ML and GNN Potential–Driven Acceleration of Thermoelectric Material Design Through Bonding Hierarchies

Ph.D. THESIS

by

HARPRIYA MINHAS



DEPARTMENT OF CHEMISTRY

INDIAN INSTITUTE OF TECHNOLOGY INDORE

January 2026

ML and GNN Potential–Driven Acceleration of Thermoelectric Material Design Through Bonding Hierarchies

A THESIS

Submitted in partial fulfillment of the

requirements for the award of the degree

of

DOCTOR OF PHILOSOPHY

by

HARPRIYA MINHAS



DEPARTMENT OF CHEMISTRY

INDIAN INSTITUTE OF TECHNOLOGY INDORE

January 2026

INDIAN INSTITUTE OF TECHNOLOGY INDORE

CANDIDATE'S DECLARATION

I hereby certify that the work which is being presented in the thesis entitled **ML and GNN Potential–Driven Acceleration of Thermoelectric Material Design Through Bonding Hierarchies** in the partial fulfillment of the requirements for the award of the degree of **DOCTOR OF PHILOSOPHY** and submitted in the **DEPARTMENT OF CHEMISTRY, Indian Institute of Technology Indore**, is an authentic record of my own work carried out during the time period from May 2021 to January 2026 under the supervision of **Prof. BISWARUP PATHAK**, Professor, Department of Chemistry, IIT Indore.

The matter presented in this thesis has not been submitted by me for the award of any other degree of this or any other institute.

Harpriya Minhas
29/01/26

Signature of the student with date
(HARPRIYA MINHAS)

This is to certify that the above statement made by the candidate is correct to the best of my/our knowledge.

29/01/26

Signature of Thesis Supervisor with date
(Prof. BISWARUP PATHAK)

HARPRIYA MINHAS has successfully given his Ph.D. Oral Examination held on 29/05/2026.

Signature of Thesis Supervisor with date
(Prof. BISWARUP PATHAK)

ACKNOWLEDGEMENTS

The completion of this Ph.D. thesis represents a demanding yet rewarding journey made possible through personal commitment and the support of numerous individuals and institutions. Looking back on these 4.5 years of growth and learning, I feel a deep sense of gratitude toward all those who contributed, directly and indirectly, to this experience.

I would like to express my sincere and foremost appreciation to my Ph.D. supervisor, ***Professor Biswarup Pathak****, whose constant guidance, academic insight, and encouragement were central to the progress of this research. Despite his many responsibilities and the size of his research group, he was always approachable and generous with his time for discussions and offering thoughtful direction. His kindness, integrity, and dedication to both research and mentorship have profoundly influenced me. I am truly thankful for the training and mentorship he provided, which shaped not only my academic development but also my personal growth. I remain deeply grateful for his unwavering support throughout my doctoral journey.*

I also extend my sincere thanks to the PSPC members, ***Professor Sanjay K. Singh*** *and* ***Professor Preeti A. Bhobe****, for their thoughtful suggestions, constructive feedback, and guidance at various stages of my Ph.D. work.*

I am grateful to the Department of Chemistry at the Indian Institute of Technology Indore for fostering a supportive academic atmosphere and providing the necessary infrastructure and resources for this research. I also acknowledge with appreciation the efforts of the administrative staff, library personnel, and technical staff for their consistent support and assistance.

I am also grateful to my academic collaborators—Dr. Subrata Kundu of CSIR–Central Electrochemical Research Institute (CECRI), Professor Yuichi Negishi of the Tokyo University of Science, and Professor Amitava Patra of the Indian Association for the Cultivation of Science.

I sincerely acknowledge the Prime Minister's Research Fellowship (PMRF), for financial support.

I would like to extend special appreciation to Dr. Sandeep Das for his guidance during the initial stages of my research, which helped establish a strong foundation for my work. I am also deeply grateful to Dr. Milan K. Jena for mentoring me like an elder brother, offering constant encouragement, and patiently guiding me through several research projects. My sincere thanks go to Rahul Kumar Sharma for always being there with support, motivation, and help whenever needed. I am thankful to all present and former group members for their camaraderie, cooperation, and for making my time in the group both productive and enriching. I truly appreciate their friendship and assistance in both technical and non-technical matters.

Finally, to my beloved family, I express my deepest gratitude to my parents, Mr. Sukhbir Singh and Mrs. Surinder Kaur, and my brother, Mr. Gurkirat Singh Minhas, for their unconditional love, unwavering encouragement, and constant belief in me, which have been the foundation of my journey. I extend special thanks to my grandmother, Mrs. Surinder Kaur, for her invaluable support throughout this journey. Their sacrifices, patience, and faith have been a continuous source of strength and motivation.

In conclusion, I gratefully acknowledge all the individuals and institutions who contributed to the successful completion of this Ph.D. thesis. Although it is not possible to name everyone who supported me along the way, their impact on my academic and personal journey has been profound and enduring.

एकं सद् विप्रा बहुधा वदन्ति (Ekam sat vipra bahudha vadanti)

Harpriya Minhas

Dedicated to
Parents and Grand Parents

Synopsis

1. Introduction

Thermoelectric (TE) materials enable direct conversion of heat into electrical energy through the Seebeck effect and provide a solid-state route for waste-heat recovery and thermal management. Their energy-conversion efficiency is quantified by the dimensionless figure of merit,

$$zT = \frac{S^2 \sigma T}{\kappa_L + \kappa_e}$$

where S is the Seebeck coefficient, σ the electrical conductivity, κ_L and κ_e the lattice and electronic thermal conductivities, respectively, and T the absolute temperature. Improving ZT requires a delicate balance between the power factor (PF = $S^2\sigma$) and lattice thermal conductivity (κ_L), as improvements in one often come at the expense of the other *[1,2]*. Advancing beyond this constraint demands a fundamental understanding of the atomic-scale factors that govern chemical bonding, crystal structure, and phonon transport in crystalline solids *[3,4]*. Such insights are critical for the rational design of materials with intrinsically low κ_L, thereby enabling the development of next-generation, high-efficiency thermoelectrics.

Semiconductors containing post-transition metal cations with stereochemically active lone pairs (SCALPs) are gaining prominence in materials research due to their remarkable thermoelectrics, and thermal data storage applications *[5,6]*. The unique characteristics of SCALP materials, including cations like Sn^{2+}, Pb^{2+}, As^{3+}, Sb^{3+}, and Bi^{3+}, induces local dipoles through non-bonding interactions, leading to strong lattice anharmonicity *[5,7]*. Such non-bonding effect introduces anharmonicity, which disrupts local symmetry, reducing thermal conductivity in thermoelectric materials. Beyond these intrinsic effects, κ_L can be further suppressed through various mechanisms such as hierarchical, complex crystal structures, rattling atoms, antibonding states near the valence architectures band edge, and Coulombic repulsion in edge- and face-sharing polyhedral *[8,9]*. In these systems,

edge-sharing polyhedral bonding brings neighboring cations into close proximity, leading to pronounced electrostatic (cation-cation) repulsion and local structural distortions, which together enhance phonon scattering and suppress κ_L.

Over the past decade, materials discovery has undergone a paradigm shift driven by the convergence of high-throughput (HT) computation, machine-learning interatomic potentials (MLIPs), and advanced machine-learning (ML) algorithms. HT-DFT workflows allow rapid screening of phase stability, electronic structure, phonon dispersion, and transport descriptors across broad chemical spaces. MLIPs including MatterSim, MACE, CHGNet, and MTP extend these capabilities by enabling large-scale molecular dynamics, anharmonic phonon renormalization, and thermal transport calculations with near-first-principles accuracy *[10]*. Concurrently, ML algorithms such as gradient boosting regressor (GBR), decision trees (DT) random forests (RF), convolutional neural networks (CNN), and graph neural networks (GNN) have demonstrated exceptional predictive power for Seebeck coefficients, electrical conductivity, thermal conductivity, and figure of merit, allowing efficient exploration and inverse design of complex chemistries. The integration of HT workflows, MLIPs, and advanced GNN models represents a transformative strategy for overcoming long-standing transport limitations and accelerating the discovery of next-generation thermoelectric materials.

In this thesis, recent advances in ultralow thermal conductivity, higher-order phonon scattering, rattling dynamics, stereochemically active lone pairs, and chemical bonding descriptors are critically examined to identify and bridge key research gaps in thermoelectric materials. Building on these insights, the work develops an integrated framework combining lattice-dynamical theory, bonding-hierarchy principles, and machine-learning–driven approaches to address complexities in predicting transport behavior. By incorporating ML models, MLIPs, and bonding descriptors that capture

anharmonicity, hybridization, and interaction strengths, this thesis aims to mitigate long-standing challenges and transform the landscape of data-driven thermoelectric materials discovery.

2. Objectives

The primary objectives of the thesis are outlined as follows:

(i) The first objective (**Chapter 2**) is to understand how dimensionality and thickness govern κ_L and thermoelectric performance in layered materials such as γ-GeSe and GeS. Building on this, the work also examines the critical role of higher-order phonon processes in shaping anharmonic heat transport, enabling the design of materials with enhanced thermoelectric efficiency.

(ii) The second objective (**Chapter 3**) is to investigate how rattling dynamics and bonding hierarchies in complex chalcotitanates systems influence anharmonicity and lattice thermal transport. Using MLIPs, this work aims to capture multi-scale vibrational behavior and identify design principles that leverage rattlers and structural heterogeneity to achieve intrinsically low κ_L and improved thermoelectric performance.

(iii) The third objective (**Chapter 4**) of the thesis is to establish a ML-driven inverse design framework for optimizing thermoelectric materials through rational dopant engineering and chemical modification. Predictive models used to identify dopants that modulate carrier concentration, electronic structure, and phonon scattering. This chapter further investigates the role of SCALPs using bonding-based descriptors to reveal how lone-pair-induced distortions, electronic asymmetry, and structural flexibility govern anharmonicity and thermal transport in pnictogen chalcogenides, ultimately enabling ML-assisted screening strategies for next-generation thermoelectric materials.

(iv) The fourth objective of this chapter (**Chapter 5**) is to resolve at atomistic precision, how SCALPs, rattling dynamics, and antibonding electronic states synergistically drive strong lattice anharmonicity and ultralow κ_L in complex and edge-sharing metal chalcogenides. By combing

MLIPs and first-principles phonon-electron analyses, this chapter quantifies bond heterogeneity, phonon softening, Grüneisen parameters, and multi-phonon scattering pathways, establishing chemically intuitive structure-property relationships for thermoelectric materials design.

(v) The fifth objective of this chapter (**Chapter 6**) is to develop a unified, bonding-aware machine-learning framework for predicting κ_L in pnictogen chalcogenides by integrating SCALP-driven asymmetry, bonding distortions, and geometric flexibility. Using a fine-tuned MatterSim and Wigner transport formulation, the chapter aims to achieve high-fidelity κ_L predictions are benchmarked against state-of-the-art MLIPs. The incorporation of quantitative bonding descriptors identifies the dominant chemical-structural factors governing κ_L and accelerates the discovery of intrinsically low-κ_L thermoelectric materials.

(vi) Finally, our objective (**Chapter 7**) is to integrate deep learning and transfer learning framework for predicting and discovering materials with ultralow κ_L in complex crystal systems. By leveraging cross-property transfer learning using graph neural network models (ALIGNN), this work aims to improve κ_L prediction accuracy under limited data conditions. Additionally, the feasibility of Transformer-based LLMs (CrystaLLM) for generating crystal structures, which are subsequently screened to accelerate the discovery of materials with intrinsically low κ_L.

3. Thesis Chapter Contribution

The contents of each chapter included in the thesis are discussed as follows.

3.1. Introduction (Chapter 1)

This chapter presents a unified overview of thermoelectrics, first-principles density functional theory (DFT), machine learning interatomic potential (MLIPs), the broader machine learning (ML) and graph neural network (GNN) framework that underpins this thesis. We begin by outlining both fundamental and advanced thermoelectric concepts, including transport physics, performance descriptors, and their relevance to solid-state and nanoscale energy-conversion devices. Emphasis is placed on strategies that

accelerate thermoelectric property prediction, particularly those leveraging chemical bonding hierarchies and structure-property relationships, along with the associated opportunities and limitations. The latter part of the chapter provides a concise introduction to the theoretical and computational tools used throughout this thesis: (a) the foundations of DFT for electronic structure and total-energy calculations; (b) electronic and lattice thermal transport formalisms essential for evaluating thermoelectric performance; and (c) ML, GNN and MLIP methodologies, including model construction, training paradigms, and their integration with quantum transport calculations.

3.2. Dimensionality, Thickness, and Higher-Order Anharmonicity (Chapter 2)

Two-dimensional chalcogenides are promising thermoelectric platforms, but achieving high ZT requires understanding structure–property evolution with dimensionality. Using first-principles calculations, we show that dimensional confinement in γ-GeSe (monolayer to quad-layer) strongly enhances phonon anharmonicity, suppresses group velocities, and weakens interlayer coupling, driving κ_L below 1 W/mK and as low as 0.15–0.17 W/mK at 900 K in bilayer and trilayer systems (Figure 1). Despite modest power-factor reduction, the drastic κ_L suppression yields exceptional ZT values (2.8-3.8), far exceeding bulk γ-GeSe. Additionally, advanced anharmonic lattice-dynamics calculations reveal that four-phonon scattering is essential for accurately describing thermal transport in GeS bilayers, where enhanced phonon scattering significantly reduces κ_L and improves high-temperature ZT. Together, these results highlight dimensional engineering and higher-order phonon processes as critical design principles for high-performance low-dimensional thermoelectrics.

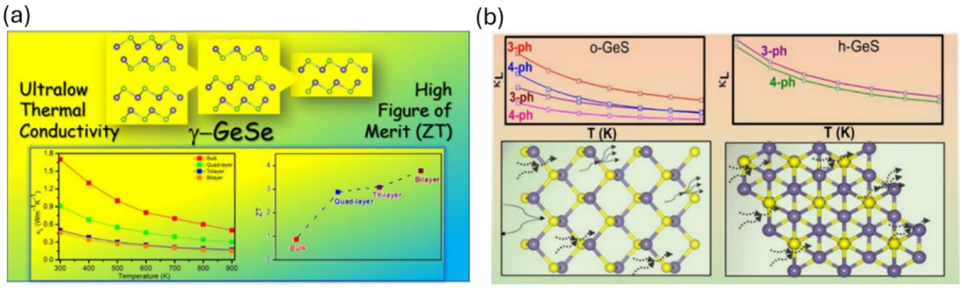


Figure 1: (a) Dimensionality and thickness dependent tuning of γ-GeSe yields low κ_L and improved thermoelectric efficiency. (b) The temperature-dependent κ_L of orthorhombic (o-GeS) and hexagonal (h-GeS) phases, highlighting the contributions from three-phonon (3-ph) and four-phonon (4-ph) scattering processes.

3.3. Rattling Ion-Induced Bonding Hierarchies in Chalcotitanates (Chapter 3)

The nature of chemical bonding in crystalline solids plays a decisive role in governing phonon transport, lattice thermal conductivity, and ultimately thermoelectric (TE) performance. In this chapter, we develop first-principles–trained MLIPs to quantitatively investigate thermal transport in chalcogenide-based materials exhibiting complex bonding environments (Figure 2). In Li–Cu–Ti chalcotitanates, the incorporation of Li induces intense rattling behavior, generating a bonding hierarchy composed of coexisting strong and weak interactions. This hierarchical bonding, reinforced by significant atomic displacement parameters for Li and Ti/Cu rattlers in $LiCu_3TiTe_4$, produces overdamped vibrational modes that efficiently scatter heat-carrying phonons. The resulting ultralow κ_L emerges directly from the coupling between rattling cations and the underlying bonding network. Our MLIP-driven framework thus provides a rigorous atomistic understanding of how rattling-induced bonding hierarchies can be exploited to enhance thermoelectric efficiency in complex chalcogenides.

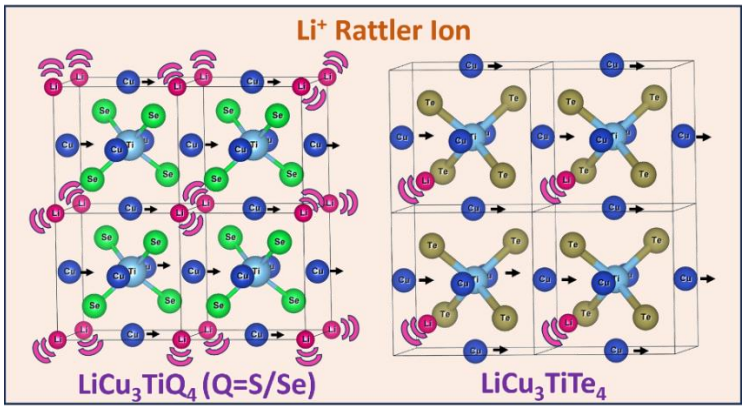


Figure 2: Schematic illustration of Li^+ rattler-ion dynamics in $LiCu_3TiQ_4$ (Q = S/Se) and $LiCu_3TiTe_4$ frameworks, showing how loosely bound Li^+ vibrations couple with the surrounding tetrahedral units and induce enhanced phonon scattering.

3.4. Interpretable ML Reveals Bonding Insights for Thermoelectrics (Chapter 4)

The integration of data-driven ML approaches with thermoelectric materials design has become a transformative strategy for accelerating materials discovery (Figure 3a). ML models trained on extensive experimental datasets spanning chalcogenides, skutterudites, and clathrates across multiple temperatures accurately predict key thermoelectric properties for hundreds of previously unexplored, doped compositions. Regression-based classification identifies high-performance chalcogenides and demonstrates the effectiveness of ML-guided dopant engineering. The chapter further introduces chemically informed bonding descriptors that capture the hidden influence of SCALPs and bonding hierarchies in pnictogen chalcogenides (Figure 3b). Incorporating these descriptors significantly improves κ_L prediction accuracy compared to conventional features and enables the identification of optimal ranges of ionicity, hybridization, polarizability, and coordination mismatch required for ultralow κ_L. The results provide both predictive capability and physical insight into lone-pair-driven thermal transport suppression.

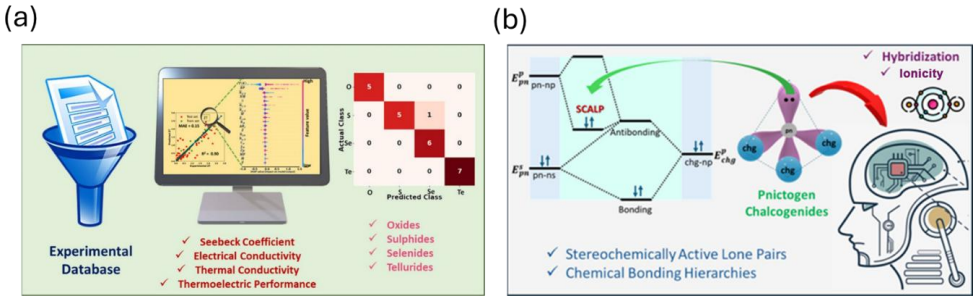


Figure 3: (a) Workflow integrating experimental thermoelectric databases with interpretable ML models for predicting electronic and thermal transport properties, including accurate classification of chalcogenide compounds. (b) Schematic illustrating the origin of SCALPs in pnictogen chalcogenides and their incorporation into bonding-based ML descriptors to capture structure–property relationships governing thermoelectric performance.

3.5. Insights into Antibonding States Drive Anharmonicity and Low κ_L (Chapter 5)

This chapter examines the synergistic roles of SCALPs, rattling dynamics, and orbital hybridization in suppressing κ_L in noncentrosymmetric pnictogen chalcogenides. Using MLIPs, thermal transport mechanisms are systematically investigated in $AAsSe_2$ (A = Li or Na) and Ba_2AsMQ_5 (M = As, Sb, Bi; Q = S, Se) systems (Figure 4a-b), where conventional ab initio approaches are computationally challenging. The analysis reveals that SCALPs, pn–pn bonding, and edge-sharing polyhedra promote antibonding electronic states near the valence band maximum, intensifying phonon scattering. A set of bonding-centric descriptors, including lone-pair geometry, ionicity, and hybridization is introduced to quantify anharmonicity and establish direct links between local bonding motifs and ultralow κ_L. This framework offers a chemically intuitive pathway for rational thermoelectric materials design.

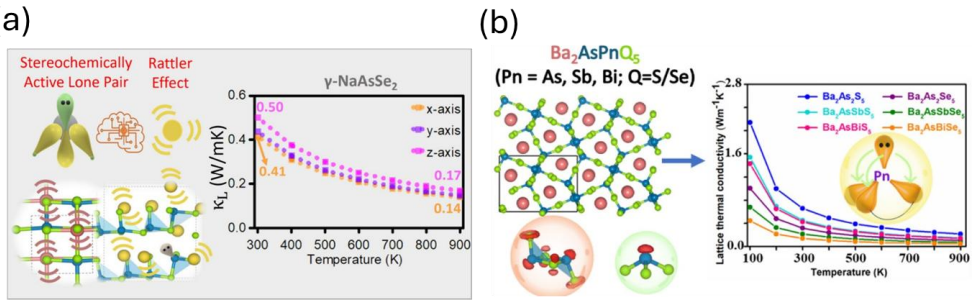


Figure 4: (a) Summary of SCALP and rattler effects in γ-$NaAsSe_2$ leading to anisotropic ultralow lattice thermal conductivity. (b) Schematic representation of the Ba_2AsPnQ_5 (Pn = As, Sb, Bi; Q = S/Se) crystal framework and its local bonding environment, highlighting the influence of pnictogen lone-pair activity on κ_L.

3.6. Scaling and Quantifying Anharmonicity using GNN Potentials (Chapter 6)

In this chapter, we develop a scalable and transferable framework for predicting κ_L in pnictogen chalcogenides using a fine-tuned universal MatterSim potential combined with the Wigner heat transport formalism (Figure 5). Benchmarking against state-of-the-art MLIPs, including MACE and CHGNet, demonstrates high-fidelity κ_L prediction at a fraction of the computational cost of first-principles calculations. The study quantitatively separates the contributions of SCALP-induced asymmetry (≈40%) and additional bonding and geometric distortions (≈60%) to κ_L suppression. By incorporating advanced bonding descriptors, this framework enables rapid, high-throughput screening of thermoelectric materials and establishes MatterSim as a robust platform for predictive thermal transport modeling.

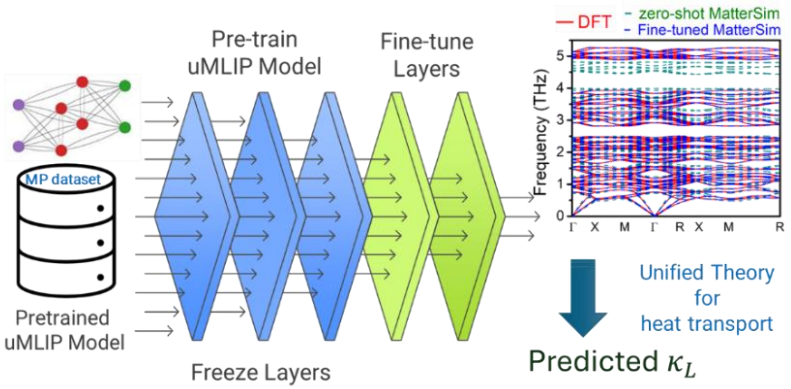


Figure 5: Workflow illustrating the fine-tuning of the universal MLIP: pretrained layers are frozen and selectively refined to reproduce DFT phonon spectra, enabling unified theory of heat transport prediction of κ_L.

3.7. Structure Generation and Deep Learning TL-strategies for Low κ_L (Chapter 7)

In this chapter, we present an integrated deep-learning and transfer-learning framework for predicting and discovering materials with ultralow lattice thermal conductivity in complex crystal systems (Figure 6). By training deep learning models such as CGCNN, GATGNN, and ALIGNN, and applying transfer learning strategies, we demonstrated the ability to overcome challenges posed by limited datasets. The chapter also demonstrates the feasibility of Transformer-based large language models (CrystaLLM) for generating novel crystal structures in CIF format. Several generated compounds are predicted to exhibit ultralow κ_L, validating the effectiveness of combining deep learning, transfer learning, and generative models for accelerated thermoelectric materials discovery.



Figure 6: Overview of the integrated transfer learning-based prediction and LLM-driven generation framework. Transfer learning improves κ_L prediction accuracy under limited data conditions, while the CrystaLLM generation engine produces novel crystal structures that are subsequently screened for ultralow predicted κ_L.

4. Conclusions

This thesis provided a comprehensive, multiscale investigation into the chemical, structural, and data-driven determinants of lattice thermal conductivity and thermoelectric performance, advancing a unified framework for the discovery of intrinsically low-κ_L materials. By integrating lattice-dynamical theory, chemical-bonding descriptors, anharmonic phonon physics, and state-of-the-art machine-learning approaches, the work systematically elucidates the mechanisms that govern heat transport in structurally diverse chalcogenide systems. **Chapter 2** established how reduced dimensionality and thickness fundamentally reshape phonon dispersion and activate higher-order scattering processes particularly four-phonon interactions in layered semiconductors such as GeX (X = S, Se). These insights highlight the central role of dimensional confinement in driving ultralow κ_L and enhancing thermoelectric efficiency. **Chapter 3** explored the interplay between rattling dynamics, bonding hierarchies, and multi-scale phonon scattering in Li–Cu–Ti chalcotitanates. Using MLIPs, the chapter revealed how local vibrational units and heterogeneous bonding landscapes induce strong anharmonicity

while maintaining favorable electronic transport, offering a transferable paradigm for designing low-κ_L frameworks. **Chapter 4** introduced a ML–driven inverse design strategy to optimize dopant chemistry and bonding environments. Through a combined analysis of SCALPs, hybridization motifs, and bonding descriptors in pnictogen chalcogenides, the chapter demonstrated how lone-pair–induced distortions and electronic asymmetry dominate thermal-transport behavior, providing predictive pathways for chemical tuning. In **Chapter 5**, deepened this understanding by uncovering how SCALPs, rattling modes, and antibonding-state–driven bond softening jointly governs lattice anharmonicity in edge-sharing metal chalcogenides. MLIP-enabled phonon-electron analyses captured phonon renormalization, broadened scattering channels, and anharmonic potentials that underlie their exceptionally low κ_L. **Chapter 6** presented a unified, bonding-aware predictive platform based on a fine-tuned MatterSim and Wigner heat-transport formulation. By quantifying SCALP strength, bonding distortions, and structural asymmetry, this framework achieved high-fidelity κ_L prediction and identified dominant bonding contributions that suppress heat transport across pn-chg chemistries. **Chapter 7** establishes a unified deep learning framework combining cross-property transfer learning and LLM-based structure generation to predict and discover materials with ultralow κ_L. ALIGNN with transfer learning delivers the highest prediction accuracy under limited data, while CrystaLLM enables the generation of novel crystal structures with promising ultralow κ_L. Together, these approaches provide an efficient pathway for accelerated materials discovery in complex lattice systems.

5. References:

1. Xiao Y., Zhao L. D. (2020), Seeking New, Highly Effective Thermoelectrics, Science, 367, 6486, 1196-1197 (DOI: 10.1126/science.aba3827)

2. Zhu T., Liu Y., Fu C., Heremans J. P., Snyder J. G., Zhao X. (2017), Compromise and Synergy in High-Efficiency Thermoelectric Materials, Adv. Mater., 29, 14, 1605884 (DOI: 10.1002/adma.201605884)

3. Snyder G. J., Toberer E. S. (2008), Complex Thermoelectric Materials, Nat. Mater., 7, 2, 105-114 (DOI: 10.1038/nmat2090)

4. Shi X. L., Zou J., Chen Z. G. (2020), Advanced Thermoelectric Design: From Materials and Structures to Devices, Chem. Rev., 120, 15, 7399-7515 (DOI:10.1021/acs.chemrev.0c00026)

5. Walsh A., Watson G. W. (2005), The Origin of the Stereochemically Active Pb(II) Lone Pair: DFT Calculations on PbO and PbS, J. Solid State Chem., 178, 5, 1422-1428. (DOI:10.1016/j.jssc.2005.01.030)

6. Wuttig M., Yamada N. (2007), Phase-Change Materials for Rewriteable Data Storage, Nat. Mater., 6, 11, 824-832. (DOI:10.1038/nmat2009)

7. Skoug E. J., Morelli D. T. (2011), Role of Lone-Pair Electrons in Producing Minimum Thermal Conductivity in Nitrogen-Group Chalcogenide Compounds, Phys. Rev. Lett., 107, 23, 235901 (DOI:10.1103/PhysRevLett.107.235901)

8. Morelli D. T., Jovovic V., Heremans J. P. (2008), Intrinsically Minimal Thermal Conductivity in Cubic I-V-VI2 Semiconductors, Phys. Rev. Lett., 101, 3, 035901 (DOI:10.1103/PhysRevLett.101.035901).

9. Walsh A., Payne D. J., Egdell R. G., Watson G. W. (2011), Stereochemistry of Post-Transition Metal Oxides: Revision of the Classical Lone Pair Model, Chem. Soc. Rev. 40, 9, 4455-4463 (DOI:10.1039/c1cs15098g)

10. Yang H., Hu C., Zhou Y., Liu X., Shi Y., Li J., Li G., Chen Z., Chen S., Zeni C., Horton M., Pinsler R., Fowler A., Zügner D., Xie T., Smith J., Sun L., Wang Q., Kong L., Liu C., Hao H., Lu Z. (2024), MatterSim: A Deep Learning Atomistic Model Across Elements, Temperatures and Pressures. (DOI: arXiv:2405.04967)

LIST OF PUBLICATIONS

Publications Included in Thesis:

1. **Minhas H.,** Das S., and Pathak B. (2022), Ultralow Thermal Conductivity and High Thermoelectric Performance of γ-GeSe: Effects of Dimensionality and Thickness, ACS Appl. Energy Mater., 5 (8), 9914-9928 (DOI: 10.1021/acsaem.2c01600) (Impact Factor: **5.6**)
2. **Minhas H.,** Das S., and Pathak B. (2023) Importance of Four Phonon Scattering Effect in Lattice Thermal Conductivity and Thermoelectrics: A Case Study, ACS Appl. Energy Mater., 6 (13), 7305-7316 (DOI: 10.1021/acsaem.3c01147) (Impact Factor: **5.6**)
3. **Minhas H.,** Jena M. K., Sharma R. K., Pathak B. (2024) Machine Learning-Driven Inverse Design and Role of Dopant for Tuning Thermoelectric Efficiency, ACS Appl. Electron. Mater., 6 (8), 5815-5826 (DOI: 10.1021/acsaelm.4c00808) (Impact Factor: **4.7**)
4. **Minhas H.,** Das S., Sharma R.K., and Pathak B. (2024) Rattling induced bonding hierarchy in Li–Cu–Ti chalcotitanates for enhanced thermoelectric efficiency: a machine learning potential approach, J. Mater. Chem. A, 12, 25988-25999 (DOI: 10.1039/D3TA07461G) (Impact Factor: **9.5**)
5. **Minhas H.,** Jena M.K., Sharma R.K., and Pathak B. (2025) Insights into Thermal Conductivity of Pnictogen Chalcogenides: Machine Learning Stereochemically Active Lone Pairs and Hybridization, Chem. Mater., 37 (1), 198-209 (DOI: 10.1021/acs.chemmater.4c02294) (Impact Factor: **7.0**)
6. **Minhas H.,** Sharma R.K., Pathak B. (2025) Exploring Combined Stereochemically Active Lone Pair and Rattling Effects in Thermoelectrics with Machine Learning Potentials, J. Phys. Chem. Lett., 16 (20), 5051-5061 (DOI: 10.1021/acs.jpclett.5c00952) (Impact Factor: **4.7**)
7. **Minhas H.,** Sharma R.K., Pathak B. (2025) Antibonding States Drive Anharmonicity and Low Thermal Conductivity in Edge-Sharing Metal Chalcogenides, ACS Appl. Mater. Interfaces, 17 (44), 60669-60681 (DOI: 10.1021/acsami.5c17211) (Impact Factor: **8.2**)

8. **Minhas H.,** Sharma R. K., Pathak B. (2026) Unravelling Lone Pair Induced Bonding Effects on Thermal Conductivity in Metal Chalcogenides using Machine Learning Potentials, J. Mater. Chem. A (DOI: 10.1039/D5TA08916F) (Impact Factor: **9.5**)
9. **Minhas H.,** Sharma R. K., Pathak B. Cross-Property Deep Transfer Learning Framework for Lattice Thermal Conductivity (Manuscript under preparation).

Publications Excluding Thesis:

10. **Minhas H.,** Majumdar A., and Pathak B. (2023) Predicting the Thermal Conductivity of 2D and 3D Group 13 Nitrides using Machine Learning Potential: The Special Case of AlN, ACS Appl. Energy Mater., 6 (19), 9851-9863 (DOI: 10.1021/acsaem.3c01161) (Impact Factor: **5.6**)
11. **Minhas H.,** Majumdar A., and Pathak B. (2024) Comparison of lattice thermal conductivity using ab-initio DFT, machine learning interatomic potentials, and temperature dependent effective potential: a case study of hexagonal BN and BP bilayer, J. Phys.: Condens. Matter, 36 (39), 395701 (DOI: 10.1088/1361-648X/ad5b42) (Impact Factor: **2.6**)
12. Sharma R.K., **Minhas H.**, Pathak B., (2024) Investigating the Metastability-Triggered Reactivity of Pt7,8 Clusters on Graphene: Unraveling Statistical Ensemble Representation for ORR in Gas and Implicit Solvent Phases, J. Phys. Chem. C, 128 (18), 7504–7517 (DOI: 10.1021/acs.jpcc.4c00376) (Impact Factor: **3.2**)
13. Devi A., **Minhas H.**, Sahoo L., Gratious S., Das A., Mandal S., Pathak B., Patra A. (2024) Insights of the efficient hydrogen evolution reaction performance in bimetallic Au4Cu2 nanoclusters, Nanoscale, 16, 1758-1769 (DOI: 10.1039/D3NR05445D) (Impact Factor: **5.1**)
14. Sharma R.K., **Minhas H.**, Pathak B., (2024) High-throughput screening of bifunctional catalysts for oxygen evolution/reduction reaction at the subnanometer regime, Nanoscale, 16, 21340-21350 (DOI: 10.1039/D4NR02787F) (Impact Factor: **5.1**)

15. Sharma R.K., Jena M.K., **Minhas H.**, Pathak B., (2024) Machine-Learning-Assisted Screening of Nanocluster Electrocatalysts: Mapping and Reshaping the Activity Volcano for the Oxygen Reduction Reaction, ACS Appl. Mater. Interfaces, 16 (46), 63589-63601 (DOI: 10.1021/acsami.4c14076) (Impact Factor: **8.2**)
16. Nagappan S., **Minhas H.**, Gurusamy H., Karmakar A., Ravichandran S., Pathak B., Kundu S. (2024) Unraveling the Synergistic Role of Sm3+ Doped NiFe-LDH as High-Performance Electrocatalysts for Improved Anion Exchange Membrane and Water Splitting Applications, Small Methods, 2401655 (DOI: 10.1002/smtd.202401655) (Impact Factor: **9.1**)
17. Nagappan S., Minhas H., Urkude R.R., Pathak B., Kundu S. (2025) Harnessing the Synergistic Effects of Ir Co-Decorated NiMn-LDH: a Multi-Analytical Approach to Boost Electrocatalytic Overall Water Splitting Activity in Alkaline Condition, Small, 21 (14), 2500081 (DOI: 10.1002/smll.202500081) (Impact Factor: **12.1**)
18. Sharma R.K., **Minhas H.**, Pathak B., (2025) Machine Learning-Guided Discovery of Alloy Nanoclusters: Steering Morphology-Based Activity and Selectivity Relationships in Bifunctional Electrocatalysts, ACS Appl. Mater. Interfaces, 17 (28), 40488–40498 (DOI: 10.1021/acsami.5c07198) (Impact Factor: **8.2**)
19. Roy S.S., **Minhas H.**, Lakshminarayanan P., Kirti KM, Sahu S., Pathak B., and Kundu S. (2025) Vertically Grown Face-to-Face Nano-assembly of In(OH)3 and NiFe-LDH Enables Interfacial Charge Separation for Enhanced Alkaline and Seawater Electrolysis, Adv. Funct. Mater., e24906 (DOI: 10.1002/adfm.202524906) (Impact Factor: **19**)
20. Tomihari S.,* Kamiyama M.,* **Minhas H.**,* Kawawaki T., Takemae K., Shingyouchi Y., Chen Z., Pathak B., Negishi Y. (2026) Exposure of Active Metal Sites on Cu14 Nanoclusters for Highly Selective Electrocatalytic Nitrate Reduction ACS Catal., 15, 24, 20853–20863 [* all authors have equally contributed] (Impact Factor: **13.1**)

Table of Contents

1. List of Figures and Schemes xxxi

2. List of Tables lxix

3. Acronyms lxxv

Chapter 1: Introduction

1.1. Introduction to Thermoelectric Materials and Advanced Design Strategies 3

1.2. "Thermoelectric Problem": Decoupling the Conflicting Variables 5

1.3. Historical Evolution of Thermoelectric Materials 6

1.4. Phonon Engineering Strategies for Achieving Ultralow Lattice Thermal Conductivity 7

1.4.1. Dimensionality Reduction 8

1.4.2. Intrinsic Rattling Effect 9

1.4.3. Stereochemically Active Lone Pairs 9

1.4.4. Bonding Heterogeneity 11

1.4.5. Higher-Order Phonon Scattering 11

1.5. Electronic Structure Engineering for Enhanced Power Factor 12

1.5.1 Band Convergence 13

1.6. Chemical Bonding Descriptors for Thermoelectric Design 14

1.6.1. Bonding Descriptors 15

1.6.2. Electronic Descriptors 16

1.6.3. Orbital Energy Descriptors 17

1.6.4. Structural Descriptors 17

1.7. Theoretical Methodology 19

1.7.1. Schrödinger Equation for Many-Body Problem 20

1.7.2. Born-Oppenheimer Approximation 21

1.7.3. Density Functional Theory 22

1.7.3.1. The Hohenberg-Kohn Theorem 24

1.7.3.2. Kohn-Sham Formalism 26

1.7.4. Exchange-Correlation Functional 28

1.6.4.1. Local Density Approximation (LDA) 28

1.7.4.2. Generalized Gradient Approximation (GGA) 29
1.7.4.3. van der Waals Density Functional (vdw-DF) 31
1.7.5. Projector Augmented Wave (PAW) Method 32
1.7.6. Electronic Structure of Periodic Solids 33
1.7.7. Bloch's Theorem 34
1.7.8. k-Points 35
1.7.9. Basis Sets 36
1.7.10. Boltzmann Transport Equation (BTE) 37
1.7.11. Relaxation Time Approximations 38
1.7.12. Scattering Rates 39
1.7.12.1. Acoustic Deformation Potential (ADP) Scattering 40
1.7.12.2. Ionized Impurity (IMP) Scattering 40
1.7.12.3. Polar Optical Phonon (POP) Scattering 41
1.7.12.4. Piezoelectric (PIE) Scattering 41
1.7.13. Carrier Transport Model: Solution to the BTE 41
1.7.13.1. Seebeck Coefficient 42
1.7.13.2. Carrier Mobility 43
1.7.13.3. Electrical Conductivity 43
1.8. Quantum Transport Theory 43
1.8.1. Lattice Vibrations and Phonons 43
1.8.2. Phonon Dispersions 44
1.8.3. Force Constants and Phonon Transport 45
1.9. Machine Learning 46
1.9.1. Machine Learning Interatomic Potentials (MLIPs) 46
1.9.1.1. Moment Tensor Potential (MTP) 48
1.9.2. Universal Machine Learning Interatomic Potentials (uMLIPs) 52
1.9.2.1. MatterSim 53
1.9.2.2. MACE 54
1.9.2.3. CHGNet 54
1.10. Supervised Learning 55
1.10.1. Regression 55

1.10.2. Classification 55
1.10.3. Unsupervised Learning 55
1.10.4. Dataset 55
1.10.4.1. Training Dataset 56
1.10.4.2. Test Dataset 56
1.10.4.3. Validation Set 56
1.10.5. Feature Selection and Correlation Analysis 56
1.10.5.1. Feature Engineering 56
1.10.5.2. Pearson Correlation Coefficient (PCC) 56
1.10.5.3. Spearman Rank Correlation Coefficient (SCC) 57
1.10.5.4. Mutual Information (MI) 58
1.10.6. Hyperparameter Tunning 58
1.10.6.1. Grid Search 58
1.10.6.2. Randomized Search 59
1.10.7. Machine Learning Algorithms 59
1.10.7.1. Linear Regression 59
1.10.7.2. Logistic Regression 59
1.10.7.3. K-Nearest Neighbours 60
1.10.7.4. Kernel Ridge Regression 60
1.10.7.5. Support Vector Machine 60
1.10.7.6. Random Forest 61
1.10.7.7. Adaptive Boosting 61
1.10.7.8. Extreme Gradient Boosting 61
1.10.7.9. Gaussian Process Regression 61
1.10.7.10. Decision Tree 61
1.10.7.11. Extra Tree Regression 62
1.11. Deep Learning Algorithms 62
1.11.1. Convolutional Graph Neural Network (CGCNN) 62
1.11.2. Graph Attention Neural Network (GATGNN) 63
1.11.3. Atomistic Line Graph Neural Network (ALIGNN) 64
1.12. Model Evaluation Metrics 65

1.12.1. Coefficient of Determination 65
1.12.2. Mean Absolute Error (MAE) 65
1.12.3. Mean Squared Error (MSE) 65
1.12.4. Root Mean Squared Error (RMSE) 65
1.12.5. Confusion Matrix 65
1.12.6. Accuracy 66
1.12.7. Precision 66
1.12.8. Recall (Sensitivity) 66
1.12.9. F1 Score 67
1.12.10. Cross-Validation 67
1.13. Feature Importance 67
1.13.1. Permutation Feature Importance 68
1.13.2. Machine Learning Explainability 68
1.13.3. Shapley Additive explanation (SHAP) 69
1.14. References 70
Chapter 2: Dimensionality, Thickness, and Higher-Order Anharmonicity
Section: A
2.1. Introduction 91
2.2. Model and Computational Details 93
2.3. Results and Discussion 95
2.3.1. Structure and Stability 95
2.3.2. Phonon Transport Properties 98
2.3.3. Electronic Transport Properties 102
2.3.4. Thermal Properties 105
2.3.5. Thermoelectric Properties 111
2.3.5.1. Seebeck Coefficient 111
2.3.5.2. Electrical Conductivity 114
2.3.5.3. Power Factor and Figure of Merit 116
2.4. Summary 119
Section B

2.5. A Case Study of Importance of 3- and 4-phonon Interactions 120
2.6. Modelling and Computational Details 121
2.7. Results and Discussion 123
2.7.1. Structural and Electronic Properties 123
2.7.2. Thermal Properties 130
2.7.3. Thermoelectric Properties 140
2.7.3.1. Seebeck Coefficient 141
2.7.3.2. Electrical Conductivity 143
2.7.3.3. Power Factor and Figure of Merit 146
2.8. Summary 150
2.9. References 150
Chapter 3: Rattling Ion-Induced Bonding Hierarchies in Chalcotitanates
3.1. Introduction 165
3.2. Model and Computational Methodology 167
3.3. Results and Discussion 170
3.3.1. Structure and Stability 170
3.3.2. Training and Testing of Moment Tensor Potentials (MTPs) 174
3.3.3. Phonon Transport Properties 175
3.3.4. Thermal Properties 179
3.3.5. Electronic Properties 183
3.3.6. Thermoelectric Properties 189
3.4. Summary 193
3.5. References 194
Chapter 4: Interpretable ML Reveals Bonding Insights for Thermoelectrics
Section: A
4.1. Introduction 205
4.2. Feature Engineering and Selection 207
4.3. Results and Discussion 212
4.3.1. Machine Learning Explainability 216

4.3.2. Machine Learning Classification 228
4.4. Summary 235
Section-B
4.5. Introduction 236
4.6. Dataset Design for Machine Learning 238
4.7. Descriptor Designing 240
4.7.1. Bonding Descriptors 241
4.7.2. Structural Descriptors 243
4.7.3. Orbital Energy Descriptors 243
4.7.4. Electronic Descriptors 244
4.8. Results and Discussion 252
4.8.1 Machine Learning Study 252
4.8.2. Prediction of Unknown Materials 262
4.8.3. Effects of Descriptors on Thermal Conductivity (κ_L) 267
4.8.4. $Bi_{14}Te_{13}S_8$, $InSbS_3$, and RbK_2BiSe_5: A Case Study 270
4.9. Summary 272
4.10. References 273
Chapter 5: Insights into Antibonding States Drive Anharmonicity and Low κ_L
5.1. Introduction 285
5.2. Computational Details 287
5.2.1. MTP Training 288
5.2.2. Thermal and Electronic Transport Properties 288
5.3. Results and Discussion 289
5.3.1. SCALP and Anharmonicity in alkali-metal chalcoarsenates 289
5.3.2. Machine Learning Potentials 292
5.3.3. Thermal Transport 293
5.3.4. Real Space Identification of SCALPs 300
5.3.5 Electronic Transport Properties 302
5.3.6. Thermoelectric Properties 307
5.4. Summary 309

Section-B

5.5. Introduction 309

5.6. Computational Details 311

5.6.1. Construction of Machine Learning Interatomic Potentials 312

5.6.2. Calculating Lattice and Electronic Transport Properties 312

5.7. Results and Discussion 313

5.7.1. Crystal Structure derived Anharmonicity 313

5.7.2. Machine Learning Interatomic Potentials 315

5.7.3. Anharmonic Phonon Dispersion 317

5.7.4. Engineering Band Valleys through Orbital Design 322

5.7.5. Capturing Chemical Bonding Heterogeneities 326

5.7.6. Bonding Descriptors as Fingerprint for Anharmonicity 329

5.7.7. Correlation Analysis of Bonding Descriptors and κ_L 332

5.7.8. Carrier Transport Mechanisms and Scattering Effects in Thermoelectric Materials 333

5.8. Summary 343

5.9. References 344

Chapter 6: Scaling and Quantifying Anharmonicity using GNN Potentials

6.1. Introduction 359

6.2. Computational Details 361

6.2.1. Density Functional Theory (DFT) Calculations 361

6.2.2. Fine-Tuning of MatterSim 361

6.2.3. Lattice Thermal Conductivity Calculations 362

6.3. Results and Discussion 362

6.3.1. High throughput screening of Pnictogen-Chalcogenide 362

6.3.2. Fine-Tuning Universal MatterSim for Accurate Interatomic Force Constants 369

6.3.3. Wigner formulation of heat transport for κ_L 371

6.3.4. Validation of uMLIP Predicted κ_L 374

6.3.5. Structural Fingerprinting of SCALPs 376

6.3.6. Quantifying SCALP and Bonding Hierarchies 378
6.3.7. Cs_3SbS_3, $Ba_3Sb_2Se_7$, and Li_3BiS_3: a case study 382
6.4. Summary 385
6.5. References 386
Chapter 7: Structure Generation and Deep Learning Transfer Learning strategies for Low κ_L
7.1. Introduction 397
7.2. Dataset Construction and Processing 399
7.3. Results and Discussion 401
7.3.1. Scratch Model Training 401
7.3.2. Fine-tuned Strategies using Transfer Learning 403
7.3.3. Transfer Learning Formulation 405
7.3.4.1. Fine Tuning Strategies 405
7.3.4. Dataset Description and Pretrained Models 407
7.3.4.1. Effect of Dataset Size 409
7.3.4.2. Energy vs Electronic vs Mechanical Properties 410
7.3.4.3. Same-Property vs Cross-Property Transfer 411
7.3.4.4. Role of Fine-Tuning Strategy 411
7.3.5. Crystal Structure Generation Using CrystaLLM 412
7.3.5.1. Validity of Generated Structures 414
7.3.5.2. Uniqueness and Novelty of Generated Structures 414
7.4. Summary 417
7.5. References 417
Chapter 8: Future Directions
8.1. Future Direction 425

List of Figures and Schemes

Chapter 1		Page No.
Figure 1.1	Schematic illustration of thermoelectric power generation via the Seebeck effect. A temperature gradient established between a high-temperature heat source (100–600 °C) and a low-temperature heat sink (30–100 °C) drives charge carrier transport in coupled p-type and n-type semiconductor thermoelectric legs, generating an electrical current.	3
Figure 1.2	Schematic illustration of a thermoelectric (TE) module for (a) Seebeck effect and (b) Peltier effect for power generation and refrigeration, respectively. Figure reprinted with permission from Ref. 5. Copyrights 2010, Springer Nature.	4
Figure 1.3	Schematic diagram of thermoelectric properties vs. carrier concentration (n_c) reflecting the intrinsic trade-off between TE parameters. Figure reprinted with permission from Ref. 6. Copyrights 2012, Elsevier.	5
Figure 1.4	Mechanisms for suppressing lattice thermal conductivity (κ_L). Schematic overview of bonding- and defect-driven phonon scattering mechanisms, including lone-pair–induced anharmonicity, lattice softening, antibonding electronic states, reduced dimensionality, and multidimensional defects such as off-center dopants and rattler ions. Their synergistic interplay disrupts phonon transport across length scales, leading to intrinsically low κ_L.	8

Figure 1.5 Schematics of energy level diagram illustrating stereochemically active lone pairs (SCALP) in pnictogen (Pn) chalcogenide (Chg) materials. Figure reprinted with permission from Ref. 46. Copyrights 2025, American Chemical Society. 10

Figure 1.6 Schematic illustration of 3-phonon and 4-phonon scattering processes, highlighting extrinsic phonon scattering induced by grain boundaries, atomic defects, vacancies, and nanoparticles. The combined action of intrinsic anharmonic phonon–phonon interactions and defect-mediated scattering across multiple length scales effectively suppresses κ_L. 12

Figure 1.7 Band-structure engineering strategies for enhancing thermoelectric performance. Schematic representation of electronic band convergence and band sharpening, illustrating how flat and sharp band features increase the effective mass and density of states near the Fermi level, thereby enhancing the Seebeck coefficient without severely compromising electrical conductivity. Figure reprinted with permission from Ref. 48. Copyrights 2025, American Chemical Society. 14

Figure 1.8 Schematic illustration of chemically motivated descriptors governing thermal transport in pnictogen chalcogenides. (a) Bonding descriptors quantify the extent of orbital overlap and bond strength anisotropy. (b) Electronic descriptors capture charge localization, ionicity, and stereochemically active lone-pair formation. (c) 15

Orbital-energy descriptors describe s–p hybridization and the emergence of antibonding states near the Fermi level (SCALP regime). (d) Structural descriptors reflect lone-pair–induced distortions and bonding asymmetry, which collectively enhance phonon anharmonicity and suppress lattice thermal conductivity. Figure reprinted with permission from Ref. 46. Copyrights 2025, American Chemical Society.

Figure 1.9 Comparative illustration of many body and DFT perspectives. 23

Figure 1.10 Illustration of interacting and non-interacting many-electron systems having the same ground-state electron density. 26

Figure 1.11 Flow chart of the self-consistent loop for the solution of Kohn-Sham equations. 27

Figure 1.12 Accuracy–cost landscape of machine-learning interatomic potentials including GAP, MTP, NNP, SNAP, and qSNAP. Model hyperparameters govern the trade-off between test error and computational efficiency. Figure reprinted with permission from Ref. 105. Copyrights 2020, American Chemical Society. 48

Figure 1.13 Schematics for data curation and training of moment tensor potentials (MTPs) using the polynomial regression and iterative optimization to define the local chemical environment representing potential energy surface. Figure reprinted with permission from Ref. 45. Copyrights 2025, American Chemical Society. 49

Figure 1.14 Schematic of the MatterSim framework illustrating large-scale pretraining and fine-tuning of graph neural network–based machine-learning interatomic potentials (e.g., CHGNet, MACE). Atomic structures are encoded as graphs and processed through message-passing layers to predict total energies, atomic forces, and stress tensors, enabling applications such as molecular dynamics, structure relaxation, phonon calculations, elastic properties, and phase stability analysis. 53

Figure 1.15 Schematic illustration of Convolutional Graph Neural Network (CGCNN), Atomistic Line Graph Neural Network (ALIGNN) and Graph Attention Neural Network (GATGNN), architecture. 63

Figure 1.16 Confusion matrix showing the true positives, true negatives, false positives, and false negatives. TP: True Positive, TN: True Negative, FN: False Negative, FP: False Positive 66

Figure 1.19 Schematic diagram showing K-fold (K=10) cross-validation. 67

Figure 1.20 Schematic illustration of the black box model and explainable AI interpreting the decision behind ML prediction. 69

Chapter 2

Figure 2.1 Optimized structures of γ-GeSe (a) bulk – top view, (b) bulk – side view, (c) quad-layer, (d) tri-layer, (e) bilayer, and (f) monolayer. 93

Figure 2.2 Electron localization function (isosurface value is 0.03 e $Å^{-3}$) of γ-GeSe (a) bulk, (b) quad-layer, (c) trilayer, (d) bilayer, and (e) monolayer. The ELF 96

plots have been prepared by considering a (100) plane cross section for all of the models.

Figure 2.3 Phonon band structures in THz of γ-GeSe (a) bulk, (b) quad-layer, (c) tri-layer, (d) bilayer and (e) monolayer. 99

Figure 2.4 Phonon density of states for γ-GeSe (a) bulk, (b) quad-layer, (c) tri-layer, and (d) bilayer. 101

Figure 2.5 Electronic band structures of γ-GeSe (a) bulk, (b) quad-layer, and (c) tri-layer and (d) bilayer using HSE06 functional. 103

Figure 2.6 Electronic projected density of states (PDOS) of γ-GeSe (a) bulk, (b) quad-layer, (c) tri-layer, and (d) bilayer structures using HSE06 functional. 104

Figure 2.7 (a) Lattice thermal conductivity (κ_L) vs temperature, (b) electronic thermal conductivity (κ_e) vs temperature, and (c) normalized cumulative lattice thermal conductivity as a function of frequency for all studied systems of γ-GeSe at 300 K. 106

Figure 2.8 Weighted phase space (three phonon process), isotopic scattering rate (ISR), anharmonic scattering rate (ASR), anharmonic emission scattering rate (ASR^-) and anharmonic absorption scattering rate (ASR^+) for (a) bulk, (b) quadlayer, (c) trilayer, and (d) bilayer systems. 108

Figure 2.9 Grüneisen parameter as a function of angular frequency for γ-GeSe bilayer at 300 K for (a) bulk, (b) quadlayer, (c) trilayer, and (d) bilayer systems. 109

Figure 2.10 Seebeck coefficients of the γ-GeSe (a) bulk, (b) quad-layer, (c) tri-layer, and (d) bilayer structures 113

as a function of carrier concentration at temperature range of 300-900 K.

Figure 2.11 Electrical conductivity of the γ-GeSe (a) bulk, (b) quad-layer, (c) tri-layer, and (d) bilayer structures as a function of carrier concentration at temperature range of 300-900 K. 115

Figure 2.12 Electronic thermal conductivity (κ_e) of the γ-GeSe (a) bulk, (b) quad-layer, (c) tri-layer, and (d) bilayer structures as a function of carrier concentration at the temperature range of 300-900 K. 116

Figure 2.13 Power factor (PF) of the γ-GeSe (a) bulk, (b) quad-layer, (c) tri-layer, and (d) bilayer structures as a function of carrier concentration at temperature range of 300-900 K. 117

Figure 2.14 Thermoelectric figure of merit (ZT) of the γ-GeSe (a) bulk, (b) quad-layer, (c) tri-layer, and (d) bilayer structures as a function of carrier concentration at temperature range of 300-900 K. 117

Section B

Figure 2.15 Optimized structures of (a) bulk top view o-GeS, (b) bulk-side view o-GeS along x-axis, (c) bulk-side view o-GeS along y-axis, (d) bulk top view h-GeS (e) bulk-side view h-GeS. 122

Figure 2.16 Electron localization function of GeS bilayer systems, (a) o-GeS top view of (001) plane at 0.77 e $Å^{-3}$ isosurface, (b) h-GeS top view of (001) plane at 0.54 e $Å^{-3}$ isosurface, (c) o-GeS side view of (100) plane at 0.77 e $Å^{-3}$ isosurface, and (d) h-GeS side view of (100) plane at 0.54 e $Å^{-3}$ isosurface. 125

Figure 2.17 Phonon band structures of (a) o-GeS bulk, (b) h-GeS bulk, (c) o-GeS bilayer, and (d) h-GeS bilayer systems. 127

Figure 2.18 Electronic band structures of GeS systems (a) o-GeS bulk and (b) h-GeS bulk (c) o-GeS bilayer and (d) h-GeS bilayer, using the HSE06 functional. 128

Figure 2.19 Partial density of states for considered GeS systems, (a) o-GeS bulk, (b) h-GeS bulk, (c) o-GeS bilayer, and (d) h-GeS bilayer. 129

Figure 2.20 Lattice thermal conductivity of (a) o-GeS and h-GeS bulk considering 3-phonon scattering, and (b) o-GeS and h-GeS bilayer considering 3-phonon and 4-phonon scattering at different temperatures. 130

Figure 2.21 Boundary and isotopic scattering rates of the considered GeS systems, (a) o-GeS bulk, (b) h-GeS bulk, (c) o-GeS bilayer (3 phonon), (d) o-GeS bilayer (3+4 phonon), (e) h-GeS bilayer (3 phonon), and (f) o-GeS bilayer (3+4 phonon) with respect to frequency (THz) at 300K. 134

Figure 2.22 Anharmonic scattering rates of the GeS systems (a) o-GeS bulk (3-phonon), (b) h-GeS bulk (3-phonon), (c) o-GeS bilayer (3-phonon), (d) o-GeS bilayer (3+4 phonon), (e) h-GeS bilayer (3-phonon) and (f) h-GeS bilayer (3+4 phonon) at 300 K. 135

Figure 2.23 Weighted phase space of the GeS systems (a) o-GeS bulk (3 phonon), (b) h-GeS bulk (3 phonon), (c) o-GeS bilayer (3 phonon), (d) o-GeS bilayer (3+4 phonon), (e) h-GeS bilayer (3 phonon) and (f) h-GeS bilayer (3+4 phonon) with respect to frequency (THz) at 300 K. 136

Figure 2.24 Umklapp and Normal scattering of the GeS systems (a) o-GeS bilayer (3+4 phonon) and (b) h-GeS bilayer (3+4 phonon) with respect to frequency (THz) at 300K. 137

Figure 2.25 Grüneisen parameter (γ) of the GeS systems (a) o-GeS bulk (3 phonon), (b) h-GeS bulk (3 phonon), (c) o-GeS bilayer (3 phonon), (d) o-GeS bilayer (3+4 phonon), (e) h-GeS bilayer (3 phonon), and (f) h-GeS bilayer (3+4 phonon) with respect to frequency (THz) at 300K. 138

Figure 2.26 Scattering Rates of (a) o-GeS bulk, (b) h-GeS bulk, (c) o-GeS bilayer, and (d) h-GeS bilayer: These represent the variation of Polar Optical Phonon (POP) Scattering, Ionized Impurity Scattering (IMP), and Acoustic Deformation Potential Scattering (ADP) with Carrier Concentrations at 300 K and 900 K for n-Type and p-Type Conduction. 141

Figure 2.27 Seebeck coefficients of (a) o-GeS bulk along x-axis, (b) o-GeS bulk along y-axis, (c) o-GeS bulk along z-axis, (d) h-GeS bulk along x and y axis, (e) h-GeS bulk along z axis, (f) o-GeS bilayer along x-axis, (g) o-GeS bilayer along y-axis and (h) h-GeS bilayer along x and y axis as a function of carrier concentration at different temperature using AMSET. 142

Figure 2.28 Electronic thermal conductivity (κ_e) of (a) o-GeS bulk along x-axis, (b) o-GeS bulk along y-axis, (c) o-GeS bulk along z-axis, (d) h-GeS bulk along x and y axis, (e) h-GeS bulk along z axis, (f) o-GeS bilayer along x-axis, (g) o-GeS bilayer along y-axis 144

and (h) h-GeS bilayer along x and y axis as a function of carrier concentration using AMSET.

Figure 2.29 Electrical conductivity of (a) o-GeS bulk along x-axis, (b) o-GeS bulk along y-axis, (c) o-GeS bulk along z-axis, (d) h-GeS bulk along x and y axis, (e) h-GeS bulk along z axis, (f) o-GeS bilayer along x-axis, (g) o-GeS bilayer along y-axis and (h) h-GeS bilayer along x and y axis as a function of carrier concentration at different temperature using AMSET. 145

Figure 2.30 ZT of the considered GeS bulk systems, (a) o-GeS bulk along x-axis, (b) o-GeS bulk along y-axis, (c) o-GeS bulk along z-axis, (d) o-GeS bulk along x and y-axis, and (e) h-GeS bulk along z-axis (3-phonon) using AMSET. 148

Figure 2.31 ZT of the considered GeS systems, (a) o-GeS bilayer along x-axis (3-phonon), (b) o-GeS bilayer along x-axis (3+4 phonon), (c) o-GeS bilayer along y-axis (3-phonon), (d) o-GeS bilayer along y-axis (3+4 phonon), (e) h-GeS bilayer along x and y-axis (3-phonon), and (f) h-GeS bilayer along x and y-axis (3+4 phonon), as a function of carrier concentration at different temperatures using AMSET. 149

Chapter 3

Figure 3.1 The conventional unit cell of cubic lithium copper chalcotitanates (a) $LiCu_3TiS_4$, (b) $LiCu_3TiSe_4$, and (c) $LiCu_3TiTe_4$ where $LiCu_3TiS_4$ and $LiCu_3TiSe_4$ adopt an isostructural cubic 3D stuffed diamond structure, while $LiCu_3TiTe_4$ exhibits a closer resemblance to a sulvanite structure. (d-f) The 168

electron localization function (ELF) visualized at an iso-surface value of 0.9 eVÅ^{-3} revealing the presence of lone pairs around S/Se/Te atoms. (g-i) The atomic displacement parameters (ADP) for $LiCu_3TiQ_4$ across the equilibrium positions.

Figure 3.2 Convergence of the lattice thermal conductivity of $LiCu_3TiQ_4$ (Q = S, Se, and Te) against q-point mesh at 300 K. Lattice thermal conductivities are found to converge at 17 × 17 × 17 q-point mesh. 170

Figure 3.3 The total electronic charge distribution contour plots for (a) $LiCu_3TiS_4$, (b) $LiCu_3TiSe_4$ along (1 -1 0) plane, and (c) $LiCu_3TiTe_4$ along (-1 -1 0) plane. 172

Figure 3.4 The position of Li in (a) $LiCu_3TiS_4$, (b) $LiCu_3TiSe_4$, and (c) $LiCu_3TiTe_4$. 173

Figure 3.5 The schematic illustrates the development of moment tensor potentials (MTPs), incorporating the local environment to generate a potential energy surface. The trained MTPs employed for the prediction of interatomic force constants, phonon dispersion relations, and lattice thermal conductivity. 174

Figure 3.6 Scatter plots illustrating the comparison between predicted vs DFT calculated **(A)** energy parity plots and **(B)** force parity plots for $LiCu_3TiQ_4$ (Q = S, Se, and Te) systems along with their respective test and train root mean square error (RMSE) and mean absolute error (MAE) scores in meV for energies and meV/Å for forces. 175

Figure 3.7 The phonon dispersion and projected phonon density of states for (a) $LiCu_3TiS_4$, (b) $LiCu_3TiSe_4$, (c) $LiCu_3TiTe_4$ across the high symmetry points in 177

the first Brillouin zone. (d-f) Group velocity (km/sec) and (g-i) mode average Grüneisen parameter (γ) for the considered systems.

Figure 3.8 The phonon dispersion relations in $LiCu_3TiTe_4$, reflect the avoided crossing between LA acoustic and optical branch at 1.6 THz of frequency. 178

Figure 3.9 The total lattice thermal conductivity ($\kappa_L = \kappa_L^p + \kappa_L^c$) of $LiCu_3TiQ_4$ (where Q = S, Se, or Te) as a function of temperature (K). 181

Figure 3.10 The calculated total anharmonic scattering (TAS) rates of (a) $LiCu_3TiS_4$, (b) $LiCu_3TiSe_4$, and (c) $LiCu_3TiTe_4$ at 300 K and 900 K along with absorption and emission scattering channels at 300 K. The weighted phase space (WP_3) as a function of frequency (THz) for (d) $LiCu_3TiS_4$, (e) $LiCu_3TiSe_4$, and (f) $LiCu_3TiTe_4$ at 300 K with absorption (P_3^+) and emission (P_3^-) weighted phase space. 182

Figure 3.11 Boundary and isotopic scattering rates of (a) $LiCu_3TiS_4$, (b) $LiCu_3TiSe_4$, (c) $LiCu_3TiTe_4$ with respect to frequency (THz) at 300K. 184

Figure 3.12 The electronic band structures along with the projected density of states (PDOS) calculated within HSE03 functional for (a) $LiCu_3TiS_4$, (b) $LiCu_3TiSe_4$, and (c) $LiCu_3TiTe_4$ with their respective band gaps (Eg) and the pink arrow defining the direct/indirect path along the Brillouin zone points. 185

Figure 3.13 Scattering rates as a function of energy of n-type for (a, d) $LiCu_3TiS_4$, (b, e) $LiCu_3TiSe_4$, and (c, f) $LiCu_3TiTe_4$. These represent their scattering 187

mechanisms including polar optical phonon (POP), ionized impurity (IMP), and acoustic deformation potential (ADP) scattering at carrier concentrations of 10^{20} cm^{-3} at 300 K and 900 K for n-type conduction.

Figure 3.14 Scattering rates as a function of energy of p-type for (a, d) $LiCu_3TiS_4$, (b, e) $LiCu_3TiSe_4$, and (c, f) $LiCu_3TiTe_4$. These represent their scattering mechanisms including polar optical phonon (POP), ionized impurity (IMP), and acoustic deformation potential (ADP) scattering at carrier concentrations of 10^{20} cm^{-3} at 300 K and 900 K for p-type conduction. 188

Figure 3.15 Mobility (cm^2/Vs) as a function of temperature for n- and p-type doping of (a, d) $LiCu_3TiS_4$, (b, e) $LiCu_3TiSe_4$, and (c, f) $LiCu_3TiTe_4$ under three scattering mechanisms namely, polar optical phonon (POP), ionized impurity (IMP), and acoustic deformation potential (ADP) scattering with carrier concentrations of 10^{20} cm^{-3}. 189

Figure 3.16 The calculated electronic transport properties including electrical conductivity (S/m), Seebeck coefficient (μV/K), and electronic thermal conductivity ($Wm^{-1}K^{-1}$) for (a) $LiCu_3TiS_4$, (b) $LiCu_3TiSe_4$, and (c) $LiCu_3TiTe_4$. 190

Figure 3.17 The evaluated thermoelectric properties for $LiCu_3TiQ_4$ (Q = S, Se, or Te) **(a)** Seebeck coefficient (S), **(b)** electrical conductivity (σ), **(c)** power factor (PF), and **(d)** thermoelectric figure of merit (ZT), at 10^{19} cm^{-1} calculated based on relaxation times obtained transport coefficients 192

using AMSET. The negative and positive signs of the carrier concentrations represent n- and p-type doping. Here, the blue, red, and olive green represent the $LiCu_3TiS_4$, $LiCu_3TiSe_4$, and $LiCu_3TiTe_4$, respectively. The dotted line and straight line represent temperature scales of 300 K and 500 K.

Figure 3.18 The evaluated thermoelectric properties for $LiCu_3TiQ_4$ (Q = S, Se, or Te) **(a)** Seebeck coefficient (S), **(b)** electrical conductivity (σ), **(c)** power factor (PF), and **(d)** thermoelectric figure of merit (ZT), calculated based on relaxation times obtained transport coefficients using AMSET at carrier concentration of 10^{20} cm^{-3}. The negative and positive signs of the carrier concentrations represent n- and p-type doping. 193

Chapter 4

Figure 4.1 Schematic illustration of database generation with elements of the periodic table reflects the total database and stepwise machine learning workflow for the prediction of TE properties. 206

Figure 4.2 The Pearson correlation coefficient (PCC) plot for the top 21 features and figure of merit (*ZT*). The scale at the bottom represents the range of the correlation where dark purple and pale yellow signify the perfect negative (-1) and perfect positive (+1) correlation. 209

Figure 4.3 The Spearman's rank correlation plot for the top 21 features and figure of merit (*ZT*). The scale at the bottom represents the range of the correlation 210

where light purple and purple signify the perfect negative (-1) and perfect positive (+1) correlation.

Figure 4.4 Mutual information feature importance plot of optimized XGBR model for (a) Seebeck coefficient (S), (b) electrical conductivity (σ), (c) thermal conductivity (κ_L), (d) power factor (PF) and (e) figure of merit (ZT). 211

Figure 4.5 The vertical bar plots represent the test mean absolute error (MAE) and the adjacent color bar reflects the test R^2 Scores for the prediction of (a) Seebeck coefficient (S), (b) electrical conductivity (σ), (c) thermal conductivity (κ_L), and (d) figure of merit (ZT). 213

Figure 4.6 Parity plots of ML predicted versus experimental values for **(a)** Seebeck coefficient (S) in μVK^{-1}, **(b)** electrical conductivity(σ) in Scm^{-1}, **(c)** lattice thermal conductivity (κ_L) in $Wm^{-1}K^{-1}$, and **(d)** figure of merit (ZT) along with their test MAE values of XGBR models. 215

Figure 4.7 SHAP bar plot showing the global feature importance of each considered input feature on the prediction of (a) Seebeck coefficient (S), (b) electrical conductivity (σ), (c) lattice thermal conductivity (κ_L), and (d) figure of merit (ZT). 218

Figure 4.8 The SHAP beeswarm plot displays an information-dense summary of how individual feature in a dataset influences the prediction of the ML model, where each dot on the feature row represents a particular instance with its corresponding SHAP value for the prediction of (a) Seebeck coefficient 220

(S), (b) electrical conductivity (σ), (c) lattice thermal conductivity (κ_L), and (d) figure of merit (ZT).

Figure 4.9 SHAP waterfall plots showing the local explanation for the prediction of (a) Seebeck coefficient (S), (b) electrical conductivity (σ), (c) thermal conductivity (κ_L), and (d) figure of merit (ZT). The $E[f(x)]$ stands for the expected value of model prediction and $f(x)$ indicates the final prediction. The red/blue color denotes positive/negative contribution of each feature towards the prediction. 222

Figure 4.10 SHAP force plot for the prediction of (a) Seebeck coefficient, (b) electrical conductivity, (c) thermal conductivity, (d) power factor, and (e) figure of merit (ZT) for a particular instance. The base value indicates the average model predicted value and $f(x)$ denotes the final predicted value. 223

Figure 4.11 The calculated electron localization function (ELF) at isosurface value of 0.75 eV/Å^3 for (a) pristine GeTe, (b) Ba doped GeTe, (c) Co doped, (d) Cu doped GeTe, and (e) Li/Sb co-doped GeTe revealing the presence of lone pairs around Te atoms. 227

Figure 4.12 The ML classification analysis. Train-test accuracy (%) score of considered ML models with (a) 'dataset-A' based on elemental composition descriptors and (b) 'dataset-B' based on their five TE properties as descriptors for all four chalcogenides TE materials. (c-d) confusion matrix of quaternary classification, and (e-f) SHAP feature 232

importance plot of RFC model with dataset-A and dataset-B, respectively.

Figure 4.13 The ML binary classification of chalcogenide terminated thermoelectric materials with **"Dataset-B"**: (a) the train-test accuracy for best fitted RFC model of all six combinations "O-S", "O-Se", "O-Te", "S-Se", "S-Te", and "Se-Te"; the confusion matrix of binary classification along with their classification report, and SHAP feature importance plot for (b)"O-S", (c) "O-Se", (d) "O-Te", (e) "S-Se", (f) "S-Te", and (g) "Se-Te". 234

Section-B

Figure 4.14 Illustrative workflow for ML screening of pnictogen (Pn) chalcogenide (Chg) materials with ultralow κ_L values. The workflow illustrated the screening of pnictogen chalcogenides with pnictogen atoms in the +3-oxidation state. The feature space was designed using chemical bonding descriptors to reveal the role of stereochemically active lone pairs (SCALPs). 239

Figure 4.15 Distribution of 233 materials in terms of (a) pnictogen cation (b) chalcogen anion element proportion in materials, and (c) number of constituent elements in the composition. 240

Figure 4.16 Schematics of energy level diagram illustrating stereochemically active lone pairs (SCALP) in pnictogen (Pn) chalcogenide (Chg) materials. (a) Orbital interactions between the Pn(ns) and Chg(p) orbitals lead to the formation of filled bonding and antibonding combinations. Owing to the lower energy of Pn(ns) compared to the Chg(p) states, the 242

bonding combination predominantly exhibits Pn(ns) character, and the antibonding combination contains Chg(p) states. (b) The anti-bonding combination is stabilized by orbital coupling with Chg(p), resulting in a filled upper valence band (VB). The contribution of the Chg(p) orbitals to the upper VB creates an asymmetric electron density on Pn, resulting in a stereochemically active lone pair (SCALP).

Figure 4.17 The Pearson correlation coefficient (PCC) represents the considered feature-feature and feature-target (κ_L) relationship for chemical bonding descriptors. The color represents the direction and range of the correlation, where dark red and dark blue signifies the perfect positive (+1) and perfect negative (-1) correlation. 245

Figure 4.18 The Pearson correlation coefficient (PCC) represents the feature-feature and feature-target (κ_L) relationship for chemical bonding descriptors after removing highly correlated features. The color represents the direction and range of the correlation, where dark purple and pale yellow signifies the perfect positive (+1) and perfect negative (-1) correlation. 246

Figure 4.19 The Pearson correlation coefficient (PCC) represents the feature-feature and feature-target (κ_L) relationship for conventional features. The color represents the direction and range of the correlation, where dark purple and pale yellow signifies the perfect positive (+1) and perfect negative (-1) correlation. 247

Figure 4.20 The Spearman's rank correlation matrix illustrates Spearman's rank correlation coefficient between feature-feature and feature-target (κ_L) for chemical bonding descriptors after removing highly correlated features. 248

Figure 4.21 The Spearman's rank correlation matrix illustrates Spearman's rank correlation coefficient between feature-feature and feature-target (κ_L) for conventional features after removing highly correlated features. 249

Figure 4.22 The feature importance plot with the mutual information (MI) method for the chemical bonding dataset. 250

Figure 4.23 Performance comparison of ML algorithms for κ_L prediction using **(a)** conventional features and **(b)** theory-guided chemical bonding descriptors. Bar plots show the mean absolute error (MAE), root mean square error (RMSE), and R^2 scores for both the training and testing datasets across various regression models, including kernel ridge regression (KRR), decision tree regression (DTR), CatBoost, gradient boosting regression (GBR), extra tree regression (ETR), Adaboost, random forest regression (RFR), and eXtreme gradient boosting regression (XGBR). The XGBR model demonstrated the lowest RMSE/MAE and high R^2 values, indicating its superior performance in predicting κ_L. 252

Figure 4.24 Performance metrics and feature importance of the XGBR Model with different feature sets: (a) scatter plot for the conventional set of features, (b) scatter 254

plot for the chemical bonding descriptor sets considering ~5% experimental error margin, and **(c)** global interpretability by SHAP summary plot and beeswarm feature importance plots for the considered input features for the output lattice thermal conductivity (κ_L) for chemical bonding descriptors. Each solitary dot placed on the feature row represents an instance with a SHAP value (x-axis), effectively conveying valuable information in a visually compact manner. The color gradient (y-axis) represents the magnitude of the feature, ranging from low (blue) to high (green).

Figure 4.25 The 7-fold cross-validation score of root mean square error (RMSE) using XGBR model. 255

Figure 4.26 The learning rate with increasing training data size corresponding to the mean absolute error (MAE). 256

Figure 4.27 (a) The train-test parity plot of the XGBR model highlighting the model outliers, (b) the radar plot consists of outliers with key chemical bonding descriptors values, including with their predicted κ_L^{ML} values. 257

Figure 4.28 The scatter plot for the chemical bonding descriptor sets (a) with and (b) without removing polycrystalline materials, considering a 5% experimental error margins. 258

Figure 4.29 (a) The train-test parity plot of XGBR model for the chemical bonding descriptor sets after introducing various non-SCALP materials with high κ_L values, considering a 5% experimental error margins (b) ML predicted lattice thermal conductivity (κ_L^{ML}) 258

and experimentally measured κ_L values (κ_L^{Exp}) of non-SCALP materials with high κ_L values, and the difference between predicted and experimental values reported in the literature.

Figure 4.30 SHAP global interpretability analysis ML model prediction with conventional features: The bar plot showing overall contribution of individual features and the solitary dots on its right represents the bee-swarm plot providing a comprehensive summary of how each feature in the dataset impact the thermal conductivity (κ_L). Each dot in the bee-swarm plot represents an instance, with its SHAP value indicating the impact on the prediction of κ_L. 260

Figure 4.31 The comparison between the ML-predicted *versus* experimentally reported κ_L values from the test dataset. Prototype structures with different κ_L values ($\kappa_L^{Exp}/\kappa_L^{ML}$): **(a)** Tl_3SbS_3 (0.42/0.44), *[41]* **(b)** $BiSbSe_3$ (0.60/0.60) *[73]* **(c)** $CdPbBi_4Se_8$ (0.64/0.68), *[74]* **(d)** $TlPbBiS_3$ (0.88/0.89), *[46]* **(e)** $MnSbS_2Cl$ (1.10/1.00), *[75]* and **(f)** $K_2Bi_8Se_{13}$ (1.28/1.28), *[41]* illustrate the model's predictive performance. 261

Figure 4.32 List of top 14 predicted pnictogen chalcogenides at 300 K along with their OQMD IDs. The predicted κ_L^{ML} values of $MnTl_2As_2S_5$ and $AgCu_2PbBiS_4$ materials are consistent with previously reported values *[76]*. 263

Figure 4.33 Crystal structures, projected density of states (PDOS), and crystal orbital overlap population (COOP) analysis of **(a)** $MnTl_2As_2S_5$ and **(b)** 265

$Ba_2As_2Se_5$. The 3D view of the electron localization function (ELF) at isosurface values of 4.58 $\times 10^{-4}$ eV/Å^3 and 8.59 $\times$ 10^{-4} eV/Å^3, respectively. PDOS and COOP analyses were used to visualize the bonding characteristics of the SCALP near the Fermi energy, where a positive overlap population indicates a bonding interaction, while a negative overlap population indicates an antibonding interaction.

Figure 4.34 The calculated electron localization function (ELF) exhibiting the presence of lone pair clouds around pnictogen atoms in best five materials with low κ_L values: (a) $MnTl_2As_2S_5$ (isosurface value of 8.6 $\times$ 10^{-4} eV/Å^3), (b) $Ba_2As_2Se_5$ (isosurface value of 9.4 $\times$ 10^{-4} eV/Å^3), (c) $Bi_{14}Te_{13}S_8$ (isosurface value of 3.1 $\times$ 10^{-3} eV/Å^3), (d) $AgCu_2PbBiS_4$ (isosurface value of 1.2 $\times$ 10^{-3} eV/Å^3), and (e) $Tl_2SnAs_2S_6$ (isosurface value of 4.6 $\times$ 10^{-4} eV/Å^3). 266

Figure 4.35 A scatter heat map highlighting the relationship between the lattice thermal conductivity (κ_L) and the chemical bonding descriptors, using **(a)** ionicity and hybridization and **(b)** mismatch and polarizability. Radar plots characterizing the change in κ_L via the difference in mismatch (δ), ionicity (r'_σ), hybridization (r_π^{-1}), and polarizability ($\overline{\alpha}$) for **(c)** the best five materials with ultralow κ_L $\leq$ 0.40 Wm^{-1}K^{-1}, and **(d)** materials with κ_L > 1.0 Wm^{-1}K^{-1}. The highlighted materials with * are in close agreement with ML predicted vs reported κ_L.[50] 268

Figure 4.36 The radar plot representing the interplay between mismatch (δ), ionicity (r'_σ), hybridization (r_π^{-1}), and polarizability ($\overline{\alpha}$) for **(a)** $Bi_{14}Te_{13}S_8$, **(b)** $InSbS_3$, and **(c)** RbK_2BiSe_5 materials. **(d-f)** The partial density of states (PDOS) of each element in the $Bi_{14}Te_{13}S_8$, $InSbS_3$, and RbK_2BiSe_5 systems, and **(g-i)** 3D visualization of the electron localization function (ELF) for $Bi_{14}Te_{13}S_8$, $InSbS_3$, and RbK_2BiSe_5 materials at isosurface value of 18.3 × 10^{-4} eV/Å^3, 8.8 × 10^{-4} eV/Å^3 and 7.9 × 10^{-4} eV/Å^3, respectively. 271

Chapter 5

Figure 5.1 **(a)** Orbital interactions in the lone-pair containing As-Se bonds that facilitate stereochemically active lone pair (SCALP) formation, **(b)** Expanding the chemical space using *ab initio* molecular dynamics (AIMD) simulations to represent energy of an atomic configuration ($E^{mtp}(chg)$) comprised of local potential (V) of neighboring atoms (n_i), **(c)** Local chemical environment descriptors defining the moment tensor, where neighboring atoms within a cut-off radius (R_{cut}) interact with the central atom, where f_u encodes the radial information and $r_{ij} \otimes ... \otimes r_{ij}$ contains the angular information, **(d)** constructing invariant features through atomic permutations, rotations, and reflections by computing tensor contractions and eliminating linear dependencies, defining radial basis function which uses polynomial operator on interatomic distances (r_{ij}), $c = \{c^{(\beta)}_{\mu,z_i,z_j}\}$ is radical 286

basis function, $Q^{(\beta)}(|r_{ij}|)$ uses polynomial functions operated on interatomic distances based on cutoff radius **(e)** training moment tensor potentials (MTPs) using the polynomial regression and iterative optimization to define the local chemical environment representing potential energy surface, and **(f)** performance matrix illustrating the accuracy of trained MTPs through scatter plots comparing AIMD calculated energies/forces with MTP predicted energies/forces used to predict thermal transport properties of $LiAsSe_2$ and $NaAsSe_2$ materials.

Figure 5.2 The unit cell of (a) lithium chalcoarsenate $LiAsSe_2$, (b) sodium chalcoarsenate $NaAsSe_2$ along with total electronic charge distribution (TECD) contour plots along the (010) plane and the 3D electron localization function (ELF) visualized at an iso-surface value of 0.9 $eVÅ^{-3}$ reveal the presence of lone pairs around As and Se atoms (c) Scatter plots comparing MTP-predicted with AIMD calculated values: energy and force parity plots for $LiAsSe_2$ and $NaAsSe_2$. (d) The error matrix of trained MTPs evaluated in root mean square error (RMSE) and mean absolute error (MAE) for energies (in meV) and forces (meV $Å^{-1}$) for both the training and testing sets. 290

Figure 5.3 (a) The machine learning interatomic potential predicted lattice thermal conductivity (κ_L) of $LiAsSe_2$ and $NaAsSe_2$ as a function of temperature (K) along three axes. (b) The comparison of κ_L with ABX_2 compounds featuring lone pair electrons, 294

with data obtained from Ref. 5 and 33 Atomic displacement parameters for (c) $LiAsSe_2$ and (d) $NaAsSe_2$ across the equilibrium positions.

Figure 5.4 The machine learning interatomic potential predicted phonon dispersion, phonon density of states and Grüneisen parameter (γ), group velocity across the high symmetry points in the first Brillouin zone for **(a)** $LiAsSe_2$, **(b)** $NaAsSe_2$. In the plot, the longitudinal acoustic (LA) mode is highlighted in green, and the two-transverse acoustic (TA) phonon modes are highlighted in blue and red. 295

Figure 5.5 The calculated total anharmonic scattering rates and weighted phase space (WP_3) as a function of frequency (THz) for (a) $LiAsSe_2$ (b) $NaAsSe_2$ at 300 K highlighting absorption and emission scattering channels. 298

Figure 5.6 Boundary and isotopic scattering rates of (a) $LiAsSe_2$, and (b) $NaAsSe_2$ with respect to frequency (THz) at 300K. 300

Figure 5.7 Electronic band structures, projected density of states (PDOS) calculated using the HSE06 functional, and the crystal orbital Hamilton population (COHP) plot for (a) $LiAsSe_2$ and (b) $NaAsSe_2$. The dark yellow arrow defines the direct band gap along the Brillouin zone points. The pairwise orbital interactions shown in COHP plot highlight the presence of SCALP electrons where, positive overlap populations indicate bonding interactions, and negative overlap population indicates antibonding interactions. 301

Figure 5.8 Scattering rates as a function of energy of p-type for $LiAsSe_2$. These represent their scattering mechanisms including polar optical phonon (POP), ionized impurity (IMP), and acoustic deformation potential (ADP) scattering at carrier concentration ranges from 10^{19} cm^{-3} - 10^{21} cm^{-3} at 300 K and 600 K. 302

Figure 5.9 Scattering rates as a function of energy of n-type for $LiAsSe_2$. These represent their scattering mechanisms including polar optical phonon (POP), ionized impurity (IMP), and acoustic deformation potential (ADP) scattering at carrier concentration ranges from 10^{19} cm^{-3} - 10^{21} cm^{-3} at 300 K and 600 K. 303

Figure 5.10 Scattering rates as a function of energy of p-type for $NaAsSe_2$. These represent their scattering mechanisms including polar optical phonon (POP), ionized impurity (IMP), and acoustic deformation potential (ADP) scattering at carrier concentration ranges from 10^{19} cm^{-3} - 10^{21} cm^{-3} at 300 K and 600 K. 303

Figure 5.11 Scattering rates as a function of energy of n-type for $NaAsSe_2$. These represent their scattering mechanisms including polar optical phonon (POP), ionized impurity (IMP), and acoustic deformation potential (ADP) scattering at carrier concentration ranges from 10^{19} cm^{-3} - 10^{21} cm^{-3} at 300 K and 600 K. 304

Figure 5.12 Mobility (cm^2/Vs) as a function of temperature for n- and p-type doping for $LiAsSe_2$, under three scattering mechanisms namely, polar optical 305

phonon (POP), ionized impurity (IMP), and acoustic deformation potential (ADP) scattering with carrier concentrations ranges from 10^{19} cm^{-3} - 10^{21} cm^{-3}.

Figure 5.13 Mobility (cm^2/Vs) as a function of temperature for n- and p-type doping for $NaAsSe_2$, under three scattering mechanisms namely, polar optical phonon (POP), ionized impurity (IMP), and acoustic deformation potential (ADP) scattering with carrier concentrations ranges from 10^{19} cm^{-3} - 10^{21} cm^{-3}. 306

Figure 5.14 The direction dependent electronic thermal conductivity, κ_e ($Wm^{-1}K^{-1}$), as a function of carrier concentration N (10^{21} cm^{-3}) for (a) $LiAsSe_2$, and (b) $NaAsSe_2$. The dotted and solid lines represent the κ_e at 300 K and 600 K, respectively. 306

Figure 5.15 The direction dependent power factor ($mWK^{-2}m^{-1}$), as a function of carrier concentration N (10^{21} cm^{-3}) for (a) $LiAsSe_2$, and (b) $NaAsSe_2$. The dotted and solid lines represent the κ_e at 300 K and 600 K, respectively. 307

Figure 5.16 Thermoelectric properties including Seebeck coefficient (S), electrical conductivity (σ), thermoelectric figure of merit (ZT) for (a) $LiAsSe_2$ and (b) $NaAsSe_2$, calculated based on relaxation times and transport coefficient obtained using AMSET. The negative and positive signs of the carrier concentrations represent n- and p-type doping, respectively, with dotted and solid line representing 300 K and 600 K. 308

Section-B

Figure 5.17 (a) Optimized conventional unit cell structures of $Ba_2As_2S_5$, $Ba_2As_2Se_5$, Ba_2AsSbQ_5 (Q = S/Se), and Ba_2AsBiQ_5 (Q = S/Se). (b) 3D electron localization function (ELF) map of $[Pn_2Q_4]^{2-}$ unit and (c) PnQ_3 units (Pn = As, Sb, Bi; Q = S, Se) at an iso-surface value of 0.90 eÅ^{-3}, highlighting the lone-pair regions around the pnictogen atoms. (d) Lattice thermal conductivity (κ_L) values predicted using machine learning interatomic potentials as a function of temperature along three crystallographic directions. Red circles mark the $Ba_2AsBiSe_5$ system, which exhibits ultralow κ_L. 314

Figure 5.18 Scatter plots comparing MTP-predicted and AIMD-calculated energies and forces for (a) $Ba_2As_2S_5$, (b) Ba_2AsSbS_5, (c) Ba_2AsBiS_5, (d) $Ba_2As_2Se_5$, (e) $Ba_2AsSbSe_5$, and (f) $Ba_2AsBiSe_5$. Each panel reports the mean absolute error (MAE) and root mean square error (RMSE) for energies (meV) and forces (meV Å^{-1}) for both the training and testing datasets, quantifying the accuracy of the trained MTP models. 316

Figure 5.19 Machine learning interatomic potential (MLIP)-predicted phonon dispersion, phonon density of states, Grüneisen parameter (γ), and group velocity across the high-symmetry points in the first Brillouin zone for (a) $Ba_2AsSbSe_5$, (b) $Ba_2AsBiSe_5$. Panels (c-d) show the potential energy landscape of Ba_2AsPnQ_5 (where Pn=As, Sb, Bi; Q=S, Se) as a function of atomic displacement from their equilibrium positions. 319

Figure 5.20 The machine learning interatomic potential predicted phonon dispersion, phonon density of states and Grüneisen parameter (γ), group velocity across the high symmetry points in the first Brillouin zone for (a) $Ba_2As_2S_5$, (b) $Ba_2As_2Se_5$, (c) Ba_2AsSbS_5, (d) $Ba_2AsSbSe_5$. 320

Figure 5.21 The calculated (a) total anharmonic scattering rates and (b) weighted phase space (WP_3) as a function of frequency (THz) for Ba_2AsPnS_5 (Pn = As, Sb and Bi) at 300 K along with absorption and emission scattering channels and absorption (P_3^+) and emission (P_3^-) weighted phase space. 321

Figure 5.22 The calculated (a) total anharmonic scattering rates and (b) weighted phase space (WP_3) as a function of frequency (THz) for $Ba_2AsPnSe_5$ (Pn = As, Sb and Bi) at 300 K along with absorption and emission scattering channels and absorption (P_3^+) and emission (P_3^-) weighted phase space. 322

Figure 5.23 Boundary and isotopic scattering rates of (a) Ba_2AsPnS_5 (Pn = As, Sb and Bi) and (b) $Ba_2AsPnSe_5$ (Pn = As, Sb, and Bi) with respect to frequency (THz) at 300K. 322

Figure 5.24 The electronic band structures along with the total and projected density of states (Total DOS and PDOS) calculated using the HSE03 functional for (a) Ba_2AsPnS_5 (Pn = As, Sb and Bi) and (b) $Ba_2AsPnSe_5$ (Pn = As, Sb and Bi) along the Brillouin zone points, highlighting the band degeneracies in the valence band (V1, V2, V3) and conduction band (C1, C2). 323

Figure 5.25 (a) Schematic illustration of band valley engineering through modifications in the band structure and density of states. (b) Calculated band gaps for Ba_2AsPnQ_5 materials (Pn = As, Sb, Bi; Q = S, Se). (c-d) Electronic band structure of $Ba_2As_2Se_5$ and $Ba_2AsBiSe_5$ highlighting valence band (V_1, V_2, V_3) and conduction band (C_1, C_2) degeneracies. (e) Partial density of states (PDOS) and crystal orbital Hamilton population (COHP) analysis for $Ba_2AsBiSe_5$. (f) Schematic representation of orbital interactions near the Fermi level in $Ba_2AsBiSe_5$, derived from PDOS and COHP analysis. 325

Figure 5.26 Total and Partial density of states (Total DOS/PDOS) and crystal orbital Hamilton population (COHP) analysis of (a) $Ba_2As_2S_5$, (b) Ba_2AsSbS_5 and (c) $Ba_2AsSbSe_5$. 327

Figure 5.27 Total and Partial density of states (Total DOS/PDOS) and crystal orbital Hamilton population (COHP) analysis of (a) $Ba_2As_2Se_5$ and (b) $Ba_2AsSbSe_5$. 327

Figure 5.28 Mobility (cm^2/Vs) as a function of temperature for **(a)** n- doping and **(b)** p-type doping for Ba_2AsPnS_5 (Pn = As, Sb, and Bi) under three scattering mechanisms namely, polar optical phonon (POP), ionized impurity (IMP), and acoustic deformation potential (ADP) scattering with carrier concentrations of 10^{20} cm^{-3}. 334

Figure 5.29 Mobility (cm^2/Vs) as a function of temperature for **(a)** n- doping and **(b)** p-type doping for $Ba_2AsPnSe_5$ (Pn = As, Sb, and Bi) under three scattering 335

mechanisms namely, polar optical phonon (POP), ionized impurity (IMP), and acoustic deformation potential (ADP) scattering with carrier concentrations of 10^{20} cm^{-3}.

Figure 5.30 Scattering rates as a function of energy of n-type at **(a)** 300 K and **(b)** 700 K for Ba_2AsPnS_5 (Pn = As, Sb, and Bi). These represent their scattering mechanisms including polar optical phonon (POP), ionized impurity (IMP), and acoustic deformation potential (ADP) scattering at carrier concentrations of 10^{20} cm^{-3}. 335

Figure 5.31 Scattering rates as a function of energy of p-type at (a) 300 K and (b) 700 K for Ba_2AsPnS_5 (Pn = As, Sb, and Bi). These represent their scattering mechanisms including polar optical phonon (POP), ionized impurity (IMP), and acoustic deformation potential (ADP) scattering at carrier concentrations of 10^{20} cm^{-3}. 336

Figure 5.32 Scattering rates as a function of energy of n-type at (a) 300 K and (b) 700 K for $Ba_2AsPnSe_5$ (Pn = As, Sb, and Bi). These represent their scattering mechanisms including polar optical phonon (POP), ionized impurity (IMP), and acoustic deformation potential (ADP) scattering at carrier concentrations of 10^{20} cm^{-3}. 336

Figure 5.33 Scattering rates as a function of energy of p-type at (a) 300 K and (b) 700 K for $Ba_2AsPnSe_5$ (Pn = As, Sb, and Bi). These represent their scattering mechanisms including polar optical phonon (POP), ionized impurity (IMP), and acoustic deformation 337

potential (ADP) scattering at carrier concentrations of 10^{20} cm^{-3}.

Figure 5.34 The calculated electronic transport properties including electrical conductivity (S/m), Seebeck coefficient (μV/K), and electronic thermal conductivity ($Wm^{-1}K^{-1}$) for **(a)** $Ba_2As_2S_5$, **(b)** Ba_2AsSbS_5, and **(c)** Ba_2AsBiS_5. 338

Figure 5.35 The calculated electronic transport properties including electrical conductivity (S/m), Seebeck coefficient (μV/K), and electronic thermal conductivity ($Wm^{-1}K^{-1}$) for (a) $Ba_2As_2Se_5$, (b) $Ba_2AsSbSe_5$, and (c) $Ba_2AsBiSe_5$. 339

Figure 5.36 The calculated electronic thermal properties (κ_L) in $Wm^{-1}K^{-1}$ for (a) Ba_2AsPnS_5 (Pn = As, Sb, and Bi) and (b) $Ba_2AsPnSe_5$ (Pn = As, Sb, and Bi) systems. 341

Figure 5.37 The evaluated thermoelectric properties for **(a)** $Ba_2As_2S_5$, **(b)** Ba_2AsSbS_5, and **(c)** Ba_2AsBiS_5 containing Seebeck coefficient (S), electrical conductivity (σ), and thermoelectric figure of merit (ZT), calculated based on relaxation times obtained transport coefficients using AMSET. The negative and positive signs of the carrier concentrations represent n- and p-type doping. Here, the orange, blue and olive green represents the x-axis, y-axis, and z-axis, respectively. The dotted line and straight line represent temperature scale of 300 K and 700 K. 341

Figure 5.38 Thermoelectric properties of (a) $Ba_2As_2Se_5$, (b) $Ba_2AsSbSe_5$, and (c) $Ba_2AsBiSe_5$ containing Seebeck coefficient (S), electrical conductivity (σ), and thermoelectric figure of merit (ZT), computed 342

using AMSET derived relation times. Negative and positive carrier concentrations correspond to n-type and p-type doping, respectively. Orange, blue, and olive green represent the x-axis, y-axis, and z-axis, respectively. Dotted and solid lines indicate temperatures of 300K and 700K.

Chapter 6

Figure 6.1 (a) Two-dimensional t-SNE projection of the pnictogen-chalcogenide (pn-chg) chemical space based on structural and compositional descriptors (perplexity = 30, learning rate = 50, iterations = 300). Each point represents a pn-chg material, color-coded according to eight distinct clusters (C1-C8) identified through K-means clustering. Representative crystal structures are illustrated for each cluster are described in Table 6.1. Violin maps showing the distribution of key property values for pn-chg from seven prototypes identified in Materials Project database. For each prototype showing distribution for (b) atomic weight, (c) electronic band gap, (d) formation energy (E_f), and (e) energy above convex hull (E_{Hull}), the blue-dashed line denotes the selection criterion, used in current study. 364

Figure 6.2 Determination of the optimal number of clusters using k-means clustering. **(a)** Elbow method plot showing the decrease in inertia (within-cluster sum of squares) as the number of clusters (K) increases, with the optimal K suggested at the point where the decrease begins to level off. **(b)** Silhouette score plot illustrating the average silhouette coefficient 365

for each K, where higher values indicate better-defined clusters.

Figure 6.3 (a) Schematic workflow illustrating the high-throughput screening of the pnictogen chalcogenides dataset starting from 154,718 compounds in the Materials Project database. The candidate space is progressively narrowed using successive filters based on chemical criteria, thermodynamic stability ($E_f < 0$ eV/atom and $E_{Hull} < 0.50$ meV), electronic band gap ($E_g > 0.1$ eV), oxidation state constraints, and dynamical stability, ultimately yielding 78 promising thermoelectric candidates. (b) Structural classification of the final 78 screened compounds, categorized by their crystal symmetries, highlighting the diversity of crystallographic motifs, (c) Fine-tuning learning curves for the MatterSim model, showing the reduction in mean absolute error (MAE) for energy, forces, and stresses as a function of training epochs, (d) Parity plots comparing MatterSim-predicted and DFT-calculated values for energy, forces, and stresses, confirming high fidelity of the MatterSim model in reproducing DFT-level accuracy. 368

Figure 6.4 The phonon dispersion curves for (a) K_3SbTe_3 and (b) Na_3SbS_3 comparing density functional theory (DFT) results with predictions from MatterSim, both in its zero-shot and fine-tuned forms. 371

Figure 6.5 (a) Directional lattice thermal conductivity (κ_L) along the crystallographic x, y, and z-axes for 78 screened pnictogen chalcogenide systems. The materials are categorized into four regimes on their 373

κ_L values: ultralow (<0.20 W/mK, blue), low (0.20-0.50 W/mK, green), medium (0.50-1.10 W/mK, yellow), and high (>1.10 W/mK, red). The background gradient represents the magnitude of the κ_C value defines wave-like conductivity, (b) representative crystal structures of ten materials with average κ_L ~0.40 W/mK at room temperature, along with their corresponding Materials Project (MP-ids).

Figure 6.6 Comparative performance of CHGNet, MACE and MatterSim in predicting the lattice thermal conductivity (κ_L) (a) scatter plots of uMLIP-predicted versus DFT-calculated κ_L values, showing model correlation coefficient (R^2). CHGNet displays large deviations (R^2 = 0.21), whereas MACE and MatterSim exhibit high correlations with DFT ($R^2 \approx 0.90$), highlighting substantial accuracy gains. (b) Violin plots of Symmetric Relative Error (SRE), Symmetric Relative Mean Error (SRME), and Symmetric Relative Difference (SRD). The narrower, centered distributions for MatterSim confirm their minimal bias and high predictive reliability in reproducing phonon-mediated thermal transport. 376

Figure 6.7 **(a)** Bar plot showing the correlation coefficients between κ_L and two categories of descriptors: SCALP descriptors (~40%, shown in blue) and beyond SCALP-distortion descriptors (~60%, shown in orange). Descriptor details are provided in Table 6.3-6.4. (b) Global interpretability of the GBR model obtained from SHAP feature 380

importance and beeswarm plots, highlighting the key chemical bonding descriptors contributing most significantly to κ_L based on mean SHAP values. (c) SHAP force plots illustrating the interplay between SCALP and geometric activity across representative pn-chg materials. The sequence from K_3SbSe_3 to $Cs_3Sb_5Se_9$ to $MgCu_3AsS_4$ to $Cu_6Hg_3S_{12}$ demonstrates a decrease in SCALP-activity that led to high κ_L.

Figure 6.8 Crystal structures with SCALP projection on pnictogens using electron localization function (ELF), projected density of states (PDOS), and crystal orbital Hamilton population (COHP) analysis of (a) Cs_3SbS_3, (b) $Ba_3Sb_2Se_7$, and (c) Li_3BiS_3. The 3D view of the electron localization function (ELF) at isosurface values of 0.91 eV/Å^3. The comparison of ionicity (r'_σ), hybridization (r_π^{-1}), bond angle (θ), with lattice thermal conductivity (κ_L). PDOS and COHP analyses were used to visualize the bonding characteristics of the SCALP near the Fermi energy, where a positive overlap population indicates a bonding interaction, while a negative overlap population indicates an antibonding interaction. 384

Chapter 7

Figure 7.1 Data-driven framework for scalable prediction and optimization of κ_L. (a) Distribution of crystal chemistries and structural families within the 3,925-material κ_L dataset, highlighting the chemical and topological diversity used to train the model. (b) Edge-gated graph convolution networks 400

operating on GNN models, enabling bond-centric message passing that captures anharmonic and local structural effects governing phonon transport. (c) Knowledge-transfer paradigm in which representations learned from a large materials corpus enhancing predictive accuracy and data efficiency for smaller or compositionally constrained datasets. (d) Closed-loop crystal optimization workflow integrating fine-tuned CrystaLLM generation, structural relaxation, and dynamical stability screening with pre-trained machine-learning interatomic potentials.

Figure 7.2 Model comparison and hyperparameter sensitivity. (a–c) Mean absolute error (MAE) contributions from key hyperparameters including learning rate, batch size, and number of graph convolution (GC) layers for CGCNN, deeper-CGCNN, and ALIGNN models, respectively, illustrating their relative influence on predictive performance (d–f) Predicted versus DFT-values for the training and test sets GNN models. 402

Figure 7.3 Fine-tuning strategies for a pretrained graph neural network model. Schematic illustration of four transfer-learning strategies applied to a graph-based architecture comprising atom, edge, and angle embedding layers, followed by bond and line graph message passing, pooling, and linear MLP head. Strategy 1 unfreezes all layers for full fine-tuning. Strategy 2 freezes the embedding layers while fine-tuning the downstream graph and MLP layers. Strategy 3 freezes all pretrained layers 406

except the final prediction layer. Strategy 4 retains all pretrained layers and adds an additional prediction head for task-specific learning.

Figure 7.4 Performance of same-property and cross-property transfer learning using different fine-tuning strategies. (a) Bar plots show the train, validation, and test MAE obtained for six target properties, band gap, convex hull energy (E_{hull}), formation energy, bulk modulus, dielectric constant, and lattice thermal conductivity (κ_L) using four fine-tuning strategies: S1 (unfreeze all layers), S2 (freeze embedding layers), S3 (unfreeze final layer only), and S4 (add prediction head). Results include both same-property transfer and cross-property transfer, yielding a total of 24 trained models. (b) Parity plots for the best-performing transfer learning models under the S1 strategy. 409

Figure 7.5 Evaluation of generative crystal structures and discovery of low lattice thermal conductivity candidates. (a) Violin plots comparing the distributions of lattice lengths, lattice angles, and atomic fractional coordinates for generated structures against the training dataset, demonstrating close agreement in crystallographic statistics. (b) Cumulative counts of generated, unique, and unique-novel structures, highlighting efficient novelty generation after duplicate removal. (c,d) Low-dimensional embeddings comparing generated and training structures, indicating strong coverage of the learned structural manifold while extending into previously 413

unexplored regions. (e) Workflow summarizing structure filtering from 10,000 generated candidates to dynamically stable materials. (f) Representative unique and novel crystal structures identified by the model along with the phonon dispersion relations confirming the dynamical stability of selected candidates, with no imaginary frequencies observed. Here, E_{hull}, E_f and κ_L represents convex hull (meV/atom), formation energy (eV/atom) and lattice thermal conductivity (W/mK).

Chapter 8

Figure 8.1 Schematic illustration of forward and inverse materials design paradigms enabled by machine learning. (a) Traditional forward design maps material structures to properties, while inverse design seeks to generate candidate structures conditioned on targeted properties within a highly ill-posed and non-unique design space. (b) A generative inverse 425 Chapter 8 design framework, where conditional deep neural networks learn probabilistic mappings between structure representations and physical responses, enabling efficient exploration of complex materials spaces and the discovery of novel, out-of-distribution materials with targeted functionalities, such as ultralow lattice thermal conductivity. 425

List of Tables

		Page No.
Chapter 2		
Table 2.1	Elastic Constants (C_{11}, C_{12}), Young's Modulus (Y), Shear Modulus (P), and Poisson's Ratio (ν) for the Considered Structures of γ-GeSe.	97
Table 2.2	Cohesive Energy and Formation Energy for the Considered Structures of γ-GeSe.	98
Table 2.3	Comparison of calculated, experimentally observed Raman shifts and the previously reported calculated values of phonon modes of AB′ stacked γ-GeSe. The E_1 modes are Raman active but forbidden in the back-scattering geometry and noted as N/A *[33]*.	102
Table 2.4	Electronic bandgaps (eV) of considered γ-GeSe systems using PBE and HSE06 functional.	103
Table 2.5	Longitudinal velocity (ν_L), Transverse velocity (ν_T) and Debye Temperature (θ_D) for the considered structures of γ-GeSe.	111
Table 2.6	Effective masses of the carriers along Γ → M k-path for considered systems of γ-GeSe.	113
Table 2.7	Lattice thermal conductivity (κ_L), Power Factor ($S^2\sigma$), and ZT at 300K, 600K, and 900K for all the considered systems.	118
Table 2.8	The lattice parameter, bond distance, and net effective charges of considered structures of GeS.	124
Table 2.9	Cohesive energy and formation energy for the considered structures of GeS.	126

Table 2.10	Lattice thermal conductivity ($Wm^{-1}K^{-1}$) of o-GeS bilayer with respect to 3 phonon and 3+4 phonon processes and the percentage change on considering 3+4 phonon.	131
Table 2.11	Lattice thermal conductivity ($Wm^{-1}K^{-1}$) of h-GeS bilayer with respect to 3 phonon and 3+4 phonon processes and the percentage change on considering 3+4 phonon.	132
Table 2.12	Longitudinal velocity (V_L), Transverse velocity (V_T) and Debye Temperature (θ_D) for the considered structures of GeS.	139
Table 2.13	Lattice Thermal Conductivity (κ_L) ($Wm^{-1}K^{-1}$), Power Factor (PF) ($mWK^{-2}m^{-1}$), and ZT at 300 and 900 K for o- GeS and h-GeS bulk.	147
Table 2.14	Lattice Thermal Conductivity (κ_L) ($Wm^{-1}K^{-1}$), Power Factor (PF) ($mWK^{-2}m^{-1}$), and ZT at 300 and 900 K for o- GeS and h-GeS bilayer. Here, percentage change represents the change in κ_L(3+4ph) with respect to κ_L(3-ph).	147
Chapter 3		
Table 3.1	The sum of covalent and ionic radii (Å) of respective atoms in Ti–Q, Li–Q, and Cu–Q (Q = S, Se, or Te) and the actual bond lengths are defined in blue color.	171
Table 3.2	The calculated Young's modulus (GPa), shear modulus (GPa), Poisson's ratio, and Debye Temperature, θ_D (K) for the considered structures of $LiCu_3TiQ_4$.	172
Table 3.3	The temperature-dependent lattice thermal conductivity (κ_L) including the contributions from	180

	particle-like (κ_L^p) and wave-like (κ_L^c) conduction mechanisms. The unit of thermal conductivity is $Wm^{-1}K^{-1}$.	
Table 3.4	Calculated bandgaps using different functionals for $LiCu_3TiQ_4$ systems.	185
Table 3.5	The carrier effective mass (m_o) of hole and electron for $LiCu_3TiQ_4$ systems.	186
Chapter 4		
Table 4.1	List of 35 Elemental and Structural Features Considered in the Present Study	208
Table 4.2	List of Top 21 Elemental and Structural Features Considered After Removing Highly Correlated Features	212
Table 4.3	Optimized hyperparameters of optimized XGBR models with test accuracy score.	213
Table 4.4	Mean Absolute Error (MAE) of 9-fold Cross-Validation using the XGBR Models for Seebeck Coefficient (S) μVK^{-1}, Electrical Conductivity (σ) Scm^{-1}, Thermal Conductivity (κ_L) $Wm^{-1}K^{-1}$, Power Factor (PF) $\mu Wcm^{-1}K^{-2}$, and Thermoelectric Figure of Merit (ZT) datasets. Test MAE and standard deviation (std) Values for Each XGBR Model have also been Reported.	216
Table 4.5	Experimental (Exp) and Predicted (Pred) Values of ZT and $\kappa_L(Wm^{-1}K^{-1})$ for selected TE Materials with Chalcogens (Group 16 Elements) Termination.	224
Table 4.6	Predicted Top High-Performance Doped TE Materials with ZT, κ_L $(Wm^{-1}K^{-1})$, and S (μVK^{-1}) for at 300 K, 700 K, and 1000 K Selected from 390 Unknown Dataset.	225

Table 4.7	List of Optimized Hyperparameters Considered for ML Classification with **"Dataset-A"** Model, Anong with Corresponding Test Accuracy Score.	229
Table 4.8	List of Optimized Hyperparameters Considered for ML Classification with **"Dataset-B"** Model, Anong with Corresponding Test Accuracy Score.	230
Table 4.9	List of All Considered Chemical Bonding Descriptors.	240
Table 4.10	List of All the Considered Conventional Features.	244
Table 4.11	List of Screened Final Features Considered of ML Model Training After Removing Highly Correlated Features for Chemical Bonding Descriptors.	251
Table 4.12	Optimized hyperparameters of utilized XGBR model with test accuracy score.	253
Chapter 5		
Table 5.1	The lattice parameters (Å) of the considered structures of $LiAsSe_2$ and $NaAsSe_2$ systems.	289
Table 5.2	The sum of covalent and ionic radii (Å) of respective atoms in A–Se (A = Li and Na), and As–Se and the actual bond lengths are defined in blue color.	291
Table 5.3	The optimized MTP hyperparameters for $LiAsSe_2$ and $NaAsSe_2$.	292
Table 5.4	The calculated Young's modulus (GPa), shear modulus (GPa), Poisson's ratio, Debye Temperature, θ_D (K), and mode average Grüneisen parameters ($\overline{|\gamma|}$) for the considered structures of $LiAsSe_2$ and $NaAsSe_2$ systems.	297
Table 5.5	The calculated Young's modulus (GPa), shear modulus (GPa), Poisson's ratio, and Debye	318

Temperature, θ_D (K) for the considered structures of Ba_2AsPnQ_5 (Pn=As/Sb/Bi; Q=S/Se).

Table 5.6 Geometric, bond stiffness/softness, and chemical bonding descriptors for Ba_2AsPnQ_5 (Pn = As, Sb, Bi; Q = S, Se), including lone pair angle (θ), lone pair distance from pnictogen (d_{lp}), Debye temperature (θ_D), Grüneisen parameter (γ), ionicity (r'_σ), hybridization (r_π^{-1}), integrated crystal Hamilton population (ICOHP, Pn-Chg), bond length (Pn-Chg), and lattice thermal conductivity (κ_L) along the x-axis. 328

Table 5.7 Interplay of chemical bonding parameters: lone pair angle (θ), lone pair-pnictogen distance (d_{lp}), Debye temperature (θ_D), Grüneisen parameter (γ), ionicity (r'_σ), hybridization (r_π^{-1}), and their quantitative influence on κ_L for Ba_2AsPnQ_5 systems. Panels **(a-f)** depicts the individual impact of each parameter, alongside the Pearson correlation coefficient plot summarizing their relationships. 331

Chapter 6

Table 6.1 K-means Cluster Descriptions for Pnictogen Chalcogenide (pn-chg) Systems Based on Chemical and Structural Properties. 365

Table 6.2 Mean absolute errors (MAEs) for energy, forces, and stresses across screened pnictogen chalcogenide materials at final epochs. Each row corresponds to a material, and each column represents the MAE for energy, forces, and 370

stresses on training (Train), validation (Val), and test (Test) datasets in meV, meV/Å or GPa.

Table 6.3 Pearson correlation coefficient (PCC) matrix between structural/bonding descriptors and the κ_L^{avg} of SCALP materials. The red dotted squares highlight descriptors with the strongest negative correlations with κ_L^{avg}. 377

Table 6.4 Chemical Bonding Descriptor Correlations highlighting the SCALP and Structural Distortion mechanisms influencing κ_L. 381

Chapter 7

Table 7.1 The lists the target material property, dataset size, and the mean absolute error (MAE) achieved by the corresponding pretrained ALIGNN model prior to fine-tuning. These pretrained models serve as source tasks for both same-property and cross-property transfer learning analyses. 408

Table 7.2 List of predicted low lattice thermal conductivity (κ_L), formation energy (E_f), convex hull (E_{hull}) for generated novel and unique structures. 415

Acronyms

TE: Thermoelectric

S: Seebeck Coefficient

κ_L: Lattice thermal conductivity

κ_e: Electronic Thermal Conductivity

σ: Electrical Conductivity

ZT: Figure of merit

PF: Power Factor

n_c: Carrier Concentration

SCALP: Stereochemically Active Lone Pairs

Pn: Pnictogen

Chg: Chalcogenide

VB: Valence Band

CB: Conduction Band

m*: Effective Mass

θ: Lone Pair Angle

r_c: Covalent Radii

DFT: Density Functional Theory

LDA: Local Density Approximation

GGA: Generalized Gradient Approximation

PBE: Perdew-Burke-Ernzerhof

DOS: Density of State

WF: Wavefunction

BOA: Born-Oppenheimer Approximation

vdW: van der Waals

PAW: Projector Augmented Wave

PP: Pseudopotential

LCAO: Linear Combination of Localized Numerical Atomic Orbitals

MOs: Molecular Orbitals

VASP: Vienna *ab initio* Simulation Package

DFPT: Density Functional Perturbation Theory

AIMD: *Ab Initio* Molecular Dynamics

IFCs: Interatomic Force Constants

BTE: Boltzmann transport equation

CRTA: Constant Relaxation Time Approximation

MRTA: Momentum Relaxation Time Approximation

SERTA: Self-Energy Relaxation Time Approximation

AMSET: *Ab initio* Scattering and Transport

ADP: Acoustic Deformation Potential

IMP: Ionized Impurity

POP: Polar Optical Phonon

PIE: Piezoelectric

ML: Machine Learning

MLIPs: Machine Learning Interatomic Potentials

MTP: Moment Tensor Potential

CHGNet: Crystal Hamiltonian Graph Neural Network

MACE: Multilayer Atomic Cluster Expansion

SHAP: SHapley Additive exPlanations

XGBR: Extreme Gradient Boosting Regression

KRR: Kernel Ridge Regression

LR: Linear Regression

GPR: Gaussian Process Regression

RFR: Random Forest Regression

CGCNN: Convolutional Graph Neural Network

GATGNN: Graph Attention Neural Network

ALIGNN: Atomistic Line Graph Neural Network

CHAPTER 1

Introduction

CHAPTER 1

CHAPTER 1

1.1. Introduction to Thermoelectric Materials and Advanced Design Strategies

The continuous rise in global energy consumption, driven by industrial expansion, urbanization, and technological modernization, has intensified the reliance on fossil fuels, leading to severe environmental and sustainability challenges *[1]*. A substantial fraction of the energy generated worldwide, often exceeding 60% is dissipated as waste heat across a wide range of temperature scales, from industrial processes to automotive exhaust and microelectronic devices. Harnessing this ubiquitous waste heat represents a compelling opportunity for improving overall energy efficiency and reducing carbon emissions, as described in **Figure 1.1**.

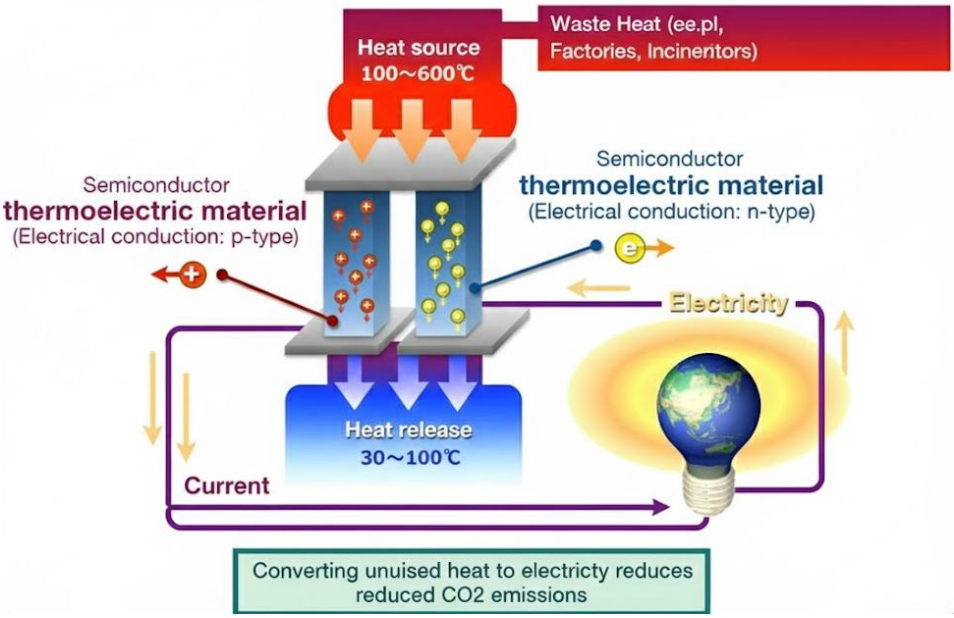


Figure 1.1: Schematic illustration of thermoelectric power generation via the Seebeck effect. A temperature gradient established between a high-temperature heat source (100–600 °C) and a low-temperature heat sink (30–100 °C) drives charge carrier transport in coupled p-type and n-type semiconductor thermoelectric legs, generating an electrical current.

Thermoelectric (TE) materials enable the direct and reversible conversion between thermal and electrical energy via solid-state transport phenomena, most notably the Seebeck and Peltier effects, without the need for moving

parts, working fluids, or greenhouse gas emissions *[2-5]*. In the Seebeck effect, an applied temperature gradient generates an electrical voltage through carrier diffusion, whereas the Peltier effect describes heat absorption or release at material junctions under an applied electric current (**Figure 1.2**). This intrinsic coupling between heat and charge transport makes thermoelectrics particularly attractive for waste-heat recovery, distributed power generation, and solid-state cooling with precise temperature control *[1-3]*. The efficiency of a thermoelectric material is quantified by the dimensionless figure of merit, ZT, defined as *[3]:*

$$ZT = \frac{\sigma S^2 T}{\kappa}, \kappa = \kappa_L + \kappa_e, \quad (1.1)$$

where σ, S, and Tdenote the electrical conductivity, Seebeck coefficient, and absolute temperature, respectively, and $\kappa$is the total thermal conductivity comprising lattice (κ_L) and electronic (κ_e) contributions. Historically, the pursuit of high-performance thermoelectric materials has focused on enhancing the power factor (σS^2) or suppressing thermal conductivity. However, these transport coefficients are strongly interdependent through the underlying electronic structure and scattering mechanisms, imposing a fundamental constraint on independent optimization and constituting a central challenge in thermoelectric materials design.

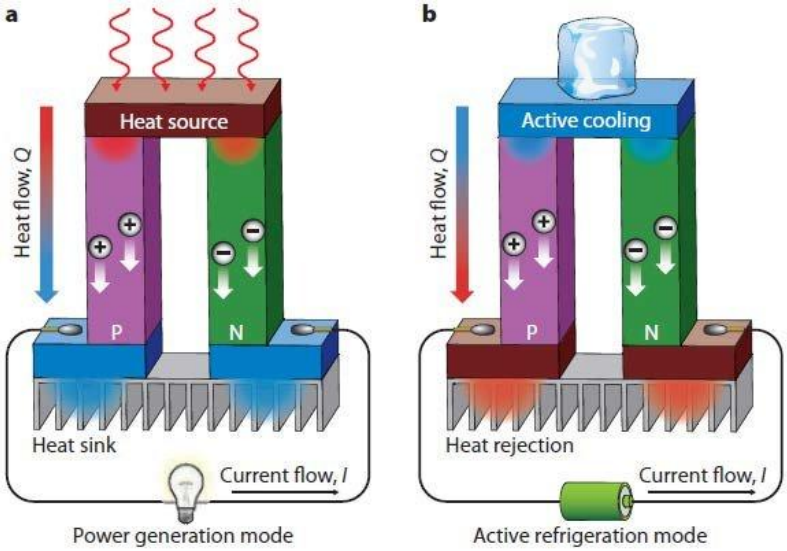


Figure 1.2: Schematic illustration of a thermoelectric (TE) module for (a) Seebeck effect and (b) Peltier effect for power generation and refrigeration, respectively. Figure reprinted with permission from Ref. 5. Copyrights 2010, Springer Nature.

1.2. "Thermoelectric Problem": Decoupling the Conflicting Variables

Despite the apparent simplicity of the *ZT* expression, its optimization is fundamentally constrained by the strong interdependence of electronic and thermal transport parameters Electrical conductivity is governed by the charge carrier concentration (n), mobility (μ), and effective mass (m^*),

$$\sigma = ne\mu = \frac{ne^2\tau}{m^*} \tag{1.2}$$

where τ is the charge carrier relaxation time. In contrast, the Seebeck coefficient increases with carrier effective mass and decreases with carrier concentration, leading to an intrinsic trade-off between σ and S (**Figure 1.3**) *[3,6]*. Consequently, efforts to enhance electrical conductivity often result in reduced power factors.

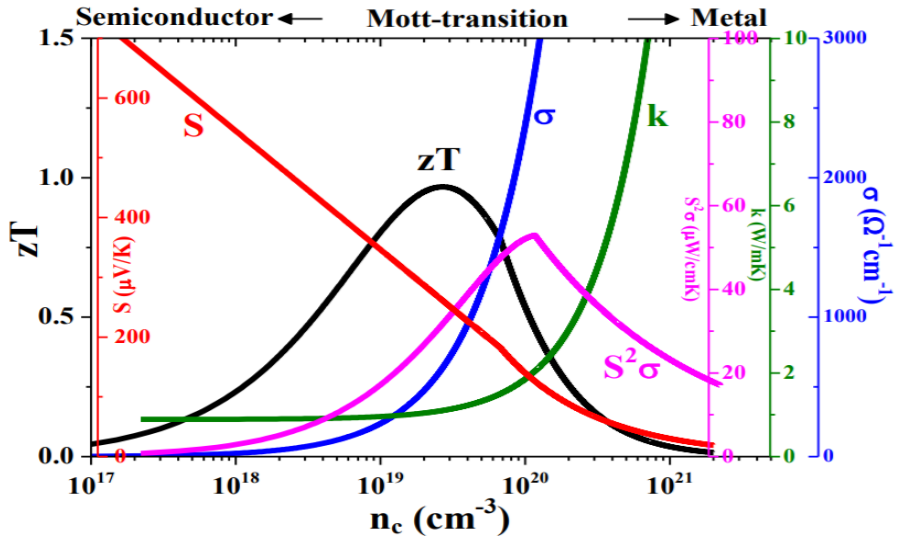


Figure 1.3: Schematic diagram of thermoelectric properties vs. carrier concentration (n_c) reflecting the intrinsic trade-off between TE parameters. Figure reprinted with permission from Ref. 6. Copyrights 2012, Elsevier.

Thermal transport introduces an additional constraint. The electronic contribution to thermal conductivity, κ_e, is intrinsically linked to σ via the Wiedemann–Franz law *[7,8]*,

$$\kappa_e = L\sigma T \tag{1.3}$$

where L is the Lorenz number. As a result, κ_e cannot be reduced independently without adversely affecting electrical transport. In contrast, the lattice contribution κ_L mediated by phonons offers greater tunability and motivating extensive efforts to suppress phonon transport while preserving favorable electronic properties. This recognition has shaped the modern paradigm of thermoelectric research, wherein phonon engineering plays a central role.

1.3. Historical Evolution of Thermoelectric Materials

Although the Seebeck effect was discovered in 1821, practical thermoelectric devices with *ZT* values approaching unity were realized only in the mid-twentieth century, primarily based on Bi_2Te_3-derived alloys. These materials, now referred to as first-generation thermoelectrics, enabled device efficiencies of ~5% and remained the technological standard for several decades *[4,9]*.

Substantial progress remained elusive until the early 1990s, when Hicks and Dresselhaus proposed that reduced dimensionality and quantum confinement could enhance thermoelectric performance by modifying the electronic density of states *[10,11]*. While these theoretical insights emphasized improvements in the power factor, subsequent experimental advances were driven predominantly by dramatic reductions in lattice thermal conductivity rather than purely electronic enhancements. This shift culminated in the emergence of second-generation thermoelectric materials, characterized by the deliberate introduction of nanoscale precipitates, point defects, and compositional disorder to scatter phonons across multiple length scales *[11]*. Bulk systems such as PbTe-based alloys, filled skutterudites, and clathrates achieved *ZT* values in the range of 1.3–1.7,

representing a substantial improvement over earlier materials *[7,12]*.

More recently, third-generation thermoelectrics have been realized through the concurrent integration of multiple optimization strategies, including band convergence, resonant impurity levels, hierarchical phonon scattering, and mobility preservation *[13]*. Materials such as SnSe,*[14]* GeTe,*[15]* $Cu_{2-x}Se$,*[16]* and advanced half-Heuslers have demonstrated *ZT* values approaching or exceeding 2.0, corresponding to predicted device conversion efficiencies surpassing 15–20%.

1.4. Phonon Engineering Strategies for Achieving Ultralow Lattice Thermal Conductivity

The fundamental strategies to achieve the low κ_L focused on discovering new crystalline materials with specific structural and electronic features such as layered structure,*[17]* rattling atoms,*[18]* lone-pair effects,*[19]* and liquid-like ionic movements *[16]* as shown in **Figure 1.4**. Additionally, introducing extrinsic point defects,*[20]* nanostructuring,*[21]* and all scale hierarchical architectures *[7]* have been explored. In each case, understanding the structure-bonding relationships within specific material classes is paramount for identifying the mechanisms responsible for their intrinsically low κ_L values. In recent decades, paradigms including *in situ* nanostructure,*[7,22]* liquid-like lattice,*[16,23]* weak chemical bonding,*[24,25]* constructing hierarchical architectures,*[7]* and off-centered atom approaches,*[26]* have been effectively employed to reduce thermal conductivity and enhance TE efficiency.

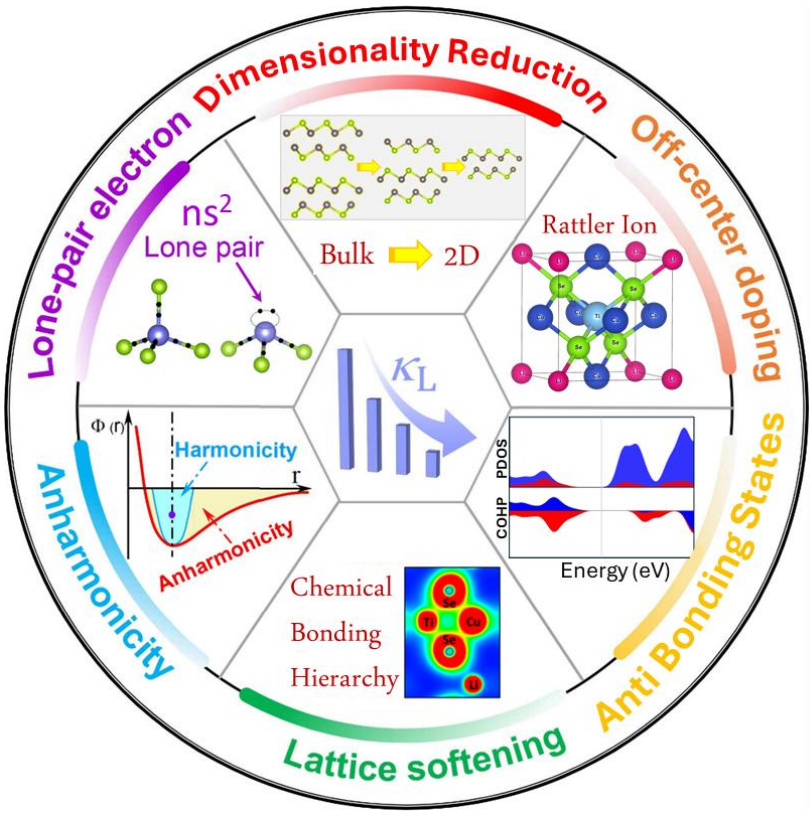


Figure 1.4: Mechanisms for suppressing lattice thermal conductivity (κ_L). Schematic overview of bonding- and defect-driven phonon scattering mechanisms, including lone-pair–induced anharmonicity, lattice softening, antibonding electronic states, reduced dimensionality, and multidimensional defects such as off-center dopants and rattler ions. Their synergistic interplay disrupts phonon transport across length scales, leading to intrinsically low κ_L.

1.4.1. Dimensionality Reduction. Until 1990, there was hardly any significant improvement in the performance of the TE figure of merit beyond the ZT value of 1 for bulk materials. In 1993, Hicks and Dresselhaus introduced the concept of quantum confinement in low-dimensional materials to increase the Power Factor overall, thereby enhancing ZT *[10,11]*. Reducing the thermal conductivity by the effect of dimensionality is a steadfast way to improve TE efficiency. Among the TE-related transport parameters, thermal transport properties uniquely exhibit weak dependence

on electronic transport properties, enabling effective minimization through tailored crystal structure and microstructure design *[20,27]*.

1.4.2. Intrinsic Rattling Effect. Materials containing loosely bound atoms within rigid structural frameworks often exhibit localized, low-frequency vibrational modes commonly described as rattling *[18,28]*. These modes strongly scatter heat-carrying phonons and have been extensively exploited in clathrates and skutterudites. Recently, Cu-based chalcogenides have attracted significant attention due to the emergence of liquid-like Cu sublattices, wherein fast ionic motion induces strong phonon damping and ultralow κ_L *[16, 29-32]*. Materials such as Cu_2Se,*[16]* Cu_3SbSe_3,*[29]* $CsCu_5Se_3$,*[30]* Cu_4TiSe_4,*[31]* and KCu_5Se_3,*[32]* have gained importance for their dynamic disorder with low κ_L can coexist with favorable electronic transport. As such factors can influence the bonding hierarchy, consequently modifying electric or thermal transport properties and leading to an enhancement in thermoelectric (TE) performance.

1.4.3. Stereochemically Active Lone Pairs

Skoug and Morelli have demonstrated a correlation between lone pair electrons, particularly the ns^2 pairs in the pnictogen chalcogenides, and their intrinsically low κ_L *[33]*. The presence of the pnictogen group (As, Sb, Bi) in a +3 oxidation state introduces local structural anharmonicity due to the presence of stereochemically active lone pairs (SCALPs) (**Figure 1.5**), a critical factor in realizing materials with ultralow κ_L *[33]*.The lone pair electrons interact with the valence electrons of chalcogen atoms through electrostatic repulsion, causing lattice anharmonicity, which can be qualitatively explained by the morphology of the electron lone pair orbital cloud *[34]*. It has been demonstrated that this effect is more pronounced in $A^IB^VX^{VI}$ materials compared to $A^IB^{III/V}X^{VI}$ materials (A^I: monovalent, B^{III}: trivalent, B^V: pentavalent, and X^{VI}: chalcogen elements), where the intrinsically low κ_L is substantially affected by SCALPs. For example, the $AgSbSe_2$ (Sb^{3+} has a SCALP) exhibits significantly lower κ_L values of 0.7

$Wm^{-1}K^{-1}$ compared to 1.7 $Wm^{-1}K^{-1}$ of $AgInSe_2$ (In^{3+} does not have a SCALP) *[35]*. Additionally, Cu_3SbSe_4 (with Sb^{5+} cations) has a thermal conductivity of 2.5–3.5 $Wm^{-1}K^{-1}$, much higher than Cu_3SbSe_3 (with Sb^{3+} cations) at 0.7–1.0 $Wm^{-1}K^{-1}$ at room temperature, even though both pnictogen chalcogenides contain the same elements and have similar stoichiometry *[36,37]*. According to the revised lone-pair model, the energy gap between the outermost s and p orbitals of pnictogen cations plays a crucial role in the formation of SCLAPs *[38]*. Although significant, the influence of SCALPs on low κ_L values originating from the nature of chemical bonding remains an elusive aspect in materials science and requires further investigation *[35, 39-41]*. These materials have appeared as the building blocks for the development of efficient energy devices, including thermoelectrics, solar cells, optoelectronic devices, and photocatalysis owing to their semiconducting properties, unique crystal structure, and tune-able stoichiometric composition *[17, 42-46]*.

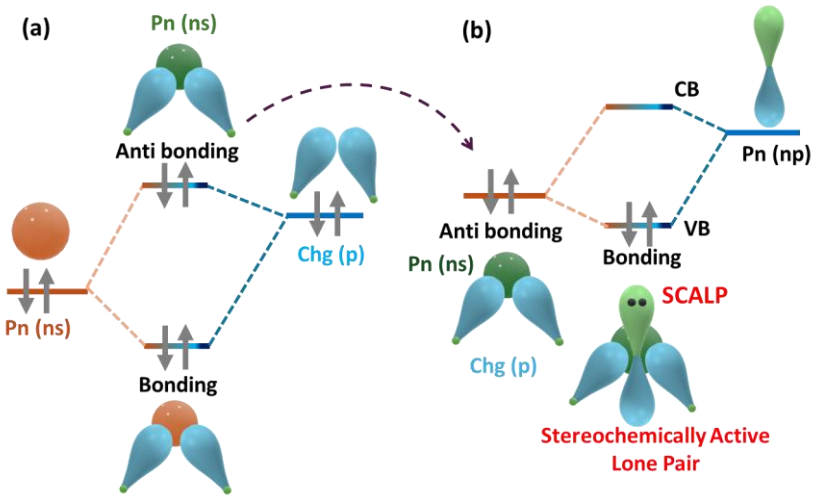


Figure 1.5: Schematics of energy level diagram illustrating stereochemically active lone pairs (SCALP) in pnictogen (Pn) chalcogenide (Chg) materials. Figure reprinted with permission from Ref. 46. Copyrights 2025, American Chemical Society.

In **Figure 1.5(a)** Orbital interactions between the Pn(ns) and Chg(p) orbitals lead to the formation of filled bonding and antibonding combinations.

Owing to the lower energy of Pn(ns) compared to the Chg(p) states, the bonding combination predominantly exhibits Pn(ns) character, and the antibonding combination contains Chg(p) states. **Figure 1.5(b)** indicates the anti-bonding combination is stabilized by orbital coupling with Chg(p), resulting in a filled upper valence band (VB). The contribution of the Chg(p) orbitals to the upper VB creates an asymmetric electron density on Pn, resulting in a stereochemically active lone pair (SCALP).

1.4.4. Bonding Heterogeneity

Bonding heterogeneity plays a crucial role in suppressing lattice thermal conductivity (κ_L) by disrupting coherent phonon transport pathways. In crystalline solids, strong and uniform chemical bonds provide continuous channels for phonon propagation, whereas weak bonds introduce local anharmonicity and large-amplitude atomic vibrations. These weakly bonded atoms act as effective phonon scattering centers, significantly reducing phonon mean free paths. Consequently, materials containing multiple bonding environments exhibit pronounced phonon scattering across a wide frequency spectrum, making bonding heterogeneity a powerful intrinsic mechanism for lowering κ_L *[3,47,48]*.

1.4.5. Higher-Order Phonon Scattering

Phonon–phonon interactions arising from lattice anharmonicity fundamentally limit κ_L. While three-phonon scattering processes dominate at moderate temperatures, recent studies have shown that four-phonon scattering becomes significant in strongly anharmonic materials and at elevated temperatures. These higher-order processes originate from quartic anharmonicity and introduce additional scattering channels, substantially reducing phonon lifetimes and κ_L. Feng and Ruan demonstrated that four-phonon interactions can reduce κ_l by ~30% in silicon at room temperature and become dominant at high temperatures *[49,50]*. Subsequent first-principles studies revealed that four-phonon scattering is essential to accurately reproduce ultralow κ_l in materials *[49,51,52]*.The recognition of

higher-order scattering has important implications for thermoelectric design, as soft bonding, heavy atoms, and structural complexity enhance anharmonicity and activate multi-phonon scattering channels, enabling intrinsically low κ_L (**Figure 1.6**) *[14,47]*.

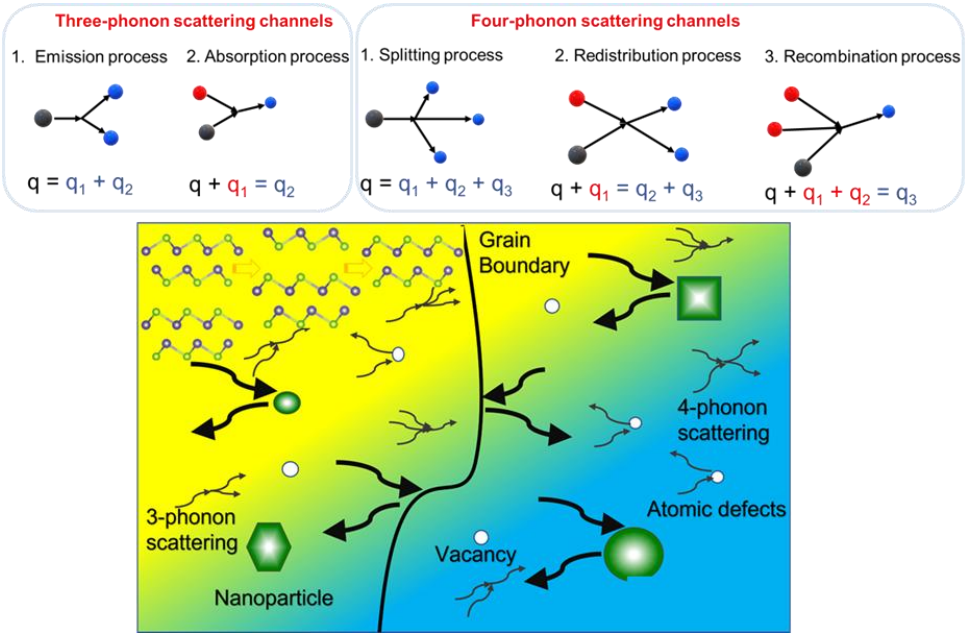


Figure 1.6: Schematic illustration of 3-phonon and 4-phonon scattering processes, highlighting extrinsic phonon scattering induced by grain boundaries, atomic defects, vacancies, and nanoparticles. The combined action of intrinsic anharmonic phonon–phonon interactions and defect-mediated scattering across multiple length scales effectively suppresses κ_L.

1.5. Electronic Structure Engineering for Enhanced Power Factor

Alongside phonon engineering, optimizing the electronic power factor (PF = $S^2\sigma$) is equally critical for achieving high thermoelectric performance. As a purely electronic parameter, the power factor is governed by the band structure and charge carrier scattering mechanisms. Consequently, electronic structure engineering has emerged as a central strategy for enhancing thermoelectric efficiency.

Current approaches to improve power factor primarily include: **(i)** precise control of carrier concentration through chemical doping, which enables

optimization of electrical conductivity while maintaining a reasonable Seebeck coefficient; **(ii)** enhancement of the density-of-states effective mass and Seebeck coefficient via band convergence and resonant impurity levels, which introduce sharp features near the Fermi level and increase carrier energy filtering; and **(iii)** improvement of carrier mobility through modulation doping, which spatially separates charge carriers from ionized impurities to suppress scattering *[8, 53-55]*.

These complementary strategies allow simultaneous enhancement of Seebeck coefficient and electrical conductivity, thereby overcoming their intrinsic trade-off. Recent advances demonstrate that rational electronic structure engineering, when combined with phonon suppression strategies, provides a powerful pathway toward designing high-performance thermoelectric materials with superior power factors *[8,47]*.

1.5.1. Band Convergence

Band convergence refers to the energetic alignment of multiple valleys (or pockets) at the valence or conduction band extrema. The presence of multiple degenerate valleys enhances the Seebeck coefficient by effectively increasing the density-of-states effective mass (m*) without significantly compromising carrier mobility (μ) *[3,8,12]*. These valleys correspond to separate pockets of the Fermi surface located at the same energy, leading to an increased number of conducting channels, as illustrated in **Figure 1.7**. Quantitatively, the total density-of-states effective mass is given by:

$$m^* = N_V^{2/3} m_b^*$$

where N_V is the valley (orbital) degeneracy and m_b^* is the single-valley effective mass *[9,12]*. This relationship demonstrates that increasing band degeneracy enhances the effective mass without directly altering the band curvature, thereby preserving carrier mobility.

Effective chemical doping or alloying is commonly employed to energetically align multiple electronic bands, thereby increasing valley degeneracy—an approach known as band convergence engineering *[8]*.

The primary objective is to improve the Seebeck coefficient while maintaining high electrical conductivity. Under heavy doping conditions, carriers redistribute among multiple valleys, resulting in an enhanced effective mass and thus a higher Seebeck coefficient, without substantially degrading mobility *[3,8]*. Consequently, band convergence significantly enhances the thermoelectric power factor (σS^2) and the figure of merit (ZT) in carrier-optimized systems. This strategy has emerged as a powerful design principle for high-performance thermoelectric materials *[47]*.

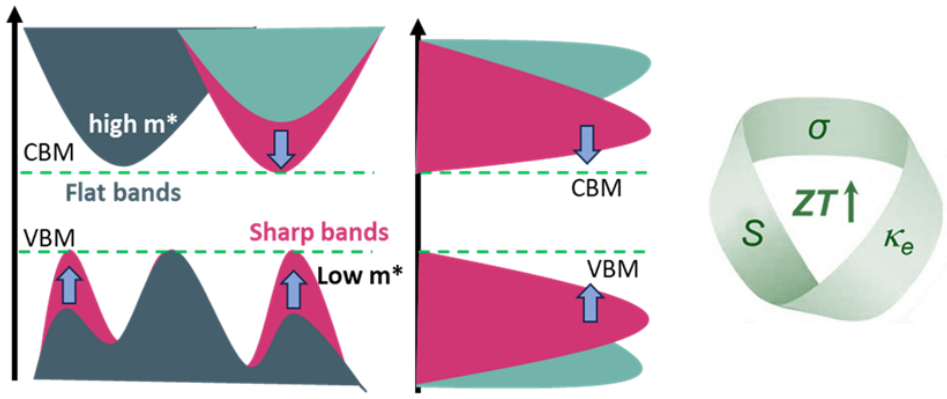


Figure 1.7: Band-structure engineering strategies for enhancing thermoelectric performance. Schematic representation of electronic band convergence and band sharpening, illustrating how flat and sharp band features increase the effective mass and density of states near the Fermi level, thereby enhancing the Seebeck coefficient without severely compromising electrical conductivity. The interdependence of electrical conductivity (σ), Seebeck coefficient (S), and electronic thermal conductivity (κ_e) in determining the thermoelectric figure of merit (ZT) is highlighted. Figure reprinted with permission from Ref. 48. Copyrights 2025, American Chemical Society.

1.6. Chemical Bonding Descriptors for Thermoelectric Design

The κ_L of thermoelectric materials is governed by phonon transport, which is intrinsically linked to the nature of chemical bonding and electronic structure. Chemical bonding descriptors influence all three terms by

modifying bond stiffness, vibrational anharmonicity, and phonon scattering rates. To rationalize low thermal conductivity in complex chalcogenides, these descriptors can be classified into bonding, electronic, orbital-energy, and structural categories, as described in **Figure 1.8(a-d)**.

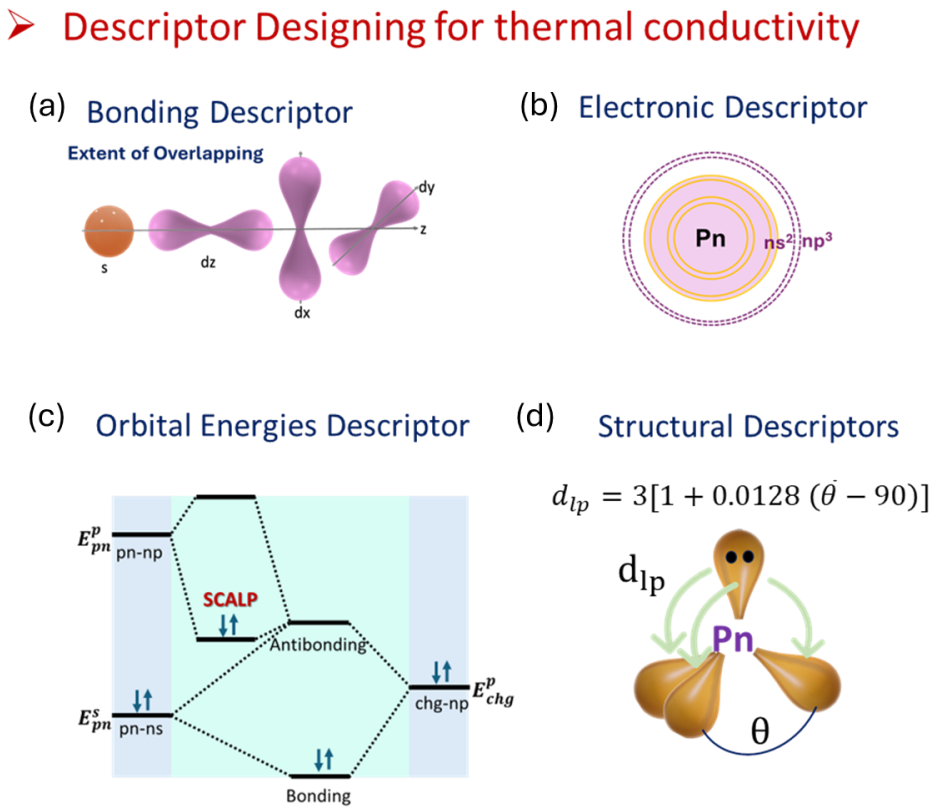


Figure 1.8: Schematic illustration of chemically motivated descriptors governing thermal transport in pnictogen chalcogenides. **(a)** Bonding descriptors quantify the extent of orbital overlap and bond strength anisotropy. **(b)** Electronic descriptors capture charge localization, ionicity, and stereochemically active lone-pair formation. **(c)** Orbital-energy descriptors describe *s*–*p* hybridization and the emergence of antibonding states near the Fermi level (SCALP regime). **(d)** Structural descriptors reflect lone-pair–induced distortions and bonding asymmetry, which collectively enhance phonon anharmonicity and suppress lattice thermal conductivity. Figure reprinted with permission from Ref. 46. Copyrights 2025, American Chemical Society.

1.6.1. Bonding Descriptors: Wuttig and co-workers introduced a chemically intuitive fingerprint to rationalize bonding characteristics in complex solids using two fundamental parameters: the degree of ionicity (r'_σ) and the tendency toward hybridization (r_π^{-1}) in the bonding *[56]*. The parameter r'_σ quantitatively captures the ionic character of chemical bonds, whereas r_π^{-1} describes the extent of covalent bonding arising from orbital hybridization. The latter can be inferred from the energetic separation between the valence s- and p-states, whose relative alignment is a critical prerequisite for the formation of stereochemically active lone pairs (SCALPs), as schematically illustrated in **Figure 1.8(a)** *[38]*. These descriptors explicitly incorporate the contribution of atomic orbital radii to bonding behavior and thereby provide insight into the presence or absence of sp-hybridized bonds between pnictogen and chalcogen species. The parameters are defined as follows:

$$r'_\sigma = \left(\frac{\sum_i n_i r_{p,i}}{\sum_i n_i}\right) - \left(\frac{\sum_j n_j r_{p,j}}{\sum_j n_j}\right) \tag{1.4}$$

$$r_\pi^{-1} = \left[\left(\frac{\sum_i n_i (r_{p,i} - r_{s,i})}{\sum_i n_i}\right) - \left(\frac{\sum_j n_j (r_{p,j} - r_{s,j})}{\sum_j n_j}\right)\right]^{-1} \tag{1.5}$$

Here, r_p and r_s denote the valence radii of the p- and s-orbitals, respectively, and the summations extend over the $i^{\text{th}}$and j^{th} atomic species constituting the material *[56,57]*. The average polarizability ($\overline{\alpha}$) serves as a complementary bonding descriptor, reflecting the degree of electronic charge localization within the lattice.

1.6.2. Electronic Descriptors: Electronic descriptors capture the average electronic configurations and elemental properties that govern bonding polarity, charge distribution, and lattice dynamics. These descriptors include the average valence electron occupations associated with the s- and p-orbitals, denoted as $\bar{V}_s^{(e^-)}$and $\bar{V}_p^{(e^-)}$, respectively. These quantities provide insight into orbital filling, bonding tendencies, and the degree of covalency, all of which influence phonon transport and thermal properties.

To further quantify bonding polarity and ionic character, we incorporate descriptors based on electronegativity, including the average electronegativity between pnictogen and chalcogen species $\bar{\chi}_{\mathrm{pn-chg}}$and the corresponding electronegativity difference $\Delta\chi_{\mathrm{pn-chg}}$. These parameters capture charge-transfer tendencies and electrostatic contributions to bonding. In addition, the ratio of ionic radii between pnictogen and chalcogen ions $\left(r_{\mathrm{pn}}^{+3}{:}\, r_{\mathrm{chg}}^{-2}\right)$ serves as a measure of size mismatch and coordination distortion, while the average atomic weight $(\bar{Z})$ accounts for mass-related phonon scattering effects *[58]*.

1.6.3. Orbital Energy Descriptors: The formation of stereochemically active lone pairs (SCALPs) and the resulting lattice distortions are governed by the interaction strength between cation s-states and anion p-states, as well as by their relative energetic alignment, as schematically illustrated in **Figure 1.8(c)**. According to the revised lone-pair model, a small energy separation between these orbitals promotes strong hybridization, leading to enhanced cation-derived character near the top of the valence band and the emergence of an active lone pair *[38]*. As the chalcogen element is varied down the group from S to Te, the interaction between anion p-states and pnictogen ns-states progressively weakens due to increasing energy mismatch. This reduction in on-site hybridization suppresses lone-pair activity and diminishes the extent of local structural distortion. The strength of these interactions can be quantitatively assessed through orbital-energy descriptors derived from the valence shell energies of the pnictogen and chalcogen atoms, including the s- and p-orbital energies, E_{pn}^{s}, E_{chg}^{s}, E_{pn}^{p}, E_{chg}^{p}, as well as their combined contributions, $E_{\mathrm{pn}}^{(s+p)}$, $E_{\mathrm{chg}}^{(s+p)}$. These descriptors provide a direct measure of orbital-energy alignment and hybridization propensity, enabling the identification of materials prone to SCALP formation, enhanced lattice anharmonicity, and reduced lattice thermal conductivity *[38]*.

1.6.4. Structural Descriptors: Structural descriptors capture the real-space manifestations of bonding asymmetry and electronic effects that govern phonon transport. One of the most effective structural indicators is the number mismatch (δ) between cations and anions, which has been reported as a reliable performance descriptor for lattice thermal conductivity in chalcogenides *[58]*. An increase in the absolute value of the number mismatch ($|\ \delta\ |$) is generally accompanied by a reduction in κ_{L}, reflecting enhanced local structural distortions, rattling-like dynamics, and the presence of stereochemically active lone pairs (SCALPs). The number mismatch is defined as:

$$\delta = \frac{N_{\mathrm{cation}} - N_{\mathrm{anion}}}{N_{\mathrm{anion}}}, \tag{1.6}$$

where N_{cation} and N_{anion} represent the number of cationic and anionic species in the formula unit, respectively *[58]*. In addition to compositional asymmetry, structural complexity plays a significant role in suppressing lattice thermal conductivity. Materials with a large number of atoms in the primitive unit cell (N) exhibit an increased density of phonon branches and scattering channels, which enhances phonon–phonon interactions and reduces heat transport.

The range of covalent radii (r_c) further serves as a descriptor of bond-strength heterogeneity in pnictogen chalcogenides. A broader distribution of covalent radii reflects variations in bond stiffness across the lattice, leading to spatially nonuniform force constants and increased phonon scattering.

A direct structural fingerprint of stereochemically active lone pairs is provided by the lone-pair angle (θ), which quantifies the angular separation between the lone-pair electron density and the bonding pnictogen nporbitals. A smaller θ enhances Coulombic repulsion between the lone pair and bonding electrons, intensifying local lattice distortions and anharmonic vibrational behavior. This effect increases phonon scattering rates and ultimately lowers κ_{L} *[33]*. Further, the lone-pair distance (d_{lp})

describes the spatial extent of the lone-pair electron density relative to the pnictogen nucleus and is given by *[33]:*

$$d_{\mathrm{lp}} = 3[1 + 0.0128(\bar{\theta} - 90)], \quad (1.7)$$

where $\bar{\theta}$ denotes the average lone-pair angle. Together, θ and d_{lp} provide quantitative structural metrics for assessing lone-pair activity, lattice anharmonicity, and their combined impact on lattice thermal conductivity.

1.7. Theoretical Methodology

Density functional theory (DFT) is one of the most extensively employed quantum mechanical frameworks for investigating the electronic properties of matter across disciplines such as chemistry, physics, materials science, and engineering. Owing to its favorable balance between computational efficiency and predictive accuracy, DFT has become a standard tool for exploring ground-state electronic structures and related properties of complex materials. In this chapter, the fundamental principles and key theorems underpinning DFT that are relevant to the present thesis are outlined. Additionally, the specific DFT-based methodologies adopted for atomic-scale simulations and ground-state electronic structure calculations are briefly described, with particular emphasis on their application to thermoelectric materials. At its core, density functional theory is rooted in the time-independent Schrödinger equation, which governs the quantum mechanical behavior of interacting particles:

$$\hat{H}\Psi(x_i, y_i, z_i) = E\Psi(x_i, y_i, z_i) \quad (1.8)$$

where $\hat{H}$ denotes the Hamiltonian operator representing the total energy of the system, Ψ is the many body wavefunction, and E is the corresponding energy eigenvalue for particles located at positions (x_i, y_i, z_i). Although this equation provides a complete description of quantum systems, it can be solved exactly only for a limited number of simple cases, such as the hydrogen atom. For systems containing many interacting electrons particularly extended solids like semiconductors and thermoelectric materials of interest in this work the exact solution becomes

computationally intractable. Consequently, a series of well-founded approximations are introduced to render the problem solvable while retaining sufficient physical accuracy.

1.7.1. Schrödinger Equation for Many-Body Problem

The quantum many-body problem constitutes a foundational challenge in condensed matter physics, quantum chemistry, and materials science with multiple interacting particles. These particles are primarily electrons and atomic nuclei, whose mutual interactions govern the structural, electronic, and functional properties of materials. A quantitative understanding of materials behavior therefore relies on an accurate description of the electronic structure, particularly the ground-state configuration. The intrinsic difficulty of the many-body problem stems from the necessity to explicitly account for interactions among all particles in the system, resulting in an exponentially increasing computational complexity with system size. he quantum mechanical behavior of a many-particle system is formally described by the time-independent Schrödinger equation. For a system consisting of N electrons and M nuclei, the equation can be in equation 1.9.

$$\widehat{H}\Psi(r_1, r_2, \dots, r_N, R_1, R_2, \dots, R_M) = E\Psi(r_1, r_2, \dots, r_N, R_1, R_2, \dots, R_M) \quad (1.9)$$

where $\Psi(r_1, r_2, r_3, \dots, r_N, R_1, R_2, R_3, \dots, R_M)$ is the many-electron wavefunction depending on the coordinates of all electrons (r_i) and the nuclei R_I, E is the energy of the system.

The Hamiltonian operator $\widehat{H}$ contains contributions from both kinetic and potential energy terms associated with electrons and nuclei, and is expressed as (equation 1.10):

$$\widehat{H} = \underbrace{-\frac{\hbar^2}{2m_e}\sum_i \nabla_i^2}_{\widehat{T}_e} \underbrace{-\frac{\hbar^2}{2}\sum_I \frac{\nabla_I^2}{M_I}}_{\widehat{T}_n} + \underbrace{\underbrace{\frac{1}{2}\sum_{i\neq j}\frac{e^2}{4\pi\varepsilon_0 r_{ij}}}_{\widehat{V}_{ee}} \underbrace{-\sum_{i,I}\frac{e^2 Z_i}{4\pi\varepsilon_0 R_{iI}}}_{\widehat{V}_{en}} + \underbrace{\frac{1}{2}\sum_{I\neq J}\frac{e^2 Z_I Z_J}{4\pi\varepsilon_0 R_{IJ}}}_{\widehat{V}_{nn}}}_{\widehat{V}} \quad (1.10)$$

Here, m_e and M_I denote the masses of the electron and the I^{th} nucleus, respectively, $e$is the elementary charge, and Z_I represents the atomic number of the I^{th} nucleus. The first two terms, $\hat{T}_e$ and $\hat{T}_n$, correspond to the kinetic energy operators of the electrons and nuclei. The remaining terms describe the Coulomb interactions arising from electron–electron ($\hat{V}_{ee}$), electron–nucleus ($\hat{V}_{en}$), and nucleus–nucleus ($\hat{V}_{nn}$) interactions.

The explicit inclusion of all these interaction terms renders the exact solution of the many-body Schrödinger equation computationally prohibitive for systems containing more than a few particles. This fundamental limitation motivates the development of approximate theoretical frameworks, such as density functional theory, which enable tractable yet accurate descriptions of complex materials systems.

1.7.2. Born-Oppenheimer Approximation

The full many-body Hamiltonian given in Equation 1.10 for many electrons is too complex to solve and feasible only for small systems like hydrogen atoms and molecules. For extended systems such as solids, which involve many interacting electrons and nuclei, physically motivated approximations are indispensable. A key simplification arises from the substantial mass disparity between electrons and nuclei: the mass of a proton is approximately 1836 times greater than that of an electron. Consequently, nuclear motion occurs on a much slower timescale compared to electronic motion *[59]*.

This separation of timescales forms the basis of the Born–Oppenheimer approximation *[59]*, in which electronic and nuclear degrees of freedom are treated independently. Within this framework, the nuclear kinetic energy can be neglected in the electronic problem, and the nucleus–nucleus interaction energy can be combined with the electron–nucleus interaction to define an external potential acting on the electrons. Physically, this implies that electrons instantaneously adjust to changes in nuclear positions, allowing the nuclei to be treated as classical, quasi-static particles.

Under the Born–Oppenheimer approximation, the total wavefunction factorizes into electronic and nuclear components,

$$\Psi_{\text{total}} = \Psi_{\text{electronic}}\,\Psi_{\text{nuclear}}, \tag{1.11}$$

and equivalently,

$$\Psi(\mathbf{r}_1, \ldots, \mathbf{r}_N, \mathbf{R}_1, \ldots, \mathbf{R}_M) = \Psi(\mathbf{r}_1, \ldots, \mathbf{r}_N)\,\Psi(\mathbf{R}_1, \ldots, \mathbf{R}_M). \tag{1.12}$$

This factorization allows the Hamiltonian to be separated into electronic and nuclear parts. The nuclear Hamiltonian consists of the kinetic energy of the nuclei and the classical electrostatic ion–ion interaction, the latter of which can be evaluated using Ewald summation in periodic systems. The electronic Hamiltonian is then given by

$$\hat{H}_{\text{el}} = \hat{T}_e + \hat{V}_{\text{ext}} + \hat{U}_{ee},$$

or explicitly,

$$\hat{H} = \underbrace{-\frac{\hbar^2}{2m_e}\sum_i \nabla_i^2}_{\hat{T}_e} + \underbrace{\underbrace{\frac{1}{2}\sum_{i\neq j}\frac{e^2}{4\pi\varepsilon_0 r_{ij}}}_{\hat{V}_{ee}} - \underbrace{\sum_{i,I}\frac{e^2 Z_i}{4\pi\varepsilon_0 R_{iI}}}_{\hat{V}_{en}}}_{\hat{V}} \tag{1.13}$$

Although the Born–Oppenheimer approximation significantly reduces the dimensionality of the problem by eliminating explicit nuclear degrees of freedom, the electronic Schrödinger equation still involves $3N$ variables due to electron–electron interactions. As a result, a direct wavefunction-based solution remains impractical for large systems. This limitation motivates a reformulation of the problem in terms of the electron density rather than individual electron coordinates, leading naturally to density functional theory (DFT), which is introduced in the following section.

1.7.3. Density Functional Theory

Density functional theory (DFT) is a quantum mechanical approach that focuses on electron density rather than many-body wavefunctions to describe interacting electron systems. The formal foundation of DFT is provided by the Hohenberg–Kohn theorems *[60]*. The first theorem establishes that the ground-state electron density uniquely determines the

external potential and, consequently, all ground-state properties of the system, including the total energy. In this formulation, the external potential plays a role analogous to the external energy term introduced previously but is expressed as a functional of the electron density rather than explicit electron coordinates. The second Hohenberg–Kohn theorem introduces a variational principle with respect to the electron density, stating that the correct ground-state density minimizes the total energy functional. Accordingly, the total energy of the system can be written as

$$E[\rho(r)] = F[\rho(r)] + E_{ext}[\rho(r)] \geq E_{gs}, \quad (1.14)$$

where ρ(r) is the electron density at a given radius, r, E_{ext} and E_{gs} are the external energy functional and ground state energy and F is the energy functional of the remaining interactions, including the electron kinetic energies, Hartree energy etc. whose form remains to be found. **Figure 1.9** represents the comparative illustration of many body perspective and DFT perspective.

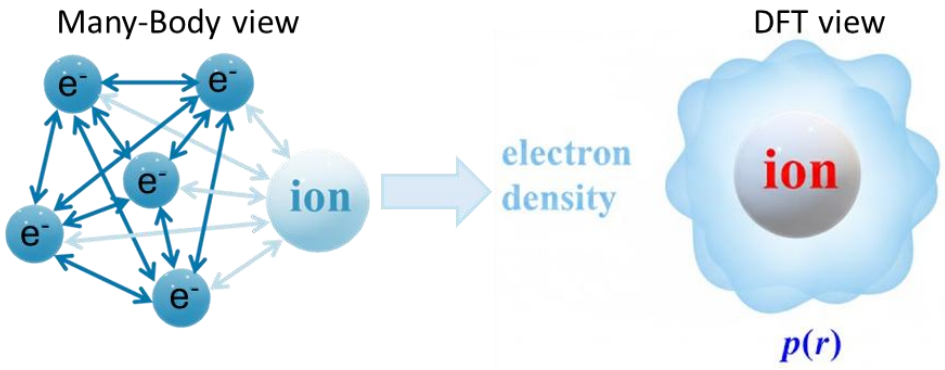


Figure 1.9: Comparative illustration of many body and DFT perspectives.

The practical realization of density functional theory is provided by the Kohn–Sham formalism,*[61,62]* which introduces an auxiliary system of non-interacting electrons designed to reproduce the exact ground-state electron density of the interacting system. Within this framework, the universal functional $F[\rho]$is decomposed as

$$F[\rho(\mathbf{r})] = T_s[\rho] + E_H[\rho] + E_{xc}[\rho], \quad (1.15)$$

where $T_s[\rho]$ is the kinetic energy of the non-interacting Kohn–Sham

electrons, $E_H[\rho]$ is the classical Hartree energy, and $E_{xc}[\rho]$ is the exchange–correlation functional. The latter incorporates all remaining many-body effects, including exchange interactions arising from the Pauli exclusion principle and correlation effects due to electron–electron Coulomb repulsion. Since the exact form of $E_{xc}[\rho]$ is unknown, it must be approximated in practical calculations. By reducing the interacting many-electron problem to a set of self-consistent single-particle equations, the Kohn–Sham approach significantly lowers the computational complexity, enabling DFT calculations for systems containing hundreds to thousands of atoms. This favorable balance between accuracy and efficiency has established DFT as the most widely used electronic structure method for determining ground-state properties of atoms, molecules, and solids. The conceptual origins of DFT can be traced to the Thomas–Fermi model *[61,62]*, which treated electrons as a homogeneous non-interacting gas but failed to capture essential interaction effects. The modern, formally exact foundation of DFT was established by the Hohenberg–Kohn theorems, with the Kohn–Sham formulation providing the practical framework used in contemporary electronic structure calculations *[63]*.

1.7.3.1. The Hohenberg-Kohn Theorem

In 1964, Hohenberg and Kohn established the theoretical foundation of DFT by demonstrating that the electronic properties of an interacting many-electron system can be expressed uniquely in terms of the electron density $\rho(\mathbf{r})$ in the presence of an external potential. Their work is formalized through two fundamental theorems, both centered on the ground-state electron density.

Theorem I: *"For a system of interacting electrons subject to an external potential $V_{ext}(\mathbf{r})$, the ground-state electron density $\rho(\mathbf{r})$ uniquely determines the external potential up to an additive constant."*

This implies that the Hamiltonian, and all ground-state properties, are uniquely described by $\rho(r)$.

Theorem II: *"A universal functional for the Energy $E[\rho]$ of the electron density, valid for any external potential. For a given V_{ext}, the exact ground-state energy corresponds to the global minimum of this functional, and the electron density that achieves this minimum is the exact ground-state density $\rho_0(\boldsymbol{r})$."*

Here, $\rho_0(\boldsymbol{r})$ uniquely determines V_{ext}, it also determines the corresponding ground-state wavefunction.

Combining the above theorems, the total ground-state energy can be expressed as a functional of the electron density,

$$E_{HK}[\rho] = F_{HK}[\rho] + \int d^3r V_{ext}(r)\rho(r) \quad (1.16)$$

where $F_{\text{HK}}[\rho]$is a universal functional containing all internal contributions to the energy, including the kinetic energy and electron–electron interactions. Accordingly, the internal energy functional may be written as,

$$E_{HK}[\rho] = T[\rho] + E_{int}[\rho] \quad (1.17)$$

This functional is independent of the external potential and depends solely on the electron density. Although the Hohenberg–Kohn theorems guarantee the existence of $F_{\text{HK}}[\rho]$, they do not provide its explicit form, necessitating the use of approximations in practical implementations. The exact ground-state energy E_0 is obtained by minimizing the energy functional with respect to the density,

$$\frac{\delta E_{\text{HK}}[\rho]}{\delta \rho(\mathbf{r})} \Big|_{\rho=\rho_0} = 0 \quad (1.18)$$

The Hohenberg–Kohn theorems thus establish a rigorous and unique relationship between the ground-state electron density and the total energy, forming the conceptual basis of modern DFT. However, while these theorems define the exact framework, they do not specify a practical route for constructing the energy functional. This limitation is addressed by the Kohn–Sham formalism, which provides an efficient and accurate scheme for treating exchange and correlation effects and enables the computation of ground-state properties of interacting many-electron system.

1.7.3.2. Kohn-Sham Formalism

In 1965, Kohn and Sham proposed that the exact ground-state electron density of an interacting many-electron system can be reproduced by an auxiliary system of non-interacting particles moving in an effective potential, as schematically illustrated in **Figure 1.10**. This key insight extends the Hohenberg–Kohn framework by replacing the interacting electron problem with a formally equivalent non-interacting reference system that yields the same electron density.

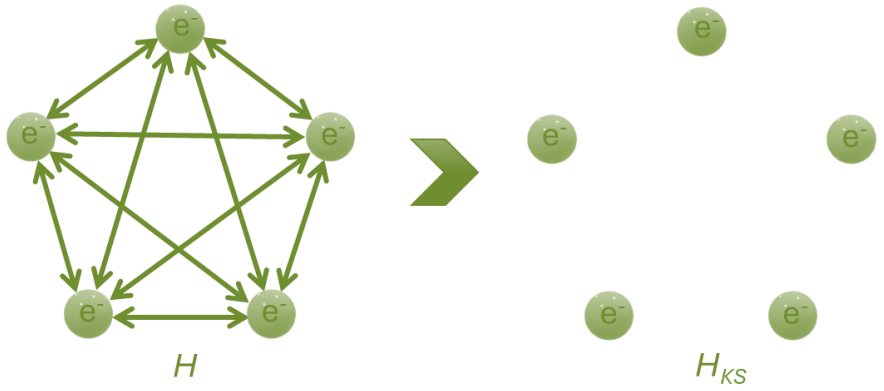


Figure 1.10: Illustration of interacting and non-interacting many-electron systems having the same ground-state electron density.

Within the Kohn–Sham formalism, the total energy functional is expressed as

$$E_{\mathrm{KS}}[n] = T_s[n] + \int d^3r\, V_{\mathrm{ext}}(\mathbf{r})n(\mathbf{r}) + \frac{1}{2}\int d^3r\, d^3r' \frac{n(\mathbf{r})n(\mathbf{r}')}{|\,\mathbf{r}-\mathbf{r}'\,|} + E_{xc}[n], \tag{1.19}$$

where $T_s[n]$ is the kinetic energy of the non-interacting electron system, the second term represents the interaction with the external potential arising from the nuclei, and the third term is the classical Hartree contribution describing electron–electron Coulomb repulsion. The final term, $E_{xc}[n]$, is the exchange–correlation functional, which incorporates all remaining many-body effects beyond the mean-field description. The nucleus–nucleus Coulomb interaction enters the total energy as an additive constant.

Since the exact analytical form of $E_{xc}[n]$ is unknown, the practical success of the Kohn–Sham approach relies on physically motivated approximations to this functional. According to the second Hohenberg–Kohn theorem, the

ground-state density is obtained by minimizing the Kohn–Sham energy functional with respect to the electron density. This minimization leads to a set of single-particle Schrödinger-like equations,

$$\widehat{H}_{\mathrm{KS}}\,\phi_i(\mathbf{r}) = \left[-\frac{\hbar^2}{2m_e}\nabla^2 + V_{\mathrm{KS}}(\mathbf{r})\right]\phi_i(\mathbf{r}) = \varepsilon_i\phi_i(\mathbf{r}), \qquad (1.20)$$

where $\phi_i(\mathbf{r})$ are the Kohn–Sham orbitals and ε_i are the corresponding eigenvalues. The effective Kohn–Sham potential is given by

$$V_{\mathrm{KS}}(\mathbf{r}) = V_{\mathrm{ext}}(\mathbf{r}) + \int d^3r' \frac{n(\mathbf{r}')}{|\mathbf{r}-\mathbf{r}'|} + V_{xc}(\mathbf{r}), \qquad (1.21)$$

with the exchange–correlation potential defined as the functional derivative

$$V_{xc}(\mathbf{r}) = \frac{\delta E_{xc}[n]}{\delta n(\mathbf{r})} \qquad (1.22)$$

Although the Kohn–Sham orbitals are not true many-electron wavefunctions and do not possess a direct physical interpretation, they provide a convenient mathematical construct for determining the ground-state electron density. The density is obtained from the occupied Kohn–Sham orbitals as

$$\rho(\mathbf{r}) = \sum_i |\,\phi_i^{\mathrm{KS}}(\mathbf{r})\,|^2 \qquad (1.23)$$

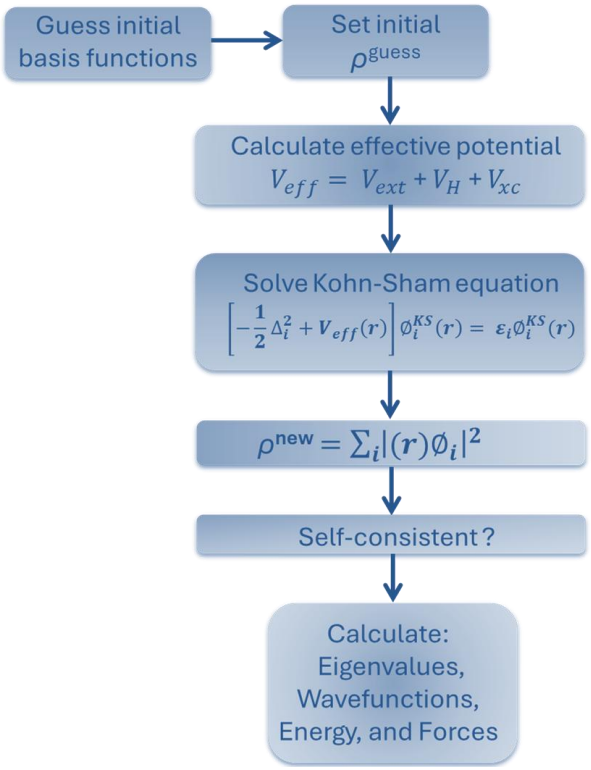


Figure 1.11: Flow chart of the self-consistent loop for the solution of Kohn-Sham equations.

To obtain the ground-state electron density, the Kohn–Sham equations are solved self-consistently using an iterative procedure, as outlined in the following algorithm (**Figure 1.11**). The process begins with an initial guess for the electron density, ρ(r). Using this density, the effective Kohn–Sham potential, $V_{\text{eff}}(r)$, is constructed, incorporating the external, Hartree, and exchange–correlation contributions. The resulting Kohn–Sham equations are then solved to yield the Kohn–Sham orbitals, $\phi_i^{\text{KS}}(r)$, from which a new electron density is calculated. This updated density is subsequently used as input for the next iteration. The cycle is repeated until self-consistency is achieved, i.e., until the input and output electron densities converge within a predefined tolerance.

1.7.4. Exchange-Correlation Functionals

Since an exact analytical expression for the exchange–correlation energy is not known, several approximate exchange–correlation (xc) functionals have been developed to balance computational efficiency and predictive accuracy. The overall reliability of density functional theory calculations critically depends on the quality of the chosen E_{xc}, as it encapsulates all many-body exchange and correlation effects beyond the classical electrostatic interactions.

1.7.4.1. Local Density Approximation (LDA)

The simplest and earliest exchange–correlation functional within the Kohn–Sham framework is the Local Density Approximation (LDA) *[63]*. In LDA, the exchange–correlation energy is treated locally by assuming that the electron density at each point in space behaves as a homogeneous electron gas. This approximation is motivated by the fact that the uniform electron gas possesses the simplest known form of the exchange–correlation

functional and provides reasonable accuracy for a wide range of systems. The LDA exchange–correlation energy is expressed as

$$E_{\mathrm{xc}}^{\mathrm{LDA}} = \int \rho(\mathbf{r})\, \varepsilon_{\mathrm{xc}}^{\mathrm{uni}}[\rho(\mathbf{r})]\, d\mathbf{r} \tag{1.16}$$

where $\varepsilon_{\mathrm{xc}}^{\mathrm{uni}}$ denotes the exchange–correlation energy density of a uniform electron gas evaluated at the local electron density $\rho(\mathbf{r})$. This term can be decomposed into exchange (ε_x) and correlation (ε_c) contributions. While the exchange component admits an analytical expression, the correlation energy lacks a closed-form solution and is therefore obtained from numerical parameterizations based on quantum Monte Carlo calculations combined with interpolation schemes *[64]*.

Despite its simplicity, LDA performs remarkably well for several model systems and is particularly suited for systems with slowly varying electron densities, such as simple metals *[65]*. Moreover, subsequent studies have demonstrated that LDA can also yield reasonably accurate structural and energetic properties for semiconductors and insulators *[66,67]*. However, LDA suffers from well-known limitations, including: (i) systematic overestimation of cohesive and binding energies, (ii) insufficient spatial localization of electrons, making it less reliable for systems involving localized $d$and $f$electrons, and (iii) the absence of long-range correlation effects, such as van der Waals interactions, due to its inherently local nature.

1.7.4.2. Generalized-Gradient Approximation (GGA)

The Generalized Gradient Approximation (GGA) represents a significant improvement over the Local Density Approximation by incorporating not only the local electron density but also its spatial gradient $\nabla\rho(\mathbf{r})$into the exchange–correlation functional *[68,69]*. Within GGA, the exchange–correlation energy is expressed as a gradient-corrected modification of the LDA energy density,

$$E_{xc}^{GGA} = \int \rho\,(\boldsymbol{r})\varepsilon_{xc}^{LDA}[\rho(\boldsymbol{r}), \nabla\rho(\boldsymbol{r})]d\boldsymbol{r} \tag{1.24}$$

$$E_{xc}^{GGA} = \int \varepsilon_x^{uni}\, \rho(\boldsymbol{r}) F_{xc}[n(\boldsymbol{r}), \nabla\rho(\boldsymbol{r})]\rho(\boldsymbol{r})d\boldsymbol{r}, \tag{1.25}$$

where $\varepsilon_x^{\text{uni}}$ denotes the exchange energy density of a uniform electron gas and F_{xc} is a dimensionless enhancement factor accounting for gradient corrections. Several widely used GGA functionals have been proposed, including PW92 *[70]*, B88 *[71]*, B95 *[72]*, LYP *[73,74]*, and PBE *[75-77]*. A well-known deficiency of both LDA and GGA is the severe underestimation of electronic band gaps, often by ~50% or more. This originates from the Kohn–Sham eigenvalue formulation, which neglects the derivative discontinuity associated with electron addition and removal, artificially narrowing the band gap. To address this limitation, higher-rung approximations have been developed. Meta-GGA functionals, such as the Tran–Blaha modified Becke–Johnson (mBJ) functional *[78,79]*, incorporate higher-order density derivatives and substantially improve band-gap predictions, although they tend to underestimate band widths and are therefore unsuitable for transport calculations *[79]*.

Hybrid functionals provide a more balanced description by mixing a fraction of exact Hartree–Fock exchange with GGA exchange,

$$E_{\text{xc}}^{\text{hybrid}} = E_{\text{xc}}^{\text{GGA}} + \alpha(E_x^{\text{HF}} - E_x^{\text{GGA}}), \tag{1.26}$$

where α is the fraction of exact exchange. This approach compensates for the opposing errors of GGA and Hartree–Fock. Two widely used hybrid functionals are PBE0, which includes 25% Hartree–Fock exchange and performs well for wide-band-gap materials, and the screened Heyd–Scuseria–Ernzerhof (HSE06) functional *[80,81]*, which applies short-range exact exchange and reverts to GGA behavior at longer distances. Due to its balanced accuracy and computational efficiency, HSE06 is employed for all electronic structure calculations in this work. Although hybrid functionals deliver substantially improved electronic properties, they are computationally demanding typically an order of magnitude more expensive than GGA and are therefore reserved for calculations where accurate electronic descriptions are essential.

1.7.4.3. van der Waals Density Functional (vdW-DF) Method

Accurate electronic-structure calculations for sparse systems must simultaneously capture (i) strong local chemical bonding and (ii) weak, long-range non-local dispersion interactions. Such sparse systems including van der Waals (vdW) complexes, layered materials, soft matter, and biomolecules are widespread and characterized by interatomic separations where long-ranged vdW forces play a decisive role. Conventional LDA and GGA functionals fail to describe these interactions adequately due to their inherently local or semi-local nature. Consequently, this thesis employs van der Waals density functionals (vdW-DF) to reliably describe both electronic structure and related properties *[82,83]*.

In 2004, the vdW-DF formalism was introduced as a non-local approximation to the exchange–correlation energy, explicitly incorporating long-range dispersion interactions within the DFT framework *[84].* A key advantage of vdW-DF is its unified treatment of vdW forces at the same electronic level as ionic, covalent, metallic, and hydrogen bonding, enabling a consistent description across diverse material classes. This approach has demonstrated robust performance for a wide range of weakly bonded systems. Within the vdW-DF framework, the total Kohn–Sham energy functional is given by

$$E^{\text{vdW-DF}}[n] = T_s[n] + E_H[n] + \int V_{\text{ext}}(\mathbf{r})n(\mathbf{r})\, d\mathbf{r} + E_{\text{xc}}^{\text{vdW-DF}}, \qquad (1.27)$$

where T_s is the kinetic energy of non-interacting electrons, E_H is the Hartree energy, and V_{ext} represents the external potential due to nuclei. The defining feature of vdW-DF lies in its treatment of exchange–correlation energy,

$$E_{\text{xc}}^{\text{vdW-DF}} = E_x^{\text{GGA}} + E_c^{\text{LDA}} + E_c^{\text{nl}}, \qquad (1.28)$$

where the exchange energy is taken from a GGA functional, the local correlation energy from LDA, and the non-local correlation term E_c^{nl} explicitly accounts for vdW interactions. Unlike LDA and GGA, vdW-DF introduces non-locality directly into the correlation energy, enabling an

accurate description of dispersion forces. The non-local correlation energy is expressed as a six-dimensional integral,

$$E_c^{\mathrm{nl}}[n] = \frac{1}{2}\int d\mathbf{r}\int d\mathbf{r}'\, n(\mathbf{r})\,\Phi(\mathbf{r},\mathbf{r}')\,n(\mathbf{r}'), \tag{1.29}$$

where $\Phi(\mathbf{r},\mathbf{r}')$ is a universal kernel function that asymptotically reproduces the characteristic $1/r^6$ behavior of vdW interactions. The kernel depends on the electron density and its gradients through a density-dependent length scale defined by

$$q_0(\mathbf{r}) = \frac{\varepsilon_{\mathrm{xc}}^0}{\varepsilon_x^{\mathrm{LDA}}}\,k_F(\mathbf{r}), \tag{1.30}$$

where $k_F = (3\pi^2 n)^{1/3}$is the Fermi wavevector.

The quantity $\varepsilon_{\mathrm{xc}}^0$ incorporates gradient corrections to the LDA exchange–correlation energy,

$$\varepsilon_{\mathrm{xc}}^0 \approx \varepsilon_{\mathrm{xc}}^{\mathrm{LDA}} - \frac{Z_{ab}}{9}\left(\frac{\nabla n}{2k_F n}\right)^2, \tag{1.31}$$

with $Z_{ab} = -0.8491$ for the vdW-DF functional. This parameter, while density dependent, is determined from first-principles considerations and governs the strength of gradient corrections. By explicitly incorporating non-local correlation effects, vdW-DF overcomes a major limitation of conventional DFT and enables a physically sound description of dispersion-dominated systems, making it particularly suitable for the sparse materials investigated in this thesis.

1.7.5. Projector Augmented Wave (PAW) Method

In first-principles simulations of electronic nanoscale devices, the Kohn–Sham (K–S) formalism of density functional theory provides an efficient and rigorous framework for describing many-electron systems. However, an explicit treatment of all electrons is computationally prohibitive, particularly for heavy elements, because tightly bound core electrons exhibit rapidly oscillating wavefunctions and contribute negligibly to chemical bonding. To overcome this limitation, a frozen-core approximation is employed, in which the nucleus and core electrons are

incorporated into an effective ionic potential, while only the chemically active valence electrons are treated explicitly. This simplification is achieved through the use of pseudopotentials, which replace the strong Coulomb potential of the nucleus and inert core states with a smoother effective potential. The pseudisation procedure removes the nodal structure from valence wavefunctions, enabling their accurate representation using a significantly reduced plane-wave basis set. Among the available schemes, the projector augmented wave (PAW) method, as implemented in the Vienna *ab initio* Simulation Package (VASP), combines the accuracy of all-electron approaches with the computational efficiency of pseudopotential methods *[85]*. Within the PAW framework, the true all-electron wavefunction is reconstructed from a smooth pseudo-wavefunction augmented by atom-centered projector functions, allowing an accurate description of valence charge density at a comparatively low computational cost.

Earlier developments in pseudopotential theory include norm-conserving pseudopotentials, which enforce agreement between all-electron and pseudo wavefunctions outside a chosen core radius while preserving charge normalization and eigenvalues for a reference atomic configuration *[86,87]*. In VASP, pseudopotentials are generated following well-established formalisms that ensure high transferability across diverse chemical environments, making them particularly well suited for large-scale simulations of nanoscale and condensed-matter systems.

1.7.6. Electronic Structure of Periodic Solids

The electronic-structure methods discussed above are formally developed for finite systems containing a limited number of electrons, such as atoms and molecules. In contrast, crystalline solids are inherently periodic and contain an effectively infinite number of electrons, rendering a direct application of these methods impractical. To extend density functional theory (DFT) to crystalline systems, periodic boundary conditions are

introduced. Owing to the translational symmetry of a crystal lattice, the effective Kohn–Sham potential is periodic and satisfies

$$V_{\text{eff}}(\mathbf{r}+\mathbf{R}) = V_{\text{eff}}(\mathbf{r}), \tag{1.32}$$

where **R** is a lattice translation vector.

This periodicity enables the application of Bloch's theorem,*[88]* which states that the single-particle Kohn–Sham wavefunctions can be written as

$$\Psi_{i\mathbf{k}}(\mathbf{r}) = e^{i\mathbf{k}\cdot\mathbf{r}} u_{i\mathbf{k}}(\mathbf{r}) \tag{1.33}$$

where $\mathbf{k}$ is the crystal wave vector and $u_{i\mathbf{k}}(\mathbf{r})$ is a function with the periodicity of the lattice, i.e., $u_{i\mathbf{k}}(\mathbf{r}) = u_{i\mathbf{k}}(\mathbf{r}+\mathbf{R})$.

The periodic function $u_{i\mathbf{k}}(\mathbf{r})$ can be expanded in a Fourier series over reciprocal lattice vectors $\mathbf{G}$,

$$u_{i\mathbf{k}}(\mathbf{r}) = \textstyle\sum_{\mathbf{G}} c_{i\mathbf{G}}\ e^{i\mathbf{G}\cdot\mathbf{r}} \tag{1.34}$$

where the reciprocal lattice vectors satisfy $\mathrm{G}\cdot\mathrm{R} = 2\pi m$, with m being an integer. Substituting Eq. (1.35) into Eq. (1.34) yields the Bloch states expressed as a linear combination of plane waves,

$$\Psi_{i\mathbf{k}}(\mathbf{r}) = \sum_{\mathbf{G}} c_{i(\mathbf{k}+\mathbf{G})}\ e^{i(\mathbf{k}+\mathbf{G})\cdot\mathbf{r}} \tag{1.35}$$

This plane-wave representation transforms the many-electron problem of a periodic solid into a problem defined over reciprocal space. Although the number of possible **k**-points is formally infinite, the smooth variation of $\Psi_{i\mathbf{k}}(\mathbf{r})$ across neighboring **k**-points allows the electronic structure to be accurately described by sampling a finite and discrete set of **k**-points within the Brillouin zone. Consequently, efficient Brillouin-zone sampling schemes enable accurate and tractable calculations of electronic properties in crystalline solids.

1.7.7. Bloch's Theorem

In crystalline solids, computational complexity can be significantly reduced by exploiting lattice periodicity. Instead of simulating the entire material, only the smallest repeating unit, the unit cell is considered, with periodic boundary conditions imposed such that each atom interacts with atoms in

the same cell and their periodic images *[89]*. This periodicity is reflected in the crystal potential,

$$V(\mathbf{r}) = V(\mathbf{r} + \mathbf{R}) \tag{1.36}$$

where **R** is a lattice translation vector. Under such a periodic potential, electron states are described by Bloch's theorem, which states that the Kohn–Sham wavefunctions take the form

$$\psi_{\mathbf{k}}(\mathbf{r}) = u_{\mathbf{k}}(\mathbf{r})e^{i\mathbf{k}\cdot\mathbf{r}} \tag{1.37}$$

where $u_{\mathbf{k}}(\mathbf{r})$ has the periodicity of the lattice and **k** is a wavevector in reciprocal space. Upon translation by a lattice vector **R**, the wavefunction satisfies

$$\psi_{\mathbf{k}}(\mathbf{r} + \mathbf{R}) = e^{i\mathbf{k}\cdot\mathbf{R}}\psi_{\mathbf{k}}(\mathbf{r}) \tag{1.38}$$

ensuring consistency with periodic boundary conditions. This formalism enables the electronic structure of an infinite periodic solid to be fully described using a single unit cell.

1.7.8. k-Points

In addition to real-space simulations of the unit cell, periodic crystals are more naturally described in reciprocal (momentum) space, commonly referred to as *k*-space. Owing to lattice periodicity, electronic states need only be evaluated within the first Brillouin zone (BZ), the reciprocal-space counterpart of the primitive unit cell, as all other zones are equivalent by translational symmetry. This reduction significantly lowers computational cost while retaining full physical accuracy. In practical implementations such as VASP, calculations are performed by efficiently switching between real and reciprocal space using fast Fourier transforms, depending on which representation is computationally favorable.

Many key material properties, including electronic band structures, phonon dispersions, and several thermal transport coefficients, are naturally expressed in reciprocal space *[89,90]*. Phonon properties are formulated in *q*-space, which is related to *k*-space through the relation $\mathbf{q} = 2\pi\mathbf{k}$, reflecting the reciprocal lattice formalism.

Due to finite computational resources, Brillouin zone integrations are carried out over a discrete set of *k*-points rather than continuously. These sampling points are typically chosen to include high-symmetry locations, such as the Γ-point $(0, 0, 0)$, where band extrema and critical electronic features frequently occur. Most calculations employ a Γ-centered Monkhorst–Pack mesh, which provides a uniform and systematic sampling of reciprocal space. For electronic band-structure calculations, additional *k*-points are explicitly selected along high-symmetry paths to resolve dispersion relations with high resolution.

1.7.9. Basis Sets

In electronic structure calculations, the electronic wavefunctions must be expanded in a suitable basis set, which plays a decisive role in determining the accuracy and efficiency of the simulations. Although localized basis functions such as atomic orbitals or real-space grids are commonly used, they can introduce Pulay stress when the basis set is incomplete *[91]*. This artificial stress arises when Hellmann–Feynman forces are evaluated and can lead to spurious forces that depend on atomic positions rather than physical interactions *[92]*.

To avoid this limitation, VASP employs a plane-wave basis set, which is independent of both atomic positions and chemical species. In the limit of an infinite basis, plane waves form a complete and unbiased representation, thereby eliminating Pulay stress *[93]*. In practice, however, the basis set is truncated at a finite kinetic energy, defined by the plane-wave energy cutoff (ENCUT) specified in the INCAR file. The ENCUT value is systematically converged to ensure accurate total energies and forces, in direct analogy to k-point convergence. Despite convergence of both the k-point mesh and energy cutoff, residual Pulay stress may still arise during variable-cell relaxations, where changes in lattice parameters alter the effective basis. To minimize this effect, the energy cutoff is typically increased by

approximately 30% during structural optimizations, leading to more reliable stress tensors and equilibrium geometries.

1.7.10. Boltzmann Transport Equation

The Boltzmann transport equation (BTE), originally formulated by Ludwig Boltzmann in 1872, provides a statistical description of particle transport under external perturbations *[94-96]*. In crystalline solids, it governs the transport of electrons under electric field and temperature gradients, and phonons under temperature gradients. Within the relaxation time approximation, the electronic conductivity tensor contribution from band i at wavevector $\mathbf{k}$ is given by

$$\sigma_{mn}(i,\mathbf{k}) = e^2\tau_{i\mathbf{k}}v_m(i,\mathbf{k})v_n(i,\mathbf{k}), \tag{1.39}$$

where $e$is the elementary charge, $\tau_{i\mathbf{k}}$ is the carrier relaxation time, and v_m and v_n are the components of the group velocity. Expressed in terms of energy, the conductivity tensor becomes

$$\sigma_{mn}(\varepsilon) = \frac{1}{N}\sum_{i,\mathbf{k}}\sigma_{mn}\,(i,\mathbf{k})\delta(\varepsilon-\varepsilon_{i\mathbf{k}}), \tag{1.40}$$

where $N$is the total number of $\mathbf{k}$-points and $\varepsilon_{i\mathbf{k}}$ is the band energy. The electronic group velocity is obtained from the band dispersion as

$$\mathbf{v}_{i\mathbf{k}} = \frac{1}{\hbar}\nabla_{\mathbf{k}}\varepsilon_{i\mathbf{k}}, \tag{1.41}$$

demonstrating that charge transport is directly linked to the curvature of the electronic bands. Using these quantities, the transport coefficients are formulated through the Onsager relations, defined as

$$L^{(\alpha)}(\mu,T) = \int \sigma(\varepsilon)(\varepsilon-\mu)^{\alpha}\left(-\frac{\partial f(\varepsilon,T)}{\partial\varepsilon}\right)d\varepsilon, \tag{1.42}$$

where $\mu$is the chemical potential (equal to the Fermi energy E_F), and $f(\varepsilon,T)$ is the Fermi–Dirac distribution,

$$f(\varepsilon,T) = \frac{1}{\exp\left[(\varepsilon-\mu)/(k_BT)\right]+1} \tag{1.43}$$

From the Onsager coefficients, the macroscopic electronic transport properties are obtained as

$$\sigma = L^{(0)}, \tag{1.44}$$

$$S = \frac{L^{(1)}}{eTL^{(0)}}, \tag{1.45}$$

$$\kappa_e = \frac{1}{e^2T}\left(\frac{[L^{(1)}]^2}{L^{(0)}} - L^{(2)}\right), \tag{1.46}$$

where σ is the electrical conductivity, S is the Seebeck coefficient, and κ_e is the electronic contribution to the thermal conductivity. It is important to note that transport is dominated by electronic states near the Fermi level, as the derivative of the Fermi–Dirac distribution sharply weights contributions around μ. While the electronic thermal conductivity is often approximated using the Wiedemann–Franz law with a fixed or temperature-dependent Lorenz number, in this work κ_e is explicitly calculated from the Onsager coefficients to ensure higher accuracy, particularly for non-metallic and thermoelectric materials.

1.7.11. Relaxation Time Approximations

Most quantities appearing in the Boltzmann transport formalism can be obtained directly from electronic energies and densities of states calculated using density functional theory (DFT), for example from VASP outputs. An exception is the carrier relaxation time τ, which encapsulates the effect of scattering processes and is not directly accessible from standard DFT calculations. A commonly adopted simplification is the constant relaxation time approximation (CRTA), where $\tau$is assumed to be energy-, momentum-, and temperature-independent, typically taken as $\tau = 1 \times 10^{-14}$s. This approximation is implemented in the widely used BoltzTraP code and allows efficient estimation of transport coefficients, although it neglects the microscopic origin of carrier scattering *[95,97]*.

In this thesis, electronic transport properties are calculated using the AMSET framework, which employs the momentum relaxation time

approximation (MRTA) to explicitly evaluate scattering rates *[98]*. These momentum-dependent relaxation times are subsequently passed to BoltzTraP2 for the computation of transport coefficients *[97]*. Within MRTA, electron lifetimes are treated as scalar quantities and are assumed to be independent of the specific scattering direction between initial and final states. AMSET adopts a particular implementation of MRTA known as the self-energy relaxation time approximation (SERTA), which neglects back-scattering contributions from the final electronic state. Under this framework, the elastic scattering rate is given by

$$\tau^{-1} = \frac{2\pi}{\hbar} \mid g_{nm}(\mathrm{k},\mathrm{q}) \mid^2 \delta\left(\varepsilon_{n\mathbf{k}} - \varepsilon_{m,\mathbf{k+q}}\right), \tag{1.47}$$

where $g_{nm}(\mathrm{k},\mathrm{q})$ is the electron–phonon coupling matrix element, and an electron in state (n, k) is scattered to state $(m, \mathrm{k}+\mathrm{q})$ by a phonon of wavevector q. For inelastic scattering, phonon absorption and emission processes must be included, leading to

$$\tau^{-1} = \frac{2\pi}{\hbar} \mid g_{nm}(\mathbf{k},\mathbf{q}) \mid^2 [(b_{\mathbf{q}} + 1 - f_{m,\mathbf{k+q}})\delta(\varepsilon_{n\mathbf{k}} - \varepsilon_{m,\mathbf{k+q}} - \hbar\omega_{\mathbf{q}}) + (b_{\mathbf{q}} + f_{m,\mathbf{k+q}})\delta(\varepsilon_{n\mathbf{k}} - \varepsilon_{m,\mathbf{k+q}} + \hbar\omega_{\mathbf{q}})], \tag{1.48}$$

where $\omega_{\mathbf{q}}$is the phonon frequency, $b_{\mathbf{q}}$ is the Bose–Einstein phonon occupation, and $f_{m,\mathbf{k+q}}$ is the Fermi–Dirac occupation of the final electronic state. In both elastic and inelastic processes, the scattering matrix element $g_{nm}(\mathbf{k},\mathbf{q})$ encapsulates the strength and nature of the underlying scattering mechanism, such as acoustic phonons, polar optical phonons, or ionized impurities. By explicitly accounting for these processes, the AMSET–BoltzTraP2 workflow enables a more physically realistic description of carrier transport beyond the constant relaxation time approximation.

1.7.12. Scattering Rates

Carrier scattering mechanisms determine the relaxation time entering the Boltzmann transport equation and therefore play a central role in governing electrical conductivity and thermoelectric performance. In this work,

scattering rates are evaluated using the physically motivated models implemented in AMSET, which explicitly account for the dominant electron–phonon and impurity scattering processes relevant to semiconductors and thermoelectric materials *[98]*.

1.7.12.1. Acoustic Deformation Potential (ADP) Scattering

The first mechanism considered is acoustic deformation potential (ADP) scattering, which arises from the interaction between charge carriers and long-wavelength acoustic phonons that locally distort the crystal lattice. The corresponding scattering matrix element is given by

$$g_{nm}^{\mathrm{ADP}}(\mathbf{k},\mathbf{q}) = \sum_{\mathbf{G}\neq-\mathbf{q}}^{\text{acoustic}} \frac{\sqrt{k_B T}\,\tilde{D}_{n\mathbf{k}}}{\sqrt{C}} \langle \psi_{m,\mathbf{k}+\mathbf{q}} | e^{i(\mathbf{q}+\mathbf{G})\cdot\mathbf{r}} | \psi_{n\mathbf{k}} \rangle, \tag{1.49}$$

where G is a reciprocal lattice vector, $\widetilde{D}_{n\mathbf{k}} = D_{n\mathbf{k}} + \mathbf{v}_{n\mathbf{k}} \otimes \mathbf{v}_{n\mathbf{k}}$, $D_{n\mathbf{k}}$is the deformation potential, $\mathbf{v}_{n\mathbf{k}}$ is the band velocity, and C is the elastic constant. Physically, the deformation potential quantifies the shift in electronic band energies induced by lattice strain. ADP scattering is unique among the mechanisms considered here in that it is not electronically screened, as it does not involve long-range Coulomb interactions.

1.7.12.2. Ionized Impurity (IMP) Scattering

The second mechanism is ionized impurity scattering, which describes carrier scattering by charged defects introduced either intrinsically or through intentional doping an essential requirement for achieving optimal carrier concentrations in thermoelectric materials. The scattering matrix element is expressed as

$$g_{nm}^{\mathrm{IMP}}(\mathbf{k},\mathbf{q}) = \sum_{\mathbf{G}\neq-\mathbf{q}} \frac{\sqrt{n_{\mathrm{IMP}}}\,Ze}{\varepsilon_s} \frac{\langle \psi_{m,\mathbf{k}+\mathbf{q}} | e^{i(\mathbf{q}+\mathbf{G})\cdot\mathbf{r}} | \psi_{n\mathbf{k}} \rangle}{|\mathbf{q}+\mathbf{G}|^2+\beta^2}, \tag{1.50}$$

where $n_{\mathrm{IMP}}$is the concentration of ionized impurities with charge Z, ε_s is the static dielectric constant (including both ionic and electronic contributions), and β is the inverse screening length. This mechanism captures long-range Coulomb interactions between charge carriers and ionized dopants, with screening effects explicitly incorporated through the dielectric constant and screening length.

1.7.12.3. Polar Optical Phonon (POP) Scattering

In polar materials, polar optical phonon (POP) scattering becomes an important mechanism due to the macroscopic electric fields generated by longitudinal optical phonons. The corresponding scattering matrix element is given by

$$g_{nm}^{\mathrm{POP}}(\mathrm{k},\mathrm{q}) = \sqrt{\frac{\hbar\omega_{\mathrm{po}}}{2}} \sum_{\mathrm{G}\neq-\mathrm{q}} \sqrt{\left(\frac{1}{\varepsilon_\infty}-\frac{1}{\varepsilon_s}\right)} \frac{\langle\psi_{m,\mathrm{k+q}}|e^{i(\mathrm{q+G})\cdot\mathrm{r}}|\psi_{n\mathrm{k}}\rangle}{|\mathrm{q+G}|^2+\beta^2}, \tag{1.51}$$

where ε_∞ is the high-frequency dielectric constant and ω_{po} is the dipole-weighted polar optical phonon frequency at the Γ-point. This formulation exploits the fact that POP scattering is dominated by long-wavelength optical phonons near the Brillouin zone center, allowing a simplified yet accurate description without explicitly sampling phonon modes at all wavevectors. Acoustic phonons are not included in this mechanism, as the dipole interaction vanishes in the low-frequency limit.

1.7.12.4. Piezoelectric (PIE) Scattering

Finally, piezoelectric (PIE) scattering arises in materials that lack inversion symmetry, where acoustic lattice distortions generate macroscopic electric fields that interact with charge carriers. The corresponding scattering matrix element is

$$g_{nm}^{\mathrm{PIE}}(\mathbf{k},\mathbf{q}) = \sum_{\mathbf{G}\neq-\mathbf{q}}^{\text{acoustic}} \frac{\sqrt{k_B T}\, h}{\sqrt{C}} \frac{\langle\psi_{m,\mathbf{k+q}}|e^{i(\mathbf{q+G})\cdot\mathbf{r}}|\psi_{n\mathbf{k}}\rangle}{|\mathbf{q+G}|^2+\beta^2}, \tag{1.52}$$

where h is the piezoelectric tensor. This mechanism reflects the coupling between mechanical strain and electric polarization and is therefore only operative in non-centrosymmetric crystals.

1.7.13. Carrier Transport Model: Solution to the Boltzmann Transport Equation

Within the semiclassical approximation, carrier transport is described through the non-equilibrium distribution function $f(\mathbf{k})$, which deviates

slightly from the equilibrium Fermi–Dirac distribution $f_0[\varepsilon(\mathbf{k})]$ under weak driving forces,

$$f(\mathbf{k}) = f_0[\varepsilon(\mathbf{k})] + \chi g(\mathbf{k}), \tag{1.53}$$

where χ is the cosine of the angle between the driving force and the wavevector $\mathbf{k}$, and $g(\mathbf{k})$ represents the perturbation induced by the applied electric field or temperature gradient.

In the reformulated BTE, both inelastic and elastic scattering processes are explicitly considered. The inelastic processes introduce *scattering-in* $S_i[g(\mathrm{k})]$ and *scattering-out* $S_o(\mathrm{k})$ terms, which depend self-consistently on the perturbed distribution function. Elastic scattering enters through the total elastic scattering rate $\nu_{\mathrm{el}}(\mathrm{k})$. The steady-state solution of the BTE is therefore obtained self-consistently as

$$g(\mathbf{k}) = \frac{S_i[g(\mathbf{k})] - v(\mathbf{k})\frac{\partial f}{\partial z} - \frac{eE\partial f}{\hbar\,\partial \mathbf{k}}}{S_o(\mathbf{k}) + \nu_{\mathrm{el}}(\mathbf{k})}, \tag{1.54}$$

where $E$is the applied electric field and $v(\mathbf{k})$is the electron group velocity. At room temperature, polar optical phonon scattering typically constitutes the dominant inelastic scattering mechanism.

Elastic scattering mechanisms influence carrier mobility through the total elastic scattering rate, which is evaluated using Matthiessen's rule,

$$\nu_{\mathrm{el}}(\mathbf{k}) = \nu_{\mathrm{ii}}(\mathbf{k}) + \nu_{\mathrm{pe}}(\mathbf{k}) + \nu_{\mathrm{de}}(\mathbf{k}) + \nu_{\mathrm{dis}}(\mathbf{k}), \tag{1.55}$$

where the subscripts denote ionized impurity, piezoelectric, deformation potential, and dislocation scattering, respectively. By explicitly accounting for all relevant elastic and inelastic processes, the BTE is solved to obtain the perturbed distribution $g(\mathbf{k})$.

1.7.13.1. Seebeck Coefficient

To compute the Seebeck coefficient S, the electric driving force term is set to zero, such that only the thermal driving force contributes to the perturbation of the distribution. Assuming a spatially uniform carrier concentration across a small temperature gradient, the Seebeck coefficient is given by

$$S = \frac{k_B}{e}\left[\frac{\varepsilon_F}{k_B T} - \frac{\int k^2 f(1-f)\frac{\varepsilon}{k_B T}\,dk}{\int k^2 f(1-f)\,dk}\right] - \frac{J/\sigma}{\partial T/\partial z}, \tag{1.56}$$

where ε_F is the Fermi energy, J is the electrical current density, and σ is the electrical conductivity.

1.7.13.2. Carrier Mobility

For mobility calculations, the thermal driving force is neglected and only the electric field contribution is retained. The carrier mobility is expressed as

$$\mu = \frac{1}{3}\frac{\int v(\mathbf{k})\left(\frac{k}{\pi}\right)^2\left(\frac{g}{E}\right)dk}{\int \left(\frac{k}{\pi}\right)^2 f\,dk} \tag{1.57}$$

Here, a free-electron density of states $(k/\pi)^2$ is used, which can limit accuracy for complex semiconductors. In this work, this limitation is mitigated by replacing free-electron quantities with ab initio–calculated band structures, densities of states, and group velocities, thereby substantially improving the predictive capability of the transport model. All quantities required to evaluate the mobility and Seebeck coefficient including band energies, density of states, group velocities, deformation potentials, conduction band wavefunctions, and polar optical phonon frequencies are obtained from first-principles calculations.

1.7.13.3. Electrical Conductivity

Once the electron and hole mobilities are known, the electrical conductivity is calculated as

$$\sigma = ne\mu_e + pe\mu_h \tag{1.58}$$

where $n$and $p$are the electron and hole concentrations, respectively, e is the elementary charge, and μ_e and μ_h denote the mobilities of electrons and holes.

1.8. Quantum Transport Theory

1.8.1. Lattice Vibrations and Phonons

Phonons are the quantized normal modes of lattice vibrations and provide a fundamental framework for describing vibrational properties, dynamical stability, and thermal transport in crystalline solids *[99]*. Phonon dispersion relations, analogous to electronic band structures, represent the phonon frequencies as a function of wavevector along high-symmetry paths in reciprocal space. The slope of these dispersions corresponds to the phonon group velocity, which governs heat transport. For a crystal containing N atoms in the primitive unit cell, there are exactly $3N$ phonon modes, comprising three acoustic modes and $(3N - 3)$ optical modes. Unlike electronic bands, phonon dispersions do not exhibit a bandgap in the conventional sense, and phonons obey Bose–Einstein statistics, allowing multiple phonons to occupy the same quantum state.

The three acoustic branches two transverse and one longitudinal necessarily approach zero frequency at the Γ point, reflecting the translational invariance of the crystal lattice. The presence of imaginary (negative) phonon frequencies indicates dynamical instability, signifying that atomic displacements experience a negative restoring force, and the structure is not kinetically stable.

1.8.2. Phonon Dispersions

Phonon Dispersion calculation is carried out to investigate the dynamic stability of any system. The term ‘phonon’ defines a collective vibration of periodic atoms in molecules as well as in condensed matter, which represents an excited state in the quantum mechanical quantization of the vibrational modes of elastic structures of interacting particles. In static model, the atoms are arranged in a crystal periodically without any movement. Lattice dynamics deals with the concept that periodically arranged atoms in the crystal lattice are capable of motion due to thermal excitation. In practical cases, all the atoms vibrate to some extent due to thermal agitation. The vibration of an atom is a superposition of vibrations of atoms around their equilibrium sites due to the interaction with neighbor

atoms. This collective vibration of atoms in the crystal lattice forms a wave having allowed wavelength and amplitude. Compared with light 'quanta' photon (which also has wave nature), quantum of lattice vibrational waves is named as 'phonon'. Phonon frequency calculation is done by density functional perturbation theory (DFPT) *[100,101]* as implemented in VASP. Phonon dispersion is plotted by the Phonopy package,*[101]* which gives the dispersion of the phonon frequencies along the high symmetry points of the Brillion zone in reciprocal space.

1.8.3. Force Constants and Phonon Transport

Phonon-mediated thermal transport is governed by the interatomic force constants (IFCs), which are obtained by expanding the crystal potential energy, Φ, as a Taylor series with respect to atomic displacements:

$$\phi = \phi_0 + \sum_{lk}\sum_{\alpha}\phi_\alpha(lk)u_\alpha(lk) + \frac{1}{2}\sum_{ll'kk'}\sum_{\alpha\beta}\phi_{\alpha\beta}(lk,l'k')u_\alpha(lk)u_\beta(l'k') + \frac{1}{3!}\sum_{ll'l"kk'k"}\sum_{\alpha\beta\gamma}\phi_{\alpha\beta\gamma}(lk,l'k',l"k")u_\alpha(lk)u_\beta(l'k')u_\gamma(l"k") + \cdots \quad (1.59)$$

where $l$labels unit cells, k denotes atoms, α,β,γ are Cartesian components, and $u$represents atomic displacements. The coefficients Φ_0, Φ_α, $\Phi_{\alpha\beta}$, and $\Phi_{\alpha\beta\gamma}$ correspond to the zeroth-, first-, second-, and third-order force constants, respectively.

Second-order IFCs were computed using the finite-displacement supercell method as implemented in Phonopy, where atoms are displaced by 0.01 Å and the resulting Hellmann–Feynman forces are evaluated using VASP *[101,102]*. The forces are related to the IFCs via

$$F_\alpha(lk) = -\frac{\partial\Phi}{\partial u_\alpha(lk)}, \Phi_{\alpha\beta}(lk,l'k') = -\frac{\partial F_\beta(l'k')}{\partial u_\alpha(lk)} \quad (1.60)$$

These IFCs are used to construct the dynamical matrix,

$$D_{kk'}^{\alpha\beta}(\mathbf{q}) = \sum_{l'} \frac{\Phi_{\alpha\beta}(0k,l'k')}{\sqrt{m_k m_{k'}}} e^{i\mathbf{q}\cdot(\mathbf{r}_{l'k'}-\mathbf{r}_{0k})} \quad (1.61)$$

where $m_k$is the atomic mass and q is the phonon wavevector. Diagonalization of the dynamical matrix yields the phonon frequencies and polarization vectors:

$$D(\mathbf{q})\,\mathbf{e}_{\mathbf{q}j} = \omega_{\mathbf{q}j}^2 \mathbf{e}_{\mathbf{q}j} \quad (1.62)$$

The resulting phonon eigenvalues are used to construct phonon dispersion relations and phonon density of states. Anharmonic effects are incorporated through third-order IFCs, calculated using Phono3py, which enable the evaluation of three-phonon scattering processes. These interactions introduce a complex phonon self-energy, leading to a frequency renormalization and a finite phonon lifetime. The phonon lifetime is given by

$$\tau_\alpha = \frac{1}{2\Gamma_\alpha(\omega_\alpha)} \quad (1.63)$$

where Γ_α is the imaginary part of the phonon self-energy. Finally, the lattice thermal conductivity is computed by solving the phonon Boltzmann transport equation within the relaxation time approximation:

$$\kappa_l = \frac{1}{NV}\sum_\alpha C_\alpha\ \mathbf{v}_\alpha \otimes \mathbf{v}_\alpha\,\tau_\alpha \quad (1.64)$$

where N is the number of unit cells of volume V, $\mathbf{v}_\alpha$ is the phonon group velocity, and C_α is the mode-specific heat capacity,

$$C_\alpha = k_B \left(\frac{\hbar\omega_\alpha}{k_B T}\right)^2 \frac{e^{\hbar\omega_\alpha/k_B T}}{\left(e^{\hbar\omega_\alpha/k_B T}-1\right)^2} \quad (1.65)$$

1.9. Machine Learning

Machine learning (ML), a subfield of artificial intelligence (AI), employs algorithms and data-driven approaches to enable systems to learn from experience and autonomously perform tasks without explicit programming *[103,104]*.

1.9.1 Machine Learning Interatomic Potentials (MLIPs)

CHAPTER 1

A fundamental challenge in computational materials science lies in balancing accuracy and computational efficiency. Conventional ab initio methods, while highly precise, are often prohibitively expensive for large-scale or long-time simulations *[105]*. Classical interatomic potentials, on the other hand, offer computational speed but frequently fail to achieve predictive accuracy for complex materials. Machine Learning Interatomic Potentials (MLIPs) provide an elegant solution to this dilemma by combining the accuracy of first-principles methods with the efficiency of empirical potential. By training on carefully curated sets of high-fidelity ab initio data, MLIPs can reproduce material properties with near-ab initio precision while delivering speedups of several orders of magnitude. Over the past decade, MLIPs have emerged as a versatile and powerful tool across a broad spectrum of materials modeling applications.

Over the past decade, various MLIPs have been developed, spanning neural network-based architectures such as Behler–Parrinello neural networks (BPNN), *[105]* Deep Potential Molecular Dynamics (DeepMD), *[106]* Neural Equivariant Interatomic Potentials (NequIP) *[107]* and kernel methods such as Gaussian approximation potentials (GAP) and sparse Gaussian process regression (SGPR) *[108, 109]*. Linear-expansion frameworks include the Spectral Neighbor Analysis Potential (SNAP), *[110]* Moment Tensor Potential (MTP), *[111, 112]* and Atomic Cluster Expansion (ACE) *[113]*. Neural networks offer high flexibility but often require extensive training datasets and hyperparameter optimization, whereas kernel methods facilitate rigorous uncertainty quantification but at a substantial computational cost *[105, 114]*. In contrast, MTPs strike an optimal balance of accuracy, transferability, and efficiency, achieving near-DFT fidelity with modest AIMD datasets and simulation speeds up to three orders of magnitude faster than DFT *[105, 111]*. By leveraging moment tensor descriptors, MTPs effectively capture mid- and long-range interactions, enabling accurate predictions of both energies and forces *[111]*.

Over time, a variety of ML-based approaches have emerged for the accurate evaluation of interatomic potentials, including Neural Networks (NNs) *[115]*, Gaussian Approximation Potentials (GAP) *[108]*, Moment Tensor Potentials (MTP) *[111]*, and Spectral Neighbor Analysis Potentials (SNAP) *[110]*. **Figure 1.12** (reprinted from Ref. *[105]*) presents a comparative assessment of several widely used MLIPs reported in the literature *[105]*. The performance of each potential is evaluated using metrics that depend on the properties of interest, such as errors in predicted energies, interatomic forces, or stress tensors. This comparative framework provides insight into the relative strengths and limitations of different MLIP formulations for various material modeling tasks.

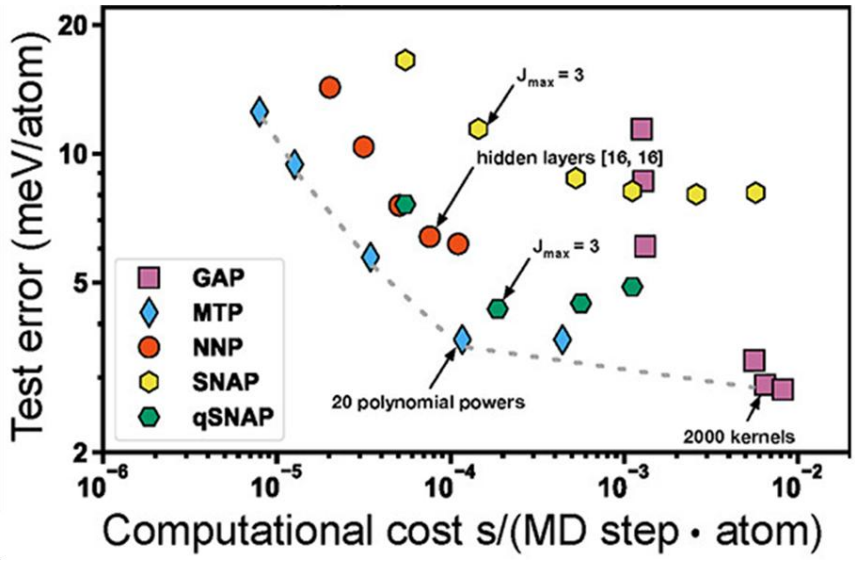


Figure 1.12: Accuracy–cost landscape of machine-learning interatomic potentials including GAP, MTP, NNP, SNAP, and qSNAP. Model hyperparameters govern the trade-off between test error and computational efficiency. Figure reprinted with permission from Ref. 105. Copyrights 2020, American Chemical Society.

1.9.1.1. Moment Tensor Potential (MTP)

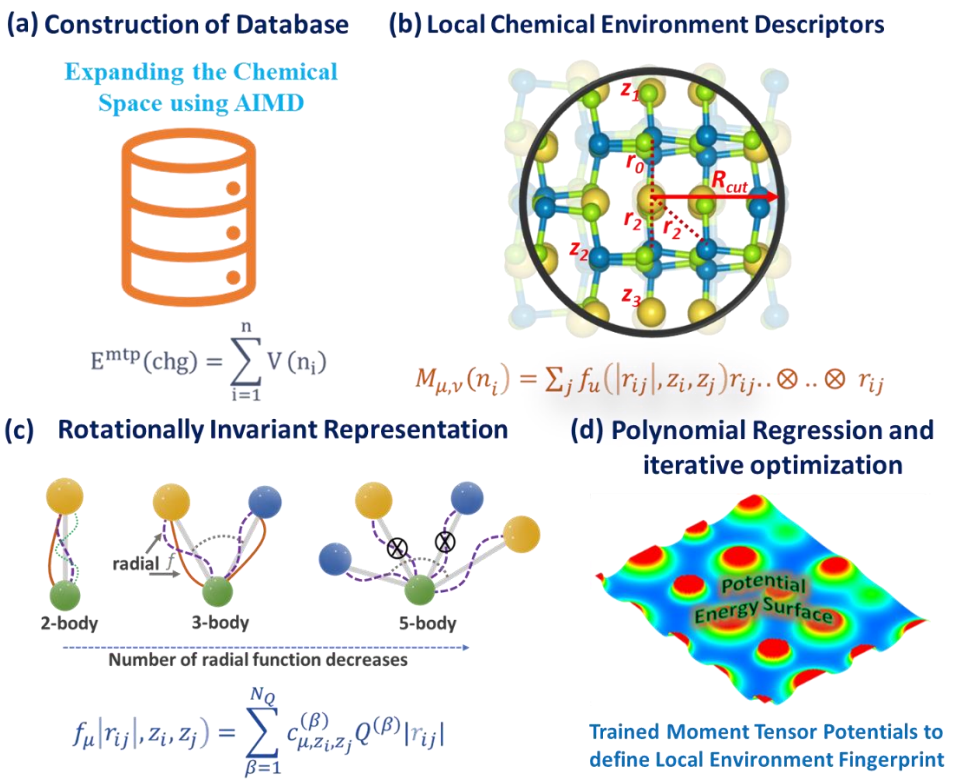


Figure 1.13: (a) Expanding the chemical space using *ab initio* molecular dynamics (AIMD) simulations to represent energy of an atomic configuration ($E^{mtp}(chg)$) comprised of local potential (V) of neighboring atoms (n_i), **(b)** Local chemical environment descriptors defining the moment tensor, where neighboring atoms within a cut-off radius (R_{cut}) interact with the central atom, where f_u encodes the radial information and $r_{ij} \otimes ... \otimes r_{ij}$ contains the angular information, **(c)** constructing invariant features through atomic permutations, rotations, and reflections by computing tensor contractions and eliminating linear dependencies, defining radial basis function which uses polynomial operator on interatomic distances (r_{ij}), $c = \{c^{(\beta)}_{\mu,z_i,z_j}\}$ is radical basis function, $Q^{(\beta)}(|r_{ij}|)$ uses polynomial functions operated on interatomic distances based on cutoff radius **(d)** training moment tensor potentials (MTPs) using the polynomial regression and iterative optimization to define the local chemical environment representing potential energy surface.

Figure reprinted with permission from Ref. 45. Copyrights 2025, American Chemical Society.

Moment Tensor Potential (MTP) belongs to the class of machine learning interatomic potentials (MLIP) were used to describe interatomic interactions, described in **Figure 1.13** *[111, 112, 116]*. These potentials represent the energy of an atomic configuration (cfg) as a sum of contributions of the local atomic environment of each atom. Therefore, the potential energy of interatomic interactions, E^{mtp}, is defined as:

$$\mathrm{E^{mtp}(cfg)} = \sum_{\mathrm{i=1}}^{\mathrm{n}} \mathrm{V(n_i)} \tag{1.66}$$

$$\mathrm{V(n_i)} = \sum_{\alpha} \xi_{\alpha} \mathrm{B_{\alpha}(n_i)} \tag{1.67}$$

where V is the local energy contribution of atom $\mathrm{n_i}$of atomic type $\mathrm{z_i}$. This function V is a linear sum of fitting parameters ξ_{α} and basis functions $\mathrm{B_{\alpha}}$. The fitting parameters ξ_{α} are trained using ridged linear regression. The basis functions $\mathrm{B_{\alpha}}$ are constructed with the help of moment tensor descriptors, which use radial and angular information to provide a fingerprint of each local atomic environment. These descriptors are written as:

$$\mathrm{M_{\mu,\nu}(n_i)} = \sum_{\mathrm{j}} \mathrm{f_u}\left(\left|\mathrm{r_{ij}}\right|, \mathrm{z_i}, \mathrm{z_j}\right) \mathrm{r_{ij}} \otimes \ldots \otimes \mathrm{r_{ij}} \tag{1.68}$$

$$\mathrm{f_{\mu}}\left|\mathrm{r_{ij}}\right|, \mathrm{z_i}, \mathrm{z_j}) = \sum_{\beta=1}^{\mathrm{N_Q}} \mathrm{c_{\mu,z_i,z_j}^{(\beta)}} \mathrm{Q^{(\beta)}}(|\mathrm{r_{ij}}|) \tag{1.69}$$

where $\mathrm{f_u}$ encodes the radial information and $\mathrm{r_{ij}} \otimes \ldots \otimes \mathrm{r_{ij}}$ contains the angular information. The terms $\mathrm{z_i}$ and $\mathrm{z_j}$ denote the atom types for atom $\mathrm{n_i}$ and its neighborhood atoms $\mathrm{n_j}$. The position of these neighbors relative to the $\mathrm{i^{th}}$ atom is written as $\mathrm{r_{ij}}$. The radial function $\mathrm{f_u}$ contains "radial" parameters,

$c = \{c^{(\beta)}_{\mu,z_i,z_j}\}$ specific to each i–j atom type interaction and another term called the radial basis function, $Q^{(\beta)}(|r_{ij}|)$ which uses polynomial functions operated on interatomic distances based on a user-defined cutoff radius. The angular part is a tensor found by performing an outer product. This information is then used to obtain "level" of moments, which is an operation over multiple moments ($M_{\mu,\nu}$) to obtain a scalar term. On the basis of a threshold set for these levels, the number of basis function B_α is determined. The basis functions are sorted according to these levels, and then the total number of basis functions B_α is decided. The radial basis function is defined as:

$$Q^{(\beta)}(|r_{ij}| = \begin{cases} \varphi^{(\beta)}(|r_{ij}|)(R_{cut} - |r_{ij}|)^2, & |r_{ij}| < R_{cut} \\ 0, & |r_{ij}| \geq R_{cut} \end{cases} \quad (1.70)$$

Here $\varphi^{(\beta)}$are polynomial functions (e.g. Chebyshev polynomials) on the interval $[R_{min}, R_{cut}]$, where R_{min} is the minimal distance between atoms in the system investigated, R_{cut} is the cutoff radius which is introduced to ensure a smooth behavior of MTP when atoms leave or enter the interaction neighborhood.

$$\sum_{k=1}^{K}\left[w_e(E_k^{AIMD} - E_k^{MTP})^2 + w_f\sum_{i}^{N}|f_{k,i}^{AIMD} - f_{k,i}^{MTP}|^2 + w_s\sum_{i,j=1}^{3}|\sigma_{k,ij}^{AIMD} - f_{k,ij}^{MTP}|^2\right] \rightarrow \min \quad (1.71)$$

Here, E_k^{AIMD}, $f_{k,i}^{AIMD}$, and $\sigma_{k,ij}^{AIMD}$ are energy, atomic forces, and stresses in the training sets, respectively, and , E_k^{MTP}, $f_{k,i}^{MTP}$, and $\sigma_{k,ij}^{MTP}$ are energy, atomic forces, and stresses calculated by MTP. The k denotes the number of configurations the in the training set and w_e, w_f, and w_s are the non-negative weights, represents the importance of energies, forces, and stresses

in the optimization. Here, in our studies these values were set to 1, 0.1, and 0.001, respectively.

1.9.2. Universal Machine Learning Interatomic Potentials (uMLIPs)

The graph neural network (GNN)-based MLIPs have shown remarkable progress due to their ability to represent atomic structures as graphs, effectively encoding local atomic environments and complex bonding topologies. This framework provides strong chemical and structural generalizability, enabling the development of "universal" or "foundational" MLIPs such as Materials 3-body Graph Network (M3GNet),*[117]* atomistic line graph neural network-based force field (ALIGNN-FF),*[118]* MACE,*[119]* Crystal Hamiltonian Graph Neural Network (CHGNet), *[120]* and MatterSim,*[121]* which are trained on chemically and structurally diverse datasets spanning the periodic table (**Figure 1.14**). While many models enable large-scale exploration of energy landscapes, thermodynamic stability, and harmonic vibrational properties, their often struggle with accuracy in certain domains and typically require fine-tuning through transfer learning *[117, 118, 122]*. In this thesis, we have done benchmarking and validating with existing MACE, CHGNet and MatterSim uMLIPs with high-fidelity predicted κ_L.

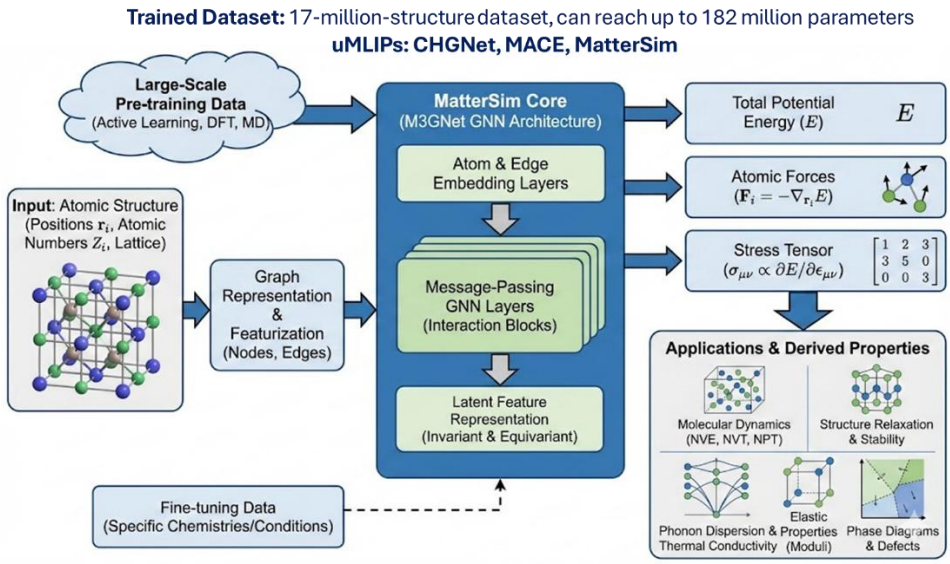


Figure 1.14: Schematic of the MatterSim framework illustrating large-scale pretraining and fine-tuning of graph neural network–based machine-learning interatomic potentials (e.g., CHGNet, MACE). Atomic structures are encoded as graphs and processed through message-passing layers to predict total energies, atomic forces, and stress tensors, enabling applications such as molecular dynamics, structure relaxation, phonon calculations, elastic properties, and phase stability analysis.

1.9.2.1. MatterSim constructs its input data from material graphs derived from the underlying three-dimensional point clouds of a structure under periodic boundary conditions *[121]*. Each point corresponds to an atom and is associated with its element type from the periodic table. Formally, a material graph is defined as $G = (Z, V, R, [L, S])$, with the following components:

- Z represents the atomic numbers $z_i$along with optional atomic features.
- R contains the atomic coordinates in Euclidean space $\mathbb{R}^3$.
- V encodes geometric relationships, such as relative vectors or bond information between atoms.
- L is the 3×3 lattice matrix representing the crystal periodicity.
- S is optional global scalar state information, such as temperature, pressure, or other material-specific conditions.

In these graphs, nodes correspond to atoms, and edges are created according to a predefined rule: any two atoms $r_i$and r_j are connected by an edge if their Euclidean distance satisfies $|| r_i - r_j ||\leq r_c$, where r_c is a radial cutoff distance. Fractional coordinates are first converted to Cartesian coordinates before graph construction.

As a geometric graph representation, material graphs inherently preserve roto-translational symmetry. MatterSim enforces roto-translational invariance for scalar properties (e.g., total energy) and equivariance for vectorial properties (e.g., atomic forces). Depending on the task and target properties, MatterSim further adapts its input representations and crystalline

features to be compatible with underlying architectures such as M3GNet and Graphormer, enabling accurate and physically consistent predictions across diverse materials.

1.9.2.2. MACE. The MACE architecture, introduced by Batatia et al. (2022),*[119]* combines O(3)-equivariant message passing with explicit many-body interactions to construct fast and highly accurate machine-learned interatomic potentials. Unlike conventional equivariant graph neural networks, which primarily rely on pairwise (two-body) messages and deep network stacking to capture complexity, MACE explicitly encodes higher-order correlations three-body and four-body interactions—directly within its message-passing layers. This design enhances the network's expressivity, data efficiency, and scalability, allowing it to achieve state-of-the-art accuracy on benchmark datasets while remaining computationally efficient. Importantly, the incorporation of many-body messages modifies the empirical power-law exponent of the learning curves, leading to faster convergence with increasing data, whereas equivariance alone shifts the curves without affecting their scaling behavior. By efficiently representing complex multi-atom interactions, MACE provides a physically grounded and robust framework, particularly suitable for modeling materials in which many body effects, such as phonon scattering and thermal transport, play a critical role.

1.9.2.3. CHGNet. The Crystal Hamiltonian Graph Neural Network (CHGNet) is a machine-learned interatomic potential pre-trained on energies, forces, stresses, and magnetic moments from 1.5 million crystal structures in the MPtrj dataset *[120]*. In CHGNet, angle information is incorporated through pairwise message-passing convolutions between bonds (the *bond graph*, where bonds serve as nodes and angles as edges), layered on top of standard pairwise convolutions between atoms (the *atom graph*, where atoms are nodes and bonds are edges). To improve physical consistency, atomic features used to predict energies, forces, and stresses are constrained by charge-state information, which is inferred from

magnetic moments and atomic orbital theory prior to the final convolution layer. This architecture allows CHGNet to efficiently capture both local atomic interactions and higher-order angular correlations, making it particularly suitable for modeling complex crystalline materials with diverse chemical environments.

Fine-tuning and transfer learning are efficient strategies for leveraging large, pre-trained deep learning models to achieve improved accuracy on small target datasets, offering significant data efficiency compared with training models from scratch *[105, 114, 122, 123]*. While pretrained universal MLIPs (uMLIPs) have demonstrated robustness across a range of applications, higher accuracy in energies and forces can often be achieved by fine-tuning the model for specific material systems, particularly when high-precision predictions are required. During fine-tuning, additional DFT-calculated data points are used to adjust the effective potential energy surface represented by the uMLIP, allowing it to better capture system-specific interactions. To maintain the pretrained knowledge and improve extrapolation, it is common to freeze the deeper layers of the network and update only the shallower layers, thereby refining the model while preserving the general physical trends learned during pretraining.

1.10. Supervised Learning

Supervised learning is a type of ML where the model is trained on a labelled dataset to train algorithms to predict outcomes and recognize patterns. Supervised learning can be divided into two main categories *[124]*:

1.10.1 Regression

The goal is to predict a continuous output variable based on input features *[124]*.

1.10.2. Classification

The aim is to categorize a discrete class label for given input data.

1.10.3. Unsupervised Learning

Unsupervised learning is a type of machine learning where the model is trained on unlabelled data. The goal is to find patterns, structures, and relationships within the data without any predefined labels *[125]*.

1.10.4. Dataset

A dataset in ML is a collection of data points used in the iterative process of building, optimizing, and validating models/algorithms. This data can be gathered from experimental measurements, simulations, or literature.

1.10.4.1. Training set

The training set is the biggest subset of original datasets that are used for train/fit models to make predictions and find insights within the data.

1.10.4.2. Test set

The test set is a subset of a dataset that is withheld from training and used to assess the performance of the trained model on unseen data.

1.10.4.3. Validation set

A validation set is a subset of the dataset used to evaluate the performance of a ML model during the training process. Its primary purposes are to perform hyperparameter tuning and model selection and prevent overfitting.

1.10.5. Feature Selection and Correlation Analysis

Effective machine learning models rely not only on robust algorithms but also on well-designed input features. Feature selection and correlation analysis play a crucial role in improving model accuracy, interpretability, and computational efficiency by identifying the most relevant variables and eliminating redundancy *[126]*.

1.10.5.1. Feature Engineering

Feature engineering is the process of creating, selecting, and transforming input variables using domain knowledge to improve the performance of machine learning algorithms *[127]*. Well-engineered features enable models to better capture underlying physical and statistical relationships within the data, often leading to enhanced predictive accuracy and generalization. In materials science, feature engineering is particularly

important for incorporating physically meaningful descriptors that reflect compositional, structural, and thermodynamic properties.

1.10.5.2. Pearson Correlation Coefficient (PCC)

The Pearson Correlation Coefficient (PCC) is a statistical metric used to quantify the strength and direction of a linear relationship between two continuous variables *[128]*. Represented by the symbol r, its value ranges from −1 to 1, where $r = 1$ indicates a perfect positive linear correlation, $r = -1$ represents a perfect negative linear correlation, and $r = 0$ implies no linear correlation.

PCC is calculated by normalizing the covariance between the two variables by the product of their standard deviations, resulting in a dimensionless quantity that enables direct comparison across different datasets. PCC is particularly useful for identifying redundant features that exhibit strong linear correlations with one another. The coefficient is given by:

$$\text{PCC} = \frac{\sum_{i=1}^{n}(x_i - \bar{x})(y_i - \bar{y})}{\sqrt{\sum_{i=1}^{n}(x_i - \bar{x})^2}\sqrt{\sum_{i=1}^{n}(y_i - \bar{y})^2}} \tag{1.72}$$

where x_i and y_i are individual observations of variables x and y, respectively, and $\bar{x}$ and $\bar{y}$ denote their mean values.

1.10.5.3. Spearman Rank Correlation Coefficient (SCC)

The SCC is a non-parametric measure that evaluates the strength and direction of a monotonic relationship between two ranked variables *[129]*. Unlike PCC, SCC does not assume linearity or normality of the data, making it robust to outliers and suitable for ordinal or nonlinearly related variables. SCC assesses how well the relationship between two variables can be described by a monotonic function and is calculated using the ranked differences between data points. It is defined as:

$$\rho = 1 - \frac{6\sum d_i^2}{n(n^2 - 1)} \tag{1.73}$$

where $d_i$is the difference between the ranks of the i^{th} observation and $n$is the total number of samples. Due to its robustness and flexibility, SCC is widely used when PCC assumptions are not satisfied.

1.10.5.4. Mutual Information (MI)

Mutual Information (MI) is a feature selection technique used to quantify the degree of dependency between two variables, capturing both linear and nonlinear relationships *[130]*. MI measures the amount of information gained about one random variable through knowledge of another.

The mutual information between two variables X and $Y$is defined as:

$$\text{MI}(X, Y) = H(X) - H(X \mid Y) \tag{1.74}$$

where $H(X)$ represents the entropy of variable X, given by:

$$H(X) = -\sum_{x \in X} p(x) \log\, p(x) \tag{1.75}$$

Here, $p(x)$ denotes the probability distribution of X, and $H(X \mid Y)$ is the conditional entropy of X given Y. MI can be interpreted as the reduction in uncertainty of X due to the knowledge of Y, making it particularly effective for detecting nonlinear dependencies between features and target variables.

1.10.6. Hyperparameter Tuning

Hyperparameter tuning is a critical step in machine learning model development, aimed at identifying the optimal configuration of hyperparameters that maximizes model performance *[131]*. Unlike model parameters, which are learned during training, hyperparameters are predefined and control the learning process, such as model complexity, learning rate, and regularization strength. Proper hyperparameter optimization helps prevent overfitting and improves generalization. In this work, two widely used tuning strategies, Grid Search and Randomized Search are employed *[131]*.

1.10.6.1. Grid Search

Grid search is a systematic hyperparameter optimization technique that exhaustively evaluates all possible combinations of predefined hyperparameter values. While it guarantees identification of the optimal

parameter set within the specified search space, grid search can become computationally expensive when the number of hyperparameters or their ranges increase.

1.10.6.2. Randomized Search

Randomized search is an alternative hyperparameter optimization method in which hyperparameter values are randomly sampled from predefined distributions. Unlike grid search, randomized search explores a broader region of the hyperparameter space using fewer evaluations, often resulting in comparable or superior performance with significantly reduced computational cost. This approach is particularly advantageous for high-dimensional or large-scale machine learning problems.

1.10.7. Machine Learning Algorithms

Machine learning algorithms provide a systematic framework for identifying patterns and relationships within data, enabling accurate prediction and classification of material properties. In this thesis, a variety of supervised learning algorithms are employed, ranging from linear models to ensemble and kernel-based methods. A brief description of each algorithm is provided below.

1.10.7.1. Linear Regression

Linear regression is a fundamental supervised learning technique used to model the linear relationship between an input variable $x$and a target output y *[132]*. The objective is to determine the best-fitting straight line that minimizes the difference between predicted and actual values. The linear regression model is expressed as:

$$y = wx + b \tag{1.76}$$

where w represents the slope of the regression line and b denotes the intercept. Linear regression is widely used due to its simplicity, interpretability, and computational efficiency.

1.10.7.2. Logistic Regression

Logistic regression is a classification algorithm used to estimate the probability of a categorical dependent variable *[133]*. Unlike linear

regression, it employs a sigmoid (logistic) function to map predicted values to the range $[0,1]$, making it suitable for binary classification problems. The sigmoid function is defined as:

$$\sigma(t) = \frac{1}{1 + e^{-t}} \tag{1.77}$$

The output represents the probability of a given input belonging to a specific class.

1.10.7.3. K-Nearest Neighbors

The K-Nearest Neighbors (KNN) algorithm is a non-parametric, instance-based learning method that makes predictions based on the proximity of data points in the feature space *[134]*. For a given input, KNN identifies the $k$closest neighbors according to a distance metric (e.g., Euclidean distance) and determines the output based on majority voting (classification) or averaging (regression). KNN is simple to implement and effective for problems with well-separated classes, although it can be computationally expensive for large datasets.

1.10.7.4. Kernel Ridge Regression

Kernel ridge regression combines ridge regression with kernel methods to model nonlinear relationships between independent and dependent variables *[135]*. By mapping the input data into a higher-dimensional feature space using kernel functions, KRR enables flexible and accurate regression even when the data is not linearly separable. This method is particularly effective for capturing complex trends while maintaining regularization to prevent overfitting.

1.10.7.5. Support Vector Machines

Support Vector Machines are supervised learning algorithms used for both classification and regression tasks *[136]*. SVM constructs a decision boundary, known as the maximum-margin hyperplane, which separates different classes while maximizing the margin between them. For a given feature vector x, the hyperplane is defined as:

$$\mathbf{w}^T x + b = 0 \tag{1.78}$$

where w is the normal vector to the hyperplane and b is the bias term. Kernel functions can be employed to extend SVMs to nonlinear classification problems.

1.10.7.6. Random Forest

Random Forest is an ensemble learning algorithm that constructs multiple decision trees using randomly selected subsets of the training data and features *[137]*. The final prediction is obtained by aggregating the predictions of individual trees through majority voting (classification) or averaging (regression). Random Forest models are robust against overfitting and perform well on high-dimensional datasets.

1.10.7.7. Adaptive Boosting

Adaptive Boosting, or AdaBoost, is a boosting technique that combines multiple weak learners to form a strong classifier *[138]*. During training, higher weights are assigned to misclassified samples, forcing subsequent learners to focus on difficult cases. This adaptive reweighting process enhances predictive accuracy and improves model performance.

1.10.7.8. Extreme Gradient Boosting

Extreme Gradient Boosting (XGBoost) is an advanced implementation of gradient boosting designed for efficiency and scalability *[139]*. It builds an ensemble of weak learners, typically decision trees, by sequentially minimizing the prediction error of previous models. XGBoost incorporates regularization, parallel processing, and optimized tree construction, making it highly effective for large and complex datasets.

1.10.7.9. Gaussian Process Regression

Gaussian Process Regression is a Bayesian, non-parametric regression method that defines a probability distribution over functions *[140]*. Instead of assuming a fixed functional form $y = f(x)$, GPR places a Gaussian process prior over the function space, enabling predictions with uncertainty quantification. This makes GPR particularly useful for modeling noisy data and estimating confidence intervals.

1.10.7.10. Decision Tree

A decision tree is a tree-based learning algorithm in which internal nodes represent decision rules based on feature values, branches correspond to possible outcomes of these decisions, and leaf nodes represent final predictions *[141]*. Decision trees are intuitive, easy to interpret, and capable of handling both numerical and categorical data.

1.10.7.11. Extra Tree Regression

Extra Trees Regression (Extremely Randomized Trees) is an ensemble learning technique that builds multiple decision trees using random feature selection and random split points *[142]*. Unlike traditional decision trees, this increased randomness enhances model diversity, leading to improved generalization and reduced variance, particularly for regression tasks.

1.11. Deep Learning Algorithms

In recent years, deep learning approaches have emerged as powerful tools for predicting materials properties directly from structural information. Unlike classical machine learning methods, which rely on handcrafted features, deep learning models can automatically learn complex relationships between atomic structures and their properties, enabling accurate, scalable, and transferable predictions. Among these, graph-based neural networks have become particularly effective because they naturally represent crystal structures as graphs, encoding both atomic identities and their spatial interactions. Key graph-based architectures include CGCNN,*[143]* GATGNN,*[144]* and ALIGNN,*[145]* each designed to capture increasingly sophisticated chemical and structural information.

1.11.1. Convolutional Graph Neural Network (CGCNN)

The Convolutional Graph Neural Network (CGCNN), introduced by Xie and Grossman (2018), represents crystal structures as graphs, where nodes correspond to atoms and edges correspond to interatomic bonds *[143]*. Atomic features, such as element type, electronegativity, and coordination environment, are encoded as node attributes, while bond lengths or other geometric information are captured as edge attributes (**Figure 1.15**). CGCNN applies graph convolution operations, which iteratively aggregate

information from an atom's neighbors to update node features, effectively capturing local chemical environments.

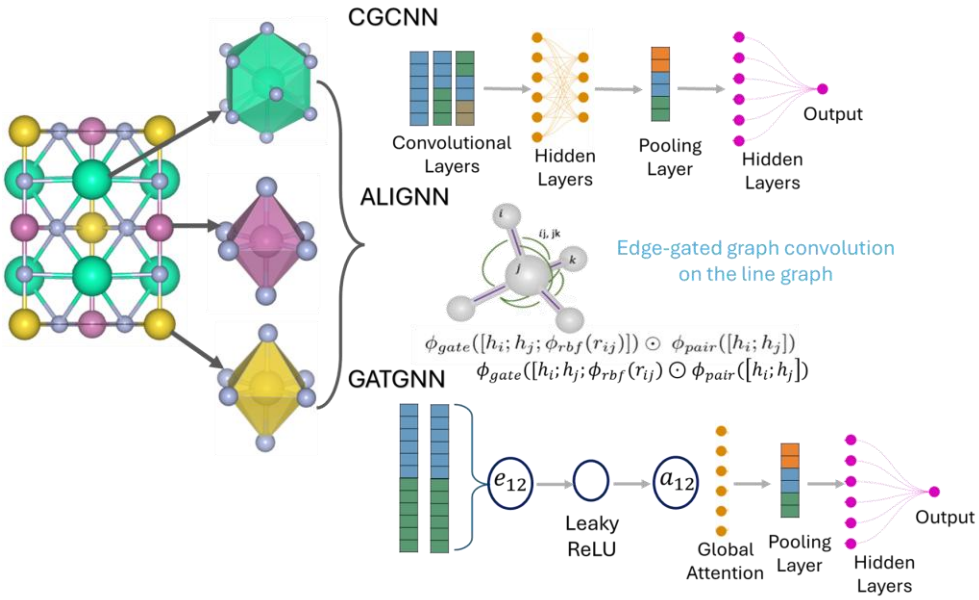


Figure 1.15: Schematic illustration of Convolutional Graph Neural Network (CGCNN), Atomistic Line Graph Neural Network (ALIGNN) and Graph Attention Neural Network (GATGNN), architecture.

Following multiple convolution layers, a readout function aggregates node features into a single vector representing the crystal, which is then fed into fully connected layers to predict target properties such as formation energy, band gap, or elastic constants. CGCNN has demonstrated strong performance on large-scale materials databases, including the Materials Project, and has become a foundational architecture in crystal graph neural networks. Its simplicity and efficiency make it suitable for predicting a wide range of properties while maintaining chemical interpretability.

1.11.2. Graph Attention Neural Network (GATGNN)

The Graph Attention Neural Network (GATGNN) enhances traditional graph convolution by incorporating attention mechanisms to weigh contributions from neighboring atoms differently. In conventional GNNs like CGCNN, all neighbors contribute equally to updating a node's

representation *[144]*. GATGNN introduces learnable attention coefficients that dynamically assign importance to each neighbor based on its chemical and spatial relevance. This mechanism enables the network to focus on the most influential atomic interactions, improving its ability to model complex, heterogeneous materials. In GATGNN, each graph convolution layer computes attention-weighted sums over neighboring nodes, followed by non-linear transformations to update node features, described in **Figure 1.15**. By stacking multiple attention layers, the model can capture both short- and long-range interactions, making it highly suitable for predicting properties sensitive to specific local motifs or long-range correlations, such as defect formation energies or lattice thermal conductivity.

1.11.3. Atomistic Line Graph Neural Network (ALIGNN)

The Atomistic Line Graph Neural Network (ALIGNN) is a recent advancement in GNN architectures, designed to explicitly capture both atomic and bond-level interactions in crystalline materials *[145]*. ALIGNN constructs a line graph from the original crystal graph, where the edges (bonds) of the original graph become the nodes of the line graph, illustrated in **Figure 1.15**. This allows the network to propagate information not only through atoms but also along bonds, effectively modeling bond-angle correlations and higher-order geometric features.

ALIGNN uses two parallel convolution pathways: one operates on the atom graph to update atomic features, and the other on the line graph to update bond features, with mutual message passing between the two. This dual-graph approach enables ALIGNN to capture subtle chemical and structural patterns, improving predictions of properties that are sensitive to bond orientation and angular interactions, such as lattice thermal conductivity, phonon properties, and elastic moduli. ALIGNN has been shown to outperform CGCNN and GATGNN on several benchmark datasets, demonstrating its effectiveness in modeling complex materials with strong directionality or anisotropy.

1.12. Model Evaluation Metrics

1.12.1. Coefficient of determination (R^2)

The coefficient of determination (R^2) is a statistical metric used to assess the goodness of fit of a regression model. It quantifies the fraction of the variance in the dependent variable that can be explained by the independent variables included in the model. The value of R^2 ranges from 0 to 1, where higher values indicate a better explanatory power of the regression model *[146]*.

$$R^2 = \frac{\sum_{i=1}^{n}(M_i - \bar{m})^2}{\sum_{i=1}^{n}(m_i - \bar{m})^2} \quad \text{where} \quad \overline{m} = \frac{\sum_{i=1}^{n} m_i}{n} \tag{1.79}$$

Here, M_i denotes the predicted output value, m_i represents the corresponding DFT/experimental value, $\bar{m}$ is the mean of the DFT/experimental values, and n is the total number of data points in the dataset.

1.12.2. Mean Absolute Error (MAE)

It is defined as the average of the absolute differences between the predicted values and the corresponding actual (reference) values.

$$\text{MAE} = \frac{1}{n}\sum_{i=1}^{n}|M_i - m_i| \tag{1.80}$$

1.12.3. Mean Squared Error (MSE)

It is defined as the average of the squared differences between the predicted values and the corresponding actual (reference) values.

$$\text{MSE} = \frac{1}{n}\sum_{i=1}^{n}(M_i - m_i)^2 \tag{1.81}$$

1.12.4. Root Mean Squared Error (RMSE)

It is defined as the square root of the average of the squared differences between the predicted values and the corresponding actual (reference) values.

$$\text{RMSE} = \sqrt{\frac{1}{n}\sum_{i=1}^{n}(M_i - m_i)^2} \tag{1.82}$$

1.12.5. Confusion Matrix

A confusion matrix is an $N \times N$ tabular representation used to evaluate the performance of a classification model, where N denotes the number of

target classes. It summarizes the predicted versus actual class labels, providing a detailed assessment of how well the machine learning classification algorithm performs across all classes. By explicitly accounting for correct and incorrect predictions, the confusion matrix offers a comprehensive view of model performance, including class-wise accuracy and misclassification patterns. (**Figure 1.18**).

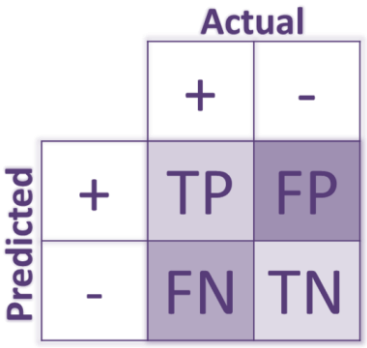


Figure 1.18: Confusion matrix showing the true positives, true negatives, false positives, and false negatives, TP: True Positive, TN: True Negative, FN: False Negative, FP: False Positive.

1.12.6. Accuracy

It measures the proportion of correct predictions made by the model across the entire dataset. The sum of true positives (TP) and true negatives (TN) is divided by the total number of datasets.

$$\text{Accuracy (\%)} = \frac{TP+TN}{TP+FP+TN+FN} \times 100 \qquad (1.83)$$

1.12.7. Precision

It measures the proportion of true positive predictions among all positive predictions made by the model. It evaluates the exactness of the model.

$$\text{Precision} = \frac{TP}{TP+FP} \qquad (1.84)$$

1.12.8. Recall (Sensitivity)

Recall, also known as sensitivity /true positive rate, measures the ratio of correctly predicted positive observations to all the actual positives in the dataset. It evaluates the completeness of a model.

$$\text{Recall} = \frac{TP}{TP+FN} \tag{1.85}$$

1.12.9. F1 Score

The F1 Score is an evaluation metric that combines precision and recall into a single metric by taking their harmonic mean.

$$\text{F1 Score} = 2 \times \frac{Precision \times recall}{precision + recall} \tag{1.86}$$

1.12.10. Cross-Validation

Cross-validation is a robust technique in machine learning used to evaluate the performance and generalizability of a model. By repeatedly testing the model on different subsets of the data, cross-validation provides a more reliable estimate of predictive accuracy than a single train–test split and helps mitigate overfitting. Several cross-validation strategies exist; in this thesis, we primarily employ the K-fold cross-validation method *[147]*. In K-fold cross-validation, the dataset is partitioned into K mutually exclusive subsets, or folds. The model is trained on $K-1$ folds and evaluated on the remaining fold, with this process repeated Ktimes such that each fold serves as the test set exactly once. The final model performance is obtained by averaging the evaluation metrics across all folds. (**Figure 1.19**).

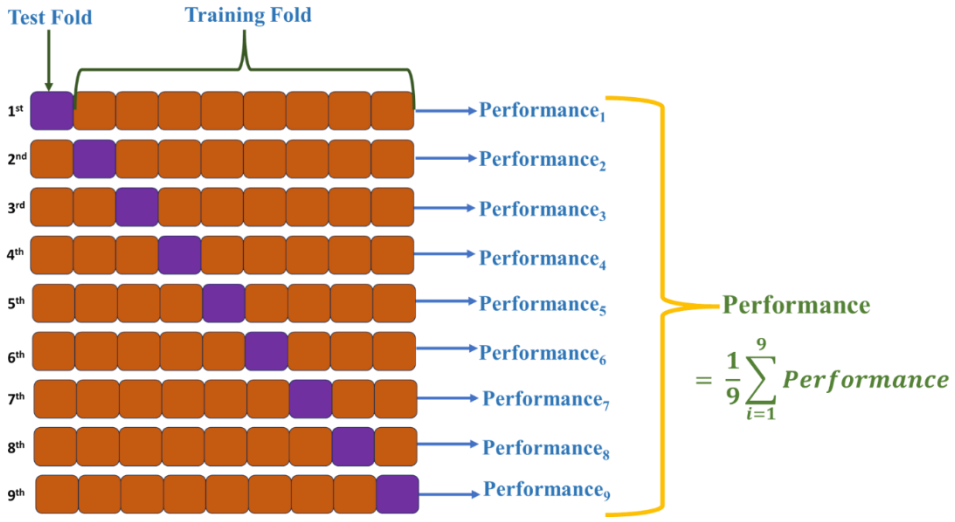


Figure 1.19: Schematic diagram showing K-fold (K=9) cross-validation.

1.13. Feature Importance

Feature importance refers to a set of techniques in machine learning used to quantify the relevance and contribution of individual features to the prediction of a target variable. Analyzing feature importance is essential for model interpretability, feature selection, and performance optimization, as it helps identify which input variables most strongly influence the model's predictions. Feature importance methods can be broadly classified into model-based approaches, which rely on the internal structure of the model, and model-agnostic approaches, which are independent of the underlying algorithm and provide more general insights into model behavior. Together, these methods enable a deeper understanding of the predictive mechanisms of the machine learning models considered in this work.

1.13.1. Permutation Feature Importance

Permutation feature importance is a model-agnostic technique used to evaluate the significance of individual features by assessing the impact of feature values shuffling on the performance of the model *[137]*. This method involves randomly permuting the values of a particular feature and then measuring the resulting change in the model's prediction error. If permuting the values of a feature significantly increases the model's error, it indicates that the model relies heavily on that feature for making accurate predictions, thereby defining it as an important feature. Conversely, if the model's error remains unchanged after permuting the feature's values, the feature is deemed as less important.

1.13.2. Machine Learning Explainability

Explainable AI arises from the fact that traditional ML models are often difficult to understand and interpret. These models are typically black boxes that make predictions based on input data but do not provide any insight into the reasoning behind their predictions. Explainable AI (XAI) is a set of tools and frameworks to help understand and interpret predictions made by ML models. Model explainability refers to the capability of a machine learning algorithm to provide understandable insights into its decision-making process or output for a human user (**Figure 1.20**). Key aspects of

XAI include transparency, fairness, causality, transferability, and accountability *[148]*.

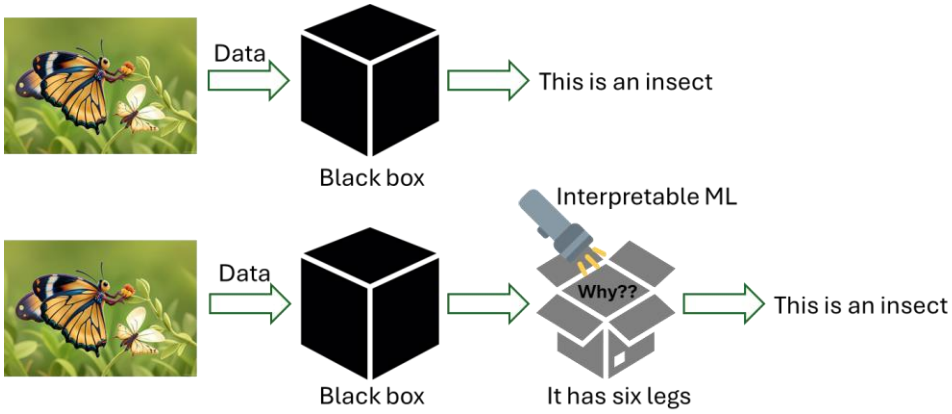


Figure 1.20: Schematic illustration of the black box model and explainable AI interpreting the decision behind ML prediction.

1.13.3. SHapley Additive exPlanations (SHAP)

SHAP is a unified and theoretically grounded framework for interpreting predictions of machine learning models. It is based on principles from cooperative game theory, where each input feature is treated as a "player" contributing to the final prediction. SHAP quantifies the contribution of each feature by assigning it a Shapley value, which represents the fair contribution of that feature to the model output. One of the key advantages of SHAP is that it is model agnostic, making it applicable to a wide range of machine learning algorithms *[149]*.

SHAP provides insights at both local and global levels. At the local level, SHAP values explain individual predictions by decomposing the difference between the model output and a baseline (expected) prediction into contributions from each feature. This enables a detailed understanding of how specific input features influence a particular prediction. At the global level, aggregating SHAP values across the entire dataset yields an overall measure of feature importance, offering valuable insight into the general behavior and decision-making patterns of the model.

The Shapley value $\phi_x(p)$ for a feature x (out of a total of $n$features) associated with a model prediction p is given by:

$$\emptyset_x(p) = \sum_{s \subseteq N/x} \frac{|S|!(n-|S|-1)!}{n!}(p(S \cup x) - p(S)) \qquad (1.87)$$

where Sdenotes a subset of features excluding x, Nrepresents the set of all features, $p(S \cup \{x\})$ is the model prediction when feature x is included, and $p(S)$ is the prediction obtained without feature x.

In this thesis, model interpretability is carried out using SHAP analysis as implemented in the Python SHAP package. This approach enables a quantitative evaluation of how individual input features contribute to the prediction outcomes. The Shapley value for the i^{th} feature is computed as:

$$\text{Shap}(i) = \sum_{S \subseteq M\{i\}} \frac{|\,S\,|\,!\,(n-|\,S\,|-1)!}{n!}[f_x(S \cup \{i\}) - f_x(S)] \qquad (1.88)$$

with

$$f_x(S) = \mathbb{E}[f(x) \mid x_S] \qquad (1.89)$$

where $n$is the total number of features, $M\{i\}$ represents all possible feature subsets excluding feature i, and $\mathbb{E}[f(x) \mid x_S]$ denotes the expected value of the model output conditioned on the subset of features S.

Using this framework, SHAP values are computed to quantify feature contributions and elucidate their relative importance in predicting target material properties, including Seebeck coefficient (S), electrical conductivity (σ), lattice thermal conductivity (κ_L), power factor (PF), and thermoelectric figure of merit (ZT).

1.14. Reference

1. Hamid Elsheikh, M., Shnawah, D. A., Sabri, M. F. M., Sopian, K., Alghoul, M. A., Rahim, N. A., Mohamed, A., (2014) A review on thermoelectric renewable energy: Principle parameters that affect their

performance, Renewable and Sustainable Energy Reviews, 30, 337–355 (DOI: 10.1016/j.rser.2013.10.047)

2. DiSalvo, F. J. (1999) Thermoelectric cooling and power generation, *Science*, **285**, 703–706. (DOI: 10.1126/science.285.5428.703)

3. Snyder, G. J., Toberer, E. S. (2008) Complex thermoelectric materials, *Nature Materials*, **7**, 105–114. (DOI: 10.1038/nmat2090)

4. Rowe, D. M. (Ed.). (2018) *CRC Handbook of Thermoelectrics*, CRC Press, Boca Raton.

5. Li, J.-F., Liu, W.-S., Zhao, L.-D., Zhou, M. (2010) High-Performance Nanostructured Thermoelectric Materials. *NPG Asia Mater*. 2010, 2 (4), 152–158. (DOI: 10.1038/asiamat.2010.138)

6. Lee, S., Bock, J. A., Trolier-McKinstry, S., Randall, C. A. (2012) Ferroelectric–thermoelectricity and Mott transition of ferroelectric oxides with high electronic conductivity, *Journal of the European Ceramic Society*, 32, 3971–3988. (DOI: 10.1016/j.jeurceramsoc.2012.06.007)

7. Biswas, K., He, J., Blum, I. D., Wu, C.-I., Hogan, T. P., Seidman, D. N., Dravid, V. P., Kanatzidis, M. G. (2012) High-performance bulk thermoelectrics with all-scale hierarchical architectures, Nature, 489, 414–418 (DOI: 10.1038/nature11439)

8. Pei, Y., Shi, X., Lalonde, A., Wang, H., Chen, L., Snyder, G. J. (2011) Convergence of electronic bands for high performance bulk thermoelectrics, *Nature*, 473, 66–69. (DOI: 10.1038/nature09996)

9. Terasaki, I. (2005) Introduction to thermoelectricity, in *Materials for Energy Conversion Devices*, Woodhead Publishing.

10. Hicks, L. D., Dresselhaus, M. S. (1993) Effect of quantum-well structures on the thermoelectric figure of merit, *Physical Review B*, 47, 12727–12731. (DOI: 10.1103/PhysRevB.47.12727)

11. Hicks, L. D., Dresselhaus, M. S. (1993) Thermoelectric figure of merit of a one-dimensional conductor, *Physical Review B*, 47, 16631–16634. (DOI: 10.1103/PhysRevB.47.16631)

12. Heremans, J. P., Jovovic, V., Toberer, E. S., Saramat, A., Kurosaki, K., Charoenphakdee, A., Yamanaka, S., Snyder, G. J. (2008) Enhancement of thermoelectric efficiency in PbTe by distortion of the electronic density of states, Science, 321, 554–557 (DOI: 10.1126/science.1159725)

13. Zhao, L.-D., Tan, G., Hao, S., He, J., Pei, Y., Chi, H., Wang, H., Gong, S., Xu, H., Dravid, V. P., Uher, C., Snyder, G. J. (2016) Ultrahigh power factor and thermoelectric performance in hole-doped single-crystal SnSe, Science, 351, 141–144 (DOI: 10.1126/science.aad3749)

14. Zhao, L.-D., Lo, S.-H., Zhang, Y., Sun, H., Tan, G., Uher, C., Wolverton, C., Dravid, V. P., Snyder, G. J. (2014) Ultralow thermal conductivity and high thermoelectric figure of merit in SnSe crystals, Nature, 508, 373–377 (DOI: 10.1038/nature13184)

15. Perumal, S., Bellare, P., Shenoy, U. S., Raj, V., Anantharaman, B., Sreekumaran Nair, P., Dheeraj, D. R., Ghosh, R. (2017) Low thermal conductivity and high thermoelectric performance in Sb and Bi codoped GeTe, Chem. Mater., 29, 10426–10435 (DOI: 10.1021/acs.chemmater.7b04023)

16. Liu, H., Shi, X., Xu, F., Zhang, W., Li, H., Zhang, Y., Bai, S., Yu, H., Zhao, L.-D., Chen, L., Snyder, G. J. (2012) Copper ion liquid-like thermoelectrics, Nat. Mater., 11, 422–425 (DOI: 10.1038/nmat3273)

17. Liu, D., Wang, D., Hong, T., Xie, H., Li, Y., Chen, L., Snyder, G. J. (2023) Lattice planarification advances highly effective SnSe crystalline thermoelectrics, Science, 380, 841–846 (DOI: 10.1126/science.adg7196)

18. Christensen, M., Abrahamsen, A. B., Christensen, N. B., Nørgaard, J., Lefmann, K., Rotter, M., McGuire, M. A., Sales, B. C., Singh, D. J. (2008) Avoided crossing of rattler modes in thermoelectric materials, Nat. Mater., 7, 811–815 (DOI: 10.1038/nmat2273)

19. Nielsen, M. D., Ozoliņš, V., Heremans, J. P. (2013) Lone pair electrons minimize lattice thermal conductivity, Energy Environ. Sci., 6, 570–578 (DOI: 10.1039/C2EE23391F)

20. Zheng, Y., Slade, T. J., Hu, L., Liu, W., Snyder, G. J., Shi, X., Uher, C., Chen, G., Zeier, W. G. (2021) Defect engineering in thermoelectric materials: What have we learned?, Chem. Soc. Rev., 50, 9022–9054 (DOI: 10.1039/D1CS00285K)

21. Chandra, S., Bhat, U., Dutta, P., Radhakrishnan, S., Saha, A., Sharma, S., Biswas, K. (2022) Modular nanostructures facilitate low thermal conductivity and ultra-high thermoelectric performance in n-type SnSe, Adv. Mater., 34, 2203725 (DOI: 10.1002/adma.202203725)

22. Biswas, K., He, J., Zhang, Q., Wang, G., Uher, C., Dravid, V. P., Kanatzidis, M. G. (2011) Strained endotaxial nanostructures with high thermoelectric figure of merit, Nat. Chem., 3, 160–166 (DOI: 10.1038/nchem.955)

23. Xie, H., Su, X., Zhang, X., Li, Y., Chen, L., Uher, C., Wolverton, C., Snyder, G. J. (2019) Origin of intrinsically low thermal conductivity in talnakhite $Cu_{17.6}Fe_{17.6}S_{32}$, J. Am. Chem. Soc., 141, 18402–18411 (DOI: 10.1021/jacs.9b05072)

24. Li, W., Lin, S., Weiss, M., Wang, H., Snyder, G. J., Wolverton, C. (2018) Crystal structure induced ultralow lattice thermal conductivity in Ag_9AlSe_6, Adv. Energy Mater., 8, 1800030 (DOI: 10.1002/aenm.201800030)

25. Ying, P., Li, X., Wang, Y., Chen, L., Wu, D., Snyder, G. J. (2017) Hierarchical chemical bonds contributing to intrinsically low thermal conductivity in α-MgAgSb, Adv. Funct. Mater., 27, 1604145 (DOI: 10.1002/adfm.201604145)

26. Luo, Z. Z., Hao, S., Zhang, X., Shi, X., Uher, C., Chen, L., Snyder, G. J. (2018) Soft phonon modes from off-center Ge atoms lead to ultralow thermal conductivity, Energy Environ. Sci., 11, 3220–3229 (DOI: 10.1039/C8EE01755G)

27. Su, X., Wei, P., Li, H., Xie, H., Snyder, G. J. (2017) Multi-scale microstructural thermoelectric materials, Adv. Mater., 29, 1602013

28. Jana, M. K., Pal, K., Warankar, A., Biswas, K. (2017) Intrinsic rattler-induced low thermal conductivity in Zintl-type $TlInTe_2$, J. Am. Chem. Soc., 139, 4350–4353 (DOI: 10.1021/jacs.7b01434)

29. Qiu, W., Xi, L., Wei, P., Zhang, Y., Li, J., Yang, J. (2014) Part-crystalline part-liquid state and rattling-like thermal damping, Proc. Natl. Acad. Sci. USA, 111, 15031–15035 (DOI: 10.1073/pnas.1410349111)

30. Tyagi, K., Gahtori, B., Bathula, S., Biswas, K. (2014) Thermoelectric properties of Cu_3SbSe_3 with intrinsically ultralow lattice thermal conductivity, J. Mater. Chem. A, 2, 15829–15835 (DOI: 10.1039/C4TA02590C)

31. Koley, B., Lakshan, A., Raghuvanshi, P. R., Biswas, K. (2021) Ultralow lattice thermal conductivity at room temperature in Cu_4TiSe_4, Angew. Chem. Int. Ed., 60, 19969–19974 (DOI: 10.1002/anie.202014222)

32. Li, F., Liu, X., Ma, N., Wu, D., Li, J., Zhang, Q. (2023) Overdamped phonon diffusion and nontrivial electronic structure in KCu_5Se_3, J. Am. Chem. Soc., 145, 14542–14552 (DOI: 10.1021/jacs.3c04871)

33. Skoug, E. J., Morelli, D. T. (2011) Role of lone-pair electrons in producing minimum thermal conductivity, *Physical Review Letters*, 107, 235901. (DOI: 10.1103/PhysRevLett.107.235901)

34. Spitzer, D. P. (1970) Lattice thermal conductivity of semiconductors: A chemical bond approach, *Journal of Physics and Chemistry of Solids*, 31, 19–40.

35. Morelli, D. T., Jovovic, V., Heremans, J. P. (2008) Intrinsically minimal thermal conductivity in cubic I–V–VI_2 semiconductors, *Physical Review Letters*, **101**, 035901. (DOI: 10.1103/PhysRevLett.101.035901)

36. Skoug, E. J., Cain, J. D., Morelli, D. T. (2010) Structural effects on lattice thermal conductivity, *Applied Physics Letters*, 96, 181905. (DOI: 10.1063/1.3425886)

37. Zhang, Y., Skoug, E., Cain, J., et al. (2012) First-principles description of anomalously low lattice thermal conductivity, *Physical Review B*, **85**, 054306. (DOI: 10.1103/PhysRevB.85.054306)

38. Walsh, A., Payne, D. J., Egdell, R. G., Watson, G. W. (2011) Stereochemistry of post-transition metal oxides, *Chemical Society Reviews*, 40, 4455–4463. (DOI: 10.1039/C1CS15098G)

39. Laurita, G., Seshadri, R. (2022) Chemistry, structure, and function of lone pairs in extended solids, *Accounts of Chemical Research*, **55**, 2255–2265. (DOI: 10.1021/acs.accounts.1c00741)

40. Rathore, E., Juneja, R., Culver, S. P., Parker, S. C., Snyder, G. J. (2019) Origin of ultralow thermal conductivity in n-type cubic $AgBiS_2$, Chem. Mater., 31, 2106–2115 (DOI: 10.1021/acs.chemmater.9b00001)

41. Maria, Ilaria; Arora, Richa; Dutta, Moumita; Bhui, Anirban; Arora, Prashant; Sanyal, Biplab; Biswas, Kanishka (2023) Metavalent bonding-mediated dual $6s^2$ lone-pair expression leads to intrinsic lattice shearing in *n*-type $TlBiSe_2$, Journal of the American Chemical Society, 145, 11045–11055 (DOI: 10.1021/jacs.3c02146)

42. Zhu, Bing; Liu, Xiaoyuan; Wang, Qing; Zhang, Qinghao; Liu, Wenjie; Yu, Bin; Zhang, Xun; Chen, Gang; Zhao, Lidong (2020) Realizing record high performance in *n*-type Bi_2Te_3-based thermoelectric materials, Energy & Environmental Science, 13, 2106–2114 (DOI: 10.1039/D0EE01349H)

43. Chen, Shiyou; Walsh, Aron; Gong, Xian-Gang; Wei, Su-Huai (2013) Classification of lattice defects in the kesterite Cu_2ZnSnS_4 and $Cu_2ZnSnSe_4$ earth-abundant solar cell absorbers, Advanced Materials, 25, 1522–1539 (DOI: 10.1002/adma.201203146)

44. Kavanagh, Samuel R.; Savory, Callum N.; Scanlon, David O.; Walsh, Aron (2021) Hidden spontaneous polarisation in the chalcohalide photovoltaic absorber $Sn_2SbS_2I_3$, Materials Horizons, 8, 270–279 (DOI: 10.1039/D1MH00764E)

45. Minhas, H.; Sharma, R. K.; Pathak, B. (2025), Exploring Combined Stereochemically Active Lone-Pair and Rattling Effects in Thermoelectrics with Machine Learning Potentials, J. Phys. Chem. Lett., 16 (20), 5051–5061 (DOI: 10.1021/acs.jpclett.5c00952)

46. Minhas, Harpriya; Jena, Milan Kumar; Sharma, Rahul Kumar; Pathak, Biswarup (2025), Insights into Thermal Conductivity of Pnictogen Chalcogenides: Machine Learning Stereochemically Active Lone Pairs and Hybridization, Chemistry of Materials, 37, 1, 198–209 (DOI: 10.1021/acs.chemmater.4c02294)

47. He, Jie; Tritt, Terry M. (2017) Advances in thermoelectric materials research: looking back and moving forward, Science, 357, eaak9997 (DOI: 10.1126/science.aak9997)

48. Minhas, Harpriya; Sharma, Rahul Kumar; Pathak, Biswarup (2025), Antibonding States Drive Anharmonicity and Low Thermal Conductivity in Edge-Sharing Metal Chalcogenides, ACS Applied Materials & Interfaces, 17 (44), 60669–60681 (DOI: 10.1021/acsami.5c17211)

49. Feng, Tongtong; Lindsay, Lucas; Ruan, Xiulin (2017) Four-phonon scattering significantly reduces intrinsic thermal conductivity of solids, Physical Review B, 96, 161201(R) (DOI: 10.1103/PhysRevB.96.161201)

50. Feng, Tongtong; Ruan, Xiulin (2016) Quantum mechanical prediction of four-phonon scattering rates and reduced thermal conductivity of solids, Physical Review B, 93, 045202 (DOI: 10.1103/PhysRevB.93.045202)

51. Yang, X., Feng, T., Li, J., Ruan, X. (2019) Stronger role of four-phonon scattering than three-phonon scattering in thermal conductivity of III–V semiconductors at room temperature, *Phys. Rev. B*, 100, 245203 (DOI: 10.1103/PhysRevB.100.245203).

52. Xie, L., Feng, J.-H., Li, R., He, J.-Q. (2020) First-principles study of anharmonic lattice dynamics in low thermal conductivity $AgCrSe_2$: Evidence for a large resonant four-phonon scattering, *Phys. Rev. Lett.*, 125, 245901 (DOI: 10.1103/PhysRevLett.125.245901).

53. Heremans, J. P., Wiendlocha, B., Chamoire, A.-M. (2012) Resonant levels in bulk thermoelectric semiconductors, *Energy Environ. Sci.*, 5, 5510–5530 (DOI: 10.1039/C2EE22464E).

54. Yu, Y., Zhou, C., Ghosh, T., Maria, I., Arora, R., Dutta, M., Bhui, A., Sanyal, B., Biswas, K. (2023) Doping by design: Enhanced thermoelectric

performance of GeSe alloys through metavalent bonding, *Adv. Mater.*, 35, 2300893 (DOI: 10.1002/adma.202300893).

55. Bhui, A., Das, S., Arora, R., Maria, I., Dutta, M., Sanyal, B., Biswas, K. (2023) Hg doping-induced reduction in structural disorder enhances the thermoelectric performance in $AgSbTe_2$, *J. Am. Chem. Soc.*, 145, 21587–21597 (DOI: 10.1021/jacs.3c09643).

56. Lencer, D., Salinga, M., Grabowski, B., Hickel, T., Neugebauer, J., Wuttig, M. (2008) A map for phase-change materials, *Nat. Mater.*, 7, 972–977 (DOI: 10.1038/nmat2330).

57. Chelikowsky, J. R., Phillips, J. C. (1978) Quantum-defect theory of heats of formation and structural transition energies of liquid and solid simple-metal alloys and compounds, *Phys. Rev. B*, 17, 2453–2477 (DOI: 10.1103/PhysRevB.17.2453).

58. Raty, J.-Y., Gatti, C., Schön, C. F., Wuttig, M. (2021) How to identify lone pairs, van der Waals gaps, and metavalent bonding using charge and pair density methods: From elemental chalcogens to lead chalcogenides and phase-change materials, *Phys. Status Solidi RRL*, 15, 2000534 (DOI: 10.1002/pssr.202000534).

59. Born, M., Oppenheimer, R. (1927) Zur Quantentheorie der Molekeln, *Ann. Phys.*, 389, 457–484 (DOI: 10.1002/andp.19273892002).

60. Hohenberg, P., Kohn, W. (1964) Inhomogeneous electron gas, *Phys. Rev.*, 136, B864–B871 (DOI: 10.1103/PhysRev.136.B864).

61. Thomas, L. H. (1927) The calculation of atomic fields, *Math. Proc. Camb. Philos. Soc.*, 23, 542–548 (DOI: 10.1017/S0305004100011683).

62. Nesbet, R. K. (2002) Thomas–Fermi theory revisited, *Int. J. Quantum Chem.*, 90, 321–334 (DOI: 10.1002/qua.10061).

63. Rajagopal, A. K., Callaway, J. (1973) Inhomogeneous electron gas, *Phys. Rev. B*, 7, 1912–1919 (DOI: 10.1103/PhysRevB.7.1912).

64. Ceperley, D. M., Alder, B. J. (1980) Ground state of the electron gas by a stochastic method, *Phys. Rev. Lett.*, 45, 566–569 (DOI: 10.1103/PhysRevLett.45.566).

65. Zupan, A., Blaha, P., Schwarz, K., Perdew, J. P. (1998) Pressure-induced phase transitions in solid Si, SiO_2, and Fe: Performance of local-spin-density and generalized-gradient-approximation density functionals, *Phys. Rev. B*, 58, 11266–11272 (DOI: 10.1103/PhysRevB.58.11266).

66. Jones, R. O., Gunnarsson, O. (1989) The density functional formalism, its applications and prospects, *Rev. Mod. Phys.*, 61, 689–746 (DOI: 10.1103/RevModPhys.61.689).

67. Grossman, J. C., Mitas, L., Raghavachari, K. (1995) Structure and stability of molecular carbon: Importance of electron correlation, *Phys. Rev. Lett.*, 75, 3870–3873 (DOI: 10.1103/PhysRevLett.75.3870).

68. Perdew, J. P., Chevary, J. A., Vosko, S. H., Jackson, K. A., Pederson, M. R., Singh, D. J., Fiolhais, C. (1992) Atoms, molecules, solids, and surfaces: Applications of the generalized gradient approximation for exchange and correlation, *Phys. Rev. B*, 46, 6671–6687 (DOI: 10.1103/PhysRevB.46.6671).

69. Perdew, J. P., Yue, W. (1986) Accurate and simple density functional for the electronic exchange energy: Generalized gradient approximation, *Phys. Rev. B*, 33, 8800–8802 (DOI: 10.1103/PhysRevB.33.8800).

70. Perdew, J. P., Wang, Y. (1992) Accurate and simple analytic representation of the electron-gas correlation energy, *Phys. Rev. B*, 45, 13244–13249 (DOI: 10.1103/PhysRevB.45.13244).

71. Becke, A. D. (1988) Density-functional exchange-energy approximation with correct asymptotic behavior, *Phys. Rev. A*, 38, 3098–3100 (DOI: 10.1103/PhysRevA.38.3098).

72. Becke, A. D. (1993) Density-functional thermochemistry. III. The role of exact exchange, *J. Chem. Phys.*, 98, 5648–5652 (DOI: 10.1063/1.464913).

73. Lee, C., Yang, W., Parr, R. G. (1988) Development of the Colle–Salvetti correlation-energy formula into a functional of the electron density, *Phys. Rev. B*, 37, 785–789 (DOI: 10.1103/PhysRevB.37.785).

74. Miehlich, B., Savin, A., Stoll, H., Preuss, H. (1989) Results obtained with the correlation energy density functionals of Becke and Lee, Yang and Parr, *Chem. Phys. Lett.*, 157, 200–206 (DOI: 10.1016/0009-2614(89)87234-3).

75. Perdew, J. P., Burke, K., Ernzerhof, M. (1996) Generalized gradient approximation made simple, *Phys. Rev. Lett.*, 77, 3865–3868 (DOI: 10.1103/PhysRevLett.77.3865).

76. Hammer, B., Scheffler, M., Jacobsen, K. W., Nørskov, J. K. (1994) Multidimensional potential energy surface for H_2 dissociation over Cu(111), *Phys. Rev. Lett.*, 73, 1400–1403 (DOI: 10.1103/PhysRevLett.73.1400).

77. Penev, E., Kratzer, P., Scheffler, M. (1999) Effect of the cluster size in modeling the H_2 desorption and dissociative adsorption on Si(001), *J. Chem. Phys.*, 110, 3986–3993 (DOI: 10.1063/1.478279).

78. Tran, F., Blaha, P. (2009) Accurate band gaps of semiconductors and insulators with a semilocal exchange-correlation potential, *Phys. Rev. Lett.*, 102, 226401 (DOI: 10.1103/PhysRevLett.102.226401).

79. Koller, D., Tran, F., Blaha, P. (2012) Improving the modified Becke–Johnson exchange potential, *Phys. Rev. B*, 85, 155109 (DOI: 10.1103/PhysRevB.85.155109).

80. Perdew, J. P., Ernzerhof, M., Burke, K. (1996) Rationale for mixing exact exchange with density functional approximations, *J. Chem. Phys.*, 105, 9982–9985 (DOI: 10.1063/1.472933).

81. Heyd, J., Scuseria, G. E., Ernzerhof, M. (2003) Hybrid functionals based on a screened Coulomb potential, *J. Chem. Phys.*, 118, 8207–8215 (DOI: 10.1063/1.1564060).

82. Berland, K., Chakarova-Käck, S. D., Cooper, V. R., Lee, K., Schröder, E., Thonhauser, T., Langreth, D. C., Lundqvist, B. I. (2011) A van der Waals density functional study of adenine on graphene: Single-molecular adsorption and overlayer binding, *J. Phys.: Condens. Matter*, 23, 135001 (DOI: 10.1088/0953-8984/23/13/135001).

83. Berland, K., Jiao, Y., Lee, J.-H., Cooper, V. R., Schröder, E. (2017) Assessment of two hybrid van der Waals density functionals for covalent and non-covalent binding of molecules, *J. Chem. Phys.*, 146, 234106 (DOI: 10.1063/1.4986522).

84. Dion, M., Rydberg, H., Schröder, E., Langreth, D. C., Lundqvist, B. I. (2004) Van der Waals density functional for general geometries, *Phys. Rev. Lett.*, 92, 246401 (DOI: 10.1103/PhysRevLett.92.246401).

85. Kresse, G., Furthmüller, J. (1996) Efficient iterative schemes for *ab initio* total-energy calculations using a plane-wave basis set, *Phys. Rev. B*, 54, 11169–11186 (DOI: 10.1103/PhysRevB.54.11169).

86. Hamann, D. R. (1989) Generalized norm-conserving pseudopotentials, *Phys. Rev. B*, 40, 2980–2987 (DOI: 10.1103/PhysRevB.40.2980).

87. Hamann, D. R. (2013) Optimized norm-conserving Vanderbilt pseudopotentials, *Phys. Rev. B*, 88, 085117 (DOI: 10.1103/PhysRevB.88.085117).

88. Bloch, F. (1931) Quantum mechanics of electrons in crystal lattices, *Proc. R. Soc. Lond. A*, 130, 275–287 (DOI: 10.1098/rspa.1931.0019).

89. Loudon, R. (1977) Quantum theory of the solid state, *Phys. Bull.*, 28, 52–53 (DOI: 10.1088/0031-9112/28/2/047).

90. Kittel, C. (2004) *Introduction to Solid State Physics*, 8th ed., Wiley, New York.

91. Pulay, P. (1969) *Ab initio* calculation of force constants and equilibrium geometries in polyatomic molecules, *Mol. Phys.*, 17, 197–204 (DOI: 10.1080/00268976900100941).

92. Nielsen, O. H., Martin, R. M. (1985) Quantum-mechanical theory of stress and force, *Phys. Rev. B*, 32, 3780–3791 (DOI: 10.1103/PhysRevB.32.3780).

93. Kresse, G., Furthmüller, J. (1996) Efficiency of *ab initio* total energy calculations for metals and semiconductors using a plane-wave basis set, *Comput. Mater. Sci.*, 6, 15–50 (DOI: 10.1016/0927-0256(96)00008-0).

94. Dowker, J. S. (1982) Many-particle physics, *Phys. Bull.*, 33, 109–110 (DOI: 10.1088/0031-9112/33/3/038).

95. Madsen, G. K. H., Singh, D. J. (2006) BoltzTraP. A code for calculating band-structure dependent quantities, *Comput. Phys. Commun.*, 175, 67–71 (DOI: 10.1016/j.cpc.2006.03.007).

96. Li, W., Carrete, J., Katcho, N. A., Mingo, N. (2014) ShengBTE: A solver of the Boltzmann transport equation for phonons, *Comput. Phys. Commun.*, 185, 1747–1758 (DOI: 10.1016/j.cpc.2014.02.015).

97. Madsen, G. K. H., Carrete, J., Verstraete, M. J. (2018) BoltzTraP2, a program for interpolating band structures and calculating semiclassical transport coefficients, *Comput. Phys. Commun.*, 231, 140–145 (DOI: 10.1016/j.cpc.2018.05.010).

98. Ganose, A. M., Park, J., Faghaninia, A., Woods-Robinson, R., Persson, K. A., Jain, A. (2021) Efficient calculation of carrier scattering rates from first principles, *Nat. Commun.*, 12, 2222 (DOI: 10.1038/s41467-021-22440-5).

99. Broido, D. A., Malorny, M., Birner, G., Mingo, N., Stewart, D. A. (2007) Intrinsic lattice thermal conductivity of semiconductors from first principles, *Appl. Phys. Lett.*, 91, 231922 (DOI: 10.1063/1.2822891).

100. Baroni, S., de Gironcoli, S., Dal Corso, A., Giannozzi, P. (2001) Phonons and related crystal properties from density-functional perturbation theory, *Rev. Mod. Phys.*, 73, 515–562 (DOI: 10.1103/RevModPhys.73.515).

101. Togo, A., Chaput, L., Tadano, T., Tanaka, I. (2023) Implementation strategies in phonopy and phono3py, *J. Phys.: Condens. Matter*, 35, 353001 (DOI: 10.1088/1361-648X/acd66a).

102. Togo, A. (2023) First-principles phonon calculations with phonopy and phono3py, *J. Phys. Soc. Jpn.*, 92, 012001 (DOI: 10.7566/JPSJ.92.012001).

103. Franklin, J. (2005) The elements of statistical learning: Data mining, inference and prediction, *Math. Intell.*, 27, 83–85 (DOI: 10.1007/BF02985802).

104. Sanchez-Lengeling, B., Aspuru-Guzik, A. (2018) Inverse molecular design using machine learning: Generative models for matter engineering, *Science*, 361, 360–365 (DOI: 10.1126/science.aat2663).

105. Zuo, Y., Chen, C., Li, X., Deng, Z., Chen, Y., Behler, J., Csányi, G., Shapeev, A. V., Thompson, A. P., Wood, M. A., Ong, S. P. (2020) Performance and cost assessment of machine learning interatomic potentials, *J. Phys. Chem. A*, 124, 731–745 (DOI: 10.1021/acs.jpca.9b08723).

106. Zhang, L., Han, J., Wang, H., Car, R., E, W. (2018) Deep potential molecular dynamics: A scalable model with the accuracy of quantum mechanics, *Phys. Rev. Lett.*, 120, 143001 (DOI: 10.1103/PhysRevLett.120.143001).

107. Batzner, S., Musaelian, A., Sun, L., Geiger, M., Mailoa, J. P., Kornbluth, M., Molinari, N., Smidt, T. E., Kozinsky, B. (2022) E(3)-equivariant graph neural networks for data-efficient and accurate interatomic potentials, *Nat. Commun.*, 13, 2453 (DOI: 10.1038/s41467-022-29939-5).

108. Hajibabaei, A., Myung, C. W., Kim, K. S. (2021) Sparse Gaussian process potentials: Application to lithium diffusivity in superionic conducting solid electrolytes, *Phys. Rev. B*, 103, 214102 (DOI: 10.1103/PhysRevB.103.214102).

109. Willow, S. Y., Hajibabaei, A., Ha, M., Kim, K. S. (2024) Sparse Gaussian process-based machine learning first-principles potentials for materials simulations: Application to batteries, solar cells, catalysts, and macromolecular systems, *Chem. Phys. Rev.*, 5, 011303 (DOI: 10.1063/5.0231265).

110. Thompson, A. P., Swiler, L. P., Trott, C. R., Foiles, S. M., Tucker, G. J. (2015) Spectral neighbor analysis method for automated generation of

quantum-accurate interatomic potentials, *J. Comput. Phys.*, 285, 316–330 (DOI: 10.1016/j.jcp.2014.12.018).

111. Shapeev, A. V. (2016) Moment tensor potentials: A class of systematically improvable interatomic potentials, *Multiscale Model. Simul.*, 14, 1153–1173 (DOI: 10.1137/15M1054183).

112. Novikov, I. S., Gubaev, K., Podryabinkin, E. V., Shapeev, A. V. (2021) The MLIP package: Moment tensor potentials with MPI and active learning, *Mach. Learn.: Sci. Technol.*, 2, 025002 (DOI: 10.1088/2632-2153/abc9fe).

113. Drautz, R. (2019) Atomic cluster expansion for accurate and transferable interatomic potentials, *Phys. Rev. B*, 99, 014104 (DOI: 10.1103/PhysRevB.99.014104).

114. Hajibabaei, A., Kim, K. S. (2021) Universal machine learning interatomic potentials: Surveying solid electrolytes, *J. Phys. Chem. Lett.*, 12, 8115–8125 (DOI: 10.1021/acs.jpclett.1c01605).

115. Behler, J., Parrinello, M. (2007) Generalized neural-network representation of high-dimensional potential-energy surfaces, *Phys. Rev. Lett.*, 98, 146401 (DOI: 10.1103/PhysRevLett.98.146401).

116. Mortazavi, B., Podryabinkin, E. V., Novikov, I. S., Shapeev, A. V., Rabczuk, T. (2021) Accelerating first-principles estimation of thermal conductivity by machine-learning interatomic potentials: A MTP/ShengBTE solution, *Comput. Phys. Commun.*, 258, 107583 (DOI: 10.1016/j.cpc.2020.107583).

117. Chen, C., Ong, S. P. (2022) A universal graph deep learning interatomic potential for the periodic table, *Nat. Comput. Sci.*, 2, 718–728 (DOI: 10.1038/s43588-022-00349-3).

118. Choudhary, K., DeCost, B., Major, L., Kalinin, S. V., Persson, K. A., Rondinelli, J. M. (2023) Unified graph neural network force field for the periodic table: Solid-state applications, Digit. Discov., 2, 346–355 (DOI: 10.1039/D2DD00096B)

119. Batatia, I., Kovács, D. P., Simm, G. N. C., Ortner, C., Csányi, G., Müller, K.-R. (2023) MACE: Higher-order equivariant message passing neural networks for fast and accurate force fields, Adv. Neural Inf. Process. Syst., 36, 11423–11437

120. Deng, B., Zhong, P., Jun, K. J., Choi, Y., Chen, Z., Tang, Q., Wu, X., Park, S., Liu, W., Galli, G. (2023) CHGNet as a pretrained universal neural network potential for charge-informed atomistic modelling, Nat. Mach. Intell., 5, 1031–1041 (DOI: 10.1038/s42256-023-00716-3)

121. Yang, H., Hu, C., Zhou, Y., Li, X., Zhang, J., Wang, Q., Chen, S., Liu, M. (2024) MatterSim: A deep learning atomistic model across elements, temperatures and pressures, (arXiv preprint arXiv: 2405.04967v2)

122. Deng, B., Choi, Y., Zhong, P., Jun, K. J., Chen, Z., Tang, Q., Wu, X., Park, S., Liu, W., Galli, G. (2024) Overcoming systematic softening in universal machine learning interatomic potentials by fine-tuning, npj Comput. Mater., 10, 94 (DOI: 10.1038/s41524-024-01500-6)

123. Friederich, P., Häse, F., Proppe, J., Aspuru-Guzik, A. (2021). Machine-learned potentials for next-generation matter simulations, *Nat. Mater.*, 20, 750–761 (DOI: 10.1038/s41563-020-0777-6).

124. Goar, V., Yadav, N. S. (2024). Foundations of machine learning, in *Intelligent Optimization Techniques for Business Analytics*, Springer, Cham.

125. Hinton, G. E. (2012). A practical guide to training restricted Boltzmann machines, *Lect. Notes Comput. Sci.*, 7700, 599–619 (DOI: 10.1007/978-3-642-35289-8_32).

126. Liu, H., Motoda, H. (1998). *Feature Selection for Knowledge Discovery and Data Mining*, Springer, Boston.

127. Bishop, C. M. (2007). Pattern recognition and machine learning, *J. Electron. Imaging*, 16, 049901 (DOI: 10.1117/1.2819119).

128. Dembczyński, K., Waegeman, W., Hüllermeier, E. (2012). An analysis of chaining in multi-label classification, *Front. Artif. Intell. Appl.*, 241, 294–301.

129. Spearman, C. (1904). The proof and measurement of association between two things, *Am. J. Psychol.*, 15, 72–101 (DOI: 10.2307/1412159).
130. Ali, Y. A., Awwad, E. M., Al-Razgan, M., Maarouf, A. (2023). Hyperparameter search for machine learning algorithms for optimizing the computational complexity, *Processes*, 11, 349 (DOI: 10.3390/pr11020349).
131. Bergstra, J., Bengio, Y. (2012) Random search for hyper-parameter optimization, J. Mach. Learn. Res., 13, 281–305
132. Su, X. G. (2009) Linear regression analysis: Theory and computing, Springer, Berlin, Germany
133. Sperandei, S. (2014) Understanding logistic regression analysis, Biochem. Med. (Zagreb), 24, 12–18 (DOI: 10.11613/BM.2014.003)
134. Nigsch, F., Bender, A., Van Buuren, B., et al. → We need full authors. Could you provide them? Otherwise: Nigsch, F., Bender, A., Van Buuren, B., Tetko, I. V., Muegge, I., et al. (2006) Melting point prediction employing k-nearest neighbor algorithms and genetic parameter optimization, J. Chem. Inf. Model., 46, 2412–2422 (DOI: 10.1021/ci060149f)
135. Zhang, L., Suganthan, P. N. (2017) Benchmarking ensemble classifiers with novel co-trained kernel ridge regression and random vector functional link ensembles [Research Frontier], IEEE Comput. Intell. Mag., 12, 40–53 (DOI: 10.1109/MCI.2017.2742867)
136. Cortes, C., Vapnik, V. (1995) Support-vector networks, Mach. Learn., 20, 273–297 (DOI: 10.1023/A:1022627411411)
137. Breiman, L. (2001) Random forests, Mach. Learn., 45, 5–32 (DOI: 10.1023/A:1010933404324)
138. Zhu, J., Zou, H., Rosset, S., Hastie, T. (2009) Multi-class AdaBoost, Stat. Interface, 2, 349–360
139. Chen, T., Guestrin, C. (2016) XGBoost: A scalable tree boosting system, In: Proc. ACM SIGKDD Int. Conf. Knowl. Discov. Data Min., 785–794

140. Challis, E., Hurley, P., Serra, L., Allsop, D., McIntosh, A., Corvin, A., Waddington, J., Weickert, C., Whelan, C., Howells, D. (2015) Gaussian process classification of Alzheimer's disease and mild cognitive impairment from resting-state fMRI, Neuroimage, 112, 232–243 (DOI: 10.1016/j.neuroimage.2015.02.037)

141. Myles, A. J., Feudale, R. N., Liu, Y., Woody, N. A., Brown, S. D. (2004) An introduction to decision tree modeling, J. Chemom., 18, 275–285

142. Criminisi, A., Shotton, J., Konukoglu, E. (2011) Decision forests: A unified framework for classification, regression, density estimation, manifold learning and semi-supervised learning, Found. Trends Comput. Graph. Vis., 7, 81–227

143. Xie, T., Grossman, J. C. (2018) Crystal graph convolutional neural networks for an accurate and interpretable prediction of material properties, Phys. Rev. Lett., 120, 145301 (DOI: 10.1103/PhysRevLett.120.145301)

144. Omee, S. S., Louis, S. Y., Fu, N., Zhang, X., Wang, Y., Lee, J. (2022) Scalable deeper graph neural networks for high-performance materials property prediction, Patterns, 3, 100491 (DOI: 10.1016/j.patter.2022.100491)

145. Choudhary, K., DeCost, B. (2021) Atomistic line graph neural network for improved materials property predictions, NPJ Comput. Mater., 7, 128 (DOI: 10.1038/s41524-021-00650-1)

146. Glantz, S. A., Slinker, B. K., Neilands, T. B. (2016) Primer of applied regression & analysis of variance, McGraw-Hill, New York, NY

147. Soper, D. S. (2021) Greed is good: Rapid hyperparameter optimization and model selection using greedy k-fold cross validation, Electronics (Switzerland), 10, 1973 (DOI: 10.3390/electronics10161973)

148. Longo, L., Brcic, M., Cabitza, F., Santucci, G., Guidotti, R. (2024) Explainable artificial intelligence (XAI) 2.0: A manifesto of open challenges and interdisciplinary research directions, Inf. Fusion, 106, 102–134

149. Lundberg, S. M., Erion, G., Chen, H., DeGrave, A., Prutkin, J. M., Nair, B., Katz, R., Himmelfarb, J., Bansal, N., Lee, S.-I. (2020) From local explanations to global understanding with explainable AI for trees, Nat. Mach. Intell., 2, 56–67 (DOI: 10.1038/s42256-019-0138-9)

CHAPTER 1

CHAPTER 2

Dimensionality, Thickness, and Higher-Order Anharmonicity

CHAPTER 2

CHAPTER 2

Section: A

2.1. Introduction

As energy demands increase with modernization and the increasing human population, the need to shift towards renewable sources for harnessing electrical energy becomes important due to the obvious challenges in using age-old non-renewable sources such as oil, gas, and fossil fuels *[1]*. Along with limited supply, usage of non-renewable sources also poses an environmental threat. Renewable sources like solar or wind energy are quite intermittent in nature *[2]*. In this context, thermoelectric (TE) technology becomes attractive with the ability to convert waste thermal energy into useful electric energy *[3, 4]*. Thermoelectric devices are ideal for use in various industries such as chemical, nuclear and steel industries, solar power plants, thermal power plants, smart gadgets and space technologies *[5–10]*. Thermoelectric materials have a long way to tread despite all the advantages before they can be applied for large-scale commercialization on par with other energy storage systems. This is because of the low efficiency in their ability to convert thermal to electrical energy due to the challenges in simultaneously achieving low thermal conductivity and high electrical conductivity in a material *[11–13]*. As of now, most of the thermoelectric research is based on improving certain materials which possess good thermoelectric properties. PbTe, SiGe, and Bi_2Te_3 are among the most commercialized materials with thermoelectric applications *[8, 14–17]*. However, all these materials suffer from a low figure of merit (ZT), an important dimensionless metric in thermoelectrics *[1]*. Some of these materials are composed of heavy metals which are not recommended for futuristic applications. Previous studies have shown that some of the effective ways to achieve a high ZT value can be by decreasing lattice thermal conductivity, called phonon engineering, and by increasing the power factor (PF) term, which is called bandgap engineering *[17, 18]*. Phonon engineering includes dimensionality reduction *[19–21]* and defect creation *[16, 22]* while band engineering can be done by doping or inducing

pressure in the system *[23–25]*. Controlling the lattice thermal conductivity (κ_L) could be achieved by introducing points defects, rattling modes, plane defects, line defects which result in an increase in low-frequency acoustic phonon scattering *[26–28]*. Another way could be choosing a complex structure material with large anharmonicity leading to intrinsically ultra-low κ_L *[1]*.

While GeSe being a member of the chalcogenide family, possess characteristics such as low electronegativity difference, and high atomic weight, the ZT value of the bulk GeSe is less due to high thermal conductivity. One of the effective ways to enhance the power factor by reducing dimensionality (1D and 2D) was first introduced in 1993 by Hicks and Dresselhaus, where the movement of electrons is confined in a particular direction *[29–31]*. Thus, it is important to model low dimensional materials of the chalcogenide family to increase their thermoelectric performance. The dimensionality reduction leads to decrease in the lattice thermal conductivity, which is the only independent parameter in the equation leading to high ZT. Two dimensional materials, being of very small size (in the order of 10^{-9} m) can find applications in various fields which require small size TE devices with high energy density. Some of the applications of high ZT low dimensional materials are in smart wearables, space technologies for energy production to sustain the satellites and space shuttles, and medical equipment *[6–8, 32]*. The metal chalcogenide materials exhibit layered interconnected structures with weak van der Waals (vdW) interactions in their bulk form, while atoms in the layered structure have covalent interactions. The layered stacking in these structures promotes the synthesis of 2D nanosheets. The theoretical studies reported that the 2D structures of these chalcogenides are thermodynamically stable and endorse ultra-low thermal conductivity. In addition to material-specific engineering approaches, recent advances in phonon interaction modeling and machine learning have opened new avenues for optimizing

thermoelectric performance. This chapter explores these developments through case studies on γ -GeSe, GeS, and data-driven design strategies.

2.2. Model and Computational Details

The various structures of γ-GeSe considered in this chapter are illustrated in **Figure 2.1**. Bulk γ-GeSe belongs to the $P6_3mc$ space group in the hexagonal crystal family *[33]*. The bulk structure of γ-GeSe has a four-layer unit cell consisting of two merged buckled honeycomb lattices held together by weak vdW interactions. The lattice parameter for the optimized unit cell of bulk γ-GeSe is calculated to be: a = b = 3.78 Å, c = 15.5 Å, α = β = 90°, γ = 120° which also agrees with experimental reports of the synthesized material experimentally grown on SiO_2/Si substrate *[33]*.

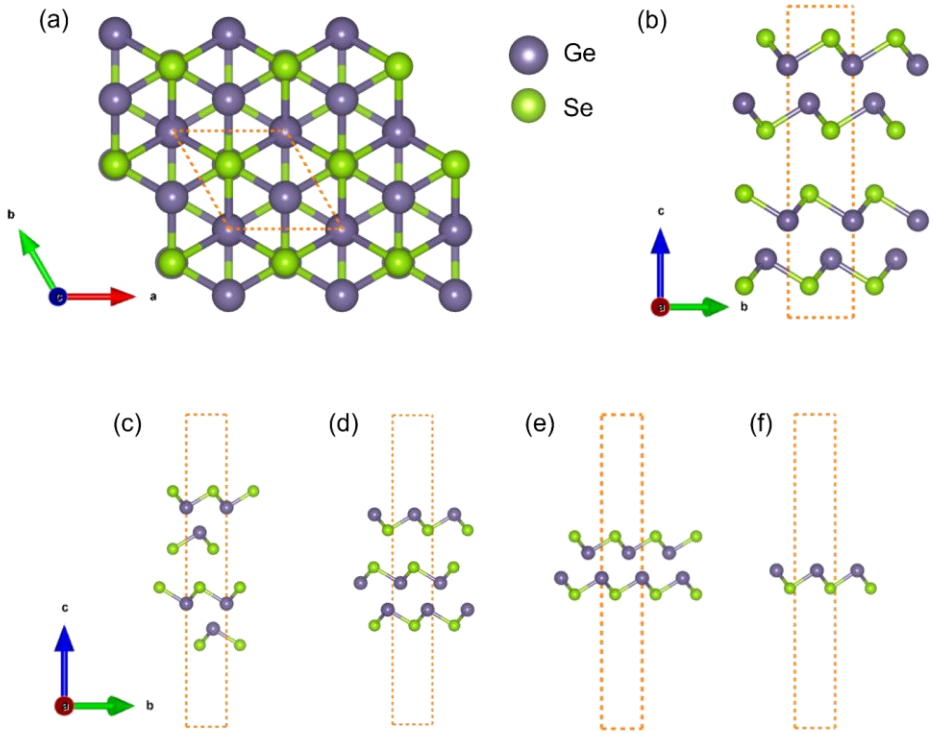


Figure 2.1: Optimized structures of γ-GeSe (a) bulk – top view, (b) bulk – side view, (c) quad-layer, (d) tri-layer, (e) bilayer, and (f) monolayer.

The first-principles calculations have been performed by considering the projector augmented wave (PAW) method as implemented in the Vienna Ab initio Simulation Package (VASP) *[34, 35]*. The generalized gradient approximation (GGA) of Perdew-Burke-Ernzerhof (PBE) is employed as the exchange-correlation functional with an energy cut-off value of 300 eV to describe the core and valence electron interactions *[36, 37]*. All the structural relaxations have been carried out by considering an energy convergence criterion of $< 10^{-6}$ eV/Å and a force convergence criterion of $< 10^{-3}$ eV/Å. The dispersion energy corrections for van der Waals interactions have been considered by Grimme's DFT-D3 method included in our calculations *[38]*. A vacuum of ~25 Å has been considered to avoid interactions between periodic images of 2D materials. 5 × 5 × 3 and 5 × 5 × 1 Γ-centred k-point meshes have been used for the Brillouin zone sampling of bulk and reduced layers, respectively. We also have considered the Heyd-Scuseria-Ernzerhof (HSE06) hybrid functional to obtain accurate electronic properties of the considered systems *[39, 40]*. The Hartree-Fock exchange parameter (α) of 25% was considered in the hybrid functional calculations. Phonon calculations have been carried out by using PHONOPY package which uses the finite displacement method to calculate second-order interatomic force constants (IFCs) *[41]*. Phonon calculations have been carried out by using PHONOPY package which uses the finite displacement method to calculate second-order interatomic force constants (IFCs) using a 3 × 3 × 1 supercell. The third order force constants calculated by ShengBTE code using 3 × 3 × 1 considering third nearest neighboring atoms. For the calculation of third-order anharmonic IFCs, the thirdorder.py code was utilized. Finally, the second-order IFCs and third-order IFCs were fed into the SHENGBTE code to obtain the κ_L of the materials *[42]*. The Seebeck coefficient and transport properties of these materials have been determined through the BoltzTrap2 code which takes into consideration the semiclassical Boltzmann theory, Boltzmann transport equation (BTE), and constant relaxation time approximation (CRTA) methods *[43]*. We have

used CRTA with t = 10^{-14} s for thermal and electrical conductivity calculations *[43]*. A constant relaxation time approximation (CRTA) has been considered with relaxation time, $\tau = 10^{-14}$ s to calculate the electrical conductivity as well as electronic thermal conductivity using BoltzTrap2 code. The BoltzTrap2 code considers a constant relaxation time across all the temperatures which has been considered as a reasonable assumption in previous report. Our considered τ value has been used in many previous reports on similar materials of 2D chalcogenide family *[43, 44]*. Ab initio molecular dynamics (AIMD) simulations are performed in the NVT ensemble at 900 K, and the temperature control is achieved by a Nosé–Hoover thermostat.

2.3. Results and Discussion

2.3.1. Structure and Stability

The calculated bond length between Ge-Se is 2.55 Å, which is comparable to the reported experimental and theoretical results of Ge-Se (2.52 Å) *[33]*. The bulk γ-GeSe has a stacking sequence of AB′, where the above layer is stacked on the below layer by one-third of unit cell shift along the armchair direction and placed by rotation of 180°. The bulk and reduced layers consist of both strong and weak bonding arrangements along with vdW interactions. Slack's theory reveals the dependency of lower κ_L on major factors like high average atomic mass, weak interatomic interactions, and high anharmonicity of a system *[45, 46]*. To understand the atomic interactions in the system, the Electron Field Localization Function (ELF) has been calculated as shown in Figure 2.2. From the ELF of γ-GeSe bulk (**Figure 2.2(a)**), it is evident that electron density is localized on the Se atoms only, whereas, for the 2D systems (**Figure 2.2(b-e)**), the electron density is localized on both the Ge and Se atoms. However, the presence of electron density between the Ge and Se atoms shows the covalent character between them. The presence of lone pair in the system interacts with bond pair and overall results in the weakening of the bond strength. Secondly, the

lone pair lone pair repulsions in the interlayer increase the anharmonicity of the system. Overall, decreases the thermal conductivity of the system.

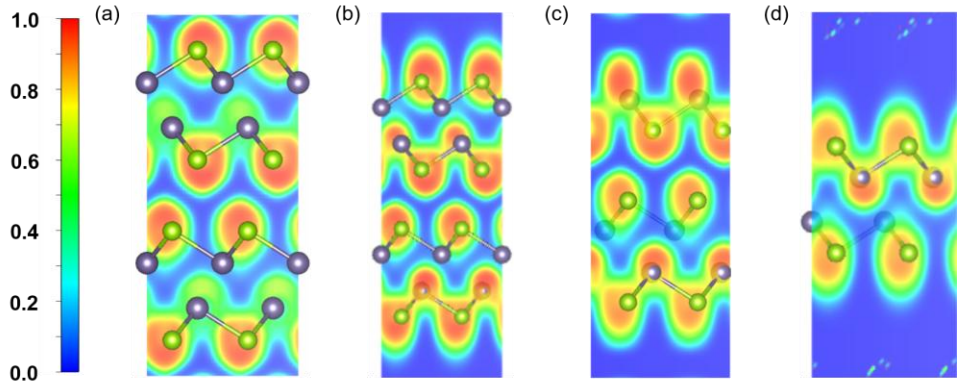


Figure 2.2: Electron localization function (isosurface value is 0.03 e $Å^{-3}$) of γ-GeSe (a) bulk, (b) quad-layer, (c) trilayer, (d) bilayer, and (e) monolayer. The ELF plots have been prepared by considering a (100) plane cross section for all of the models.

The mechanical stability of considered 2D structures has been determined by calculating their elastic constants (C_{11}, C_{12}) as presented in Table 1. The Born criteria for mechanical stability of hexagonal material have been satisfied for all the structures *[47]*. Therefore, the modeled 2D materials can be considered mechanically stable. The Young's Modulus (Y), Poisson's ratio (ν), and Shear Modulus (P) are calculated using the following equations,

$$Y_x = Y_y = Y = \frac{C_{11}^2 - C_{12}^2}{C_{11}} \quad (1)$$

$$\nu_{xy} = \nu_{yx} = \nu = \frac{C_{12}}{C_{11}} \quad (2)$$

$$P = \frac{Y}{2\,(1+\nu)} \quad (3)$$

The corresponding results of Young's modulus, Shear Modulus, and Poisson's ratio have been tabulated for all considered materials in **Table**

2.1. The Young's Modulus, as well as Shear Modulus, are found to decrease with thickness from quad-layer to monolayer. The same trend of thickness-dependent Young's modulus has also been reported for various materials like graphene and hexagonal boron nitride (hBN) *[48, 49]*. The Young's Modulus obtained in our studied materials are much lower compared to graphene (345 N/m), hexagonal boron nitride (271 N/m) but higher than silicene (60 N/m), and phosphorene (23-92 N/m) *[48, 50–52]*. The Shear modulus is also found to follow the same trend as Young's Modulus. A mechanically stable material should have Poisson's ratio within the range of 0 to 0.45. The Poisson's ratio value for all the systems considered satisfies this criterion.

Table 2.1: Elastic Constants (C_{11}, C_{12}), Young's Modulus (Y), Shear Modulus (P), and Poisson's Ratio (ν) for the Considered Structures of γ-GeSe

Structure	C_{11}	C_{12}	**Young's modulus (Y)**	**Shear modulus (P)**	**Poisson's ratio (ν)**
bulk	91.47	14.35	89.22	38.56	0.16
quad-layer	298.78	37.75	294	130.08	0.13
trilayer	130.36	22.35	126.52	54.06	0.16
bilayer	96	14.29	93.87	40.81	0.15
monolayer	53	8.51	51.63	22.25	0.16

The formation energy (E_f) and cohesive Energy (E_c) of bulk, bi, tri, and quad layers have been calculated by the following equations,

$$E_f = \frac{E_{Total} - (n_{Ge}\,\mu_{Ge} + n_{Se}\mu_{Se})}{n_{Ge} + n_{Se}} \quad (4)$$

$$E_c = \frac{E_{Total} - (n_{Ge}E_{Ge} + n_{Se}E_{Se})}{n_{Ge} + n_{Se}} \quad (5)$$

The μ_{Ge} and μ_{Se} represents the chemical potential of Ge bulk structure and Se bulk molecule, respectively. The E_{Total}, E_{Ge}, and E_{Se}, are the total

energy of system, energy of single isolated Ge atom and energy of single isolated Se atom respectively. The n_{Ge} and n_{Se} represents the number of Ge and Se atoms in unit cell of our material. The formation energy (E_f) of γ -GeSe for all the considered systems have been calculated with respect to the isolated bulk face centered cubic Ge and Se, whereas cohesive energy (E_c) has been calculated with respect to the discrete atoms. The negative value of formation energy means that the formation of all γ -GeSe systems are possible whereas, the negative cohesive energy means that once the γ -GeSe is formed, it would not get decomposed into atoms. The values of E_f shows that formation of multilayers of γ -GeSe systems are more favorable over monolayer. Therefore, the E_f is highly thickness dependent whereas cohesive energy is independent of number of layers. The cohesive and formation energy calculations provided in **Table 2.2**, also ascertain the thermodynamic stability of the studied γ-GeSe systems.

Table 2.2: Cohesive Energy and Formation Energy for the Considered Structures of γ-GeSe

Structures	Cohesive energy (eV atom^{-1})	Formation energy (eV atom^{-1})
bulk	–3.51	–0.29
quad-layer	–3.48	–0.26
trilayer	–3.44	–0.22
bilayer	–3.45	–0.23
monolayer	–3.31	–0.18

2.3.2. Phonon Transport Properties

Phonon calculations tell us about the dynamical stability of a material and reveal important information about the nature of the band structure which affects the lattice thermal properties of the material. The phonon band structure calculations show that bulk, as well as bilayer, tri-layer, and quad-layer structures of γ-GeSe are dynamically stable with all phonon bands in the positive range as shown in **Figure 2.3(a-e)**. Only the γ-GeSe monolayer

shows imaginary modes of vibration as is evident from its phonon band structure in **Figure 2.3(e)** and hence not considered for further calculations. As a characteristic of 2D materials, the acoustic modes are found to be linear at Γ position whereas, flexural out-of-plane acoustic (TA) modes are quadratic for all phonon band structures. The phonon band structures show the relevant number of phonon anti-crossing, which results in enhanced anharmonic scattering in the system. The effect of dipole-dipole interactions is incorporated into the dynamic matrix based on Born effective charges and high-frequency dielectric constants, which results in the splitting between longitudinal optical phonon frequency and transverse optical phonon frequency (LO-TO splitting) at the Γ-position.

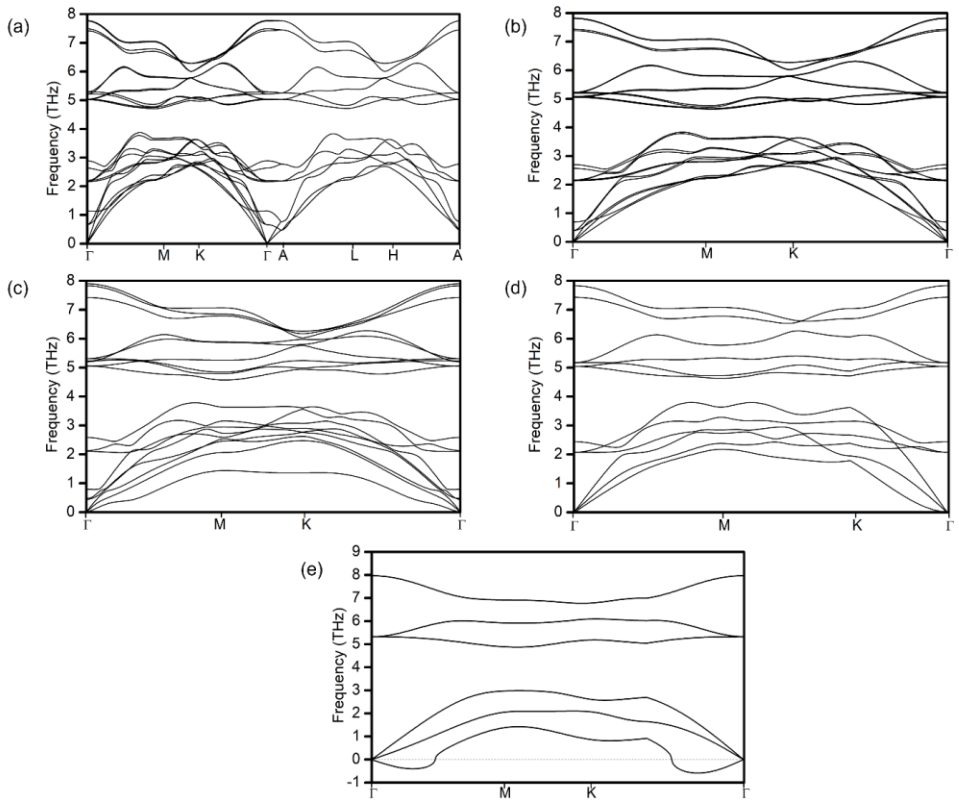


Figure 2.3: Phonon band structures in THz of γ-GeSe (a) bulk, (b) quad-layer, (c) tri-layer, (d) bilayer and (e) monolayer.

Figure 2.3(a) denotes γ-GeSe bulk with eight atoms in unit cell contributing total twenty-four modes. For quad-layer with eight atoms in the unit cell, twenty-four modes of vibration can be seen in **Figure 2.3(b)** but with lower frequency than bulk. The lowest frequency acoustic curve (TA) is quadratic in nature whereas the other two acoustic curves (TA' and LA) are linear at Γ- point. Similarly, the tri-layer γ-GeSe system with six atoms in the unit cell, shows eighteen modes, out of which the three lowest frequency vibrations are acoustic, and the rest are optical (**Figure 2.3(c)**). For a bilayer system containing four atoms in the unit cell, there are twelve vibrational degrees of freedom. Among these, the three lowest-frequency branches correspond to the acoustic modes, two transverse acoustic modes (TA and TA′) and one longitudinal acoustic mode (LA) while the remaining nine branches arise from optical vibrational modes (**Figure 2.3(d)**). As we increase the layers of the 2D material, the lowest acoustic branches in the band structures shift towards a lower frequency range along the k-path which can be depicted from bilayer and trilayer whereas, the quadlayer shows more similarity with the bulk phonon band structure. The anti-crossing is much more noticeable in bulk than in quad-layer followed by tri- and bilayer. The least anti-crossing or hybridization between acoustic and optical modes, inferred from the noticeable gap at the crossing point for the bilayer system in **Figure 2.3(d)**. Therefore, upon reducing the dimensionality from 3D to 2D, the increase in scattering rate and further reduces the acoustic mode velocities thereby predicting lower lattice thermal conductivity. The number of phonon modes are dependent on number of atoms in the unit cell so, it's highly dependent on the thickness of the layer. As the thickness changes the number of phonon modes also changes, which overall affects the crossing and anti-crossing in the system.

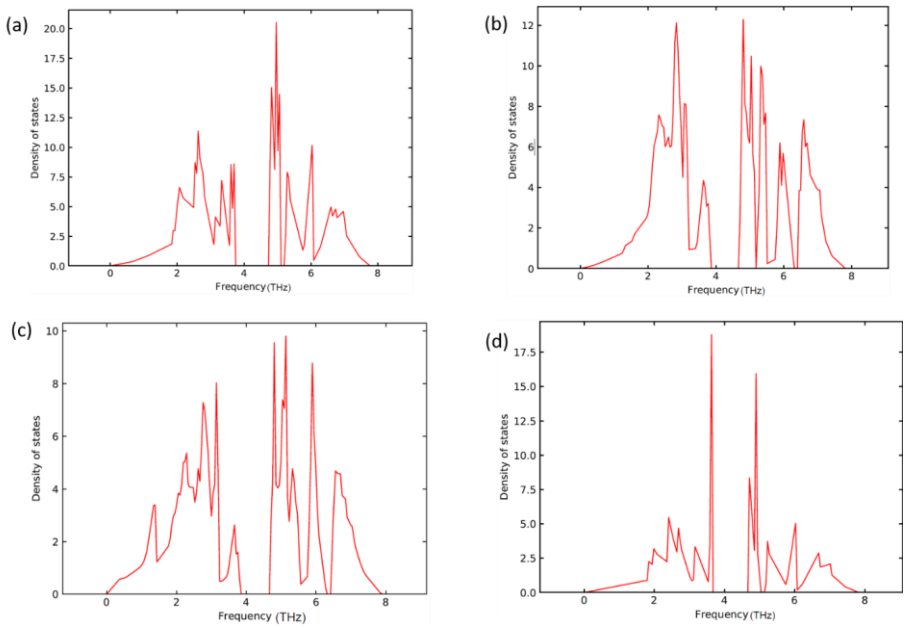


Figure 2.4: Phonon density of states for γ-GeSe (a) bulk, (b) quad-layer, (c) tri-layer, and (d) bilayer.

The phonon density of states shown in **Figure 2.4** provides a qualitative description regarding the role of chemical bonding on heat transport in bulk and 2D layered materials. The heat is mainly carried by phonon modes with a frequency below 3 THz. The acoustic modes below 3 THz are found to become dense with the increase in the number of layers. The phonon density of states (DOS) also reflects the contribution of the total acoustic and optical waves at each frequency. Since Ge and Se have comparable atomic masses, they contribute equally to the acoustic vibrational character in γ-GeSe. We have compared phonon spectra of our γ-GeSe bulk with available Raman spectra from a previous report *[33]*. As is evident from **Table 2.3**, our calculated frequencies are in good agreement with the available results. The three modes of acoustic vibrations that are more prominent are likely to be the Raman active modes (A_1^1, E_2^1, and A_2^1) in the γ-GeSe bilayer. The A_1^1 mode should correspond to the TA vibrations, i.e., out-of-plane vibrations of the Ge–Se pair in the opposite direction. The E_2^1 modes represent the in-plane vibrations and motion of Ge–Se atoms, where they

vibrate 180° out of phase. The A_2^1 mode should correspond to out-of-plane vibrations of Ge and Se atoms, where they vibrate 180° out of phase.

Table 2.3: Comparison of calculated, experimentally observed Raman shifts and the previously reported calculated values of phonon modes of AB′ stacked γ-GeSe. The E_1 modes are Raman active but forbidden in the back-scattering geometry and noted as N/A *[33]*.

Symmetry	Calculated	Experimental	Previous Results
$^1E_2$	22	22	26.2
$^2E_2$	72.1	68	59.9
$^1E_1$	73.4	NA	64.7
$^1A_1$	96.4	90	91.7
$^3E_2$	167.5	166	165.3
$^2E_1$	168	NA	169
$^3E_1$	174	NA	178.9
$^4E_2$	176.4	NA	181.4
$^2A_1$	247.6	258	240.1
$^3A_1$	259.4	266	256.4

2.3.3. Electronic Transport Properties

Moving ahead, we calculate the band gaps to infer insights regarding the electronic properties of the considered 2D materials which in turn affect the electronic conductivity and Seebeck coefficient of the material. The bandgap of γ-GeSe bulk is calculated along the high symmetry point of the first Brillion zone as shown in **Figure 2.5(a)**. Our calculated indirect bandgap of 0.36 eV for bulk γ-GeSe using HSE06 functional, shows good agreement with the experimentally calculated indirect bandgap of 0.36 eV. The γ-GeSe bulk shows the direct bandgap of 0.54 eV at Γ position. The highest valence band (VB) has a hole valley at Γ and A points whereas the lowest conduction band (CB) has electron valleys at M, Γ, A and L points. In γ-GeSe bulk, the valence band maxima and the conduction band minima lie at Γ and M, respectively. As we reduce the layer thickness, conduction band minima located at M continuously destabilizes, while the valence band

minima at Γ stabilizes. As a result, the bandgap increases as we decrease the number of layers of the 2D material.

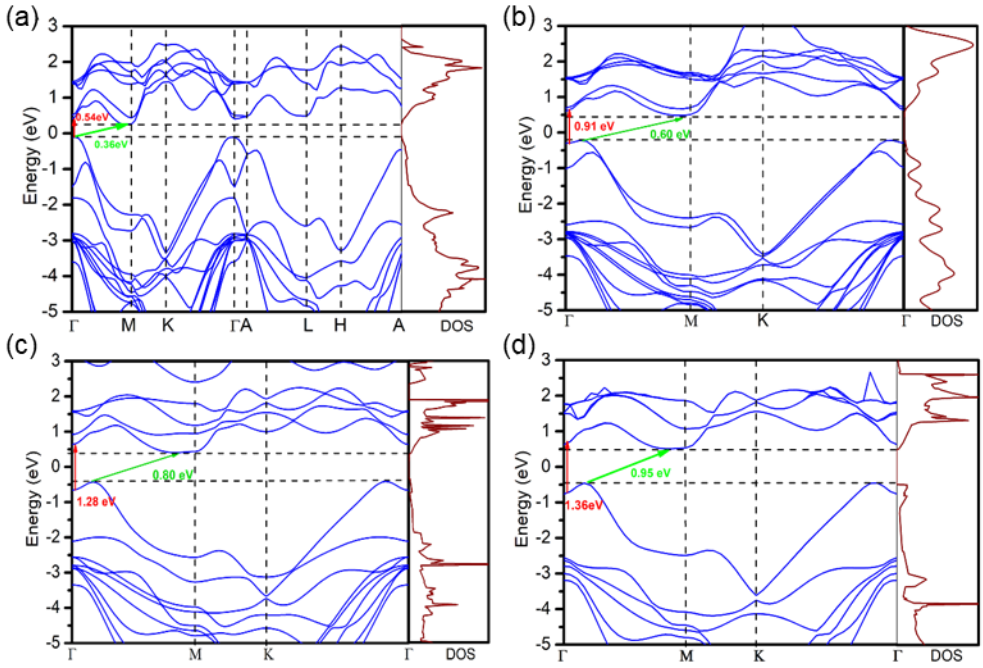


Figure 2.5: Electronic band structures of γ-GeSe (a) bulk, (b) quad-layer, and (c) tri-layer and (d) bilayer using HSE06 functional.

Table 2.4: Electronic bandgaps (eV) of considered γ-GeSe systems using PBE and HSE06 functional.

Structure	PBE functional	HSE06 functional
Bulk	0.10	0.36
Quad-layer	0.62	0.60
Tri-layer	0.48	0.80
Bilayer	0.29	0.96
Monolayer	2.17	2.96

In Table 2.4, the band gaps of the studied materials have been listed with respect to PBE as well as HSE06 results. The indirect bandgap of 0.95 eV for γ-GeSe bilayer is comparable to the previous reports *[53]*. The electronic band structures for quad-layer, and tri-layer are shown in **Figure 2.5(b-c)**. The tri-layer and quad-layer show indirect bandgaps of 0.80 eV and 0.60 eV. At the M point in all the band structures, the nature of the hole valley

does not change with number of layers. The calculated band gap of γ-GeSe monolayer using HSE06 functional is 2.96 eV which is a wide indirect bandgap. The large bandgap of monolayer has been reflected in previous reports *[33, 53]*. From previous reports the wide bandgap materials are generally not found to be suitable for thermoelectric materials. So, we have excluded γ-GeSe monolayer for further TE studies.

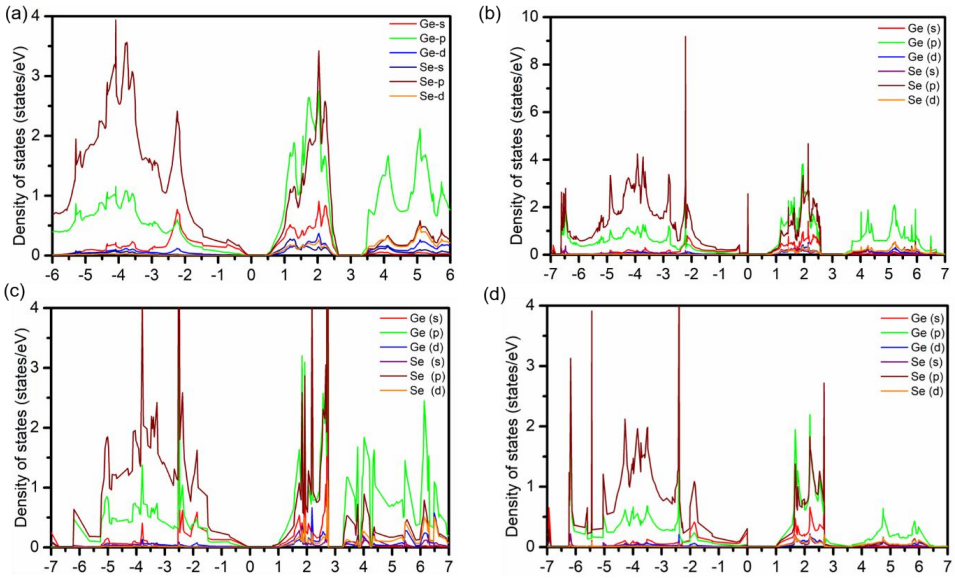


Figure 2.6: Electronic projected density of states (PDOS) of γ-GeSe (a) bulk, (b) quad-layer, (c) tri-layer, and (d) bilayer structures using HSE06 functional.

We analyzed the partial density of states for all the structures to understand the contribution of individual element states in the valence and conduction band as presented in Figure 2.6. All the structures have similar nature of DOS other than the bandgap which increases as the number of layers is decreased. The higher electronegativity of Se than Ge is also reflected in the DOS plot, as the valence band is dominated by Se and the conduction band by Ge states. Below the Fermi level (-1.50 to - 0.14 eV), the electronic states are contributed by Se-p, Ge-s and Ge-p and the maximum contribution in the valence band is shown by the Se-p states. Therefore, we can predict that the electrical conductivity and Seebeck coefficient of p-type GeSe are

mainly determined by Se-p state. Above the Fermi level (0.22 to 2.60 eV), the electronic states are contributed by Ge-p and Se-p states. The maximum contribution in the conduction band is shown by the Ge-p states which imply that the Seebeck coefficient and electrical conductivity of n-type GeSe are majorly determined by Ge-p states. Therefore, we can conclude that the thermoelectric performance of n-type and p-type can be enhanced by adjusting the carrier concentration (N) i.e., adjusting the amount of Ge and Se atoms, respectively.

2.3.4. Thermal Properties

Checking the lattice thermal conductivity (κ_L) of a material is necessary as low κ_L results in higher ZT which defines the thermoelectric efficiency of a material. The studied material γ-GeSe and their multilayer study shows here long-range Coulomb interactions which can give rise to LA – TA branch splitting, which are very crucial component while determining the thermal conductivity and phonon lifetimes. These interactions depend on Born effective charges and high frequency dielectric tensors. This LO-TO splitting of branches affects the phonon-phonon scattering space that helps in determining the κ_L. In **Figure 2.7(a)**, the variation in lattice thermal conductivity with temperature for γ-GeSe bulk, bilayer, tri-layer and quad-layer systems have been represented. For the γ-GeSe bulk, κ_L is calculated to be 1.73 $Wm^{-1}K^{-1}$ at 300 K which drops to 0.6 $Wm^{-1}K^{-1}$ at a higher temperature of 900 K. The value of κ_L significantly decreases in lower dimensional systems. For the quad-layer and tri-layer, κ_L is found to be 0.91 $Wm^{-1}K^{-1}$ and 0.50 $Wm^{-1}K^{-1}$ at 300 K, respectively. The lattice thermal conductivity further declines to 0.30 $Wm^{-1}K^{-1}$ and 0.17 $Wm^{-1}K^{-1}$ for quad- and tri-layer, respectively at 900 K. As the number of layers decreased in -GeSe bilayer, the κ_L is 0.46 $Wm^{-1}K^{-1}$ at 300 K which further lowers to 0.16 $Wm^{-1}K^{-1}$ at 900 K. The ultralow lattice thermal conductivity obtained in case of γ-GeSe bilayer especially, may play an important role in achieving higher ZT value of the material afterward.

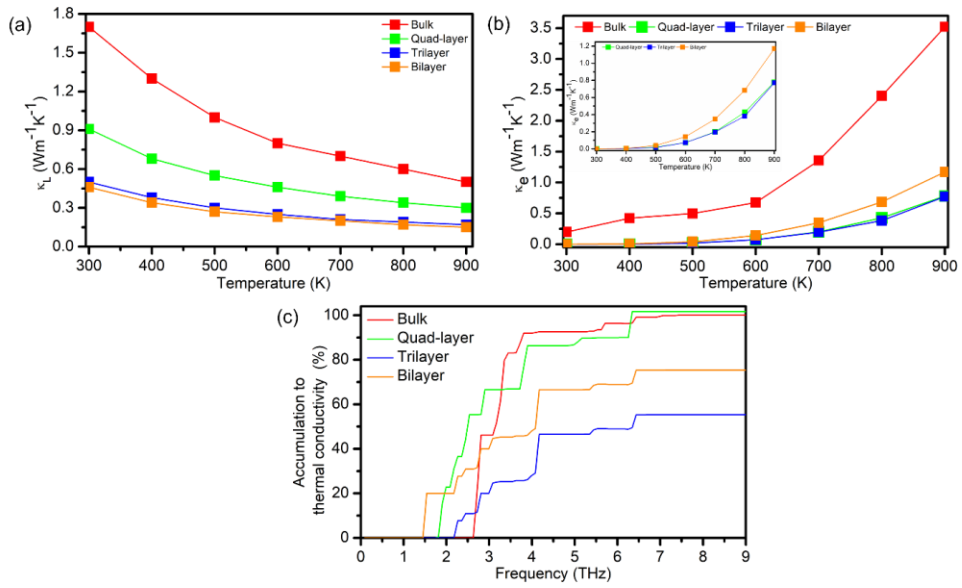


Figure 2.7: (a) Lattice thermal conductivity (κ_L) vs temperature, (b) electronic thermal conductivity (κ_e) vs temperature, and (c) normalized cumulative lattice thermal conductivity as a function of frequency for all studied systems of γ-GeSe at 300 K.

The electronic thermal conductivity (κ_e) shows dependency on the carrier concentration shown in **Figure 2.7(b)**. The κ_e decreases with the quantum confinement of the system. As a result, γ-GeSe bulk shows κ_e of 0.19 $Wm^{-1}K^{-1}$ at 300 K which increases with an increase in temperature to 3.52 $Wm^{-1}K^{-1}$ at 900 K. The 2D systems of γ-GeSe show slight change with an increment of layers. The κ_e values are 0.00011 $Wm^{-1}K^{-1}$ for quad-layer, 0.00012 $Wm^{-1}K^{-1}$ for tri-layer, and 0.00025 $Wm^{-1}K^{-1}$ for bilayer at 300 K which increases to 0.78025 $Wm^{-1}K^{-1}$ for quad-layer, 0.77172 $Wm^{-1}K^{-1}$ for tri-layer and 1.17027 $Wm^{-1}K^{-1}$ for bilayer at 900 K. Therefore, the total thermal conductivity of the system calculated by adding (κ_e) to the κ_L term, is obtained to be 4.9 $Wm^{-1}K^{-1}$ at 900 K. From the above results, we could infer an inversely proportional relation between lattice thermal conductivity and temperature. The reported thermal conductivity for well-known materials like graphene (371.66 $Wm^{-1}K^{-1}$), silicon (28.00 $Wm^{-1}K^{-1}$), MoS_2 (140 $Wm^{-1}K^{-1}$), TiS_3 (10 $Wm^{-1}K^{-1}$), SnTe (2.88 $Wm^{-1}K^{-1}$) and WSe_2 (42

$Wm^{-1}K^{-1}$) at 300 K are much higher in comparison to that of our material (0.586 $Wm^{-1}K^{-1}$ at 300 K) *[54–59]*. The bilayer of α-GeSe exhibits a thermal conductivity of ~0.5 $Wm^{-1}K^{-1}$ and ~7.5 $Wm^{-1}K^{-1}$ at 800 K in the armchair and zigzag modes respectively. The lowest frequency optic phonons provide stronger scattering channels for acoustic modes. The ultralow lattice thermal conductivity of our material can be explained by low elastic constants obtained earlier, scattering rates and Grüneisen parameters. Thus, we further calculate and discuss these parameters. In **Figure 2.7(c)**, the accumulation to lattice thermal conductivity as a function of frequency (THz) at 300 K is illustrated for all the γ-GeSe system by considering all the total modes which are below 4 THz. For γ-GeSe bulk the phonon modes below 4 THz transport more than 85% of the heat, while for other 2D system contribution further decreases, as some higher frequency optical modes are also contributing. However, most of the heat is still being carried by acoustic phonons, thus making the low-lying frequency part dominant.

In **Figure 2.8**, the distribution of weighted phase space against phonon frequency has been shown. This gives an idea regarding how the phonons are scattered, in scattering rates from three phonon interactions, the absorption (P_3^+ : λ + λ' → λ"), emission (P_3^-: λ → λ' – λ") processes and total P, written as,

$$P_3 = \frac{2}{3\Omega} \left(P_3^+ + \frac{1}{2} P_3^- \right)$$

where, Ω is the normalization factor *[60]*. The weighted phase space plot provides the scattering rate as a function of harmonic frequencies which corresponds to the intensity of phonon scattering during heat conduction. The high scattering rate of a material indicates high phonon scattering which implies the low thermal conductivity of the system. The three-phonon weighted phase space P_3 of all the systems corresponds to the number of scattering channels for phonons.

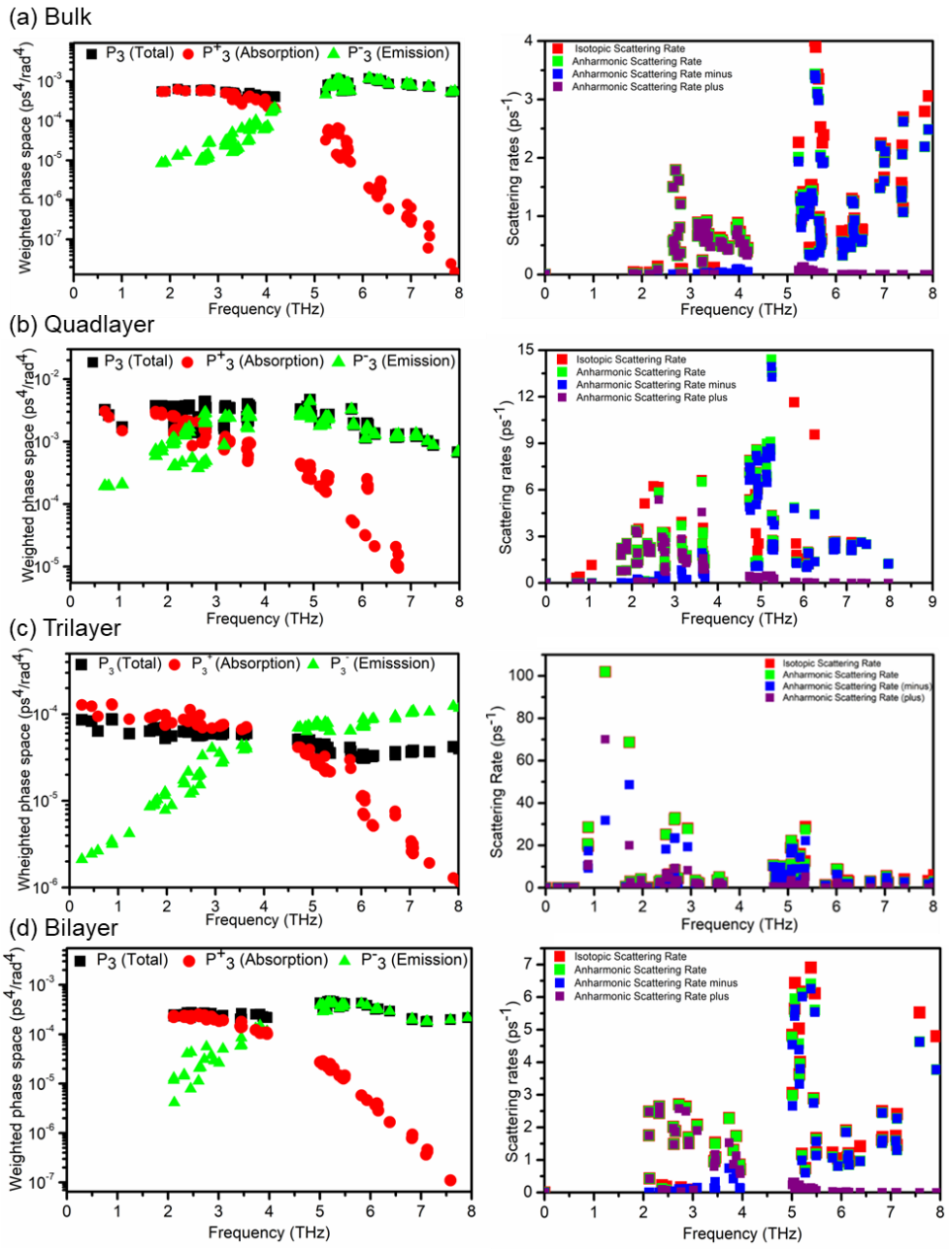


Figure 2.8: Weighted phase space (three phonon process), isotopic scattering rate (ISR), anharmonic scattering rate (ASR), anharmonic emission scattering rate (ASR^-) and anharmonic absorption scattering rate (ASR^+) for (a) bulk, (b) quadlayer, (c) trilayer, and (d) bilayer systems.

If all the other factors are similar, then the larger P_3 provides hindrance in thermal conductivity of the system. In the absorption process, the two low-frequency phonons give rise to high-frequency optical mode. In emission

the phonons are allowed to decompose into another lower frequency. Therefore, both processes obey the law of conservation of energy and momentum. The scattering of acoustic modes and low-lying optical modes (4 THz), near the crossing point consists of high scattering rates due to intercrossing of bands. The phonon modes lying between 2 to 4 THz region has been scattered in both the absorption and emission process, indicating that the low-lying optical modes increases the overall phonon scattering rates. Further, we have plotted the scattering rates for anharmonic modes as shown in **Figure 2.7**. In all the considered systems, the low-lying phonon frequency region has been dominated by frequency-dependent scattering rates (anharmonic three-phonon and isotopic scattering rates) as we increase the layers. The anharmonic three-phonon scattering is contributed by both absorption as well as emission process. The major contribution in the lower lying frequency range is by the absorption processes.

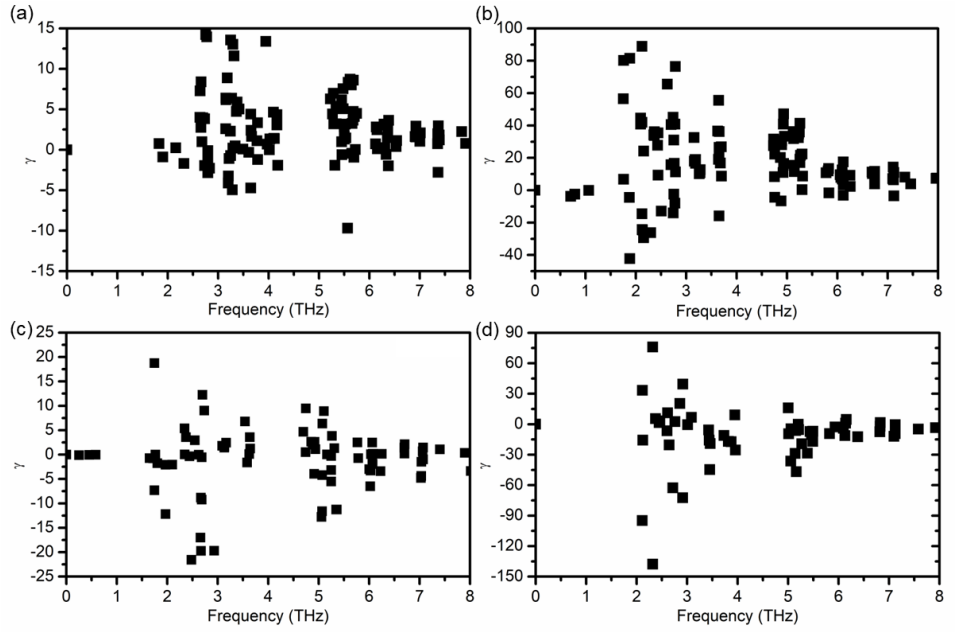


Figure 2.9: Grüneisen parameter as a function of angular frequency for γ-GeSe bilayer at 300 K for (a) bulk, (b) quadlayer, (c) trilayer, and (d) bilayer systems.

The Grüneisen parameter vs phonon frequency plots are shown in Figure 2.9. The Grüneisen parameter gives a measure of the anharmonicity of the material which inversely relates to the κ_L. The higher Grüneisen parameter for 2D systems in comparison to the bulk shows the increase in anharmonicity with the decrease in the number of layers. Also, the trend is inversely related to the trend of κ_L. The points at the low-lying frequencies (acoustic mode) in the plot corresponds to the heat carrying phonon modes. Therefore, higher the deviation of Grüneisen parameter at low lying phonon frequencies, lower will be the κ_L. The deviation of Grüneisen parameter is much higher in bilayer than the bulk, implying more reduced κ_L in bilayer. The Grüneisen parameter also relates to linear thermal expansion of the considered material. Some modes with negative value are also present in the plots which indicates that the material could have negative thermal expansion as well. This further increases the lifetime of the material. In several well-known TE materials like MoS_2, Pb_2Se_3, graphene, silicene, and germanene, negative values of Grüneisen parameter have been observed previously *[56]*. The frequency dependent Grüneisen parameter is highly scattered in the range below 4 THz. Also, from the frequency-dependent weighted phase space (**Figure 2.8**) it can be inferred that low lying optical, as well as acoustic frequency, has been dominated by harmonic scattering. The Grüneisen parameter is higher for acoustic and low-lying optical branches (below 4 THz) than that of optical branches. This implies that low-lying optical and acoustic modes are more anharmonic in comparison to higher optical phonons. Thus, we observe that with decreasing layers of γ-GeSe, the anharmonicity increases, which has been reflected in the lowering of κ_L as well. Therefore, all the factors verify the ultralow κ_L of the γ-GeSe bilayer and tri-layer.

The Debye Temperature (θ_D) is the temperature at which the highest normal mode of vibrations exists in the material. This Debye Temperature also correlates with the elastic properties, phonon thermal expansion, and

thermal conductivity *[55]*. The Debye Temperature (θ_D) of the γ-GeSe systems have been given in **Table 2.5** and is calculated by using following formula,

$$\theta_D = \frac{hv_s}{2\pi k_B}\left[6\pi^2 \frac{N}{V}\right]^{1/3} \quad (6)$$

where h is Planck's constant, k_B is Boltzmann constant, V is volume, N is number of atoms in unit cell and v_s is average sound velocity. The average sound velocity (v_s) is given by *[61]*,

$$v_s = \left[\frac{1}{3}\left(\frac{1}{v_L^3} + \frac{2}{v_T^3}\right)\right]^{-(1/3)} \quad (7)$$

where v_L and v_T are the longitudinal and transverse sound velocities of the material.

Table 2.5: Longitudinal velocity (ν_L), Transverse velocity (ν_T) and Debye Temperature (θ_D) for the considered structures of γ-GeSe.

Structures	$\boldsymbol{\nu_L}$ **(m/s)**	$\boldsymbol{\nu_T}$ **(m/s)**	$\boldsymbol{\theta_D}$ **(K)**
Bulk	3120.28	1488.72	174.8
Quad-layer	2107.78	1230.34	121.2
Tri-layer	1748.56	1152.08	109.3
Bilayer	2009.43	1231.63	95.9

The θ_D of γ-GeSe bulk corresponds to 174.8 K and it gets drastically reduced in 2D γ-GeSe systems. The θ_D is further reduced when layers are reduced. This implies that lower the θ_D softer the material and it contains lower longitudinal and transverse velocity. All these parameters further point towards lower κ_L.

2.3.5. Thermoelectric Properties

2.3.5.1. Seebeck Coefficient

The thermoelectric properties have been calculated by using the BoltzTrap2 code *[43]*. The narrow bandgap obtained for the considered structures of γ-GeSe as well as their ultra-low κ_L insinuates that it should be further investigated for thermoelectric applications. Hence, we have calculated the Seebeck coefficient and electrical properties besides electronic properties as well as thermal conductivity, to discover their potential in thermoelectric devices. On considering energy independent scattering approximation the Seebeck coefficient (S) is given as,

$$S = \frac{8\pi^2 k_B^2 m^* T}{3eh^2}\left(\frac{\pi}{3n}\right)^{3/2} \quad (8)$$

where, n is carrier concentration, T is absolute temperature, h is Planck's constant, m* is effective mass, and k_B is Boltzmann constant *[62]*. Thus, from above equation it is evident that Seebeck coefficient is directly proportional to carrier concentration and directly proportional to effective mass of carrier concentration. The narrow bandgap and DOS effective mass (m_d^*) are key factors in controlling Seebeck coefficient. According to Mott's equation, S decreases with decrease in m_d^* *[63]*. However, a very narrow bandgap can further lead to an increase in lattice thermal conductivity at higher temperatures due to the bipolar effect. Thus, for bulk, the carrier concentration should be comparatively high (10^{20} cm^{-3} -10^{21} cm^{-3}) among TE materials, which overcomes the bipolar effect. The effective mass of hole and electron concentration increases from bulk to quad and then decreases from quad to bilayer which follows a similar trend with Seebeck coefficient. On observing the band edges of the materials in the electronic band structure plots, the bulk does not have valley degeneracy whereas the 2D materials possess two-hole valley degeneracies between Γ→ M and K→ Γ in all the cases. This difference in band degeneracy between the bulk and quadlayer, trilayer and bilayers are also reflected in the effective mass as well as Seebeck coefficient which are all directly proportional to each other.

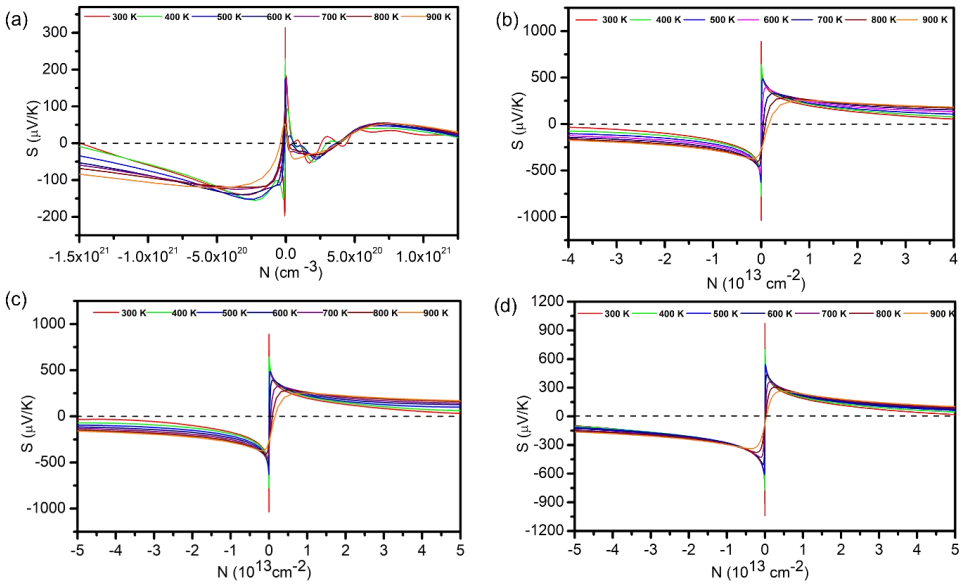


Figure 2.10: Seebeck coefficients of the γ-GeSe (a) bulk, (b) quad-layer, (c) tri-layer, and (d) bilayer structures as a function of carrier concentration at temperature range of 300-900 K.

Figure 2.10 shows the computed Seebeck coefficients of bulk and reduced layers of γ-GeSe within the temperature range of 300 to 900 K. The Seebeck coefficient is found to be three times higher for the reduced layers than γ-GeSe bulk. For bulk, S is 300 μV/K at 300 K which increases to 872.5 μV/K for quad layer, 880 μV/K for tri-layer, and 975 μV/K for bilayer. The plots show that the Seebeck coefficient increases with increase in temperature. The effective mass depends on the extent of band flattening in the electronic band structure of the material. Here, as we go from bulk to 2D, effective mass decreases. However, carrier concentration also decreases with decrease in dimension of the material due to quantum confinement. This explains the increase in Seebeck coefficient from 3D γ-GeSe bulk to 2D γ-GeSe.

Table 2.6: Effective masses of the carriers along Γ → M k-path for considered systems of γ-GeSe.

Carrier type	Bulk	quad-layer	tri-layer	bilayer
Hole ($m_h(m_o)$)	0.150	0.366	0.240	0.191
Electron ($m_e(m_o)$)	0.069	0.170	0.173	0.169

Table 2.6 shows that effective mass of hole concentration is higher than the effective mass of corresponding electron concentration. The lowest curvature in electronic band structure of γ-GeSe bulk compared to 2D layers also agrees with the high effective mass for bulk than 2D systems (**Figure 2.5**). As mobility is inversely proportional to the effective mass, the p-type is having lower mobility than that of n-type. Therefore, in all cases n-type outperforms p-type.

2.3.5.2. Electrical Conductivity

For calculating electrical conductivity as well as electrical thermal conductivity, a constant relaxation time approximation (CRTA) has been considered ($\tau = 10^{-14}$ s). In Figure 2.11-2.12, the variation of electrical conductivity (σ) and electronic thermal conductivity (κ_e) with respect to carrier concentration are presented. At 300 K, σ is 3.112 μS/m (n-type) and 1.141 μS/m (p-type) for bulk γ-GeSe. The σ value drastically decreases for quad-layer (n-type: 0.170 μS/m; p-type: 0.081 μS/m), tri-layer (n-type: 0.132 μS/m; p-type: 0.056 μS/m), and bilayer (n-type: 0.151 μS/m; p-type: 0.096 μS/m. As the electrical conductivity increases with the increase in temperature, more thermal energy is available to release free electrons from the valence band (VB) to the conduction band (CB). Consequently, the excited electrons will convert into charge carriers (electrical conductivity). The difference in electrical conductivity is also dependent on effective mass (m*). As the effective mass of holes is found to be much higher than electrons in the previous section for all systems, hole conductivity is found to be much less than electron conductivity in **Figure 2.5** and **Figure 2.11**. Therefore, in all the models, n-type conductivity is found to be higher than p-type conductivity. The variation of κ_e with carrier concentration also follows the same patterns as that of electrical conductivity (σ) with carrier

concentration as can be understood from Figure 2.11-2.12. The κ_e is calculated as 3.2 $Wm^{-1}K^{-1}$, 0.78 $W.m^{-1}K^{-1}$, 0.76 $Wm^{-1}K^{-1}$ and 1.17 $Wm^{-1}K^{-1}$, for bulk, quad-layer, tri-layer, and bilayer at 900 K, respectively which decreases at lower temperature (300 K) to 0.02 $Wm^{-1}K^{-1}$, 0.0001 $Wm^{-1}K^{-1}$, 0.018 $Wm^{-1}K^{-1}$ and 0.0023$Wm^{-1}K^{-1}$ respectively. The very low values of κ_e at low temperatures indicate that the total thermal conductivity is contributed majorly by κ_L. At higher temperature, the contribution of κ_e to total thermal conductivity (κ) also increases.

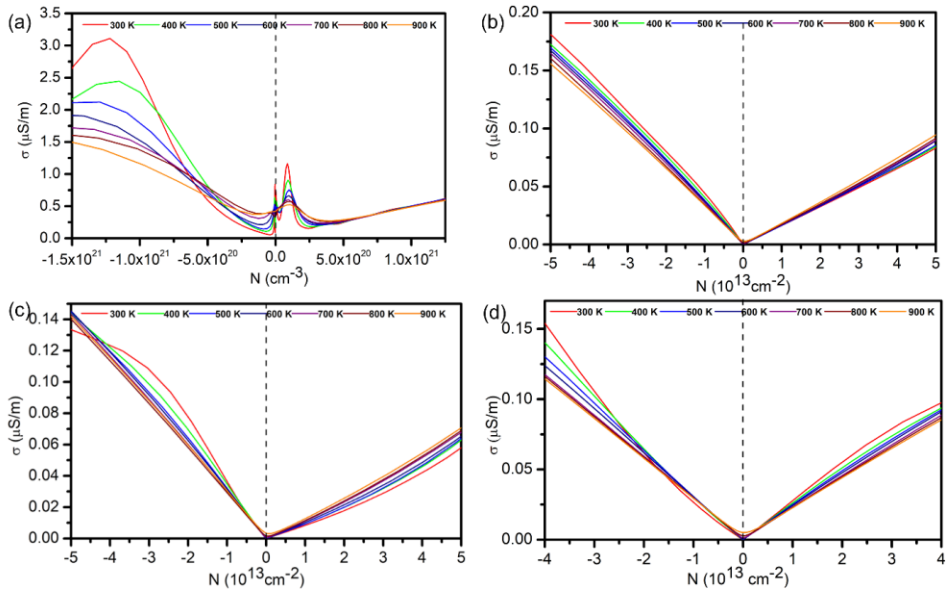


Figure 2.11: Electrical conductivity of the γ-GeSe (a) bulk, (b) quad-layer, (c) tri-layer, and (d) bilayer structures as a function of carrier concentration at temperature range of 300-900 K.

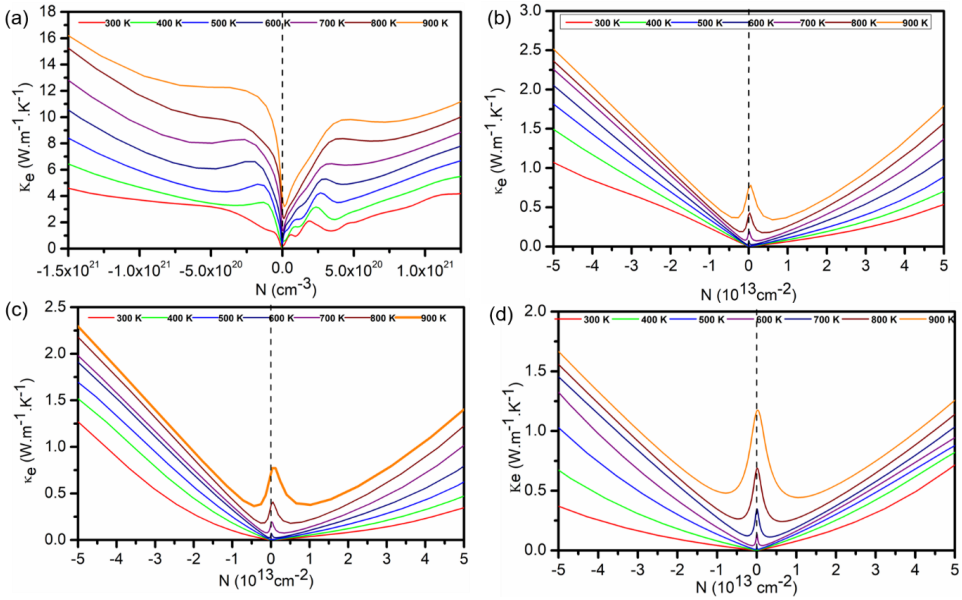


Figure 2.12: Electronic thermal conductivity (κ_e) of the γ-GeSe (a) bulk, (b) quad-layer, (c) tri-layer, and (d) bilayer structures as a function of carrier concentration at the temperature range of 300-900 K.

2.3.5.3. Power Factor and Figure of Merit

Thus, we have collected all the required parameters to evaluate the power factor (PF) and dimensionless quantity ZT known as a figure of merit, which define the efficiency of a thermoelectric material. The PF and ZT are defined as,

$$PF = S^2\sigma \tag{9}$$

$$ZT = \frac{S^2\sigma T}{(\kappa_e + \kappa_L)} \tag{10}$$

It has been observed that PF for the γ-GeSe bulk is comparatively higher than the reduced layers. The PF and ZT of the materials have been plotted for both hole and electron-doped cases as a function of carrier concentration (N) at a temperature range from 300K to 900K as shown in **Figure 2.13-2.14**.

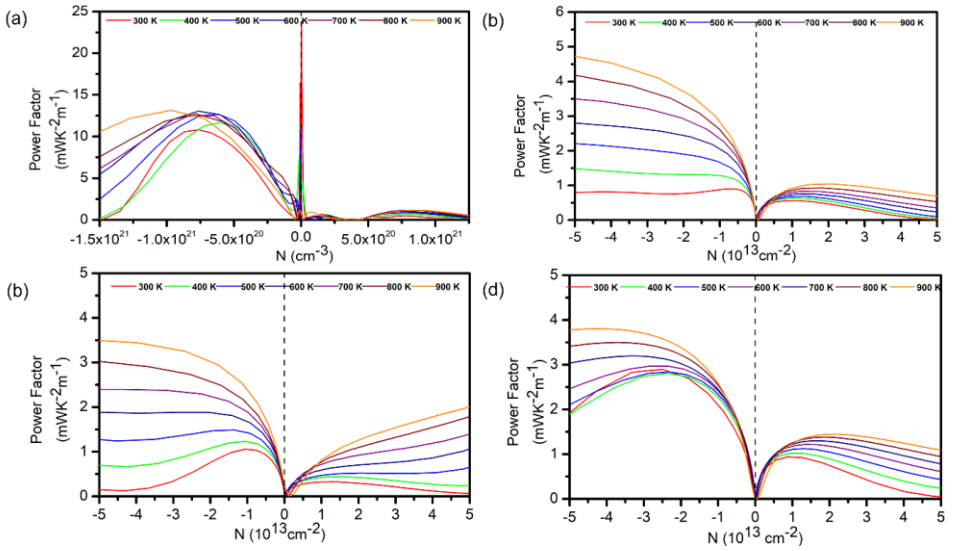


Figure 2.13: Power factor (PF) of the γ-GeSe (a) bulk, (b) quad-layer, (c) tri-layer, and (d) bilayer structures as a function of carrier concentration at temperature range of 300-900 K.

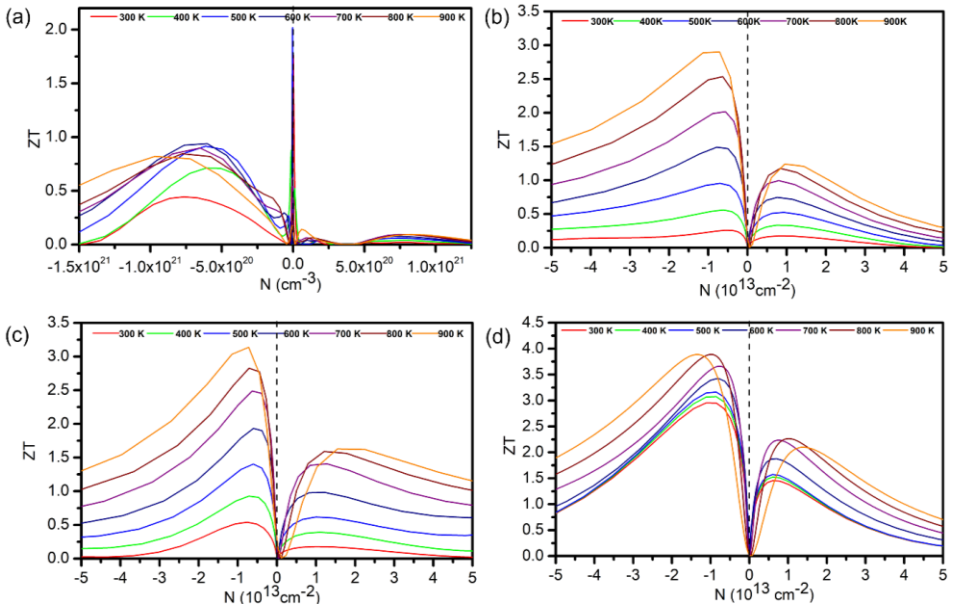


Figure 2.14: Thermoelectric figure of merit (ZT) of the γ-GeSe (a) bulk, (b) quad-layer, (c) tri-layer, and (d) bilayer structures as a function of carrier concentration at temperature range of 300-900 K.

For all the systems, the electron-doped cases show the higher ZT compared to hole-doped ones. For a better comparison and clear understanding of results, all the graphs have been plotted near the charge neutrality points of electron (n-type) and hole (p-type) cases at different temperatures. For γ-GeSe bulk, PF is 10 $mWK^{-2}m^{-1}$ at 300 K and becomes constant at higher temperatures (13 $mWK^{-2}m^{-1}$ at 600 K and 900 K). Due to the presence of high thermal conductivity, the ZT calculated for this system is found to be as low as 0.4 at 300 K, which increases to 0.9 at 900 K. In the 2D systems, thermal conductivity is reduced by quantum confinement i.e., controlling the thickness and reducing the layers. As the layers are reduced, the ZT is found to increase. Therefore, quantum confinement plays a crucial role in improving the performance of the system. For quad-layers, PF is 0.79 $mWK^{-2}m^{-1}$ at 300 K which increases to 4.5 $mWK^{-2}m^{-1}$ with a ZT of 2.8 at 900 K. For tri-layers, PF is 1 $mWK^{-2}m^{-1}$ at 300 K which increases to 3.3 $mWK^{-2}m^{-1}$ with a maximum ZT of 3.1 at 900 K. The outstanding performance is shown by the bilayer with a high ZT value of 3.8 at 900 K. Although the γ-GeSe bilayer is suitable even at room temperature with a ZT of 2.9 at 300 K, its high ZT at high temperature is remarkable. For the sake of comparison, the other phases of GeSe material show lower ZT values. The α-GeSe bulk and β-GeSe bulk shows ZT of 0.83 (n-type) and ~ 1 (n-type), respectively at 300 K, and the bilayer of α-GeSe exhibits the ZT of ~ 1.95 at 800 K *[64]*. All our results obtained have been presented in **Table 2.7**.

Table 2.7: Lattice thermal conductivity (κ_L), Power Factor ($S^2\sigma$), and ZT at 300K, 600K, and 900K for all the considered systems.

Material	Temperature (K)	κ_L ($Wm^{-1}K^{-1}$)	$S^2\sigma$ ($mWK^{-2}m^{-1}$))	ZT
γ-GeSe Bulk	300	1.73	10.0	0.4
	600	1.93	12.6	0.9
	900	0.60	12.9	0.8
	300	0.91	0.8	0.3

γ-GeSe Quadlayer	600	0.46	2.3	1.4
	900	0.30	4.5	2.8
γ-GeSe Trilayer	300	0.50	1.0	0.5
	600	0.26	1.9	1.9
	900	0.17	3.3	3.1
γ-GeSe Bilayer	300	0.46	3.1	2.9
	600	0.23	3.3	3.1
	900	0.16	3.9	3.8

All the values obtained leading to calculation of ZT may vary due to some assumptions in our calculations. A constant value of τ at all the considered temperatures (300 K - 900 K) leads to increase in the power factor with increase in temperature (**Figure 2.14**). However, with increase in temperature, the relaxation time is expected to decrease leading to a lower PF and ZT value. Hence, CRTA leads to overestimation of PF in our case. However, we have overlooked the scattering due to various defects/impurities which are also expected to overestimate the κ_L in our calculations. Thus, both the overestimations when considered together will not change the ZT value much. While γ-GeSe demonstrates promising thermoelectric properties through dimensional and band engineering, accurate modeling of thermal conductivity remains a challenge. This motivates a deeper investigation into higher-order phonon interactions, as explored in the following section on GeS systems.

2.4. Summary

In summary, we systematically investigate the thermoelectric performance of recently synthesized γ-GeSe from bulk to monolayer limits. Structural stability is confirmed through phonon spectra, elastic constants, and ab initio molecular dynamics. Dimensionality reduction strongly modifies phonon transport, with heat predominantly carried by low-frequency modes (<4 THz). While all systems exhibit indirect band gaps, the gap increases with decreasing thickness, rendering the monolayer unsuitable due to excessive band gap and dynamical instability. Remarkably, the bilayer

displays an ultralow lattice thermal conductivity (0.17 W m^{-1} K^{-1}) driven by weak bonding, lone-pair-induced anharmonicity, and strong acoustic–optical phonon anticrossing. This leads to an unprecedented ZT of 3.8 at 800 K. Our results demonstrate that dimensional confinement is a powerful strategy to enhance thermoelectric efficiency.

Section: B

2.5. A Case Study of Importance of 3- and 4-phonon Interactions

Here, we would like to bring to notice that it has been found that for some bulk materials with peculiar phonon dispersion curves such as a large frequency band gap, *[65]* the flatness of phonon branches, *[66]* and acoustic bunching,*[67]* the Boltzmann transport equation (BTE) calculations of lowest order 3-phonon scattering channels fail to give an accurate prediction of κ_L *[68–70]*. In some materials the lowest order 3-phonon interactions are restricted, and due to this BTE over-estimates the κ_L *[71–73]*. However, the discrepancy in calculating κ_L can be resolved by considering the higher-order 4-phonon scattering channels *[72]*. The κ_L of cubic boron arsenide (c-BAs) at room temperature considering the 3-phonon scattering was ~2100 $Wm^{-1}K^{-1}$, which was even higher than diamond *[44]*. Later, the κ_L value dropped to ~1400 $Wm^{-1}K^{-1}$ upon considering the effect of 3 and 4-phonon scattering rates,*[70]* which is comparable to experimentally calculated κ_L *[68]*. A recent study on 2D SnSe shows that considering 3-phonon scattering results in the κ_L of 2.42 $Wm^{-1}K^{-1}$ at room temperature, which decreases to 1.43 $Wm^{-1}K^{-1}$ on considering the 3 and 4-phonon scattering *[74]*. The calculated κ_L (~1 $Wm^{-1}K^{-1}$) is closer to the 4-phonon results *[75]*. Therefore, understanding the lattice thermal transport properties accurately is crucial for the futuristic application of thermoelectric material. Although numerous studies have been carried out evaluating the κ_L of various materials, they are majorly based on considering the 3-phonon scattering theory, predicting inaccurate results *[76, 77]*.

Motivated by these prior reports and aiming to examine the 3 and 3+4-phonon effect, we systematically study the thermal, mechanical, dynamic, and electronic properties of GeS through first-principles calculations. We have calculated the κ_L and thermoelectric performance of bulk and bilayer forms of orthorhombic GeS (o-GeS) and hexagonal GeS (h-GeS) at various temperatures and carrier concentrations, considering different relaxation times. For the bilayer systems specifically, we have considered the 4-phonon scattering effect on κ_L which in turn affects the TE performance of the material. Thereby we have tried to understand how the inclusion of 4-phonon scattering can help in calculating TE properties with higher accuracy.

2.6. Modelling and Computational details

We have considered two phases of GeS system namely, orthorhombic (o-GeS), and hexagonal (h-GeS) phases as represented in **Figure 2.15**. An orthorhombic unit cell (Figure 1(a-c)) of GeS bulk consists of eight atoms (four Ge and four S). The o-GeS structure possesses a hinge-like structure along the armchair direction, which introduces huge anisotropy in the system.[38] The lattice parameter (x = 3.67 Å, y = 4.35 Å, and z = 10.67 Å) of o-GeS found to be in good agreement with previous experimental (x = 3.64 Å, y = 4.29 Å, and z = 10.42 Å) and theoretical reports (x = 3.67 Å, y = 4.34 Å, and z = 10.67 Å) *[79, 80]*.

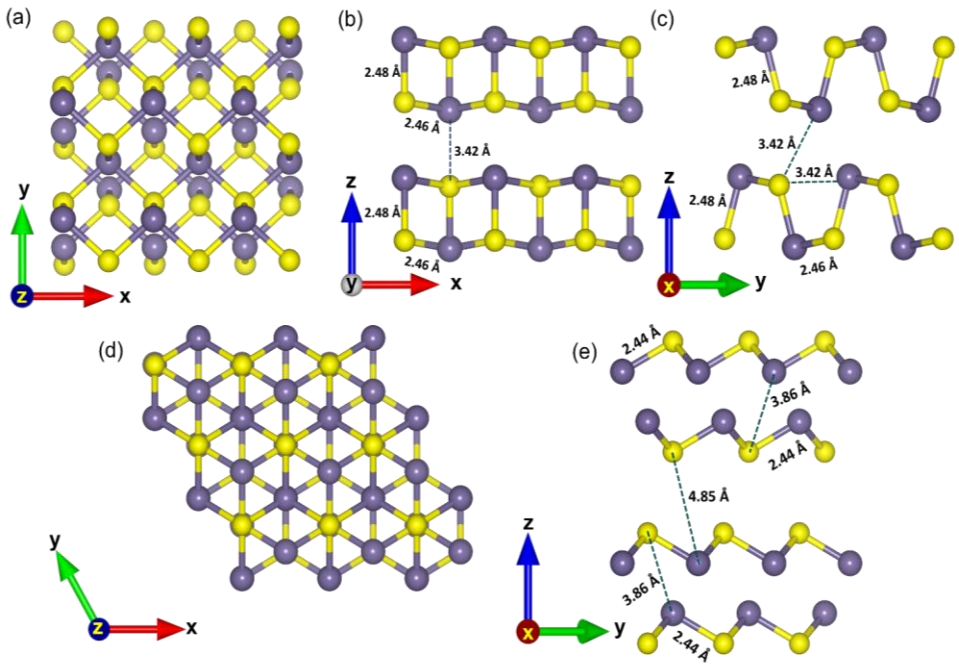


Figure 2.15: Optimized structures of (a) bulk top view o-GeS, (b) bulk-side view o-GeS along x-axis, (c) bulk-side view o-GeS along y-axis, (d) bulk top view h-GeS (e) bulk-side view h-GeS.

The first-principles calculations have been performed by considering the projected augmented wave (PAW) method as implemented in the Vienna Ab initio Simulation Package (VASP) *[34, 35]*. The generalized gradient approximation (GGA) of Perdew-Burke-Ernzerhof (PBE) is employed as the exchange-correlation functional with an energy cut-off value of 600 eV to describe the core and valence electron interactions *[36, 37]*. All the structural relaxations have been carried out, considering an energy convergence criterion of less than 10^{-6} eV and a force convergence criterion of less than 10^{-3} eV/Å. The dispersion energy corrections have been included in the calculations by considering Grimme's DFT-D3 method.[39, 40] A vacuum of ~20 Å has been considered to avoid interactions between periodic images of 2D materials. 5 × 5 × 5 and 8 × 7 × 3 Γ-centred k-point meshes have been used for the Brillouin zone sampling of hexagonal GeS (h-GeS) and orthorhombic GeS (o-GeS) bulk, respectively and 4 × 4 × 1 and 8 × 7 × 1 Γ-centred k-point meshes have been used for the Brillouin

zone sampling of h-GeS and o-GeS bilayer, respectively. We also have considered the Heyd-Scuseria-Ernzerhof (HSE06) hybrid functional to obtain accurate electronic properties of the considered systems *[39, 40]*. The Hartree-Fock exchange parameter (α) of 25% was considered in the hybrid functional calculations. Phonon calculations have been carried out with the help of the PHONOPY package which uses the finite displacement method to calculate second-order interatomic force constants (IFCs) *[41]*. Ab initio molecular dynamics (AIMD) simulations have been performed in the NVT ensemble at 300 K, 700 K, and 900 K, where the temperature control was achieved by a Nosé–Hoover thermostat. For the calculation of third-order anharmonic IFCs (interatomic force constants), the thirdorder.py code was utilized *[82]*. Optimized 3 × 3 × 2 supercell for bulk and 3 × 3 × 1 for bilayer structures have been considered for the 2^{nd} order IFCs and 3^{rd} order IFCs. Finally, the 2^{nd} order IFCs and 3^{rd} order IFCs were fed into the SHENGBTE code to obtain the κ_L of the materials *[42]*. A 2 × 2 × 1 supercell for bilayer have been considered for the 4^{th} order IFCs upto 2^{nd} nearest neighbouring atom *[83]*. The size of the supercell was sufficiently larger than the cut-off interaction of the third order and fourth-order force constants, and similar treatment has also been extensively used in previous studies *[74, 84]*. The dense k-mesh 9 × 9 × 9 for bulk and 17 × 17 × 1 for bilayer have been considered for the calculation of κ_L. All the electronic transport properties have been calculated using both BoltzTrap2 code as well as AMSET. Boltztrap2 considers the semiclassical Boltzmann theory, constant relaxation time approximation (CRTA), and the Boltzmann transport equation (BTE) methods *[44, 85]*. On the other hand, AMSET package considers ionized impurity, acoustic deformation, and piezoelectric scattering mechanisms to provide accuracy similar to the state-of-art methods *[86, 87]*.

2.7. Results and Discussion

2.7.1. Structural and Electronic Properties

The hexagonal unit cell of GeS also consists of eight atoms with a lattice parameter of x = y = 3.63 Å and z= 15.39 Å as shown in **Figure 2.15(d-e)**. The bulk structure of h-GeS has a four-layer unit cell consisting of two merged buckled honeycomb lattices, where the second and third layers are held together by weak van der Waals interactions. In h-GeS bulk and bilayer contains a single type of bond 2.44 Å. The unit cell parameters and essential information regarding bonding for all considered structures have been given in **Table 2.8**.

Table 2.8: The lattice parameter, bond distance, and net effective charges of considered structures of GeS.

Composition	a (Å)	b (Å)	c (Å)	Inter-layer distance (Å)	Ge-S (Å)	Net Effective Charge (|e|)	
						Ge	S
o-GeS bulk	3.68	4.47	10.67	2.63	2.48, 2.46	+0.800	-0.800
h-GeS bulk	3.63	3.63	15.39	2.43 (average)	2.47	+0.690	-0.690
o-GeS bilayer	3.67	4.47	25.00	2.65	2.44, 2.46	+0.826	-0.826
h-GeS bilayer	3.63	3.63	25.00	2.01	2.47	+0.685	-0.685

The Ge-S bond length in o-GeS bilayer shows huge anisotropy compared to the o-GeS bulk and the interlayer distance between the two layers also increases in o-GeS bilayer by 0.02 Å, whereas the bond length and interlayer distance remain the same in h-GeS systems. The interlayer distance between the bottom layers is 2.01 Å and the interlayer distance after every two layers is 3.27 Å. Therefore, we have mentioned the average distance between all layers in **Table 2.8**. In the o-GeS system, two kinds of Ge-S interactions are present in the xy plane as shown in **Figure 2.15 (c,e)**. The distance between Ge and S atoms is calculated to be 2.46 Å and 3.42 Å. The weaker Ge-S interaction (3.42 Å) contributes more towards the y-axis, while the stronger Ge-S interaction (2.46 Å) is reflected along the x-

axis. The nature of chemical bonding in GeS systems has been revealed by electron localization function (ELF) as plotted in **Figure 2.16** *[88]*.

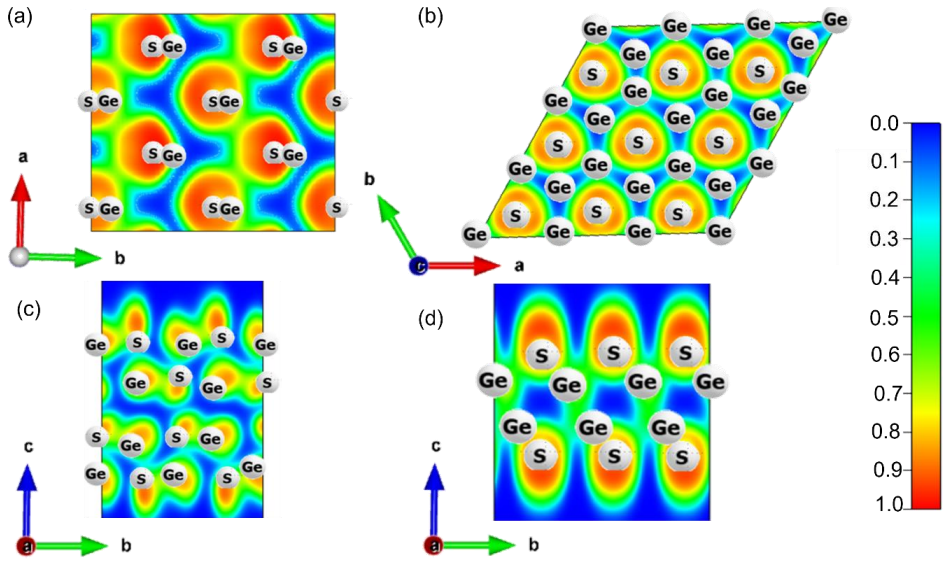


Figure 2.16: Electron localization function of GeS bilayer systems, (a) o-GeS top view of (001) plane at 0.77 e $Å^{-3}$ isosurface, (b) h-GeS top view of (001) plane at 0.54 e $Å^{-3}$ isosurface, (c) o-GeS side view of (100) plane at 0.77 e $Å^{-3}$ isosurface, and (d) h-GeS side view of (100) plane at 0.54 e $Å^{-3}$ isosurface.

From the top view of ELF plots of o-GeS and h-GeS bilayer, it is evident that electron density is localized on the S atoms. The outermost two 4p electrons of Ge are shared with the 3p orbital of S during the covalent bond formation of Ge-S, resulting in the two 4s electrons of Ge remaining as lone-pair electrons as evident in **Figure 2.16(c)**. The presence of lone pair in the system interacts with the bond pair thereby resulting in the weakening of the bond strength. Secondly, the lone pair-lone pair repulsions in the interlayer increase the anharmonicity of the system. These factors can potentially decrease the thermal conductivity of the system *[89]*. It has been observed that there is the presence of Ge – Ge interactions (indicated in green colour) in two different layers of h-GeS bilayer.

Bader charge analysis has been carried out to identify the charge distribution on constituent atoms by using the Atoms in Molecules (AIM) theory *[90]*.

The Ge atoms are positively charged whereas S atoms are negatively charged, due to the high electronegativity of S by 0.52 *[91]*, which is further supported by Bader charge results (**Table 2.8**). Therefore, in GeS it is evident that charge transfer occurs from Ge to S. The charge transfer for each Ge –S bond has been observed to be 0.80 |e| and 0.83 |e| for o- GeS bulk and bilayer, respectively. For h- GeS bulk and bilayer, the charge transfer for each Ge-S bond is 0.69 |e|. The higher charge transfer in o-GeS results in more polarised covalent bonds compared to h-GeS. Additionally, the shorter bond lengths observed for o-GeS compared to h-GeS, as indicated in **Table 2.8** are consistent with the higher charge transfer and more polarized covalent bonds in o-GeS.

Table 2.9: Cohesive energy and formation energy for the considered structures of GeS.

Composition	Cohesive Energy (eV/atom)	Formation Energy (eV/atom)
h-GeS bulk	-3.77	-0.30
h-GeS bilayer	-3.75	-0.27
o-GeS bulk	-3.81	-0.33
o-GeS bilayer	-3.75	-0.27

The negative formation and cohesive energy values indicate that the formation of considered systems is feasible, and they would not decompose after formation (**Table 2.9**). The calculated mechanical properties of considered systems follow the criteria of stability (**Table 2.8-2.9**). As mechanical properties of the material are associated with the stiffness of the structure, they affect the phonon modes as well as their propagation. The low values of elastic properties indicate the weak chemical bonding in the system, which reduces the speed of phonon propagation.

The dynamic stability of o-GeS and h-GeS bulk and bilayer has been confirmed from the phonon dispersion graphs as shown in **Figure 2.17**. The absence of any imaginary phonon frequency in the phonon band structures

indicates their dynamical stability *[85, 92]*. However, o-GeS and h-GeS monolayers possess imaginary frequency. Therefore, we have not considered the monolayers of respective systems for our studies. The phonon band structures show a considerable number of phonons crossing and anti-crossing, which affects the anharmonic scattering in the two distinct phases. The heat is carried by the low-lying phonon modes (< 4 THz). The phonon band gap (a-o gap) is ~2.07 THz in o-GeS bulk, which increases in o-GeS bilayer to ~2.20 THz (Figure 2.17). Similarly, the a-o gap in the case of h-GeS bulk is ~ 0.74 THz which increases to ~ 0.87 THz for h-GeS bilayer as shown in **Figure 2.17**. The optical branches below a-o gap lead to more scattering probability by weakly coupling with the acoustic phonon branches *[67]*. In o-GeS and h-GeS bulk, the acoustic band crosses the low-frequency optical (LFO) bands. However, in the o-GeS bilayer, there is presence of one avoided crossing between longitudinal acoustic (LA) and LFO in Y to Γ direction (**Figure 2.17(c)**). Similarly, in h-GeS bilayer, the presence of avoided crossing between acoustic bands (LA and (TA and ZA)) along Γ to M, M to K, and K to Γ directions (**Figure 2.17(d)**) and crossing between LA and LFO modes causes the flattening of acoustic bands, which lowers the phonon group velocity and that further reflects in κ_L. .

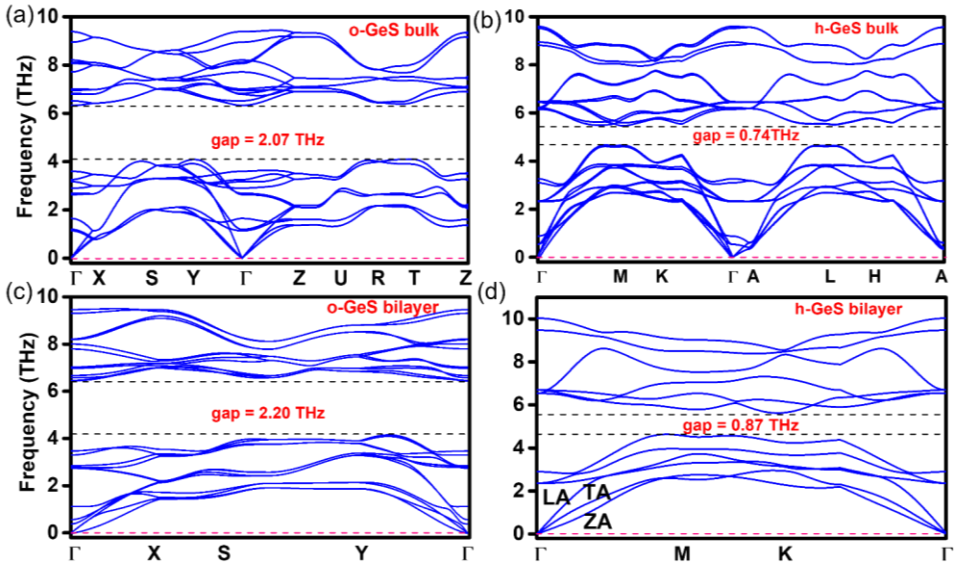


Figure 2.17: Phonon band structures of (a) o-GeS bulk, (b) h-GeS bulk, (c) o-GeS bilayer, and (d) h-GeS bilayer systems.

Moving ahead, we have calculated the electronic properties of o-GeS and h-GeS structures. These properties affect the Seebeck coefficient and electronic conductivity of the material. The electronic band gap of bulk and 2D materials of o-GeS and h-GeS has been calculated along the high symmetry k-path of the Brillouin zone (BZ) as shown in **Figure 2.18**. The indirect band gap of 1.80 eV from Γ → X' for o-GeS bulk using HSE06 functional, shows good agreement with experimental (1.7 – 1.9 eV) and previous computational reports (1.71 eV) *[79, 80, 93, 94]*. The hole valley at valence band maxima (VBM) is found to degenerate at Γ, Y', and T positions. Similarly, the conduction band minima (CBM) have electron valleys at X', S', Γ, Y' and T positions for o-GeS bulk. The band gap of o-GeS bilayer (2.09 eV) is higher than o-GeS bulk (1.80 eV) which could be due to the quantum confinement effect.

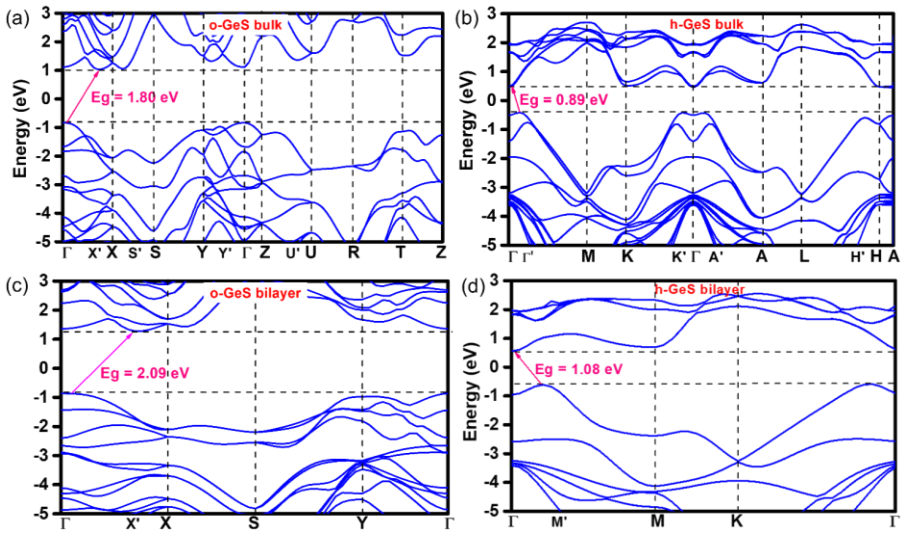


Figure 2.18: Electronic band structures of GeS systems (a) o-GeS bulk and (b) h-GeS bulk (c) o-GeS bilayer and (d) h-GeS bilayer, using the HSE06 functional.

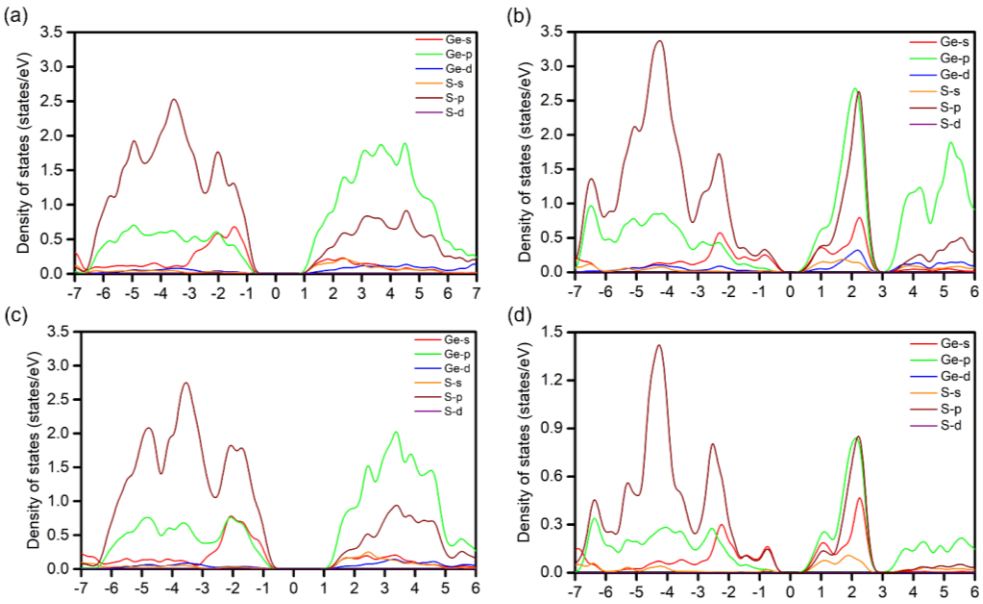


Figure 2.19: Partial density of states for considered GeS systems, (a) o-GeS bulk, (b) h-GeS bulk, (c) o-GeS bilayer, and (d) h-GeS bilayer.

For the h-GeS bulk, we find an indirect band gap of 0.89 eV from Γ'→ Γ. The degenerate VBM has a hole valley at Γ', K', A' and H' an electron valley at Γ, K, A, and H. Similarly, h-GeS bilayer has an indirect band gap of 1.08 eV from M'→ Γ position. Furthermore, we have analysed the partial density of states (PDOS) for all the considered materials to understand the contribution of individual element states in valence and conduction band as presented in **Figure 2.19**. The electronegativity of S is higher than Ge by 0.52 *[91]*, which is evident in PDOS plots. The valence band (VB) is majorly dominated by S p-orbital, whereas the conduction band (CB) is composed of Ge p-orbitals majorly. In the case of o-GeS bulk and bilayer, the electronic states below Fermi level are contributed maximum by S-p, followed by Ge-s and Ge-p orbitals. Above Fermi level (0.80 – 2.90 eV) maximum contribution is by p orbitals of Ge and S, followed by s orbital of Ge and S orbitals. Moreover, the contribution of all the states remains the same in o-GeS bulk and bilayer systems. In the case of h-GeS, though all the elemental state contribution remains the same, the peak intensity declines in the h-GeS bilayer. Overall, the thermoelectric performance of n-

and p-type can be improved by adjusting the concentration of Ge and S atoms, respectively.

2.7.2. Thermal Properties

The role and importance of 3-phonon and 4-phonon interactions on the lattice thermal conductivity (κ_L). The calculated κ_L values obtained from 3-phonon scattering for o-GeS and h-GeS bulk have been presented in Figure 2.20 covering a temperature range of 300-900 K. For the 2D o-GeS bilayer system, the 3-phonon calculated values are $\kappa_{L,3}$ = 14.59 $Wm^{-1}K^{-1}$ along the x-axis and $\kappa_{L,3}$ = 7.55 $Wm^{-1}K^{-1}$ along the y-axis at 300 K as shown in **Figure 2.20**.

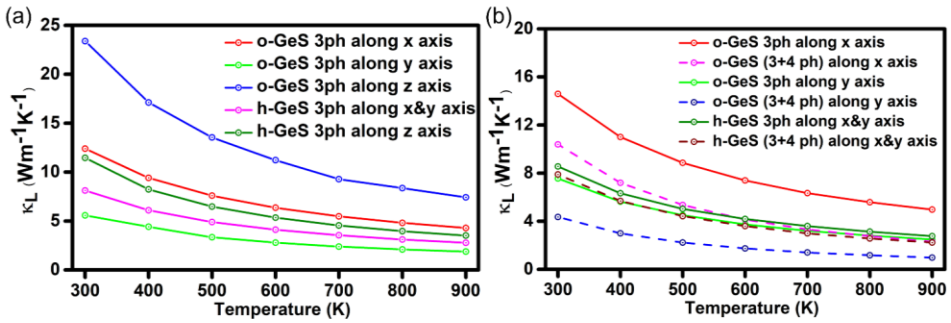


Figure 2.20: Lattice thermal conductivity of (a) o-GeS and h-GeS bulk considering 3-phonon scattering, and (b) o-GeS and h-GeS bilayer considering 3-phonon and 4-phonon scattering at different temperatures.

The calculated $\kappa_{L,3}$ values for our o-GeS bilayer is found to be lower than the reported $\kappa_{L,3}$ values for o-GeS monolayer (11.76 $Wm^{-1}K^{-1}$ along the x-axis and 12.53 $Wm^{-1}K^{-1}$ along the y-axis) at 300 K *[95]*. In the o-GeS system, two kinds of Ge-S interactions are present (**Figure 2.15**) as discussed previously. The weaker bonding along the y-axis compared to the x-axis results in lower κ_L along the y-axis. The studied Young's and shear modulus of o-GeS along both axes shows higher along the x-axis (~51 GPa) than along the y-axis (~17 GPa), which agrees with the observed anisotropy in the κ_L. For h-GeS bilayer, the $\kappa_{L,3}$ = 8.55 $Wm^{-1}K^{-1}$ along the x and y axis

as shown in **Figure 2.20(b)**. Thus, the o-GeS phase is found to show higher κ_L than the h-GeS phase. However, the κ_L value decreases on increasing the temperature for all the systems as is evident from **Figure 2.20**. The lattice thermal conductivities that have been reported for α-GeSe, γ-GeSe, and GeTe bulk at 300 K are 7.5 $Wm^{-1}K^{-1}$, 1.73 $Wm^{-1}K^{-1}$, and 2.5 $Wm^{-1}K^{-1}$, respectively *[19, 96]*. SnSe bulk exhibits a thermal conductivity value of 0.62 $Wm^{-1}K^{-1}$ at 300 K. Similarly, the calculated thermal conductivity values for PbS, PbSe, and PbTe bulk at 300 K are 2.80, 2.64, and 2.30 $Wm^{-1}K^{-1}$, respectively *[97]*. All these values are higher than the calculated thermal conductivity value of considered o-GeS and h-GeS bulk systems.

Further, we have investigated the effect of higher-order scattering rates on o-GeS and h-GeS bilayers. The calculated κ_L from 4-phonon scattering theory is $\kappa_{L,3+4}$ = 10.39 $Wm^{-1}K^{-1}$ along the x-axis and $\kappa_{L,3+4}$ = 4.35 $Wm^{-1}K^{-1}$ along the y-axis for o-GeS bilayer at 300 K. Therefore, the percentage change in κ_L at 300 K is 28.78% and 42.38% along x and y axis, respectively. This uneven percentage change along x and y-axis in κ_L of the o-GeS system arises due to its bonding anisotropy, as shown in **Figure 2.15**. The stronger bonds along x-axis scatter less than the weaker bonds along y-axis compared to the x-axis. The observation is consistent with the bonding patterns of the system. The h-GeS bilayer system the calculated κ_L from 4-phonon scattering theory $\kappa_{L,3+4}$ = 8.55 $Wm^{-1}K^{-1}$ along the x and y-axis. The h-GeS bilayer shows a change of 7.71% in κ_L on considering 4-phonon. The percentage change of κ_L on considering 4-phonon interactions increases with increasing the temperature as tabulated in **Table 2.10-2.11**.

Table 2.10: Lattice thermal conductivity ($Wm^{-1}K^{-1}$) of o-GeS bilayer with respect to 3 phonon and 3+4 phonon processes and the percentage change on considering 3+4 phonon.

o-GeS Bilayer

T (K)	$\kappa_{L,x}$ (3ph)	$\kappa_{L,y}$ (3ph)	$\kappa_{L,x}$ (3+4ph)	$\kappa_{L,y}$ (3+4ph)	% change in κ_L along x-axis	% change in κ_L along y-axis
300	14.59	7.55	10.39	4.35	28.78	42.38
400	11.00	5.63	7.19	2.99	34.63	46.89
500	8.85	4.50	5.35	2.22	39.54	50.66
600	7.39	3.73	4.14	1.74	43.97	53.35
700	6.34	3.20	3.32	1.40	47.63	56.25
800	5.58	2.81	2.76	1.17	50.53	58.36
900	4.96	2.48	2.30	0.97	53.63	60.88

Table 2.11: Lattice thermal conductivity ($Wm^{-1}K^{-1}$) of h-GeS bilayer with respect to 3 phonon and 3+4 phonon processes and the percentage change on considering 3+4 phonon.

h-GeS Bilayer			
T (K)	**κ_L (3ph)**	**κ_L (3+4ph)**	**% change in κ_L**
300	8.55	7.89	7.71
400	6.32	5.69	9.96
500	5.02	4.42	11.95
600	4.19	3.59	14.32
700	3.59	2.99	16.71
800	3.13	2.56	18.21
900	2.76	2.23	19.20

At 900 K, the percentage change of κ_L is found to be more prominent for o-GeS bilayer (~54% and ~61% along the x and y-axis), whereas the 4-phonon interaction effect is negligible for h-GeS bilayer ~19%. This change

in κ_L can be attributed to the increase in the number of scattering channels (4-phonon) with temperature as compared to 3-phonon scattering channels *[65, 84]*. The 4-phonon scattering is more prominent in o-GeS bilayer compared to the h-GeS bilayer due to the presence of weaker Ge-S bonding and larger a-o gap in o-GeS system as shown in Figure 2.16 *[67]*. As in some materials, the large band gap will forbid two acoustic phonons from combining into an optical phonon and thus weaken the coupling between acoustic and optical phonons, due to the strong restriction of simultaneous energy and momentum conservations. However, it will not be restrictive for 4-phonon processes between acoustic and optical phonons *[67]*.

The materials with low κ_L can exhibit high anharmonicity, scattering rates, high Grüneisen parameter, and low group velocity. κ_L is also impacted by the boundary and isotopic scattering in the material (**Figure 2.21**). It has been observed from the graph that isotopic phonon scattering has the least impact on the κ_L whereas, phonon boundary scattering shows a larger effect on κ_L. On considering 4-phonon scattering, both the scattering rates contribute in the same order but for o-GeS bilayer the scattering rate is more in the acoustic region compared to h-GeS bilayer.

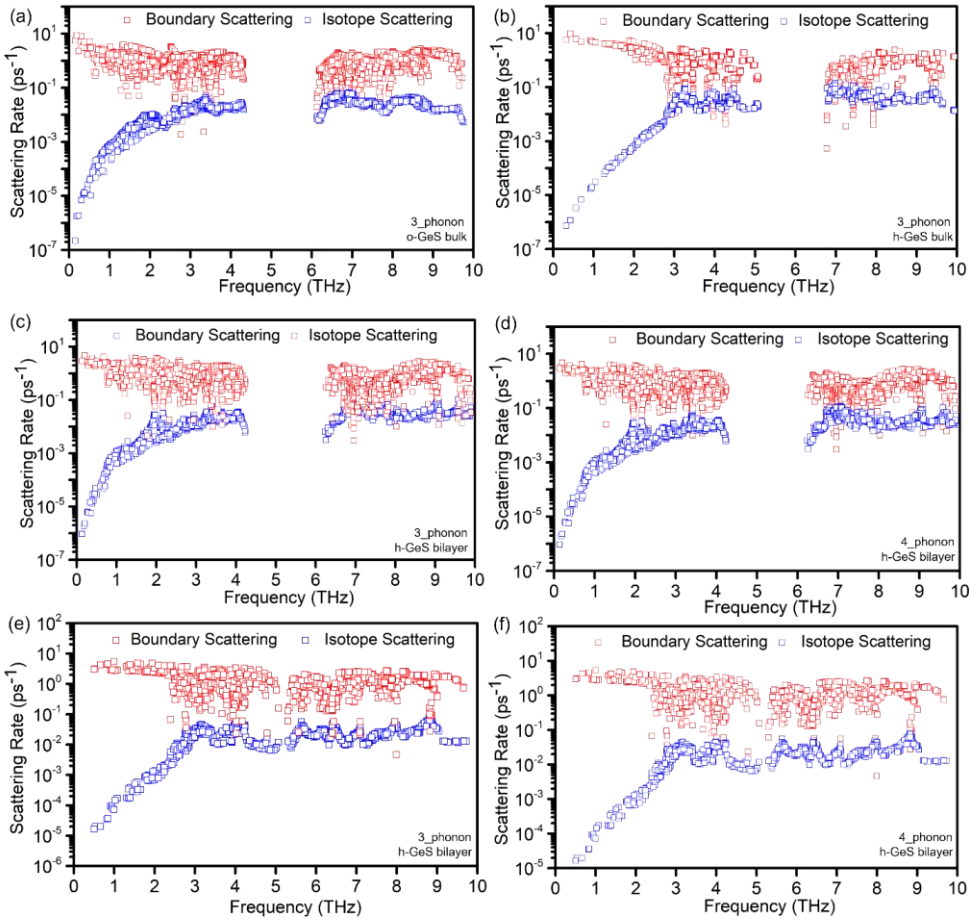


Figure 2.21: Boundary and isotopic scattering rates of the considered GeS systems, (a) o-GeS bulk, (b) h-GeS bulk, (c) o-GeS bilayer (3 phonon), (d) o-GeS bilayer (3+4 phonon), (e) h-GeS bilayer (3 phonon), and (f) o-GeS bilayer (3+4 phonon) with respect to frequency (THz) at 300K.

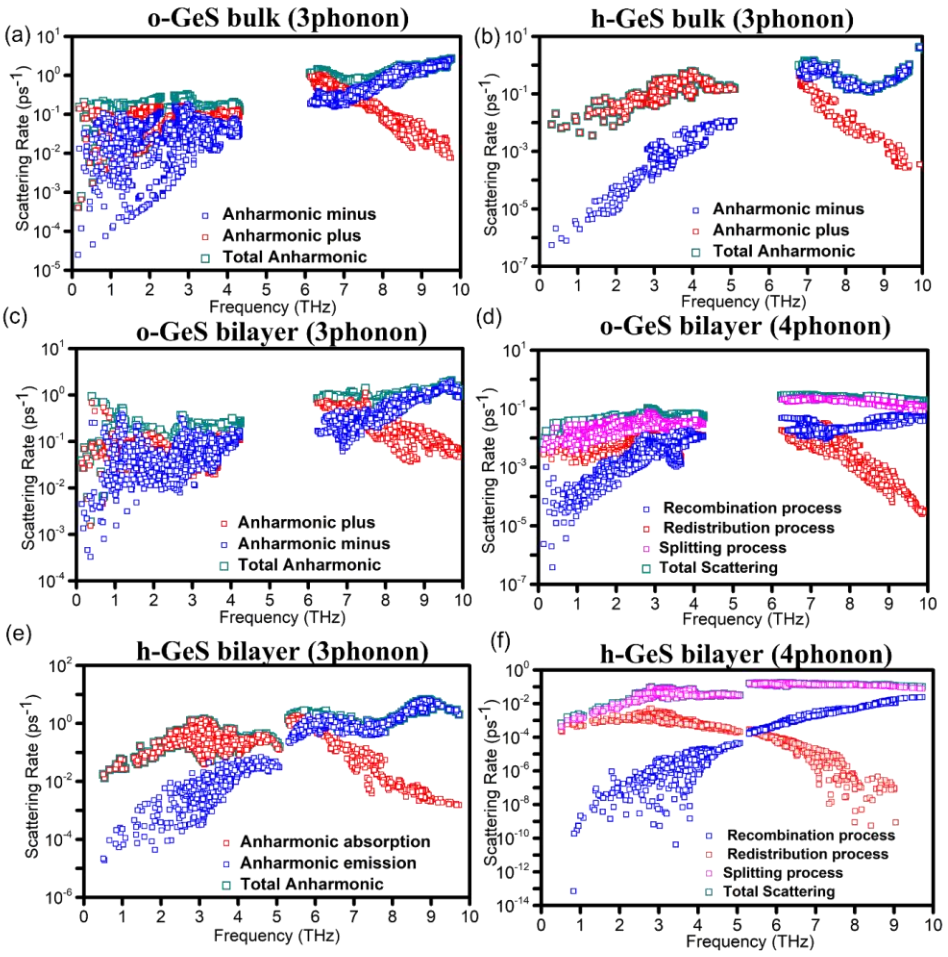


Figure 2.22: Anharmonic scattering rates of the GeS systems (a) o-GeS bulk (3-phonon), (b) h-GeS bulk (3-phonon), (c) o-GeS bilayer (3-phonon), (d) o-GeS bilayer (3+4 phonon), (e) h-GeS bilayer (3-phonon) and (f) h-GeS bilayer (3+4 phonon) at 300 K.

Moving to anharmonic scattering rates, more amount of acoustic scattering supports the low κ_L of o-GeS bulk and bilayer than the h-GeS bulk and bilayer. The a-o band gap increases in o-GeS bilayer and h-GeS bilayer with respect to that of o-GeS and h-GeS bulk (Figure 2). The lower a-o gap in h-GeS systems also supports the lower κ_L of h-GeS systems as depicted in **Figure 2.22(e, f)**. The lowest κ_L is observed along the o-GeS y-axis in both bulk and bilayer with 2.48 $Wm^{-1}K^{-1}$ and 0.97 $Wm^{-1}K^{-1}$ values at 900 K, respectively. Considering the 3-phonon scattering process, the acoustic

region is dominated by anharmonic absorption ($q + q' \rightarrow q''$), while considering 4-phonon scattering process, anharmonic splitting ($q \rightarrow q' + q'' + q'''$) is found to dominate.

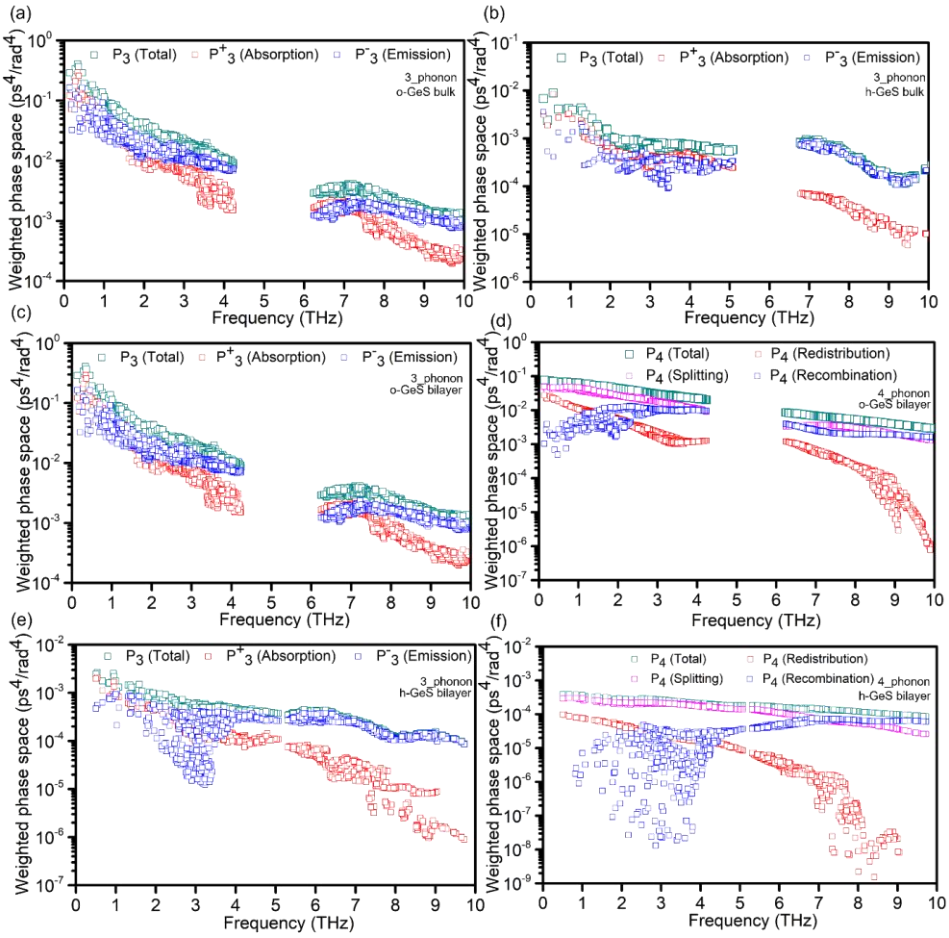


Figure 2.23: Weighted phase space of the GeS systems (a) o-GeS bulk (3 phonon), (b) h-GeS bulk (3 phonon), (c) o-GeS bilayer (3 phonon), (d) o-GeS bilayer (3+4 phonon), (e) h-GeS bilayer (3 phonon) and (f) h-GeS bilayer (3+4 phonon) with respect to frequency (THz) at 300 K.

The distribution of weighted phase space (P) with respect to phonon frequency has been represented in **Figure 2.23**. This gives an overall idea regarding phonon scattering channels from three phonon interactions, absorption (P_3^+: $q + q' \rightarrow q''$) and emission (P_3^-: $q \rightarrow q' + q''$) processes. In 4-phonon interactions the dominant scattering channel in acoustic mode is splitting process ($q \rightarrow q' + q'' + q''' + k$), followed by redistribution

process $(q + q' \rightarrow q'' + q''' + k)$. However, the contribution of redistribution process decreases with an increase in phonon frequency, and the contribution of recombination process increases as shown in **Figure 2.23(d, f)**. The major channels for optical modes are splitting process $(q + q' \rightarrow q'' + q''' + k)$ followed by recombination process. The P_3 and P_4 plots provide the phonon scattering rates as a function of harmonic frequency during heat conduction. Also, we find that in both the bilayer systems of GeS, the 4-phonon Umklapp process, and normal process are almost contributing in equal proportions as shown in **Figure 2.24**. The Umklapp scattering, which is directly proportional to thermal resistance, typically occurs for the higher frequency acoustic phonons for which the wave vector is the substantial fraction of the Brillouin zone (BZ) *[98]*.

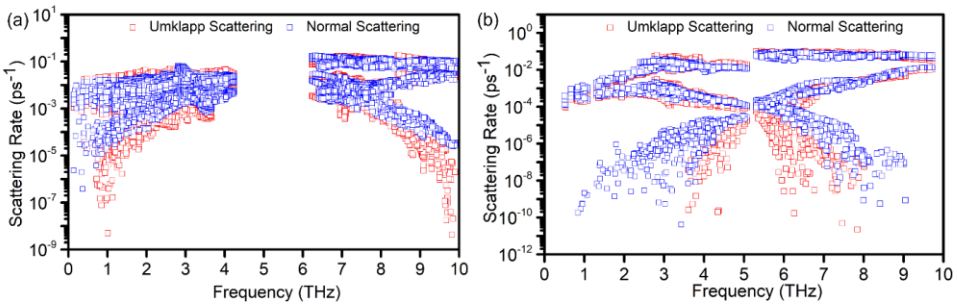


Figure 2.24: Umklapp and Normal scattering of the GeS systems (a) o-GeS bilayer (3+4 phonon) and (b) h-GeS bilayer (3+4 phonon) with respect to frequency (THz) at 300K.

For further insight, we calculated another parameter that explains the extent of phonon scattering, the Grüneisen parameter (γ), a dimensionless quantity that describes the anharmonic interactions within the system which results in a lowering of κ_L. It can be calculated based on the change in phonon frequency with respect to the change in volume,

$$\gamma = -\frac{V}{\omega}\frac{\partial \omega}{\partial V} \qquad (1)$$

where V and ω are the volume of the unit cell and angular frequency, respectively. The larger value of γ implies stronger anharmonicity in the

system and more phonon-phonon scattering, resulting in the shorter relaxation time of phonons and overall resulting in lower κ_L. The average γ for o-GeS and h-GeS bulk is calculated to be 0.69 and 1.00, respectively.

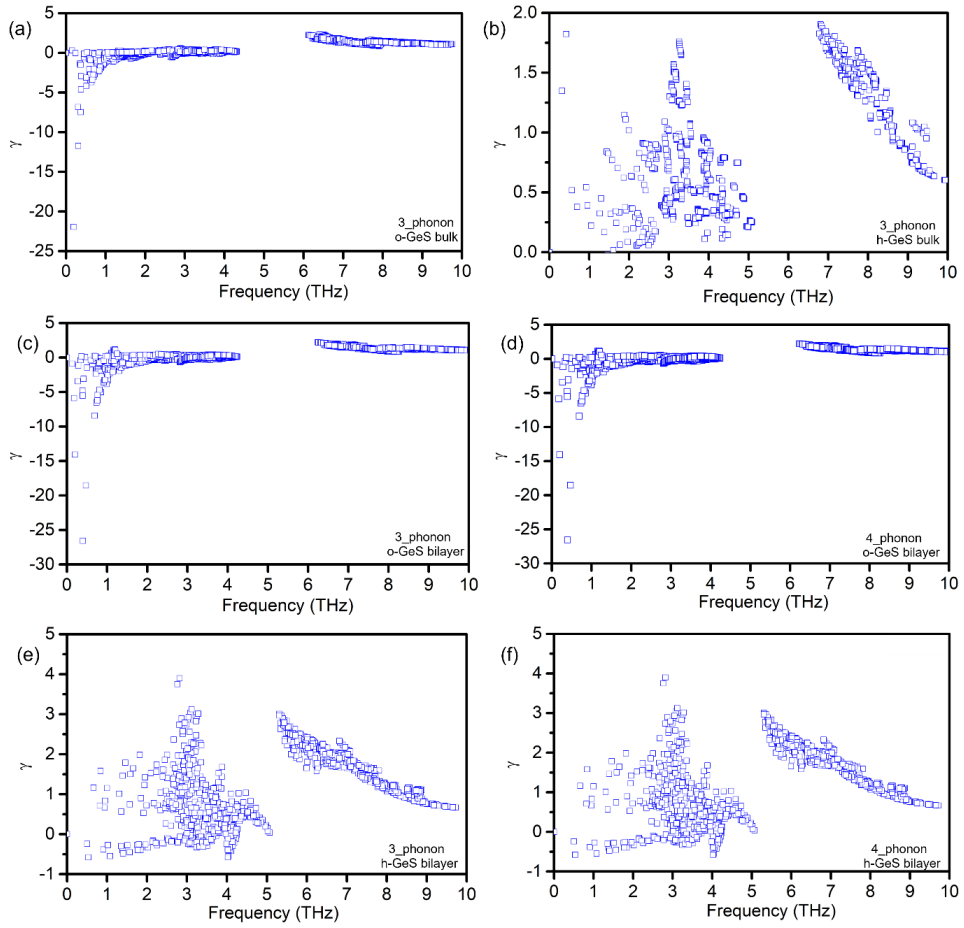


Figure 2.25: Grüneisen parameter (γ) of the GeS systems (a) o-GeS bulk (3 phonon), (b) h-GeS bulk (3 phonon), (c) o-GeS bilayer (3 phonon), (d) o-GeS bilayer (3+4 phonon), (e) h-GeS bilayer (3 phonon), and (f) h-GeS bilayer (3+4 phonon) with respect to frequency (THz) at 300K.

For o-GeS and h-GeS bilayer, the average γ is calculated to be 0.52 and 1.19, respectively at 300 K, considering 3-phonon scattering. On including the 4-phonon scattering process as well, we didn't observe much change in o-GeS bilayer ($\gamma_3 = 0.52$ and $\gamma_{3+4} = 0.53$), whereas the change in γ has been found to be much noticeable in h-GeS bilayer ($\gamma_3 = 1.19$ and $\gamma_{3+4} = 1.90$). The γ parameter upon considering 3-phonon scattering for some well-

known systems with low thermal conductivity like PbTe and PbSe are 1.62 and 1.69, respectively *[56]*. **Figure 2.25** shows the deviation of γ at the acoustic region majorly contributes towards heat conduction. Therefore, the higher the deviation of γ below 4 THz, the lower will be the κ_L. The concentration and deviation of γ parameter is higher in o-GeS than the h-GeS both in the 3-phonon and 4-phonon processes. The γ also shows the direct relation with the linear thermal expansion of the material. All the considered systems show negative γ at different frequency regions except h-GeS bulk. As the γ is directly related to linear thermal expansion, a negative γ signifies that the material can have negative linear thermal expansion. Materials like Pb_2Se_3, MoS_2, graphene, germanene, and silicene have been found to exhibit negative γ parameters *[56]*. All the discussed parameters support the low thermal conductivity in o-GeS than h-GeS systems. The phonon conductivity is directly proportional to the κ_L.

Table 2.12: Longitudinal velocity (V_L), Transverse velocity (V_T) and Debye Temperature (θ_D) for the considered structures of GeS.

Material	Longitudinal velocity (V_L) (m/s)	Transverse velocity (V_T) (m/s)	Debye Temperature (θ_D) (K)
o-GeS bulk	4695	2552	364
h-GeS bulk	4260	2580	353
o-GeS bilayer	5153	4035	390
h-GeS bilayer	4704	2789	259

The longitudinal velocity is almost twice of transverse velocity as shown in **Table 2.12**. The Debye temperature (θ_D) defines the critical temperature above which all phonon modes get excited. The θ_D values for o-GeS bulk, o-GeS bilayer, h-GeS bulk, and h-GeS bilayer are found to be 364 K, 353 K, 390 K, and 259 K, respectively. These values agree with the trends

observed for κ_L in our considered systems. The values are typically lower than that in graphene (2539 K) and comparable to stanene 198 K *[55]*. However, a low value of θ_D indicates damping of phonons. This damping of phonons refers to the loss of energy by phonons as they propagate through a material leading to low κ_L.

2.7.3. Thermoelectric Properties

The majority of the studies on TE properties are based on constant relaxation time approximation (CRTA). The thermoelectric performance (ZT) calculated using CRTA is represented in Table 2.11-2.12. However, the CRTA approach could be highly inaccurate because of complex scattering in the system which highly affects the carrier relaxation time *[85]*. Thus we have further calculated the thermoelectric properties using the AMSET package which calculates the energy and temperature-dependent carrier scattering rates. These scattering mechanisms include the full anisotropic nature of ionized impurity (IMP), polar optical phonon (POP), acoustic deformation potential (ADP), and piezoelectric (PIE) scatterings processes *[86]*. Here, in our study the PIE scattering is zero, therefore we have neglected the piezoelectric tensor. However, the ADP, IMP, and POP scattering rates as a function of temperature vary at different carrier concentrations as shown in **Figure 2.26**. The differential scattering rate is calculated based on the Fermi's golden rule and the mode-dependent scattering rates are calculated using the Born approximation.

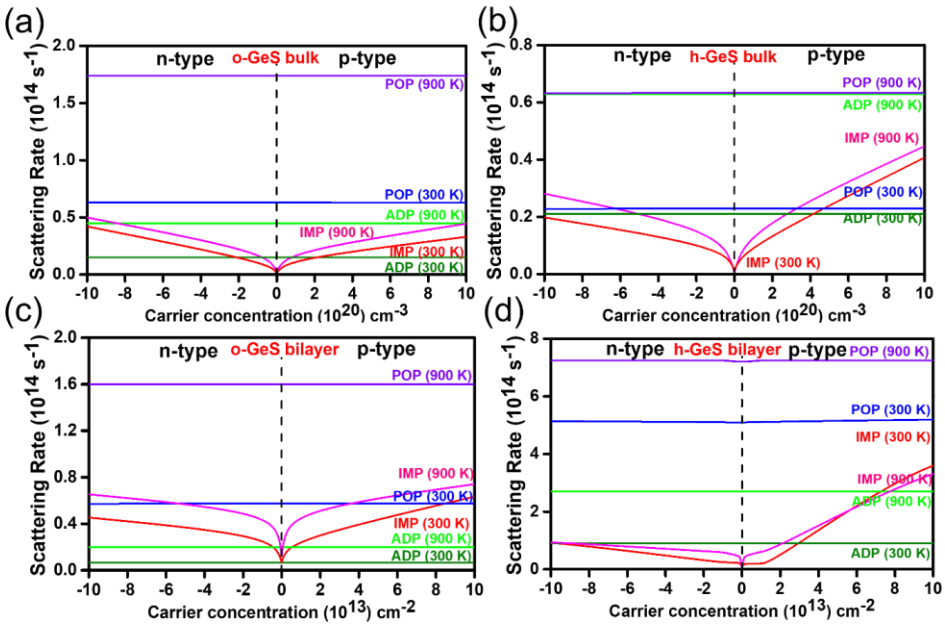


Figure 2.26: Scattering Rates of (a) o-GeS bulk, (b) h-GeS bulk, (c) o-GeS bilayer, and (d) h-GeS bilayer: These represent the variation of Polar Optical Phonon (POP) Scattering, Ionized Impurity Scattering (IMP), and Acoustic Deformation Potential Scattering (ADP) with Carrier Concentrations at 300 K and 900 K for n-Type and p-Type Conduction.

2.7.3.1. Seebeck Coefficient

The considered GeS systems have been further examined for their thermoelectric performance. To know TE performance, it is imperative to study the Seebeck coefficient and electrical properties besides their electronic and thermal properties. By considering the energy-independent scattering approximation, the Seebeck coefficient (S) is formulated as

$$S = \frac{8\pi^2 k_B^2 m^* T}{3eh^2}\left(\frac{\pi}{3n}\right)^{2/3} \qquad (2)$$

where k_B is Boltzmann constant, m^* is effective mass, T is absolute temperature, h is Planck's constant and n is the carrier concentration *[91]*. Thus, the optimum band gap should be at least $10k_BT_{max}$, to eradicate the simultaneous excitation of intrinsic holes and electrons, which decreases the

S at elevated temperature scale. We observed that the |S| value of h-GeS bulk gradually decreases with an increase in temperature till the carrier concentration of $1x10^{20}$ cm^{-3}. Above this carrier concentration, an opposite trend is observed, where |S| increases with increase in temperature. This is due to bipolar conduction as observed in other reports *[99]*.

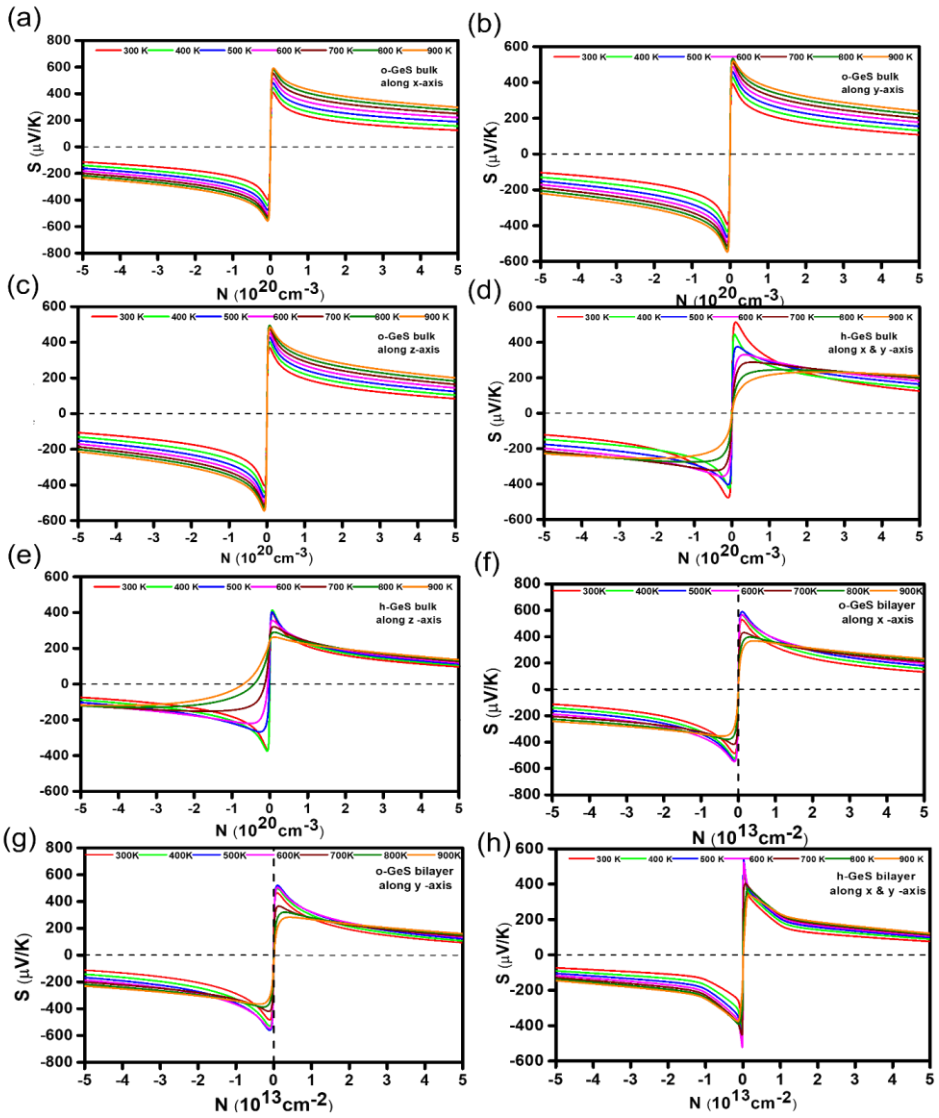


Figure 2.27: Seebeck coefficients of (a) o-GeS bulk along x-axis, (b) o-GeS bulk along y-axis, (c) o-GeS bulk along z-axis, (d) h-GeS bulk along x and y axis, (e) h-GeS bulk along z axis, (f) o-GeS bilayer along x-axis,

(g) o-GeS bilayer along y-axis and (h) h-GeS bilayer along x and y axis as a function of carrier concentration at different temperature using AMSET.

At room temperature (RT), the S of h-GeS bulk is 538 μVK^{-1} which decreases to 210 μVK^{-1} at 900 K. At higher concentration (> 10^{20} cm^{-3}), the S increases to 443 μVK^{-1} at 900 K for n-type. This bipolar conduction is majorly caused because of the low band gap, due to which both electrons and holes participate in conduction resulting in decrease in Seebeck coefficient. The carrier concentration (N) for o-GeS and h-GeS bulk is 10^{20} cm^{-3} – 10^{21} cm^{-3} and for o-GeS and h- GeS bilayer is 10^{13} cm^{-2}. This decrease in N could be due to quantum confinement *[100]*. This is because the confinement restricts the movement of the carriers in the two dimensions, leading to the quantization of energy levels and the formation of discrete energy states. As a result, the carriers are distributed over a smaller number of available states, leading to a reduced carrier density per unit area *[100]*. Moreover, the S for bilayer increases with an increase in temperature. At RT, S is 224 μVK^{-1} and on increasing temperature to 900 K, S spikes up to 390 μVK^{-1}. The o-GeS is an anisotropic system, which has S_x= 527 μVK^{-1}; S_y= 508 μVK^{-1} and S_z= 526 μVK^{-1} at 300 K which increases to S_x= 697 $\mu VK^{-1}$$S_y$= 673 $\mu VK^{-1}$$S_z$= 670 μVK^{-1} at 900 K. Similarly, for the o-GeS bilayer the S_x= 420 μVK^{-1} and S_y= 425 μVK^{-1} at 300 K and S_x= 430 μVK^{-1} and S_y= 510 μVK^{-1} at 900 K as shown in **Figure 2.27**.

2.7.3.2. Electrical Conductivity

To avoid the CRTA, we have evaluated the scattering rate i.e., relaxation time with carrier concentration and varying temperature, which has been considered for calculating the electronic thermal conductivity (κ_e) and electrical conductivity (σ) using AMSET. **Figures 2.28-2.29**, Supporting Information represents the electrical conductivity and electronic thermal conductivity with respect to the carrier concentrations, respectively. At RT,

σ is 0.47 μSm^{-1} for h-GeS bulk and 0.06 μSm^{-1} for h-GeS bilayer. Similarly, o-GeS exhibits σ_x = 0.21 μSm^{-1}; σ_y = 0.31 μSm^{-1} and σ_z = 0.62 μSm^{-1} at 300 K and o-GeS bilayer exhibits σ_x = 0.06 μSm^{-1} and σ_y = 0.08 μSm^{-1} at room temperature.

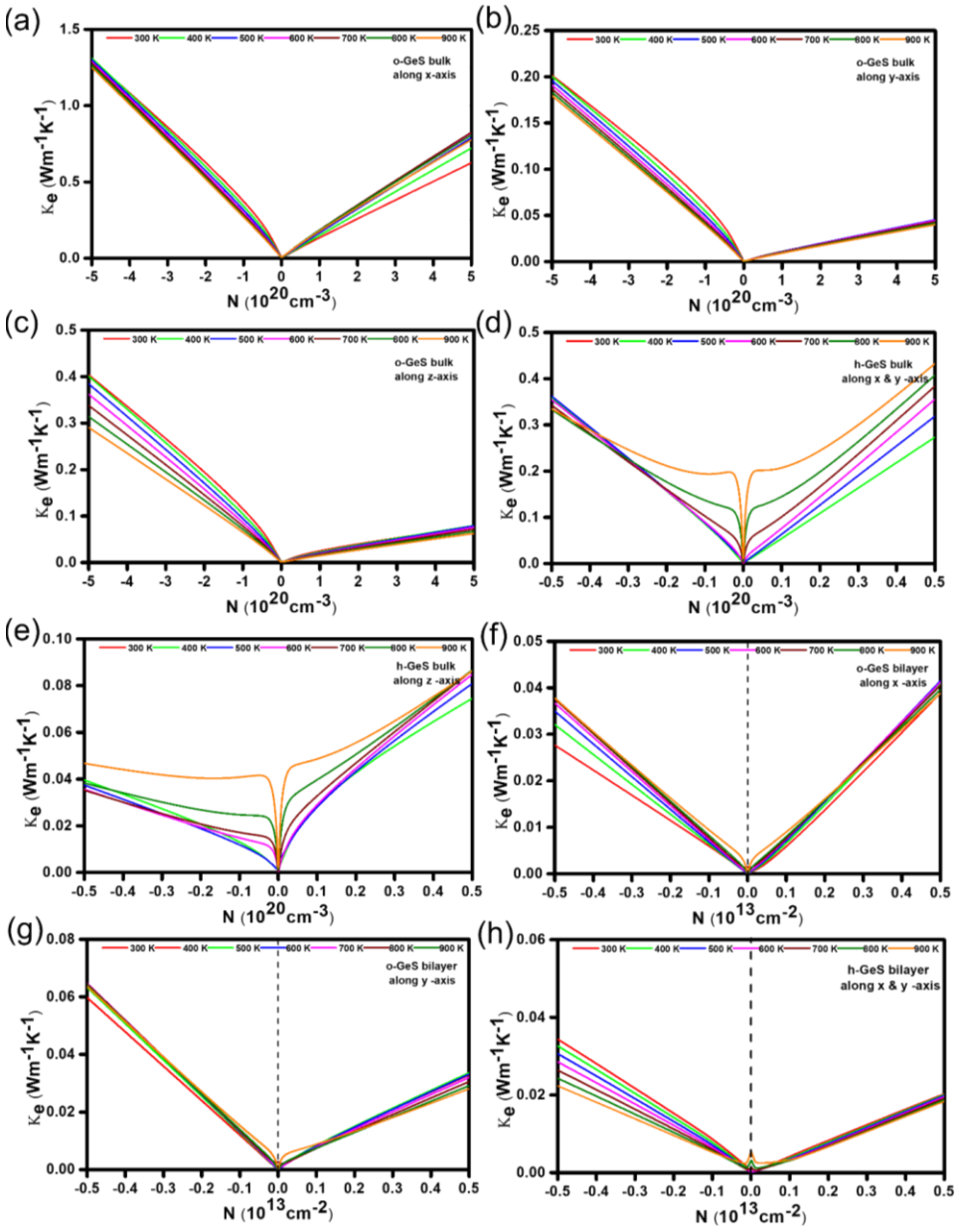


Figure 2.28: Electronic thermal conductivity (κ_e) of (a) o-GeS bulk along x-axis, (b) o-GeS bulk along y-axis, (c) o-GeS bulk along z-axis, (d) h-GeS bulk along x and y axis, (e) h-GeS bulk along z axis, (f) o-GeS bilayer along

x-axis, (g) o-GeS bilayer along y-axis and (h) h-GeS bilayer along x and y axis as a function of carrier concentration using AMSET.

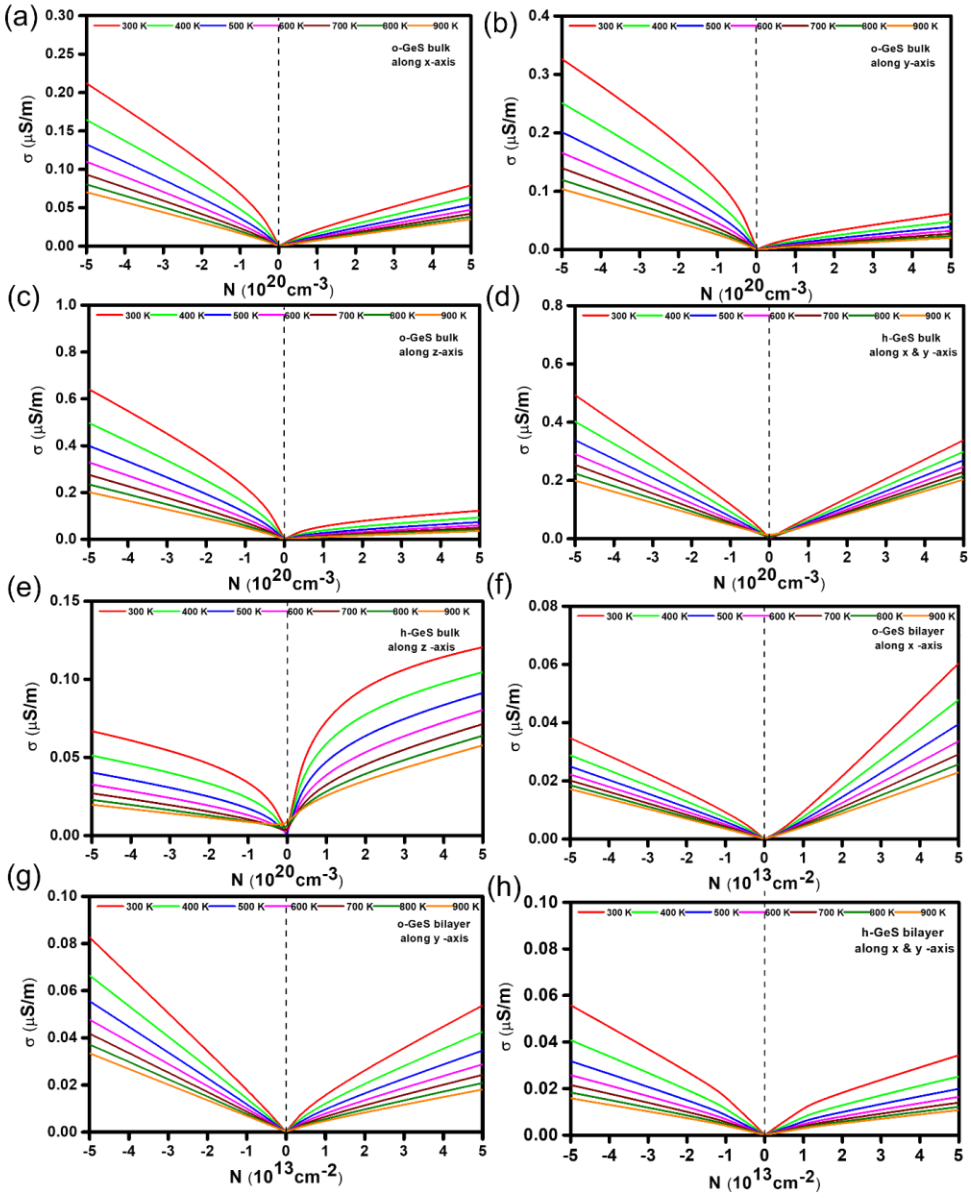


Figure 2.29: Electrical conductivity of (a) o-GeS bulk along x-axis, (b) o-GeS bulk along y-axis, (c) o-GeS bulk along z-axis, (d) h-GeS bulk along x and y axis, (e) h-GeS bulk along z axis, (f) o-GeS bilayer along x-axis, (g) o-GeS bilayer along y-axis and (h) h-GeS bilayer along x and y axis as a function of carrier concentration at different temperature using AMSET.

In all the considered systems, the n-type conductivity is found to be higher than p-type conductivity except h-GeS bulk along z-axis and o-GeS bilayer along x-axis as shown in **Figure 2.26**. The κ_e follows the direct relation with temperature. As the temperature increases the κ_e also increases. At RT, the κ_e is 0.35 $Wm^{-1}K^{-1}$ and 0.02 $Wm^{-1}K^{-1}$ for h-GeS bulk and bilayer, respectively. For the anisotropic o-GeS material, κ_e is 1.27 $Wm^{-1}K^{-1}$; 1.19 $Wm^{-1}K^{-1}$ and 0.39 $Wm^{-1}K^{-1}$ along x, y, and z-axis for bulk. However, κ_e decreases to 0.027 $Wm^{-1}K^{-1}$ and 0.06 $Wm^{-1}K^{-1}$ for the x and y-axis, respectively at 300 K for o-GeS bilayer. The ultralow values of κ_e at low temperatures reflect that κ_L is contributing majorly towards total thermal conductivity. But as the temperature increases the contribution of κ_e towards total thermal conductivity also increases.

2.7.3.3. Power Factor and Figure of Merit

Finally, we have all the parameters to calculate power factor (PF) and figure of merit (ZT). ZT is a dimensionless quantity, which defines the net efficiency of the TE material at different temperature scales. The PF and ZT can be formulated as,

$$PF = S^2\sigma \quad (3)$$

$$ZT = \frac{S^2\sigma}{\kappa_e + \kappa_L} T \quad (4)$$

All the important parameters related to the thermoelectric performance of the considered GeS bulk and bilayer has been presented in **Table 2.13-2.14**. The plots of ZT with respect to carrier concentration at the temperature range from 300 K to 900 K with both hole and electron-doped cases are represented in **Figures 2.30-2.31**.

It has been observed that PF is higher for bulk rather than the bilayer for both phases of GeS system. The n-type shows a higher value than the p-type for both PF and ZT except o-GeS bulk along the x-axis and h-GeS along x and y axis (**Table 2.13**). For the h-GeS bulk, the p-type shows peak at 5.54 $mWK^{-2}m^{-1}$ at 300 K whereas, at the same temperature n- type shows 8.16

$mWK^{-2}m^{-1}$ as can be seen in Table 1. For h-GeS bilayer at RT, n- type shows PF value of 0.27 $mW^{-2}K^{-1}$.

Table 2.13. Lattice Thermal Conductivity (κ_L) ($Wm^{-1}K^{-1}$), Power Factor (PF) ($mWK^{-2}m^{-1}$), and ZT at 300 and 900 K for o- GeS and h-GeS bulk.

Material	T (K)	κ_L (3ph)			PF			ZT (AMSET)			ZT (CRTA)		
		x	y	z	x	y	z	x	y	z	x	y	z
o-GeS Bulk	300	12.40	5.57	23.39	2.21	2.91	6.63	0.03	0.16	0.08	0.02	0.06	0.03
	900	4.29	1.87	7.42	2.34	3.28	10.5	0.34	0.97	0.52	0.67	1.28	0.82
h-GeS Bulk	300	8.11	8.11	11.45	5.54	5.54	1.96	0.12	0.12	0.17	0.77	0.76	0.02
	900	2.77	2.77	3.51	8.16	8.16	2.75	0.96	0.96	0.29	1.28	1.29	0.25

Table 2.14: Lattice Thermal Conductivity (κ_L) ($Wm^{-1}K^{-1}$), Power Factor (PF) ($mWK^{-2}m^{-1}$), and ZT at 300 and 900 K for o- GeS and h-GeS bilayer. Here, percentage change represents the change in κ_L(3+4ph) with respect to κ_L(3-ph).

Material	T (K)		κ_L (3ph)	κ_L (3+4ph)	Percentage change	PF	AMSET		CRTA	
							ZT (3ph)	ZT (3+4ph)	ZT (3ph)	ZT (3+4ph)
o-GeS Bilayer	300	x	14.59	10.39	28.78	0.43	0.008	0.011	0.02	0.03
		y	7.55	4.35	42.38	0.59	0.023	0.039	0.05	0.09
	900	x	4.96	2.30	53.63	0.89	0.160	0.264	0.36	0.69
		y	2.48	0.97	60.88	1.48	0.303	0.508	1.12	2.12
h-GeS Bilayer	300	x=y	8.55	7.89	7.71	0.27	0.009	0.012	0.05	0.06
	900	x=y	2.76	2.23	19.20	0.33	0.08	0.09	0.72	0.86

On comparing the TE performance of o-GeS bulk using CRTA and AMSET approaches, a significant difference in the results has been observed. The maximum TE performance of o-GeS bulk is observed along the y-axis 1.28 using the CRTA approach. However, when considering the relaxation time, the TE value declines to 0.97 at 900 K. Similarly, for h-GeS bulk, the TE performance drops from 1.29 to 0.96 upon considering the relaxation time as shown **Table 2.13**. In the case of o-GeS bilayers, the TE value shows

significant decrease when the relaxation time is considered. The resulting ZT values are found to be half of the values calculated with the CRTA approach. In the case of h-GeS bilayers, the TE performance declines from 0.86 to 0.09 (**Table 2.14**) due to higher scattering rates caused by various factors such as phonon-phonon interactions (POP), impurities (IMP), and alloy scattering (ADP). This is due to the high scattering rate in the bilayer, as shown in **Figure 2.26 (d)**.

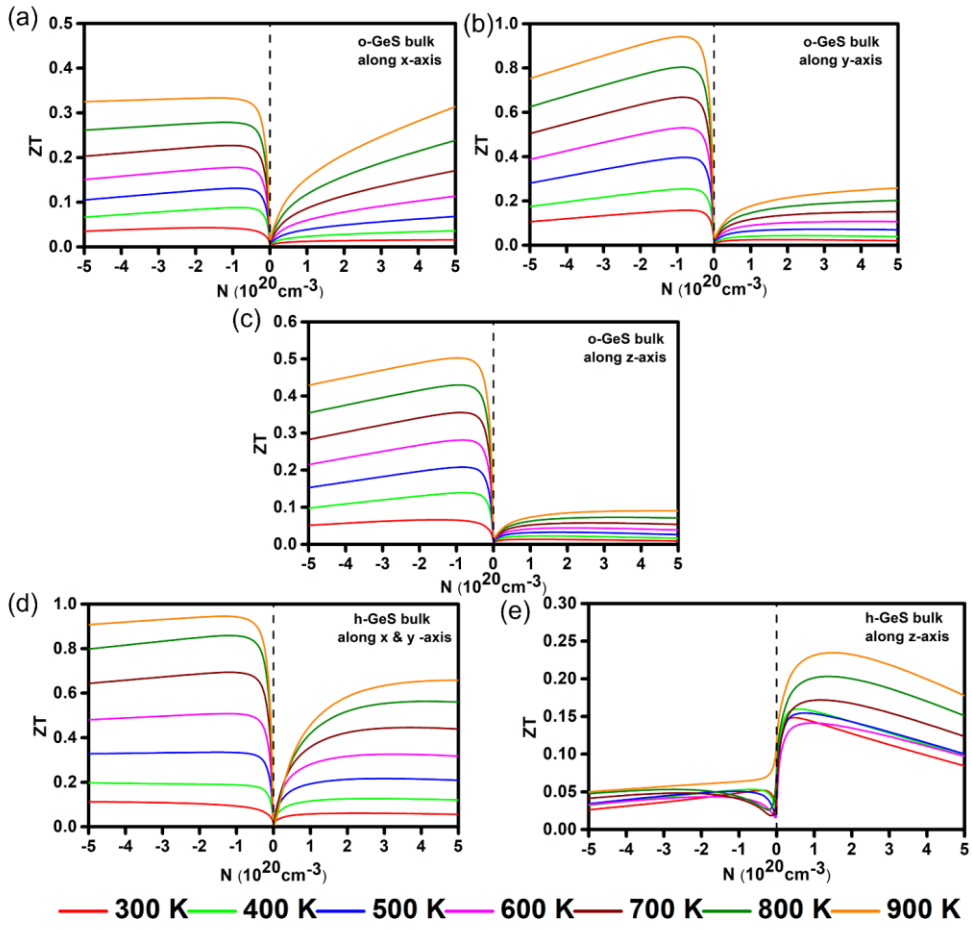


Figure 2.30: ZT of the considered GeS bulk systems, (a) o-GeS bulk along x-axis, (b) o-GeS bulk along y-axis, (c) o-GeS bulk along z-axis, (d) o-GeS bulk along x and y-axis, and (e) h-GeS bulk along z-axis (3-phonon) using AMSET.

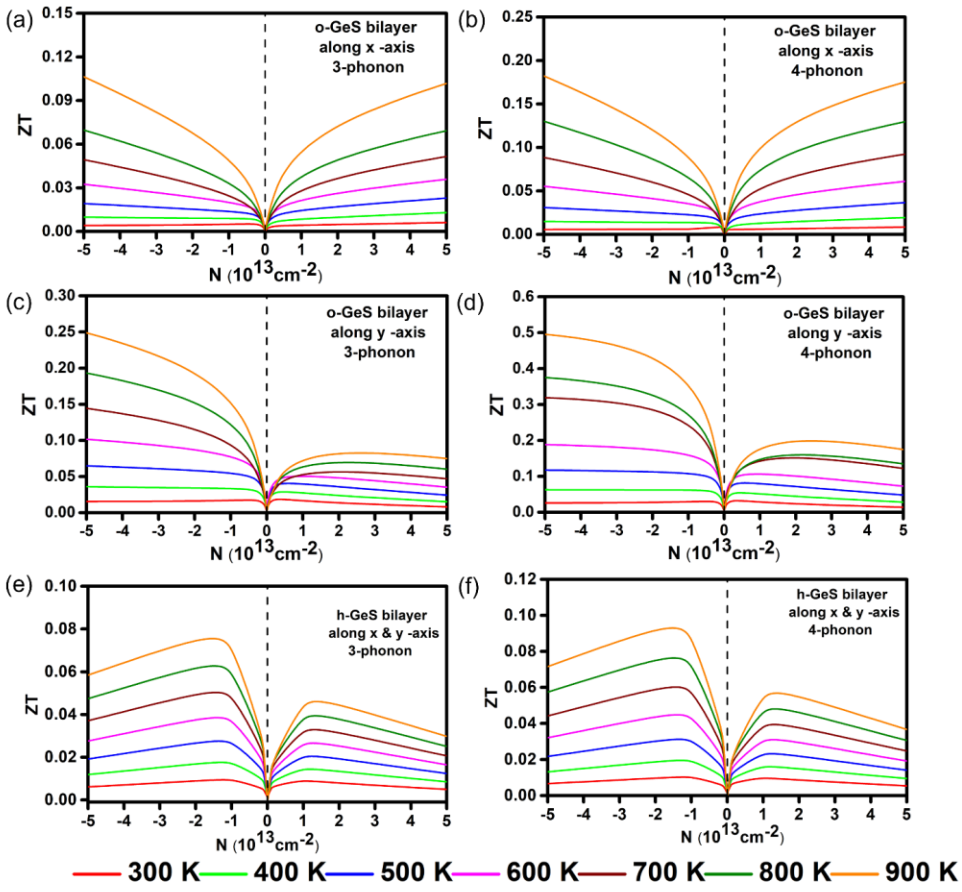


Figure 2.31: ZT of the considered GeS systems, (a) o-GeS bilayer along x-axis (3-phonon), (b) o-GeS bilayer along x-axis (3+4 phonon), (c) o-GeS bilayer along y-axis (3-phonon), (d) o-GeS bilayer along y-axis (3+4 phonon), (e) h-GeS bilayer along x and y-axis (3-phonon), and (f) h-GeS bilayer along x and y-axis (3+4 phonon), as a function of carrier concentration at different temperatures using AMSET.

The introduction of 4-phonon interactions in the calculations leads to a variation in the calculated value of thermal conductivity (κ_L), which in turn affects the calculated value of the ZT for the system as demonstrated in **Figure 2.31** and **Table 2.14**. The calculated ZT value at 900 K for o-GeS bilayer, considering 3-phonon interactions along the y-axis results in a ZT value of 0.30. However, on including 3+4 phonon interactions, the ZT value increases to 0.508. On the other hand, there is no significant change in the

ZT value for h-GeS bilayer (0.09) which is significantly lower compared ZT (0.96) calculated using CRTA approach. Although first-principles calculations provide valuable insights into phonon dynamics and electronic properties, they are computationally intensive and limited in scope. To overcome these challenges, machine learning offers a powerful alternative for rapid screening and inverse design of thermoelectric materials.

2.8. Summary

In summary, we systematically explore the thermal and thermoelectric properties of bulk and bilayer GeS in orthorhombic and hexagonal phases. All structures are confirmed to be dynamically and mechanically stable. For o-GeS, κ_L increases upon dimensional reduction, leading to lower ZT values for the bilayer compared to bulk at 900 K. In contrast, h-GeS exhibits nearly unchanged κ_L from bulk to bilayer, but a drastic reduction in ZT for the bilayer due to enhanced phonon scattering. Incorporation of four-phonon interactions significantly reduces κ_L in the o-GeS bilayer, resulting in notable enhancement of ZT, whereas h-GeS remains largely unaffected. These results highlight the critical importance of higher-order phonon scattering for accurate prediction of κ_L and thermoelectric performance.

2.9. References

1. Snyder G. J., Toberer E. S. (2008), Complex thermoelectric materials *Nat. Mater.*, 7, 105–114 (DOI:10.1038/nmat2090)

2. Chu S., Majumdar A. (2012), Opportunities and challenges for sustainable energy future, *Nature*, 488, 294–303 (DOI:10.1038/nature11475)

3. He J., Tritt T. M. (2017), Advances in thermoelectric materials research: looking back and moving forward, *Science*, 357, eaak9997 (DOI:10.1126/science.aak9997)

4. Zhu T., Liu Y., Fu C., Heremans J. P., Snyder G. J., Zhao X. (2017), Compromise and synergy in high-efficiency thermoelectric materials, *Adv. Mater.*, 29, 1605884 (DOI:10.1002/adma.201605884)

5. Bisht N., More P., Khanna P. K., Abolhassani R., Mishra Y. K., Madsen M. (2021), Progress of hybrid nanocomposite materials for thermoelectric applications, *Mater. Adv.*, 2, 1927–1956 (DOI:10.1039/D0MA01030H)

6. Wang C., Xia K., Wang H., Liang X., Yin Z., Zhang Y. (2019), Advanced carbon for flexible and wearable electronics, *Adv. Mater.*, 31, 1801072 (DOI:10.1002/adma.201801072)

7. DiSalvo F. J. (1999), Thermoelectric cooling and power generation, *Science*, 285, 703–706 (DOI:10.1126/science.285.5428.703)

8. Yang J., Caillat T. (2006), Thermoelectric materials for space and automotive power generation, *MRS Bull.*, 31, 224–229 (DOI:10.1557/mrs2006.49)

9. Witze A. (2014), Nuclear power: desperately seeking plutonium, *Nature*, 515, 484–486 (DOI:10.1038/515484a)

10. He R., Schierning G., Nielsch K. (2018), Thermoelectric devices: a review of devices, architectures, and contact optimization, *Adv. Mater. Technol.*, 3, 1700256 (DOI:10.1002/admt.201700256)

11. Vining C. B. (2009), An inconvenient truth about thermoelectrics, *Nat. Mater.*, 8, 83–85 (DOI:10.1038/nmat2361)

12. Xiao C., Li Z., Li K., Huang P., Xie Y. (2014), Decoupling interrelated parameters for designing high-performance thermoelectric materials, *Acc. Chem. Res.*, 47, 1287–1295 (DOI:10.1021/ar400290f)

13. Urban J. J. (2015), Prospects for thermoelectricity in quantum dot hybrid arrays, *Nat. Nanotechnol.*, 10, 997–1001 (DOI:10.1038/nnano.2015.289)

14. Gelbstein Y. (2011), $Pb_{1}–xSn_{x}Te$ alloys: application considerations, *J. Electron. Mater.*, 40, 533–536 (DOI:10.1007/s11664-010-1435-6)

15. Wu H. J., Zhao L.-D., Zheng F. S., Wu D., Pei Y. L., Tong X., Kanatzidis M. G., He J. Q. (2014), Broad temperature plateau for

thermoelectric figure of merit ZT > 2 in phase-separated $PbTe_{0.7}S_{0.3}$, *Nat. Commun.*, 5, 4515 (DOI:10.1038/ncomms5515)

16. Zhu T., Hu L., Zhao X., He J. (2016), New insights into intrinsic point defects in V_2VI_3 thermoelectric materials, *Adv. Sci.*, 3, 1600004 (DOI:10.1002/advs.201600004)

17. Hu L., Wu H., Zhu T., Fu C., He J., Ying P., Zhao X. (2015), Tuning multiscale microstructures to enhance thermoelectric performance of n-type bismuth-telluride-based solid solutions, *Adv. Energy Mater.*, 5, 1500411 (DOI:10.1002/aenm.201500411)

18. Hong M., Zou J., Chen Z.-G. (2019), Thermoelectric GeTe with diverse degrees of freedom having secured superhigh performance, *Adv. Mater.*, 31, 1807071 (DOI:10.1002/adma.201807071)

19. Minnich A. J., Dresselhaus M. S., Ren Z. F., Chen G. (2009), Bulk nanostructured thermoelectric materials: current research and future prospects, *Energy Environ. Sci.*, 2, 466–479 (DOI:10.1039/B822664B)

20. Li J., Shen J., Ma Z., Wu K. (2017), Thickness-controlled electronic structure and thermoelectric performance of ultrathin SnS_2 nanosheets, *Sci. Rep.*, 7, 8914 (DOI:10.1038/s41598-017-09572-9)

21. Qin D., Yan P., Ding G., Ge X., Song H., Gao G. (2018), Monolayer $PdSe_2$: a promising two-dimensional thermoelectric material, *Sci. Rep.*, 8, 2764 (DOI:10.1038/s41598-018-20918-9)

22. Liu Y., Zhao L.-D., Zhu Y., Liu Y., Li F., Yu M., Liu D.-B., Xu W., Lin Y.-H., Nan C.-W. (2016), Synergistically optimizing electrical and thermal transport properties of BiCuSeO via a dual-doping approach, *Adv. Energy Mater.*, 6, 1502423 (DOI:10.1002/aenm.201502423)

23. Yuan K., Sun Z., Zhang X., Tang D. (2019), Tailoring phononic, electronic, and thermoelectric properties of orthorhombic GeSe through hydrostatic pressure, *Sci. Rep.*, 9, 9490 (DOI:10.1038/s41598-019-45949-8)

24. Liu W., Kim H. S., Chen S., Jie Q., Lv B., Yao M., Ren Z., Opeil C. P., Wilson S., Chu C.-W., Ren Z. (2015), N-type thermoelectric material

$Mg_2Sn_{0.75}Ge_{0.25}$ for high power generation, *Proc. Natl. Acad. Sci. U.S.A.*, 112, 3269–3274 (DOI:10.1073/pnas.1424388112)

25. Yan J., Gorai P., Ortiz B., Miller S., Barnett S. A., Mason T., Stevanović V., Toberer E. S. (2015), Material descriptors for predicting thermoelectric performance, *Energy Environ. Sci.*, 8, 983–994 (DOI:10.1039/C4EE03157A)

26. Li Z., Xiao C., Zhu H., Xie Y. (2016), Defect chemistry for thermoelectric materials, *J. Am. Chem. Soc.*, 138, 14810–14819 (DOI:10.1021/jacs.6b08748)

27. Hu L., Zhu T., Liu X., Zhao X. (2014), Point defect engineering of high-performance bismuth-telluride-based thermoelectric materials, *Adv. Funct. Mater.*, 24, 5211–5218 (DOI:10.1002/adfm.201400474)

28. Deng H., Lou X., Lu W., Zhang J., Li D., Li S., Zhang Q., Zhang X., Chen X., Zhang D., Zhang Y., Tang G. (2021), High-performance eco-friendly MnTe thermoelectrics through introducing SnTe nanocrystals and manipulating band structure, *Nano Energy*, 81, 105649 (DOI:10.1016/j.nanoen.2020.105649)

29. Hicks L. D., Dresselhaus M. S. (1993), Use of quantum-well superlattices to obtain a high figure of merit from nonconventional thermoelectric materials, *Appl. Phys. Lett.*, 63, 3230–3232 (DOI:10.1063/1.110207)

30. Hicks L. D., Dresselhaus M. S. (1993), Effect of quantum-well structures on the thermoelectric figure of merit, *Phys. Rev. B*, 47, 12727–12731 (DOI:10.1103/PhysRevB.47.12727)

31. Dresselhaus M. S., Chen G., Tang M. Y., Yang R. G., Lee H., Wang D. Z., Ren Z. F., Fleurial J.-P., Gogna P. (2007), New directions for low-dimensional thermoelectric materials, *Adv. Mater.*, 19, 1043–1053 (DOI:10.1002/adma.200600527)

32. Shi W., Qu S., Chen H., Zhang Y., Wang Y., Zhang Q., Zhang W. (2018), One-step synthesis and enhanced thermoelectric properties of

polymer–quantum dot composite films, *Angew. Chem. Int. Ed.*, 57, 14762–14766 (DOI:10.1002/anie.201802681)

33. Lee S., Jung J.-E., Kim H., Lee Y., Park J. M., Jang J., Yoon S., Ghosh A., Kim M., Kim J., Na W., Kim J., Choi H. J., Cheong H., Kim K. (2021), γ-GeSe: a new hexagonal polymorph from group IV–VI monochalcogenides, *Nano Lett.*, 21, 4305–4313 (DOI:10.1021/acs.nanolett.1c00714)

34. Blöchl P. E. (1994), Projector augmented-wave method, *Phys. Rev. B*, 50, 17953–17979 (DOI:10.1103/PhysRevB.50.17953)

35. Kresse G., Furthmüller J. (1996), Efficient iterative schemes for ab initio total-energy calculations using a plane-wave basis set, *Phys. Rev. B*, 54, 11169–11186 (DOI:10.1103/PhysRevB.54.11169)

36. Perdew J. P., Burke K., Ernzerhof M. (1996), Generalized gradient approximation made simple, *Phys. Rev. Lett.*, 77, 3865–3868 (DOI:10.1103/PhysRevLett.77.3865)

37. Perdew J. P., Chevary J. A., Vosko S. H., Jackson K. A., Pederson M. R., Singh D. J., Fiolhais C. (1992), Atoms, molecules, solids, and surfaces: applications of the generalized gradient approximation for exchange and correlation, *Phys. Rev. B*, 46, 6671–6687 (DOI:10.1103/PhysRevB.46.6671)

38. Grimme S., Antony J., Ehrlich S., Krieg H. (2010), A consistent and accurate ab initio parametrization of density functional dispersion correction (DFT-D) for the 94 elements H–Pu, *J. Chem. Phys.*, 132, 154104 (DOI:10.1063/1.3382344)

39. Perdew J. P., Ernzerhof M., Burke K. (1996), Rationale for mixing exact exchange with density functional approximations, *J. Chem. Phys.*, 105, 9982–9985 (DOI:10.1063/1.472933)

40. Heyd J., Scuseria G. E., Ernzerhof M. (2003), Hybrid functionals based on a screened Coulomb potential, *J. Chem. Phys.*, 118, 8207–8215 (DOI:10.1063/1.1564060)

41. Togo A., Tanaka I. (2015), First-principles phonon calculations in materials science, *Scr. Mater.*, 108, 1–5 (DOI:10.1016/j.scriptamat.2015.07.021)

42. Li W., Lindsay L., Broido D. A., Stewart D. A., Mingo N. (2012), Thermal conductivity of bulk and nanowire $Mg_2Si_xSn_{1-x}$ alloys from first principles, *Phys. Rev. B*, 86, 174307 (DOI:10.1103/PhysRevB.86.174307)

43. Madsen G. K. H., Carrete J., Verstraete M. J. (2018), BoltzTraP2: a program for interpolating band structures and calculating semi-classical transport coefficients, *Comput. Phys. Commun.*, 231, 140–145 (DOI:10.1016/j.cpc.2018.05.010)

44. Morales-Ferreiro J. O., Diaz-Droguett D. E., Celentano D., Luo T. (2017), First-principles calculations of thermoelectric properties of IV–VI chalcogenide 2D materials, *Front. Mech. Eng.*, 3, 15 (DOI:10.3389/fmech.2017.00015)

45. Slack G. A. (1973), Nonmetallic crystals with high thermal conductivity, *J. Phys. Chem. Solids*, 34, 321–335 (DOI:10.1016/0022-3697(73)90092-9)

46. Lindsay L., Broido D. A., Reinecke T. L. (2013), First-principles determination of ultrahigh thermal conductivity of boron arsenide, *Phys. Rev. Lett.*, 111, 025901 (DOI:10.1103/PhysRevLett.111.025901)

47. Born M. (1940), On the stability of crystal lattices. I, *Math. Proc. Cambridge Philos. Soc.*, 36, 160–172 (DOI:10.1017/S0305004100017138)

48. Andrew R. C., Mapasha R. E., Ukpong A. M., Chetty N. (2012), Mechanical properties of graphene and boronitrene, *Phys. Rev. B*, 85, 125428 (DOI:10.1103/PhysRevB.85.125428)

49. Song L., Ci L., Lu H., Sorokin P. B., Jin C., Ni J., Kvashnin A. G., Kvashnin D. G., Lou J., Yakobson B. I., Ajayan P. M. (2010), Large-scale growth and characterization of atomic hexagonal boron nitride layers, *Nano Lett.*, 10, 3209–3215 (DOI:10.1021/nl1022139)

50. Kudin K. N., Scuseria G. E., Yakobson B. I. (2001), C_2F, BN, and C nanoshell elasticity from ab initio computations, *Phys. Rev. B*, 64, 235406 (DOI:10.1103/PhysRevB.64.235406)

51. Wang L., Kutana A., Zou X., Yakobson B. I. (2015), Electro-mechanical anisotropy of phosphorene, *Nanoscale*, 7, 9746–9751 (DOI:10.1039/C5NR00355E)

52. Mukhopadhyay T., Mahata A., Adhikari S., Zaeem M. A. (2018), Probing the shear modulus of two-dimensional multiplanar nanostructures and heterostructures, *Nanoscale*, 10, 5280–5294 (DOI:10.1039/C7NR07261A)

53. Li L., Zhao C., Zhang L., Zhu Y. (2021), γ-GeSe nanotubes: a one-dimensional semiconductor with high carrier mobility potential for photocatalytic water splitting, *J. Mater. Chem. C*, 9, 15158–15164 (DOI:10.1039/D1TC04204A)

54. Li S., Li X., Ren Z., Zhang Q. (2018), Recent progress towards high performance of tin chalcogenide thermoelectric materials, *J. Mater. Chem. A*, 6, 2432–2453 (DOI: 10.1039/C7TA10136B)

55. Peng B., Zhang H., Shao H., Xu Y., Ni G., Zhang R., Zhu H. (2016), Phonon transport properties of two-dimensional group-IV materials from ab initio calculations, *Phys. Rev. B*, 94, 245420 (DOI:10.1103/PhysRevB.94.245420)

56. Cai Q., Scullion D., Gan W., Falin A., Zhang S., Watanabe K., Taniguchi T., Chen Y., Santos E. J. G., Li L. H. (2019), High thermal conductivity of high-quality monolayer boron nitride and its thermal expansion, *Sci. Adv.*, 5, eaav0129 (DOI:10.1126/sciadv.aav0129)

57. Yan R., Simpson J. R., Bertolazzi S., Brivio J., Watson M., Wu X., Kis A., Luo T., Hight Walker A. R., Xing H. G. (2014), Thermal conductivity of monolayer molybdenum disulfide obtained from temperature-dependent Raman spectroscopy, *ACS Nano*, 8, 986–993 (DOI:10.1021/nn405826k)

58. Patel A., Singh D., Sonvane Y., Thakor P. B., Ahuja R. (2020), High thermoelectric performance in two-dimensional Janus monolayer material

WS–X (X = Se, Te), *ACS Appl. Mater. Interfaces*, 12, 46212–46219 (DOI:10.1021/acsami.0c13960)

59. Shen Y., Wang F. Q., Wang Q. (2020), Ultralow thermal conductivity and negative thermal expansion of CuSCN, *Nano Energy*, 73, 104822 (DOI:10.1016/j.nanoen.2020.104822)

60. Lindsay L., Broido D. A. (2008), Three-phonon phase space and lattice thermal conductivity in semiconductors, *J. Phys.: Condens. Matter*, 20, 165209 (DOI:10.1088/0953-8984/20/16/165209)

61. Majumdar A., Chowdhury S., Ahuja R. (2021), Drastic reduction of thermal conductivity in hexagonal AX (A = Ga, In, Tl; X = S, Se, Te) monolayers, *Nano Energy*, 88, 106248 (DOI:10.1016/j.nanoen.2021.106248)

62. Heremans J. P., Jovovic V., Toberer E. S., Saramat A., Kurosaki K., Charoenphakdee A., Yamanaka S., Snyder G. J. (2008), Enhancement of thermoelectric efficiency in PbTe by distortion of the electronic density of states, *Science*, 321, 554–557 (DOI:10.1126/science.1159725)

63. Ono Y. A., Taylor P. L. (1980), Theory of the low-temperature Seebeck coefficient in dilute alloys, *Phys. Rev. B*, 22, 1109–1114 (DOI:10.1103/PhysRevB.22.1109)

64. Fan Q., Zhang W., Qing H., Yang J. (2022), Exceptional thermoelectric properties of bilayer GeSe: first-principles calculation, *Materials*, 15, 971 (DOI:10.3390/ma15030971)

65. Ravichandran N. K., Broido D. A. (2020), Phonon–phonon interactions in strongly bonded solids: selection rules and higher-order processes, *Phys. Rev. X*, 10, 021063 (DOI:10.1103/PhysRevX.10.021063)

66. Xie L., Feng J. H., Li R., He J. Q. (2020), First-principles study of anharmonic lattice dynamics in low thermal conductivity $AgCrSe_2$: evidence for a large resonant four-phonon scattering, *Phys. Rev. Lett.*, 125, 245901 (DOI:10.1103/PhysRevLett.125.245901)

67. Yang X., Feng T., Li J., Ruan X. (2019), Stronger role of four-phonon scattering than three-phonon scattering in thermal conductivity of III–V

semiconductors at room temperature, *Phys. Rev. B*, 100, 245203 (DOI:10.1103/PhysRevB.100.245203)

68. Kang J. S., Li M., Wu H., Nguyen H., Hu Y. (2018), Experimental observation of high thermal conductivity in boron arsenide, *Science*, 361, 575–578 (DOI:10.1126/science.aat5522)

69. Li S., Zheng Q., Lv Y., Liu X., Wang X., Huang P. Y., Cahill D. G., Lv B. (2018), High thermal conductivity in cubic boron arsenide crystals, *Science*, 361, 579–581 (DOI:10.1126/science.aat8982)

70. Tian F., Song B., Chen X., Ravichandran N. K., Lv Y., Chen J., Ding Z., Sun J., Chen G. (2018), Unusual high thermal conductivity in boron arsenide bulk crystals, *Science*, 361, 582–585 (DOI:10.1126/science.aat7932)

71. Feng T., Ruan X. (2018), Four-phonon scattering reduces intrinsic thermal conductivity of graphene and the contributions from flexural phonons, *Phys. Rev. B*, 97, 045202 (DOI:10.1103/PhysRevB.97.045202)

72. Feng T., Ruan X. (2016), Quantum mechanical prediction of four-phonon scattering rates and reduced thermal conductivity of solids, *Phys. Rev. B*, 93, 045202 (DOI:10.1103/PhysRevB.93.045202)

73. Kundu A., Yang X., Ma J., Feng T., Ruan X. (2021), Ultrahigh thermal conductivity of θ-phase tantalum nitride, *Phys. Rev. Lett.*, 126, 115901 (DOI:10.1103/PhysRevLett.126.115901)

74. Sun J., Zhang C., Yang Z., Liu X., Wang Y., Zhao L.-D. (2022), Four-phonon scattering effect and two-channel thermal transport in two-dimensional paraelectric SnSe, *ACS Appl. Mater. Interfaces*, 14, 21365–21373 (DOI:10.1021/acsami.1c24488)

75. Zhou Y., Zhao L.-D. (2017), Promising thermoelectric bulk materials with two-dimensional structures, *Adv. Mater.*, 29, 1702676 (DOI:10.1002/adma.201702676)

76. Shafique A., Shin Y.-H. (2017), Thermoelectric and phonon transport properties of two-dimensional IV–VI compounds, *Sci. Rep.*, 7, 506 (DOI:10.1038/s41598-017-00598-7)

77. Hao S., Shi F., Dravid V. P., Wolverton C., Kanatzidis M. G. (2016), Computational prediction of high thermoelectric performance in hole-doped layered GeSe, *Chem. Mater.*, 28, 3218–3226 (DOI:10.1021/acs.chemmater.6b01164)

78. Qin G., Qin Z., Fang W. Z., et al. (2016), Diverse anisotropy of phonon transport in two-dimensional group IV–VI compounds, *Nanoscale*, 8, 11306–11319 (DOI:10.1039/C6NR01349J)

79. Tołłoczko A., Oliva R., Woźniak T., et al. (2020), Anisotropic optical properties of GeS investigated by optical absorption and photoreflectance, *Mater. Adv.*, 1, 225–233 (DOI:10.1039/D0MA00146E)

80. Yabumoto T. (1958), Electrical and optical properties of GeS, *J. Phys. Soc. Jpn.*, 13, 559–564 (DOI:10.1143/JPSJ.13.559)

81. Ji Y., Yang M., Dong H., et al. (2017), Two-dimensional germanium monochalcogenide photocatalyst for water splitting, *Nanoscale*, 9, 8608–8615 (DOI:10.1039/C7NR00688H)

82. Li W., Lindsay L., Broido D. A., et al. (2012), Thermal conductivity of bulk and nanowire $Mg_2Si_xSn_{1-x}$ alloys from first principles, *Phys. Rev. B*, 86, 174307 (DOI:10.1103/PhysRevB.86.174307)

83. Han Z., Yang X., Li W., Ruan X. (2022), FourPhonon: an extension module to ShengBTE for computing four-phonon scattering rates, *Comput. Phys. Commun.*, 270, 108179 (DOI:10.1016/j.cpc.2021.108179)

84. Feng T., Lindsay L., Ruan X. (2017), Four-phonon scattering significantly reduces intrinsic thermal conductivity of solids, *Phys. Rev. B*, 96, 161201 (DOI:10.1103/PhysRevB.96.161201)

85. Madsen G. K. H., Singh D. J. (2006), BoltzTraP: a code for calculating band-structure dependent quantities, *Comput. Phys. Commun.*, 175, 67–71 (DOI:10.1016/j.cpc.2006.03.007)

86. Ganose A. M., Park J., Faghaninia A., Woods-Robinson R., Persson K. A., Jain A. (2021), Efficient calculation of carrier scattering rates from first principles, *Nat. Commun.*, 12, 2222 (DOI:10.1038/s41467-021-22440-5)

87. Vikram, Sahni B., Jain A., Alam A. (2022), Quasi-two-dimensional carrier transport in KMgBi for promising thermoelectric performance, *ACS Appl. Energy Mater.*, 5, 12290–12300 (DOI:10.1021/acsaem.2c01685)

88. Silvi B., Savin A. (1994), Classification of chemical bonds based on topological analysis of electron localization functions, *Nature*, 371, 683–686 (DOI:10.1038/371683a0)

89. Qin G., Xu J., Wang H., Zhang Y., Hu M. (2023), Activated lone-pair electrons lead to low lattice thermal conductivity: a case study of boron arsenide, *J. Phys. Chem. Lett.*, 14, 1123–1130 (DOI:10.1021/acs.jpclett.2c03255)

90. Henkelman G., Arnaldsson A., Jónsson H. (2006), A fast and robust algorithm for Bader decomposition of charge density, *Comput. Mater. Sci.*, 36, 354–360 (DOI:10.1016/j.commatsci.2005.04.010)

91. Okhotin A. S., Krestovnikov A. N., Aivazov A. A., Pushkarskii A. S. (1969), Thermal conductivity of GeS and GeSe, *Phys. Status Solidi B*, 31, 927–934 (DOI:10.1002/pssb.19690310206)

92. Garg P., Rawat K. S., Bhattacharyya G., et al. (2019), Hexagonal CuCl monolayer for water splitting: a DFT study, *ACS Appl. Nano Mater.*, 2, 5975–5983 (DOI:10.1021/acsanm.9b00699)

93. Feng M., Liu S. C., Hu L., et al. (2021), Interfacial strain engineering in wide-bandgap GeS thin films for photovoltaics, *J. Am. Chem. Soc.*, 143, 9664–9671 (DOI:10.1021/jacs.1c04734)

94. Vaughn D. D., Patel R. J., Hickner M. A., Schaak R. E. (2010), Single-crystal colloidal nanosheets of GeS and GeSe, *J. Am. Chem. Soc.*, 132, 15170–15172 (DOI:10.1021/ja107520b)

95. Wang Y., Yang X., Shang Y. (2019), Thermal transport properties in monolayer GeS, *Phys. Lett. A*, 383, 2155–2160 (DOI:10.1016/j.physleta.2019.04.063)

96. Minhas H., Das S., Pathak B. (2022), Ultralow thermal conductivity and high thermoelectric performance of γ-GeSe: effects of dimensionality and

thickness, *ACS Appl. Energy Mater.*, 5, 9914–9928 (DOI:10.1021/acsaem.2c01600)

97. Xiao Y., Chang C., Pei Y., et al. (2016), Origin of low thermal conductivity in SnSe, *Phys. Rev. B*, 94, 125203 (DOI:10.1103/PhysRevB.94.125203)

98. Broido D. A., Lindsay L., Reinecke T. L. (2013), Ab initio study of the unusual thermal transport properties of boron arsenide, *Phys. Rev. B*, 88, 214303 (DOI:10.1103/PhysRevB.88.214303)

99. Pathak R., Dutta P., Singh A. K., Alam A. (2022), Strong anharmonicity-induced low thermal conductivity and high n-type mobility in $Bi_{1.1}Sb_{0.9}Te_2S$, *Angew. Chem. Int. Ed.*, 61, e202203456 (DOI: 10.1002/anie.202203456)

100. Zeng J., He X., Liang S.-J., Liu E., Zhang X., Chen X., Wang F., Liu Z. (2018), Experimental identification of critical condition for drastically enhancing thermoelectric power factor of two-dimensional layered materials, *Nano Lett.*, 18, 7538–7544 (DOI:10.1021/acs.nanolett.8b03026)

CHAPTER 2

CHAPTER 3

Rattling Ion-Induced Bonding Hierarchies in Chalcotitanates

CHAPTER 3

CHAPTER 3

3.1. Introduction

Achieving highly efficient advanced thermoelectric (TE) materials hinges on minimizing heat propagation within crystalline solids *[1]*. This reduction primarily involves the modification of lattice vibrations that, in turn, depend on the rigid and weak chemical bonds *[2, 3]*. Therefore, the rattling model has emerged as the most significant phenomenon affecting the bonding hierarchy, lowering the lattice thermal conductivity in the crystal system *[4–6]*. These rattler atoms occupy the large chemical space with weak bonding, exhibiting higher displacement and vibrations at distinct frequencies when compared with atoms present in the rigid crystalline framework. This phenomenon establishes a coexisting bonding hierarchy, combining both fluctuating and rigid sublattice frameworks further assisting the improvements in TE performance *[7]*. Hence, to devise advanced thermoelectric materials, it becomes crucial to comprehensively explore the impact of bonding hierarchies among the constituent atoms.

Among the TE-related transport parameters, thermal transport properties uniquely exhibit weak dependence on electronic transport properties, enabling effective minimization through tailored crystal structure and microstructure design *[8, 9]*. In recent decades, paradigms including *in situ* nanostructure,*[10, 11]* liquid-like lattice,*[12, 13]* weak chemical bonding, *[14, 15]* constructing hierarchical architectures, *[10]* and off-centered atom approaches,*[16]* have been effectively employed to reduce thermal conductivity and enhance TE efficiency. Recently, the combination of copper's high natural abundance, cost-effectiveness, and availability of chalcogens (S, Se, and Te) with suitable band gaps has positioned Cu-based chalcogenides as highly promising candidates for TE applications *[5, 13, 17–19*. The Cu-based chalcogenides such as Cu_2Se,*[13]* Cu_3SbSe_3,*[5]* $CsCu_5Se_3$,*[17]* Cu_4TiSe_4,*[18]* and KCu_5Se_3,*[19]* have gained importance for their low κ_L. Therefore, we believe that the presence of more than one rattling cation (such as Li, Ti or Cu) in $LiCu_3TiQ_4$ (S, Se, or Te) can further

influence the phonon scattering and enhancing the TE efficiency. As such factors can influence the bonding hierarchy, consequently, modify electric or thermal transport properties and leading to an enhancement in thermoelectric (TE) performance.

Although density functional theory (DFT) can accurately determine the thermal transport properties, the computational cost of these calculations increases exponentially with higher k-points, larger supercell sizes, and higher plane wave cutoff energies of the systems. These constraints result in dynamic instability, impeding the analysis of phonon dispersions and interatomic force constants (IFCs) crucial for determining κ_L. In this regard, recently, the advancement of machine learning interatomic potentials (MLIPs) has revolutionized materials simulations across diverse applications *[20, 21]*. MLIPs are described by the potential energy surfaces (PES), which are defined as a function of local environment descriptors that remain invariant to rotations, translations, and permutations of homonuclear atoms *[22]*. In particular, the moment tensor potentials (MTPs) have enabled the development of efficient MLIPs that can achieve high computational speed along with accuracy comparable to density functional theory (DFT) *[22]*. The minimal computational costs associated with generating interatomic force constants (IFCs) using MLIP provide a significant acceleration in the evaluation of anharmonic IFCs compared with the DFT-based approach, thereby facilitating the prediction of lattice thermal conductivity *[21]*. Previous reports suggest that phonon dispersion relations computed using MLIPs precisely align with DFT-based results *[20, 23, 24]*. More importantly, the calculated lattice thermal conductivity using MLIPs is found to be reasonably accurate as they are capable of dealing with large supercell systems where conventional DFT approaches struggle to address effectively. This provides motivation for the adoption of this methodology in predicting material properties.

CHAPTER 3

In this chapter, we have utilized first principles calculations to develop MLIPs used to investigate the thermal and electronic transport properties for recently synthesized cubic lithium copper chalcotitanate ($LiCu_3TiQ_4$, Q = S, Se, Te) materials *[25]*. We have considered these systems as we would like to see whether the presence of chalcogen lone pairs and the rattling cations can affect the bonding hierarchy in the system. Furthermore, our investigation extends towards identifying whether the presence of more than one rattling cation (such as Li, Cu, and Ti) can further improve the phonon scattering in the system to further improve the thermoelectric efficiency.

3.2. Model and Computational Details

The proposed $LiCu_3TiQ_4$ (Q = S, Se, and Te) adopt cubic structures are shown in Figure 3.1. structure with $P\bar{4}3m$ space group and lattice parameters of 5.51 Å, 5.70 Å, and 6.06 Å for $LiCu_3TiS_4$, $LiCu_3TiSe_4$, and $LiCu_3TiTe_4$ respectively. These values closely agree with the previously experimentally reported parameters of 5.51 Å, 5.71 Å, and 5.99 Å for $LiCu_3TiS_4$, $LiCu_3TiSe_4$, and $LiCu_3TiTe_4$ respectively *[41]*. These materials exhibit distinct diamond sublattice structures, augmented by the inclusion of Li atom to the Cu_3TiQ_4, known as “stuffed diamond”, as represented in **Figure 3.1**.

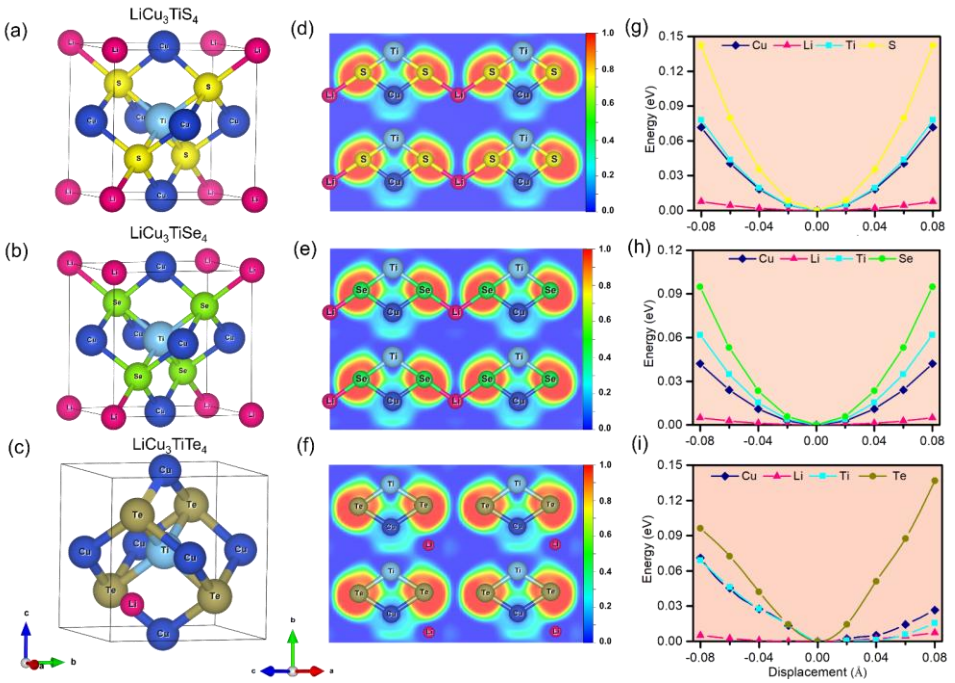


Figure 3.1: The conventional unit cell of cubic lithium copper chalcotitanates **(a)** $LiCu_3TiS_4$, **(b)** $LiCu_3TiSe_4$, and **(c)** $LiCu_3TiTe_4$ where $LiCu_3TiS_4$ and $LiCu_3TiSe_4$ adopt an isostructural cubic 3D stuffed diamond structure, while $LiCu_3TiTe_4$ exhibits a closer resemblance to a sulvanite structure. **(d-f)** The electron localization function (ELF) visualized at an iso-surface value of 0.9 $eVÅ^{-3}$ revealing the presence of lone pairs around S/Se/Te atoms. **(g-i)** The atomic displacement parameters (ADP) for $LiCu_3TiQ_4$ across the equilibrium positions.

The first principles calculations have been carried out employing projector augmented wave (PAW) pseudopotentials, which are implemented in the Vienna *ab initio* simulation package (VASP) *[26, 27]*. The generalized gradient approximation (GGA) within the Perdew-Burke-Ernzerhof (PBE) functional is employed as exchange-correlation potential with the cutoff energy 600 eV and Γ k-point grid of 5 x 5 x 5 *[28, 29]*. The structural relaxations were carried out considering the Hellmann−Feynman force convergence criterion of 0.001 eV/Å, and the energy convergence criterion of 10^{-6} eV. Furthermore, we have conducted a detailed comparison of the

electronic properties of $LiCu_3TiQ_4$ using various functionals including PBE, HSE06, HSE03, MBJ, and SCAN. Our findings indicate that the Heyd−Scuseria−Ernzerhof (HSE03) hybrid functional, incorporating a Hartree−Fock exchange parameter (α) of 10% and 5%, accurately calculates the electronic properties of the $LiCu_3TiQ_4$ (Q = S/Se) and $LiCu_3TiTe_4$ systems respectively *[30, 31]*.

To prepare a training set of MTPs, *ab initio* molecular dynamics (AIMD) simulations were conducted using the VASP code. A supercell of 2 x 2 x 2 was used for the AIMD simulations with an isobaric-isothermal NPT ensemble from 100 K to 700 K by the difference of 100 K. For each lithium copper chalcotitanates, AIMD simulation was carried out for a total of 2000 steps with the timestep of 1 fs and were conducted at each temperature. This generated a total of 14000 data points (original dataset "OD") with their respective energies, forces, and stresses for each material. From OD, a dataset of 2800 datapoints was constructed by taking every 5^{th} datapoint of 14000 data points. This prevents similar data points from being represented too frequently. This dataset is split with an 80:20 ratio to give the training set with 2240 data points and the test set with 560 data points. Finally, the training set with the 2240 structural configurations with their respective energies, stresses, and forces was trained using the MLIP package to generate trained MTP using the polynomial-based linear regression method *[32, 33]*. These MTPs were further used for the prediction of phonon dispersion relations, 2^{nd} order interatomic force constants, and 3^{rd} order interatomic force constants *[32]*.

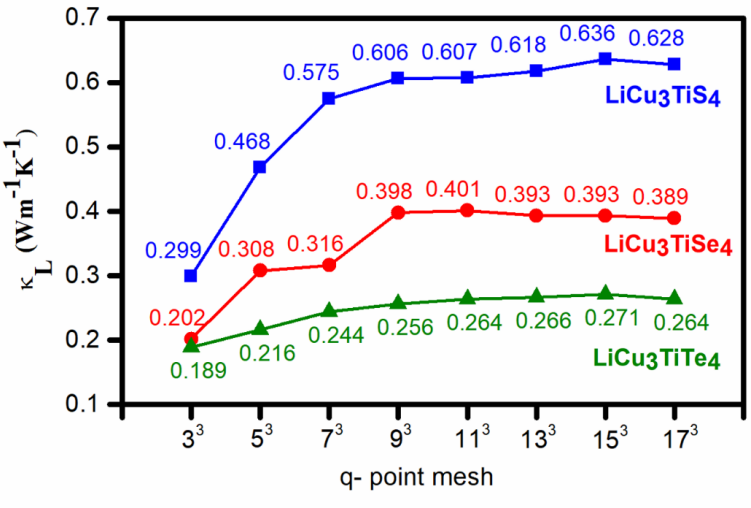


Figure 3.2: Convergence of the lattice thermal conductivity of $LiCu_3TiQ_4$ (Q = S, Se, and Te) against q-point mesh at 300 K. Lattice thermal conductivities are found to converge at 17 × 17 × 17 q-point mesh.

To calculate the lattice transport properties, the 2nd and 3rd order IFCs were employed as input data for the SHENGBTE code, which facilitated the determination of the lattice thermal conductivity of the materials *[34]*. The dense q points mesh of 17 × 17 × 17 for $LiCu_3TiQ_4$ systems have been considered to precisely determine the lattice thermal conductivity (κ_L) and the convergence of lattice thermal conductivity for $LiCu_3TiQ_4$ has been shown in **Figure 3.2.** The particle-like phonon thermal transport properties were computed by using the ShengBTE package, while the wave-like tunneling of phonon channels was evaluated using the code from the reported literature *[35–38]*. All the electronic transport properties have been calculated using the *ab initio* Scattering and Transport (AMSET) model that incorporates various scattering rates such as the ionized impurities, acoustic deformation, and piezoelectric scattering mechanisms to provide accurate results as it calculates the relaxation time *[39, 40]*.

3.3. Results and Discussion

3.3.1. Structure and Stability

In $LiCu_3TiQ_4$ (where Q = S and Se), the Li, Cu, and Ti cations are present at the corner, face center, and body center positions, respectively. Concurrently, anions (Q) occupy tetrahedral positions within the cubic unit cell. The S/Se form bonds with three Cu atoms and a Li atom, forming a tetrahedral arrangement, while Ti occupies the plane formed by the Cu atoms, resulting in a coordination number of five. However, in $LiCu_3TiTe_4$, there is a slight change in the positioning of the Li, shifting to a trigonal pyramidal arrangement, though Ti, Cu, and Te maintain similar atomic positions. The Li-Q bond lengths in the materials are 2.48 Å for S, 2.54 Å for Se, and 2.83 Å for Te, while the Cu-Q, and Ti-Q bond lengths are reported in **Table 3.1**.

Table 3.1: The sum of covalent and ionic radii (Å) of respective atoms in Ti–Q, Li–Q, and Cu–Q (Q = S, Se, or Te) and the actual bond lengths are defined in blue color.

Q	Ti–Q (Å)			Li–Q (Å)			Cu–Q (Å)		
	Actual	**Covalent**	**Ionic**	**Actual**	**Covalent**	**Ionic**	**Actual**	**Covalent**	**Ionic**
S	2.29	2.36	2.52	2.48	2.32	2.60	2.35	2.32	2.80
Se	2.40	2.48	2.66	2.54	2.34	2.74	2.45	2.44	2.94
Te	2.66	2.69	2.89	2.83	2.65	2.97	2.68	2.65	3.17

By comparing the sum of the covalent and ionic radii of all three bonds, we aimed to understand the bonding hierarchies between the constituent atoms in each system. The observed Cu-Q and Ti-Q bond distances in our systems closely align with the sum of covalent radii of the constituent atoms, indicating a strong covalent character that contributes to the rigidity of the systems. On the other hand, Li-Q bonds are more loosely bonded with lower covalent character, between the sum of covalent and the ionic radii of Li-Q suggesting the rattling characteristics of Li, originating from weak interactions. Furthermore, the bonding hierarchy has been confirmed by the total electronic charge density plots as shown in **Figure 3.3**. The Li atoms exhibit distinct spherical charge contours along the (1 -1 0) plane for

$LiCu_3TiS_4$ and $LiCu_3TiSe_4$ and (-1 -1 0) plane for $LiCu_3TiTe_4$, confirming the presence of Li in its ionic state. Conversely, the covalent bonding nature of Ti-Q, and Cu-Q (where Q = S, Se, or Te) is evidenced by the elliptical shape of charge distribution around the Ti, Cu, and Q atoms. The Cu-Q overlapping region decreases moving from S to Te and the contours around Cu and Ti atoms become more elliptical, signifying the decrease in covalent bonding of Ti-Q and Cu-Q.

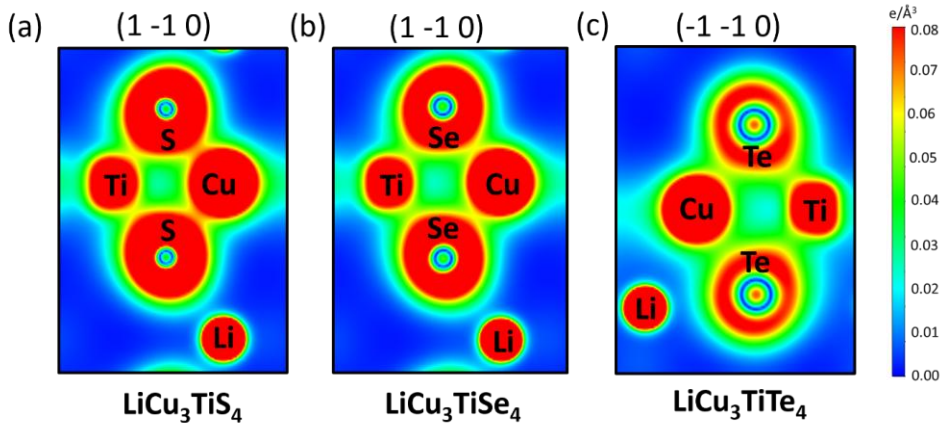


Figure 3.3: The total electronic charge distribution contour plots for (a) $LiCu_3TiS_4$, (b) $LiCu_3TiSe_4$ along (1 -1 0) plane, and (c) $LiCu_3TiTe_4$ along (-1 -1 0) plane.

Table 3.2: The calculated Young's modulus (GPa), shear modulus (GPa), Poisson's ratio, and Debye Temperature, θ_D (K) for the considered structures of $LiCu_3TiQ_4$.

Materials	Young's modulus	Shear modulus	Poisson's ratio	θ_D
$LiCu_3TiS_4$	78.62	31.036	0.38	338
$LiCu_3TiSe_4$	59.88	22.54	0.22	240
$LiCu_3TiTe_4$	30.58	11.8	0.39	157

The mechanical stability of $LiCu_3TiQ_4$ systems has been evaluated by calculating Young's modulus, shear modulus, and Poisson's ratio as shown in **Table 3.2**. The elastic constants satisfy all the elastic stability criteria,

confirming the mechanical stability of the systems *[41]*. The sulfide exhibits the highest Young's and shear modulus which decreases in the case of Se and Te, illustrating the weakening of the chemical bond strength moving from S to Te. Such bonding hierarchies can be further demonstrated by the electron localization function (ELF) *[42]*. In **Figure 3.1(d-f),** the presence of high electron density arises from the nonbonding electrons on Q, specifically from the $3s^2$ (S), $4s^2$ (Se), and $5s^2$ (Te) lone pairs. These lone pairs induce significant nonlinear repulsive electrostatic repulsions between the Q atoms and the adjacent bonds, leading to a decrease in lattice symmetry and obstructing the path of lattice vibrations ultimately resulting in high anharmonicity and reduced κ_L. For a deeper understanding of the bonding hierarchy and atomic level dynamics, we have calculated the atomic displacement parameter (ADP) which evaluates the mean-squared displacement amplitudes of each atom from their equilibrium positions in the crystal (**Figure 3.1(g-i)**). The Li shows the typical energy curve of rattling atoms that are in shallow potential wells (flatter variation), whereas Cu, Ti, and Q (S, Se, Te) are confined in a comparatively deep energy well.

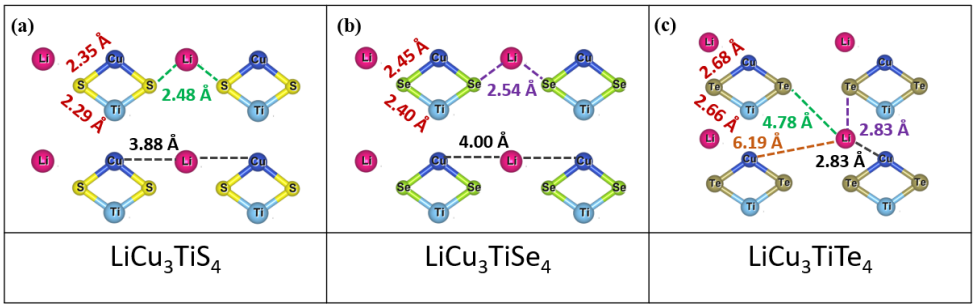


Figure 3.4: The position of Li in (a) $LiCu_3TiS_4$, (b) $LiCu_3TiSe_4$, and (c) $LiCu_3TiTe_4$.

In $LiCu_3TiS_4$ and $LiCu_3TiSe_4$ structures, Li atoms are symmetrically positioned (**Figure 3.4**), resulting in equal displacement along the +x and -x direction. However, the asymmetric positioning of Li in $LiCu_3TiTe_4$ leads to non-uniform interactions between Li and Cu/Ti/Te along the +x and -x

direction. This asymmetry affects the overall bonding hierarchy, resulting in distinct behaviour in Cu and Ti curves along the +x direction. The weak bonding of Li atoms allows for larger vibrational amplitudes compared to other atoms, enhancing vibrational motion and increasing scattering of acoustics phonons. Specifically, for $LiCu_3TiTe_4$ material with soft lattice or weak chemical bonding, some of their optical phonons could have extremely low vibration frequency, which sits very close to the acoustic phonons. These low-frequency optical phonons can involve in the phonon scattering processes and cause additional scattering with the acoustic phonons, leading to ultralow κ_L.

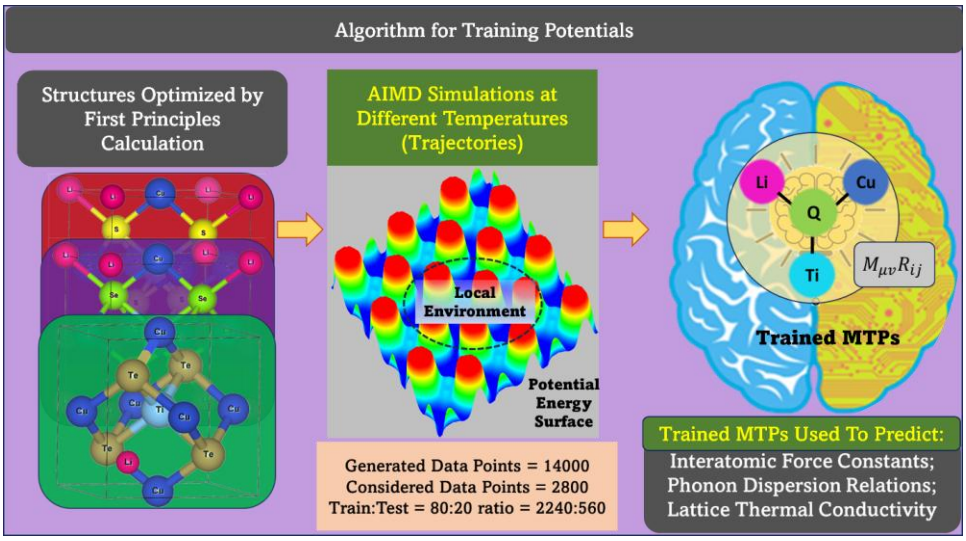


Figure 3.5: The schematic illustrates the development of moment tensor potentials (MTPs), incorporating the local environment to generate a potential energy surface. The trained MTPs employed for the prediction of interatomic force constants, phonon dispersion relations, and lattice thermal conductivity.

3.3.2. Training and Testing of Moment Tensor Potentials (MTPs)

Initially, the methodology employed for developing MTPs from the AIMD configurations is represented in **Figure 3.5**. The effectiveness of the trained MTPs were assessed through scatter plots comparing the energies and

forces obtained by AIMD with those predicted by MTPs, both for test and training data of $LiCu_3TiQ_4$ materials, as represented in **Figure 3.6**. The mean absolute error (MAE) and root-mean-square error (RMSE) scores for all systems are represented within the plots. These trained potentials (MTPs) have demonstrated their capability to accurately compute energies and forces, as they consider interactions beyond first neighbour atoms, enabling them to capture mid and long-range interactions effectively. To assess the performance of MTPs, the trained MTPs were evaluated with the "test set" data and were found to be best-fitted potentials for $LiCu_3TiS_4$, $LiCu_3TiSe_4$, and $LiCu_3TiTe_4$ with the lowest test RMSE scores of 0.5, 0.7, and 2.4 meV, respectively for energy plots. Similarly, the low RMSE values of 5.9, 8.5, and 12.3 meV/Å for $LiCu_3TiS_4$, $LiCu_3TiSe_4$, and $LiCu_3TiTe_4$ for forces also signify the best fitting of considered MLIPs. These small RMSE and MAE values demonstrate that MTPs are well-trained which further drives us to investigate its efficiency toward accurate prediction of the thermal transport properties of the $LiCu_3TiQ_4$ material.

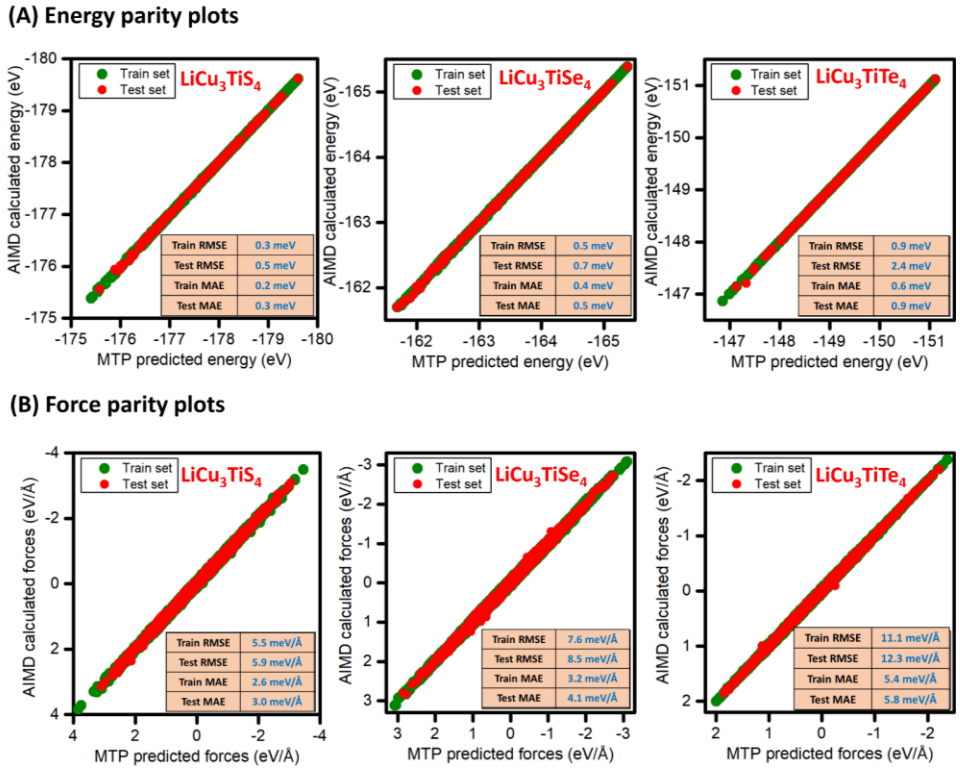


Figure 3.6: Scatter plots illustrating the comparison between predicted vs DFT calculated **(A)** energy parity plots and **(B)** force parity plots for $LiCu_3TiQ_4$ (Q = S, Se, and Te) systems along with their respective test and train root mean square error (RMSE) and mean absolute error (MAE) scores in meV for energies and meV/Å for forces.

3.3.3. Phonon Transport Properties

To analyze the dynamical stability of $LiCu_3TiQ_4$, we performed phonon dispersion calculations along the high symmetry points of the Brillouin zone. The absence of imaginary frequencies confirms its stability, as depicted in **Figure 3.7(a-c)**. The nature of acoustic phonon mode propagation plays a crucial role in determining κ_L. The phonon softening has been observed from $LiCu_3TiS_4$ to $LiCu_3TiTe_4$ and can be attributed to the weakening of bond strength with increasing atomic weight leads to lowering the frequencies of acoustic and optical phonon modes with flattened two transverse acoustic branches *[44]*. This phenomenon significantly enhances the phonon scattering rates of localized acoustic bands by introducing additional scattering channels which has been observed in the weighted phase space as discussed in section 3.4.

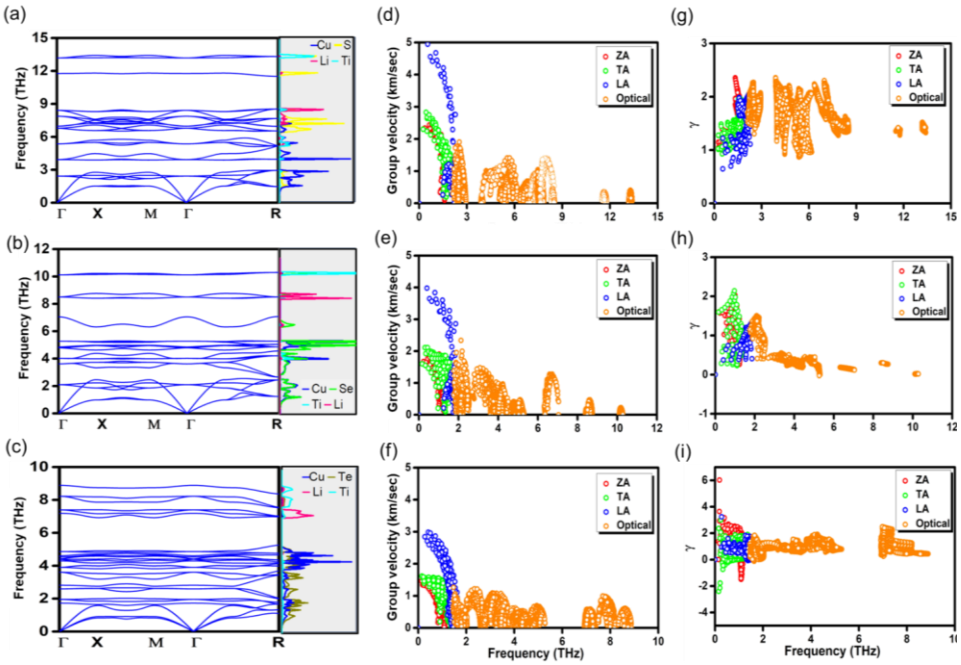


Figure 3.7: The phonon dispersion and projected phonon density of states for **(a)** $LiCu_3TiS_4$, **(b)** $LiCu_3TiSe_4$, **(c)** $LiCu_3TiTe_4$ across the high symmetry points in the first Brillouin zone. **(d-f)** Group velocity (km/sec) and **(g-i)** mode average Grüneisen parameter (γ) for the considered systems.

The TA branches exhibit low dispersion, presenting a nearly flat band across the Brillouin zone. This behaviour is similar to that observed in $AgCrSe_2$[42] and $YbFe_4Sb_{12}$,[43] highlighting the localized vibrations and rattling effects. This also suggests that the confined TA phonons result in low propagation velocities. In the low-frequency region, there exists a hybridization between the acoustic and optical branches attributed to the incoherent vibrations of localized oscillators in $LiCu_3TiS_4$ and $LiCu_3TiSe_4$. In contrast, $LiCu_3TiTe_4$ exhibits avoided crossings between acoustic and optical phonon bands as illustrated in **Figure 3.8**.

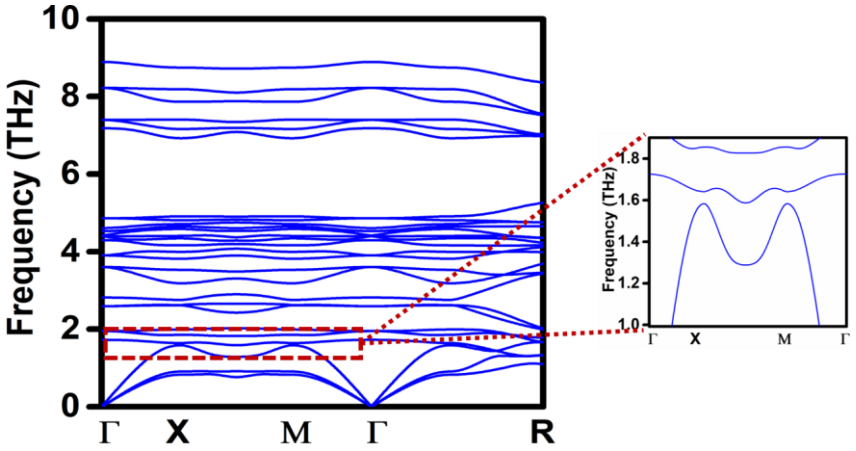


Figure 3.8: The phonon dispersion relations in $LiCu_3TiTe_4$, reflect the avoided crossing between LA acoustic and optical branch at 1.6 THz of frequency.

This avoided crossing, characteristic of acoustic-optical phonon coupling is driven by the weakened chemical bonding in $LiCu_3TiTe_4$, due to weaker covalent interactions along with the strong rattling effect of Li atoms. These atoms evolve continuously from an undistorted ground state to a locally distorted state while retaining average crystallographic symmetry *[44, 47]*. The projections of phonon density of states demonstrate that the low-frequency acoustic phonons in $LiCu_3TiS_4$ are predominantly associated with Cu atom vibrational modes, with their contribution diminishing in $LiCu_3TiSe_4$ and $LiCu_3TiTe_4$. However, in $LiCu_3TiTe_4$, the Te atoms show more dominance than the Cu and Ti atoms since heavier atoms vibrate at a lower frequency than the lighter atoms. These Cu and Ti also reflect some quiescent behavior in the acoustic region in $LiCu_3TiTe_4$. Further, the phonon vibrations are more localized near 7-9 THz of frequency, showing the hybridization of Li with Ti in the case of $LiCu_3TiTe_4$. The presence of dispersionless and localized phonon branches exhibits the characteristics of rattling atoms. Therefore, the Li^+ is nearly quiescent in the acoustic and higher frequency regions which results in a weak transfer of phonons between anionic $[Cu_3TiQ_4]^-$ and Li^+ cationic moieties of $LiCu_3TiQ_4$. Thus,

the heat flux within the $[Cu_3TiQ_4]^-$ moiety is blocked, which suppresses the thermal transport.

Furthermore, due to the presence of weaker interatomic bonds, the acoustic phonon modes in $LiCu_3TiTe_4$ are characterized as softer compared to $LiCu_3TiSe_4$ and $LiCu_3TiS_4$, which signifies that $LiCu_3TiTe_4$ has a lower Debye temperature (**Table 3.2**). The computed Debye temperatures are 338 K, 240 K, and 157 K for $LiCu_3TiS_4$, $LiCu_3TiSe_4$, and $LiCu_3TiTe_4$, respectively. Additionally, the efficiency of heat conduction relies on the phonon group velocities, which are determined by the slopes of the linear regions within the acoustic phonon branches. As represented in **Figure 3.7(d-f)**, the speed of group velocities decreases from S to Te, which can result in ultralow κ_L. Further, the large deviation in the Grüneisen parameter (γ) values of $LiCu_3TiTe_4$ indicates a stronger lattice anharmonicity than $LiCu_3TiSe_4$ and $LiCu_3TiS_4$, as shown in **Figure 3.7(g-i)**. The materials $LiCu_3TiS_4$ and $LiCu_3TiSe_4$ exhibit positive γ, causing expansion with increasing temperature and contraction with decreasing temperature. In contrast, $LiCu_3TiTe_4$ demonstrates negative thermal expansion (NTE) with negative γ, resulting in contraction with increase in temperature. The transition from S to Te is associated with a decrease in bond strength and a decrease in the frequency of longitudinal acoustic (LA) phonon modes, leading to a narrowing of the gap between the LA and transverse acoustic (TA) phonon branches. This reduction indicates that $LiCu_3TiTe_4$ phonon modes are relatively more easily excited at lower temperatures compared to the S and Se materials *[48]*. This presence of NTE relies on the presence of low-energy phonons with negative γ and a distinct phonon gap, further separating these modes from the high-energy phonons within the material's structure *[48]*. Further, the calculated mode average Grüneisen parameter ($\overline{|\gamma|}$) are 1.06, 1.41, 1.62 for S, Se, and Te, respectively in $LiCu_3TiQ_4$ systems reflecting the average anharmonicity. Additionally, $\overline{|\gamma|}$ has been compared to other high-performing thermoelectric materials like PbTe

(1.4),*[49]* BiCuOSe (1.5),*[50]* and Cu_6Te_3S (1.58),*[51]* where $LiCu_3TiTe_4$ stands out with a higher γ values, representing strong lattice anharmonicity, leading to ultralow thermal transport properties.

3.3.4. Thermal Properties

The three phonon anharmonic scattering rates were assessed to extract the effect of lattice dynamics on the thermal transport properties, using IFCs generated from MTPs, and were analyzed through the ShengBTE code and in-house provided in literature *[35, 36]*. The total κ_L which incorporates population conductivity κ_L^p from a particle-like propagation channel and coherence conductivity (κ_L^c) from the wave-like tunneling channel, within the framework of the Wigner formalism of quantum mechanics *[35, 36]*. As depicted in **Table 3.3,** the lattice thermal conductivity κ_L^p (κ_L^c) values at 300 K are 0.63 (0.10), 0.39 (0.06), and 0.26 (0.06) $Wm^{-1}K^{-1}$ for $LiCu_3TiS_4$, $LiCu_3TiSe_4$, and $LiCu_3TiTe_4$ systems, respectively.

Table 3.3: The temperature-dependent lattice thermal conductivity (κ_L) including the contributions from particle-like (κ_L^p) and wave-like (κ_L^c) conduction mechanisms. The unit of thermal conductivity is $Wm^{-1}K^{-1}$.

Systems		300 K	400 K	500 K	600 K	700 K	800 K	900 K
$LiCu_3TiS_4$	κ_L^p	0.63	0.47	0.37	0.31	0.26	0.23	0.20
	κ_L^c	0.10	0.10	0.11	0.12	0.13	0.13	0.13
	κ_L	0.73	0.57	0.48	0.43	0.39	0.36	0.33
$LiCu_3TiSe_4$	κ_L^p	0.39	0.29	0.24	0.19	0.17	0.15	0.13
	κ_L^c	0.06	0.07	0.08	0.09	0.09	0.10	0.10
	κ_L	0.45	0.36	0.32	0.28	0.26	0.25	0.23
$LiCu_3TiTe_4$	κ_L^p	0.26	0.20	0.16	0.14	0.12	0.10	0.09
	κ_L^c	0.06	0.07	0.08	0.08	0.08	0.09	0.09
	κ_L	0.32	0.27	0.24	0.22	0.20	0.19	0.18

Therefore, κ_L is majorly dominated by the conventional Peierls-Boltzmann thermal conductivity in crystals which give rise to particle-like propagation

channels. Further, **Figure 3.9** represents the total change in κ_L as a function of temperature. Interestingly, $LiCu_3TiTe_4$ exhibits an ultralow κ_L, even lower than that of many well-known materials at room temperature such as $TlInTe_2$ (0.50 $Wm^{-1}K^{-1}$),*[4]* Cu_3SbSe_3 (0.60 $Wm^{-1}K^{-1}$),*[17]* Cu_2Se (0.60 $Wm^{-1}K^{-1}$),*[13]* KCu_5Se_3 (0.48 $Wm^{-1}K^{-1}$),*[19]* $CsAg_5TeS_2$ (0.40 $Wm^{-1}K^{-1}$), *[52]* and $BaAu_2P_4$ (0.90 $Wm^{-1}K^{-1}$) *[53]*.

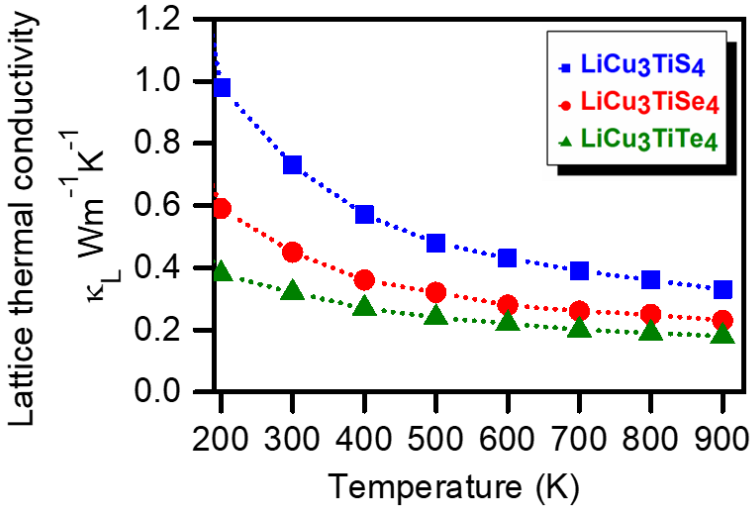


Figure 3.9: The total lattice thermal conductivity ($\kappa_L = \kappa_L^p + \kappa_L^c$) of $LiCu_3TiQ_4$ (where Q = S, Se, or Te) as a function of temperature (K).

To account for the low κ_L for $LiCu_3TiQ_4$ materials, we have analyzed the scattering rates and weighted phase space, represented in **Figure 3.10**. Notably, at 300 K, the scattering rates exhibit lower values below the acoustic cutoff region and significantly higher values above this cutoff region (**Figure 3.10(a-c)**).

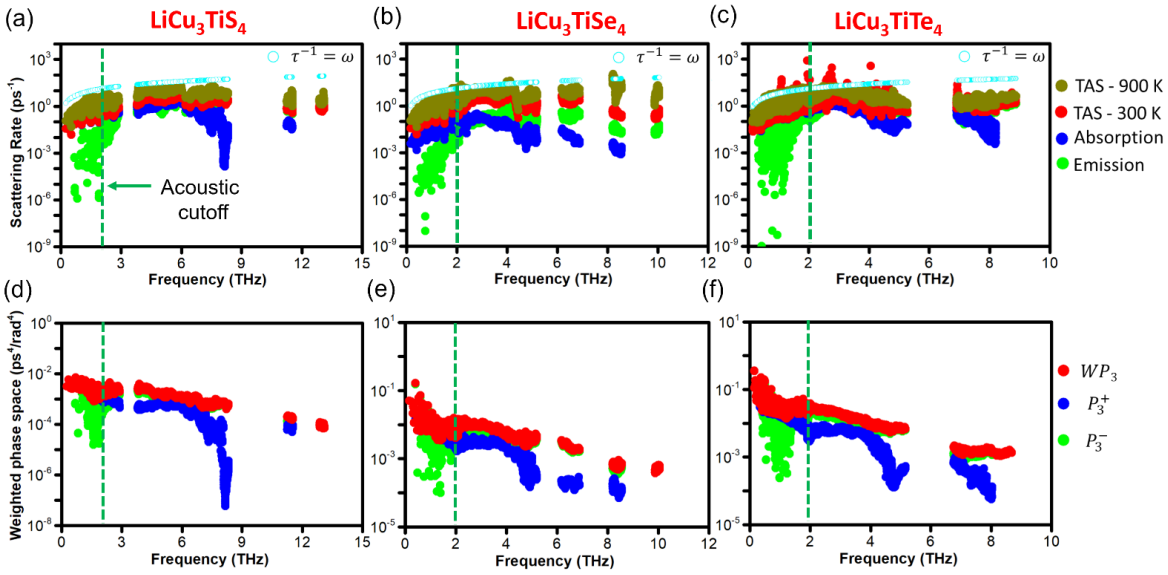


Figure 3.10: The calculated total anharmonic scattering (TAS) rates of **(a)** $LiCu_3TiS_4$, **(b)** $LiCu_3TiSe_4$, and **(c)** $LiCu_3TiTe_4$ at 300 K and 900 K along with absorption and emission scattering channels at 300 K. The weighted phase space (WP_3) as a function of frequency (THz) for **(d)** $LiCu_3TiS_4$, **(e)** $LiCu_3TiSe_4$, and **(f)** $LiCu_3TiTe_4$ at 300 K with absorption (P_3^+) and emission (P_3^-) weighted phase space.

In the context of the particle-like nature of phonons, weak inter-phonon interactions should result in scattering rates below vibrational frequencies (ω),*[54]* ($\tau^{-1} \leq \omega$) referring to "Wigner limit of time" *[55]*. The phonon vibrations below the Wigner limit of time with a long lifetime (less scattering rate) contribute mainly to particle-like conductivity whereas phonon vibrations with a short lifetime (larger scattering rate) contribute mainly to wavelike conductivity *[54]*. As shown in **Figure 3.10(a-c)**, all the phonon scattering rates lie below the Wigner limit of time showing the particle-like nature of phonons. Further, the phonon vibrations at 900 K exhibit larger scattering rates compared to those at 300 K. Consequently, phonons with short lifetimes contribute less to particle-like propagation since they are rapidly suppressed, preventing them from propagating

further. Therefore, this reflects that the $LiCu_3TiQ_4$ crystalline materials exhibit ultralow thermal conductivity following the particle-like nature of phonons *[56]*.

Further, the weighted phase space increases from S to Te as illustrated in **Figure 3.10(d-f)**, which strongly indicates the three-phonon transition probability contributes to the enhancement of the overall scattering rate and consequently results in a lower κ_L *[57]*. At 300 K, the phonon scattering channel related to the adsorption $\left(P_3^+: q_{0,\omega 0} + q_{1,\omega 1} \rightarrow q_{2,\omega 2}\right)$ exhibits a greater density and higher scattering rate compared to the emission $\left(P_3^-: q_{0,\omega 0} \rightarrow q_{1,\omega 1} + q_{2,\omega 2}\right)$ for acoustic modes, where q and ω are phonon mode and phonon frequencies. Further, it is generally feasible to identify a mode (q_1, $\omega_0 - \omega_{flat}$,) within the flat modes region that facilitates the scattering processes for any given mode ($q_0 - q_1$, ω_{flat}). Consequently, when ω_0 is greater than ω_{flat}, the number of emission channels can expand compared to cases without flat modes. The extent of this increase depends on the availability of q_1 values for $\omega_0 - \omega_{flat}$. As the number of states reaches its local maximum at ω_{flat}, the increase in number of channels attains its maximum at $\omega_0 = 2\omega_{flat}$ *[45]*. This elucidates how the augmented number of scattering channels in the presence of flat modes accounts for the distinctive behaviour of P^-. Considering the same factors, P^+ also increases from $LiCu_3TiS_4$ to $LiCu_3TiTe_4$. Additionally, boundary scatterings occur at a higher magnitude than isotopic scattering, as shown in **Figure 3.11**. Thus, boundary scattering is found to contribute more to the reduction in κ_L than isotopic scattering.

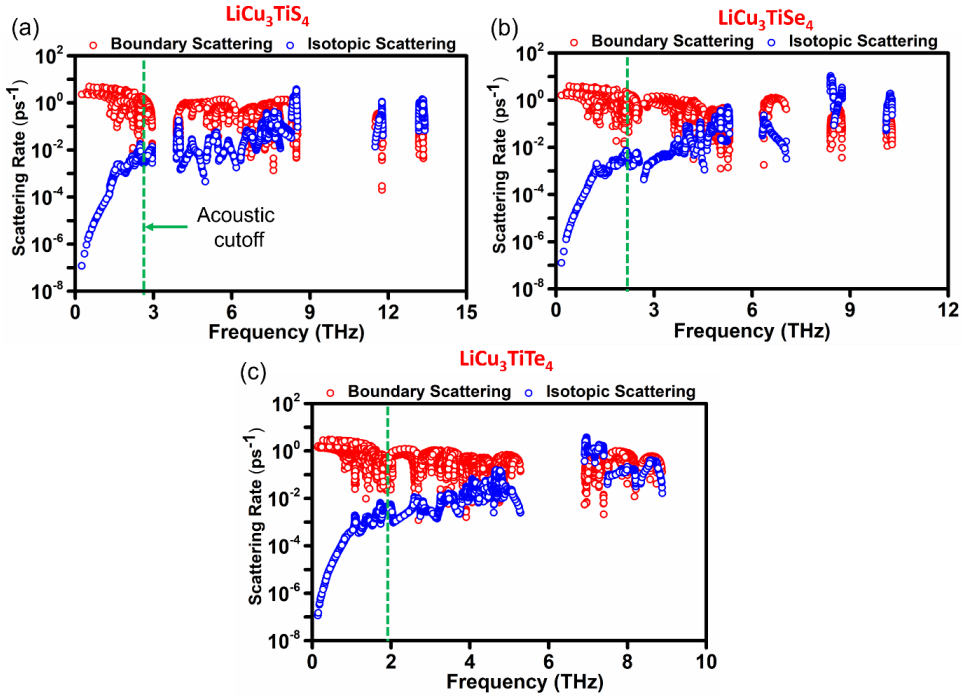


Figure 3.11: Boundary and isotopic scattering rates of **(a)** $LiCu_3TiS_4$, **(b)** $LiCu_3TiSe_4$, **(c)** $LiCu_3TiTe_4$ with respect to frequency (THz) at 300K.

3.3.5. Electronic Properties

Further, we focused on the electronic transport properties of $LiCu_3TiQ_4$, as depicted in **Figure 3.12**. We have performed band gaps using different functionals as shown in **Table 3.4**. The HSE03 functional with 10% Hartree-Fock exchange and 90% PBE worked well to calculate the electronic band structures for $LiCu_3TiS_4$ and $LiCu_3TiSe_4$ while 5% Hartree-Fock exchange and 95% PBE worked well for $LiCu_3TiTe_4$, which were found to be in coherence with experimental band gaps.[41] The electronic band structures for $LiCu_3TiS_4$ and $LiCu_3TiSe_4$ are found to have indirect band gaps of 2.23 eV and 1.93 eV, respectively, along the high symmetry Brillouin zone k-points from $R \rightarrow X$.[41] Further the $LiCu_3TiTe_4$ exhibits a direct band gap of 1.39 eV.[41] This decrease in the band gap from S to Te can be explained due to the presence of more electropositive atoms in the compound.

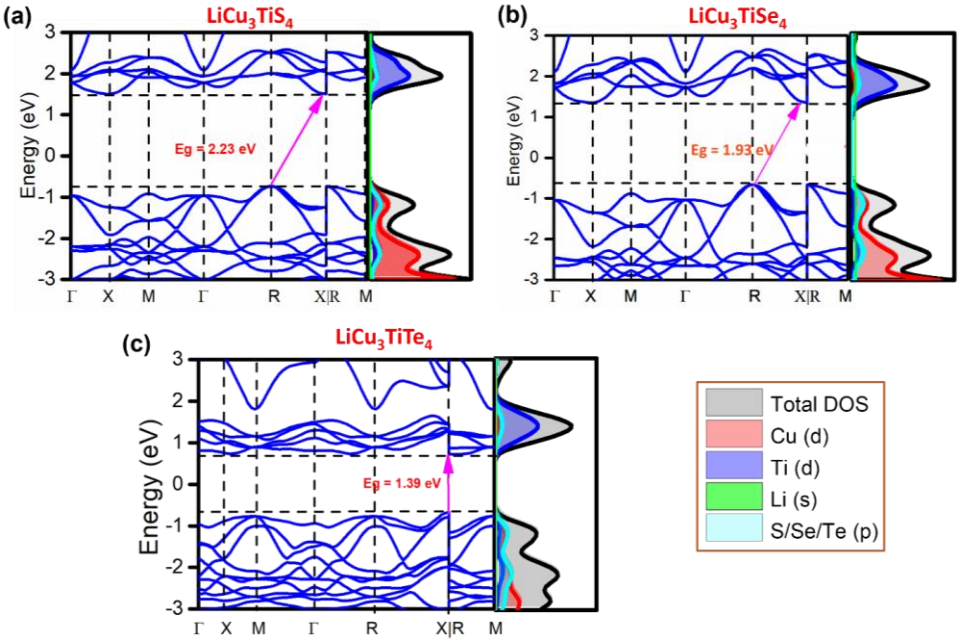


Figure 3.12: The electronic band structures along with the projected density of states (PDOS) calculated within HSE03 functional for **(a)** $LiCu_3TiS_4$, **(b)** $LiCu_3TiSe_4$, and **(c)** $LiCu_3TiTe_4$ with their respective band gaps (Eg) and the pink arrow defining the direct/indirect path along the Brillouin zone points.

Table 3.4: Calculated bandgaps using different functionals for $LiCu_3TiQ_4$ systems.

Functional	**$LiCu_3TiS_4$**	**$LiCu_3TiSe_4$**	**$LiCu_3TiTe_4$**
PBE	1.52	1.25	1.11
HSE06 (25%)	3.50	3.20	2.30
HSE06 (20%)	3.16	2.83	2.19
HSE06 (10%)	2.32	2.02	2.38
HSE06 (5%)	1.92	1.64	1.43
HSE03 (25%)	3.30	2.97	2.15
HSE03 (20%)	2.94	2.62	2.03
HSE03 (10%)	**2.22**	**1.92**	1.63
HSE03 (5%)	1.86	1.59	**1.39**

MBJ	1.52	1.31	1.22
SCAN	1.67	1.44	1.32
SCAN_RPR	1.67	1.44	1.32
SCAN_rVV10	1.73	1.50	1.36
Exp4	**2.3**	**1.86**	**1.34**

The partial density of states (PDOS) is presented alongside the band structure of each material in **Figure 3.12**. The valence band edges (VBE) in each material are primarily composed of Cu 3d orbitals (represented by red) due to its less electropositive characteristics than Ti and Li. In contrast, the conduction band edges (CBE) exhibit high dominance of Ti 3d orbitals due to its electropositive properties. The increasing electronegative behaviour of chalcogens from S to Te increases their contribution to VBE, as observed in **Figure 3.12.**

Table 3.5: The carrier effective mass (m_o) of hole and electron for $LiCu_3TiQ_4$ systems.

Carrier	**Effective mass**		
	$LiCu_3TiS_4$	**$LiCu_3TiSe_4$**	**$LiCu_3TiTe_4$**
electron	1.17	1.62	1.83
hole	0.27	0.93	1.19

The calculated electron effective mass is heavier than the hole effective mass (**Table 3.5**), leading to a significant improvement in the transport properties of p-type carriers compared to n-type carriers. In the cases of $LiCu_3TiS_4$ and $LiCu_3TiSe_4$, a dispersive valance band edge with a light effective mass is observed, while $LiCu_3TiTe_4$ features a flat band with a significant effective mass from $\Gamma \rightarrow X$ region (**Figure 3.12**). The effective mass of the hole changes significantly as we move from S to Te, which is associated with the formation of less dispersed valence bands, as described in the following equation,

$$m^* = \hbar^2 \left(\frac{d^2 E}{dk_i dk_j} \right)^{-1} \quad \text{(S3)}$$

where E and k represents the energy and wave vector. These electronic transport properties have been calculated considering the relaxation time as a function of carrier concentration and temperature. Here, we have evaluated the various scattering rates such as polar optical phonons (POP), ionized impurity (IMP), and acoustic deformation potential (ADP) using AMSET. These scattering rates provide a better reflection of how they contribute to transportation under different conditions. Further, we have plotted the scattering rates for n- and p-type at 300 K at a carrier concentration of 10^{20} cm^{-3} as shown in **Figures 3.13-3.14**.

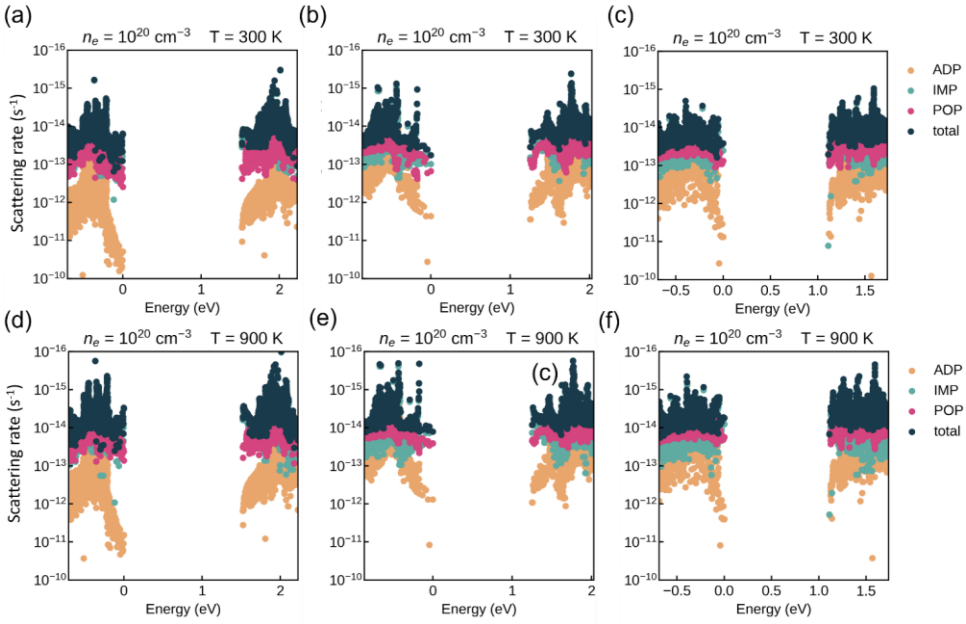


Figure 3.13: Scattering rates as a function of energy of n-type for **(a, d)** $LiCu_3TiS_4$, **(b, e)** $LiCu_3TiSe_4$, and **(c, f)** $LiCu_3TiTe_4$. These represent their scattering mechanisms including polar optical phonon (POP), ionized impurity (IMP), and acoustic deformation potential (ADP) scattering at carrier concentrations of 10^{20} cm^{-3} at 300 K and 900 K for n-type conduction.

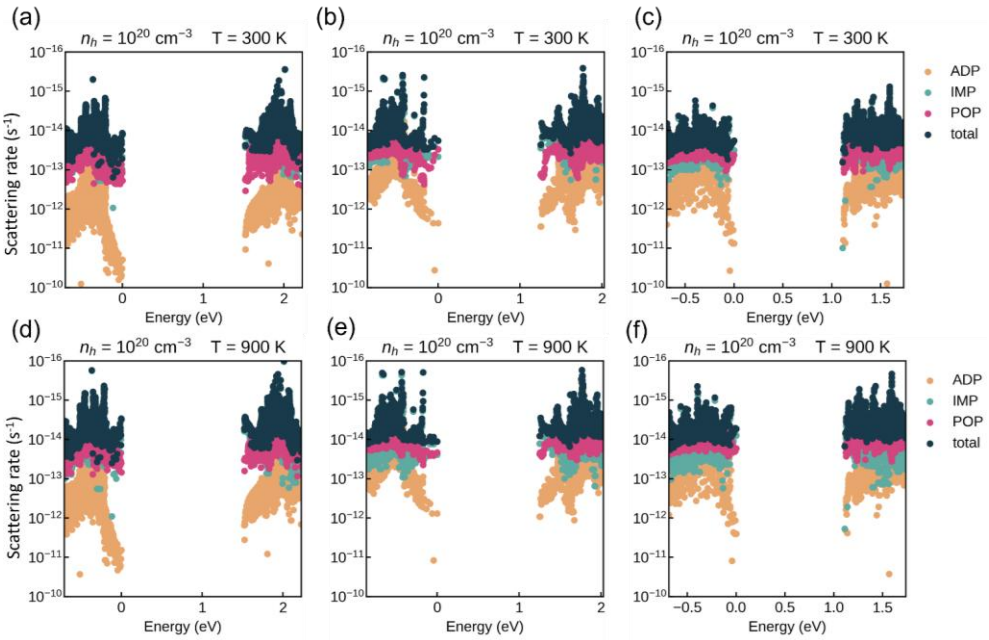


Figure 3.14: Scattering rates as a function of energy of p-type for **(a, d)** $LiCu_3TiS_4$, **(b, e)** $LiCu_3TiSe_4$, and **(c, f)** $LiCu_3TiTe_4$. These represent their scattering mechanisms including polar optical phonon (POP), ionized impurity (IMP), and acoustic deformation potential (ADP) scattering at carrier concentrations of 10^{20} cm^{-3} at 300 K and 900 K for p-type conduction.

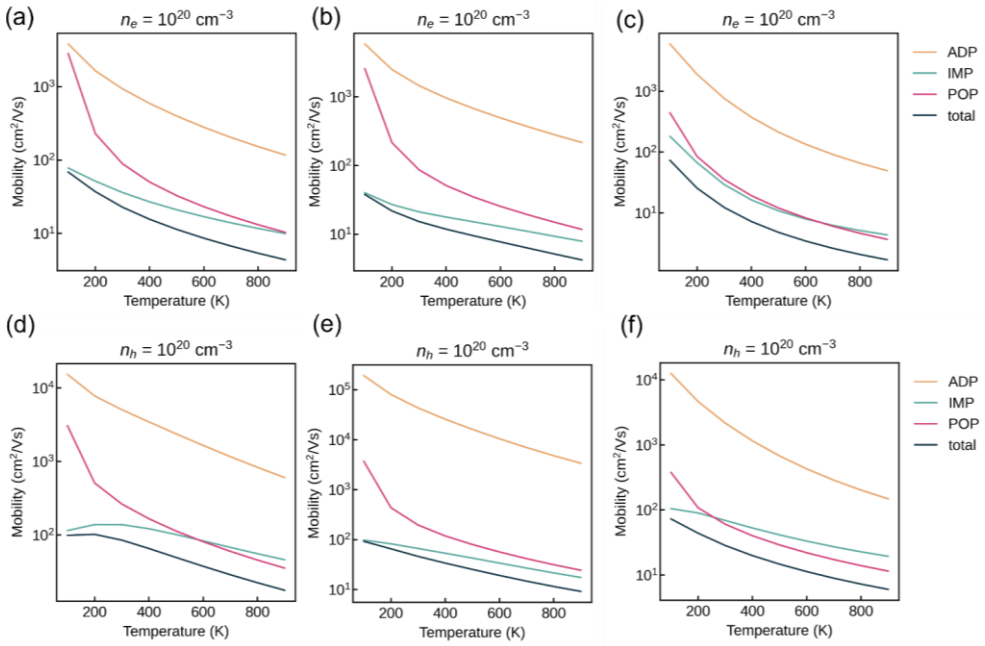


Figure 3.15: Mobility (cm^2/Vs) as a function of temperature for n- and p-type doping of **(a, d)** $LiCu_3TiS_4$, **(b, e)** $LiCu_3TiSe_4$, and **(c, f)** $LiCu_3TiTe_4$ under three scattering mechanisms namely, polar optical phonon (POP), ionized impurity (IMP), and acoustic deformation potential (ADP) scattering with carrier concentrations of 10^{20} cm^{-3}.

We observe that the IMP scattering rate does not differ much with temperature, whereas ADP and POP scattering rates decrease with an increase in temperature. The ADP has the highest scattering rate followed by the IMP and POP. Collectively, these effects lead to the lowest total scattering rates occurring at a carrier concentration of 10^{20} cm^{-3}, resulting in the highest achievable ZT value, as discussed in detail in Section 3.6. Subsequently, the scattering rates (τ^{-1}), and effective mass (m^*) are inversely proportional to the mobility according to the equation, $\mu = \left({}^{q\,\tau}/_{m^*}\right)$. Therefore, in **Figure 3.15** in all cases, ADP has the maximum mobility followed by POP and IMP, whereas the mobility of all scattering types decreases upon moving from $LiCu_3TiS_4$ to $LiCu_3TiTe_4$. The electronic transport properties, including electrical conductivity, the Seebeck coefficient, and electronic thermal conductivity of $LiCu_3TiQ_4$ at different

temperatures and carrier concentration have been represented in **Figure 3.16**.

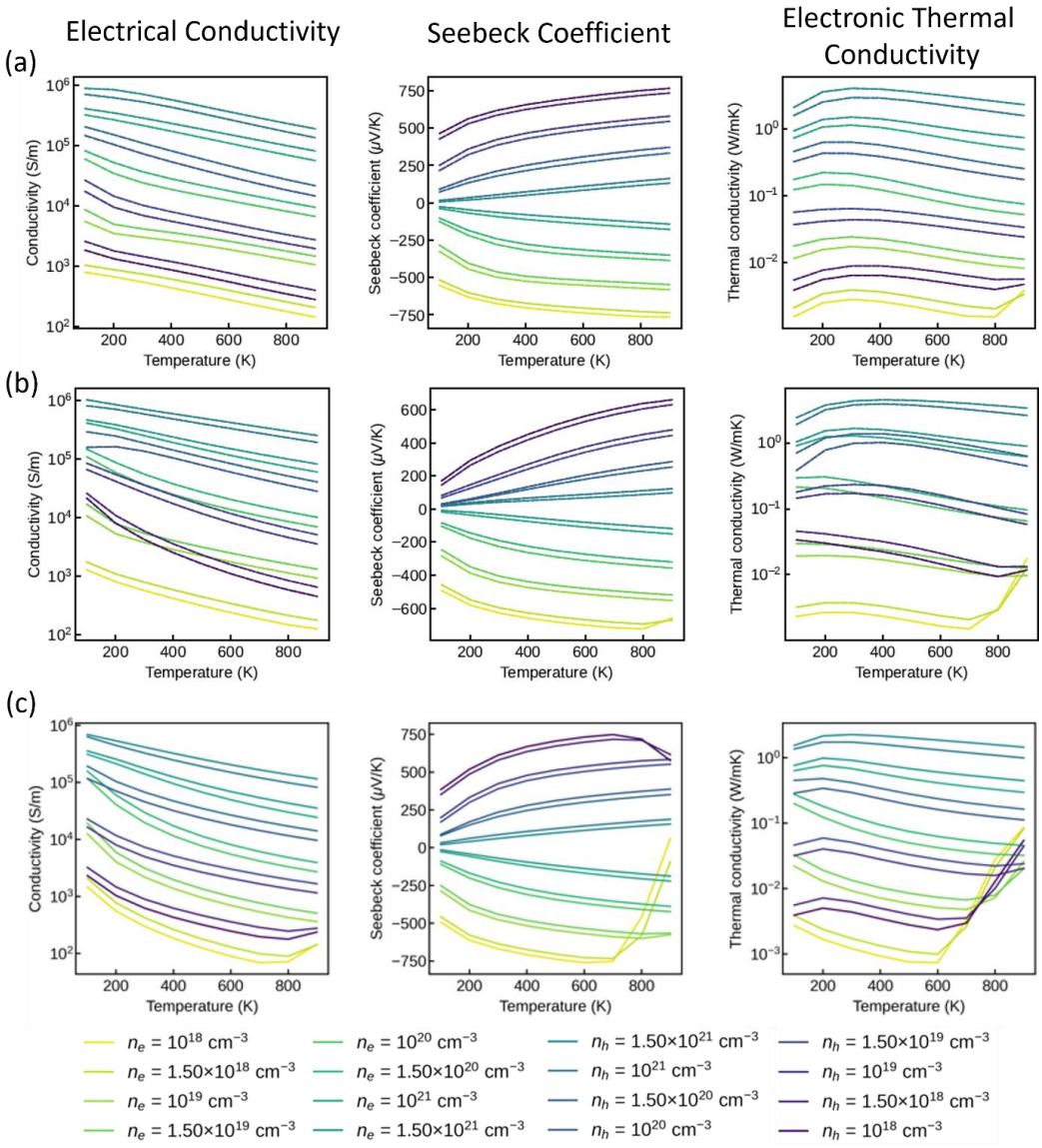


Figure 3.16: The calculated electronic transport properties including electrical conductivity (S/m), Seebeck coefficient (μV/K), and electronic thermal conductivity ($Wm^{-1}K^{-1}$) for (a) $LiCu_3TiS_4$, (b) $LiCu_3TiSe_4$, and (c) $LiCu_3TiTe_4$.

3.3.6. Thermoelectric Properties

The electrical conductivity (σ), Seebeck coefficient (S), and power factor (PF) for the n- and p-type $LiCu_3TiQ_4$ has been calculated at 300 K and 500 K as represented in **Figure 3.17-3.18**. The Seebeck coefficient (S) and figure of merit (ZT) are formulated as follows:*[58]*

$$S = \frac{8\pi^2 k_B^2 m^* T}{3eh^2}\left(\frac{\pi}{3n}\right)^{2/3} \quad (1)$$

$$ZT = \frac{S^2\sigma}{\kappa_e+\kappa_l}T = (S^2 n)\left(\frac{\mu}{\kappa}\right)eT \quad (2)$$

where k_B is Boltzmann constant, m^* is effective mass, T is absolute temperature, h is Planck's constant, e is an electrical charge and n is the carrier concentration. The electrical conductivity is defined as $\sigma = nq\mu$, where μ is mobility and q is the charge. Mobility increases with a decrease in effective mass, resulting in increased electrical conductivity along with electronic thermal conductivity. However, in the case of the Seebeck coefficient, a direct relation with m^* is observed, as depicted in **Figure 3.17**. Thus, the Seebeck coefficient, in accordance with m^* values, follows the order: $LiCu_3TiS_4$ < $LiCu_3TiSe_4$ < $LiCu_3TiTe_4$. Additionally, the Seebeck coefficient is higher for Te (-498 μVK^{-1}), followed by Se (-440 μVK^{-1}) and S (-398 μVK^{-1}) at 300 K for n-type doping with a carrier concentration of 10^{19} cm^{-3}.

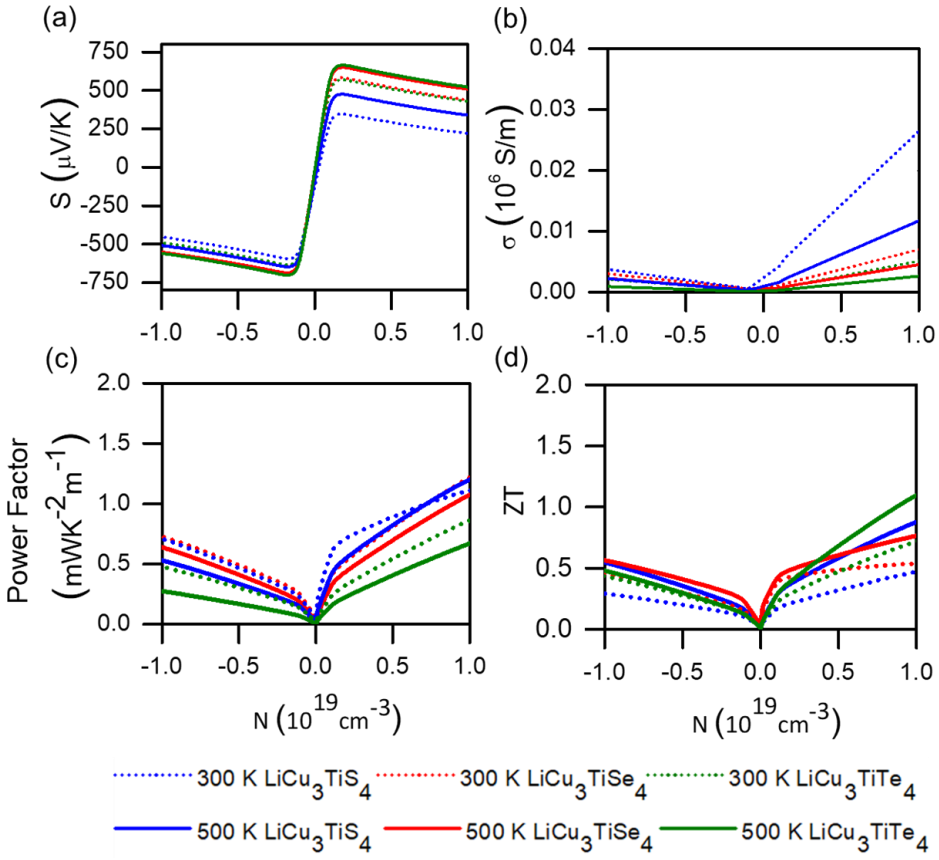


Figure 3.17: The evaluated thermoelectric properties for $LiCu_3TiQ_4$ (Q = S, Se, or Te) **(a)** Seebeck coefficient (S), **(b)** electrical conductivity (σ), **(c)** power factor (PF), and **(d)** thermoelectric figure of merit (ZT), at 10^{19} cm^{-3} calculated based on relaxation times obtained transport coefficients using AMSET. The negative and positive signs of the carrier concentrations represent n- and p-type doping. Here, the blue, red, and olive green represent the $LiCu_3TiS_4$, $LiCu_3TiSe_4$, and $LiCu_3TiTe_4$, respectively. The dotted line and straight line represent temperature scales of 300 K and 500 K.

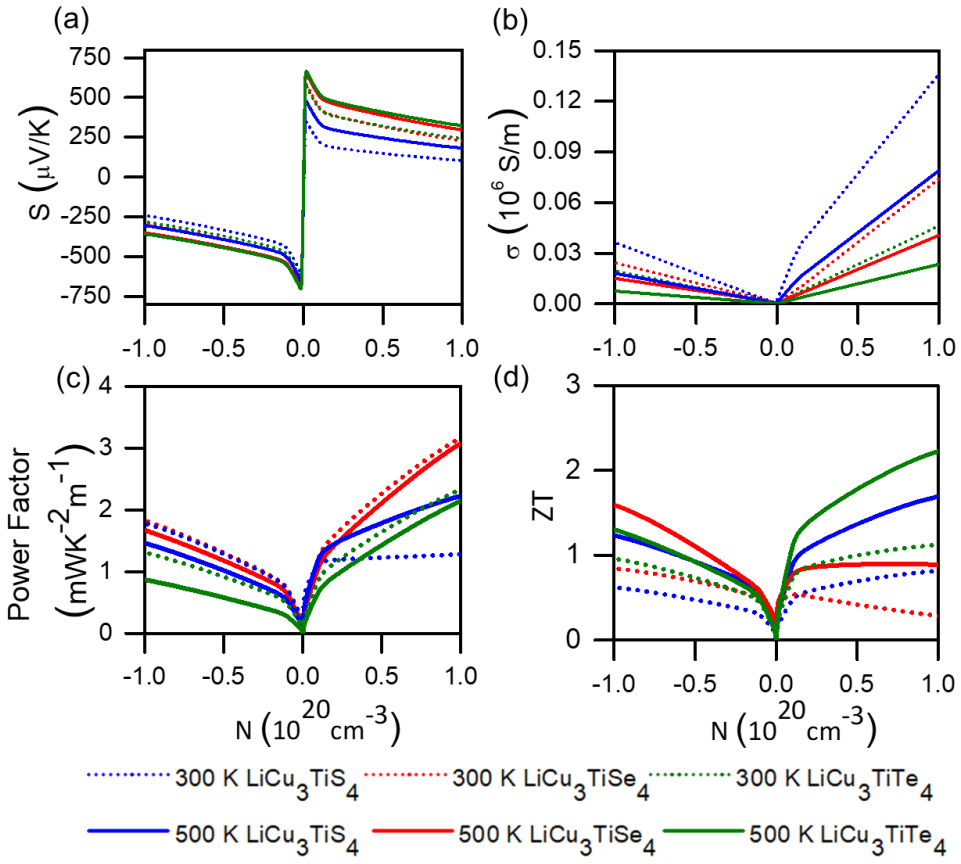


Figure 3.18. The evaluated thermoelectric properties for $LiCu_3TiQ_4$ (Q = S, Se, or Te) **(a)** Seebeck coefficient (S), **(b)** electrical conductivity (σ), **(c)** power factor (PF), and **(d)** thermoelectric figure of merit (ZT), calculated based on relaxation times obtained transport coefficients using AMSET at carrier concentration of 10^{20} cm^{-3}. The negative and positive signs of the carrier concentrations represent n- and p-type doping.

On the other hand, the σ follows the inverse order to m^* i.e., 4106 Sm^{-1} for S, followed by 3763 Sm^{-1} for Se, and 3043 Sm^{-1} for Te at 300 K for n-type doping with a carrier concentration of 10^{20} cm^{-3}. This further supports our observation that the bonding weakens as we move from S to Te in the $LiCu_3TiQ_4$ system. Finally, the calculated ZT values are 0.48 (0.78), 0.55 (0.91), and 0.75 (1.14) at 300 K (500 K) for p-type doping with a carrier concentration of 10^{19} cm^{-3} for $LiCu_3TiS_4$, $LiCu_3TiSe_4$, and $LiCu_3TiTe_4$ respectively. Therefore, $LiCu_3TiQ_4$ systems exhibit ZT values within the range of 0.78-0.89 for S, 0.91-1.68 for Se, and 1.14-2.20 for Te at carrier

concentration between 10^{19}- 10^{20} cm^{-3} at 500 K. The remarkably high ZT values result from low κ_L and optimum electronic transport properties, making them comparable to other renowned TE materials such as PbTe,*[59]* SnSe,*[60]* Cu_2Se,*[13]* Cu_3SbSe_3,*[17]* and KCu_5Se_3 *[19]*. A promising direction for future research involves exploring the effect of dopants on increasing carrier concentration to improve the ZT value. This could further enhance the performance of $LiCu_3TiQ_4$ systems, making them even more competitive with leading thermoelectric materials.

3.4. Summary

In summary, using the moment tensor potentials belonging to the class of machine learning interatomic potentials, we show that cubic lithium copper chalcotitanates exhibit remarkable thermoelectric performance. The ultralow lattice thermal conductivity originates from bonding hierarchy, phonon spectra with flat bands, and acoustic-optical hybridization resulting in an increased number of heat-carrying phonon scattering rates. The presence of rattling-like vibrations of cations is evidenced through the large atomic displacement parameters, dispersionless phonon partial density of states, and quiescence characteristics. Thus, the weakly bound sublattice efficiently suppresses thermal transport between the Li^+ ions and $[Cu_3TiQ_4]^-$ moieties. Also, lone pairs around the chalcogen atoms (S, Se, and Te) induce lattice anharmonicity reflected by the significant deviation in the Grüneisen parameter. This anharmonicity is supported by overdamped atomic vibrations and the presence of flat band modes, contributing to an enhanced scattering channels in $LiCu_3TiQ_4$ further results in ultralow κ_L. These mechanistic insights, elucidating the various routes for achieving ultralow thermal conductivity, serve as a valuable guide for designing next-generation TE materials with remarkable TE performance.

3.5. References

1. He J., Tritt T.M. (2017), Advances in thermoelectric materials research: Looking back and moving forward, Science, 357(6358), eaak9997 (DOI: 10.1126/science.aak9997)

2. Zeier W.G., Zevalkink A., Gibbs Z.M., Hautier G., Kanatzidis M.G., Snyder G.J. (2016), Thinking like a chemist: Intuition in thermoelectric materials, Angew Chem Int Ed, 55(24), 6826–6841 (DOI: 10.1002/anie.201510998)

3. Yu Y., Zhou C., Ghosh T., Schön C.F., Zhou Y., Wahl S., Raghuwanshi M., Kerres P., Bellin C., Shukla A., Cojocaru-Mirédin O., Wuttig M. (2023), Local bonding hierarchy and fluctuations in thermoelectric materials, Adv Mater, 35(19), 2300893 (DOI: 10.1002/adma.202300893)

4. Jana M.K., Pal K., Warankar A., Mandal P., Waghmare U.V., Biswas K. (2017), Intrinsic rattling of atoms in thermoelectric materials, J Am Chem Soc, 139(12), 4350–4353 (DOI: 10.1021/jacs.6b13250)

5. Qiu W., Xi L., Wei P., Ke X., Yang J., Zhang W. (2014), Part-crystalline part-liquid state and its effect on thermoelectric performance, Proc Natl Acad Sci USA, 111(42), 15031–15035 (DOI: 10.1073/pnas.1412262111)

6. Jana M.K., Pal K., Waghmare U.V., Biswas K. (2016), Rattling-induced ultralow thermal conductivity, Angew Chem Int Ed, 55(27), 7792–7796 (DOI: 10.1002/anie.201602147)

7. Christensen M., Abrahamsen A.B., Christensen N.B., Juranyi F., Andersen N.H., Lefmann K., Andreasson J., Bahl C.R.H., Iversen B.B. (2008), Avoided crossing of rattler modes in thermoelectric materials, Nat Mater, 7(10), 811–815 (DOI: 10.1038/nmat2265)

8. Zheng Y., Slade T.J., Hu L., Tan X.Y., Luo Y., Luo Z.Z., Xu J., Yan Q., Kanatzidis M.G. (2021), Defect engineering in thermoelectric materials, Chem Soc Rev, 50(16), 9022–9054 (DOI: 10.1039/D1CS00216E)

9. Su X., Wei P., Li H., Liu W., Yan Y., Li P., Su C., Xie C., Zhao W., Zhai P., Zhang Q., Tang X., Uher C. (2017), Multi-scale microstructural

engineering for high thermoelectric performance, Adv Mater, 29(20), 1602013 (DOI: 10.1002/adma.201602013)

10. Biswas K., He J., Blum I.D., Wu C.I., Hogan T.P., Seidman D.N., Dravid V.P., Kanatzidis M.G. (2012), High-performance bulk thermoelectrics with all-scale hierarchical architectures, Nature, 489(7416), 414–418 (DOI: 10.1038/nature11439)

11. Biswas K., He J., Zhang Q., Wang G., Uher C., Dravid V.P., Kanatzidis M.G. (2011), Strained endotaxial nanostructures with high thermoelectric performance, Nat Chem, 3(2), 160–166 (DOI: 10.1038/nchem.955)

12. Xie H., Su X., Zhang X., Hao S., Bailey T.P., Stoumpos C.C., Douvalis A.P., Hu X., Wolverton C., Dravid V.P., Uher C., Tang X., Kanatzidis M.G. (2019), Ultralow lattice thermal conductivity and high thermoelectric performance, J Am Chem Soc, 141(27), 10905–10914 (DOI: 10.1021/jacs.9b04641)

13. Liu H., Shi X., Xu F., Zhang L., Zhang W., Chen L., Li Q., Uher C., Day T., Snyder G.J. (2012), Copper ion liquid-like thermoelectrics, Nat Mater, 11(5), 422–425 (DOI: 10.1038/nmat3273)

14. Li W., Lin S., Weiss M., Chen Z., Li J., Xu Y., Zeier W.G., Pei Y. (2018), Band convergence engineering for high thermoelectric performance, Adv Energy Mater, 8(18), 1800030 (DOI: 10.1002/aenm.201800030)

15. Ying P., Li X., Wang Y., Yang J., Fu C., Zhang W., Zhao X., Zhu T. (2017), Hierarchical phonon scattering for high thermoelectric efficiency, Adv Funct Mater, 27(1), 1604145 (DOI: 10.1002/adfm.201604145)

16. Luo Z.Z., Hao S., Zhang X., Hua X., Cai S., Tan G., Bailey T.P., Ma R., Uher C., Wolverton C., Dravid V.P., Yan Q., Kanatzidis M.G. (2018), Electronic origin of high thermoelectric performance, Energy Environ Sci, 11(11), 3220–3230 (DOI: 10.1039/C8EE02001H)

17. Tyagi K., Gahtori B., Bathula S., Srivastava A.K., Shukla A.K., Auluck S., Dhar A. (2014), Thermoelectric transport properties of lead

chalcogenides, J Mater Chem A, 2(38), 15829–15835 (DOI: 10.1039/C4TA02815E)

18. Koley B., Lakshan A., Raghuvanshi P.R., Singh C., Bhattacharya A., Jana P.P. (2021), Strong phonon scattering and thermoelectric performance, Angew Chem Int Ed, 60, 9106–9113 (DOI: 10.1002/anie.202015593)

19. Li F., Liu X., Ma N., Yang Y.C., Yin J.P., Chen L., Wu L.M. (2023), Complex chalcogenide thermoelectric materials, J Am Chem Soc, 145(27), 14981–14993 (DOI: 10.1021/jacs.3c04529)

20. Mortazavi B., Podryabinkin E.V., Novikov I.S., Roche S., Rabczuk T., Zhuang X., Shapeev A.V. (2020), Machine-learning interatomic potentials for materials modeling, J Phys Mater, 3(2), 02LT02 (DOI: 10.1088/2515-7639/ab6c6e)

21. Mortazavi B., Podryabinkin E.V., Novikov I.S., Rabczuk T., Zhuang X., Shapeev A.V. (2021), Accelerated atomistic simulations using machine-learning potentials, Comput Phys Commun, 258, 107583 (DOI: 10.1016/j.cpc.2020.107583)

22. Zuo Y., Chen C., Li X., Deng Z., Chen Y., Behler J., Csányi G., Shapeev A.V., Thompson A.P., Wood M.A., Ong S.P. (2020), Performance and cost assessment of machine-learning interatomic potentials, J Phys Chem A, 124(4), 731–745 (DOI: 10.1021/acs.jpca.9b08723)

23. Minhas H., Majumdar A., Pathak B. (2023), Machine-learning-assisted screening of thermoelectric materials, ACS Appl Energy Mater, 6(19), 9851–9863 (DOI: 10.1021/acsaem.3c02092)

24. Wang C., Wang Q., Zhang Q., Chen C., Chen Y. (2022), Predictive modeling of thermoelectric properties using machine learning, Chem Mater, 34(17), 7837–7844 (DOI: 10.1021/acs.chemmater.2c01879)

25. Quintero M.A., Shen J., Laing C.C., Wolverton C., Kanatzidis M.G. (2022), Metastability and thermoelectric performance, J Am Chem Soc, 144(28), 12789–12799 (DOI: 10.1021/jacs.2c03942)

26. Blöchl P.E. (1994), Projector augmented-wave method, Phys Rev B, 50(24), 17953–17979 (DOI: 10.1103/PhysRevB.50.17953)

27. Kresse G., Furthmüller J. (1996), Efficient iterative schemes for ab initio total-energy calculations, Phys Rev B, 54(16), 11169–11186 (DOI: 10.1103/PhysRevB.54.11169)

28. Perdew J.P., Burke K., Ernzerhof M. (1996), Generalized gradient approximation made simple, Phys Rev Lett, 77(18), 3865–3868 (DOI: 10.1103/PhysRevLett.77.3865)

29. Perdew J.P., Chevary J.A., Vosko S.H., Jackson K.A., Pederson M.R., Singh D.J., Fiolhais C. (1997), Atoms, molecules, solids, and surfaces: Applications of the generalized gradient approximation, Phys Rev B, 56(12), 7197–7203 (DOI: 10.1103/PhysRevB.56.7197)

30. Perdew J.P., Ernzerhof M., Burke K. (1996), Rationale for mixing exact exchange with density functional approximations, J Chem Phys, 105(22), 9982–9985 (DOI: 10.1063/1.472933)

31. Heyd J., Scuseria G.E., Ernzerhof M. (2003), Hybrid functionals based on a screened Coulomb potential, J Chem Phys, 118(18), 8207–8215 (DOI: 10.1063/1.1564060)

32. Mortazavi B., Podryabinkin E.V., Roche S., Rabczuk T., Zhuang X., Shapeev A.V. (2020), Exploring phononic properties using machine-learning potentials, Mater Horiz, 7(9), 2359–2367 (DOI: 10.1039/D0MH00733A)

33. Novikov I.S., Gubaev K., Podryabinkin E.V., Shapeev A.V. (2021), The MLIP package: Moment tensor potentials, Mach Learn Sci Technol, 2(2), 025002 (DOI: 10.1088/2632-2153/abc9fe)

34. Li W., Carrete J., Katcho N.A., Mingo N. (2014), ShengBTE: A solver of the Boltzmann transport equation, Comput Phys Commun, 185(6), 1747–1758 (DOI: 10.1016/j.cpc.2014.02.015)

35. Zheng J., Lin C., Hautier G., Guo R., Huang B. (2024), High-throughput prediction of lattice thermal conductivity, npj Comput Mater, 10(1), 30 (DOI: 10.1038/s41524-024-01130-7)

36. Zheng J., Shi D., Liu S., Yang Y., Lin C., Chang Z., Guo R., Huang B. (2022), Anharmonic lattice dynamics and thermal transport, Phys Rev Mater, 6(9), 093801 (DOI: 10.1103/PhysRevMaterials.6.093801)

37. Zheng J., Shi D., Yang Y., Lin C., Huang H., Guo R., Huang B. (2022), Phonon scattering and thermal conductivity, Phys Rev B, 105(22), 224303 (DOI: 10.1103/PhysRevB.105.224303)

38. Yue J., Zheng J., Li J., Guo S., Ren W., Liu H., Liu Y., Cui T. (2024), Pressure-driven thermoelectric performance, ACS Appl Mater Interfaces, 16, 20597–20609 (DOI: 10.1021/acsami.4c01234)

39. Ganose A.M., Park J., Faghaninia A., Woods-Robinson R., Persson K.A., Jain A. (2021), Efficient calculation of carrier scattering, Nat Commun, 12(1), 2222 (DOI: 10.1038/s41467-021-22440-5)

40. Minhas H., Das S., Pathak B. (2023), Descriptor-based screening of thermoelectrics, ACS Appl Energy Mater, 6(13), 7305–7316 (DOI: 10.1021/acsaem.3c00648)

41. Mouhat F., Coudert F.X. (2014), Necessary and sufficient elastic stability conditions, Phys Rev B, 90(22), 224104 (DOI: 10.1103/PhysRevB.90.224104)

42. Silvi B., Savin A. (1994), Classification of chemical bonds by topological analysis, Nature, 371(6499), 683–686 (DOI: 10.1038/371683a0)

43. Nielsen M.D., Ozolins V., Heremans J.P. (2013), Lone pair electrons and thermoelectric performance, Energy Environ Sci, 6(2), 570–578 (DOI: 10.1039/C2EE23391F)

44. Xie H. (2023), Perspective on lattice thermal conductivity, Mater Lab, 2, 220051 (DOI: 10.1002/mala.20220051)

45. Xie L., Feng J.H., Li R., He J.Q. (2020), Resonant bonding and phonon softening, Phys Rev Lett, 125(24), 245901 (DOI: 10.1103/PhysRevLett.125.245901)

46. Li W., Mingo N. (2015), Ultralow thermal conductivity in crystalline solids, Phys Rev B, 91(14), 144304 (DOI: 10.1103/PhysRevB.91.144304)

47. Delaire O., Ma J., Marty K., May A.F., McGuire M.A., Du M.H., Singh D.J., Podlesnyak A., Ehlers G., Lumsden M.D., Sales B.C. (2011), Giant anharmonic phonon scattering, Nat Mater, 10(8), 614–619 (DOI: 10.1038/nmat3035)

48. Yang K., Xiao J., Luo J.W., Li S.S., Wei S.H., Deng H.X. (2019), Defect physics and transport properties, New J Phys, 21(12), 123015 (DOI: 10.1088/1367-2630/ab5c5a)

49. Morelli D.T., Jovovic V., Heremans J.P. (2008), Intrinsically low thermal conductivity, Phys Rev Lett, 101(3), 035901 (DOI: 10.1103/PhysRevLett.101.035901)

50. Zhao L.D., He J., Berardan D., Lin Y., Li J.F., Nan C.W., Dragoe N. (2014), High-performance thermoelectrics, Energy Environ Sci, 7(9), 2900–2924 (DOI: 10.1039/C4EE00997H)

51. Liu Z., Zhang W., Gao W., Mori T. (2021), Band engineering for thermoelectrics, Energy Environ Sci, 14(6), 3579–3587 (DOI: 10.1039/D1EE00766E)

52. Hodges J.M., Xia Y., Malliakas C.D., Alexander G.C.B., Chan M.K.Y., Kanatzidis M.G. (2018), Phase stability and transport properties, Chem Mater, 30(20), 7245–7254 (DOI: 10.1021/acs.chemmater.8b03319)

53. Pal K., He J., Wolverton C. (2018), Thermodynamic descriptors for thermoelectrics, Chem Mater, 30(21), 7760–7768 (DOI: 10.1021/acs.chemmater.8b03451)

54. Simoncelli M., Marzari N., Mauri F. (2022), Unified theory of thermal transport, Phys Rev X, 12(4), 041011 (DOI: 10.1103/PhysRevX.12.041011)

55. Lanigan-Atkins T., He X., Krogstad M.J., Pajerowski D.M., Abernathy D.L., Xu G., Xu Z., Chung D.Y., Kanatzidis M.G., Rosenkranz S., Osborn R., Delaire O. (2021), Anharmonic phonon dynamics, Nat Mater, 20(7), 977–983 (DOI: 10.1038/s41563-021-00977-1)

56. Luo Y., Yang X., Feng T., Wang J., Ruan X. (2020), Phonon hydrodynamics in solids, Nat Commun, 11(1), 2554 (DOI: 10.1038/s41467-020-16448-6)

57. Tadano T., Gohda Y., Tsuneyuki S. (2015), First-principles phonon calculations, Phys Rev Lett, 114(9), 095501 (DOI: 10.1103/PhysRevLett.114.095501)

58. Tan G., Zhao L.D., Kanatzidis M.G. (2016), Rational design of thermoelectric materials, Chem Rev, 116(19), 12123–12149 (DOI: 10.1021/acs.chemrev.6b00255)

59. Heremans J.P., Jovovic V., Toberer E.S., Saramat A., Kurosaki K., Charoenphakdee A., Yamanaka S., Snyder G.J. (2008), Enhancement of thermoelectric efficiency, Science, 321(5888), 554–557 (DOI: 10.1126/science.1159725)

60. Zhao L.D., Tan G., Hao S., He J., Pei Y., Chi H., Wang H., Gong S., Xu H., Dravid V.P., Uher C., Snyder G.J., Wolverton C., Kanatzidis M.G. (2016), Ultrahigh power factor and thermoelectric performance, Science, 351(6269), 141–144 (DOI: 10.1126/science.aad3749)

CHAPTER 3

CHAPTER 4

Interpretable ML Reveals Bonding Insights for Thermoelectrics

CHAPTER 4

CHAPTER 4

Section-A

4.1. Introduction

In materials science, the search for novel materials presents a significant challenge. Traditionally, researchers have addressed this challenge by combining density-functional theory (DFT) with laboratory-based trial-and-error synthesis methods. Recently, the application of machine learning (ML) techniques has emerged as a powerful tool for rapidly exploring diverse composition spaces to identify potential stable compounds, thereby circumventing the demand for computationally intensive DFT calculations *[1, 2]*. Advancements in high-performance computing, along with initiatives like the materials genome initiative (GMI), have led to the development of platforms such as the Materials Project, AFLOWLIB, and the Open Quantum Materials Database, which facilitates the screening of materials with desired properties *[2–4]*. The ML methods have also proven to be invaluable for accurately predicting electrical and thermal transport properties, thereby facilitating the discovery of promising TE materials *[5–8]*. However, predicting the TE properties of doped materials poses a challenge due to insufficient crystal structure information. Nevertheless, the properties of doped materials can significantly alter those of the host materials, and these materials remain highly prominent in TE materials due to their superior TE performance. Therefore, to address these challenges, the synergistic use of interpretable ML with a wide-range experimental database could enhance TE material discovery and deepen the understanding of the correlation between molecular properties and target properties.

We explored an experimental database of doped TE materials to predict five key properties using composition-based feature vectors. The trained ML model can predict all TE properties based on various temperature constraints and understand the hidden feature output relations using

explainable AI. To validate our results, we considered an external database to assess the model's performance. We have also prepared an unknown dataset by varying doping concentration to identify the most effective dopant composition at an optimal concentration level. Additionally, we classified unlabelled TE materials of functionalized terminating groups based on their performance and input features. Our approach offers a promising strategy for designing cost-effective TE materials by strategically adjusting dopant and composition ratios, which will likely interest experimentalists in this field.

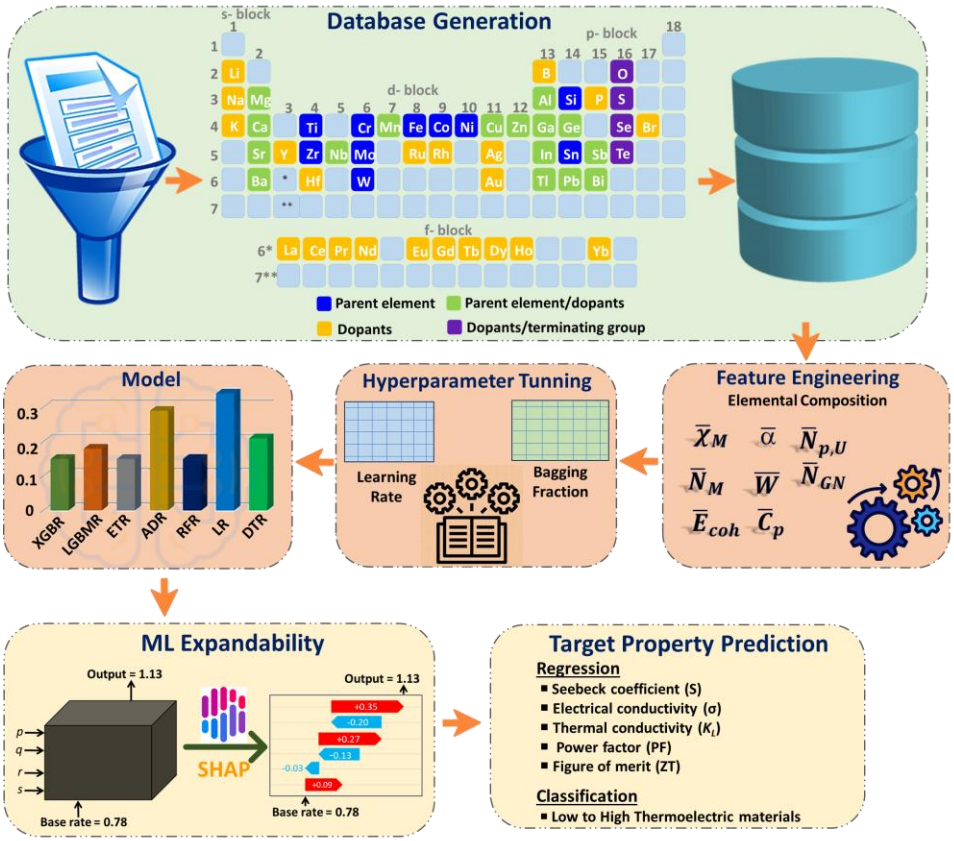


Figure 4.1: Schematic illustration of database generation with elements of the periodic table reflects the total database and stepwise machine learning workflow for the prediction of TE properties.

Figure 4.1 shows the schematic representation of the step-by-step ML workflow considered in our study to predict the five important TE properties: (a) Seebeck coefficient (S), (b) electrical conductivity (σ), (c) thermal conductivity (κ_L), (c) power factor (PF), and (d) figure of merit (ZT) for the considered database. These databases are built by collecting the TE properties of 640 unique experimentally synthesized materials from the materials research laboratory (MRL) repository and the previous literature *[9, 10]*. Based on the data, we have created five experimental databases based on TE properties: S, σ, κ_L, PF, and ZT with 3200 observations at varying temperatures. The considered database consists of experimentally synthesized materials with wide compositions including chalcogenides (GeTe, SnTe, PbTe, $Sn_{1-x}Se$, $Bi_{2-x}Sb_xTe_3$), skutterudite ($CoSb_3$, As_2Te_3), clathrates ($Ba_8Ga_{16}Ge_{30}$), and transition metal-based chalcogenides ($Cu_{2-x}Se$, $Ag_{2-x}Te_2$) at 300K to 1000K temperature range.

4.2. Feature Engineering and Selection

Features are the fundamental and critical component of the ML framework. For this, we have extracted a set of elemental and compositional features of materials that potentially can have a direct or indirect relation with their TE properties. The chemical compositions are transformed into practical input features utilizing composition-based feature vectors (CBFVs) *[11]*. These CBFVs effectively convert chemical compositions into readily applicable input features, thereby facilitating the exploration of the elemental and compositional effects on the desired TE properties. These generated features can be broadly grouped into three categories: (a) molecular descriptors (melting point, boiling point, specific heat, and metalloid properties), (b) chemical descriptors (atomic number, ionic and covalent radii, electronegativity, and valence electrons), and (c) electronic descriptors (polarizability and ionization potential). Since the TE properties of materials are experimentally measured at specific TE temperatures *[12]*.

Thus, we carefully included temperature as a feature along with 34 other features, as shown in **Table 4.1**.

Table 4.1: List of 35 Elemental and Structural Features Considered in the Present Study

Sl.No.	Feature	Feature Description	Symbol
1	F1	Average Atomic Weight	$\overline{W}$
2	F2	Average Period	$\overline{P}$
3	F3	Average Group	$\overline{G}$
4	F4	Average Family	$\overline{F}$
5	F5	Average Metal	$\overline{M}$
6	F6	Average Non-Metal	$\overline{NM}$
7	F7	Average Metalloid	$\overline{ML}$
8	F8	Average Atomic Number	$\overline{Z}$
9	F9	Average Atomic Radius	$\overline{r}_{at}$
10	F10	Average Covalent Radius	$\overline{r}_{cov}$
11	F11	Average Ionic Radius	$\overline{r}_{ion}$
12	F12	Average Pauling Electronegativity	$\overline{\chi}_P$
13	F13	Average Mulliken Electronegativity	$\overline{\chi}_M$
14	F14	Average Metallic Valence	$\overline{N}_M$
15	F15	Average Gilmor Number of Valence Electron	$\overline{N}_{GN}$
16	F16	Average Valence s Orbital	$\overline{N}_s$
17	F17	Average Valence p Orbital	$\overline{N}_p$
18	F18	Average Valence d Orbital	$\overline{N}_d$
19	F19	Average Valence of Orbital	$\overline{N}_f$
20	F20	Average Number of Unfilled Electrons in s	$\overline{N}_{s,U}$
21	F21	Average Number of Unfilled Electrons in p	$\overline{N}_{p,U}$
22	F22	Average Number of Unfilled Electrons in d	$\overline{N}_{d,U}$
23	F23	Average Number of Unfilled Electrons in f	$\overline{N}_{f,U}$
24	F24	Average Outer Shell Electrons	$\overline{N}_{Oe}$
25	F25	Average First Ionization Potential	$\overline{IE}$
26	F26	Average Polarizability	$\overline{\alpha}$
27	F27	Average Melting Point	$\overline{MP}$
28	F28	Average Boiling Point	$\overline{BP}$
29	F29	Average Density	$\overline{\delta}$
30	F30	Average Specific Heat	$\overline{C}_p$

31	**F31**	Average Heat of Fusion	$\Delta\bar{H}_f$
32	**F32**	Average Heat of Vaporization	$\Delta\bar{H}_v$
33	**F33**	Average Heat of Atomization	$\Delta\bar{H}_{atom}$
34	**F34**	Average Cohesive Energy	$\bar{E}_{coh}$
35	**F35**	Temperature (K)	$\boldsymbol{T(K)}$

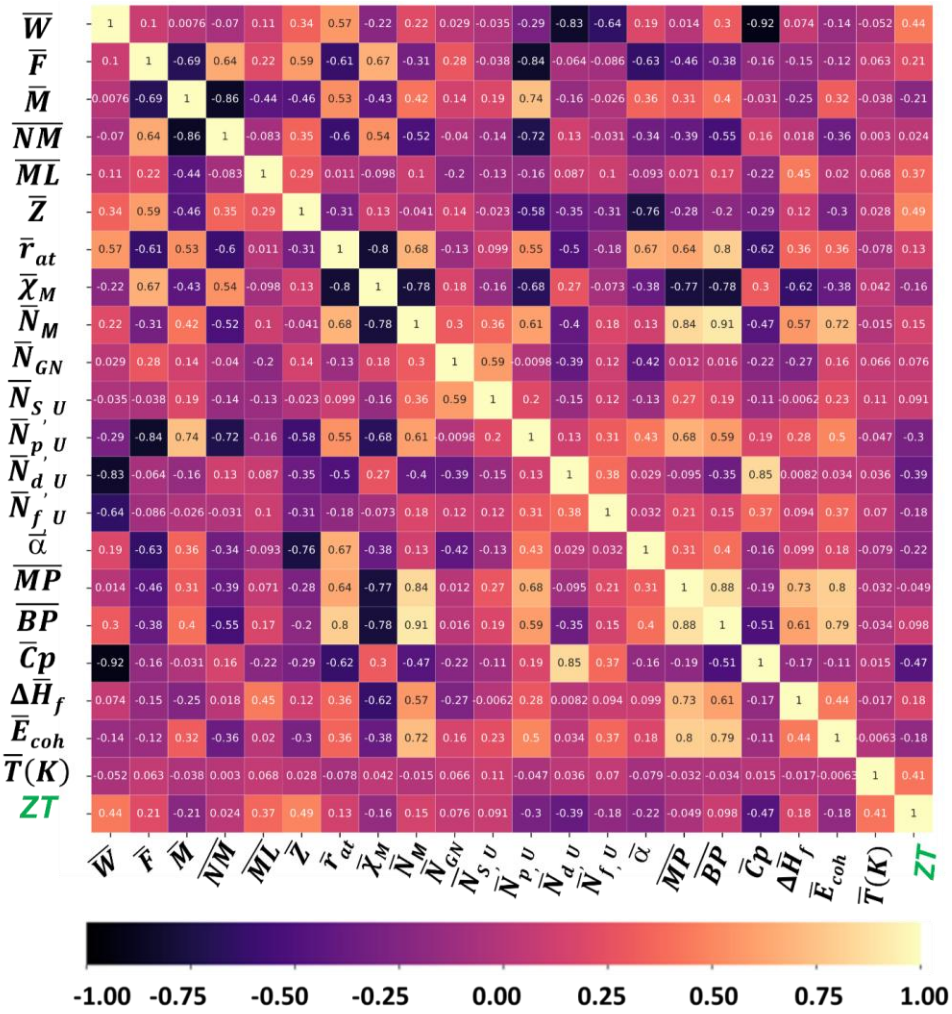


Figure 4.2: The Pearson correlation coefficient (PCC) plot for the top 21 features and figure of merit (ZT). The scale at the bottom represents the range of the correlation where dark purple and pale yellow signify the perfect negative (-1) and perfect positive (+1) correlation.

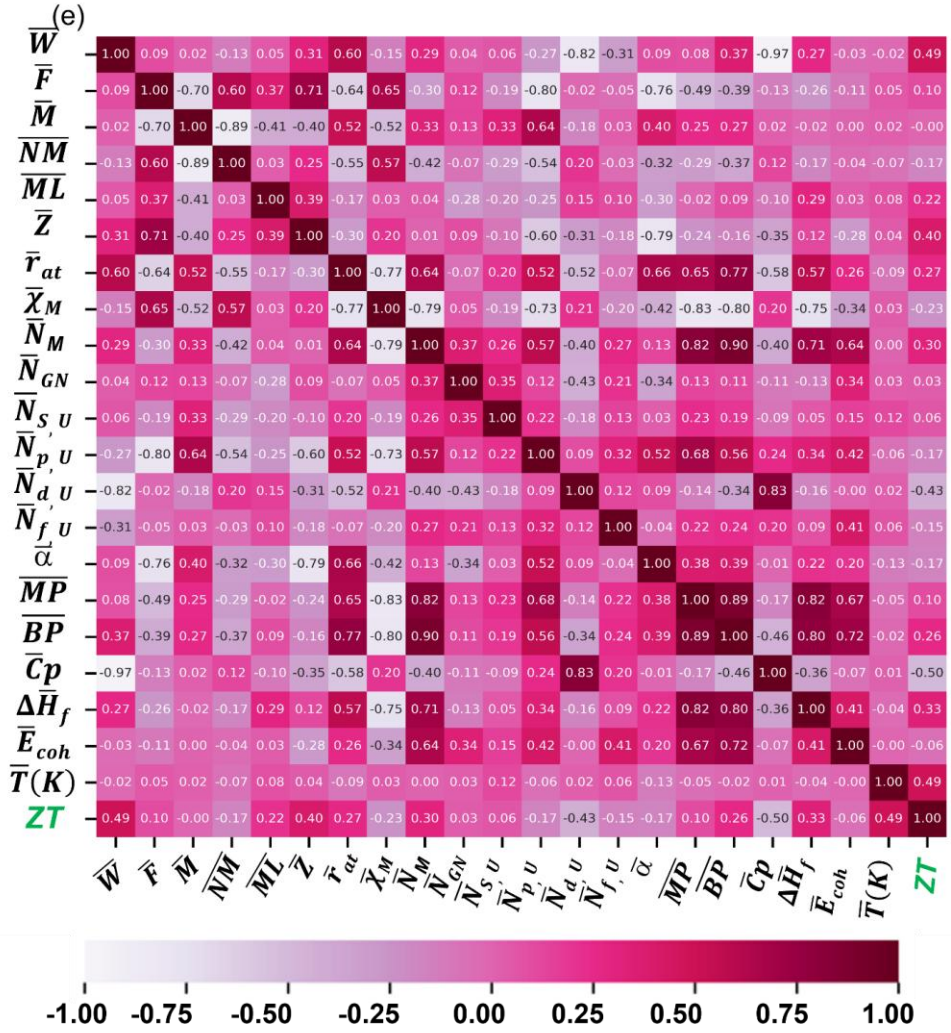


Figure 4.3: The Spearman's rank correlation plot for the top 21 features and figure of merit (ZT). The scale at the bottom represents the range of the correlation where light purple and purple signify the perfect negative (-1) and perfect positive (+1) correlation.

To elucidate the linear, monotonic, and nonlinear dependencies among these features and feature-target properties, we have quantified Pearson correlation coefficient (PCC), Spearman's rank correlation coefficient (SCC), and mutual information (MI) analysis *[13, 14]*. From PCC and SCC analysis, the average atomic weight ($\overline{W}$), average atomic number ($\bar{Z}$), and temperature T(K) are noted to have a positive correlation whereas, the

average specific heat ($\bar{C}_p$), and the average number of unfilled electrons in the d orbital ($\bar{N}_{d,U}$) show a negative correlation towards the output ZT (**Figure 4.2-4.3**). These observation highlights both linear and nonlinear dependencies between variables, providing a more comprehensive understanding of the dataset. Further, the MI method assesses the level of uncertainty reduction in the output when considering each input feature as shown in **Figure 4.4** *[15]*. From the above analysis, we systematically dropped the strongly correlated features such as average density, average heat of vaporization, and atomization, among others, to enhance the efficiency and minimize redundancy in our database. Consequently, we arrived at a refined feature count from 35 to 21 (**Table 4.1-4.2**), optimizing the dataset for ML applications.

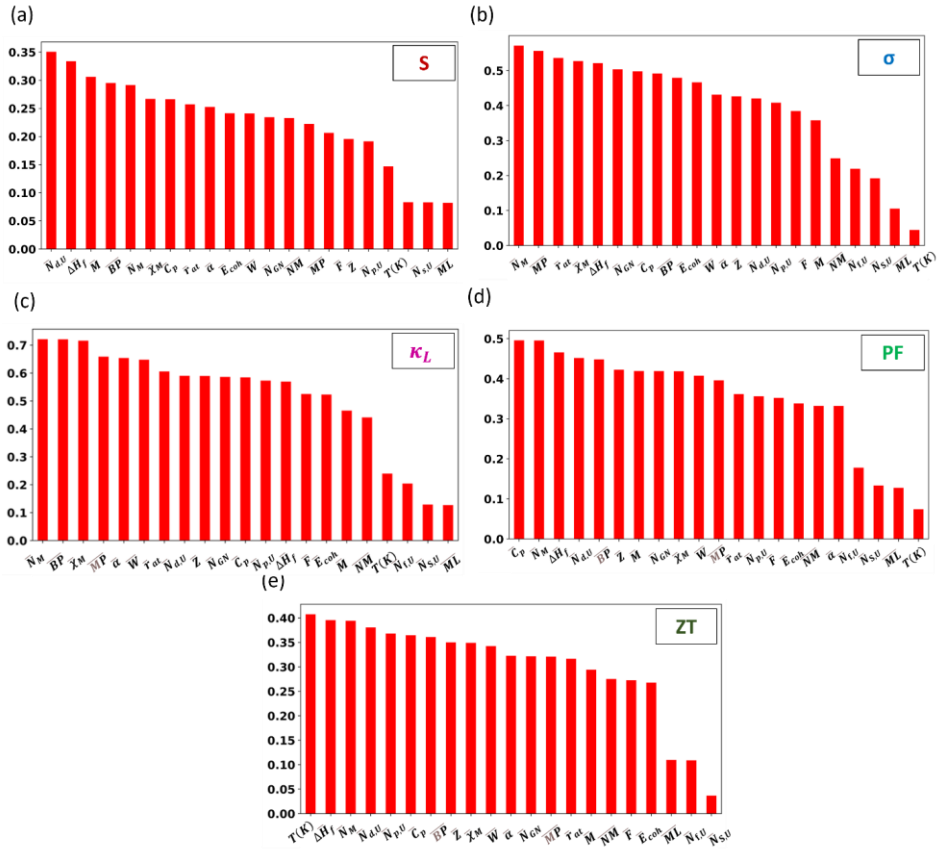


Figure 4.4: Mutual information feature importance plot of optimized XGBR model for (a) Seebeck coefficient (*S*), (b) electrical conductivity

(σ), (c) thermal conductivity (κ_L), (d) power factor (PF) and (e) figure of merit (ZT).

Table 4.2: List of Top 21 Elemental and Structural Features Considered After Removing Highly Correlated Features

S.No.	Feature	Feature Description	Symbol
1	**F1**	Average Atomic Weight	$\overline{W}$
2	**F4**	Average Family	$\overline{F}$
3	**F5**	Average Metal	$\overline{M}$
4	**F6**	Average Non-Metal	$\overline{NM}$
5	**F7**	Average Metalloid	$\overline{ML}$
6	**F8**	Average Atomic Number	$\overline{Z}$
7	**F9**	Average Atomic Radius	$\overline{r}_{at}$
8	**F13**	Average Mulliken Electronegativity	$\overline{\chi}_M$
9	**F14**	Average Metallic Valence	$\overline{N}_M$
10	**F15**	Average Gilmor Number of Valence Electron	$\overline{N}_{GN}$
11	**F20**	Average Number of Unfilled Electrons in s	$\overline{N}_{s,U}$
12	**F21**	Average Number of Unfilled Electrons in p	$\overline{N}_{p,U}$
13	**F22**	Average Number of Unfilled Electrons in d	$\overline{N}_{d,U}$
14	**F23**	Average Number of Unfilled Electrons in f	$\overline{N}_{f,U}$
15	**F26**	Average Polarizability	$\overline{\alpha}$
16	**F27**	Average Melting Point	$\overline{MP}$
17	**F28**	Average Boiling Point	$\overline{BP}$
18	**F30**	Average Specific Heat	$\overline{C}_p$
19	**F31**	Average Heat of Fusion	$\Delta\overline{H}_f$
20	**F34**	Average Cohesive Energy	$\overline{E}_{coh}$
21	**F35**	Temperature (K)	$T(K)$

4.3. Results and Discussion

After feature engineering, each database is randomly split into train and test sets in an 80:20 ratio, respectively, ensuring that the test set is completely unknown to the model during training. Subsequently, we have employed various ML algorithms, namely, extreme gradient boosting regressor

(XGBR), extra tree regression (ETR), adaptive boosting regression (ADR), random forest regression (RFR), decision tree regression (DTR), support vector regression (SVR) and other linear regression-based methods as available in the open-source Scikit-learn library *[16]*. The hyperparameter tuning of the considered models is performed by employing the RandomizedsearchCV strategy to find the optimal combination of hyperparameters (**Table 4.3**) *[17]*.

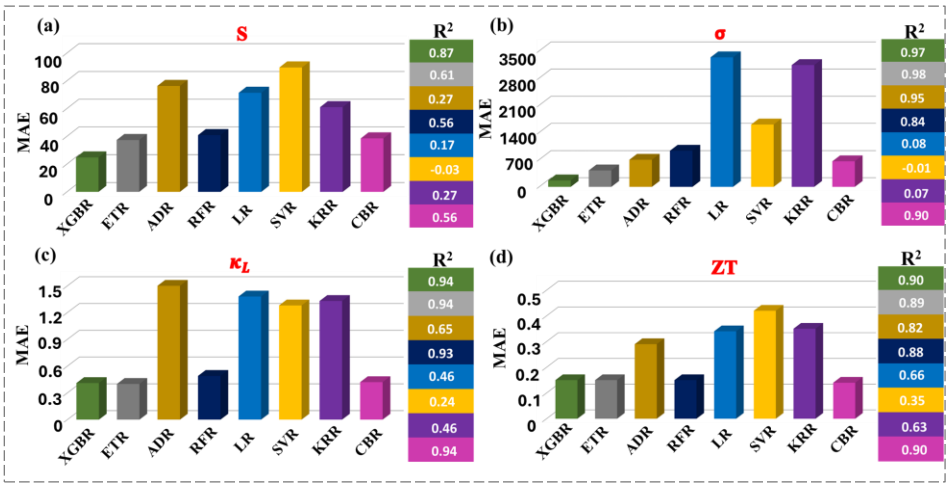


Figure 4.5: The vertical bar plots represent the test mean absolute error (MAE) and the adjacent color bar reflects the test R^2 Scores for the prediction of (a) Seebeck coefficient (S), (b) electrical conductivity (σ), (c) thermal conductivity (κ_L), and (d) figure of merit (ZT).

Table 4.3: Optimized hyperparameters of optimized XGBR models with test accuracy score.

Sl. No.	Datasets	Optimized Hyperparameters	Test MAE
1	**Figure of merit (ZT)**	'verbose': '20,' 'n_estimators': 2000, 'min_child_weight': '8,' 'max_depth': '25', 'learning_rate': '0.05', 'cv': '2', 'booster': 'gbtree', 'base_score': '1.45'	**0.15**
2	**Seebeck coefficient (S)**	'verbose': '10,' 'n_estimators': 2200, 'min_child_weight': '1 ' 'max_depth': '3',	**32.29**

		'learning_rate': '0.15', 'cv': '4', 'booster': 'gbtree', 'base_score': '0.1'	
3	**Electrical conductivity (σ)**	'verbose': '10,' 'n_estimators': 2200, 'min_child_weight': '1 ' 'max_depth': '3', 'learning_rate': '0.15', 'cv': '4', 'booster': 'gbtree', 'base_score': '0.1'	**165.20**
4	**Power factor (PF)**	'verbose': '20,' 'n_estimators': 2600, 'min_child_weight': '8 ' 'max_depth': '10', 'learning_rate': '0.1', 'cv': '2', 'booster': 'gbtree', 'base_score': '0.75'	**3.47**
5	**Thermal Conductivity (κ_L)**	'verbose': '10,' 'n_estimators': 2200, 'min_child_weight': '1 ' 'max_depth': '3', 'learning_rate': '0.15', 'cv': '4', 'booster': 'gbtree', 'base_score': '0.1'	**0.41**

It is evident that the predictive performance of XGBR and ETR, analyzed by mean absolute error (MAE), and R^2 scores are comparable for the prediction of κ_L, PF, and ZT, as shown in **Figure 4.5**. However, XGBR outperforms ETR for the prediction of S and σ. Therefore, we proceeded with the XGBR model due to its superior predictive capabilities for all five TE properties. The train-test parity plots with test MAE and R^2 have been summarized in **Figure 4.6**. The MAE values for TE properties were 24.77 μVK^{-1} for S, 165 Scm^{-1} for σ, 0.41 $Wm^{-1}K^{-1}$ for κ_L, 3.47 $\mu Wcm^{-1}K^{-2}$ for PF, and 0.15 for ZT datasets. XGBR is an ensemble algorithm rooted in gradient-boosted trees that excels at managing complex, non-linear correlations. Through its iterative training technique, it simultaneously integrates new trees to rectify errors, resulting in exceptional generalization and scalability across diverse tasks *[18]*.

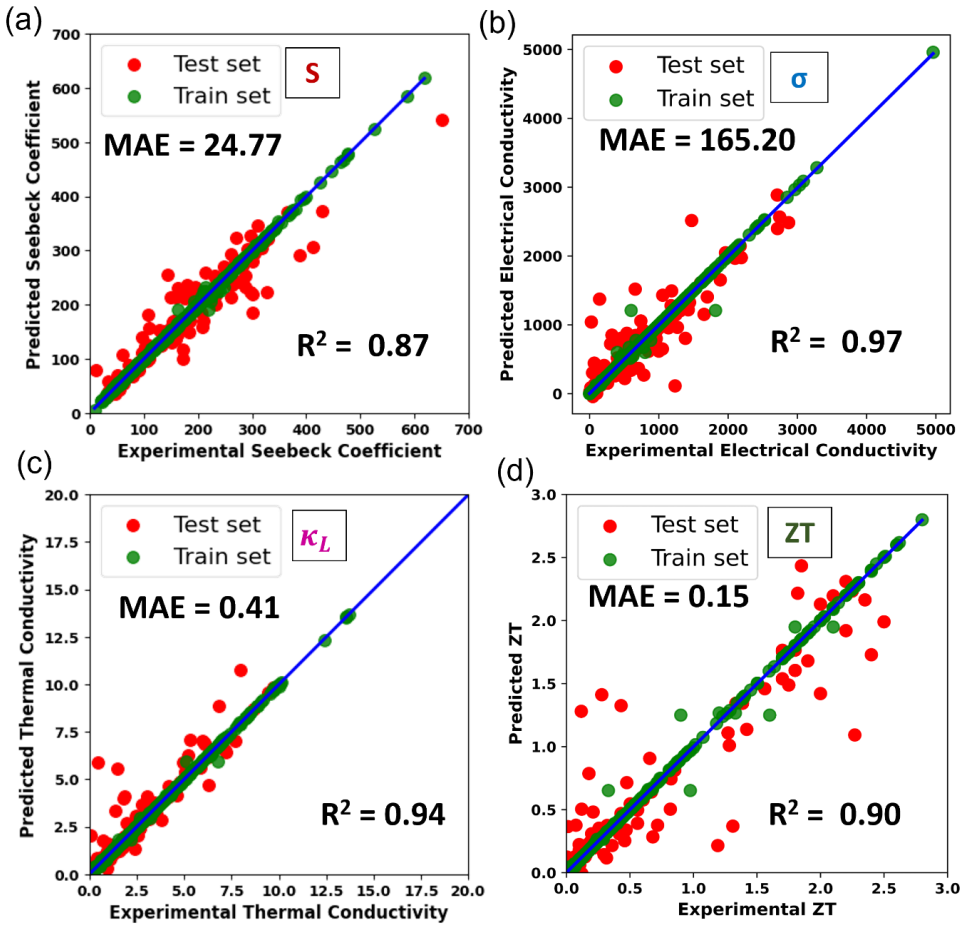


Figure 4.6: Parity plots of ML predicted versus experimental values for **(a)** Seebeck coefficient (S) in μVK^{-1}, **(b)** electrical conductivity(σ) in Scm^{-1}, **(c)** lattice thermal conductivity (κ_L) in $Wm^{-1}K^{-1}$, and **(d)** figure of merit (ZT) along with their test MAE values of XGBR models.

To avoid any risk of overfitting and ensure the stability and reliability of the best ML models, we implemented a rigorous 9-fold cross-validation (CV) analysis. This technique is renowned for its effectiveness in evaluating and stabilizing model performance. The mean MAE and individual CV MAE scores obtained from the CV datasets using optimized ML algorithms have similar test MAE scores as presented in **Table 4.4**. This alignment signifies the generalizability of the ML algorithm and reduces the risk of overfitting.

Table 4.4: Mean Absolute Error (MAE) of 9-fold Cross-Validation using the XGBR Models for Seebeck Coefficient (S) μVK^{-1}, Electrical Conductivity (σ) Scm^{-1}, Thermal Conductivity (κ_L) $Wm^{-1}K^{-1}$, Power Factor (PF) μWcm^{-1}K^{-2}, and Thermoelectric Figure of Merit (ZT) datasets. Test MAE and standard deviation (std) Values for Each XGBR Model have also been Reported.

CV Folds	S	σ	κ_L	PF	ZT
C1	38.32	163.46	0.37	3.36	0.15
C2	28.20	164.09	0.52	3.07	0.12
C3	34.45	189.68	0.77	3.71	0.10
C4	26.67	183.049	0.58	2.95	0.11
C5	25.14	164.66	0.76	2.57	0.13
C6	21.89	118.59	0.28	4.26	0.10
C7	34.18	125.73	0.62	3.84	0.14
C8	24.32	202.36	0.37	3.98	0.15
C9	26.01	184.11	0.63	3.44	0.15
$\overline{MAE} \pm std$	28.79 ± 5.22	166.19 ± 27.17	0.54 ± 0.16	3.46 ± 0.50	0.13 ± 0.02
Test *MAE*	32.29	165	0.45	3.47	0.15

Further, we aimed to validate the performance of our trained model on unseen data, which is crucial for ensuring its reliability and generalization ability. To accomplish this, we carefully constructed a validation dataset with 120 observations of 40 experimental materials at different temperatures, given in ref *[8]*. We have noted that MAE for the predicted validation set closely matched our test MAE scores, with values of 37.23 μVK^{-1} for S, 155 Scm^{-1} for σ, 0.10 Wm^{-1}K^{-1} for κ_L, and 0.15 for ZT. These results demonstrate the superior training performance and robustness of our trained XGBR model, providing a more accurate predictive capability across the evaluated TE properties.

4.3.1. Machine Learning Explainability

Furthermore, we have conducted the ML interpretability study with SHapley Additive explanations (SHAP) analysis, which is based on cooperative game theory, as implemented in the Python package *[17]*. The bar plots describe the global feature importance of individual features on the ability of the XGBR model to make predictions. Each feature in these plots, along with its Shapley values, displays its impact on ML model predictions of TE properties as shown in **Figure 4.7**. This trend can be attributed to the inherent nature of these properties, which are strongly influenced by temperature parameters. Aside $T(K)$, noteworthy contributions of $\overline{N}_M$, $\overline{\alpha}$, $\overline{NM}$, and $\overline{W}$ are demonstrated towards S.

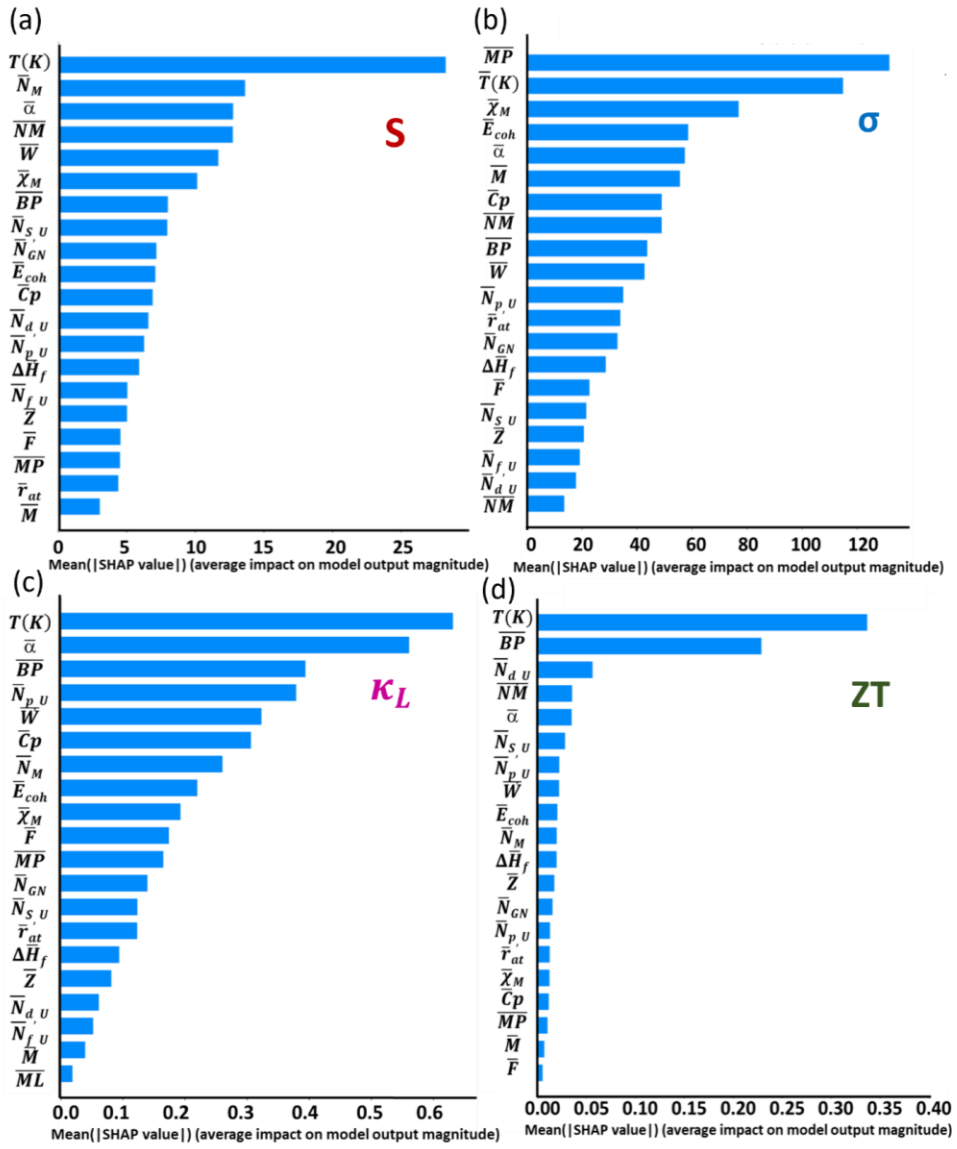


Figure 4.7: SHAP bar plot showing the global feature importance of each considered input feature on the prediction of (a) Seebeck coefficient (S), (b) electrical conductivity (σ), (c) lattice thermal conductivity (κ_L), and (d) figure of merit (ZT).

Interestingly, the positive impact of $\overline{NM}$, $\overline{W}$, and $\overline{\alpha}$ on enhancing the Seebeck coefficient (S) has also been demonstrated in previous studies, *[20, 21]* emphasizing their significant role in ML prediction. In the prediction of electrical conductivity (σ), $\overline{MP}$, $\bar{\chi}_M$, and $\bar{E}_{coh}$ exert the most substantial

influence. Similarly, $\overline{\alpha}$, $\overline{BP}$, $\overline{N}_{p,U}$, $\overline{W}$, and $\bar{C}_p$ features strongly influence the prediction of thermal conductivity (κ). Conversely, $\overline{BP}$, $\overline{N}_{d,U}$, and $\overline{\alpha}$ emerged as most impactful features for prediction of ZT.

Figure 4.8 illustrates the SHAP beeswarm plot, providing more insights into global feature importance with distribution feature instances. Each instance is represented by a solitary dot on the feature row with a Shapley value, and colour gradient on the y-axis indicates the magnitude of the feature, ranging from low (blue) to high (red). The most impactful feature $T(K)$ exhibits is driving the S and ZT prediction towards the higher values while exhibiting an inverse relation with σ and κ_L prediction consistent with the TE performance equation. The higher feature values of $\overline{N}_M$ and $\overline{\alpha}$ have a negative contribution, while those with low feature values contribute positively towards the prediction of S. The $\bar{\chi}_M$ holds positive influence, while $\bar{\bar{E}}_{coh}$ exerts a negative impact on σ. In case of κ_L, the $\overline{\alpha}$ emerges as the second most prominent feature which could be due to the presence of high electron density. The high polarizability indicates that the atoms are loosely bound to the nucleus and can be easily distorted by an external electrical field, contributing to higher anharmonicity, which in turn reduces the κ_L as shown in **Figure 4.8(c)** *[22]*. Meanwhile, the $\overline{BP}/\overline{N}_{d,U}$ has high positive/negative feature importance towards the prediction of ZT. It is noted that materials featuring late transitions d-block elements with a minimum number of unpaired d electrons ($\overline{N}_{d,U}$), exhibit the potential for high TE efficiency.

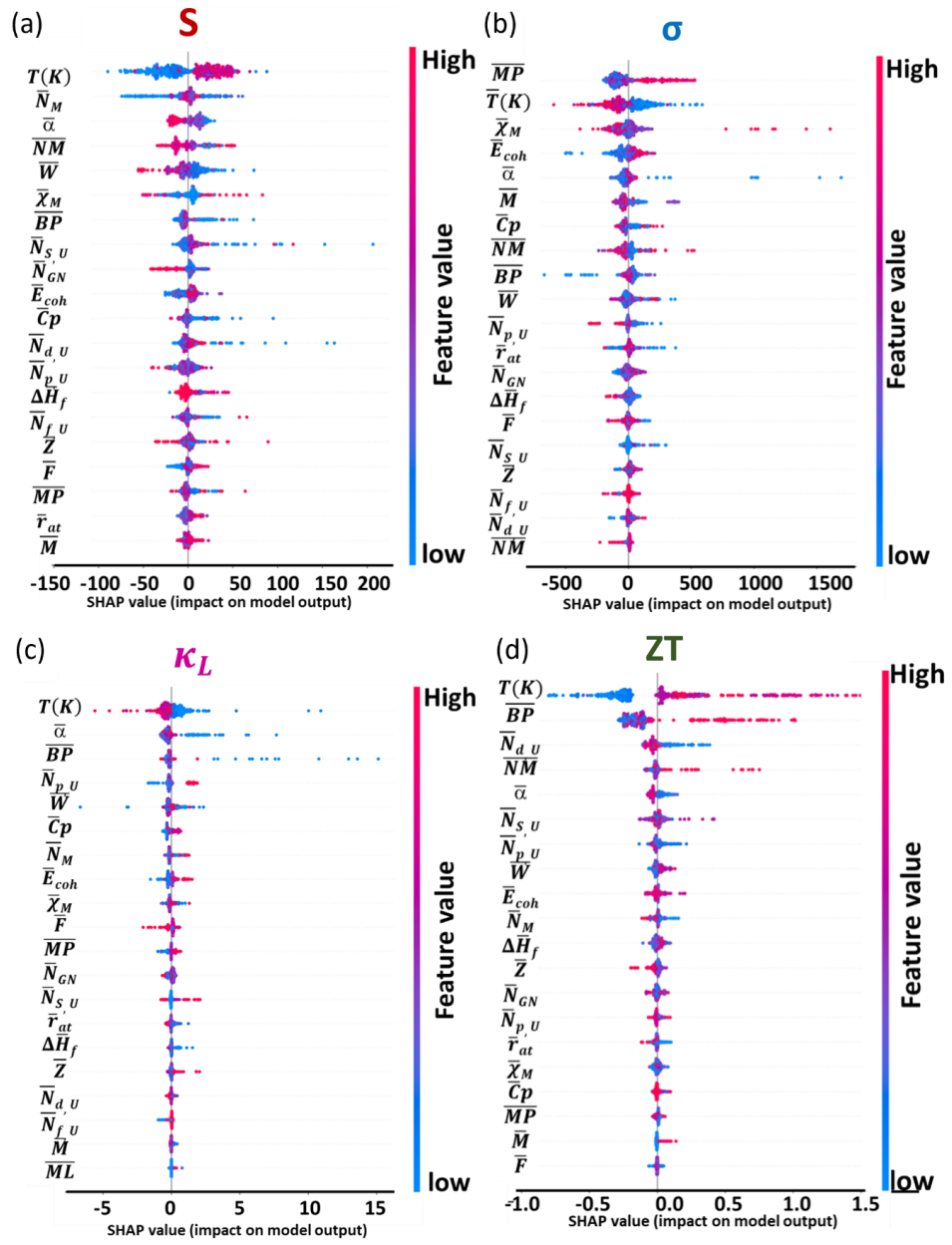


Figure 4.8: The SHAP beeswarm plot displays an information-dense summary of how individual feature in a dataset influences the prediction of the ML model, where each dot on the feature row represents a particular instance with its corresponding SHAP value for the prediction of (a) Seebeck coefficient (S), (b) electrical conductivity (σ), (c) lattice thermal conductivity (κ_L), and (d) figure of merit (ZT).

Moreover, the SHAP waterfall plots are analyzed to visualize the local interpretation of individual data points, as shown in **Figure 4.9**. The x-axis signifies a range of predicted values of target property and y-axis shows features along with their respective feature values. In this plot, $f(x)$ represents the predicted value of the model given input x, and $E[f(x)]$ represents the expected/baseline value of the target variable, which is the mean of all predictions. The direction and magnitude of each bar in the plot indicate the extent of influence of a feature value on output, with the length of bars either shifting towards a higher value (right-pointing red arrow) or lower value (left-pointing blue arrow) of the target output. The predicted value $f(x)$ of the model can be represented as:

$$f(x) = E[f(x)] + \sum_i^n Shap(i) \quad (1)$$

where, $E[f(x)]$ is the expected/baseline SHAP value of prediction and $\sum_i^n Shap(i)$ represents the sum of the SHAP values of each feature. In **Figure 4.9(a),** $\overline{BP}$, $\overline{r_{at}}$, α, $\overline{N}_{GN}$, and $\overline{F}$ features contribute positively to increase the Seebeck coefficient value from the base value $E[f(x)] = 184.59$. Therefore, the overall feature impact leads to an increase in $f(x) = 335.69$. In contrast, in the case of electrical conductivity (σ), thermal conductivity (κ_L), and power factor (PF), $f(x)$ values are lower than the $E[f(x)]$, indicating that the cumulative effect of the features causes a decrease in the overall outputs, as represented in **Figure 4.9(b-c)**. Nevertheless, in **Figure 4.9(d),** the $f(x)$ value increases from the base value due to the positive influences of $T(K)$, $\bar{\alpha}$, $\overline{ML}, \overline{N}_{d,U}$, and χ_M, all of which collectively contribute to an increase in ZT.

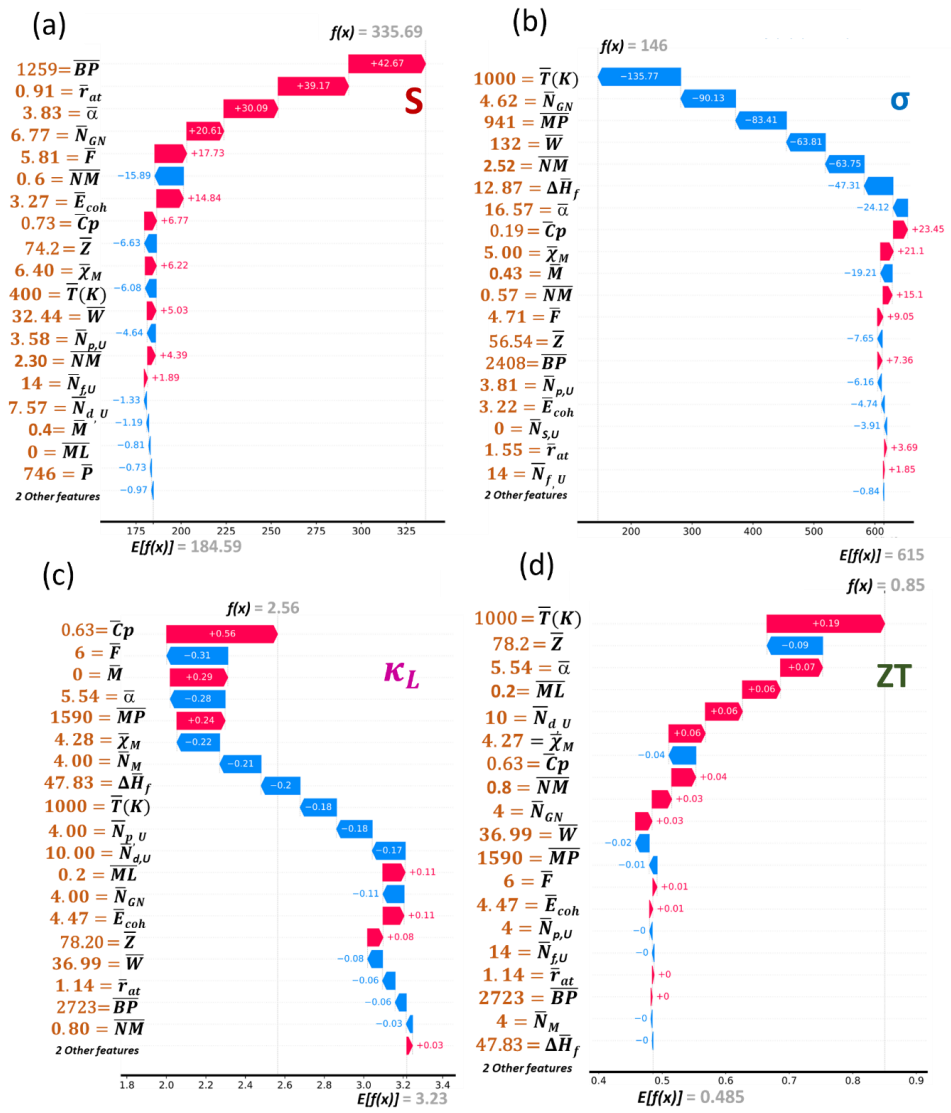


Figure 4.9: SHAP waterfall plots showing the local explanation for the prediction of (a) Seebeck coefficient (S), (b) electrical conductivity (σ), (c) thermal conductivity (κ_L), and (d) figure of merit (ZT). The $E[f(x)]$ stands for the expected value of model prediction and $f(x)$ indicates the final prediction. The red/blue color denotes positive/negative contribution of each feature towards the prediction.

Additionally, to shed more light on the role of influential features, we have visualized SHAP force plots that provide local explanations for individual

feature contribution to the XGBR model prediction of five TE properties for a specific instance as shown in **Figure 4.10**.

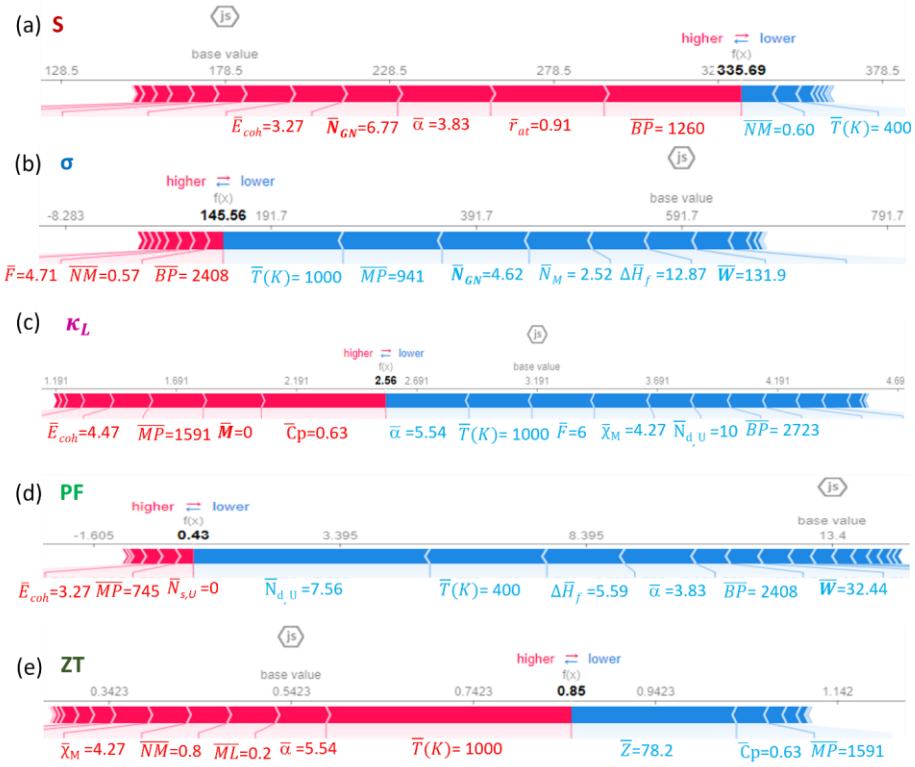


Figure 4.10: SHAP force plot for the prediction of (a) Seebeck coefficient, (b) electrical conductivity, (c) thermal conductivity, (d) power factor, and (e) figure of merit (ZT) for a particular instance. The base value indicates the average model predicted value and $f(x)$ denotes the final predicted value.

The plot highlights influential features that push the prediction value higher (toward right direction) than the base value (mean) are depicted in red color, while features responsible for driving the prediction lower (toward left direction) than the base value are presented in blue colour. The "tug-of-war" among important features, with some features pulling in one direction and others in the opposite, ultimately decides the predicted target value for each instance. For instance, in **Figure 4.10(e)**, T(K) feature with a feature value of 1000 is strongly pushing (largest arrow size) the ZT prediction away from

the base value (0.54) towards the XGBR model predicted value $f(x)$ of 0.85, while $\bar{Z}$ feature strongly driving the ZT prediction towards the lower value. Similarly, the features ($\overline{\alpha}$, $\overline{ML}$, $\overline{NM}$, and $\bar{\chi}_M$) are contributing towards higher ZT prediction, whereas features ($\overline{MP}$ and $\bar{C}_p$) are pushing for lower ZT prediction.

Table 4.5: Experimental (Exp) and Predicted (Pred) Values of ZT and $\kappa_L(Wm^{-1}K^{-1})$ for selected TE Materials with Chalcogens (Group 16 Elements) Termination

Sl. No	Formula	T(K)	ZT			κ_L $(Wm^{-1}K^{-1})$		
			Exp	Pred	Error	Exp	Pred	Error
1	$SrDy_{0.08}Ti_{0.92}O_3$	700	0.10	0.08	0.02	2.51	2.46	0.05
2	$Zn_{0.95}Al_{0.05}O$	300	0.02	0.03	-0.01	4.76	4.98	-0.22
3	$Ca_3Co_4O_9$	700	0.37	0.46	-0.09	1.47	1.37	0.1
4	$Ni_{2.0}Mo_6S_8$	1000	0.04	0.09	-0.05	0.37	1.05	-0.68
5	$Pb_{1.8}S_{1.8}Ti_2S_4$	300	0.06	0.06	0	0.24	0.23	0.01
6	$Cu_{4.0}Mo_6S_8$	700	0.26	0.61	-0.35	1.97	1.80	0.17
7	Cu_2Se	1000	1.90	1.21	0.69	0.27	0.26	0.01
8	$SnSe_{0.97}Br_{0.03}PbSe$	723	2.40	1.72	0.68	0.33	0.56	-0.23
9	$Ge_{0.92}Cr_{0.03}Bi_{0.05}Te$	623	2.00	2.08	-0.08	4.95	6.02	-1.07
10	$Ge_{0.9}Sb_{0.1}Te$	800	2.35	2.28	0.07	3.60	3.82	-0.22

Analysing ML-predicted results is crucial for understanding the quality of predicted materials and the reasons behind their high/low values of predicted properties. In this regard, we analyzed the XGBR model predicted ZT and κ_L values for an unknown test materials dataset at specific temperatures, as detailed in ref *[8]*. We observed that materials terminated with Se/Te demonstrated higher TE performance compared to O/S terminated materials. To further understand this effect, we conducted a comparison among the selected chalcogenide materials dataset, as shown in **Table 4.5**. The ML predicted ZT and κ_L values closely matched the experimental values. However, it can be noted that the ZT values were slightly underestimated for Cu_2Se and $SnSe_{0.97}Br_{0.03}PbSe$ materials, and κ_L

values were overestimated for $Ni_{2.0}Mo_6S_8$, and $Ge_{0.92}Cr_{0.03}Bi_{0.05}Te$ materials, which can be ascribed to diverse datasets.

The doped materials find widespread use in real-world applications and are particularly dominant among TE materials owing to their exceptional TE performances and stability. Our study aims to discover new doped materials with high TE properties with high ZT values by tuning suitable dopants with optimum composition using an inverse design methodology, which involves a material database-driven ML approach. Based on the test and validation results, it is evident that our model can effectively predict TE properties for unknown dopant compositions. We have prepared a database of 390 unknown materials by varying the doping ratio (making minute changes to the elemental composition) of already synthesized materials. The prediction of TE properties at temperature constraints of 300 K, 700 K, and 1000 K, represented in ref *[8]*.

Table 4.6: Predicted Top High-Performance Doped TE Materials with ZT, κ_L $(Wm^{-1}K^{-1})$, and S (μVK^{-1}) for at 300 K, 700 K, and 1000 K Selected from 390 Unknown Dataset

Sl. No	Formula	ZT			κ_L $(Wm^{-1}K^{-1})$		
		300 K	700 K	1000 K	300 K	700 K	1000 K
1	$Bi_{0.1}Sb_{1.9}Te_3$	1.74	2.08	2.20	0.40	0.37	0.40
2	$Bi_2Te_{2.8}Se_{0.2}$	1.25	-	-	0.89	-	-
3	$Bi_2Te_{1.7}Se_{1.3}$	1.19	-	-	1.62	-	-
4	$Sn_{0.90}Bi_{0.10}Se$	0.12	1.96	2.32	1.52	0.66	0.43
5	$Sn_{0.88}Se$	0.07	2.00	2.43	1.42	0.62	0.48
6	$Sn_{0.95}Na_{0.05}Se$	0.15	2.00	2.29	1.06	0.75	0.67
7	$Ge_{0.89}Cd_{0.03}Sb_{0.08}Te$	0.19	1.83	2.29	1.43	1.11	1.45
8	$Ge_{0.90}Sb_{0.07}In_{0.03}Te$	0.42	2.10	2.36	1.43	1.12	1.33
9	$Ge_{0.95}Sb_{0.05}Te$	0.24	1.86	2.33	1.51	1.26	1.48
10	$Pb_{0.953}Na_{0.04}Cd_{0.007}Te$	0.10	1.64	1.97	2.31	0.94	1.09

11	**$Pb_{0.95}Na_{0.05}Te$**	0.12	1.71	2.05	2.33	0.92	1.18
12	**$Pb_{0.95}Na_{0.05}Te_{0.10}Se_{0.90}$**	0.06	1.68	1.94	2.55	1.24	1.39

From this comprehensive predicted materials dataset, we have listed the best twelve predicted doped materials with high ZT and low κ_L values at 300K, 700K, and 1000K temperatures, as shown in **Table 4.6**. We have observed that the TE performance of these materials can be dramatically altered with a slight change in dopant concentration compared to their parent materials. These radical changes in κ_L of doped materials can be ascribed to the generation of point defects and boundary scattering *[23–25]*. The presence of defects target the higher-frequency phonons, whereas boundary defects target the lower-frequency phonons, resulting material to exhibit ultralow κ_L. We have identified $Bi_{0.1}Sb_{1.9}Te_3$ as top performing TE material with very high ZT values of 1.74, 2.08, and 2.20 at 300 K, 700 K, and 1000 K, respectively along with ultralow κ_L< 0.4 $Wm^{-1}K^{-1}$. This observation is also consistent with experimental reports on $Bi_{0.5}Sb_{1.5}Te_3$ material which has shown varying ZT values of 1.24 at 350 K and 1.86 at 320 K *[24, 25]*. Therefore, the high ZT value can be attributed to point defects created by Bi-Sb disorder that scatters heat carrying phonons, thereby reducing $\kappa_L$and allowing high ZT values. Se-doped $Bi_2Te_{2.8}Se_{0.2}$ and $Bi_2Te_{1.7}Se_{1.3}$ exhibit high ZT values of 1.25 and 1.19 at 300 K, along with low κ_L values. However, predicting ZT values for Bi_2Te_3-based compositions at high-temperature scales is not feasible due to their low melting point of 860 K *[25, 26]*. Bi/Na-doped SnSe materials have resulted in a significant increase in ZT (~2) and low κ_L above 700 K *[27, 28]*. Thus, the doping effect in parent materials such as Sb_2Te_3, Bi_2Te_3, and SnSe have been observed to increase the scattering rate, leading to lower κ_L values with higher ZT across a wide temperature range. In contrast, co-doped with (Cd/Sb and Sb/In) in GeTe and (Na/Cd/Se) in PbTe has led to higher ZT and κ_L values at higher temperatures. Permula et al. experimentally demonstrated that $Ge_{0.9}Sb_{0.1}Te$ exhibited higher ZT value than

$Ge_{0.95}Sb_{0.05}Te$ at 725 K *[29]*. For the $Ge_{0.95}Sb_{0.05}Te$ composition, our model predicts a ZT value of 1.86 at 700 K, which is comparable to the experimentally reported ZT value of 1.85 at 725 K for $Ge_{0.90}Sb_{0.10}Te$ *[29]*. This signifies the importance of precise changes in composition and temperature in achieving different ZT value. The doping in GeTe/PbTe could tune their electronic band structure, which in turn facilitates the conduction of the heavy hole valence band over the light hole valence band, leading to a high-power factor *[30–33]*. These doped GeTe and PbTe exhibit higher κ_L values and lower ZT at 300 K but their ZT values increase notably from 700 K onwards indicating an effective strategy with enhanced power factor.

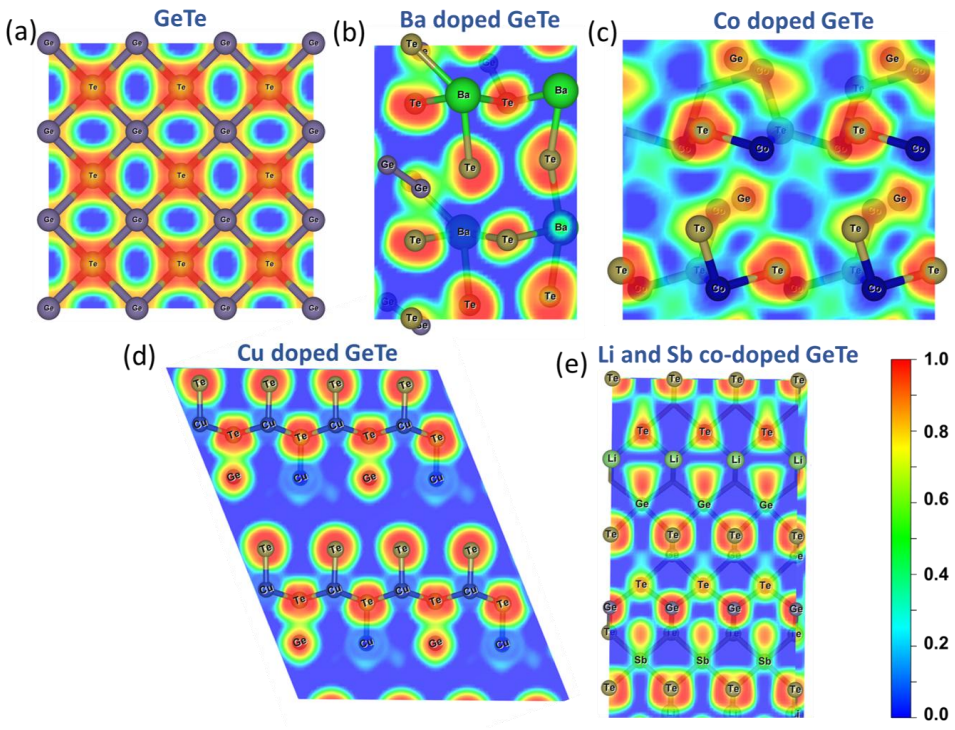


Figure 4.11: The calculated electron localization function (ELF) at isosurface value of 0.75 eV/Å^3 for (a) pristine GeTe, (b) Ba doped GeTe, (c) Co doped, (d) Cu doped GeTe, and (e) Li/Sb co-doped GeTe revealing the presence of lone pairs around Te atoms.

Additionally, the TE performance influenced by the presence of lone pairs and weak bonding, which leads to high polarizability ($\bar{\alpha}$) *[34]*. These lone pairs create strong distortion around the metal atom and lower the structural symmetry contributing to higher anharmonicity and low κ_L *[25]*. To get more insights about the role of such lone pair of electrons, we have performed electron localization function (ELF) studies on GeTe and doped GeTe materials based on the above discussion to verify the presence of lone pairs as shown in **Figure 4.11**. Here, we observe that the Ge and Sb contain cationic and anionic Te lone pairs, which contribute to lowering the κ_L. Whereas these dopants provide the additional route that either engineer the electronic transport properties or act as defects that further restrict the heat-carrying phonon pathways.

4.3.2. Machine Learning Classification

From ML prediction of all key TE properties, a noteworthy pattern emerges that chalcogenide termination has a strong influence on the TE performance of materials. Building upon the insights from regression analysis, we have attempted to classify TE materials according to their performance, with a particular focus on materials terminated with chalcogens. This classification can serve as a different perspective to understand elemental compositions and termination strategies that contribute to shaping the TE properties of materials. To facilitate the study, we have tailored two different types of datasets from our total database: (i) dataset-A: Structured around elemental composition-based descriptors, providing insights into the influence of different elements on TE performance, and dataset-B: Focused on TE properties of chalcogenide (oxides, sulphides, selenides, and tellurides) materials. Further, we have evaluated the performance accuracy of five different classifier algorithms (RFC, LR, SVM, KNN, and DTC) as available in the sci-kit learn library *[20]*. The details regarding the

optimized hyperparameters of considered models and their accuracy scores for both datasets are provided in **Table 4.7-4.8**.

Table 4.7: List of Optimized Hyperparameters Considered for ML Classification with **"Dataset-A"** Model, Anong with Corresponding Test Accuracy Score

Sl. No.	ML models	Optimized Hyperparameters	Test Accuracy
1	**RFC**	'bootstrap': True, 'ccp_alpha': 0.0, 'class_weight': None, 'criterion': 'gini', 'max_depth': None, 'max_features': 'sqrt', 'max_leaf_nodes': None, 'max_samples': None, 'min_impurity_decrease': 0.0, 'min_samples_leaf': 1, 'min_samples_split': 2, 'min_weight_fraction_leaf': 0.0, 'n_estimators': 50, 'n_jobs': None, 'oob_score': False, 'random_state': None, 'verbose': 0, 'warm_start': False	**100%**
2	**DTC**	'ccp_alpha': 0.0, 'class_weight': None, 'criterion': 'gini', 'max_depth': None, 'max_features': None, 'max_leaf_nodes': None, 'min_impurity_decrease': 0.0, 'min_samples_leaf': 1, 'min_samples_split': 2, 'min_weight_fraction_leaf': 0.0, 'random_state': None, 'splitter': 'best'	**83%**
3	**KNN**	'algorithm': 'auto', 'leaf_size': 30, 'metric': 'minkowski', 'metric_params': None, 'n_jobs': None, 'n_neighbors': 3, 'p': 2, 'weights': 'uniform'	**79%**
4	**SVM**	'C': 0.1, 'break_ties': False, 'cache_size': 200, 'class_weight': None, 'coef0': 0.0, 'decision_function_shape': 'ovr', 'degree': 3, 'gamma': 'scale', 'kernel': 'linear', 'max_iter': -1, 'probability': False, 'random_state': None, 'shrinking': True, 'tol': 0.001, 'verbose': False	**88%**
5	**LRC**	'C': 0.1, 'class_weight': None, 'dual': False, 'fit_intercept': True, 'intercept_scaling': 1, 'l1_ratio': None, 'max_iter': 100, 'multi_class': 'auto', 'n_jobs': None, 'penalty': 'l2', 'random_state': None, 'solver': 'lbfgs', 'tol': 0.0001, 'verbose': 0, 'warm_start': False	**92%**

Table 4.8: List of Optimized Hyperparameters Considered for ML Classification with **"Dataset-B"** Model, Anong with Corresponding Test Accuracy Score.

Sl. No.	ML models	Optimized Hyperparameters	Test Accuracy
1	**RFC**	'bootstrap': True, 'ccp_alpha': 0.0, 'class_weight': None, 'criterion': 'gini', 'max_depth': None, 'max_features': 'sqrt', 'max_leaf_nodes': None, 'max_samples': None, 'min_impurity_decrease': 0.0, 'min_samples_leaf': 1, 'min_samples_split': 2, 'min_weight_fraction_leaf': 0.0, 'n_estimators': 100, 'n_jobs': None, 'oob_score': False, 'random_state': None, 'verbose': 0, 'warm_start': False	**96%**
2	**DTC**	'ccp_alpha': 0.0, 'class_weight': None, 'criterion': 'gini', 'max_depth': 5, 'max_features': None, 'max_leaf_nodes': None, 'min_impurity_decrease': 0.0, 'min_samples_leaf': 1, 'min_samples_split': 2, 'min_weight_fraction_leaf': 0.0, 'random_state': None, 'splitter': 'best'	**88%**
3	**KNN**	'algorithm': 'auto', 'leaf_size': 30, 'metric': 'minkowski', 'metric_params': None, 'n_jobs': None, 'n_neighbors': 7, 'p': 2, 'weights': 'uniform'	**50%**
4	**SVM**	'C': 1, 'break_ties': False, 'cache_size': 200, 'class_weight': None, 'coef0': 0.0, 'decision_function_shape': 'ovr', 'degree': 3, 'gamma': 'scale', 'kernel': 'linear', 'max_iter': -1, 'probability': False, 'random_state': None, 'shrinking': True, 'tol': 0.001, 'verbose': False	**88%**

5	**LRC**	'C': 1, 'class_weight': None, 'dual': False, 'fit_intercept': True, 'intercept_scaling': 1, 'l1_ratio': None, 'max_iter': 100, 'multi_class': 'auto', 'n_jobs': None, 'penalty': 'l2', 'random_state': None, 'solver': 'lbfgs', 'tol': 0.0001, 'verbose': 0, 'warm_start': False	**88%**

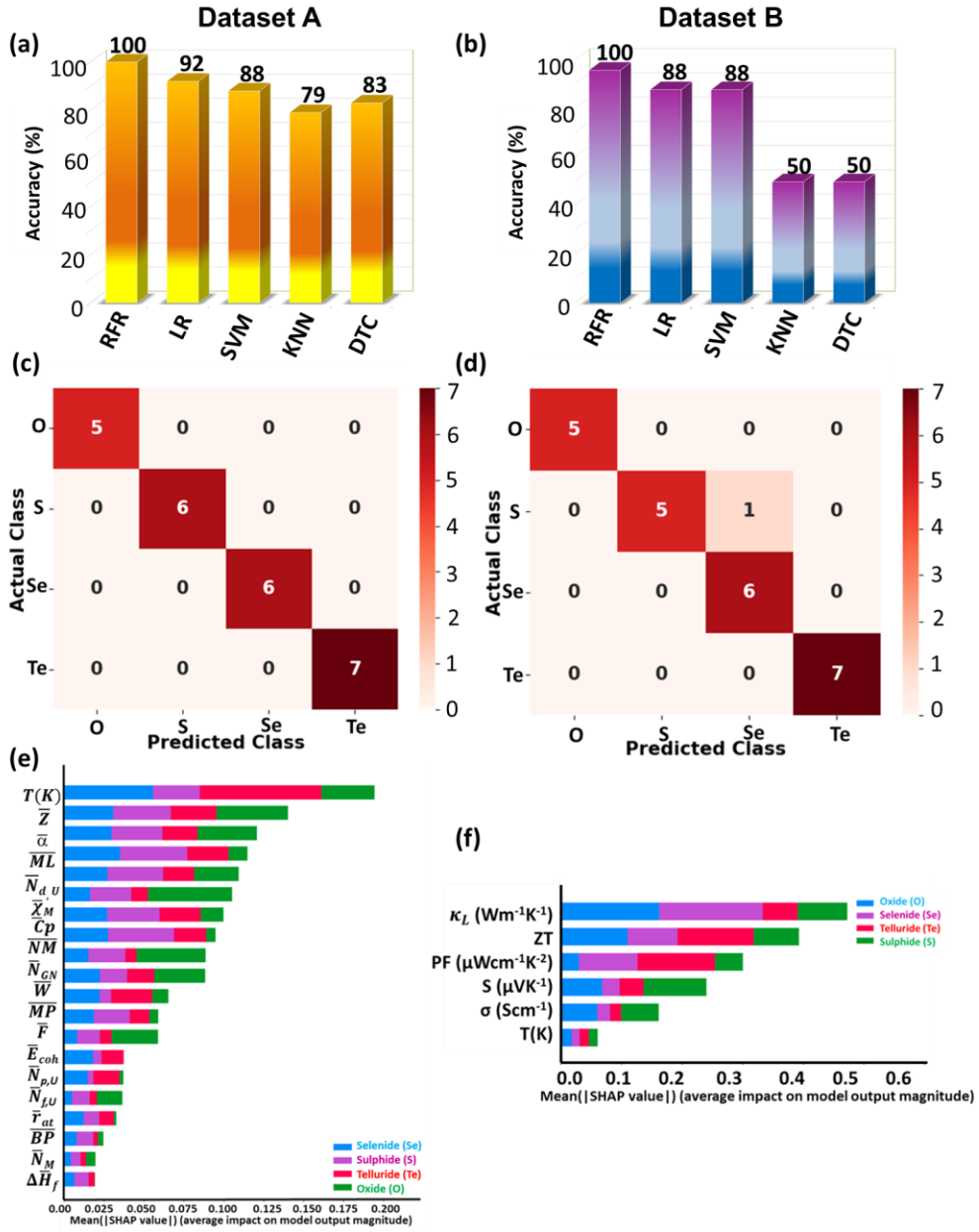


Figure 4.12: The ML classification analysis. Train-test accuracy (%) score of considered ML models with (a) 'dataset-A' based on elemental composition descriptors and (b) 'dataset-B' based on their five TE properties as descriptors for all four chalcogenides TE materials. (c-d) confusion matrix of quaternary classification, and (e-f) SHAP feature importance plot of RFC model with dataset-A and dataset-B, respectively.

The RFC model has classified the oxides, sulphides, selenides, and tellurides classes with best test accuracy scores of 100% with ‘dataset-A’ and 95.80% with ‘dataset-B’, highlighting its proficiency in ML classification. With ‘dataset-B’, the S terminated material is misclassified as Se terminated material, which is a reason behind the drop in RFC accuracy compared to ‘dataset-A’ as evident from **Figure 4.12(c-d)**. Expanding on our discussion, we have also discussed binary classification in **Figure 4.13**.

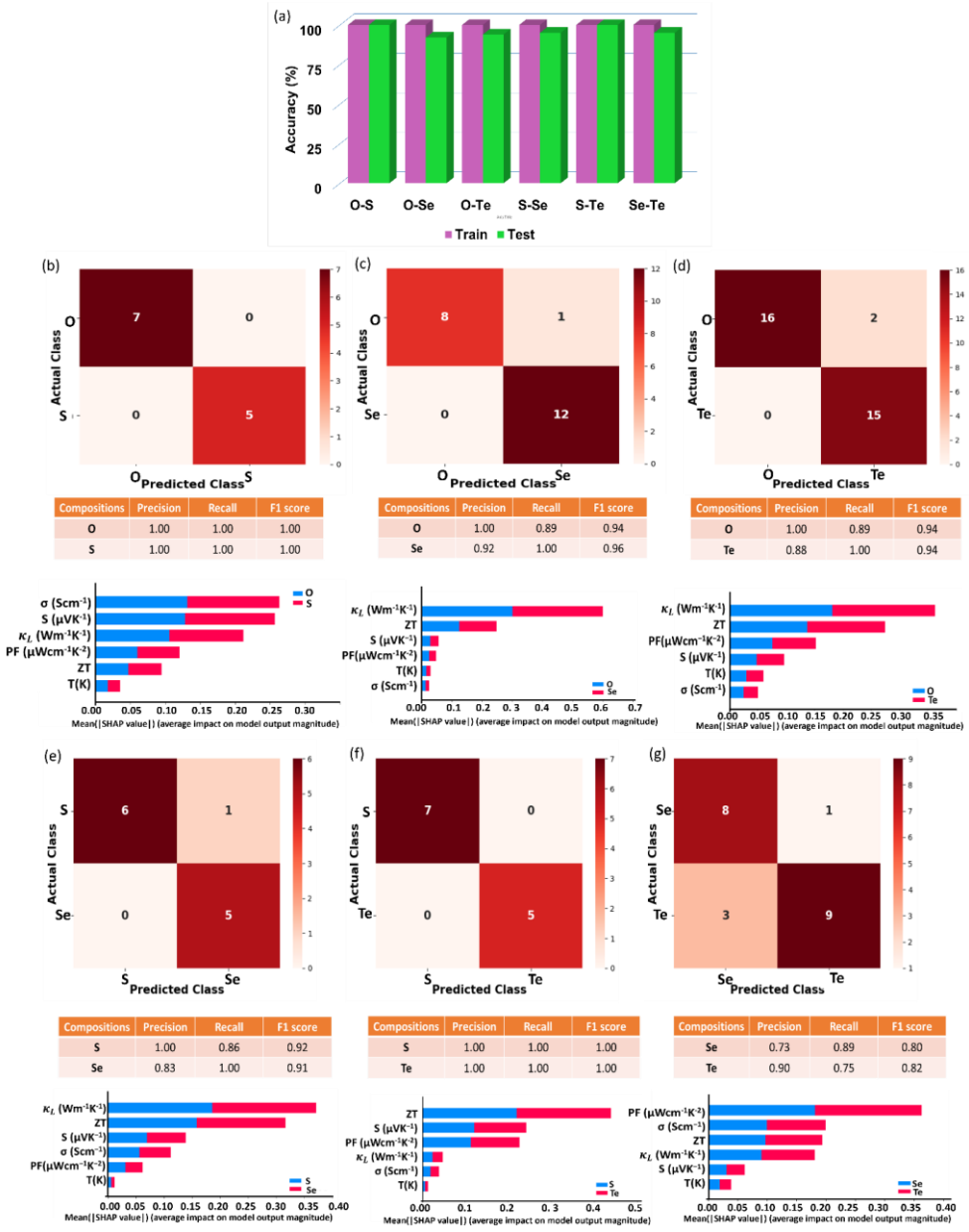


Figure 4.13: The ML binary classification of chalcogenide terminated thermoelectric materials with **"Dataset-B"**: (a) the train-test accuracy for best fitted RFC model of all six combinations "O-S", "O-Se", "O-Te", "S-Se", "S-Te", and "Se-Te"; the confusion matrix of binary classification along with their classification report, and SHAP feature importance plot for (b)"O-S", (c) "O-Se", (d) "O-Te", (e) "S-Se", (f) "S-Te", and (g) "Se-Te".

To delve into the role of features in RFC classification, we constructed SHAP (SHapley Additive exPlanations) feature importance plots which offer a global perspective on each feature role in predicting each class independently within ML model. **Figure 4.12(e-f)** shows the feature importance plot of various features of 'dataset-A' and 'dataset-B', respectively. Notably, the '$T(K)$' feature has emerged to have the highest influence on RFC prediction, particularly dominating the identification of Te terminated materials. This observation is also in agreement with our regression results, as shown in **Figure 4.12(e)**. Moreover, the strong impact of average composition atomic number '$\bar{Z}$', metalloids '$\overline{ML}$', and polarizability '$\bar{\alpha}$' descriptors could be attributed to their robust correlation with thermoelectric (TE) properties, highlighting their important role in classifying the TE materials. On the other hand, thermal conductivity (κ_L) descriptor has a strong impact on the RFC classification of chalcogenide materials with 'dataset-B'. Surprisingly, the temperature 'T(K)' demonstrates the least influence on the prediction. Interestingly, both 'κ_L' and 'ZT' descriptors are mainly driving the classification of four classes. Additionally, the 'PF' is noted to be biased towards Se and Te class, whereas 'S' and 'σ' are biased towards the oxide(O^{2-}) and sulphide(S^{2-}) class of materials. Thus, we believe that these findings contribute to a deeper understanding of TE materials and pave the way for the targeted design of materials with enhanced TE properties.

4.4. Summary

In summary, we develop a machine-learning framework that establishes quantitative relationships between doped compositions and five thermoelectric properties, elucidating the role of dopant ratios in enhancing thermoelectric performance. The model is trained on a diverse experimental database comprising chalcogenides (GeTe, SnTe, PbTe, $Sn_{1-x}Se$, $Bi_{2-x}Sb_xTe_3$), skutterudites ($CoSb_3$), clathrates ($Ba_8Ga_{16}Ge_{30}$), and transition-

metal chalcogenides across a wide temperature range. Validation on an unseen dataset of 120 compounds shows strong agreement with experiments. Leveraging this validated model, we screen 390 unexplored doped systems and identify $Bi_{0.1}Sb_{1.9}Te_3$ as the top performer, exhibiting ultralow lattice thermal conductivity (<0.4 W m^{-1} K^{-1}) and high ZT values up to 2.20. Doping-induced phonon scattering and electronic band tuning collectively enhance thermoelectric efficiency, while classification further reveals termination-dependent performance trends.

Section-B

4.5. Introduction

The fundamental strategies to achieve the low κ_L focused on discovering new crystalline materials with specific structural and electronic features such as layered structure, *[35]* rattling atoms, *[36]* lone-pair effects, *[22]* and liquid-like ionic movements *[37*. Additionally, introducing extrinsic point defects,*[38]* nanostructuring,*[39]* and all scale hierarchical architectures*[40]* have been explored. In each case, understanding the structure-bonding relationships within specific material classes is paramount for identifying the mechanisms responsible for their intrinsically low κ_L values.

Skoug and Morelli have demonstrated a correlation between lone pair electrons, particularly the ns^2 pairs in the pnictogen chalcogenides, and their intrinsically low κ_L *[41]*. The presence of the pnictogen group (As, Sb, Bi) in a +3 oxidation state introduces local structural anharmonicity due to the presence of stereochemically active lone pairs (SCALPs), a critical factor in realizing materials with ultralow κ_L *[41]*. The lone pair electrons interact with the valence electrons of chalcogen atoms through electrostatic repulsion, causing lattice anharmonicity, which can be qualitatively explained by the morphology of the electron lone pair orbital cloud *[42]*. It has been demonstrated that this effect is more pronounced in $A^IB^VX^{VI}$ materials compared to $A^IB^{III/V}X^{VI}$ materials (A^I: monovalent, B^{III}: trivalent,

B^{V}: pentavalent, and X^{VI}: chalcogen elements), where the intrinsically low κ_L is substantially affected by SCALPs. For example, the $AgSbSe_2$ (Sb^{3+} has a SCALP) exhibits significantly lower κ_L values of 0.7 $Wm^{-1}K^{-1}$ compared to 1.7 $Wm^{-1}K^{-1}$ of $AgInSe_2$ (In^{3+} does not have a SCALP) *[43]*. Additionally, Cu_3SbSe_4 (with Sb^{5+} cations) has a thermal conductivity of 2.5–3.5 $Wm^{-1}K^{-1}$, much higher than Cu_3SbSe_3 (with Sb^{3+} cations) at 0.7–1.0 $Wm^{-1}K^{-1}$ at room temperature, even though both pnictogen chalcogenides contain the same elements and have similar stoichiometry *[44, 45]*. According to the revised lone-pair model, the energy gap between the outermost s and p orbitals of pnictogen cations plays a crucial role in the formation of SCLAPs *[46]*. Although significant, the influence of SCALPs on low κ_L values originating from the nature of chemical bonding remains an elusive aspect in materials science and requires further investigation *[43, 47–49]*. These materials have appeared as the building blocks for the development of efficient energy devices, including thermoelectrics, solar cells, optoelectronic devices, and photocatalysis owing to their semiconducting properties, unique crystal structure, and tune-able stoichiometric composition *[26, 35, 50–53]*.

Understanding the correlation between SCALPs and κ_L is crucial for discovering new materials with high thermoelectric performances. However, microscopic insights into how SCALPs affect chemical bonding and enhance anharmonicity remain obscure. Moreover, detailed investigations into lattice structures and chemical bonding are necessary to uncover these relationships within the vast chemical space of the material genome. Recently, machine learning (ML) has emerged as a powerful technique with successful applications in various fields, including materials science, catalysis,*[54–56]* design of crystal structures, *[57, 58]* and prediction of material properties *[59, 60]*. This advancement enables ML to provide insights into the complex relationships between composition and

properties *[61, 62]*, particularly valuable for understanding the behavior of materials with SCALPs and low κ_L.

In this section, we focus on the chemistry of SCALPs of pnictogen cations, which impacts the intrinsic κ_L in the screened pnictogen chalcogenide material dataset. We demonstrated that integrating chemical bonding descriptors, such as structural, bonding, electronic, and orbital energies, significantly improves ML prediction compared to conventional features. These chemical bonding descriptors can be regarded as performance indicators that directly capture the SCALP and chemical bonding hierarchies to screen the materials with low κ_L values. Furthermore, we expanded our predictive analysis to estimate κ_L values for 245 unexplored materials and identified the best five materials exhibiting ultralow κ_L (< 0.40 $Wm^{-1}K^{-1}$). We have extended our dataset to demonstrate the capabilities of chemical bonding descriptors to capture the bonding environment of non-SCALP materials. Additionally, we investigated the origins of SCALPs by delineating the specific ranges for ionicity (r_σ), hybridization (r_π), and polarizability ($\overline{\alpha}$) required for ultralow κ_L at room temperature. This study defines the systematic changes in bonding, structure, and physical properties necessary to achieve a low κ_L.

4.6. Dataset Design for Machine Learning

To design our material dataset with a focus on investigating SCALPs, we established specific criteria for the material selection. To encode this crucial phenomenon, our initial design space encompasses a wide range of materials sourced from three different databases: the Open Quantum Materials Database (OQMD), *[60]* the Materials Project (MP), *[4]* and the experimentally reported κ_L values reported in the literature (κ_L^{Exp}) *[41, 63]*. We refined this dataset based on screening criteria inspired by Petrov and Shtrum, focusing on the lone pair effect in pnictogens as illustrated in **Figure 4.14** *[42]*.

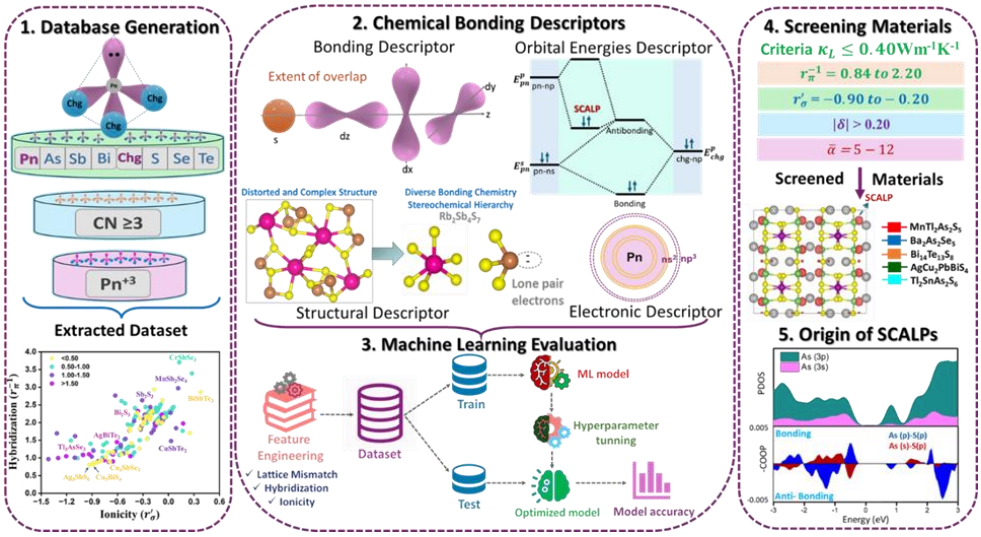


Figure 4.14: Illustrative workflow for ML screening of pnictogen (Pn) chalcogenide (Chg) materials with ultralow κ_L values. The workflow illustrated the screening of pnictogen chalcogenides with pnictogen atoms in the +3-oxidation state. The feature space was designed using chemical bonding descriptors to reveal the role of stereochemically active lone pairs (SCALPs).

According to these criteria, the material must: (i) include at least one pnictogen element (As, Sb, and Bi) in the +3 oxidation state, (ii) contain one or more chalcogen elements (S, Se, Te) excluding the radioactive elements and (iii) have each pnictogen atom must be bonded to a chalcogen atom with a coordination number ≥3. The screened database comprises 478 pnictogen chalcogenide materials. Within this database, 233 chalcogenides have been reported with κ_L at a temperature of 300 K. The elemental distribution of the dataset revealed 47% Bi, 40% Sb, and 13% As compositions, along with chalcogen ratios of 37% Te, 41% Se, and 22% S, indicating the prevalent ternary configurations (**Figure 4.15**). Additionally, we prepared another dataset of 245 materials with unknown κ_L values for predictive analysis at 300 K, which will be discussed in a later section.

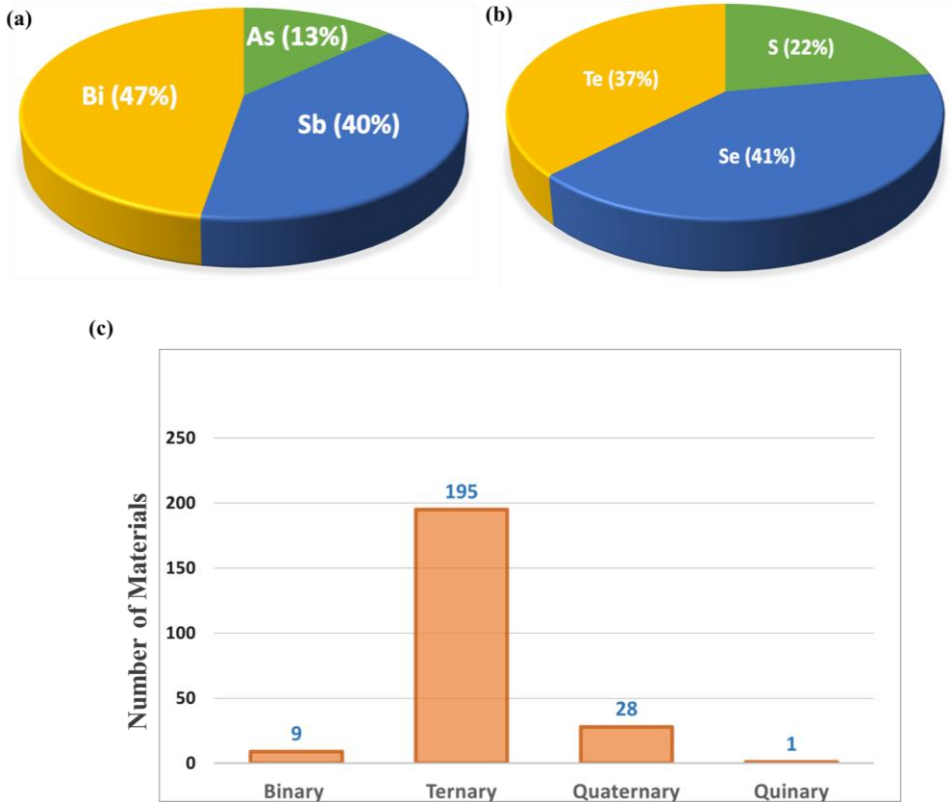


Figure 4.15: Distribution of 233 materials in terms of (a) pnictogen cation (b) chalcogen anion element proportion in materials, and (c) number of constituent elements in the composition.

4.7. Descriptor Designing

Incorporating physical and chemical properties into ML models has proven to be highly effective for enhancing prediction accuracy. In this study, we focused on descriptors related to SCALPs and chemical bonding hierarchies that define the chemical environment, as these are key factors for directly identifying materials with low κ_L in complex chalcogenides. Each of the chemical bonding descriptors utilized in our study is listed in **Table 4.9**.

Table 4.9: List of All Considered Chemical Bonding Descriptors.

S.No.	Descriptors	Symbols
1	Total number of anions and cations	N
2	Mismatch	δ

3	Average atomic weight	$\overline{Z}$
4	Average s valence electron	$\overline{V}_s^{e-}$
5	Average p valence electron	$\overline{V}_p^{e-}$
6	Pnictogen s+p energy	E_{pn}^{s+p}
7	Chalcogen s+p energy	E_{chg}^{s+p}
8	Pnictogen s energy	E_{pn}^{s}
9	Chalcogen s energy	E_{chg}^{s}
10	Pnictogen p energy	E_{pn}^{p}
11	Chalcogen p energy	E_{chg}^{p}
12	Average pnictogen and chalcogen electronegativity	$\overline{\chi}_{pn-chg}$
13	Pnictogen and chalcogen electronegativity difference	$\Delta\chi_{pn-chg}$
14	Ionicity	r'_{σ}
15	Hybridization	r_{π}^{-1}
16	Ratio of +3 pnictogen and -2 chalcogen	$r_{pn}^{+3}: r_{chg}^{-2}$
17	Average ionic character	$\overline{IC}$
18	Average polarizability	$\overline{\alpha}$
19	Covalent radii	r_c

4.7.1. Bonding Descriptors: Wuttig and coworkers have demonstrated a unique fingerprint for understanding the bonding characteristics, defined by two key parameters: the **degree of ionicity (r'_{σ})** and the tendency toward **hybridization (r_{π}^{-1})** in the bonding.[45] The parameter r'_{σ} quantitatively measures the ionicity of bonds, while r_{π}^{-1} describes the extent of covalency, which can be inferred from the energetic splitting of the s- and p-states, and their relative energy is critical for SCALP formation (**Figure 4.16**) *[23]*.

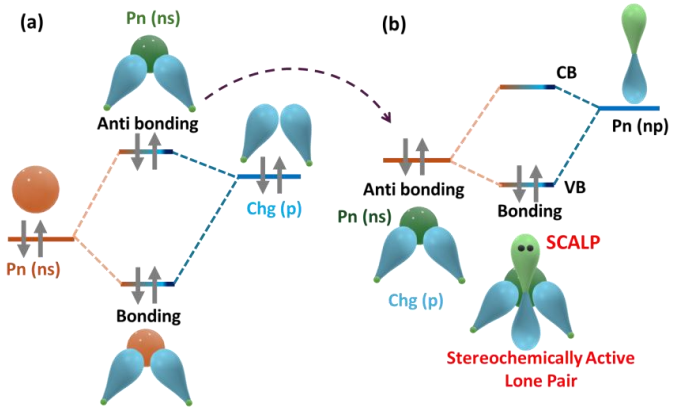


Figure 4.16: Schematics of energy level diagram illustrating stereochemically active lone pairs (SCALP) in pnictogen (Pn) chalcogenide (Chg) materials. **(a)** Orbital interactions between the Pn(ns) and Chg(p) orbitals lead to the formation of filled bonding and antibonding combinations. Owing to the lower energy of Pn(ns) compared to the Chg(p) states, the bonding combination predominantly exhibits Pn(ns) character, and the antibonding combination contains Chg(p) states. **(b)** The anti-bonding combination is stabilized by orbital coupling with Chg(p), resulting in a filled upper valence band (VB). The contribution of the Chg(p) orbitals to the upper VB creates an asymmetric electron density on Pn, resulting in a stereochemically active lone pair (SCALP).

Furthermore, these parameters reflect the contribution of orbital radii to the bonding characteristics, specifically indicating the presence or absence of sp hybridized bonds between the pnictogen and chalcogen elements. These parameters are defined as:

$$r'_{\sigma} = \left(\frac{\sum_i n_i r_{p,i}}{\sum_i n_i}\right) - \left(\frac{\sum_j n_j r_{p,j}}{\sum_j n_j}\right)$$

$$r_{\pi}^{-1} = \left[\left(\frac{\sum_i n_i (r_{p,i} - r_{s,i})}{\sum_i n_i}\right) - \left(\frac{\sum_j n_j (r_{p,j} - r_{s,i})}{\sum_j n_j}\right)\right]^{-1}$$

Here, r_p and r_s denote the valence radii of the p- and s- orbitals of atoms, summed over the i^{th} and j^{th} atoms of the material *[64, 65]*. The **average polarizability ($\bar{\alpha}$)** defines the localization of electronic density. These coordinates address the case of covalent bonding with unsaturated bonds with resonance bonding in a crystalline state.

4.7.2. Structural Descriptors: This includes the number **mismatch (δ)** between cations and anions, also reported as a performance indicator for κ_L in chalcogenides where the κ_L decreases with an increase in a number mismatch ($|\delta|$), demonstrating local distortions, rattling effects, and lone pairs (SCALP) *[66]*. The number mismatch (δ) is defined as:

$$\delta = \frac{N_{cation} - N_{anion}}{N_{anion}}$$

where N_{cation} and N_{anion} denote the number of cationic and anionic species in the formula unit, respectively *[66]*. Next, the complex crystal structure with a large number of atoms in the unit cell ($\boldsymbol{N}$) also affects κ_L. Moreover, the range of covalent radii ($\boldsymbol{r_c}$) describes the overall bond strength of pnictogen chalcogenides.

4.7.3. Orbital Energy Descriptors: The formation of SCALPs and the associated distorted crystal structure are influenced by the interaction strength between the cation s and the anion p orbitals, along with their relative energies, as depicted in **Figure 4.16**. According to the revised lone-pair model, closer energies between these states suggest stronger interactions, leading to more pronounced cation states in the upper valence band and the formation of an active lone pair *[46]*. As we descend in the chalcogen group (S to Te), the interaction strength between anion p states and pnictogen ns states weakens, leading to reduced on-site hybridization and less effective lone pairs. The weakening of these interactions can be analyzed by examining the orbital energies of the pnictogen and chalcogen valence shells for s **($\boldsymbol{E^s_{pn}}$, $\boldsymbol{E^s_{chg}}$)**, p **($\boldsymbol{E^p_{pn}}$, $\boldsymbol{E^p_{chg}}$)**, and s+p **($\boldsymbol{E^{s+p}_{pn}}$, $\boldsymbol{E^{s+p}_{chg}}$)** *[46]*.

Electronic Descriptors: The electronic descriptors account for the average valence electron configurations from s orbital ($\overline{V}_s^{e-}$) and p orbital ($\overline{V}_p^{e-}$), which are essential for understanding their bonding and thermal properties. Additionally, we have incorporated the average and difference of electronegativity between pnictogen and chalcogen elements ($\overline{\chi}_{pn-chg}$)/$\Delta\chi_{pn-chg}$, as well as the ratio of atomic radii of pnictogen and chalcogen (r_{pn}^{+3}: r_{chg}^{-2}), and average atomic weight ($\overline{Z}$) *[67]*. For a detailed comparison, we have also included common conventional features, generated by transforming the chemical compositions of materials into usable input features using composition-based feature vectors (**Table 4.10)** *[11]*.

Table 4.10: List of All the Considered Conventional Features.

S.No.	Descriptors	Symbols
1	Average atomic weight	$\overline{Z}$
4	Average Family	$\overline{F}$
5	Average Metal	$\overline{M}$
6	Average Metalloid	$\overline{ML}$
7	Average atomic Radius	$\bar{r}$
8	Average Mulliken electronegativity	$\overline{\chi}_m$
9	Average Metallic valence	$\overline{M}_v$
10	Average s electron	$\overline{V}_s^{e-}$
11	Average p electron	$\overline{V}_p^{e-}$
12	Average d electron	$\overline{V}_d^{e-}$
13	Average Melting Point	$\overline{MP}$
14	Average Boiling Point	$\overline{BP}$
15	Average polarizability	$\overline{\alpha}$
16	Average Specific heat	$\overline{C}$
17	Average Cohesive Energy	$\overline{E}_C$

Subsequently, we characterized the correlation between features and their impact on κ_L values within the dataset using Pearson's and Spearman's correlation matrices for both conventional features and chemical bonding descriptors, as shown in **Figure 4.17-4.21** *[13, 14]*.

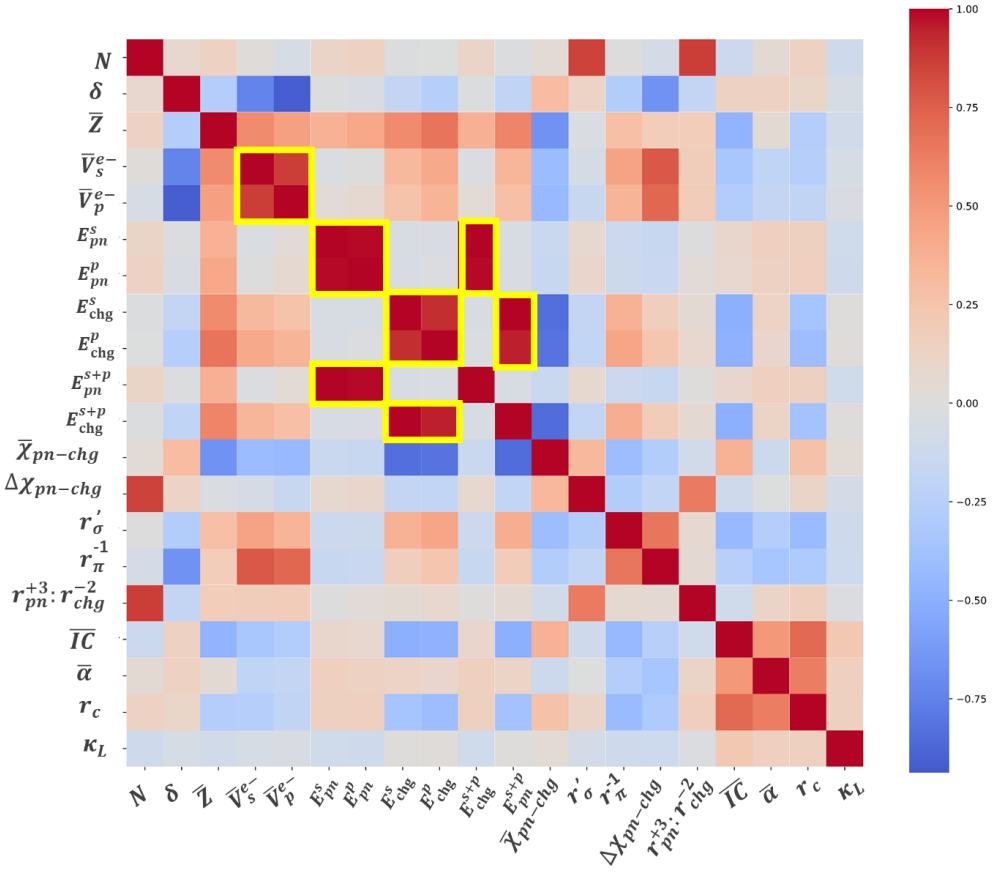


Figure 4.17: The Pearson correlation coefficient (PCC) represents the considered feature-feature and feature-target (κ_L) relationship for chemical bonding descriptors. The color represents the direction and range of the correlation, where dark red and dark blue signifies the perfect positive (+1) and perfect negative (-1) correlation.

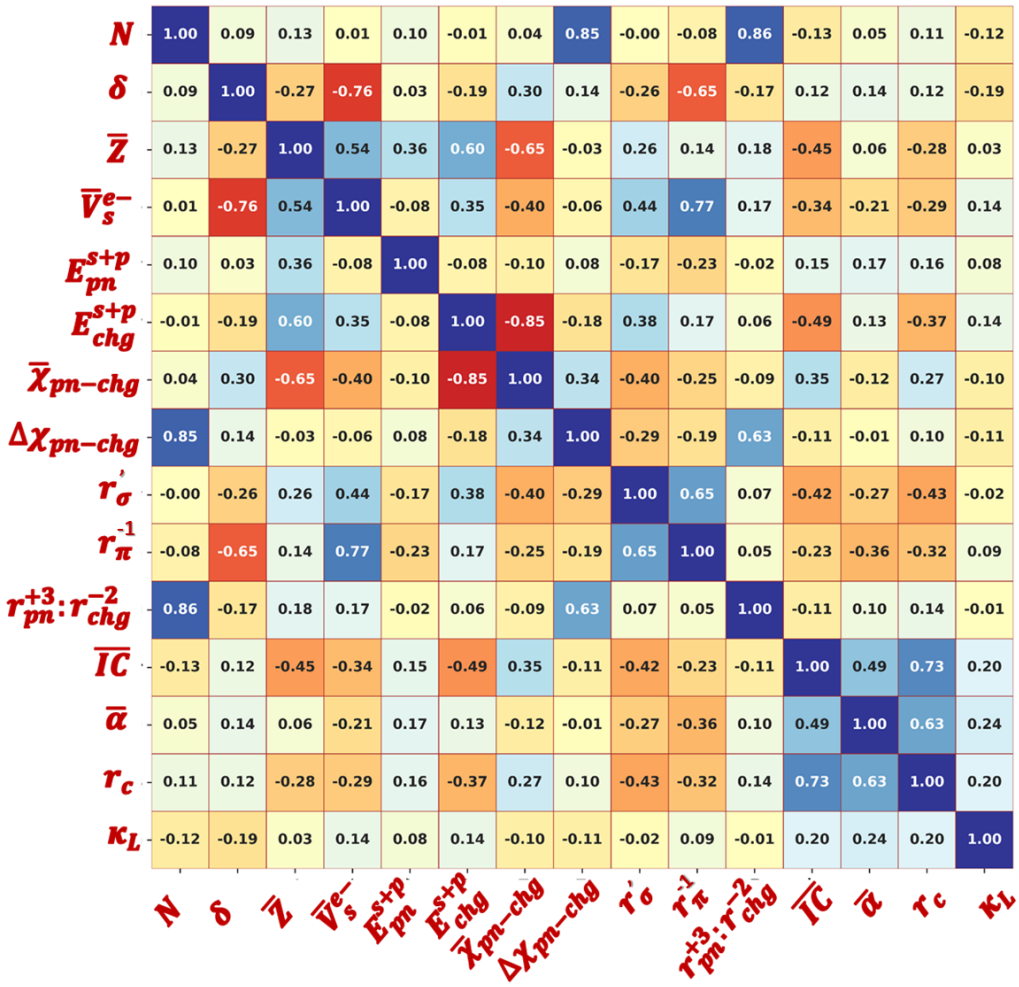


Figure 4.18: The Pearson correlation coefficient (PCC) represents the feature-feature and feature-target (κ_L) relationship for chemical bonding descriptors after removing highly correlated features. The color represents the direction and range of the correlation, where dark purple and pale yellow signifies the perfect positive (+1) and perfect negative (-1) correlation.

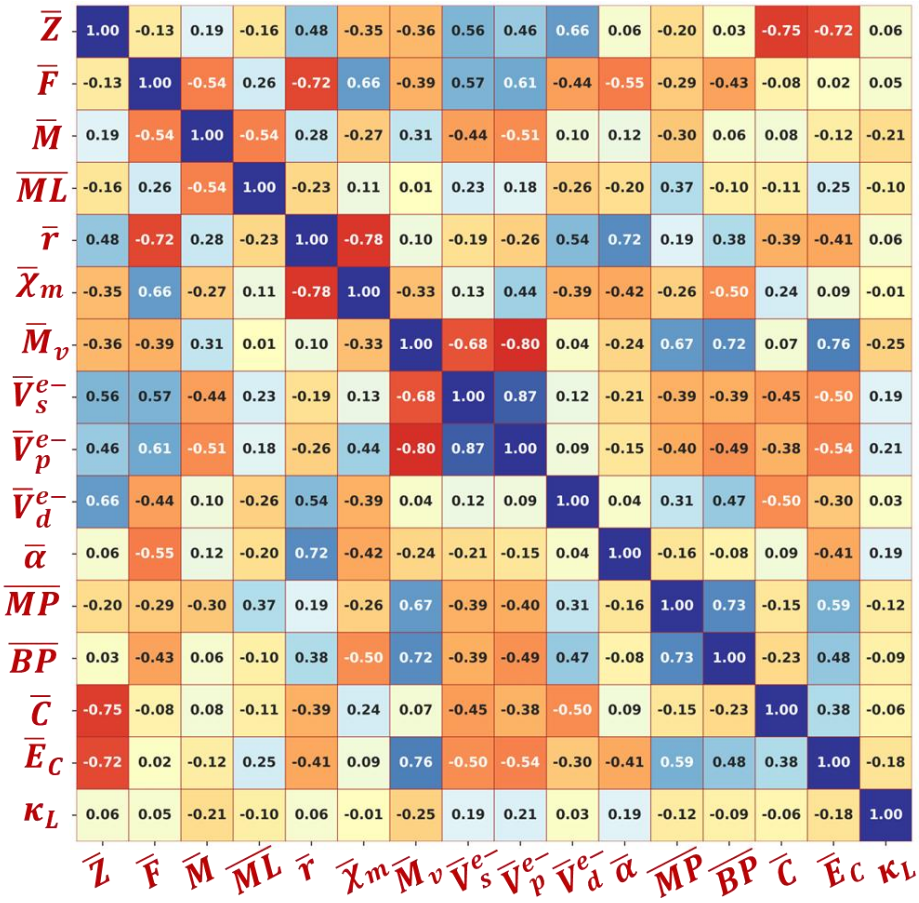


Figure 4.19: The Pearson correlation coefficient (PCC) represents the feature-feature and feature-target (κ_L) relationship for conventional features. The color represents the direction and range of the correlation, where dark purple and pale yellow signifies the perfect positive (+1) and perfect negative (-1) correlation.

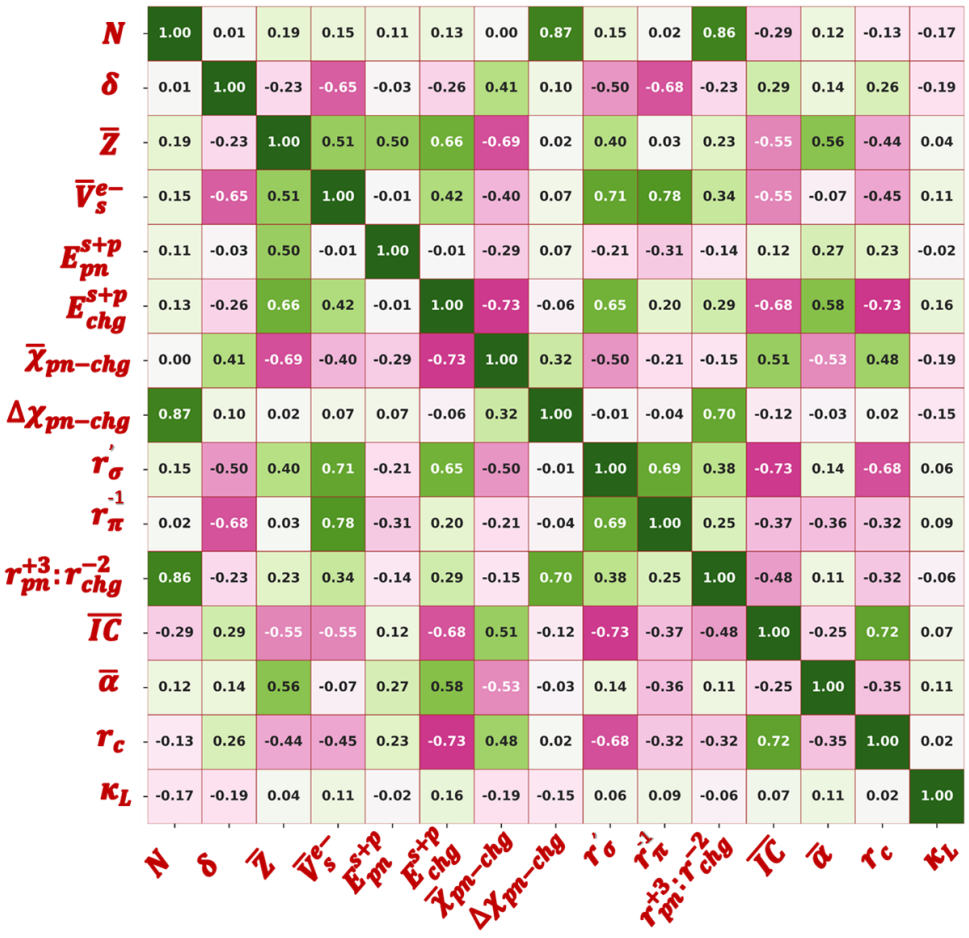


Figure 4.20: The Spearman's rank correlation matrix illustrates Spearman's rank correlation coefficient between feature-feature and feature-target (κ_L) for chemical bonding descriptors after removing highly correlated features.

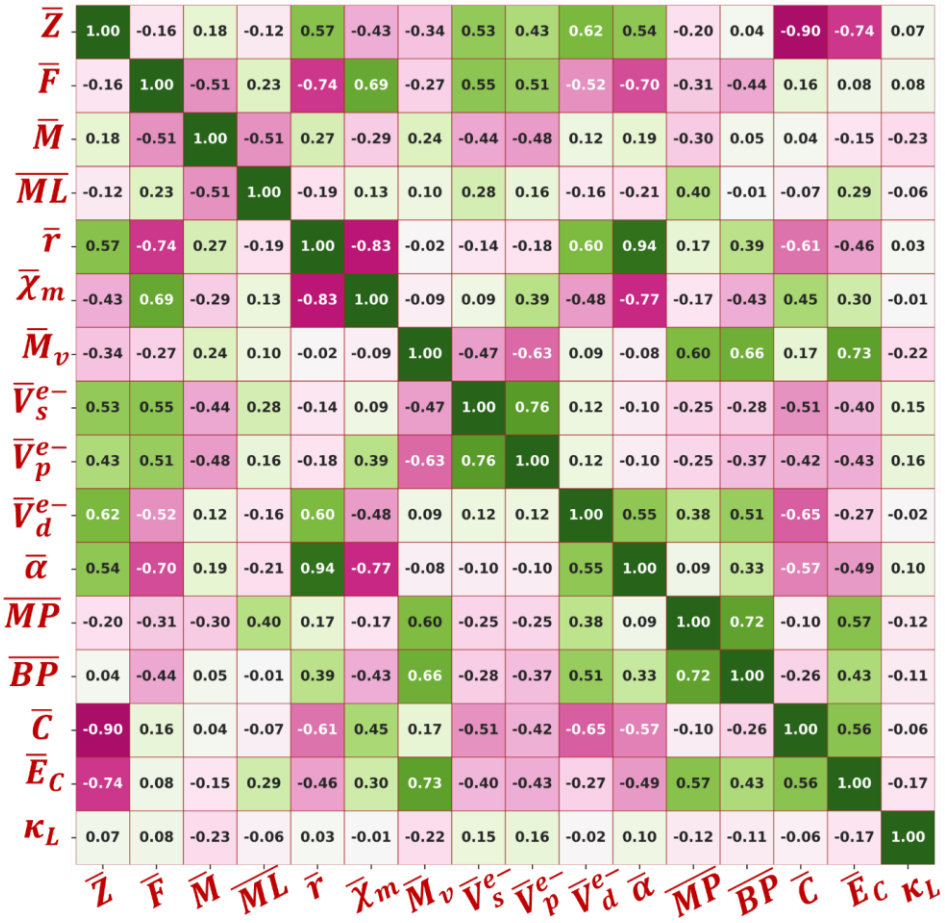


Figure 4.21: The Spearman's rank correlation matrix illustrates Spearman's rank correlation coefficient between feature-feature and feature-target (κ_L) for conventional features after removing highly correlated features.

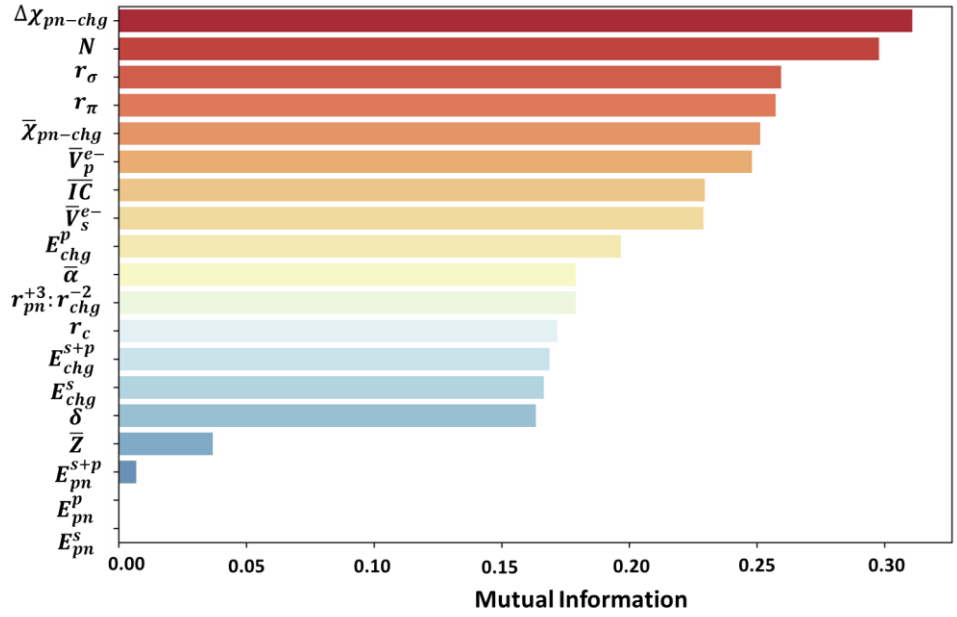


Figure 4.22: The feature importance plot with the mutual information (MI) method for the chemical bonding dataset.

From Pearson correlation coefficient (PCC) analysis, we observed that E_{pn}^s, E_{chg}^s, E_{pn}^p, E_{chg}^p, and $\overline{V}_p^{e^-}$ are highly redundant features with strong correlations among themselves (**Figure 4.17**). Interestingly, the features $\overline{\alpha}$, $\overline{IC}$, $r_{c,}$ and δ exhibited stronger correlations with κ_L. Furthermore, Spearman's correlation coefficient (SCC), which measures the monotonic relationship between features, shows a similar trend, as illustrated in **Figure 4.20-4.21**. To understand both linear and nonlinear associations between the chemical bonding descriptors and κ_L values, we studied the feature analysis using the mutual information (MI) method *[15]*. A high MI value signifies a large reduction of uncertainty, while a low MI value indicates a small reduction. If the MI is zero, the two variables are independent. **Figure 4.22** shows the feature importance of ranking calculated using the MI method for the XGBR model on the chemical bonding dataset. The E_{pn}^s and E_{pn}^p are independent of κ_L values, whereas E_{chg}^s, E_{chg}^p, and $\overline{V}_p^{e-}$ are also highly correlated in Pearson correlation coefficient (PCC) plot with E_{chg}^{s+p}

and $\overline{V}_s^{e-}$ (**Figure 4.17**). Therefore, we have dropped E_{pn}^s, E_{pn}^p, E_{chg}^s, E_{chg}^p, and $\overline{V}_p^{e-}$ features which don't affect the model performance. Based on both the PCC, SCC and MI analysis, we discarded the most redundant features, retaining 14 chemical bonding descriptor-guided features that efficiently describe the thermal conductivity (**Table 4.11**). For conventional features to screen out important features, where we proceeded with 15 features (**Figure 4.19 and 4.21**).

Table 4.11: List of Screened Final Features Considered of ML Model Training After Removing Highly Correlated Features for Chemical Bonding Descriptors

S.No.	Descriptors	Symbols
1	Total number of anions and cations	N
2	Mismatch	δ
s	Average atomic weight	$\overline{Z}$
4	Average s valence electron	$\overline{V}_s^{e-}$
5	Pnictogen s+p energy	E_{pn}^{s+p}
6	Chalcogen s+p energy	E_{chg}^{s+p}
7	Average pnictogen and chalcogen electronegativity	$\overline{\chi}_{pn-chg}$
8	Pnictogen and chalcogen electronegativity difference	$\Delta\chi_{pn-chg}$
9	Ionicity	r'_σ
10	Hybridization	r_π^{-1}
11	Ratio of +3 pnictogen and -2 chalcogen	$r_{pn}^{+3}:r_{chg}^{-2}$
12	Average ionic character	$\overline{IC}$
13	Average polarizability	$\overline{\alpha}$
14	Covalent radii	r_c

Further, we have utilized various supervised regression models, including eXtreme Gradient Boosting Regressor (XGBR), Random Forest Regressor (RFR), Adaptive Boosting Regressor (AdaBoost), extra tree regressor (ETR), Gradient Boosting Regressor (GBR), Cat-Boost Regressor (CatBoost), Decision Tree Regressor (DTR), and Kernel Ridge Regressor (KRR) algorithms from the open-source Scikit-learn library *[16]*.

4.8. Results and Discussion

4.8.1. Machine learning study

Subsequently, we conducted an ML regression analysis using two different sets of feature vectors derived from both conventional and theory-guided chemical bonding descriptors for the prediction of κ_L. The collected database was thoroughly shuffled and split into training (80%) and external test (20%) datasets, and the performances of the regression models were evaluated. We utilized above-mentioned ML models and employed five-fold hyperparameter tuning to get the best hyperparameters and the calculated test MAE/RMSE and R^2 scores as summarized in **Figure 4.23**.

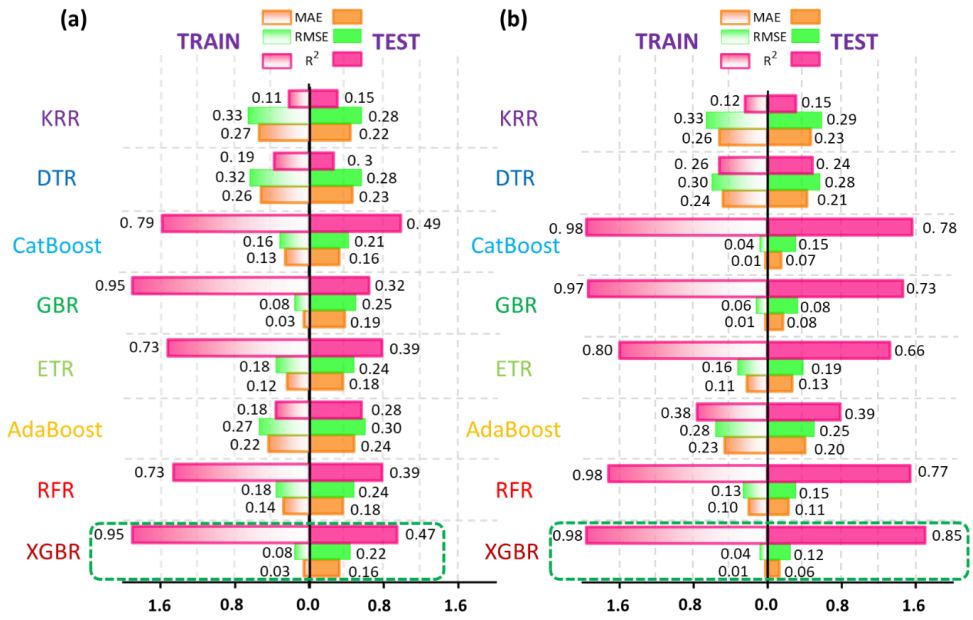


Figure 4.23: Performance comparison of ML algorithms for κ_L prediction using **(a)** conventional features and **(b)** theory-guided chemical bonding descriptors. Bar plots show the mean absolute error (MAE), root mean square error (RMSE), and R^2 scores for both the training and testing datasets across various regression models, including kernel ridge regression (KRR), decision tree regression (DTR), CatBoost, gradient boosting regression (GBR), extra tree regression (ETR), Adaboost, random forest regression (RFR), and eXtreme gradient boosting regression (XGBR). The XGBR model demonstrated the lowest RMSE/MAE and high R^2 values, indicating its superior performance in predicting κ_L.

The XGBR model emerged as the optimal choice, exhibiting the lowest RMSE and MAE scores for the κ_L dataset, comprising both conventional features and chemical bonding descriptors. The XGBR model adopts an ensemble methodology, sequentially integrating decision trees to intricately map the complex interactions between input features and κ_L, leading to more precise predictions.[46] The optimized hyperparameters utilized for XGBR model used for the chemical bonding descriptor and conventional feature dataset have been listed in **Table 4.12**.

Table 4.12: Optimized hyperparameters of utilized XGBR model with test accuracy score.

Sl. No.	Datasets	Optimized Hyperparameters	Test MAE/RMSE
1	**Chemical Bonding Descriptor**	'verbose': '20,' 'n_estimators': 2000, 'min_child_weight': '8,' 'max_depth': '25', 'learning_rate': '0.05', 'cv': '5', 'booster': 'gbtree', 'base_score': '1.45'	0.06/0.12
2	**Conventional Features**	'verbose': '10,' 'n_estimators': 500, 'min_child_weight': '5' 'max_depth': '10', 'learning_rate': '0.01', 'cv': '5', 'booster': 'gbtree', 'base_score': '1.5'	0.16/0.22

Figure 4.24(a-b) shows the parity plots of the predicted *versus* experimental κ_L values for both sets of descriptors. Additionally, we incorporated a 5% experimental error margin in the best fitted XGBR model for the predicted κ_L values, based on previous reports *[22, 68, 69]*. This margin accounts for minor variations in the predictions, as shown in **Figure 4.24(a-b)**.

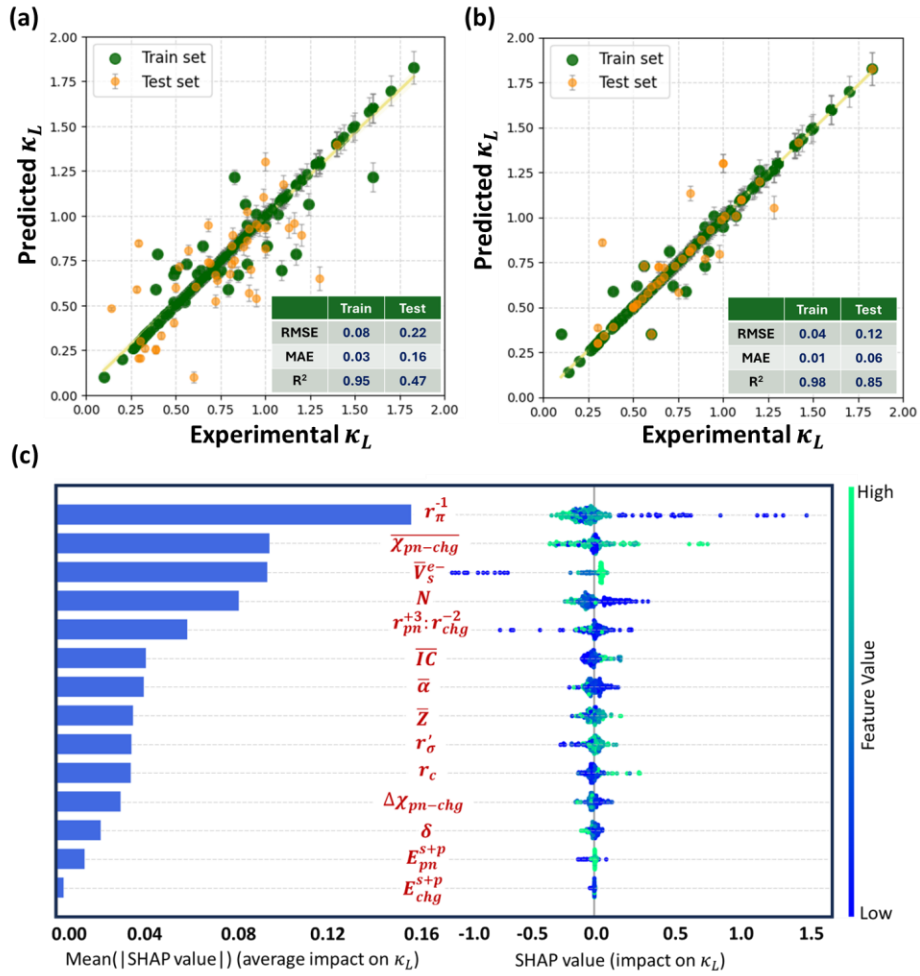


Figure 4.24. Performance metrics and feature importance of the XGBR Model with different feature sets: (a) scatter plot for the conventional set of features, (b) scatter plot for the chemical bonding descriptor sets considering ~5% experimental error margin, and **(c)** global interpretability by SHAP summary plot and beeswarm feature importance plots for the considered input features for the output lattice thermal conductivity (κ_L) for

chemical bonding descriptors. Each solitary dot placed on the feature row represents an instance with a SHAP value (x-axis), effectively conveying valuable information in a visually compact manner. The color gradient (y-axis) represents the magnitude of the feature, ranging from low (blue) to high (green).

Notably, theory-guided chemical bonding descriptors significantly improved prediction accuracy. The test RMSE scores were reduced by over 45%, decreasing from 0.22 $Wm^{-1}K^{-1}$ with conventional features to 0.12 $Wm^{-1}K^{-1}$. Additionally, the test MAE showed an improvement, dropping from 0.16 $Wm^{-1}K^{-1}$ with conventional features to 0.06 $Wm^{-1}K^{-1}$ when chemical bonding descriptors were considered. The testing dataset also exhibited a remarkable improvement in R^2 scores, increasing from 0.47 with conventional features to 0.85 with chemical bonding descriptors. Further, we have also evaluated the model's performance for the chemical bonding descriptors dataset using 7-fold cross-validation with the optimized XGBR, where the average RMSE (0.15) was comparable to the test RMSE (0.12), as shown in **Figure 4.25**.

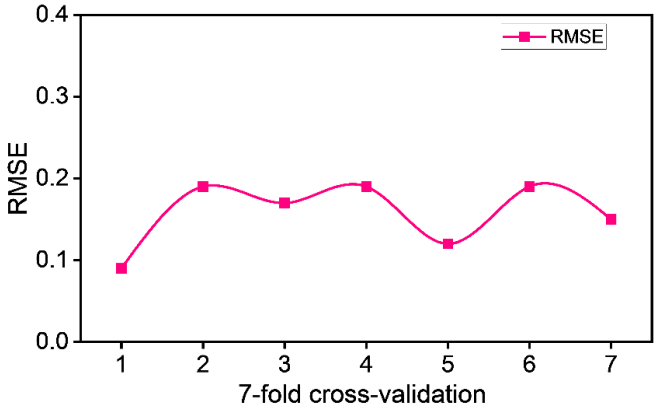


Figure 4.25: The 7-fold cross-validation score of root mean square error (RMSE) using XGBR model.

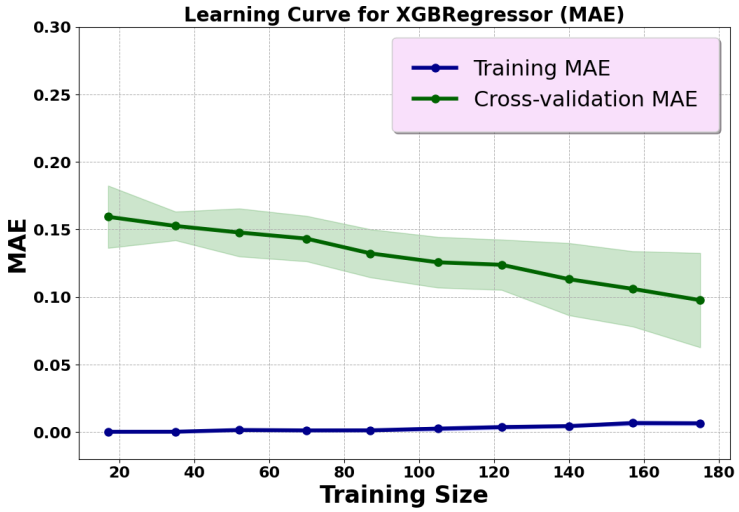


Figure 4.26: The learning rate with increasing training data size corresponding to the mean absolute error (MAE).

Furthermore, we predicted the learning rate to illustrate how the model's performance evolves with the increase in the number of training data, as shown in **Figure 4.26**. Therefore, this improvement highlights the superior effectiveness of chemical bonding descriptors in enhancing the predictive accuracy of the model for κ_L.

Further, to explain the outliers in the ML predictions, we examined the chemical bonding descriptor values and their defined ranges for each material. A common issue among these outliers is that their chemical bonding descriptors, such as number mismatch ($|\delta|$), ionicity (r'_σ), hybridization (r_π^{-1}), and polarizability ($\bar{\alpha}$) fall outside the desired ranges, leading to inconsistencies in the ML predicted κ_L values (**Figure 4.27**). For instance, Bi_8Te_9 and $PbBi_4Se_7$, the model underestimates κ_L due to higher r'_σ and $\bar{\alpha}$ values indicating significant orbital overlapping with weaker covalent bonds. Conversely, Sb_2S_3, Sb_2TeSe_2 and $SnSb_2Te_4$, the model overestimates κ_L because it overpredicted the effect of stronger bonding reflected by more negative r'_σ and large number mismatch $|\delta|$ in Sb_2TeSe_2 and slightly higher r_π^{-1} in Sb_2S_3 and $SnSb_2Te_4$. These significant differences

arise from the complex bonding behaviours when multiple descriptors deviate from their desired ranges (discussed later).

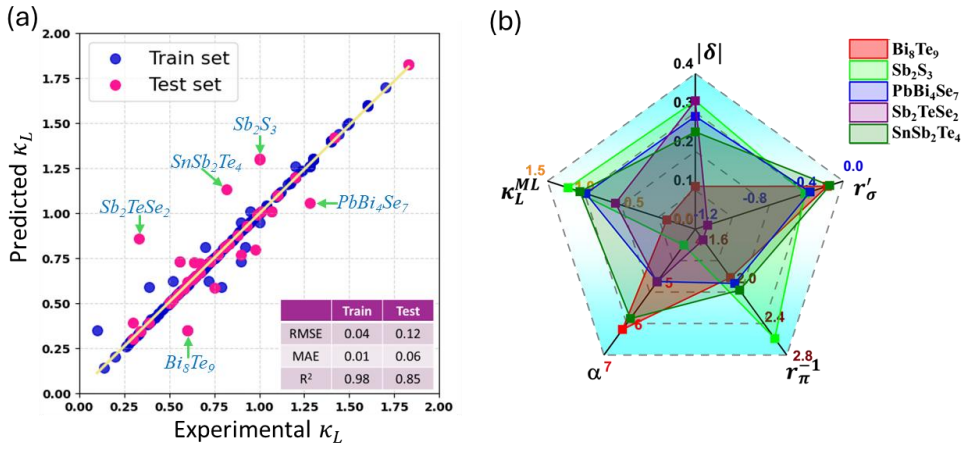


Figure 4.27. (a) The train-test parity plot of the XGBR model highlighting the model outliers, **(b)** the radar plot consists of outliers with key chemical bonding descriptors values, including with their predicted $\boldsymbol{\kappa_L^{ML}}$ values.

Furthermore, to avoid the spurious effects of grain boundaries and defects, we excluded polycrystalline data from our dataset and retained only single crystalline materials 95.5% [10 polycrystalline materials out of 219 materials]. We observed that MAE (0.06) remains same with negligible change in their R^2 values, as shown in **Figure 4.28**. Additionally, we have expanded our database size from 219 to 358 materials by introducing various new non-SCALP materials and increased the κ_L range up to 4.50 $Wm^{-1}K^{-1}$. The optimized XGBR model predicted the unknown materials with the test MAE (0.21) and R^2 (0.90), The experimental error values are found to be within ~5% for the experimentally measured κ_L of materials.[47, 48] In our case, the ML predicted error values (MAE: 0.21) for the expanded dataset (with maximum κ_L value of 4.50 $Wm^{-1}K^{-1}$) is lying within the expected average experimental error value (~0.06). Therefore, the average error in the training dataset is inherently low, making it reliable for training models with minimal experimental errors. Therefore, ML model is also able to capture the chemical bonding characteristic features of non-

SCALP materials which is evident from the accurate prediction of non-SCALP materials with high κ_L values, as shown in **Figure 4.29**. Moreover, this also demonstrates the XGBR model's ability to perform well across the broader range of κ_L values by providing more reliable predictions for thermoelectric materials outside the SCALP group.

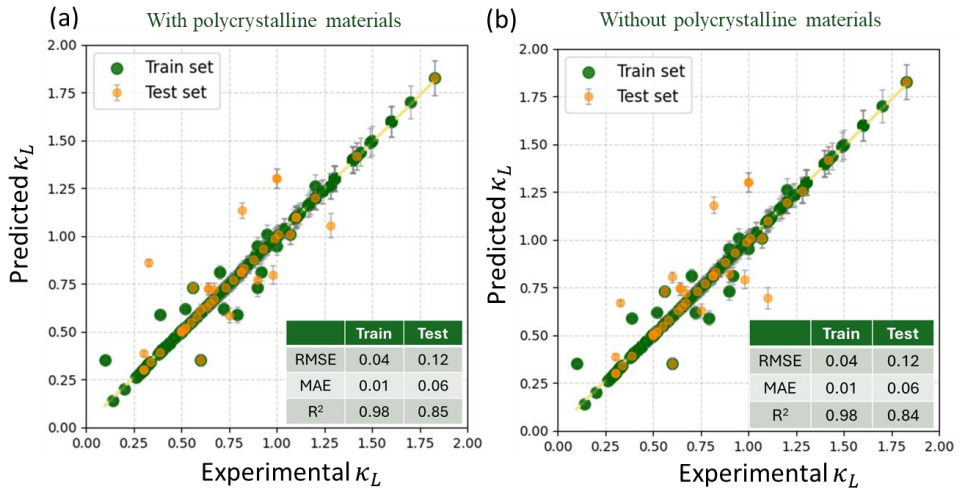
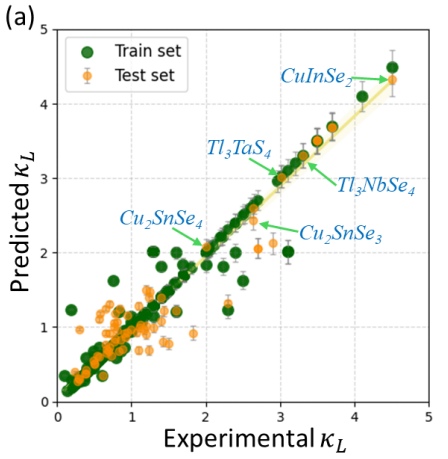


Figure 4.28: The scatter plot for the chemical bonding descriptor sets (a) with and (b) without removing polycrystalline materials, considering a 5% experimental error margins.



(b)

Materials	κ_L^{ML}	κ_L^{Exp}	difference
Cu_2SnSe_4	2.00	2.08	0.08
Tl_3TaS_4	3.50	3.48	0.02
$CuInSe_2$	4.50	4.32	0.17
Tl_3NbSe_4	3.32	3.30	0.02
Cu_2SnSe_3	2.63	2.43	0.20

Figure 4.29: (a) The train-test parity plot of XGBR model for the chemical bonding descriptor sets after introducing various non-SCALP materials with high κ_L values, considering a 5% experimental error margins **(b)** ML

predicted lattice thermal conductivity ($\boldsymbol{\kappa_L^{ML}}$) and experimentally measured κ_L values ($\boldsymbol{\kappa_L^{Exp}}$) of non-SCALP materials with high κ_L values, and the difference between predicted and experimental values reported in the literature.

The ML algorithm excels in handling complex relationships within datasets, leveraging the intricate interactions learned by its ensemble of decision trees, which classify it as a 'black box'. However, this complexity often obscures understanding of how predictions are generated, thereby compromising transparency and interpretability. To address this, we employed the model-agnostic interpretability technique SHapley Additive exPlanation (SHAP) analysis, based on cooperative game theory *[45]*. This approach facilitates unravelling the underlying design principles of ML models and understanding how the considered features contribute to the model's predictive capability for κ_L. Feature importance analysis provides a comprehensive explanation of individual feature contributions to the entire dataset or specific data instance, offering interpretations at a global level.

Figure 4.24(c) illustrates the SHAP summary plot and beeswarm plot, presenting the hierarchical ranking of the most significant global feature importance in descending order, along with the summary of how these important features affect the prediction of κ_L. Interestingly, hybridization (r_π^{-1}) was identified as the most influential descriptor, exhibiting an inverse relationship with κ_L. The covalent bonding characteristics of materials weakens with decrease in hybridization typically leads to lower thermal conduction *[64, 70, 71]*. Additionally, average electronegativity of pnictogen and chalcogen ($\bar{\chi}_{pn-chg}$) is another crucial parameter significantly effects κ_L, which attributes to different bonding environments by separating ionic, metallic, and covalent bonding *[72]*. Furthermore, $\bar{V}_s^{e-}$ with a low feature value, certainly providing the SCALP properties which

strongly interact with the pnictogen p-states in the valence band giving rise to chalcogen states in upper valence bands (discussed in later section) leading to an active lone pair *[46]*. The N and Z are well known parameters with a high feature value, r_{pn}^{+3}: r_{chg}^{-2} with low feature value, and $\bar{\alpha}$ providing the signature phenomena for relatively weak bonding with high electronic polarizability, lowering κ_L values *[64]*. For r'_σ/r_π^{-1}, clusters with a high/low feature value had a positive/negative contribution, leading to an increase/decrease in κ_L, This implies that low the r'_σ and limited degree of r_π^{-1} enables the weak bonding that is crucial for low κ_L materials. E_{chg}^{s+p} and E_{chg}^{s+p} provides the energies require for the formation of SCALP and to capture the relativistic stabilization of ns^2 lone pair *[46]*. This relativistic effect directly influences the presence or absence of SCALPs, with heavy elements (Te) tightly bound electrons that prevent the formation of SCALP, while lighter elements like (Sb) allow for active lone pairs due to weaker relativistic stabilization. However, E_{chg}^{s+p} and E_{chg}^{s+p} contributed the least to the prediction of κ_L. The global interpretability of conventional feature-based XGBR prediction is shown in **Figure 4.30**.

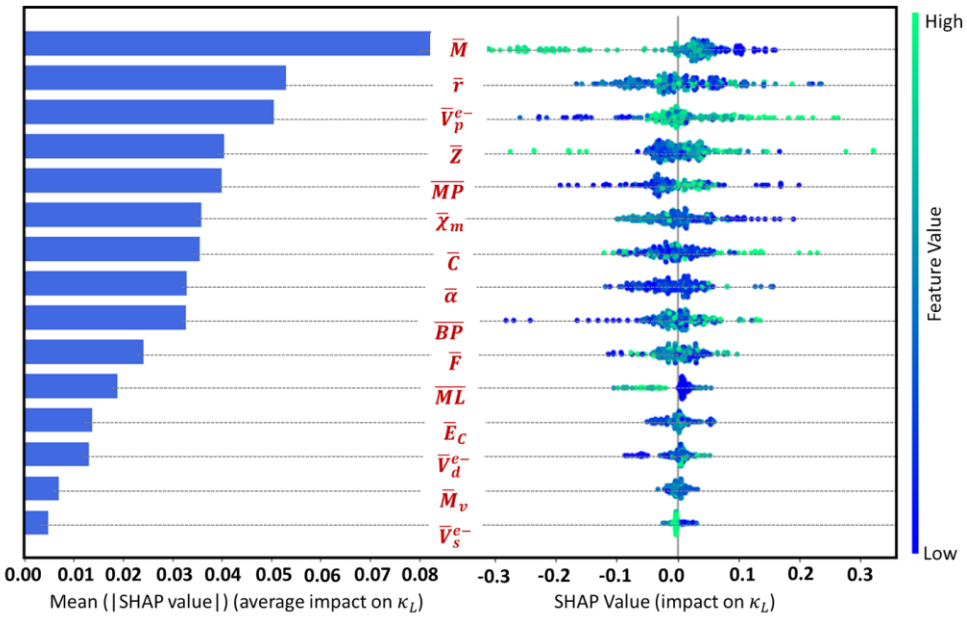
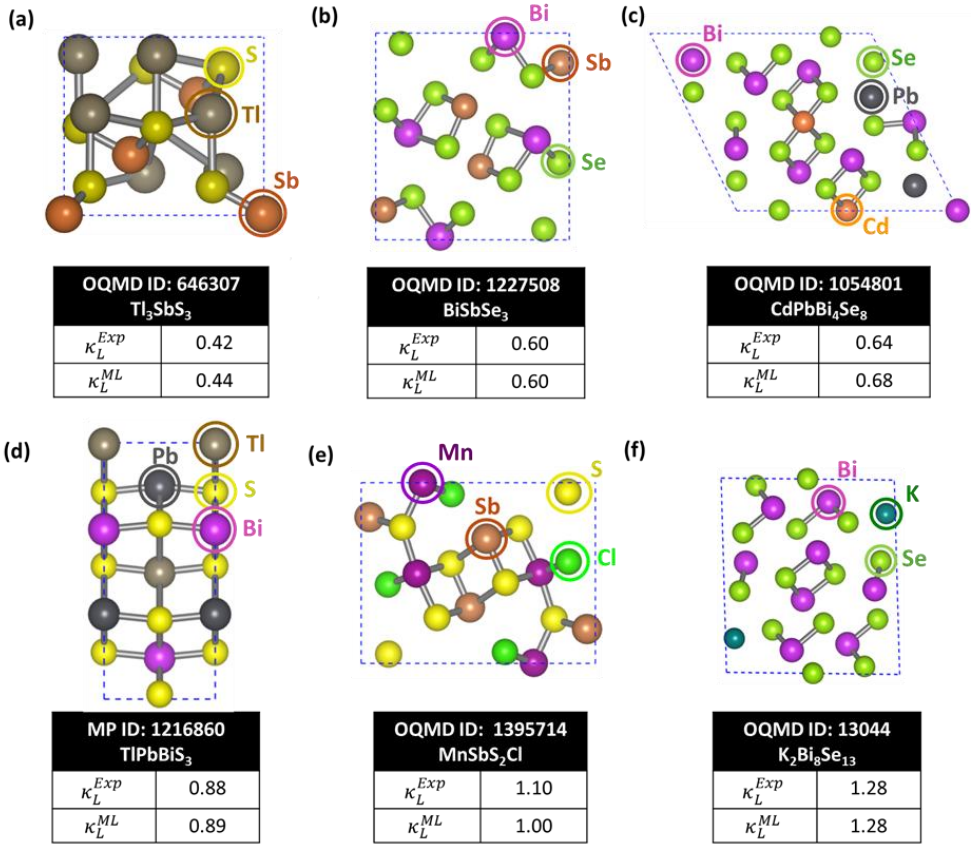


Figure 4.30: SHAP global interpretability analysis ML model prediction with conventional features: The bar plot showing overall contribution of individual features and the solitary dots on its right represents the bee-swarm plot providing a comprehensive summary of how each feature in the dataset impact the thermal conductivity (κ_L). Each dot in the bee-swarm plot represents an instance, with its SHAP value indicating the impact on the prediction of κ_L.

We observed that most of the ML predicted κ_L values of materials in the test dataset closely matched the experimentally reported κ_L values (**Figure 4.24 (b**). In **Figure 4.31**, we list a few materials along with their OQMD IDs, highlighting the model's accuracy, as the predicted κ_L values align well with the experimental data. This strong correlation confirms that our ML model is highly effective in predicting the κ_L values of unknown materials.



OQMD ID: 646307 Tl_3SbS_3	
κ_L^{Exp}	0.42
κ_L^{ML}	0.44

OQMD ID: 1227508 $BiSbSe_3$	
κ_L^{Exp}	0.60
κ_L^{ML}	0.60

OQMD ID: 1054801 $CdPbBi_4Se_8$	
κ_L^{Exp}	0.64
κ_L^{ML}	0.68

MP ID: 1216860 $TlPbBiS_3$	
κ_L^{Exp}	0.88
κ_L^{ML}	0.89

OQMD ID: 1395714 $MnSbS_2Cl$	
κ_L^{Exp}	1.10
κ_L^{ML}	1.00

OQMD ID: 13044 $K_2Bi_8Se_{13}$	
κ_L^{Exp}	1.28
κ_L^{ML}	1.28

Figure 4.31: The comparison between the ML-predicted *versus* experimentally reported κ_L values from the test dataset. Prototype structures with different κ_L values ($\kappa_L^{Exp}/\kappa_L^{ML}$): **(a)** Tl_3SbS_3 (0.42/0.44), *[41]* **(b)** $BiSbSe_3$ (0.60/0.60) *[73]* **(c)** $CdPbBi_4Se_8$ (0.64/0.68), *[74]* **(d)** $TlPbBiS_3$ (0.88/0.89), *[46]* **(e)** $MnSbS_2Cl$ (1.10/1.00), *[75]* and **(f)** $K_2Bi_8Se_{13}$ (1.28/1.28), *[41]* illustrate the model's predictive performance.

4.8.2. Prediction of Unknown Materials

To further explore potential thermoelectric materials with low lattice thermal conductivity (κ_L), we curated a dataset comprising 245 previously unexplored materials that met our initial screening criteria. Using our trained ML model, we predicted κ_L values for each material, detailed in ref *[51]*. Among these, the top 14 materials with the lowest predicted κ_L values at 300 K are represented in **Figure 4.32.**

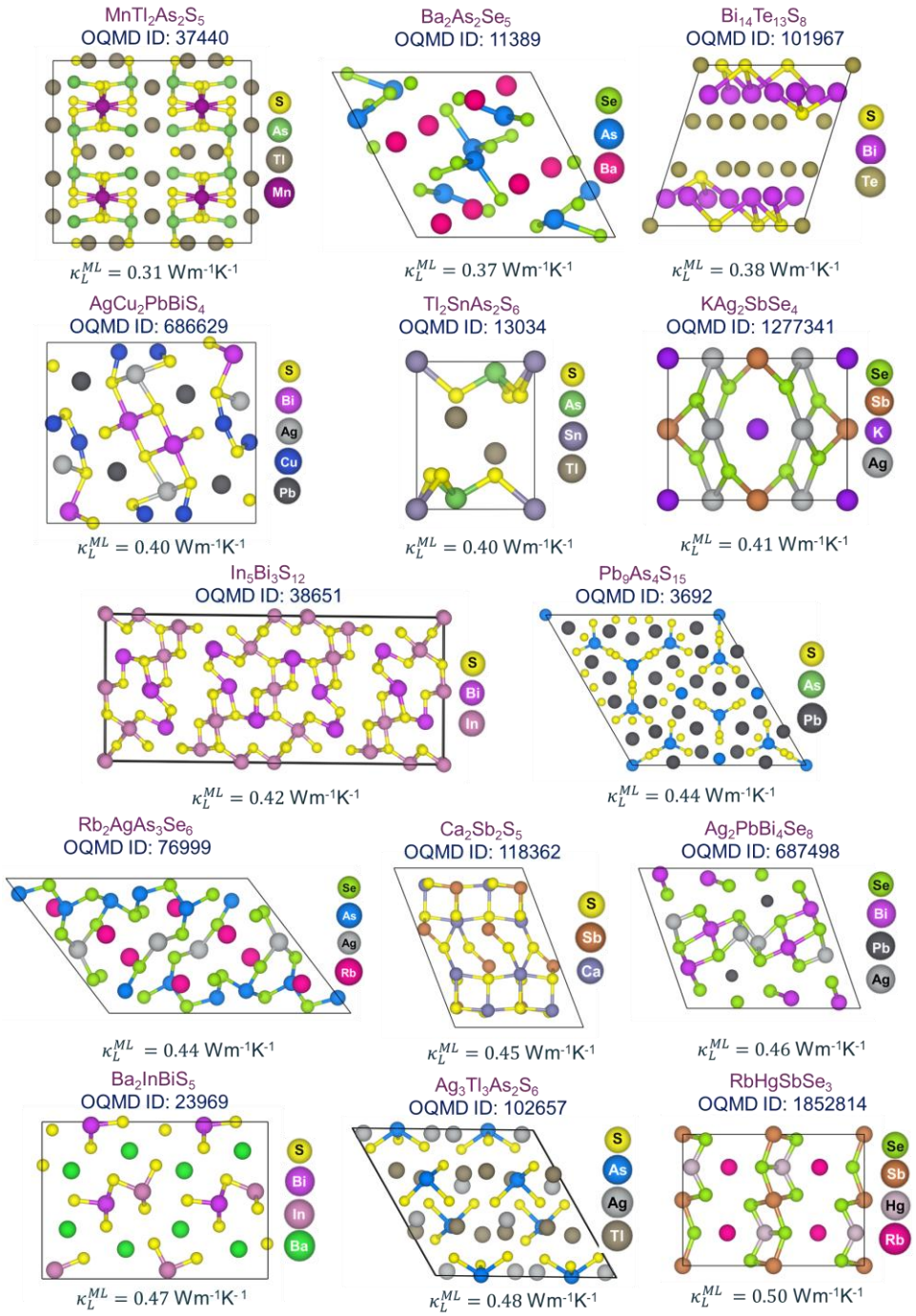


Figure 4.32: List of top 14 predicted pnictogen chalcogenides at 300 K along with their OQMD IDs. The predicted κ_L^{ML} values of $MnTl_2As_2S_5$ and $AgCu_2PbBiS_4$ materials are consistent with previously reported values *[76]*.

The presented materials exhibited low κ_L values, primarily due to the presence of SCALPs associated with their pnictogen elements. These SCALPs are known to induce intrinsic phonon scattering owing to localized lattice distortions in the bonding arrangement, effectively reducing κ_L. Additionally, these materials possess complex crystal structures (**Figure 4.33**), featuring multiple types of bonding environments, with varying degrees of ionicity, and a tendency towards covalent character, which are essential for effective phonon scattering *[64]*. In addition, we identified the best five materials showing ultralow κ_L ($\leq$ 0.40 $Wm^{-1}K^{-1}$) predicted as follows: $MnTl_2As_2S_5$ (0.31 $Wm^{-1}K^{-1}$), $Ba_2As_2Se_5$ (0.37 $Wm^{-1}K^{-1}$), $Bi_{14}Te_{13}S_8$ (0.38 $Wm^{-1}K^{-1}$), $AgCu_2PbBiS_4$ (0.40 $Wm^{-1}K^{-1}$), and $Tl_2SnAs_2S_6$ (0.41 $Wm^{-1}K^{-1}$). Interestingly, these materials have a higher number of atoms in the unit cell (N values), reflecting their complex crystal structures. Moreover, the ML predicted κ_L values for $MnTl_2As_2S_5$ (0.31 $Wm^{-1}K^{-1}$) and $AgCu_2BiPbS_4$ (0.40 $Wm^{-1}K^{-1}$) materials are consistent with the first principles calculated κ_L values reported by Wolverton and coworkers (**Figure 4.33**) *[76]*. These findings validate the accuracy and quality of the prediction of κ_L values for previously unknown materials by using chemical bonding descriptors.

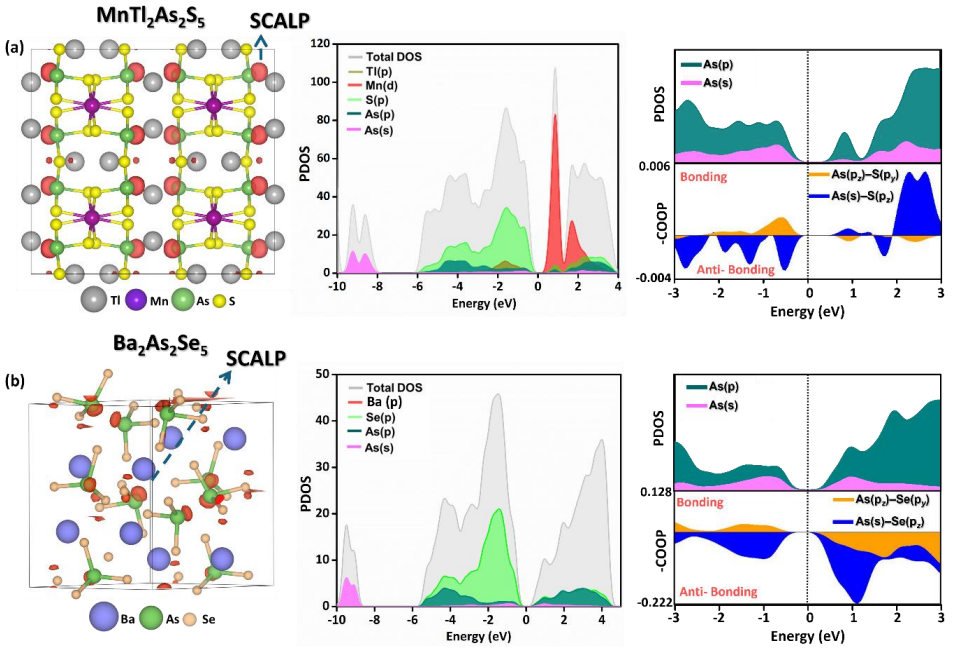


Figure 4.33: Crystal structures, projected density of states (PDOS), and crystal orbital overlap population (COOP) analysis of **(a)** $MnTl_2As_2S_5$ and **(b)** $Ba_2As_2Se_5$. The 3D view of the electron localization function (ELF) at isosurface values of 4.58 $\times 10^{-4}$ eV/Å^3 and 8.59 $\times$ 10^{-4} eV/Å^3, respectively. PDOS and COOP analyses were used to visualize the bonding characteristics of the SCALP near the Fermi energy, where a positive overlap population indicates a bonding interaction, while a negative overlap population indicates an antibonding interaction.

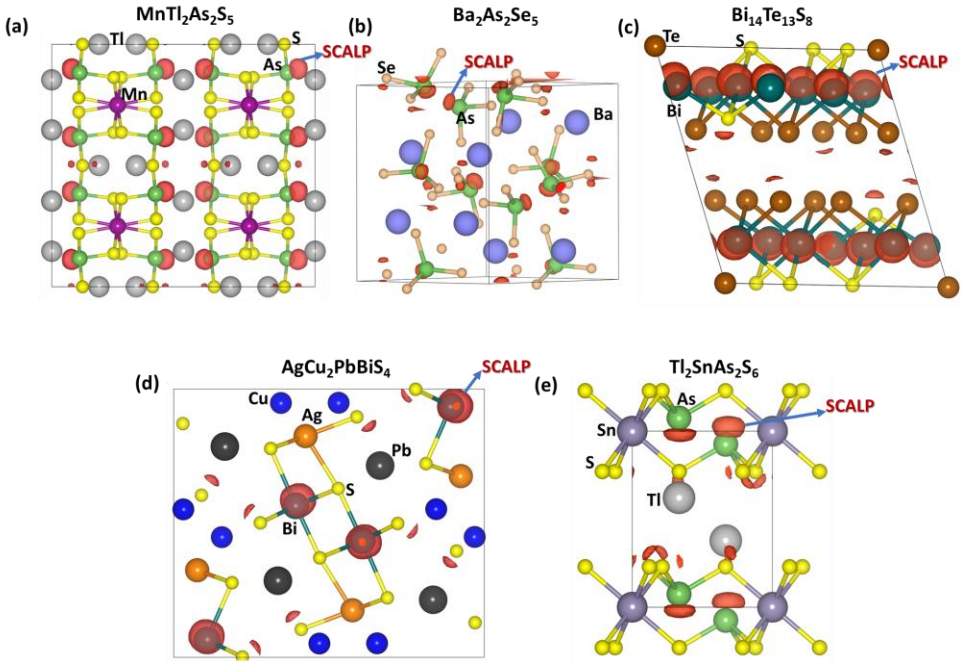


Figure 4.34: The calculated electron localization function (ELF) exhibiting the presence of lone pair clouds around pnictogen atoms in best five materials with low κ_L values: (a) $MnTl_2As_2S_5$ (isosurface value of 8.6×10^{-4} eV/Å^3), (b) $Ba_2As_2Se_5$ (isosurface value of 9.4×10^{-4} eV/Å^3), (c) $Bi_{14}Te_{13}S_8$ (isosurface value of 3.1×10^{-3} eV/Å^3), (d) $AgCu_2PbBiS_4$ (isosurface value of 1.2×10^{-3} eV/Å^3), and (e) $Tl_2SnAs_2S_6$ (isosurface value of 4.6×10^{-4} eV/Å^3).

To visualize the presence of pnictogen cationic SCALPs and understand their chemical bonding characteristics, we plotted the electron localization function (ELF) for the five best materials with ultralow κ_L (**Figure 4.34**) *[77]*. The ELF estimates the degree of electron localization on the pnictogen elements considering the local influence of Pauli exclusion and provides additional information about the morphology of the electron lone pair orbital cloud. The asymmetric spherical electron localization around the As atoms in $MnTl_2As_2S_5$ and $Ba_2As_2Se_5$ is associated with their $4s^2$ electrons (**Figure 4.33**). The impact of the SCALP expression can also be determined by analyzing the energy levels of As-s states and S/Se-p states. To

investigate this, we calculated the partial density of states (PDOS) to determine the positions of the s/p states relative to the Fermi level. The lowest energy valence band, located near −8 eV, is attributed to the bonding interaction between the As-4s and S/Se-3p/4p orbitals. Furthermore, from −6 eV onward, there is a band arising from the bonding interaction between the As-4p and S/Se-3p/4p orbitals. This localization of $4s^2$ (As) electrons at the valence band maxima (VBM) indicates the presence of SCALPs in the $MnTl_2As_2S_5$ and $Ba_2As_2Se_5$ systems. Additionally, crystal orbital overlap population (COOP) analysis was performed to understand the nature of chemical bonding in these materials. As reported by Walsh et al., the expressions of cation lone pair in heavy metal chalcogenides are driven by the interaction and synergistic stabilization of the occupied metal through the cation p-states and the antibonding interactions between As-4s and S-3p/Se-4p states *[53, 78, 79]*. The COOP analysis revealed bonding interactions between the As-4p and S-3p/Se-4p orbitals just below the Fermi level, contrary to their expected position above the Fermi level. Subsequently, antibonding interactions between the As-4s and S-3p/Se-4p orbitals were observed below the Fermi level. This can be explained by the mixing of the As-4p orbital with the antibonding state (As-4s and S-3p/Se-4p), which lowers the energy of the highest occupied states and stabilizes these states in the $MnTl_2As_2S_5$ and $Ba_2As_2Se_5$ systems, resulting in an unexpected As lone pair contribution near the Fermi level.

4.8.3. Effects of Descriptors on Thermal Conductivity (κ_L)

Further, we attempted to scrutinize the role of important descriptors in the thermal conductivity (κ_L) of the predicted unknown materials. As discussed, ionicity (r'_σ) quantifies the degree of ionic character of the bonds, whereas hybridization (r_π^{-1}) measures the energetic splitting of the s and p orbitals of valence electrons.[46] The mismatch ($|\delta| > 0$) indicates structural distortion, while polarizability defines the localization of electronic density. To understand this, we first illustrated the impact of bonding descriptor

characteristics on κ_L using a database of 233 materials with known κ_L values, as shown in **Figure 4.35(a-b).**

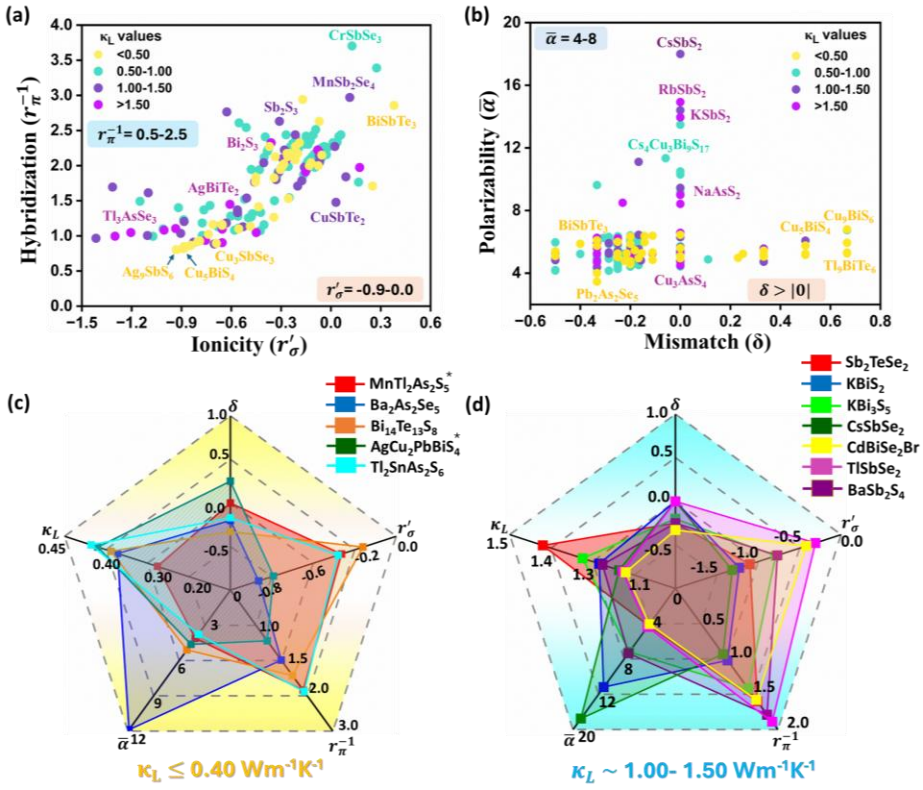


Figure 4.35: A scatter heat map highlighting the relationship between the lattice thermal conductivity (κ_L) and the chemical bonding descriptors, using **(a)** ionicity and hybridization and **(b)** mismatch and polarizability. Radar plots characterizing the change in κ_L via the difference in mismatch (δ), ionicity (r'_σ), hybridization (r_π^{-1}), and polarizability ($\bar{\alpha}$) for **(c)** the best five materials with ultralow $\kappa_L \leq 0.40$ $Wm^{-1}K^{-1}$, and **(d)** materials with $\kappa_L > 1.0$ $Wm^{-1}K^{-1}$. The highlighted materials with * are in close agreement with ML predicted vs reported κ_L *[50]*.

The analysis reveals that Ag_9SbS_6, Cu_5BiS_4, and Cu_3SbSe_3 exhibit low $\kappa_L < 0.50$ $Wm^{-1}K^{-1}$, characterized by low r'_σ $(-0.9\text{-}0.0)$ and moderate to high r_π^{-1} $(0.5 - 2.5)$ values. The higher upshifts in the values of r'_σ and r_π^{-1} for $AgBiTe_2$, Cu_3AsS_4, Tl_3AsSe_3, Cu_3AsSe_4, and Bi_2Se_3 demonstrate an

increase in κ_L values, as shown in **Figure 4.35(a)**. This suggests that pnictogen chalcogenide materials can be characterized by a unique range of hybridization and a small area of ionicity, enabling resonance bonding, which can screen a number of materials with low κ_L properties. Subsequently, Cu_5BiS_4, $Pb_2As_2Se_5$, Tl_9BiTe_6, and $BiSbTe_3$ materials, which exhibited large deviations in the mismatch ($|\delta| > 0.20$) and high $\overline{\alpha}$ $(4-8)$ values, also exhibited low κ_L, indicating optimum bonding characteristics (**Figure 4.35(b)**). Thus, a large deviation in $|\delta|$ persists with lower symmetry, which tends to adopt larger unit cells with diverse bonding hierarchies *[66]*. All these factors lead to a significant reduction in κ_L.

Further, to explore the interplay between our defined chemical bonding descriptor ranges for low κ_L values, we prepared radar plots highlighting the five best new materials identified from our database of 245 unknown materials, along with their four bonding descriptors, as shown in **Figure 4.35(c)**. These best five materials with ultralow $\kappa_L(\leq 0.40 \mathrm{Wm^{-1}K^{-1}})$ values exhibit distinct bonding characteristics with lower r'_σ $(-0.90\ to -0.20)$ values, a limited degree of r_π^{-1} $(0.84\ to\ 2.20)$, ($|\delta| > 0.20$), and high $\overline{\alpha}$ $(5-12)$ values, which are consistent with the above-defined ranges of unique bonding characteristics analyzed with known materials. Additionally, an increase in r_π^{-1} for $MnTl_2As_2S_5$, $Bi_{14}Te_{13}S_8$, and $Tl_2SnAs_2S_6$ materials led to enhanced saturated covalent bonding, reducing charge localization and reduced electronic polarizability (α). Conversely, a decrease in the degree of orbital interactions (r_π^{-1}) and r'_σ in $Ba_2As_2Se_5$ results in higher electronic polarizability ($\overline{\alpha}$), indicating a resonating bonding mechanism *[60]*.

Similarly, we have also mapped radar plots for a set of seven materials with high κ_L $(1.0-1.5\ \mathrm{Wm^{-1}K^{-1}})$, displaying varying chemical bonding descriptors, as shown in **Figure 4.35(d)**. Intriguingly, a minor deviation in any single bonding parameter can result in higher κ_L values. The high κ_L values of $KBiS_2$, $CsSbSe_2$, and $TlSbSe_2$ can be attributed to their mismatch values $(\delta = 0)$. However, Sb_2TeSe_2, KBi_3S_5, $BaSb_2S_4$, and $CdBiSe_2Br$

materials still exhibited higher κ_L values with high $\delta \geq 0.20$. The deviation in the trend for the KBi_3S_5, $BaSb_2S_4$, and Sb_2TeSe_2 materials is attributed to the higher r'_σ that exceeds the above-defined limit required to achieve low κ_L. In the case of $CdBiSe_2Br$ materials, $\overline{\alpha} > 12$ no longer contributes to reducing κ_L.

4.8.4. $Bi_{14}Te_{13}S_8$, $InSbS_3$, and RbK_2BiSe_5: A Case Study

In this case study, we aimed to elucidate how the intensity of lone pair (ns^2) electrons on pnictogen atoms affects the κ_L values of the considered complex chalcogenide materials. In this regard, we focused on three complex materials ($Bi_{14}Te_{13}S_8$, $InSbS_3$, and RbK_2BiSe_5) that were selected from our database of predicted unknown materials based on their varying κ_L values. These materials exhibit significant structural distortion, as reflected by performance indicator $\delta = |0.33|$, and display a range of κ_L^{ML} values: 0.38 $Wm^{-1}K^{-1}$ for $Bi_{14}Te_{13}S_8$, 0.50 $Wm^{-1}K^{-1}$ for $InSbS_3$, and 1.00 $Wm^{-1}K^{-1}$ for RbK_2BiSe_5 as shown in **Figure 4.36(a-c)**.

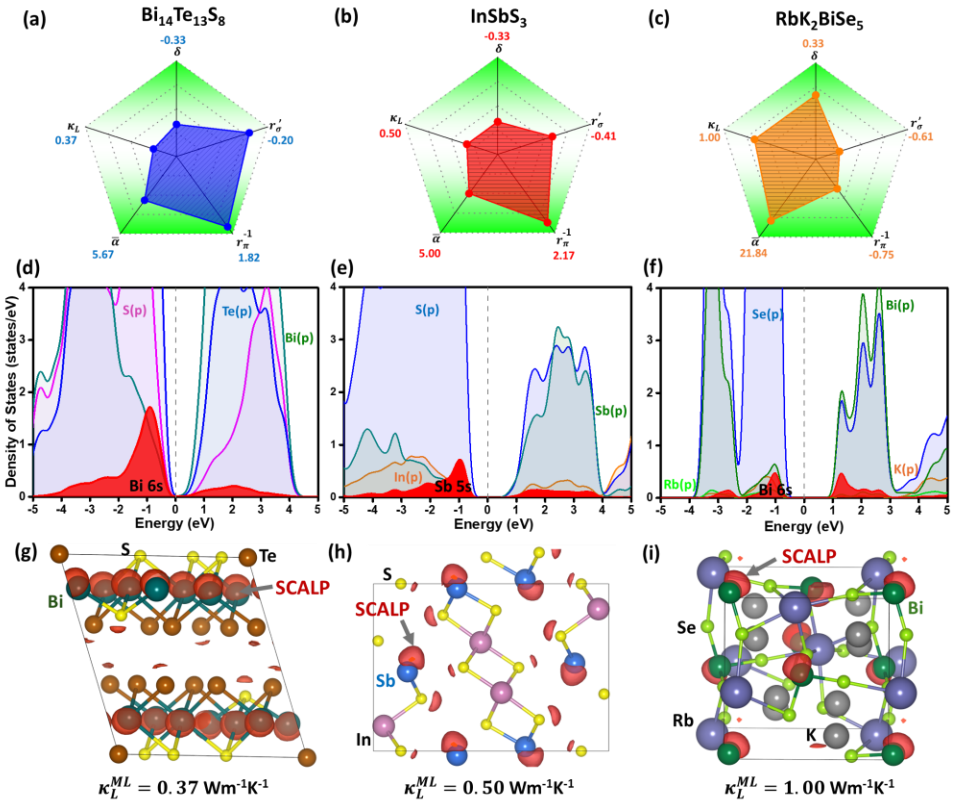


Figure 4.36: The radar plot representing the interplay between mismatch (δ), ionicity (r_σ'), hybridization (r_π^{-1}), and polarizability ($\bar{\alpha}$) for **(a)** $Bi_{14}Te_{13}S_8$, **(b)** $InSbS_3$, and **(c)** RbK_2BiSe_5 materials. **(d-f)** The partial density of states (PDOS) of each element in the $Bi_{14}Te_{13}S_8$, $InSbS_3$, and RbK_2BiSe_5 systems, and **(g-i)** 3D visualization of the electron localization function (ELF) for $Bi_{14}Te_{13}S_8$, $InSbS_3$, and RbK_2BiSe_5 materials at isosurface value of 18.3 × 10^{-4} eV/Å^3, 8.8 × 10^{-4} eV/Å^3 and 7.9 × 10^{-4} eV/Å^3, respectively.

$Bi_{14}Te_{13}S_8$ possesses a low r_σ', moderate $\bar{\alpha}$, and specific r_π^{-1}, contributing to its ultralow κ_L. In contrast, $InSbS_3$ deviated from the defined hybridization range with a higher r_π^{-1} value, resulting in an increased κ_L values. Furthermore, RbK_2BiSe_5 presents a distinct scenario in which r_σ' exceeds the defined limit, coupled with low r_π^{-1} and very high $\bar{\alpha}$, resulting in a higher κ_L of 1.00 Wm^{-1}K^{-1}. In **Figures 4.36(d-f)**, the varying intensities of the ns² lone pair contributions from pnictogen elements (Bi 6s/Sb 5s) near

the Fermi level of the VBM reflect the presence of SCALPs. It serves as the highest occupied molecular orbital (HOMO) that influences bonding within the crystal structure. Notably, moving from $Bi_{14}Te_{13}S_8$ to RbK_2BiSe_5, the intensity of the ns^2 orbitals near the Fermi level decreases with an increase in their κ_L values. The lone pairs on the pnictogen atoms with an asymmetric electronic density can be visualized using the ELF study, *[77]* as shown in **Figure 4.36(g-i)**. We observed a spherical electronic 'mushroom cloud' appears around Bi in $Bi_{14}Te_{13}S_8$, a 'bean' shaped lone pair on Sb in $InSbS_3$, and 'crescent-moon' shape lone pairs on Bi in RbK_2BiSe_5, which are clear indicators of the presence of SCALPs. Our methodology not only identifies materials with ultralow κ_L but also guides the new possibilities for the design of pnictogen-based thermoelectric materials, emphasizing the significant effects of SCALPs and chemical bonding hierarchies.

4.9. Summary

In summary, we systematically explored the influence of stereochemically active lone pairs (SCALPs) and bonding descriptors such as ionicity (r'_σ), hybridization (r_π^{-1}), and polarizability ($\overline{\alpha}$) on the thermal conductivity (κ_L) of pnictogen chalcogenide materials. We developed an ML strategy that incorporates a comprehensive set of chemical bonding descriptors to capture the empirical hidden influence using bonding, structural, orbital energies, and electronic descriptors. These descriptors elucidate the critical role of SCALPs and bonding hierarchies in influencing κ_L. We identified five new materials [$MnTl_2As_2S_5$ (0.31 $Wm^{-1}K^{-1}$), $Ba_2As_2Se_5$ (0.37 $Wm^{-1}K^{-1}$), $Bi_{14}Te_{13}S_8$ (0.38 $Wm^{-1}K^{-1}$), $AgCu_2PbBiS_4$ (0.40 $Wm^{-1}K^{-1}$), and $Tl_2SnAs_2S_6$ (0.41 $Wm^{-1}K^{-1}$)], with complex crystal structure which could be promising for low κ_L values ($\leq$ 0.40 $Wm^{-1}K^{-1}$). These findings suggest that ultralow κ_L materials can be systematically screened by characterizing the bonding descriptors such as hybridization, ionicity, polarizability, and number mismatch. Furthermore, the impact of SCALPs on bonding

interactions was characterized based on the presence of asymmetrical ns^2 states below the Fermi level and the nature of chemical bonding. Thus, this study not only identifies promising candidates for thermoelectric applications but also provides novel insights into the underlying factors affecting thermal conductivity. The elucidation of the relationship between bonding descriptors for SCALPs and thermal conductivity in pnictogen chalcogenide materials represents a significant advancement in understanding material behavior, paving the way for the design of high-performance thermoelectric materials.

4.10. References

1. Jain A., Shin Y., Persson K.A. (2016), Computational predictions of energy materials using density functional theory, *Nat Rev Mater*, 1, 15004 (DOI: 10.1038/natrevmats.2015.4)

2. Kirklin S., Saal J.E., Meredig B., Thompson A., Doak J.W., Aykol M., Rühl S., Wolverton C. (2015), The Open Quantum Materials Database (OQMD): Assessing the accuracy of DFT formation energies, *npj Comput Mater*, 1, 15010 (DOI: 10.1038/npjcompumats.2015.10)

3. Curtarolo S., Setyawan W., Wang S., Xue J., Yang K., Taylor R.H., Nelson L.J., Hart G.L.W., Sanvito S., Buongiorno Nardelli M., Mingo N., Levy O. (2012), AFLOWLIB.ORG: A distributed materials properties repository from high-throughput ab initio calculations, *Comput Mater Sci*, 58, 218–226 (DOI: 10.1016/j.commatsci.2012.02.002)

4. Jain A., Ong S.P., Hautier G., Chen W., Richards W.D., Dacek S., Cholia S., Gunter D., Skinner D., Ceder G., Persson K.A. (2013), Commentary: The Materials Project: A materials genome approach to accelerating materials innovation, *APL Mater*, 1, 011002 (DOI: 10.1063/1.4812323)

5. Furmanchuk A., Saal J.E., Doak J.W., Meredig B. (2018), Prediction of Seebeck coefficient for compounds without restriction to fixed stoichiometry: A machine learning approach, *J Comput Chem*, 39, 191–202 (DOI: 10.1002/jcc.25067)

6. Yuan H.M., Han S.H., Hu R., Zhou Y., Zhang C., Chen Y. (2022), Machine learning for accelerated prediction of the Seebeck coefficient at arbitrary carrier concentration, *Mater Today Phys*, 25, 100706 (DOI: 10.1016/j.mtphys.2022.100706)

7. Chen L., Tran H., Batra R., Kim C., Ramprasad R. (2019), Machine learning models for the lattice thermal conductivity prediction of inorganic materials, *Comput Mater Sci*, 170, 109155 (DOI: 10.1016/j.commatsci.2019.109155)

8. Minhas, H.; Jena, M. K.; Sharma, R. K.; Pathak, B. (2024), Machine Learning-Driven Inverse Design and Role of Dopant for Tuning Thermoelectric Efficiency, ACS Appl. Electron. Mater., 6 (8), 5815–5826 (DOI: 10.1021/acsaelm.4c00808)

9. Andersson S., Wadsley A.D., Biswas K., Snyder G.J. (2011), Data-driven review of thermoelectric materials: Performance and resource considerations, *Appl Phys Lett*, 99, 143901 (DOI: 10.1063/1.3641888)

10. Shi X.L., Zou J., Chen Z.G. (2020), Advanced thermoelectric design: From materials and structures to devices, *Chem Rev*, 120, 7399–7515 (DOI: 10.1021/acs.chemrev.0c00026)

11. Wang A.Y.T., Murdock R.J., Kauwe S.K., Sparks T.M. (2020), Machine learning for materials scientists: An introductory guide toward best practices, *Chem Mater*, 32, 4954–4965 (DOI: 10.1021/acs.chemmater.0c01907)

12. Vaitesswar U.S., Bash D., Huang T., Jain A. (2024), Machine learning based feature engineering for thermoelectric materials by design, *Digital Discovery*, 3, 403–416 (DOI: 10.1039/D3DD00131H)

13. Zhou H., Deng Z., Xia Y., Fu M. (2016), A new sampling method in particle filter based on Pearson correlation coefficient, *Neurocomputing*, 216, 208–215 (DOI: 10.1016/j.neucom.2016.07.036)

14. Ritter M., Li Y., Wang Y., Heller E. (2018), Efficient test for nonlinear dependence of two continuous variables, *Phys Rev E*, 98, 012130 (DOI: 10.1103/PhysRevE.98.012130)

15. Lin H., Eggesbø M., Das Peddada S. (2022), Linear and nonlinear correlation estimators unveil undescribed taxa interactions in microbiome data, *Nat Commun*, 13, 4946 (DOI: 10.1038/s41467-022-32243-x)

16. Pedregosa F., Varoquaux G., Gramfort A., Michel V., Thirion B., Grisel O., Blondel M., Prettenhofer P., Weiss R., Dubourg V., VanderPlas J., Passos A., Cournapeau D., Brucher M., Perrot M., Duchesnay É. (2011), Scikit-learn: Machine learning in Python, *J Mach Learn Res*, 12, 2825–2830

17. Douglass M.J.J. (2020), Book review: Hands-on machine learning with Scikit-Learn, Keras, and TensorFlow, *Phys Eng Sci Med*, 43, 1343–1345 (DOI: 10.1007/s13246-020-00913-z)

18. Chen T., Guestrin C. (2016), XGBoost: A scalable tree boosting system, *Proc ACM SIGKDD*, 785–794 (DOI: 10.1145/2939672.2939785)

19. Lundberg S.M., Erion G., Chen H., DeGrave A., Prutkin J.M., Nair B., Katz R., Himmelfarb J., Lee S. (2020), From local explanations to global understanding with explainable AI for trees, *Nat Mach Intell*, 2, 56–67 (DOI: 10.1038/s42256-019-0138-9)

20. Horike S., Wei Q., Kirihara K., Kitagawa S. (2020), Outstanding electrode-dependent Seebeck coefficients in ionic hydrogels for thermally chargeable supercapacitors near room temperature, *ACS Appl Mater Interfaces*, 12, 40747–40755 (DOI: 10.1021/acsami.0c11752)

21. Zhou H., Liu P. (2018), High Seebeck coefficient electrochemical thermocells for efficient waste heat recovery, *ACS Appl Energy Mater*, 1, 1423–1430 (DOI: 10.1021/acsaem.8b00247)

22. Nielsen M.D., Ozoliņš V., Heremans J.P. (2013), Lone pair electrons minimize lattice thermal conductivity, *Energy Environ Sci*, 6, 570–578 (DOI: 10.1039/C2EE23391F)

23. Qian X., Zhou J., Chen G. (2021), Phonon-engineered extreme thermal conductivity materials, *Nat Mater*, 20, 1188–1202 (DOI: 10.1038/s41563-021-01008-9)

24. Deng R., Su X., Zheng Z., Yan Y., Xie H., Liu W., Yang L., Uher C., Tang X., Zhang Q. (2018), Thermal conductivity in $Bi_{0.5}Sb_{1.5}Te_{3+x}$ and the role of dense dislocation arrays at grain boundaries, *Sci Adv*, 4, eaar5606 (DOI: 10.1126/sciadv.aar5606)

25. Kim S.I., Lee K.H., Mun H.A., Kim H.S., Hwang S.W., Roh J.W., Yang D.J., Shin W.H., Li X.S., Lee Y.H., Snyder G.J., Kim S.W. (2015), Dense dislocation arrays embedded in grain boundaries for high-performance bulk thermoelectrics, *Science*, 348, 109–114 (DOI: 10.1126/science.aaa4166)

26. Zhu B., Liu X., Wang Q., Qiu Y., Shu Z., Guo Z., Tong Y., Cui J., Gu M., He J. (2020), Realizing record high performance in n-type Bi_2Te_3-based thermoelectric materials, *Energy Environ Sci*, 13, 2106–2114 (DOI: 10.1039/D0EE01349H)

27. Sun P., Wei B., Zhang J., Li Y., Zhao X., Liu Y., Liu S., He J. (2015), Large Seebeck effect by charge-mobility engineering, *Nat Commun*, 6, 7475 (DOI: 10.1038/ncomms8475)

28. Liu H., Yuan X., Lu P., Shi X., Xu F., He Y., Tang Y., Bai S., Zhang W., Chen L., Snyder G.J. (2013), Ultrahigh thermoelectric performance by electron and phonon critical scattering in $Cu_2Se_{1-x}I_x$, *Adv Mater*, 25, 6607–6612 (DOI: 10.1002/adma.201302660)

29. Perumal S., Roychowdhury S., Negi D.S., Datta R., Biswas K. (2015), High thermoelectric performance and enhanced mechanical stability of p-type $Ge_{1-x}Sb_xTe$, *Chem Mater*, 27, 7171–7178 (DOI: 10.1021/acs.chemmater.5b03434)

30. Perumal S., Bellare P., Shenoy U.S., Biswas K. (2017), Low thermal conductivity and high thermoelectric performance in Sb and Bi codoped GeTe, *Chem Mater*, 29, 10426–10435 (DOI: 10.1021/acs.chemmater.7b04023)

31. Nshimyimana E., Hao S., Su X., Zhang X., Wolverton C., Uher C., Dravid V.P., Yan Q., Kanatzidis M.G. (2020), Discordant nature of Cd in GeTe enhances phonon scattering and improves band convergence, *J Mater Chem A*, 8, 1193–1204 (DOI: 10.1039/C9TA10436D)

32. Heremans J.P., Jovovic V., Toberer E.S., Saramat A., Kurosaki K., Charoenphakdee A., Yamanaka S., Snyder G.J. (2008), Enhancement of thermoelectric efficiency in PbTe by distortion of the electronic density of states, *Science*, 321, 554–557 (DOI: 10.1126/science.1159725)

33. Volkov B.A., Ryabova L.I., Khokhlov D.R. (2002), Mixed-valence impurities in lead telluride-based solid solutions, *Phys Usp*, 45, 819–846 (DOI: 10.1070/PU2002v045n08ABEH001146)

34. Woods-Robinson R., Han Y., Zhang H., Schelhas T.J., Stevanović D.A., Zakutayev A. (2020), Wide band gap chalcogenide semiconductors, *Chem Rev*, 120, 4007–4055 (DOI: 10.1021/acs.chemrev.9b00416)

35. Liu D., Wang D., Hong T., Li J., Tang X., He J. (2023), Lattice planarification advances highly effective SnSe crystalline thermoelectrics, *Science*, 380, 841–846 (DOI: 10.1126/science.adg7196)

36. Christensen M., Abrahamsen A.B., Christensen N.B., Jurányi F., Andersen N.H., Lefmann K., Andreasson J., Bahl C.R.H., Iversen B.B. (2008), Avoided crossing of rattler modes in thermoelectric materials, *Nat Mater*, 7, 811–815 (DOI: 10.1038/nmat2265)

37. Liu H., Shi X., Xu F., Zhang L., Zhang W., Chen L., Li Q., Uher C., Day T., Snyder G.J. (2012), Copper ion liquid-like thermoelectrics, *Nat Mater*, 11, 422–425 (DOI: 10.1038/nmat3273)

38. Zheng Y., Slade T.J., Hu L., Tan X., Luo Y., Luo Z., Xu J., Yan Q., Kanatzidis M.G. (2021), Defect engineering in thermoelectric materials: What have we learned?, *Chem Soc Rev*, 50, 9022–9054 (DOI: 10.1039/D1CS00216E)

39. Chandra S., Bhat U., Dutta P., Banerjee R., Biswas K. (2022), Modular nanostructures facilitate low thermal conductivity and ultra-high thermoelectric performance in n-type SnSe, *Adv Mater*, 34, 2203725 (DOI: 10.1002/adma.202203725)

40. Biswas K., He J., Blum I.D., Wu C.-I., Hogan T.P., Seidman D.N., Dravid V.P., Kanatzidis M.G. (2012), High-performance bulk

thermoelectrics with all-scale hierarchical architectures, *Nature*, 489, 414–418 (DOI: 10.1038/nature11439)

41. Skoug E.J., Morelli D.T. (2011), Role of lone-pair electrons in producing minimum thermal conductivity in nitrogen-group chalcogenide compounds, *Phys Rev Lett*, 107, 235901 (DOI: 10.1103/PhysRevLett.107.235901)

42. Spitzer D.P. (1970), Lattice thermal conductivity of semiconductors: A chemical bond approach, *J Phys Chem Solids*, 31, 347–355 (DOI: 10.1016/0022-3697(70)90284-2)

43. Morelli D.T., Jovovic V., Heremans J.P. (2008), Intrinsically minimal thermal conductivity in cubic I–V–VI2 semiconductors, *Phys Rev Lett*, 101, 035901 (DOI: 10.1103/PhysRevLett.101.035901)

44. Skoug E.J., Cain J.D., Morelli D.T. (2010), Structural effects on the lattice thermal conductivity of ternary antimony- and bismuth-containing chalcogenide semiconductors, *Appl Phys Lett*, 96, 061902 (DOI: 10.1063/1.3425886)

45. Zhang Y., Skoug E., Cain J., Morelli D.T. (2012), First-principles description of anomalously low lattice thermal conductivity in thermoelectric Cu–Sb–Se ternary semiconductors, *Phys Rev B*, 85, 054306 (DOI: 10.1103/PhysRevB.85.054306)

46. Walsh A., Payne D.J., Egdell R.G., Watson G.W. (2011), Stereochemistry of post-transition metal oxides: Revision of the classical lone pair model, *Chem Soc Rev*, 40, 4455–4463 (DOI: 10.1039/c1cs15098g)

47. Laurita G., Seshadri R. (2022), Chemistry, structure, and function of lone pairs in extended solids, *Acc Chem Res*, 55, 1194–1206 (DOI: 10.1021/acs.accounts.1c00741)

48. Rathore E., Juneja R., Culver S.P., Biswas K., Snyder G.J., Kanatzidis M.G. (2019), Origin of ultralow thermal conductivity in n-type cubic bulk AgBiS2: Soft Ag vibrations and local structural distortion induced by the

Bi 6s2 lone pair, *Chem Mater*, 31, 2469–2479 (DOI: 10.1021/acs.chemmater.9b00001)

49. Maria I., Arora R., Dutta M., Saha S., Nath P., Biswas K. (2023), Metavalent bonding-mediated dual 6s2 lone pair expression leads to intrinsic lattice shearing in n-type TlBiSe2, *J Am Chem Soc*, 145, 12345–12354 (DOI: 10.1021/jacs.3c02146)

50. Chen S., Walsh A., Gong X.G., Wei S.H. (2013), Classification of lattice defects in the kesterite Cu2ZnSnS4 and Cu2ZnSnSe4 earth-abundant solar cell absorbers, *Adv Mater*, 25, 1522–1539 (DOI: 10.1002/adma.201203146)

51. Minhas, H.; Jena, M. K.; Sharma, R. K.; Pathak, B. (2025), Insights into Thermal Conductivity of Pnictogen Chalcogenides: Machine Learning Stereochemically Active Lone Pairs and Hybridization, Chem. Mater., 37 (1), 198–209 (DOI: 10.1021/acs.chemmater.4c02294)

52. He J., Hu X., Liu Z., Xia Y., Li W., Sun Y., Yan Y., Pan W., Chen Q., Yang W., Zhang L. (2023), Prospect for bismuth/antimony chalcohalides-based solar cells, *Adv Funct Mater*, 33, 2301457 (DOI: 10.1002/adfm.202301457)

53. Ogawa K., Abe R., Walsh A. (2024), Band gap narrowing by suppressed lone-pair activity of Bi3+, *J Am Chem Soc*, 146, 11234–11244 (DOI: 10.1021/jacs.4c00150)

54. Zafari M., Kumar D., Umer M., Kim K.S. (2020), Machine learning-based high throughput screening for nitrogen fixation on boron-doped single atom catalysts, *J Mater Chem A*, 8, 24692–24702 (DOI: 10.1039/c9ta12608b)

55. Umer M., Umer S., Zafari M., Chen W., Zhang L., Li H., Sun Q., Yin H., (2022), Machine learning assisted high-throughput screening of transition metal single atom based superb hydrogen evolution electrocatalysts, *J Mater Chem A*, 10, 10123–10135 (DOI: 10.1039/d1ta09878k)

56. Ha M., Hajibabaei A., Kim D.Y., et al. (2022), Al-doping driven suppression of capacity and voltage fadings in 4d-element containing Li-ion-battery cathode materials: Machine learning and density functional theory, *Adv Energy Mater*, 12, 2201497 (DOI: 10.1002/aenm.202201497)

57. Long T., Fortunato N.M., Opahle I., Li X., Chen C., (2021), Constrained crystals deep convolutional generative adversarial network for the inverse design of crystal structures, *NPJ Comput Mater*, 7, 87 (DOI: 10.1038/s41524-021-00526-4)

58. Ryan K., Lengyel J., Shatruk M. (2018), Crystal structure prediction via deep learning, *J Am Chem Soc*, 140, 10158–10168 (DOI: 10.1021/jacs.8b03913)

59. Pal K., Park C.W., Xia Y., He J., (2022), Scale-invariant machine-learning model accelerates the discovery of quaternary chalcogenides with ultralow lattice thermal conductivity, *NPJ Comput Mater*, 8, 76 (DOI: 10.1038/s41524-022-00732-8)

60. Saal J.E., Kirklin S., Aykol M., Meredig B., Wolverton C., (2013), Materials design and discovery with high-throughput density functional theory: The open quantum materials database (OQMD), *JOM*, 65, 1501–1509 (DOI: 10.1007/s11837-013-0755-4)

61. Choudhary K., DeCost B., Chen C., Tavazza F., (2022), Recent advances and applications of deep learning methods in materials science, *NPJ Comput Mater*, 8, 180 (DOI: 10.1038/s41524-022-00782-0)

62. Ryu B., Wang L., Pu H., Xie M., Zhou Y., (2022), Understanding, discovery, and synthesis of 2D materials enabled by machine learning, *Chem Soc Rev*, 51, 7289–7325 (DOI: 10.1039/d1cs00947j)

63. Spitzer D.P. (1970), Lattice thermal conductivity of semiconductors: A chemical bond approach, *J Phys Chem Solids*, 31, 347–355 (DOI: 10.1016/0022-3697(70)90284-2)

64. Lencer D., Salinga M., Grabowski B., Hickel T., Neugebauer J., Wuttig M., (2008), A map for phase-change materials, *Nat Mater*, 7, 972–977 (DOI: 10.1038/nmat2330)

65. Chelikowsky J.R., Phillips J.C. (1978), Quantum-defect theory of heats of formation and structural transition energies of liquid and solid simple metal alloys and compounds, *Phys Rev B*, 17, 2453–2467 (DOI: 10.1103/PhysRevB.17.2453)

66. Deng T., Wei T.R., Huang H., Chen C., Chen S. (2020), Number mismatch between cations and anions as an indicator for low lattice thermal conductivity in chalcogenides, *NPJ Comput Mater*, 6, 90 (DOI: 10.1038/s41524-020-00355-x)

67. Raty J.Y., Gatti C., Schön C.F., Wuttig M. (2021), How to identify lone pairs, van der Waals gaps, and metavalent bonding using charge and pair density methods: From elemental chalcogens to lead chalcogenides and phase-change materials, *Phys Status Solidi RRL*, 15, 2000534 (DOI: 10.1002/pssr.202000534)

68. Barua N.K., Golabek A., Oliynyk A.O., Kleinke H. (2023), Experimentally validated machine learning predictions of ultralow thermal conductivity for SnSe materials, *J Mater Chem C*, 11, 2145–2156 (DOI: 10.1039/d3tc01450a)

69. Skoug E.J., Cain J.D., Morelli D.T. (2011), Lattice thermal conductivity of the Cu3SbSe4–Cu3SbS4 solid solution, *J Appl Phys*, 110, 063717 (DOI: 10.1063/1.3610385)

70. Tolborg K., Gatti C., Iversen B.B. (2020), Expression and interactions of stereochemically active lone pairs and their relation to structural distortions and thermal conductivity, *IUCrJ*, 7, 1089–1102 (DOI: 10.1107/S2052252520003619)

71. Chang C., Zhao L.D. (2018), Anharmonicity and low thermal conductivity in thermoelectrics, *Materials Today Physics*, 4, 50–60 (DOI: 10.1016/j.mtphys.2018.03.001)

72. Kooi B.J., Wuttig M. (2020), Chalcogenides by design: Functionality through metavalent bonding and confinement, *Adv Mater*, 32, 1908302 (DOI: 10.1002/adma.201908302)

73. Liu X., Wang D., Wu H., Wang J., Zhang Y., Wang G., Pennycook S.J., Zhao L.-D. (2019), Intrinsically low thermal conductivity in BiSbSe3: A promising thermoelectric material with multiple conduction bands, *Adv Funct Mater*, 29, 1806558 (DOI: 10.1002/adfm.201806558)

74. Zhao J., Islam S.M., Hao S., Tan G., Su X., Chen H., Lin W., Wolverton C., Kanatzidis M.G. (2017), Semiconducting pavonites CdMBi4Se8 (M = Sn and Pb) and their thermoelectric properties, *Chem Mater*, 29, 5322–5331 (DOI: 10.1021/acs.chemmater.7b03328)

75. Sato N., Kuroda N., Nakamura S., Katsura Y., Kanazawa I., Kimura K., Mori T. (2021), Bonding heterogeneity in mixed-anion compounds realizes ultralow lattice thermal conductivity, *J Mater Chem A*, 9, 17150–17159 (DOI: 10.1039/d1ta04958e)

76. Isaacs E.B., Lu G.M., Wolverton C. (2020), Inverse design of ultralow lattice thermal conductivity materials via materials database screening of lone pair cation coordination environment, *J Phys Chem Lett*, 11, 7810–7818 (DOI: 10.1021/acs.jpclett.0c01077)

77. Silvi B., Savin A. (1994), Classification of chemical bonds based on topological analysis of electron localization functions, *Nature*, 371, 683–686 (DOI: 10.1038/371683a0)

78. Walsh A., Watson G.W. (2005), The origin of the stereochemically active Pb(II) lone pair: DFT calculations on PbO and PbS, *J Solid State Chem*, 178, 1422–1428 (DOI: 10.1016/j.jssc.2005.01.030)

79. Walsh A., Watson G.W. (2005), Influence of the anion on lone pair formation in Sn(II) monochalcogenides: A DFT study, *J Phys Chem B*, 109, 18868–18875 (DOI: 10.1021/jp051822r)

CHAPTER 5

Insights into Antibonding States Drive Anharmonicity and Low κ_L

CHAPTER 5

CHAPTER 5

Section: A

5.1. Introduction

Semiconductors containing post-transition metal cations with stereochemically active lone pairs (SCALPs) are gaining prominence in materials research due to their remarkable thermoelectrics, *[1, 2]* and thermal data storage applications *[3]*. The unique characteristics of SCALP materials, including cations like Sn^{2+}, Pb^{2+}, As^{3+}, Sb^{3+}, and Bi^{3+}, induces local dipoles through non-bonding interactions, leading to strong lattice anharmonicity *[1, 4–6]*. Such non-bonding effect introduces anharmonicity, which disrupts local symmetry, reducing thermal conductivity in thermoelectric materials. The high efficiency of advanced thermoelectric materials in converting waste heat into electricity is primarily due to the strong anharmonicity resulting from changes in the electronic configuration within SCALP systems *[2]*. In pnictogen chalcogenide materials such as $CuBiS_2$, *[7]* $AgSbSe_2$, *[8]* $AgSbTe_2$, *[9]* $AgBiSe_2$, *[10]* and $AgBiS_2$ *[11]* the high phonon anharmonicity and low lattice thermal conductivity (κ_L) values originate from strong electrostatic repulsions between the pnictogen SCALP and valence p-orbital of chalcogenide *[12]*. This alteration in electronic configuration is driven by orbital interactions in SCALP materials, as described by the revised lone-pair model, as shown in **Figure 5.1a** *[13]*.

Additionally, loosely bonded rattler atoms affect the chemical bonding hierarchies in materials such as $AsBi_3S_5$, *[14]* $TlInTe_2$, *[15]* $LiCu_3TiQ_4$ (Q = S, Se or Te), *[16]* $AgPbBiSe_3$, *[17]* and $NaCuZeSe_3$, *[18]* amplifying anharmonicity. Therefore, the combined effect of SCALP effects and rattling atoms further enhance phonon scattering without significantly impacting charge carrier mobility. Therefore, in this study, we have investigated the impact of rattling atoms on SCALP-containing $AAsSe_2$ (where A = Li/Na) systems, have been synthesized and characterized. *[19, 20]* However, capturing anharmonicity in non-centrosymmetric materials requires precise vibrational Hamiltonians to accurately describe phonon

interactions, making it computationally expensive *[21–23]*. To mitigate this challenge, machine learning-based approaches have been emerged as efficient alternatives for interatomic potential fitting, enabling accurate descriptions within the Born-Oppenheimer approximations, as illustrated in **Figure 5.1(b-f)** *[24–26]*. These approaches provide an efficient means of predicting anharmonic interatomic force constants and κ_L, which are crucial for designing high-efficiency thermoelectric materials *[24, 26]*.

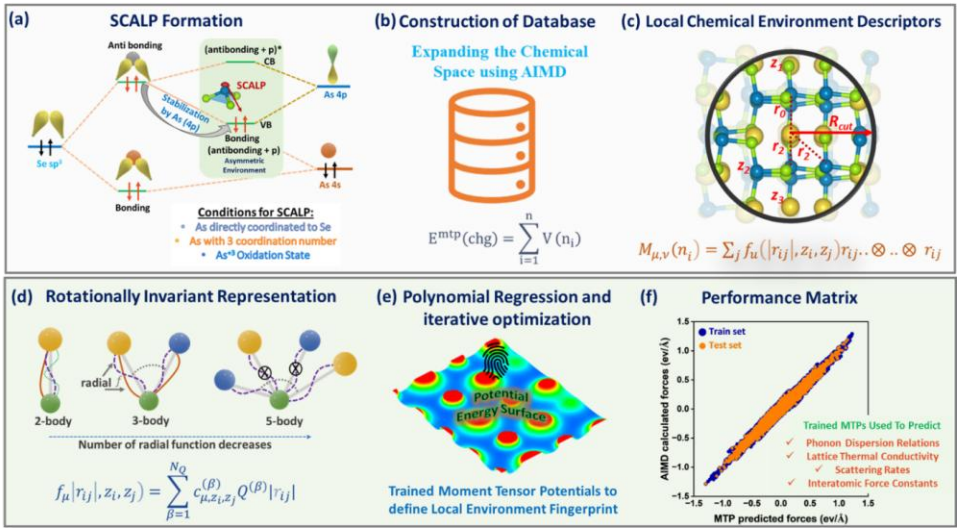


Figure 5.1. (a) Orbital interactions in the lone-pair containing As-Se bonds that facilitate stereochemically active lone pair (SCALP) formation, **(b)** Expanding the chemical space using *ab initio* molecular dynamics (AIMD) simulations to represent energy of an atomic configuration ($E^{mtp}(chg)$) comprised of local potential (V) of neighboring atoms (n_i), **(c)** Local chemical environment descriptors defining the moment tensor, where neighboring atoms within a cut-off radius (R_{cut}) interact with the central atom, where f_u encodes the radial information and $r_{ij} \otimes ... \otimes r_{ij}$ contains the angular information, **(d)** constructing invariant features through atomic permutations, rotations, and reflections by computing tensor contractions and eliminating linear dependencies, defining radial basis function which uses polynomial operator on interatomic distances (r_{ij}), $c = \{c^{(\beta)}_{\mu,z_i,z_j}\}$ is radical basis function, $Q^{(\beta)}(|r_{ij}|)$ uses polynomial functions operated on

interatomic distances based on cutoff radius **(e)** training moment tensor potentials (MTPs) using the polynomial regression and iterative optimization to define the local chemical environment representing potential energy surface, and **(f)** performance matrix illustrating the accuracy of trained MTPs through scatter plots comparing AIMD calculated energies/forces with MTP predicted energies/forces used to predict thermal transport properties of $LiAsSe_2$ and $NaAsSe_2$ materials.

In this study, we generated over 10,500 configurations for $LiAsSe_2$ and $NaAsSe_2$, using *ab initio* molecular dynamics to train MTPs, which efficiently captures structural energies and atomic forces, enabling rapid thermal transport calculations and uncovering key mechanistic pathways responsible for low κ_L. We analysed the strong SCALP expression enhancing electrostatic forces results in small bond angle impacting the high anharmonicity. We also analyzed the electronic behaviour of SCALP (As^{+3}) and the rattling effect of Li and Na atoms to understand high anharmonicity using orbital hybridization theory. The sp hybridization orbital interactions were studied through atom-projected density of states and crystal orbital Hamilton population methods, highlighting the potential of materials combining SCALP and rattler atoms for thermoelectric applications.

5.2. Computational Details

The first-principles calculations were performed using the projector augmented wave (PAW) method, as implemented in the Vienna ab initio simulation package (VASP) *[27, 28]*. The exchange-correlation interactions were treated using the generalized gradient approximation (GGA) within the Perdew-Burke-Ernzerhof (PBE) functional *[29, 30]*. A plane-wave cutoff energy of 500 eV was applied, with Gamma centered *k*-point grids of $5 \times 5 \times 5$ for $LiAsSe_2$ and $5 \times 8 \times 5$ for $NaAsSe_2$. The structural relaxations were conducted with convergence criteria set to Hellmann−Feynman forces below 0.001 eV/Å and total energy converged within 10^{-6} eV. Van der Waals and long-range interactions were accounted

using Grimme's DFT-D3 method *[31]*. To achieve an accurate prediction of electronic structures, calculations were performed using Heyd–Scuseria–Ernzerhof (HSE06) hybrid functional with Hartree–Fock exchange parameter (α) of 25% *[32, 33]*.

5.2.1. MTP Training To model interatomic interactions via the potential energy surface, machine learning interatomic potentials (MTPs) were developed. The training dataset for MTPs was generated through *ab initio* molecular dynamics (AIMD) simulations using VASP *[34, 35]*. A 2 x 2 x 2 supercell for $LiAsSe_2$ and 1 x 1 x1 supercell for $NaAsSe_2$ were used in AIMD simulations with an *NPT* thermostat, spanning temperatures from 100 K to 700 K in 100 K increments. Each temperature step included 1500 simulation steps with a time step of 1fs, resulting in a total of 10,500 data points comprising energies, forces, and stresses. To minimize redundancy, every fourth datapoint was selected, yielding a refined dataset of 2800 points. This dataset was subsequently split into a training set (2100 points) and a test set (525 points) following an 80:20 ratio. The training set was then used to develop MTPs through polynomial-based linear regression using the MLIP package *[24, 36]*. These trained potentials were employed for predicting phonon dispersion relations, and computing 2^{nd} and 3^{rd} order interatomic force constants (IFCs).[51]

5.2.2. Thermal and Electronic Transport Properties. Lattice transport properties were derived from 2^{nd} and 3^{rd} order IFCs, which were used as input in the SHENGBTE code to calculate the lattice thermal conductivity (κ_L) of the materials *[37]*. A q-points mesh of 17 × 17 × 17 was applied to the $AAsSe_2$ systems (A= Li/Na) to ensure convergence and accuracy in κ_L calculations. Phonon-mediated thermal transport properties were evaluated using the ShengBTE package. [52] Additionally, the *ab initio* Scattering and Transport (AMSET) code was used to calculate electronic transport properties, incorporating ionized impurity, acoustic deformation potential, and piezoelectric scatterings to enable accurate relaxation time calculations *[38]*.

5.3. Results and Discussion

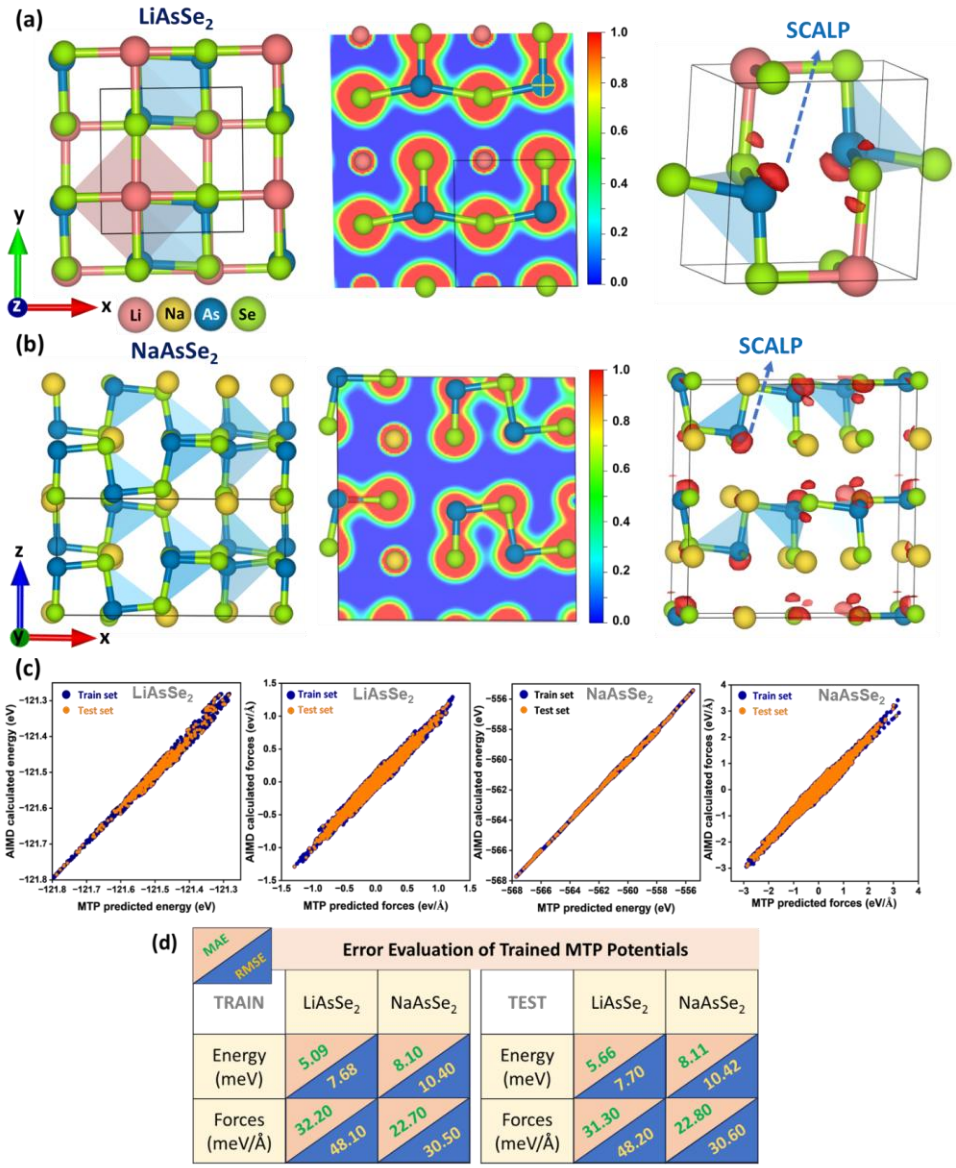
5.3.1. SCALP and Anharmonicity in alkali-metal chalcoarsenates

To understand the formation of SCALP and the anharmonicity in alkali-metal chalcoarsenates, we have thoroughly investigated their geometric and molecular orbital properties The ternary compounds $AAsSe_2$ (A= Li, Na) belong to the I-V-VI_2 family and exhibits cation-disordered structures suitable for thermoelectric applications.[53, 54] The calculated lattice parameters for $AAsSe_2$ (A= Li, and Na) systems closely align with experimental values (**Table 5.1**) *[19]*.

Table 5.1: The lattice parameters (Å) of the considered structures of $LiAsSe_2$ and $NaAsSe_2$ systems.

Systems	Considered			Experimental		
	a	**b**	**c**	**a**	**b**	**c**
$LiAsSe_2$	5.58	5.58	5.58	5.55	5.55	5.55
$NaAsSe_2$	11.77	5.96	11.96	11.68	5.90	11.82

$LiAsSe_2$ crystallizes in the cubic space group $Fm\bar{3}m$, adopting a NaCl-type structure (**Figure 5.2(a)**), while also featuring a distinctive layered arrangement along the x-axis, consisting of alternating $AsSe_3$ pyramids and $LiSe_6$ octahedra, with the layers interconnected through As–Se or Li–Se bonds. In contrast, γ-$NaAsSe_2$ displays a unique atomic arrangement, featuring dense, one-dimensional, infinite pyramidal polymeric $[AsSe_2]^-$ anionic chains interspersed with Na^+ ions, as depicted in **Figure 5.2(b)**.



(d)

MAE / RMSE	Error Evaluation of Trained MTP Potentials					
TRAIN	$LiAsSe_2$		$NaAsSe_2$	TEST	$LiAsSe_2$	$NaAsSe_2$	
Energy (meV)	5.09	7.68	8.10	10.40	Energy (meV)	5.66	7.70	8.11	10.42
Forces (meV/Å)	32.20	48.10	22.70	30.50	Forces (meV/Å)	31.30	48.20	22.80	30.60

Figure 5.2: The unit cell of **(a)** lithium chalcoarsenate $LiAsSe_2$, **(b)** sodium chalcoarsenate $NaAsSe_2$ along with total electronic charge distribution (TECD) contour plots along the (010) plane and the 3D electron localization function (ELF) visualized at an iso-surface value of 0.9 $eVÅ^{-3}$ reveal the presence of lone pairs around As and Se atoms **(c)** Scatter plots comparing MTP-predicted with AIMD calculated values: energy and force parity plots for $LiAsSe_2$ and $NaAsSe_2$. **(d)** The error matrix of trained MTPs evaluated in root mean square error (RMSE) and mean absolute error (MAE) for

energies (in meV) and forces (meV $Å^{-1}$) for both the training and testing sets.

In both the systems, each As atom forms bonds with three Se atoms, resulting in the formation of pyramidal $AsSe_3$ units due to the presence of the $4s^2$ SCALP in As^{3+}. In γ-$NaAsSe_2$, the average Se-As-Se bond angle is 99.23°, slightly lower than the 99.98° observed in $LiAsSe_2$. The significant deviation from the ideal tetrahedral angle (109°) in both systems can be attributed to strong, non-linear repulsive electrostatic interactions between the lone pairs and adjacent As atoms, contributing to higher lattice anharmonicity *[26]*. Interestingly, the slightly reduced Se-As-Se bond angle in γ-$NaAsSe_2$ is reflected in the calculated mechanical properties (Table 5.3), where γ-$NaAsSe_2$ exhibits lower bulk, Young's, and shear moduli compared to $LiAsSe_2$. This suggests that the weaker bonding in γ-$NaAsSe_2$ may contribute to increased phonon anharmonicity *[27]*.

Table 5.2: The sum of covalent and ionic radii (Å) of respective atoms in A–Se (A = Li and Na), and As–Se and the actual bond lengths are defined in blue color.

Systems	**A–Se (Å)**			**As–Se (Å)**		
	Actual	**Covalent**	**Ionic**	**Actual**	**Covalent**	**Ionic**
$LiAsSe_2$	2.82	2.49	2.79	2.51	2.37	2.75
$NaAsSe_2$	3.00	2.71	3.04	2.45	2.37	2.75

To understand bonding hierarchies, we analysed asymmetric As-Se and Li/Na-Se interactions, as tabulated in **Table 5.2**. The Li/Na-Se bond distance closely matches the sum of the ionic radii, indicating a strong ionic character and rattling behavior of Li/Na due to weak interactions. In contrast, As-Se bonds exhibit greater covalency, contributing to system's rigidity. This bonding hierarchy is further evident in total electronic charge density (TECD) contour plots (**Figure 5.2(a-b)),** where the spherical charge contours around Li and Na confirm their ionic nature, while elliptical charge

distributions around As and Se indicate covalent bonding interactions. The reduction in As-Se overlap from $LiAsSe_2$ to $NaAsSe_2$ indicates a decrease in covalency, which could lead to an increase in anharmonicity. Such coexistence of various bonding interactions and bond strengths creates a chemical bonding hierarchies at the microscopic scale, crucial for achieving high thermoelectric performance *[39–41]*. To visualize ns^2 lone-pair electrons in As^{+3} SCALP atoms, we plotted the 3D electron localization function (ELF) *[42]*, which quantifies electron localization and captures the influence of Pauli electrostatic repulsion. The resulting red mushroom-shaped electron density clouds (**Figure 5.2**) around nonbonding $4s^2$ lone pairs on As and Se atoms confirm their spatial distribution. These lone pairs induce nonlinear electrostatic repulsions, disrupting lattice symmetry. This can affect Li/Na rattling, and lattice vibrations, ultimately leading to increased anharmonicity and reduced κ_L *[12]*.

5.3.2. Machine Learning Potentials.

Accurately quantifying thermal conductivity, phonon transport and anharmonicity requires high throughput calculations of interatomic force constants, which are computationally expensive for large, non-centrosymmetric unit cells. To overcome this, we trained machine learning interatomic potentials (MTPs) using ab initio molecular dynamics (AIMD) simulations, enabling efficient prediction of the important thermal properties for the complex crystal structure. As described in the computational details, MTPs were developed by mapping the potential energy surface (PES) using AIMD configurations and optimizing hyperparameters, achieving a basis function size of 581 and an outer cutoff radius of 5 Å. Additionally, nonlinear optimization of the element-pair-dependent coefficients in the radial functions increased model robustness, as listed in **Table 5.3**. These trained MTPs effectively capture mid and long-range interactions beyond first neighbors.[51]

Table 5.3: The optimized MTP hyperparameters for $LiAsSe_2$ and $NaAsSe_2$

Hyperparameters	$LiAsSe_2$	$NaAsSe_2$
scaling	0.119	0.016
species_count	3	3
radial_basis_type	RBChebyshev	RBChebyshev
min_dist	2.11	1.64
max_dist	5.00	5.00
radial_basis_size	6	6
radial_funcs_count	6	6
alpha_moments_count	4991	4991
alpha_index_basic_count	581	581
alpha_scalar_moments	864	864
alpha_index_times_count	36170	36170

To evaluate the stability and reliability of the trained MTPs, their performance was evaluated through scatter plots and statistical metrics, including mean absolute error (MAE) and root mean square error (RMSE) for energies (*E*) and forces (*F*) prediction, as shown in **Figure 5.2(c-d)**. The test RMSE scores were 5.66 meV for energy and 31.30 meV/Å for forces in $LiAsSe_2$ and 8.11 meV for energy and 22.80 meV/Å for forces in $NaAsSe_2$. These low errors validate the high accuracy of MTPs, providing a strong foundation for further predictions of thermal transport properties, including 2^{nd} and 3^{rd} order interatomic force constants (IFCs), and extracted anharmonic scattering rates to analyze lattice dynamics and their influence on thermal transport. These rates were then analyzed through the phonon Boltzmann transport equation *[37]*.

5.3.3. Thermal Transport Figure 5.3(a) presents the direction-dependent κ_L as a function of temperature. At 300 K and 900 K, $LiAsSe_2$ exhibits higher κ_L values of 2.05 W/m K and 0.66 W/m K along the x-axis, respectively. Whereas $NaAsSe_2$ demonstrates an ultralow κ_L of 0.41 W/m K at 300 K, further decreasing to 0.14 W/m K at 900 K. Notably, $NaAsSe_2$

exhibits a lower κ_L than many ABX_2-type materials calculated at room temperature, such as $TlAsS_2$ (0.95 W/m K), $AgSbSe_2$ (0.77 W/m K), $AgSbTe_2$ (0.68 W/m K), as shown in **Figure 5.3(b)** *[5]*.

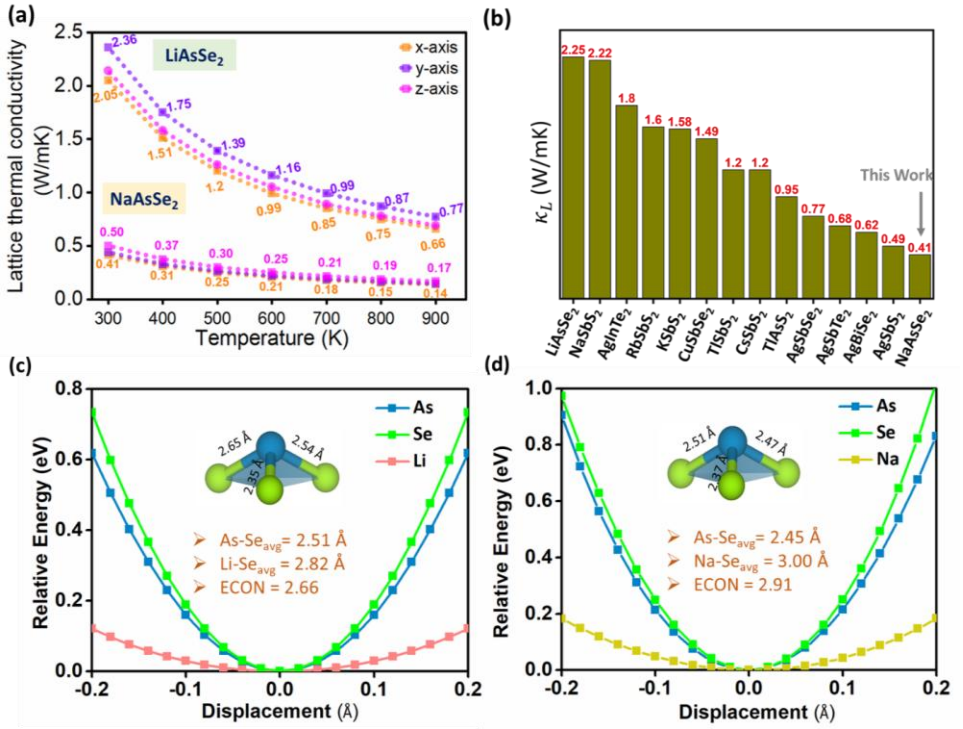


Figure 5.3: (a) The machine learning interatomic potential predicted lattice thermal conductivity (κ_L) of $LiAsSe_2$ and $NaAsSe_2$ as a function of temperature (K) along three axes. **(b)** The comparison of κ_L with ABX_2 compounds featuring lone pair electrons, with data obtained from Ref. 5 and 33 Atomic displacement parameters for **(c)** $LiAsSe_2$ and **(d)** $NaAsSe_2$ across the equilibrium positions.

To understand the rationale behind the low κ_L in $NaAsSe_2$, we analyzed the bonding hierarchy and atomic-level dynamics using atomic displacement parameter. **Figure 5.3(c-d)** illustrates that Li and Na atoms exhibit shallow potential well with relatively flat variations, reflecting a characteristic energy profile associated with rattling behaviour. Whereas, As and Se atoms reside in deeper energy wells, due to strong chemical bonding. This disparity arises from the weak chemical bonding of Li/Na atoms, which

permits larger vibrational amplitudes compared to the more rigidly bounded As/Se atoms. As a result, the enhanced vibrational motion of Li/Na atoms may increase the scattering of low-lying optical and acoustic phonons, which in turn contribute towards ultralow κ_L. Furthermore, the MTP-predicted phonon dispersions allow us to capture the vibrational modes in detail, providing distinctive fingerprints of the chemical species along with the high-symmetry points of the Brillouin zone *[7, 44]*. The absence of imaginary frequencies in **Figure 5.4(a,b)** confirms the dynamical stability of $LiAsSe_2$ and $NaAsSe_2$ systems across the Brillouin zone, where the propagation of phonon modes describes the nature of heat transport *[41]*. The acoustic phonon modes, highlighted in red, blue, and green, predominantly govern lattice heat transport.

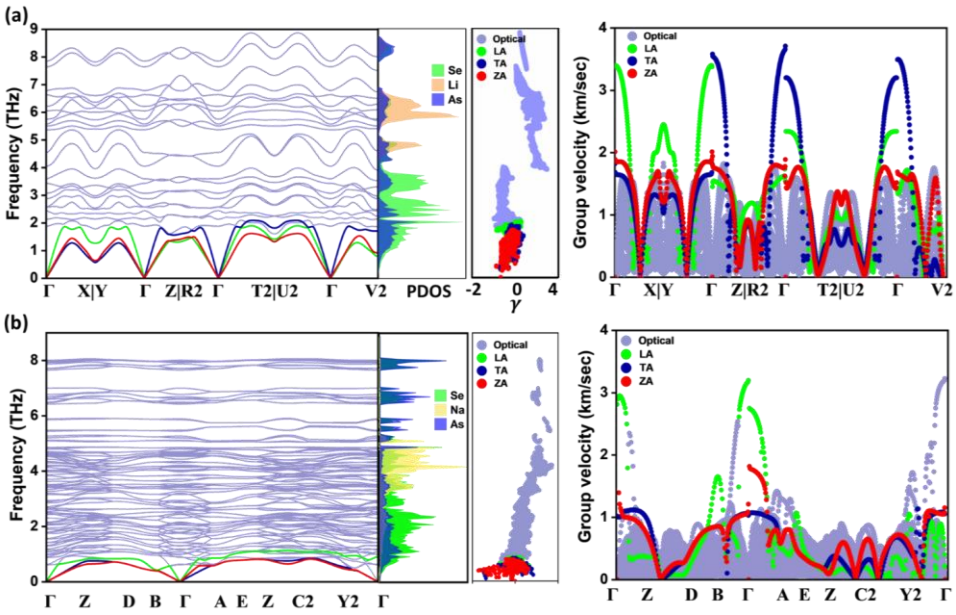


Figure 5.4: The machine learning interatomic potential predicted phonon dispersion, phonon density of states and Grüneisen parameter (γ), group velocity across the high symmetry points in the first Brillouin zone for **(a)** $LiAsSe_2$, **(b)** $NaAsSe_2$. In the plot, the longitudinal acoustic (LA) mode is highlighted in green, and the two-transverse acoustic (TA) phonon modes are highlighted in blue and red.

The phonon dispersion curves and phonon density of states (PDOS), reveal significant phonon softening from $LiAsSe_2$ to $NaAsSe_2$, attributed to SCALP electrons associated with the As atoms. This softening in $NaAsSe_2$ enhances acoustic-optical phonon interactions in the low-frequency region (below 2 THz), leading to incoherent vibrations akin to host−guest structures *[45]*. Additionally, the flattening of two transverse acoustic (ZA and TA) branches along high-symmetry directions $\Gamma \rightarrow Z$ and $A \rightarrow Z$ introduces additional scattering channels, enhancing phonon scattering and reducing κ_L *[7]*. Similar phonon flattening trends observed in $AgCrSe_2$ *[43]* and $YbFe_4Sb_{12}$, *[55]* highlight the localized vibrations and rattling effects contribute to lower group velocities and higher scattering rates. The phonon group velocity, derived from the phonon dispersion curves (**Figure 5.4**), directly influences κ_L *[48]*. The flattened phonon bands along the $Z \rightarrow D$ and $A \rightarrow Z$ directions result in lower phonon group velocities, which reduce κ_L values and indicate a decrease in group velocity from $LiAsSe_2$ to $NaAsSe_2$, contributing to the ultralow κ_L in $NaAsSe_2$. The PDOS further reveals that acoustic branches are dominated by heavier As^{+3} and Se^{-2} species, while Li and Na contribute to mid-energy optical phonons (4-7 THz for Li, 3-5 THz for Na). The dispersionless, localized phonon branches, characteristic of rattling atoms, *[18]* results in weak phonon transfer between the anionic $[AsS_2]^-$ anionic framework and the cationic Li^+/Na^+ moieties. This weak coupling effectively supresses thermal transport in $NaAsSe_2$, where the infinite polymeric $[AsSe_2]^-$ chains interspersed with Na^+ ions further disrupts heat conduction. Furthermore, the transition from Li to Na weakens bonding interactions, reducing in longitudinal acoustic (LA) phonon frequencies, and narrowing the gap between the LA and TA branches.

$NaAsSe_2$ exhibits softer acoustic phonons compared to $LiAsSe_2$, indicating a lower Debye temperature for $NaAsSe_2$ (161 K) than for $LiAsSe_2$ (220 K), as tabulated in **Table 5.4**.

Table 5.4: The calculated Young's modulus (GPa), shear modulus (GPa), Poisson's ratio, Debye Temperature, θ_D (K), and mode average Grüneisen parameters ($\overline{|\gamma|}$) for the considered structures of $LiAsSe_2$ and $NaAsSe_2$ systems.

Materials	Young's modulus	Bulk modulus	Shear modulus	Poisson's ratio	θ_D	$\overline{\lvert\gamma\rvert}$
$LiAsSe_2$	53.43	39.99	22.30	0.37	220	1.02
$NaAsSe_2$	42.77	19.86	15.50	0.56	161	1.30

The quantify the anharmonicity within the periodic crystals, we have calculated the Grüneisen parameter (γ) defined as,

$$\gamma = \frac{-dln\ \omega_q}{dln\ V}$$

where ω_q and V represents the phonon frequencies and volume, respectively. The calculated mode average Grüneisen parameters ($\overline{|\gamma|}$) for $NaAsSe_2$ and $LiAsSe_2$ are 1.30 and 1.02. Additionally, the large Grüneisen parameter (γ) values for $NaAsSe_2$ suggests stronger lattice anharmonicity compared to $LiAsSe_2$, as shown in **Figure 5.4**. Notably, $NaAsSe_2$ exhibits negative thermal expansion (NTE), with a negative γ, indicating contraction upon heating. This suggests that phonon modes in $NaAsSe_2$ are easily excited at lower temperatures compared to $LiAsSe_2$ *[48]*. The mode average Grüneisen parameters ($\overline{|\gamma|}$) for $NaAsSe_2$ (1.30) is close to the calculated high-performing thermoelectric materials, including PbTe (1.4), *[43]* BiCuOSe (1.5), *[49]* and Cu_6Te_3S (1.58), *[50]* indicating its strong lattice anharmonicity and ultralow thermal transport properties.

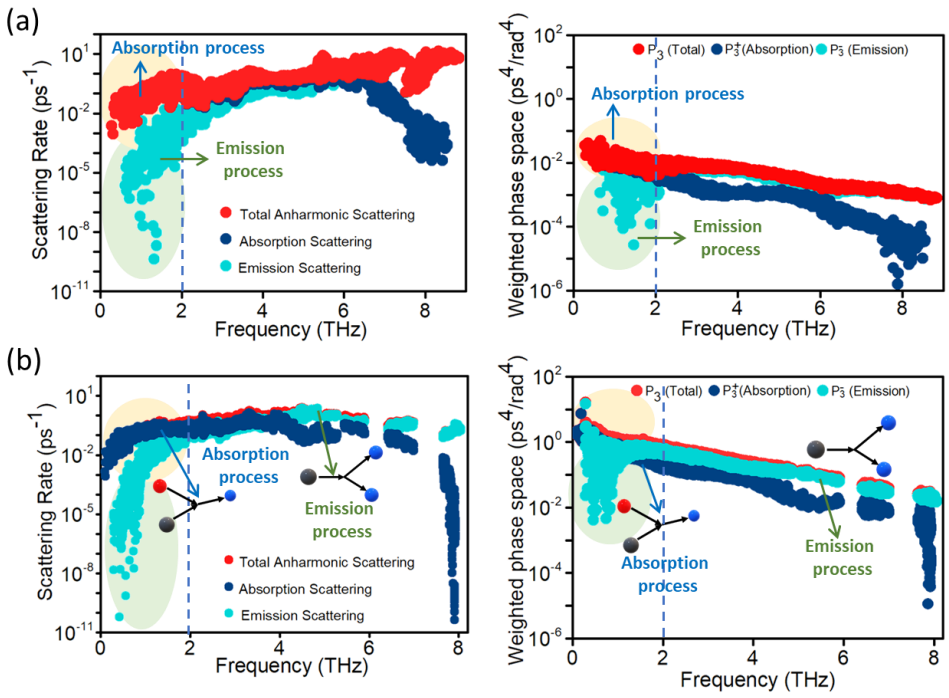


Figure 5.5: The calculated total anharmonic scattering rates and weighted phase space (WP_3) as a function of frequency (THz) for **(a)** $LiAsSe_2$ **(b)** $NaAsSe_2$ at 300 K highlighting absorption and emission scattering channels.

To explain further the low κ_L observed in these materials, we analyzed the phonon scattering rates and weighted phase space (WP3), as shown in **Figure 5.5**. The strong third-order anharmonic interactions in $NaAsSe_2$ lead to pronounced three-phonon interactions, resulting in higher phonon scattering rates and shorter phonon lifetimes. Notably, $NaAsSe_2$ exhibits higher phonon mode-resolved scattering rates than $LiAsSe_2$ below the acoustic frequency range of 2 THz. To gain deeper insights, we focused on three-phonon scattering processes, particularly absorption channels and their effects on flat phonon bands. The absorption process ($q_0 + q_1 \rightarrow q_2$) dominates in the low-frequency region (< 2 THz) and primarily involves SCALP-containing As atoms in $NaAsSe_2$. In contrast, higher-energy phonon modes (> 2 THz) exhibit elevated phonon scattering rates, mainly driven by emission processes ($q_0 \rightarrow q_1 + q_2$).

The weighted phase space (W_q^{total})is evaluated which is obtained from the following equation,[56]

$$P_q^{\pm} = \frac{1}{N}\sum_{q'q''} \begin{Bmatrix} n_q'' - n_q' \\ n_q'' + n_q' + 1 \end{Bmatrix} \delta\left(\omega_q - \omega_q' \pm \omega_q''\right) \quad \text{(S8)}$$

where P_q^+ and P_q^- denotes the energy and momentum conserved scattering phase spaces for phonon mode q in the absorption (+) and emission (-) processes, where the summation is restricted to the pairs $(\mathrm{q}_1, \mathrm{q}_2)$ satisfying $q + \mathrm{q}_1 + \mathrm{q}_2 = G$, where G is the inverse lattice vector. The weighted phase space increases from $LiAsSe_2$ to $NaAsSe_2$, as illustrated in **Figure 5.5**. At 300 K, the adsorption phonon scattering channel $\left(\mathrm{P}_3^+\colon \mathrm{q}_{0,\omega 0} + \mathrm{q}_{1,\omega 1} \rightarrow \mathrm{q}_{2,\omega 2}\right)$ exhibits a higher density and greater scattering rate than the emission process $\left(\mathrm{P}_3^-\colon \mathrm{q}_{0,\omega 0} \rightarrow \mathrm{q}_{1,\omega 1} + \mathrm{q}_{2,\omega 2}\right)$ for acoustic modes. Here, q and ω represent the phonon mode and phonon frequency, respectively. The presence of flat bands further enhances absorption processes by introducing additional scattering channels along high-symmetry pats (Z → D and A → Z) in the Brillouin zone. As ω_0 supresses ω_{flat}, the number of absorption channels increases, reaching a local maximum at ω_{flat}, and maximizes at $\omega_0 = 2\omega_{flat}$ *[46]*. This explains how an increased number of flat modes enhances the number of absorption channels, contributing the dominance of P_3^+, and leading to reduced κ_L. Additionally, boundary scattering is observed to have a greater magnitude than isotopic scattering (**Figure 5.6)**, indicating its significant role in supressing κ_L.

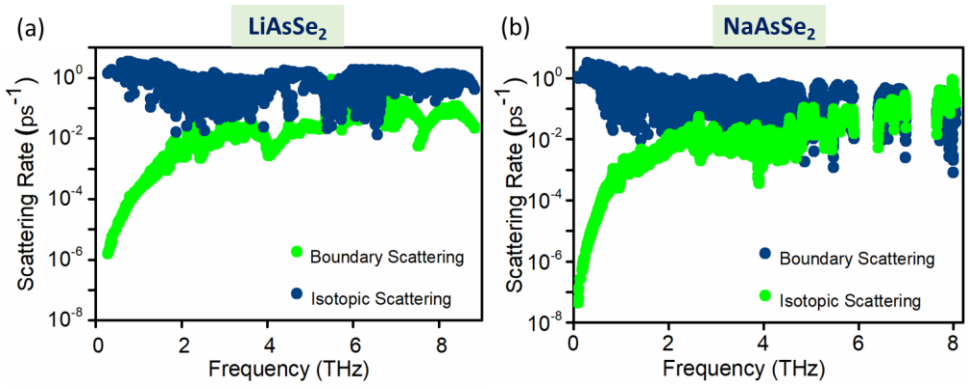


Figure 5.6: Boundary and isotopic scattering rates of **(a)** $LiAsSe_2$, and **(b)** $NaAsSe_2$ with respect to frequency (THz) at 300K.

5.3.4. Real Space Identification of SCALPs. To understand role of SCALP in governing anharmonicity, we examined their real space projection's electronic structure, partial density of states (PDOS), and crystal orbital Hamilton population (COHP) analysis, as shown in **Figure 5.7**. These analyses highlight the impact of orbital hybridization and chemical bonding on lattice dynamics and electronic properties. The electronic structure reveals a direct bandgap of 0.76 eV at the $Z|R_2$ for $LiAsSe_2$ and 1.85 eV at the C_2 points for $NaAsSe_2$, aligning closely with experimental values of 1.10 eV and 1.87 eV, respectively *[19, 20]*. The sharp peak at the $Z|R_2$ in $LiAsSe_2$ indicate the light hole effective mass, while the flattened peaks near the C_2 points in $NaAsSe_2$ suggest heavy hole effective masses *[57]*. The asymmetric coordination environment induced by SCALPs is explained through the revised lone pair model *[13]*. In these systems, SCALP cations, such as As^{3+} ($4s^2$) exhibit stereochemical activity due to orbital interactions and stabilization mechanisms. The occupied antibonding states, originating from As (4s)-Se (4p) interactions, are stabilized by As (4p) states, leading to local symmetry breaking and facilitating on-site sp mixing (**Figure 5.2)**.

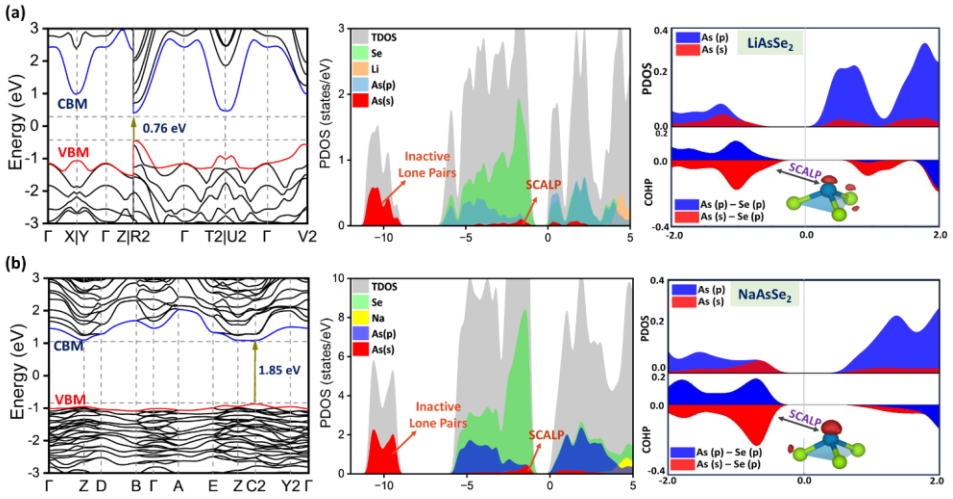


Figure 5.7: Electronic band structures, projected density of states (PDOS) calculated using the HSE06 functional, and the crystal orbital Hamilton population (COHP) plot for **(a)** $LiAsSe_2$ and **(b)** $NaAsSe_2$. The dark yellow arrow defines the direct band gap along the Brillouin zone points. The pairwise orbital interactions shown in COHP plot highlight the presence of SCALP electrons where, positive overlap populations indicate bonding interactions, and negative overlap population indicates antibonding interactions.

PDOS and COHP analysis indicate stronger lone-pair effect in $NaAsSe_2$ compared to $LiAsSe_2$. In PDOS, As ($4s^2$) lone pair electrons interact with the Se (4p) states in the valence band, forming stable bonding and unstable antibonding states. The hybridization of unoccupied As (4p) orbitals with anti-bonding (As 4s + Se 4p)* states further stabilize the occupied states (**Figure 5.7**), particularly within energy region of -0.5 to -2.0 eV at the valence state maxima (VBM) in $NaAsSe_2$. When these states are positioned deeper in the valence band (< -9.0 eV), they act as "inactive lone pairs" and do not influence the lattice dynamics. The VBM is primarily derived from As^{+3} 4s and 4p orbitals, while the conduction band minima (CBM) originate from Se 4p orbitals, as illustrated in **Figure 5.7**. Crystal orbital Hamilton populations (COHP) analysis provides insights into bonding interactions, where positive overlap populations indicate bonding states and negative

populations correspond to antibonding states *[52]*. The VBM states in As 4s near the Fermi level (E_f) exhibits antibonding interactions with Se 4p orbitals, weakening As-Se bonds by reducing electron density between the atoms *[1, 13]*. The presence of high intensity antibonding states near the E_f in $NaAsSe_2$, serves as a key indicator of ultralow κ_L *[53]*.

5.3.5. Electronic Transport Properties. The electronic transport properties of $LiAsSe_2$ and $NaAsSe_2$ were analyzed by evaluating scattering rates from ionized impurity (IMP), polar optical phonons (POP), and acoustic deformation potential (ADP) mechanisms using the AMSET package. These scattering mechanisms influence carrier mobility under different conditions, as shown in **Figures 5.8-5.11.**

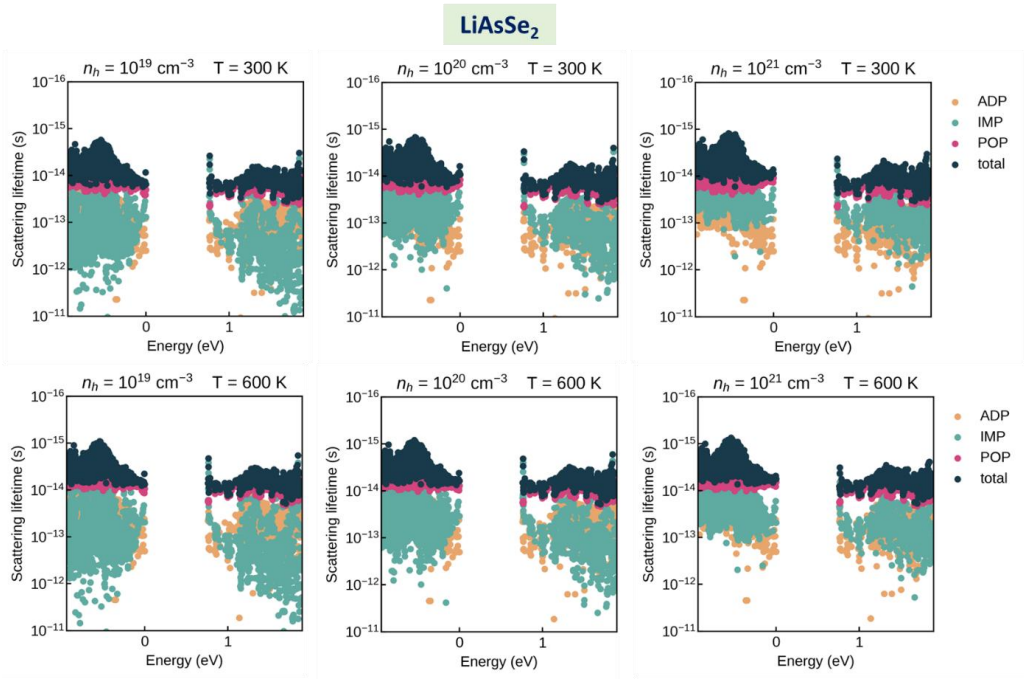


Figure 5.8: Scattering rates as a function of energy of p-type for $LiAsSe_2$. These represent their scattering mechanisms including polar optical phonon (POP), ionized impurity (IMP), and acoustic deformation potential (ADP) scattering at carrier concentration ranges from 10^{19} cm^{-3} - 10^{21} cm^{-3} at 300 K and 600 K.

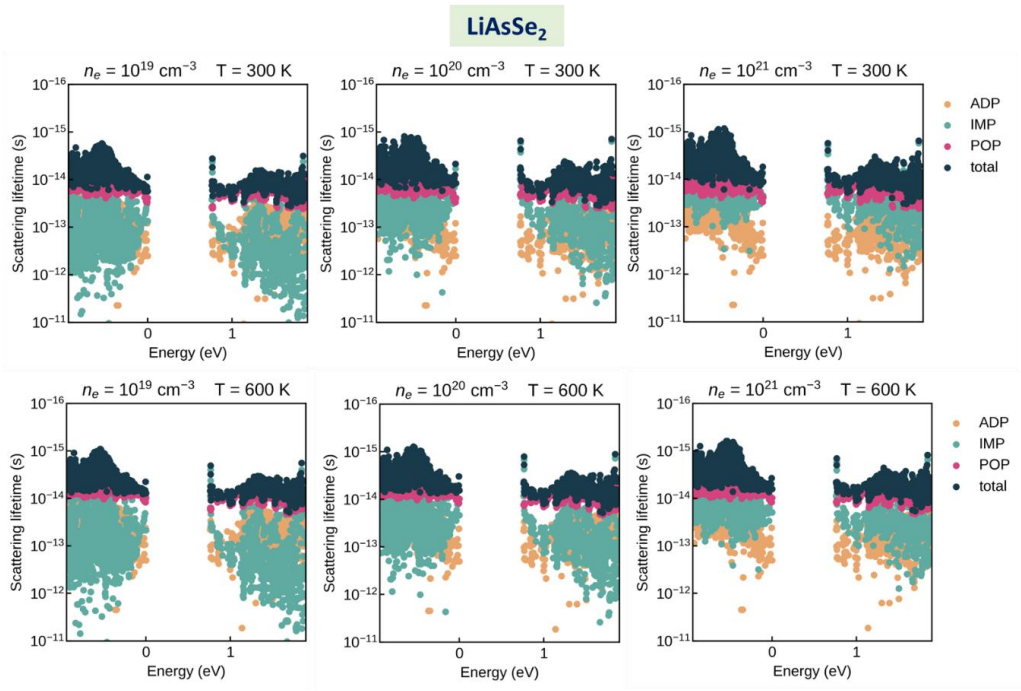


Figure 5.9: Scattering rates as a function of energy of n-type for $LiAsSe_2$. These represent their scattering mechanisms including polar optical phonon (POP), ionized impurity (IMP), and acoustic deformation potential (ADP) scattering at carrier concentration ranges from 10^{19} cm^{-3} - 10^{21} cm^{-3} at 300 K and 600 K.

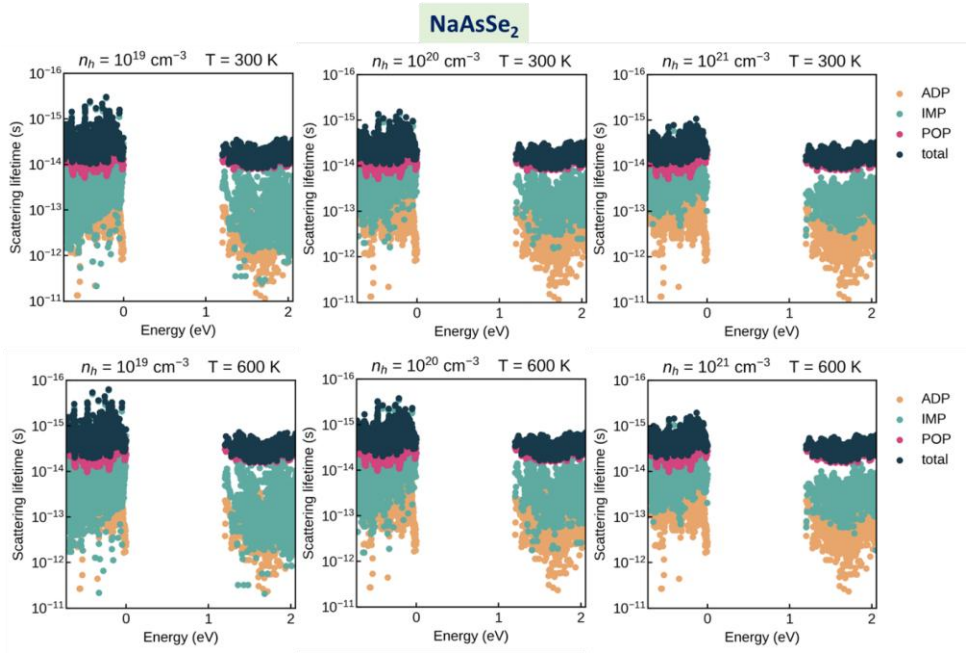


Figure 5.10: Scattering rates as a function of energy of p-type for $NaAsSe_2$. These represent their scattering mechanisms including polar optical phonon (POP), ionized impurity (IMP), and acoustic deformation potential (ADP) scattering at carrier concentration ranges from 10^{19} cm^{-3} - 10^{21} cm^{-3} at 300 K and 600 K.

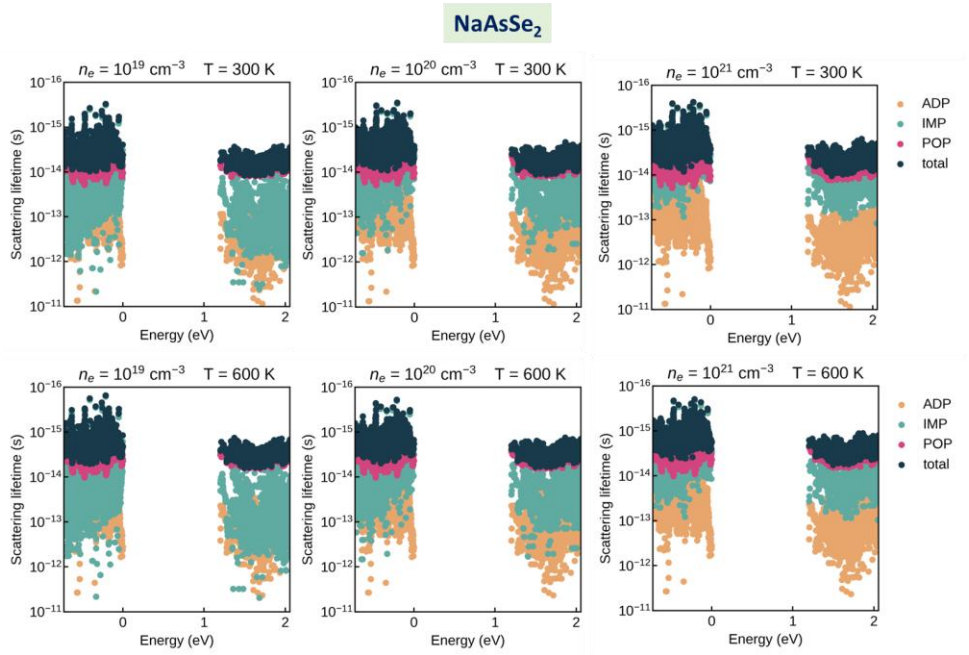


Figure 5.11: Scattering rates as a function of energy of n-type for $NaAsSe_2$. These represent their scattering mechanisms including polar optical phonon (POP), ionized impurity (IMP), and acoustic deformation potential (ADP) scattering at carrier concentration ranges from 10^{19} cm^{-3} - 10^{21} cm^{-3} at 300 K and 600 K.

The dominant scattering mechanism varies based on doping level, carrier concentration, and temperature in $LiAsSe_2$ and $NaAsSe_2$ (**Figure 5.12-5.13**). At conditions maximizing the thermoelectric figure of merit (ZT), ADP scattering plays the most significant role, followed by IMP and POP scattering. In $NaAsSe_2$, ADP scattering typically results in the highest mobility, whereas in n-type $LiAsSe_2$, IMP scattering dominates at higher temperatures. Additionally, the electronic transport properties, including the power factor (PF) and electronic thermal conductivity (κ_e) across various

temperatures and carrier concentrations are presented in **Figure 5.14-5.15**. These results highlight the intricate interplay of scattering mechanisms in governing charge transport and emphasize the critical role of ADP scattering in optimizing thermoelectric performance.

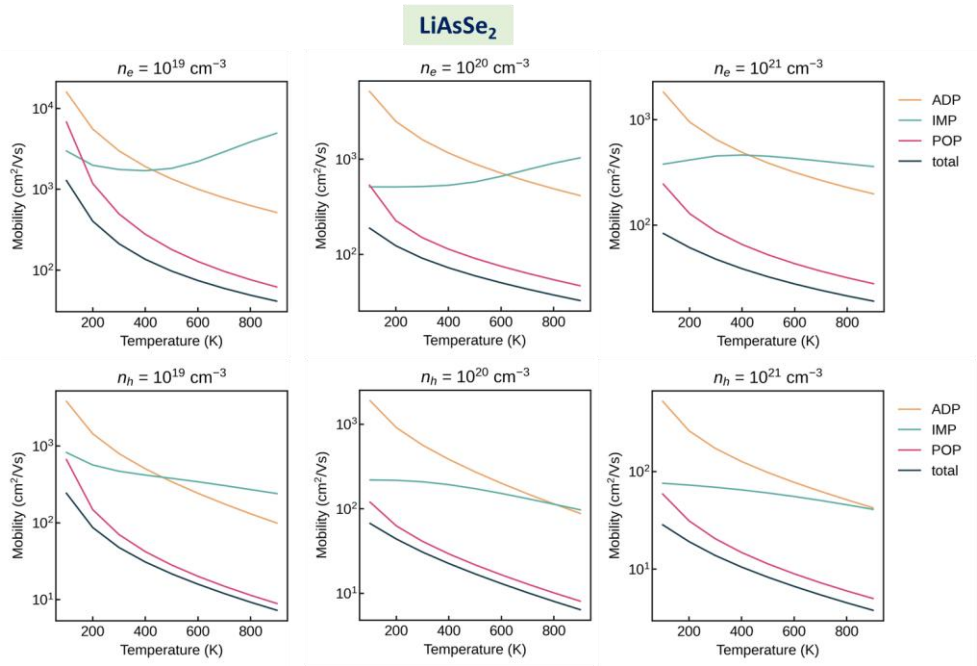


Figure 5.12: Mobility (cm^2/Vs) as a function of temperature for n- and p-type doping for $LiAsSe_2$, under three scattering mechanisms namely, polar optical phonon (POP), ionized impurity (IMP), and acoustic deformation potential (ADP) scattering with carrier concentrations ranges from 10^{19} cm^{-3} - 10^{21} cm^{-3}.

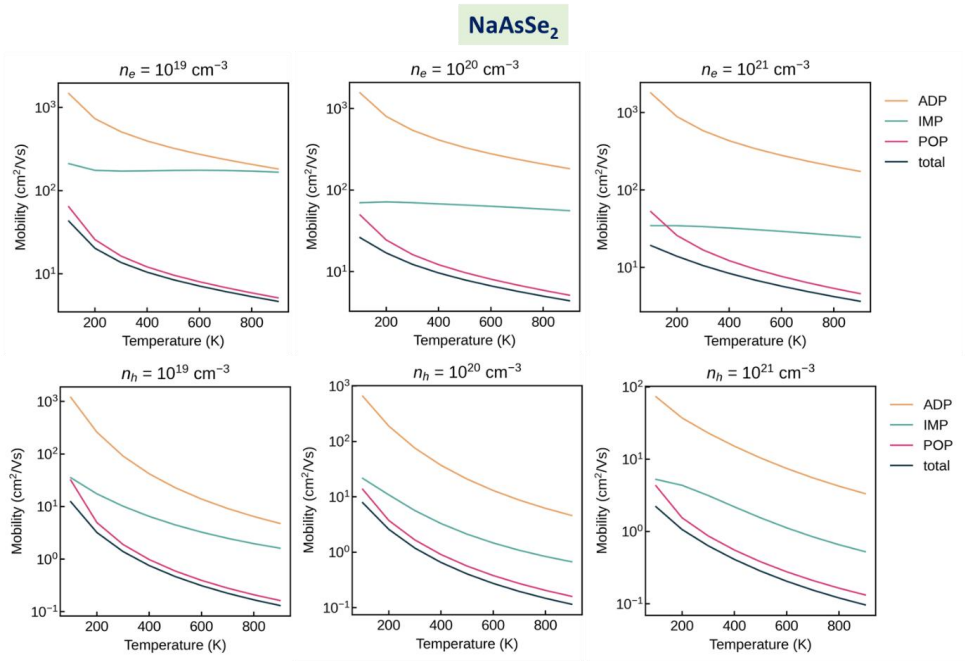


Figure 5.13: Mobility (cm^2/Vs) as a function of temperature for n- and p-type doping for $NaAsSe_2$, under three scattering mechanisms namely, polar optical phonon (POP), ionized impurity (IMP), and acoustic deformation potential (ADP) scattering with carrier concentrations ranges from 10^{19} cm^{-3} - 10^{21} cm^{-3}.

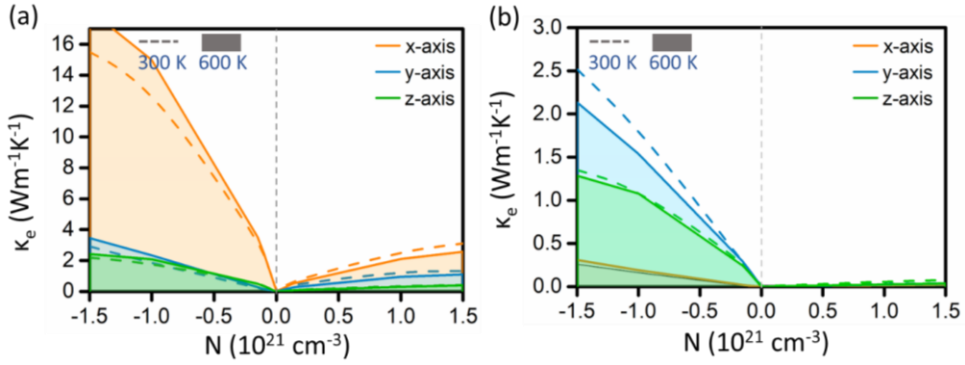


Figure 5.14: The direction dependent electronic thermal conductivity, κ_e ($Wm^{-1}K^{-1}$), as a function of carrier concentration N (10^{21} cm^{-3}) for **(a)** $LiAsSe_2$, and **(b)** $NaAsSe_2$. The dotted and solid lines represent the κ_e at 300 K and 600 K, respectively.

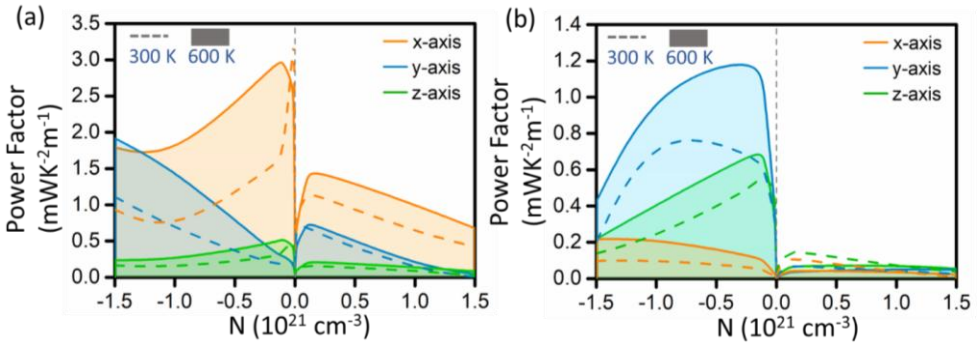


Figure 5.15: The direction dependent power factor ($mWK^{-2}m^{-1}$), as a function of carrier concentration N (10^{21} cm^{-3}) for **(a)** $LiAsSe_2$, and **(b)** $NaAsSe_2$. The dotted and solid lines represent the κ_e at 300 K and 600 K, respectively.

5.3.6. Thermoelectric Properties. The thermoelectric properties of $LiAsSe_2$ and $NaAsSe_2$, including electrical conductivity (σ), Seebeck coefficient (S), and power factor (PF) were evaluated at 300 K and 600 K, as represented in **Figure 5.16**. The Seebeck coefficient (S) and figure of merit (ZT) are given by the following equations: *[54]*

$$S = \frac{8\pi^2 k_B^2 m^* T}{3eh^2}\left(\frac{\pi}{3n}\right)^{2/3}$$

$$ZT = \frac{S^2\sigma}{\kappa_e+\kappa_L}T = (S^2 n)\left(\frac{\mu}{\kappa}\right)eT$$

where k_B is Boltzmann constant, m^* is effective mass, T is absolute temperature, h is Planck's constant, e is an electrical charge, n is the carrier concentration and μ is mobility. The electrical conductivity is defined as $\sigma = nq\mu$, indicating that an increase in mobility enhances both electrical and electronic thermal conductivity.

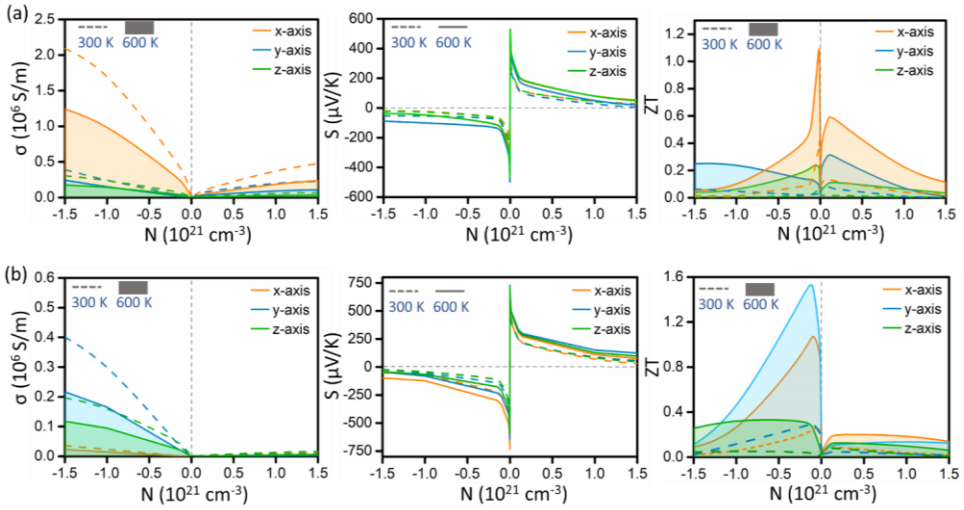


Figure 5.16: Thermoelectric properties including Seebeck coefficient (S), electrical conductivity (σ), thermoelectric figure of merit (ZT) for **(a)** $LiAsSe_2$ and **(b)** $NaAsSe_2$, calculated based on relaxation times and transport coefficient obtained using AMSET. The negative and positive signs of the carrier concentrations represent n- and p-type doping, respectively, with dotted and solid line representing 300 K and 600 K.

At 300 K for n-type doping at 10^{20} cm^{-3}, $NaAsSe_2$ exhibits higher Seebeck coefficient than $LiAsSe_2$, due to presence of flat band degeneracies in the electronic band structures near the Fermi energy. Conversely, the σ follows the inverse trend of Seebeck coefficient, with values of 3831 Sm^{-1} for $LiAsSe_2$, and 2390 Sm^{-1} for $NaAsSe_2$ at 300 K along the y-axis for n-type doping at 10^{20} cm^{-3}. This further supports weaker bonding interactions from $LiAsSe_2$ to $NaAsSe_2$. The calculated ZT values for n-type doping at 10^{20} cm^{-3} in $LiAsSe_2$ reach 0.42 at 300 K and 1.10 at 600 K along the x-axis, while in $NaAsSe_2$, ZT values of 0.30 at 300 K and 1.59 at 600 K are obtained along the y-axis for 10^{20} cm^{-3}. The superior ZT in $NaAsSe_2$ result from its lower κ_L and optimized electronic transport properties, making it comparable to popular TE materials for instance PbTe, *[55]* Cu_2Se, *[56]* Cu_3SbSe_3, *[57]* and KCu_5Se_3. *[58]* A promising direction for future research is exploring the effect of dopants on carrier concentration to further enhance

the ZT value, potentially improving the performance of $NaAsSe_2$ and making it more competitive with leading thermoelectric materials.

5.4. Summary

In summary, we highlight the unique chemical bonding hierarchies introduced by stereochemically active lone pairs (SCALPs) and rattler atoms, enhances the thermoelectric performance of $NaAsSe_2$, compared to $LiAsSe_2$. Leveraging machine learning interatomic potentials (MLIPs), we demonstrate the intricate role of SCALPs and rattler atoms improving thermoelectric performance. The presence of SCALP enhances the electrostatic repulsions between lone pairs and reduced bond angles, leading to increased structural distortions and anharmonicity with an ultralow κ_L of 0.42 W/m K at room temperature in $NaAsSe_2$. The presence of localized, dispersionless phonon branches, characteristic of rattling atoms, supresses phonon transfer between the anionic $[AsS_2]^-$ and the cationic Li^+/Na^+ sublattices. The anharmonicity is further evidenced by strong acoustic-optical phonon coupling, phonon softening, and flat transverse acoustic branches, which collectively enhance phonon scattering and suppress thermal transport. The synergy between the electronic structure and the anharmonic phonon dynamics results in a high thermoelectric figure of merit (ZT) of 1.59 at 600 K, surpassing many conventional ABX_2-type materials. By combining first-principles calculations with MLIPs, we developed an efficient prediction framework that reduces computational costs while preserving quantum-mechanical accuracy. Overall, this study highlights the transformative potential of trained MLIPs in capturing anharmonicity in SCALP materials and enhancing their thermoelectric efficiency, paving the way for the discovery of advanced thermoelectric materials.

Section: B

5.5. Introduction

Here, we would like to bring to notice that beyond these intrinsic effects, κ_L can be further suppressed through various mechanisms such as hierarchical,

[43, 59] complex crystal structures, *[16]* rattling atoms, *[14, 60, 61]* antibonding states near the valence architectures band edge, *[1, 13, 43, 62]* and Coulombic repulsion in edge- and face-sharing polyhedral *[63, 64]*. The focus on edge-sharing metal chalcogenides, particularly non-centrosymmetric pnictogen chalcogenides, is motivated by their distinctive bonding environments that inherently increase strong lattice anharmonicity and ultralow κ_L. In these systems, edge-sharing polyhedral bondings bring neighboring cations into close proximity, leading to pronounced electrostatic (cation-cation) repulsion and local structural distortions, which together enhance phonon scattering and suppress κ_L *[65]*. Additionally, unique metal-metal interactions, explained by Fajan's polarization theory and observed in subvalent bismuth species (e.g., Bi_2^{4+}, Bi_5^{3+}, Bi_8^{2+}), exhibit rare metal-metal bonding motifs, contribute further to structural complexity and anharmonic vibrational behavior *[63, 64]*. Our work uncovers inherent low κ_L in this unexplored class of edge-sharing non-centrosymmetric metal chalcogenides which should open opportunities for applications of these compounds in various thermal energy management devices.

Despite the recognized importance of bonding heterogeneities in governing thermal transport, the detailed interplay between such heterogeneities and lattice anharmonicity remains underexplored In this study, we use chemical bonding principles to systematically examine how antibonding states from SCALP, pnictogen-pnictogen bonding, rattling ions, and edge-sharing polyhedral affect bonding characteristics, lattice dynamics, and anharmonicity, with the aim of developing materials with intrinsically low κ_L. To build a robust framework for analyzing these effects, we consider key geometric and bonding descriptors: lone pair angle, *[43]* degree of ionicity (r_σ') and the hybridization tendency (r_π^{-1}) which together capture the SCALP, orbital-mixing tendencies between pnictogen (Pn) and chalcogen (Chg) atoms and the bonding characteristics associated with edge sharing polyhedra motifs *[66]*. Since the design of meaningful descriptors is crucial for capturing domain-specific characteristics, they play a key role

in effectively encoding information for machine learning models *[67–70]*. We further examine the role of lone pair geometry that led to local distortions in shaping the structural environment and influencing anharmonic behavior *[5, 43]*. Along with that, special attention is given to the interplay between SCALPs, bonding heterogeneity, and local structural motifs, which collectively dictate lattice dynamics.

Herein, we focus on a class of non-centrosymmetric pnictogen chalcogenides, Ba_2AsPnQ_5 (Pn = As, Sb, Bi; Q = S, Se), *[71]* and employ machine learning interatomic potentials (MLIPs) based on moment tensor descriptors to capture lattice anharmonicity. To uncover the origin of this anharmonicity, we perform molecular orbital analysis, which reveals key electronic mechanisms, including the influence of SCALP, Pn-Pn bonding, edge-sharing polyhedra motifs, and the rattling atoms in forming antibonding valence band maxima. We further demonstrate that orbital design can be used to engineer electronic band valleys, achieving band degeneracy near both the conduction and valence band edges to optimize carrier transport properties and enhance overall thermoelectric performance. To systematically capture these effects, we construct a descriptor space that encodes the complex relationships among bonding topology, lone pair geometry, vibrational dynamics and κ_L values, enabling predictive mapping of structure-property relationships. This work provides a comprehensive understanding of how bonding hierarchies and structural features govern lattice anharmonicity, supporting the rational design of next-generation thermoelectric materials.

5.6. Computational Details

First-principles calculations were performed using the projector augmented wave (PAW) pseudopotentials, as implemented in the Vienna *ab initio* simulation package (VASP) *[27, 28]*. The generalized gradient approximation (GGA) within the Perdew-Burke-Ernzerhof (PBE) functional was employed for the exchange-correlation potential, with a

plane-wave cutoff energy 450 eV and Γ k-point mesh of 5 x 5 x 5 *[29, 72]*. Structural relaxations were carried out considering the Hellmann-Feynman force convergence criterion of 0.001 eV/Å, and the total energy convergence criterion was set to 10^{-6} eV. Furthermore, to accurately describe the electronic properties of Ba_2AsPnQ_5 (Pn = As, Sb, Bi; Q = S, Se), we performed electronic calculations considering the Heyd−Scuseria−Ernzerhof (HSE06) hybrid functional, incorporating a Hartree−Fock exchange parameter (α) of 15% to calculates the electronic properties of the Ba_2AsPnQ_5 (Pn = As, Sb, Bi; Q = S, Se) systems *[32, 33]*.

5.6.1. Construction of Machine Learning Interatomic Potentials: To construct machine learning interatomic potentials (MLIPs), we first generated training data via *ab initio* molecular dynamics (AIMD) simulations using the VASP code. AIMD was performed on a 2 x 2 x 2 supercell in an isobaric-isothermal NPT ensemble over temperature ranging from 100 K to 700 K in 100 K increments. For each Ba_2AsPnQ_5 system, simulations at each temperature were run for 2000 steps with a 1fs timestep, producing a total of 14,000 configurations (original dataset "OD") each with corresponding energies, forces, and stresses. To reduce redundancy, every 5^{th} configuration from the OD was retained, yielded a curated dataset of 2,800 configurations. This dataset was split in an 80:20 ratio, with 2,240 structures forming the training set and 560 structures reserved for testing. The training set was used in the MLIP package to parameterize MTPs via a polynomial-based linear regression approach *[24, 36]*. The resulting MTPs were subsequently used to predict phonon dispersion relations, as well as second and third order interatomic force constants *[36]*.

5.6.2. Calculating Lattice and Electronic Transport Properties: Lattice transport properties were evaluated using second and third order IFCs as input data to the SHENGBTE code, which facilitated the determination of the lattice thermal conductivity of the materials *[37]*. The dense 9 × 9 × 9 q-points mesh was employed for the Ba_2AsPnQ_5 (Pn = As, Sb, Bi; Q = S,

Se) systems to ensure the accurate lattice thermal conductivity (κ_L) predictions. Electronic transport properties were computed using the *ab initio* Scattering and Transport (AMSET) framework, which accounts for multiple scattering rates including ionized impurities, acoustic deformation, and piezoelectric scattering mechanisms to estimate relaxation times and predict transport coefficients with high accuracy *[38, 73]*.

5.7. Results and Discussion

5.7.1. Crystal Structure derived Anharmonicity

Non-centrosymmetric pnictogen chalcogenides containing stereochemically active lone pairs (SCALPs) on the pnictogen elements (Pn = As, Sb, and Bi), together with Pn-Pn bonding networks and edge-shearing polyhedra, represent an emerging class of materials *[63, 65, 74, 75]*. A distinctive feature of these compounds is their band degeneracy near the conduction and valence band edges, which enables the optimization of carrier transport. Combined with their unique structural motifs, these characteristics give rise to tunable electronic and thermal transport properties, making them promising candidates for applications in thermoelectrics, nonlinear optics, and piezoelectrics *[76–78]*. Within this material family, $Ba_2As_2Q_5$, Ba_2AsSbQ_5, and Ba_2AsBiQ_5 (Q = S and Se) systems crystallize in the monoclinic space group $P2_1$, and belong to the class of non-centrosymmetric complex calcoarenates (**Figure 5.17(a)**) *[71]*. Notably, $Ba_2As_2Q_5$, (Q =S/Se) and $Ba_2AsSbSe_5$ have been synthesized by Kanatzidis and coworkers.[58] The Ba_2AsPnQ_5 (Pn = As, Sb, Bi; Q = S, Se) systems feature two primary structural motifs: $[Pn_2Q_4]^{2-}$ dimer units and PnQ_3 trigonal pyramids (**Figure 5.17(b-c)**). The $[Pn_2Q_4]^{2-}$ dimer consists of edge-sharing polyhedra formed by puckered four-membered (Pn-Q-Pn-Q) rings, which retain monoclinic $P2_1$ symmetry upon substituting As with Sb or Bi and Se with S. In contrast, $Ba_2As_2S_5$ crystallizes in the orthorhombic $Pca2_1$ space group, exhibiting distinct structural properties.

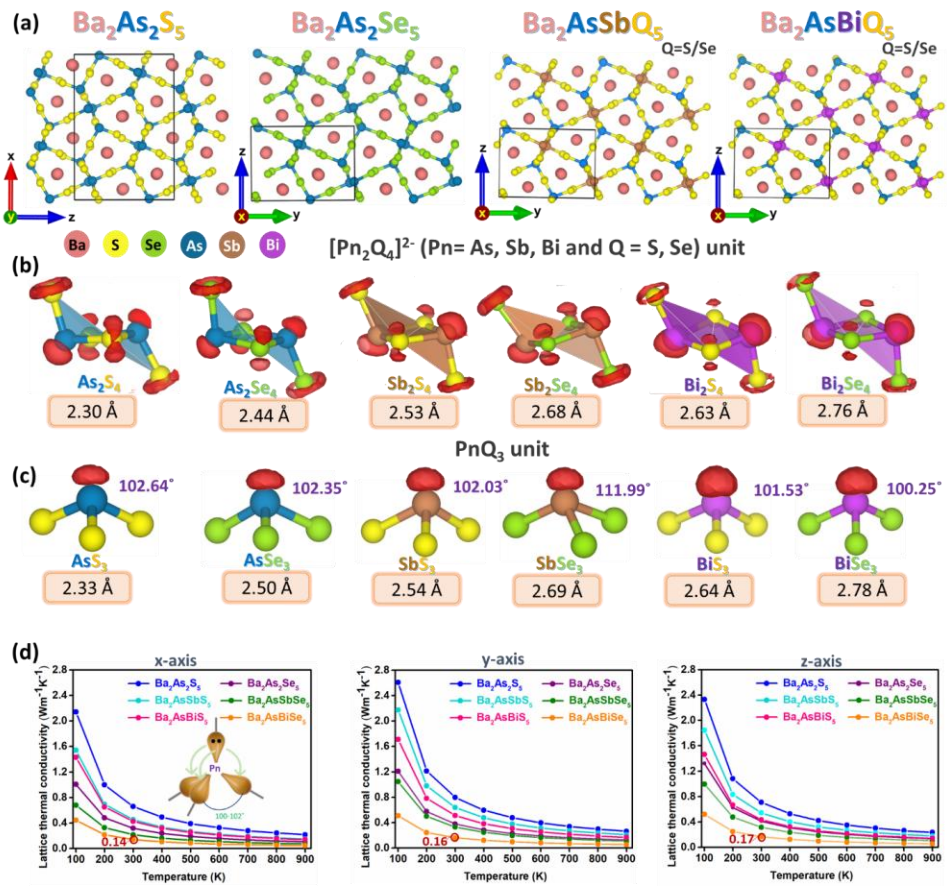


Figure 5.17: (a) Optimized conventional unit cell structures of $Ba_2As_2S_5$, $Ba_2As_2Se_5$, Ba_2AsSbQ_5 (Q = S/Se), and Ba_2AsBiQ_5 (Q = S/Se). **(b)** 3D electron localization function (ELF) map of $[Pn_2Q_4]^{2-}$ unit and **(c)** PnQ_3 units (Pn = As, Sb, Bi; Q = S, Se) at an iso-surface value of 0.90 eÅ^{-3}, highlighting the lone-pair regions around the pnictogen atoms. **(d)** Lattice thermal conductivity (κ_L) values predicted using machine learning interatomic potentials as a function of temperature along three crystallographic directions. Red circles mark the $Ba_2AsBiSe_5$ system, which exhibits ultralow κ_L.

To investigate the localization of electronic densities and its implications for anharmonicity, we performed electron localization function (ELF) analysis for the Ba_2AsPnQ_5 systems, as shown in **Figure 5.17(b-c)** *[42, 79]*. In the $[Pn_2Q_4]^{2-}$ substructure, the red mushroom-shaped lobes in the 3D ELF reveal lone-pair electrons on the Pn atoms, positioned opposite to the Pn-Q

bond due to bond-pair repulsion. The edge-shared chalcogenide polyhedra exert additional electron-electron repulsion between neighboring atoms *[65]*. Consequently, the presence of SCALP and edge-sharing polyhedra enhances orbital overlap with adjacent atoms, leading to electrostatic repulsion and structural distortion. As a result, bond angles deviate from the ideal 109.5˚ to a reduced range of 100.25˚-102.64˚, amplifying lattice anharmonicity *[5]*. Moreover, interactions between the $[Pn_2Q_4]^{2-}$ and PnQ_3 units give rise to As-As, As-Sb, and As-Bi bonds within ~3.0 Å distance, further reinforcing covalency and contributing to structural distortions. The combined effect of lone-pair-driven distortions, bond-pair repulsion, edge-sharing polyhedral, and weak Pn-Pn interactions enhance lattice anharmonicity, significantly influencing thermal transport. **Figure 5.17(d)** shows the lattice thermal conductivity (κ_L) values for the Ba_2AsPnQ_5 systems as a function of temperature along different crystallographic directions. A systematic decrease in κ_L is observed across the substitution series, both from As to Bi and from S to Se, demonstrating a clear correlation between chemical substitution, structural distortions, and anharmonicity. Among these, $Ba_2AsBiSe_5$ exhibits the highest degree of anharmonicity, resulting in the lowest κ_L value of 0.14 $Wm^{-1}K^{-1}$ along the x-axis. A detailed mechanistic analysis of these trends, focusing on bonding hierarchies, phonon dynamics, and the role of anharmonicity in thermal and electronic transport, is presented in the following section.

5.7.2. Machine Learning Interatomic Potentials. Calculating the anharmonic lattice dynamics and thermal conductivity of Ba_2AsPnQ_5 systems requires extensive evaluation of interatomic force constants (IFCs), a task that is computationally demanding due to their large, non-centrosymmetric unit cells. To address this challenge, we employed moment tensor potentials (MTPs), an efficient machine learning-based surrogate model trained on *ab initio* molecular dynamics (AIMD) data *[24]*. MTPs provide a computationally efficient alternative while retaining the

accuracy required for large-scale simulations of phonon dispersion, IFCs, and anharmonic effects *[16, 80]*.

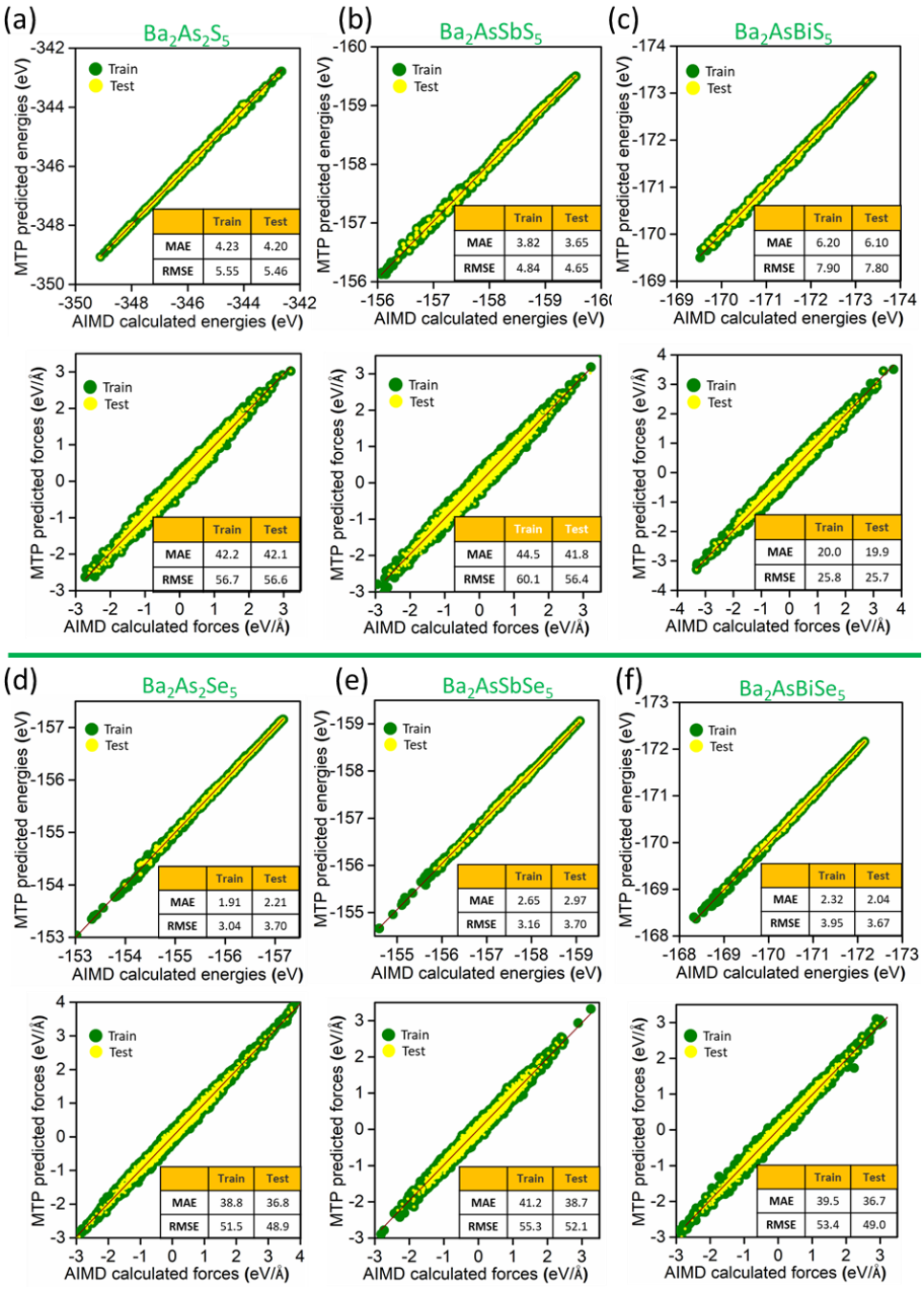


Figure 5.18: Scatter plots comparing MTP-predicted and AIMD-calculated energies and forces for **(a)** $Ba_2As_2S_5$, **(b)** Ba_2AsSbS_5, **(c)** Ba_2AsBiS_5, **(d)** $Ba_2As_2Se_5$, **(e)** $Ba_2AsSbSe_5$, and **(f)** $Ba_2AsBiSe_5$. Each panel reports the mean absolute error (MAE) and root mean square error (RMSE) for

energies (meV) and forces (meV $Å^{-1}$) for both the training and testing datasets, quantifying the accuracy of the trained MTP models.

Over the past decade, various MLIPs have been developed, spanning neural network-based architectures such as Behler–Parrinello neural networks (BPNN), *[81]* Deep Potential Molecular Dynamics (DeepMD), *[82]* Neural Equivariant Interatomic Potentials (NequIP) *[83]* and kernel methods such as Gaussian approximation potentials (GAP) and sparse Gaussian process regression (SGPR) *[84, 85]*. Linear-expansion frameworks include the Spectral Neighbor Analysis Potential (SNAP), *[86]* Moment Tensor Potential (MTP), *[24, 87]* and Atomic Cluster Expansion (ACE) *[88]*. Neural networks offer high flexibility but often require extensive training datasets and hyperparameter optimization, whereas kernel methods facilitate rigorous uncertainty quantification but at a substantial computational cost *[81, 89]*. In contrast, MTPs strike an optimal balance of accuracy, transferability, and efficiency, achieving near-DFT fidelity with modest AIMD datasets and simulation speeds up to three orders of magnitude faster than DFT *[81, 87]*. By leveraging moment tensor descriptors, MTPs effectively capture mid- and long-range interactions, enabling accurate predictions of both energies and forces *[87]*. The trained MTPs were validated against AIMD data using energy and force scatter plots (**Figure 5.18(a-f)**), yielding root-mean-square errors (RMSE) of 3.67-7.80 meV for energies and 0.025-0.056 eV/Å for forces. These errors are substantially smaller than the intrinsic DFT uncertainties in formation or cohesive energies (≈0.1-0.2 eV/atom) demonstrating that the MTPs reproduce the DFT potential energy surface with high fidelity.48–50 Comparable RMSE ranges have been reported for MTP-based models achieving DFT-level accuracy confirming the reliability of the present MTPs in capturing anharmonic effects and predicting thermal transport properties with near-DFT precision.

5.7.3. Anharmonic Phonon Dispersion. The MTP-predicted phonon dispersions provide detailed insights into the vibrational modes, serving as

distinct fingerprints of chemical species along high-symmetry points of the Brillouin zone. **Figure 5.19(a-b)** present the phonon dispersion relations for $Ba_2AsSbSe_5$ and $Ba_2AsBiSe_5$, ultralow κ_L materials of the $Ba_2AsPnSe_5$ family, highlighting their distinct phonon-suppressing mechanisms. The absence of imaginary frequencies in **Figure 5.19(a-b)** and **Figure 5.20** confirms the dynamical stability of all $Ba_2AsPnSe_5$ systems, reinforcing the reliability of the predicted phonon properties for describing heat transport mechanisms. The phonon dispersion curves display low-energy optical branches (1.0 - 2.5 THz) with small dispersion, which couple strongly with acoustic and low-energy optical modes, introducing additional scattering channels that further supress κ_L. The effect is amplified as the atomic mass increases from As to Bi, progressively flattening the phonon dispersion curves, lowering phonon group velocities, and enhancing anharmonic vibrations *[46, 90]*. Supported by the weaker mechanical properties from As to Bi (**Table 5.5**), this trend reflects the intrinsic softness of the lattice and its strong coupling to anharmonic effects.

Table 5.5: The calculated Young's modulus (GPa), shear modulus (GPa), Poisson's ratio, and Debye Temperature, θ_D (K) for the considered structures of Ba_2AsPnQ_5 (Pn=As/Sb/Bi; Q=S/Se)

	Bulk modulus	**Young's modulus**	**Shear modulus**	**Poisson's ratio**	v_L	v_T	θ_D
$Ba_2As_2S_5$	34.54	49.45	21.23	0.40	3529	2002	222
$Ba_2As_2Se_5$	27.81	45.51	20.65	0.47	2951	1700	182
Ba_2AsSbS_5	34.45	50.83	22.06	0.42	3506	1948	214
$Ba_2AsSbSe_5$	37.06	48.82	20.29	0.50	3031	1701	181
Ba_2AsBiS_5	39.96	52.08	22.13	0.43	3451	1919	210
$Ba_2AsBiSe_5$	39.96	44.60	17.30	0.48	2925	1549	164

Notably, despite the overall flattening of the phonon branches, certain modes exhibit anomalously high group velocities (~3.5-4.0 km/s) along the Γ-Z, B-Γ-A, Y_2-Γ path (**Figure 5.19(a)**), highlighting the intricate interplay between phonon transport and anharmonicity. The Grüneisen parameters

(γ), which quantify lattice anharmonicity through the dependence of phonon frequencies on volume, show particularly large values in the acoustic phonon region below 1.5 THz *[48]*. This strong anharmonicity effectively suppresses phonon propagation, with γ following the trend $Ba_2As_2Q_5$ < Ba_2AsSbQ_5 < Ba_2AsBiQ_5 (Q = S < Se), consistent with the inverse trend in κ_L. Furthermore, localized low-frequency vibrations, typically associated with rattling atoms, further amplify anharmonic phonon scattering and reduce κ_L. Similar effects have been reported in high-performing thermoelectric materials such as $Ba_8Ga_{16}Ge_{30}$, *[45]* $TlCuHfSe_3$, *[18]* and $TlInTe_2$ *[15]*. Atom-projected phonon density of states highlights that low-energy phonon modes (~2 THz) originate predominantly from Ba rattling atoms, and weakly bonded Pn-Pn cations (**Figure 5.19(a-b) and Figure 5.20**). The weak Ba-Q ionic interactions create a tunnel-like structural framework, enabling rattling-like dynamics.

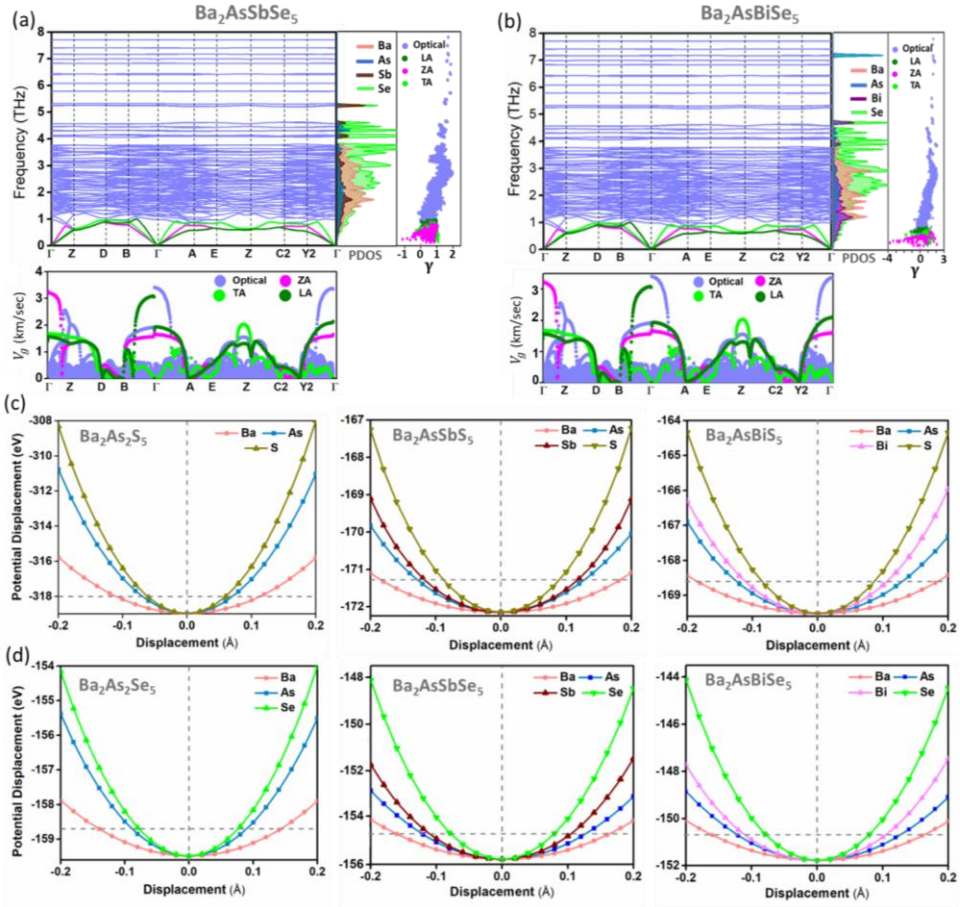


Figure 5.19: Machine learning interatomic potential (MLIP)-predicted phonon dispersion, phonon density of states, Grüneisen parameter (γ), and group velocity across the high-symmetry points in the first Brillouin zone for **(a)** $Ba_2AsSbSe_5$, **(b)** $Ba_2AsBiSe_5$. Panels **(c-d)** show the potential energy landscape of Ba_2AsPnQ_5 (where Pn=As, Sb, Bi; Q=S, Se) as a function of atomic displacement from their equilibrium positions.

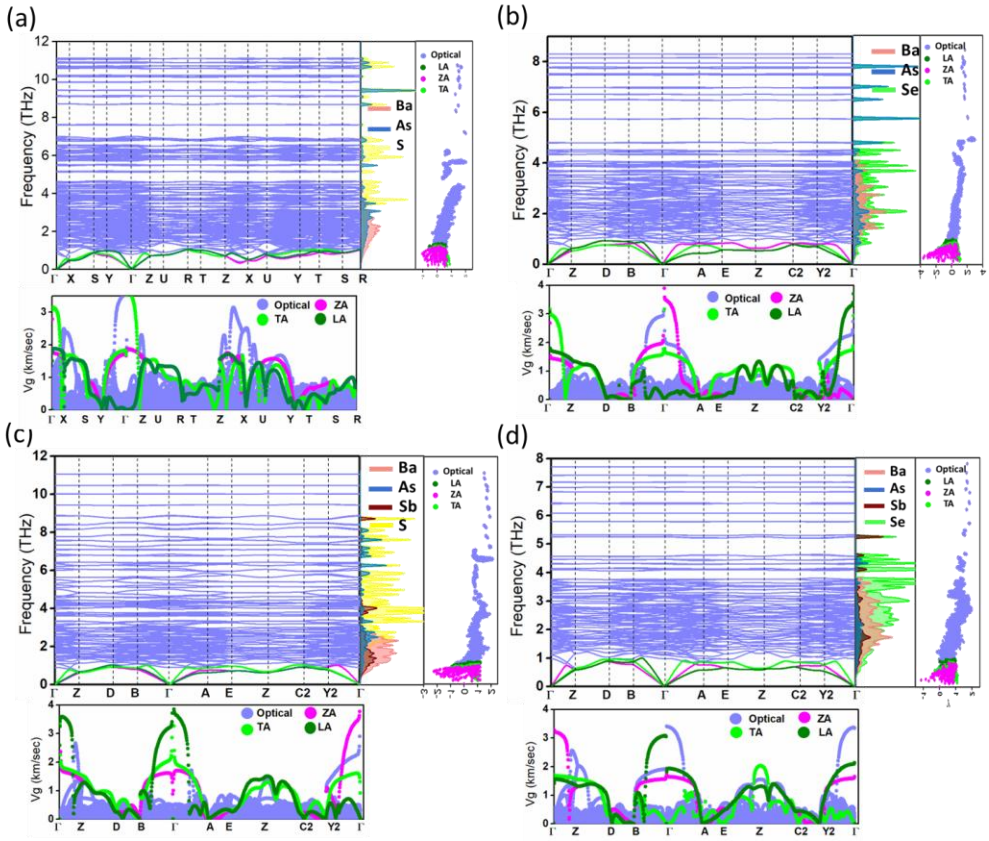


Figure 5.20. The machine learning interatomic potential predicted phonon dispersion, phonon density of states and Grüneisen parameter (γ), group velocity across the high symmetry points in the first Brillouin zone for **(a)** $Ba_2As_2S_5$, **(b)** $Ba_2As_2Se_5$, **(c)** Ba_2AsSbS_5, **(d)** $Ba_2AsSbSe_5$.

This behavior is confirmed by the potential energy surfaces for atomic displacements in Ba_2AsPnQ_5. The shallow potential wells (~1 eV; **Figure 5.19(c-d)**) indicate weak Ba-lattice bonding, promoting significant rattling motion. These rattling vibrations couple strongly with acoustic phonon

modes, playing a crucial role in the ultralow κ_L observed for $Ba_2AsBiSe_5$. Similar, rattling effect has been experimentally observed in the related systems such as $AgSb_xBi_{3-x}S_5$ and $Cu_4Bi_4Se_9$, where the low-frequency localized vibrations and strong lattice anharmonicity associated with cation "rattling" within similar edge-shared chalcogenide frameworks *[91, 92]*. The suppression of κ_L is primarily driven by increased three-phonon scattering rates and weighted phase space when moving from As to Bi and from S to Se (**Figure 5.21-5.22**). Furthermore, boundary scattering exerts a more pronounced effect than isotopic scattering, further reducing κ_L (**Figure 5.23**).

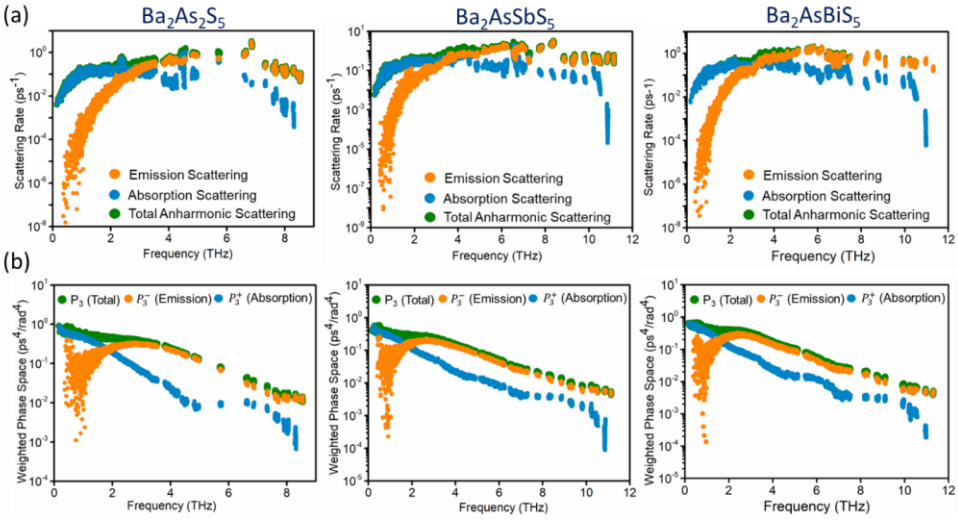


Figure 5.21: The calculated **(a)** total anharmonic scattering rates and **(b)** weighted phase space (WP_3) as a function of frequency (THz) for Ba_2AsPnS_5 (Pn = As, Sb and Bi) at 300 K along with absorption and emission scattering channels and absorption (P_3^+) and emission (P_3^-) weighted phase space.

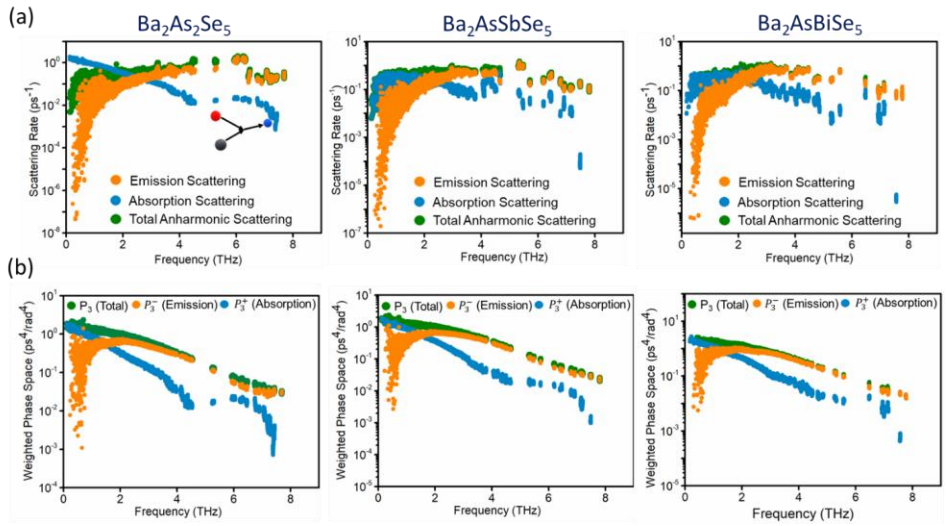


Figure 5.22: The calculated **(a)** total anharmonic scattering rates and **(b)** weighted phase space (WP_3) as a function of frequency (THz) for $Ba_2AsPnSe_5$ (Pn = As, Sb and Bi) at 300 K along with absorption and emission scattering channels and absorption (P_3^+) and emission (P_3^-) weighted phase space.

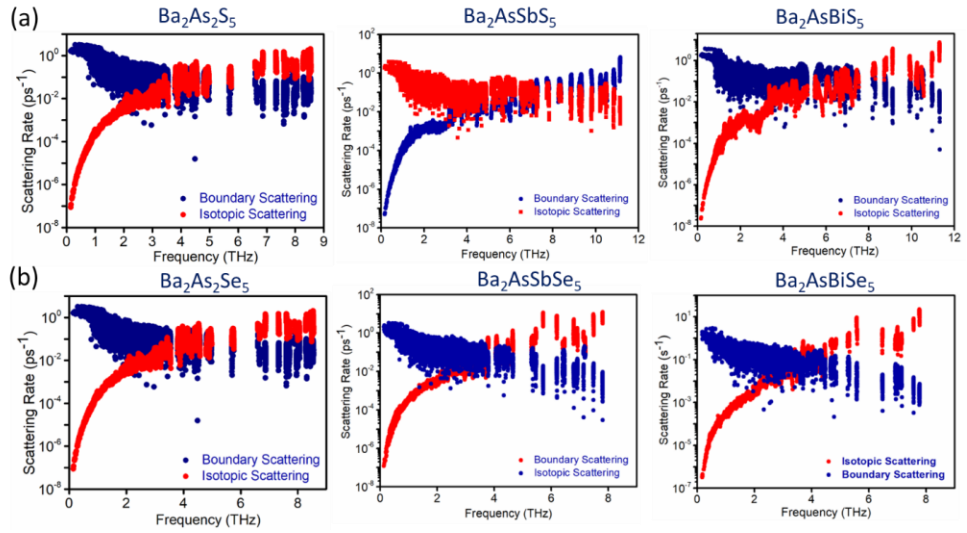


Figure 5.23: Boundary and isotopic scattering rates of **(a)** Ba_2AsPnS_5 (Pn = As, Sb and Bi) and **(b)** $Ba_2AsPnSe_5$ (Pn = As, Sb, and Bi) with respect to frequency (THz) at 300K.

5.7.4. Engineering Band Valleys through Orbital Design. To improve electronic transport and thermoelectric performance in the Ba_2AsPnQ_5

systems, we strategically tailored orbital interactions to engineer band valleys near the band edges *[93]*. By modifying the Pn-Q bonding environment, we induce the convergence of multiple band extrema, thereby increasing valley degeneracy particularly in the valence band. These materials exhibit indirect band gaps ranging from 1.71 to 2.12 eV (**Figure 5.24**), with the valence band maxima (VBM) located at the Γ point and the conduction band minima (CBM) at the E point of the Brillouin zone (**Figure 5.24**), consistent with reported experimental values *[71]*.

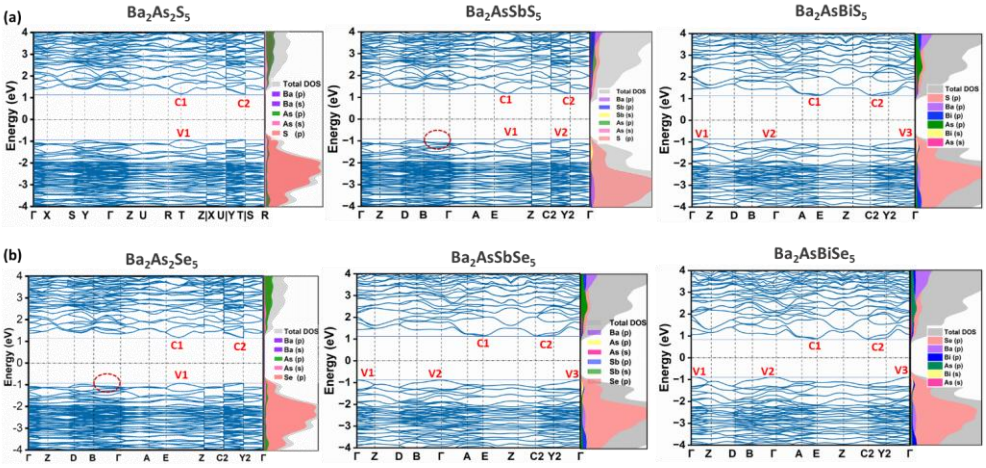


Figure 5.24: The electronic band structures along with the total and projected density of states (Total DOS and PDOS) calculated using the HSE03 functional for **(a)** Ba_2AsPnS_5 (Pn = As, Sb and Bi) and **(b)** $Ba_2AsPnSe_5$ (Pn = As, Sb and Bi) along the Brillouin zone points, highlighting the band degeneracies in the valence band (V1, V2, V3) and conduction band (C1, C2).

The presence of multiple VBM (V_1, V_2, V_3) and CBM (C_1, C_2) at different high symmetry k-points increases the overall band degeneracy in $Ba_2AsBiSe_5$ compared to $Ba_2As_2Se_5$ system (**Figure 5.25(a-d)**). This band-edge convergence near the Fermi level enhances the effective density of states for charge carriers, thereby boosting the thermoelectric power factor. The projected density of states (PDOS) (**Figure 5.25(e)**) reveals that the VBM are primarily consist of Se-4p orbitals, with notable contributions from Pn (As,

Sb, Bi) p-states. The presence of stereochemically active lone pairs (SCALP) originating from hybridization between As-4s/Bi-6s and Se-4p orbitals, highlight the role of Pn (ns) orbital near the VBM. [24, 32] Consequently, both the VBM and CBM are mainly dominated by Se-4p orbitals, with significant contributions from Bi-6p, As-4p, and the active lone pairs from Bi-6s, As-4s, underscoring the critical role of the $[Pn_2Q_4]^{2-}$ unit in tuning the band gap and influencing lattice anharmonicity. In contrast, deeply positioned As-4s /Bi-6s near -10 eV act as inactive lone pairs. Collectively, these orbital characteristics shape the band structure and strongly influence charge-carrier transport properties.

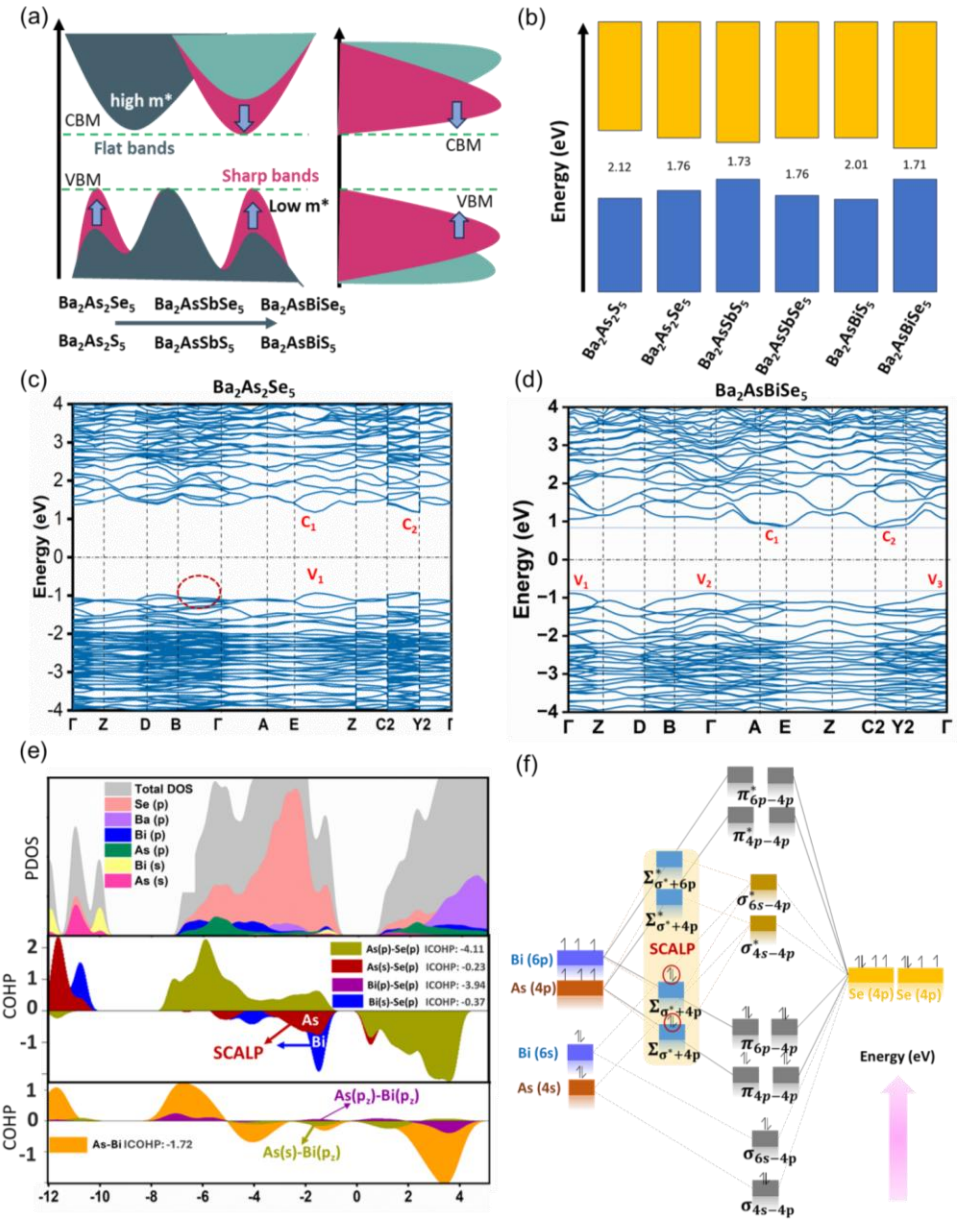


Figure 5.25: (a) Schematic illustration of band valley engineering through modifications in the band structure and density of states. **(b)** Calculated band gaps for Ba_2AsPnQ_5 materials (Pn = As, Sb, Bi; Q = S, Se). **(c-d)** Electronic band structure of $Ba_2As_2Se_5$ and $Ba_2AsBiSe_5$ highlighting valence band (V_1, V_2, V_3) and conduction band (C_1, C_2) degeneracies. **(e)** Partial density of states (PDOS) and crystal orbital Hamilton population (COHP) analysis for $Ba_2AsBiSe_5$. **(f)** Schematic representation of orbital

interactions near the Fermi level in $Ba_2AsBiSe_5$, derived from PDOS and COHP analysis**.**

5.7.5. Capturing Chemical Bonding Heterogeneities. To investigate the nature of bonding interactions governing lattice dynamics, we performed crystal orbital Hamilton population (COHP) analysis (**Figure 5.25(e)**) *[52]*. COHP quantitatively evaluates bonding and antibonding interactions by projecting Hamiltonian-weighted orbital populations, where positive values indicate bonding states, and negative values indicate antibonding states. The results reveal strong covalent interactions in Pn-Q bonds, such as As($4p_x$)-Se($4p_x$) and Bi($6p_y$)-Se($4p_y$) orbitals, with highly negative integration of COHP (ICOHP) (**Figure 5.25(e)**). In contrast, weak antibonding interactions are observed for As(4s)-Se($4p_x$) and Bi(6s)-Se($4p_y$), reflected by smaller-magnitude negative ICOHP values. Additionally, Pn-Pn bonding exhibits weak As(p_z)-Bi(p_z) interactions, which introduce additional anharmonicity due to repulsive forces between atoms. This effect can be rationalized through Fajans' polarization concept, *[94, 95]* where the highly polarizing Bi^{3+} ion distorts the adjacent As^{3+} 4pz electron cloud, inducing net polarization and weakening As-Bi bonds. Such a weak bonding network promotes structural asymmetry, disrupts phonon transport pathways, and enhances phonon scattering, thereby reducing κ_L, a key factor in thermoelectric performance. These bonding characteristics are consistently observed across the Ba_2AsPnQ_5 (Pn = As, Sb, Bi; Q = S, Se) family (**Figures 5.26-5.27**), underscoring the critical role of orbital-specific bonding heterogeneity in controlling κ_L for thermoelectric optimization.

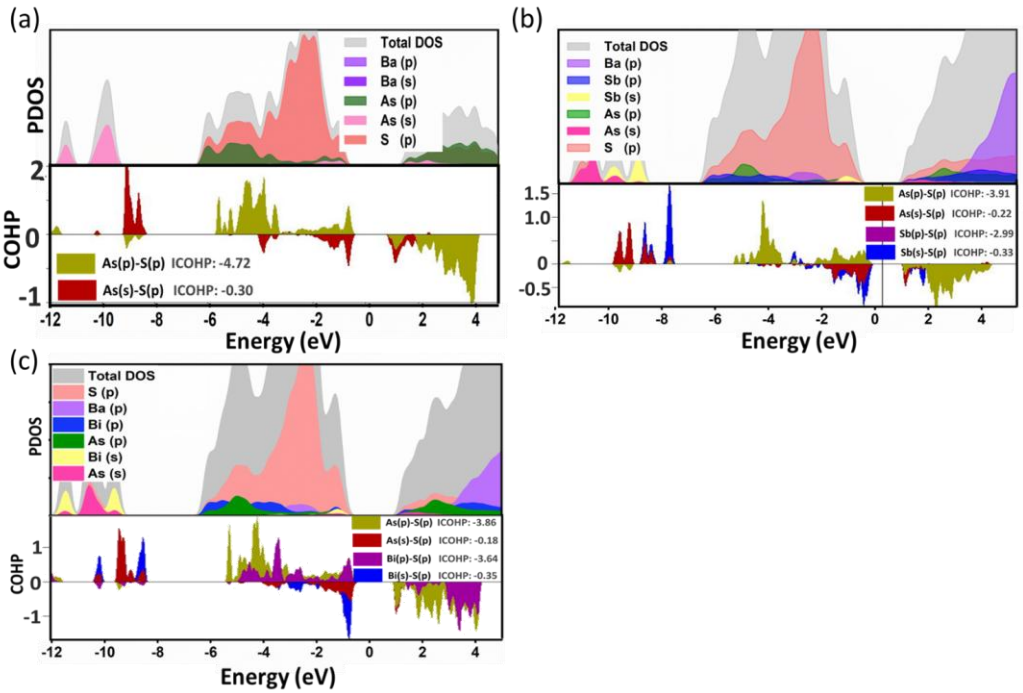


Figure 5.26: Total and Partial density of states (Total DOS/PDOS) and crystal orbital Hamilton population (COHP) analysis of **(a)** $Ba_2As_2S_5$, **(b)** Ba_2AsSbS_5 and **(c)** $Ba_2AsSbSe_5$.

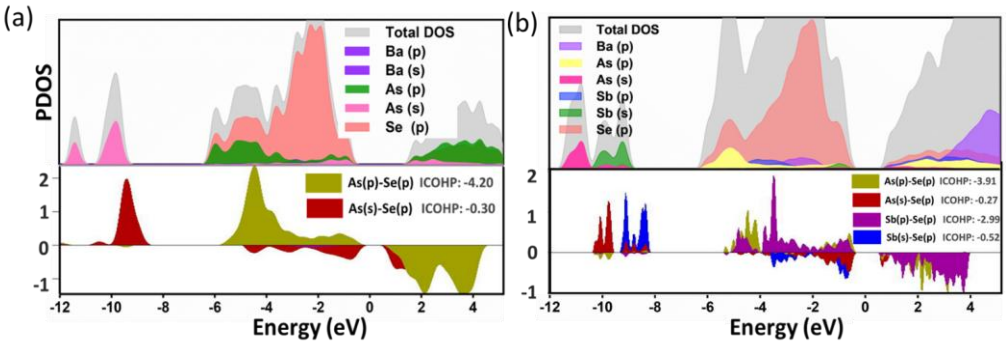


Figure 5.27: Total and Partial density of states (Total DOS/PDOS) and crystal orbital Hamilton population (COHP) analysis of **(a)** $Ba_2As_2Se_5$ and **(b)** $Ba_2AsSbSe_5$.

To further explore the role of lone-pair electrons in the ultralow κ_L material $Ba_2AsBiSe_5$, we analysed the molecular orbital (MO) interactions governing its bonding and antibonding states (**Figure 5.25(f)**). The energy

offset between Bi and As states arise from their electronegativity difference. The lowest energy states (~ -11 eV) originate from σ (4s-4p) bonding between As(4s)-Se($4p_y$), while states at ~ -10 eV correspond to σ (6s-4p) bonding between Bi(6s)-Se($4p_x$). Higher energy bands (~ -6 eV) are dominated by π(6p/4p-4p) bonding between Bi($6p_y$)-Se($4p_y$) and As($4p_x$)-Se($4p_x$). Notably, stabilized antibonding states derived from σ * (6s-4p) and σ* (4s-4p) interactions appear just below the Fermi level, indicating the presence of SCALP. This observation aligns with the revised lone pair model, wherein active lone-pair expression in heavy-metal chalcogenides arises from synergistic stabilization between occupied metal cation p-states and antibonding σ*-interaction states formed by metal s-states and chalcogen p-states *[13]*. Consequently, the antibonding states near the VBM weakens chemical bonds, softens the lattice, and promotes bonding hierarchies, collectively enhancing phonon scattering and leading to ultralow κ_L *[96]*.

Table 5.6: Geometric, bond stiffness/softness, and chemical bonding descriptors for Ba_2AsPnQ_5 (Pn = As, Sb, Bi; Q = S, Se), including lone pair angle (θ), lone pair distance from pnictogen (d_{lp}), Debye temperature (θ_D), Grüneisen parameter (γ), ionicity (r'_σ), hybridization (r_π^{-1}), integrated crystal Hamilton population (ICOHP, Pn-Chg), bond length (Pn-Chg), and lattice thermal conductivity (κ_L) along the x-axis.

Descriptors	$Ba_2As_2S_5$	Ba_2AsSbS_5	Ba_2AsBiS_5	$Ba_2As_2Se_5$	$Ba_2AsSbSe_5$	$Ba_2AsBiSe_5$
θ	102.64	102.03	101.53	102.35	101.99	100.25
d_{lp}	3.48	3.46	3.44	3.47	3.46	3.39
Y (GPa)	49.45	50.83	52.08	45.51	48.82	44.60
θ_D **(K)**	222	214	210	182	181	164
γ	0.89	1.05	1.14	0.88	1.17	1.16
r'_σ	-0.95	-0.96	-0.97	-0.82	-0.86	-0.87
r_π^{-1}	1.59	1.56	1.53	1.49	1.47	1.44
ICOHP	-0.30	-0.22	-0.18	-0.29	-0.27	-0.19

[As(s)-Q(p)]						
ICOHP [Pn(s)-Q(p)]	-0.30	-0.33	-0.35	-0.29	-0.52	-0.37
Bond Length As - Q	3.35	3.23	3.26	3.23	3.27	3.26
Bond Length Pn - Q	3.35	3.36	3.40	3.23	3.28	3.41
κ_L	0.66	0.45	0.42	0.32	0.21	0.14

5.7.6. Bonding Descriptors as Fingerprint for Anharmonicity

Deciphering the origin of ultralow κ_L in Ba_2AsPnQ_5 requires a comprehensive analysis of chemical bonding descriptors that influence phonon transport. These descriptors can be broadly classified into three main categories: **(i)** Geometrical descriptors: bond angles and lone pair distances; **(ii)** Bond stiffness/softness descriptors: elastic modulus, Debye temperature, and Grüneisen parameter; **(iii)** Chemical bonding features: ionicity, hybridization, and bond strength. As summarized in **Table 5.6**, each descriptor plays a pivotal role in tunning anharmonicity, enhancing phonon scattering, and thereby supressing κ_L. Together, they serve as a fingerprint of the complex relationship between bonding and lattice dynamics in Ba_2AsPnQ_5 compounds.

Geometric Descriptors. The lone pair angle (θ) serves as an indicator of SCALP and directly influences lattice anharmonicity. A smaller θ increases Coulombic repulsion with the bonding pnictogen np orbitals, which intensifies local lattice distortions, enhances phonon scattering, and ultimately lowers κ_L *[5]*. In Ba_2AsPnQ_5, each pnictogen is coordinated to three chalcogen atoms in a trigonal pyramidal configuration, with average Q-Pn-Q bond angles ranging from 100.25˚-102.64˚. In $Ba_2As_2S_5$, the relatively larger θ of 102.64° corresponds to a more symmetric lattice, contributing to a higher κ_L. In contrast, $Ba_2AsBiSe_5$ exhibits a smaller bond angle of 100.25°, leading to stronger lone pair-induced distortions, greater

phonon scattering, and the lowest κ_L values among the family. The lone pair distance (d_{lp}) describes the spatial extent of lone pair electron density from the pnictogen nucleus and is given by *[5]*:

$$d_{lp} = 3[1 + 0.0128\ (\bar{\theta} - 90)]$$

This relationship shows that enhanced lone-pair activity simultaneously alters both θ and d_{lp}, thereby modifying local bond stiffness and increasing anharmonicity. Nevertheless, the relative weights of these descriptors vary in their contribution to the predicted κ_L, reflecting their distinct but complementary roles within the model. The overlapping wave functions between the lone pair and nearby valence electrons generate a nonlinear electrostatic repulsion, which increases lattice anharmonicity. As the lone pairs moves closer to the pnictogen nucleus (d_{lp} decreases), these anharmonic interactions intensify, further reducing κ_L. For instance, $Ba_2As_2S_5$ has a larger d_{lp}, indicating weaker lone pair interaction and higher κ_L, whereas $Ba_2AsBiSe_5$ shows smaller d_{lp}, reflecting enhanced stereochemical activity of lone pairs that strongly suppresses κ_L. These observations confirm that increased lone pair repulsion enhances anharmonicity, leading to a more pronounced reduction in thermal conductivity.

Bond Stiffness/Softness Descriptors. The Young's modulus (Y) measures lattice stiffness, with lower Y values indicating a softer lattice that promotes stronger phonon scattering and consequently reduces κ_L. In Ba_2AsPnQ_5, Y decreases systematically from As to Sb to Bi, and from S to Se, reflecting progressive lattice softening that facilitates enhanced phonon-phonon interactions and lower κ_L. Similarly, the Grüneisen parameter (γ) quantifies lattice anharmonicity, with higher γ values corresponding to stronger phonon-phonon interactions and reduced κ_L. These trends indicate that a softer lattice, characterized by a lower Debye temperature (θ_D) and higher γ leads to stronger phonon scattering, thereby reducing κ_L.

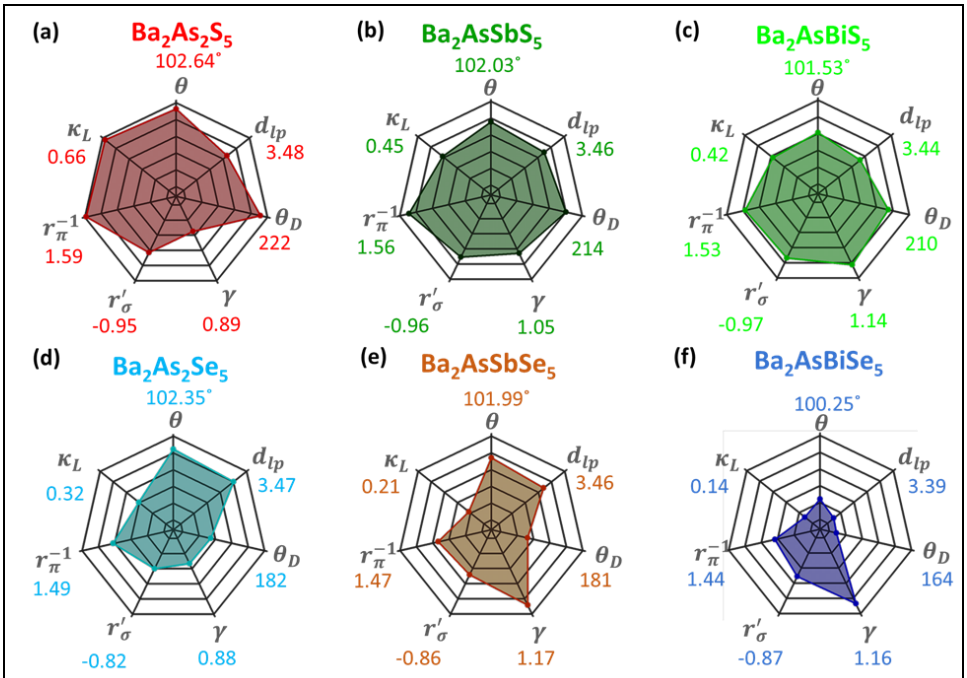
Chemical Bonding Features. The unique bonding characteristics of the studied systems are described by the degree of ionicity (r'_σ), and hybridization (r_π^{-1}). Here, r'_σ quantifies the extent of bond ionicity, while r_π^{-1} measures the degree of covalency in the Pn-Chg bond *[66]*. These parameters are derived from the energetic splitting between the s- and p-states, which plays crucial role in forming stereochemically active lone pairs and edge shared polyhedra. These parameters are defined as:

$$r'_\sigma = \left(\frac{\sum_i n_i r_{p,i}}{\sum_i n_i}\right) - \left(\frac{\sum_j n_j r_{p,j}}{\sum_j n_j}\right)$$

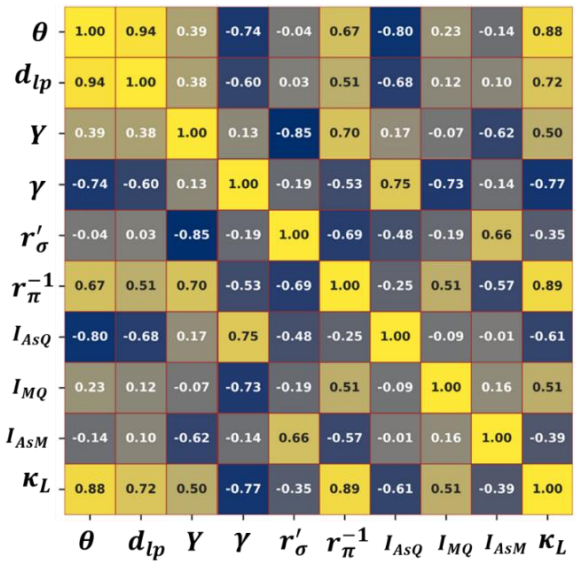
$$r_\pi^{-1} = \left|\left(\frac{\sum_i n_i (r_{p,i} - r_{s,i})}{\sum_i n_i}\right) - \left(\frac{\sum_j n_j (r_{p,j} - r_{s,j})}{\sum_j n_j}\right)\right|^{-1}$$

Here, r_p and r_s denote the valence radii of the p- and s- orbitals of atoms, summed over the i^{th} and j^{th} atoms in the material *[66, 97]*. For instance, more negative r'_σ values in $Ba_2As_2S_5$ indicate a more localized bonding environment, whereas the less negative r'_σ in $Ba_2AsBiSe_5$ reflects greater charge delocalization, which weaken bonds and lowers κ_L. Similarly, the higher r_π^{-1} in $Ba_2As_2S_5$ suggests stronger hybridization, while the reduced r_π^{-1} in $Ba_2AsBiSe_5$, indicate weaker covalency. These bonding trends, influences by SCALPs and edge-sharing polyhedral through Pn-Chg interactions, enhance phonon scattering and thereby reduce κ_L.

Table 5.7: Interplay of chemical bonding parameters: lone pair angle (θ), lone pair-pnictogen distance (d_{lp}), Debye temperature (θ_D), Grüneisen parameter (γ), ionicity (r'_σ), hybridization (r_π^{-1}), and their quantitative influence on κ_L for Ba_2AsPnQ_5 systems. Panels **(a-f)** depicts the individual impact of each parameter, alongside the Pearson correlation coefficient plot summarizing their relationships.



Descriptors	Symbol	Pearson correlation coefficient
Lone Pair Angle	θ	
Lone Pair distance	d_{lp}	
Young's modulus	Y	
Grüneisen Parameter	γ	
Ionicity	r'_{σ}	
Hybridization	r_{π}^{-1}	
ICOHP [As(s)-Q(p)]	I_{AsQ}	
ICOHP [As(s)-Q(p)]	I_{MQ}	
ICOHP [As(p)-M(p)]	I_{AsM}	
Lattice thermal conductivity	κ_L	



5.7.7. Correlation Analysis of Bonding Descriptors and κ_L. To explore the fundamental relationships between chemical bonding descriptors and κ_L, we performed a Pearson correlation coefficient (PCC) analysis of key features (**Table 5.7)** *[98, 99]*. The correlation matrix reveals that most

feature-κ_L pairs exhibit |PCC|>0.50, indicating strong statistical dependencies. Among these descriptors, hybridization (r_π^{-1}) emerges as the most influential factor, showing the highest correlation with κ_L (PCC ~ 0.89). This underscores the cumulative impact of SCALP and edge-sharing polyhedra on Pn-Chg bond, which significantly enhances phonon scattering, and reduce κ_L. The lone pair angle (θ) also correlates strongly with d_{lp} (PCC = 0.94), underscoring the intrinsic relationship between SCALP activity and lattice anharmonicity. Furthermore, r_π^{-1} is strongly correlated with r'_σ, θ, d_{lp}, and γ emphasizing the pivotal role of orbital hybridization in modulating the structural rigidity, charge distribution, and anharmonicity, all of which critically affect phonon transport *[67]*. Collectively, these findings suggest that κ_L in Ba_2AsPnQ_5 materials can be expressed as a function of key bonding parameters:

$$\kappa_L = f(\theta, d_{lp}, \gamma, r'_\sigma, r_\pi^{-1}, \mathrm{I_{AsQ}}, \mathrm{I_{MQ}})$$

While our descriptors remain transferable and robust in capturing bonding anharmonicity trends within structural families, *[67]* their predictive strength is highly dependent on dimensionality, being strongest in layered systems, moderate in chain structures, and relatively weak in complex 3-D frameworks. However, it is important to note that each of these material classes exhibit unique bonding characteristics and lattice dynamics, which require detailed, structure-specific investigations that go beyond the scope of the present data-driven framework.

5.8.8. Carrier Transport Mechanisms and Scattering Effects in Thermoelectric Materials

Electronic transport properties were evaluated using the AMSET (Ab Initio Model for Seebeck and Transport) framework, integrates first-principles electronic structure calculations with key carrier scattering mechanisms. This approach allows determination of carrier mobility and thermoelectric transport coefficients by incorporating electron-phonon (ADP and POP), ionized impurity (IMP), and defect scattering. In this chapter, all electronic

transport calculations are based on ideal single-crystal properties. As a future direction, the impact of extrinsic scattering in polycrystalline samples particularly from grain boundaries and extended defects will be investigated, as these factors are expected to further reduce carrier mobility and degrade electronic transport performance, consistent with experimental observations. The individual contributions of these scattering mechanisms as functions of temperature, carrier concentration, and electronic energy, are shown in **Figures 5.28-5.33**.

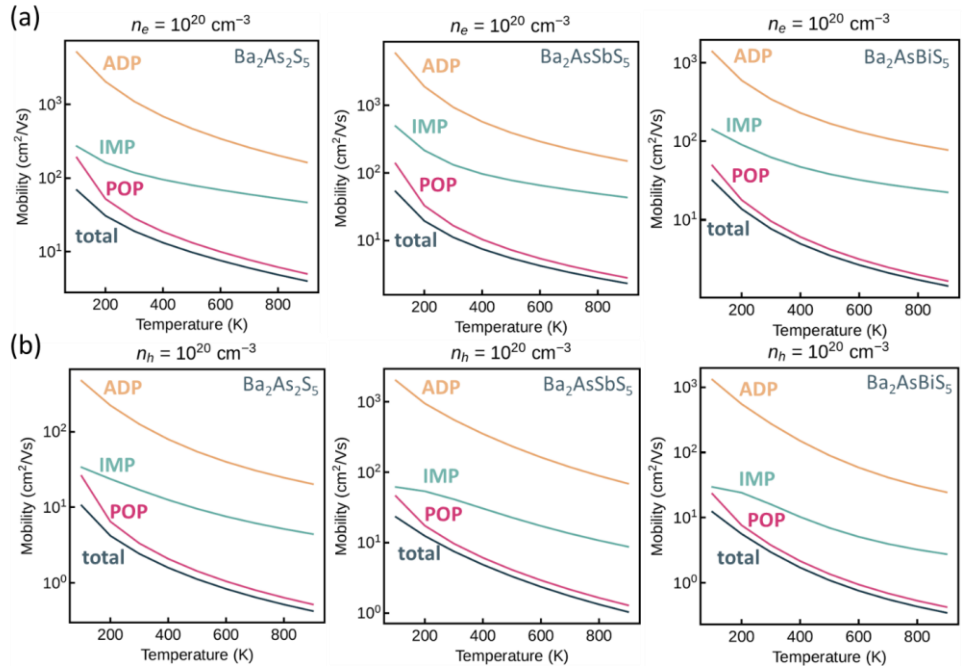


Figure 5.28: Mobility (cm^2/Vs) as a function of temperature for **(a)** n-doping and **(b)** p-type doping for Ba_2AsPnS_5 (Pn = As, Sb, and Bi) under three scattering mechanisms namely, polar optical phonon (POP), ionized impurity (IMP), and acoustic deformation potential (ADP) scattering with carrier concentrations of 10^{20} cm^{-3}.

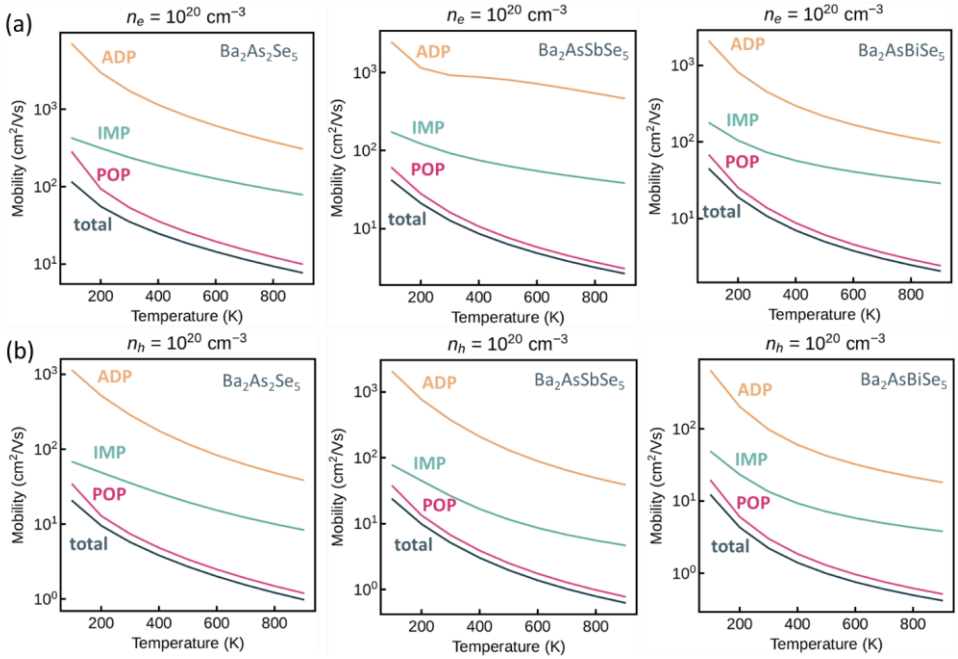


Figure 5.29: Mobility (cm^2/Vs) as a function of temperature for **(a)** n-doping and **(b)** p-type doping for $Ba_2AsPnSe_5$ (Pn = As, Sb, and Bi) under three scattering mechanisms namely, polar optical phonon (POP), ionized impurity (IMP), and acoustic deformation potential (ADP) scattering with carrier concentrations of 10^{20} cm^{-3}.

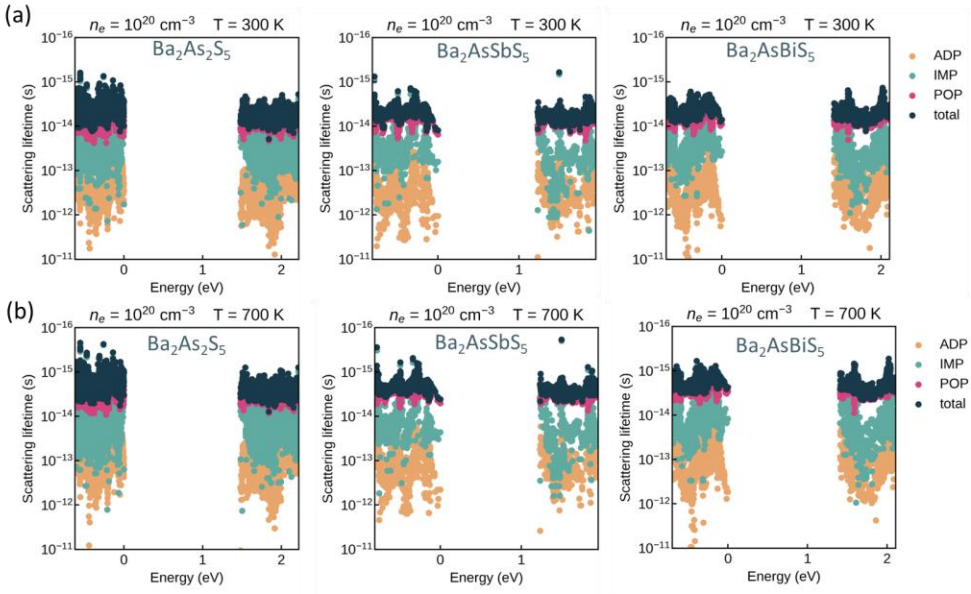


Figure 5.30: Scattering rates as a function of energy of n-type at **(a)** 300 K and **(b)** 700 K for Ba_2AsPnS_5 (Pn = As, Sb, and Bi). These represent their

scattering mechanisms including polar optical phonon (POP), ionized impurity (IMP), and acoustic deformation potential (ADP) scattering at carrier concentrations of 10^{20} cm^{-3}.

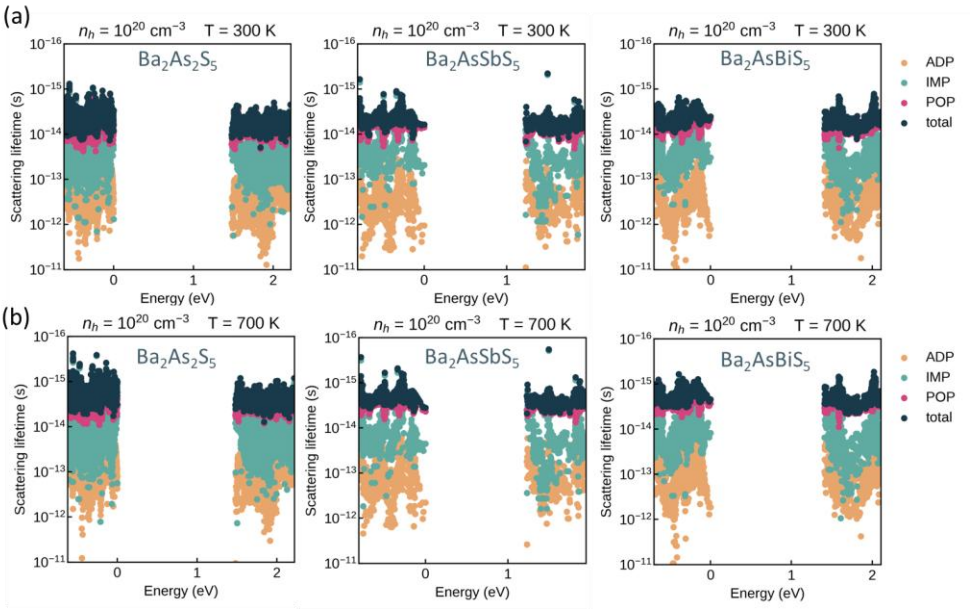


Figure 5.31: Scattering rates as a function of energy of p-type at **(a)** 300 K and **(b)** 700 K for Ba_2AsPnS_5 (Pn = As, Sb, and Bi). These represent their scattering mechanisms including polar optical phonon (POP), ionized impurity (IMP), and acoustic deformation potential (ADP) scattering at carrier concentrations of 10^{20} cm^{-3}.

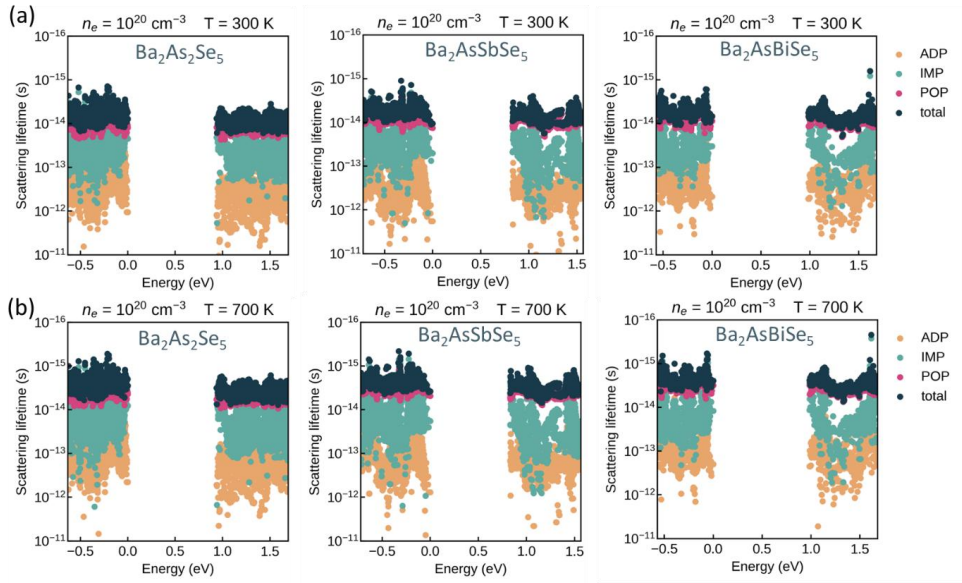


Figure 5.32 Scattering rates as a function of energy of n-type at **(a)** 300 K and **(b)** 700 K for $Ba_2AsPnSe_5$ (Pn = As, Sb, and Bi). These represent their scattering mechanisms including polar optical phonon (POP), ionized impurity (IMP), and acoustic deformation potential (ADP) scattering at carrier concentrations of 10^{20} cm^{-3}.

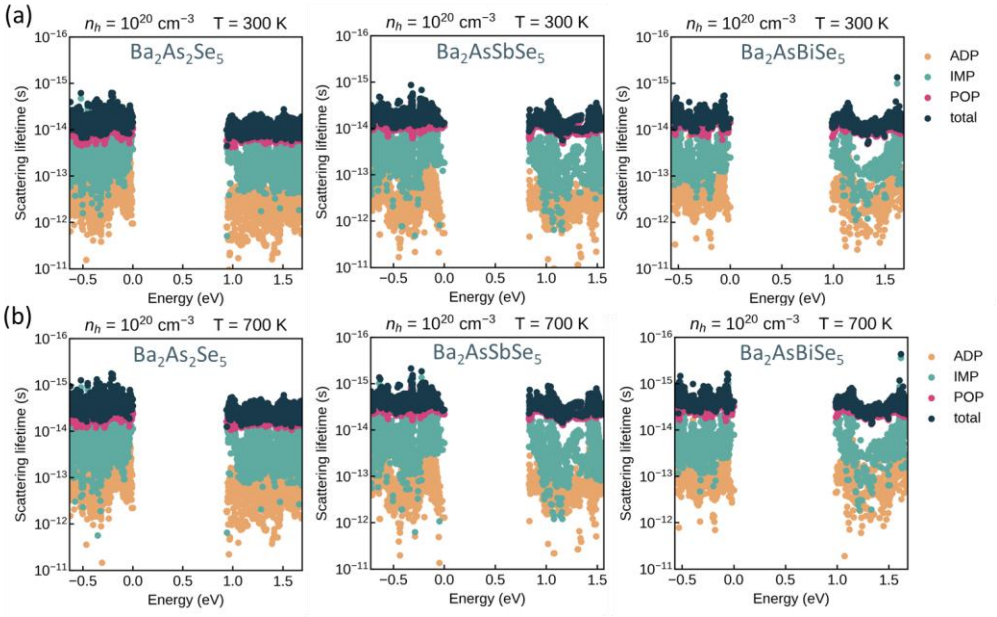


Figure 5.33: Scattering rates as a function of energy of p-type at **(a)** 300 K and **(b)** 700 K for $Ba_2AsPnSe_5$ (Pn = As, Sb, and Bi). These represent their scattering mechanisms including polar optical phonon (POP), ionized impurity (IMP), and acoustic deformation potential (ADP) scattering at carrier concentrations of 10^{20} cm^{-3}.

As anticipated, the dominant mobility-limiting scattering mechanism depends strongly on both doping concentration and temperature. The primary contributors include polar-optical phonon (POP) scattering, ionized impurity (IMP) scattering, and acoustic deformation potential (ADP) scattering. Under conditions of high thermoelectric figure of merit (ZT), ADP scattering dominates in Ba_2AsPnQ_5 (Pn = As, Sb, Bi; Q = S, Se). This behaviour is primarily attributed to the lower-energy phonon modes introduced by the presence of rattler ion, SCALP effect and edge sharing polyhedra (**Figure 5.28-5.29**). In all cases, ADP scattering is followed by

IMP and POP for both n- and p-type doping, are presented in **Figures 5.34-5.35**. The observed transport anisotropy reflects the layered crystal structure, with the highest mobilities along crystallographic directions minimizing scattering from $Pn_2Q_4^{2-}$ dimer chains. However, at high carrier concentrations and temperature, this effect is relatively reduced due to the increase in lattice vibrations, leading to greater ADP scattering and reduced mobility.

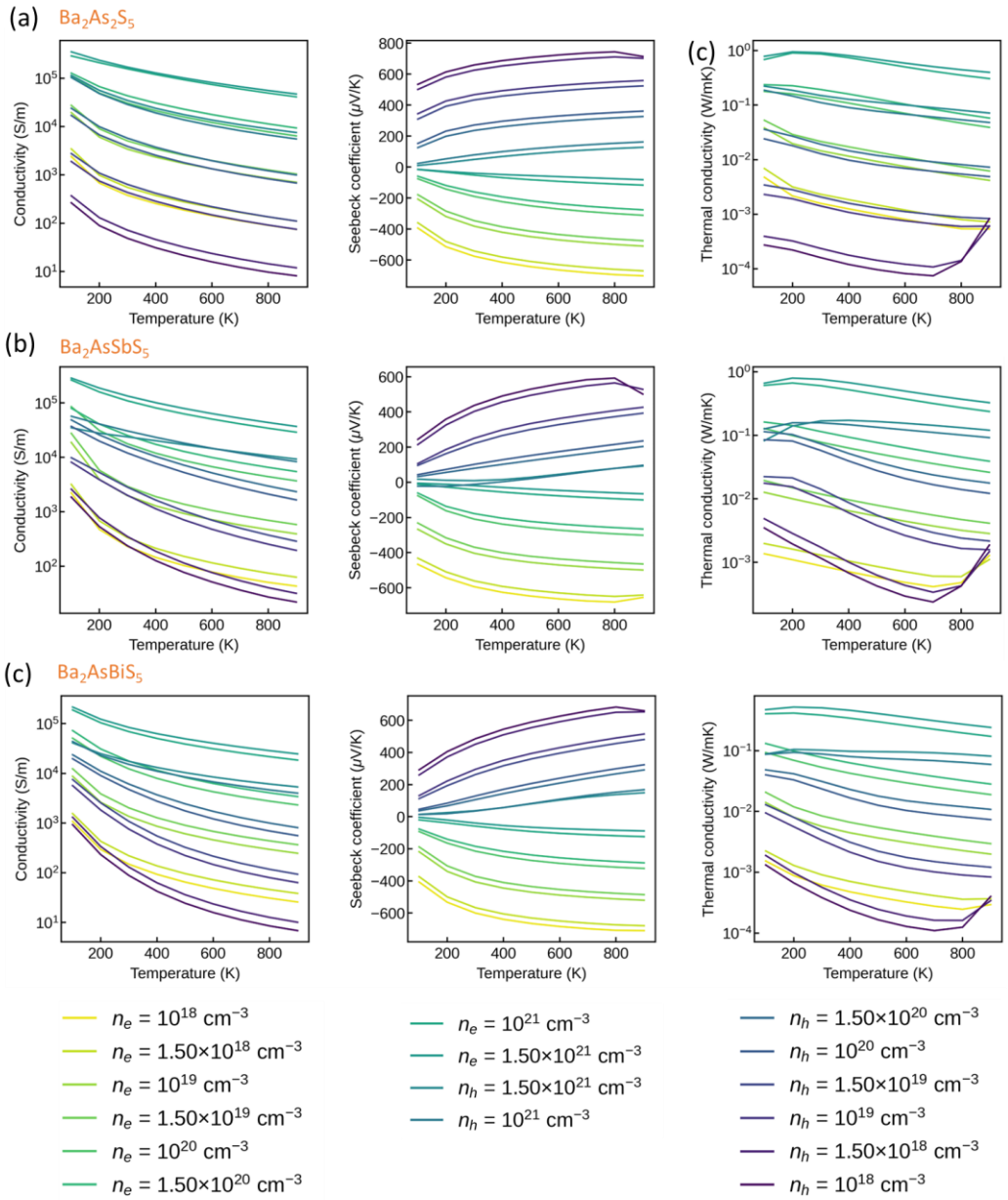


Figure 5.34: The calculated electronic transport properties including electrical conductivity (S/m), Seebeck coefficient (μV/K), and electronic thermal conductivity ($Wm^{-1}K^{-1}$) for **(a)** $Ba_2As_2S_5$, **(b)** Ba_2AsSbS_5, and **(c)** Ba_2AsBiS_5.

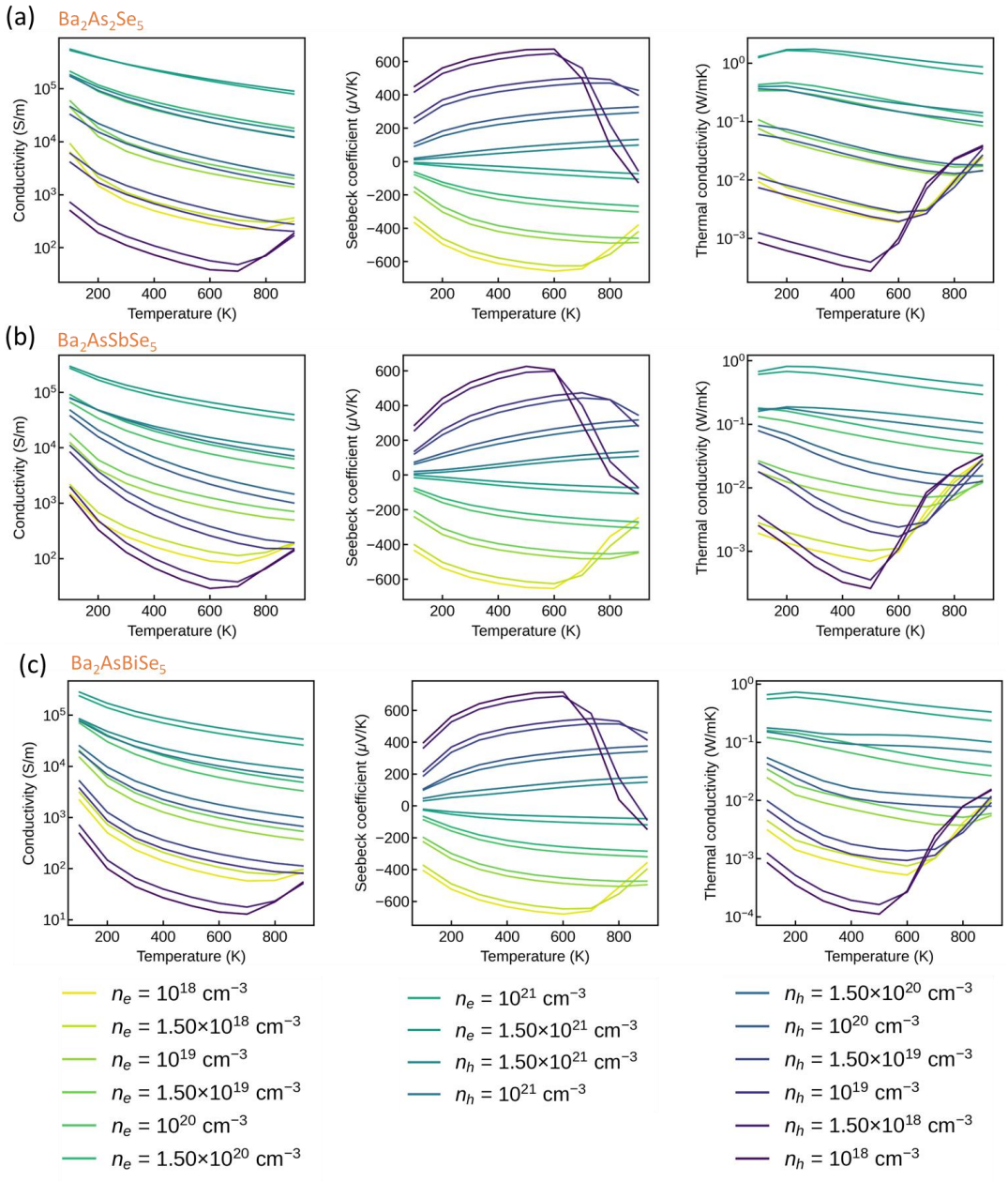


Figure 5.35: The calculated electronic transport properties including electrical conductivity (S/m), Seebeck coefficient (μV/K), and electronic

thermal conductivity ($Wm^{-1}K^{-1}$) for **(a)** $Ba_2As_2Se_5$, **(b)** $Ba_2AsSbSe_5$, and **(c)** $Ba_2AsBiSe_5$.

The interplay of these scattering mechanisms directly correlates with the exceptional thermoelectric performance: as temperature increases from 300 K to 800 K, higher phonon populations increase ADP and IMP scatterings, but the simultaneous reduction in κ_L due to stronger anharmonic phonon-phonon interactions drives the overall increase in ZT, reaching a peak value of ZT = 2.92 for $Ba_2AsBiSe_5$. However, at high carrier concentrations, this effect is relatively minor due to the dominance of impurity scattering, which is largely temperature-independent, over carrier-phonon scattering. Following the Wiedemann-Franz law ($\kappa_e = L\sigma T$), where L is the Lorentz number and T is temperature), the electronic thermal conductivity (κ_e) trends align closely with those of electrical conductivity as shown in **Figure 5.36**. Additionally, the electrical conductivity (σ), Seebeck coefficient (S), and figure of merit (ZT) for n-type and p-type Ba_2AsPnQ_5 systems were calculated at 300 K and 700 K, as depicted in **Figure 5.37-5.38**. For n-type doping at 300 K, $Ba_2AsBiSe_5$ exhibits highest Seebeck coefficient (-247 μVK^{-1}), followed by $Ba_2AsSbSe_5$ (-211 μVK^{-1}) and $Ba_2As_2Se_5$ (-182 μVK^{-1}). The calculated ZT values for n-type $Ba_2As_2S_5$, Ba_2AsSbS_5, and Ba_2AsBiS_5 are 0.11 (0.45), 0.79 (1.12), and 0.49 (1.75) at 300 K (700 K), respectively, for a carrier concentration of 10^{20} cm^{-3} as represented in **Figure 5.37**.

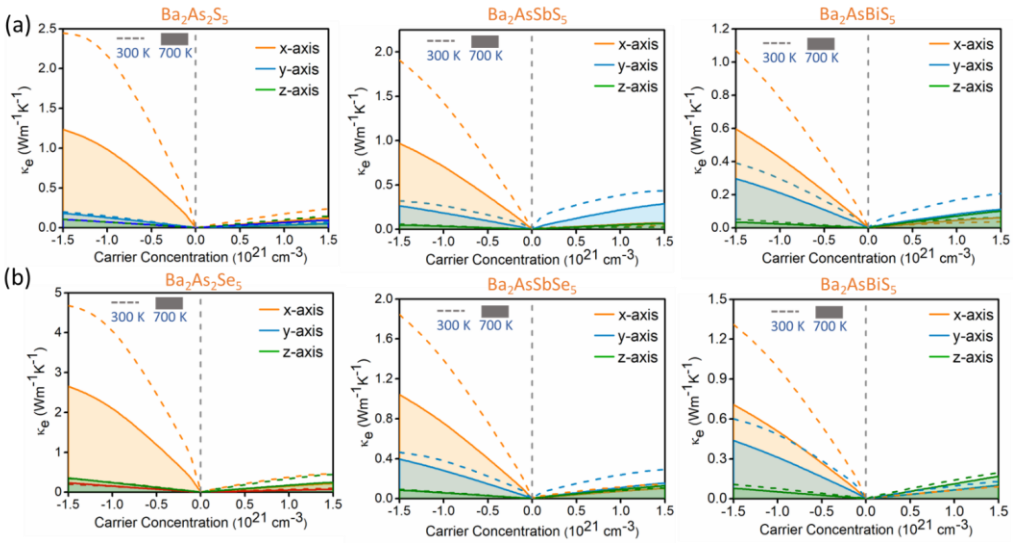


Figure 5.36: The calculated electronic thermal properties (κ_L) in $Wm^{-1}K^{-1}$ for **(a)** Ba_2AsPnS_5 (Pn = As, Sb, and Bi) and **(b)** $Ba_2AsPnSe_5$ (Pn = As, Sb, and Bi) systems.

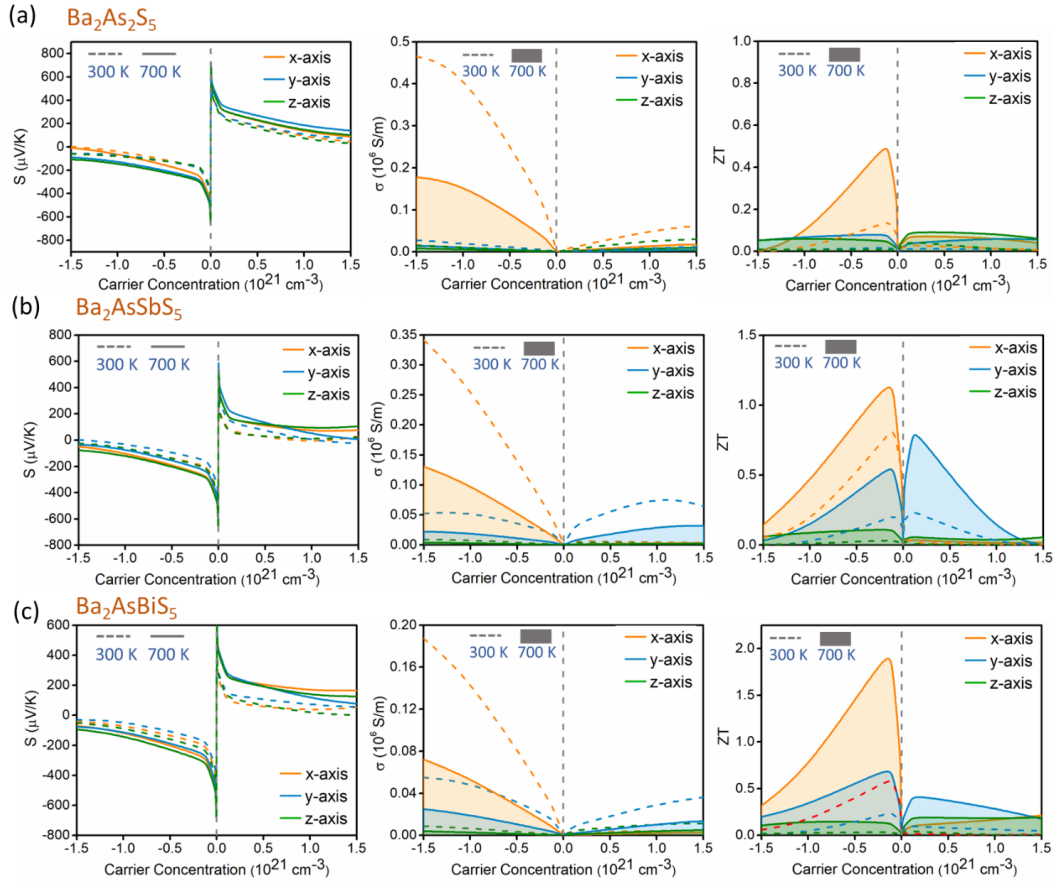


Figure 5.37: The evaluated thermoelectric properties for **(a)** $Ba_2As_2S_5$, **(b)** Ba_2AsSbS_5, and **(c)** Ba_2AsBiS_5 containing Seebeck coefficient (S), electrical conductivity (σ), and thermoelectric figure of merit (ZT), calculated based on relaxation times obtained transport coefficients using AMSET. The negative and positive signs of the carrier concentrations represent n- and p-type doping. Here, the orange, blue and olive green represents the x-axis, y-axis, and z-axis, respectively. The dotted line and straight line represent temperature scale of 300 K and 700 K.

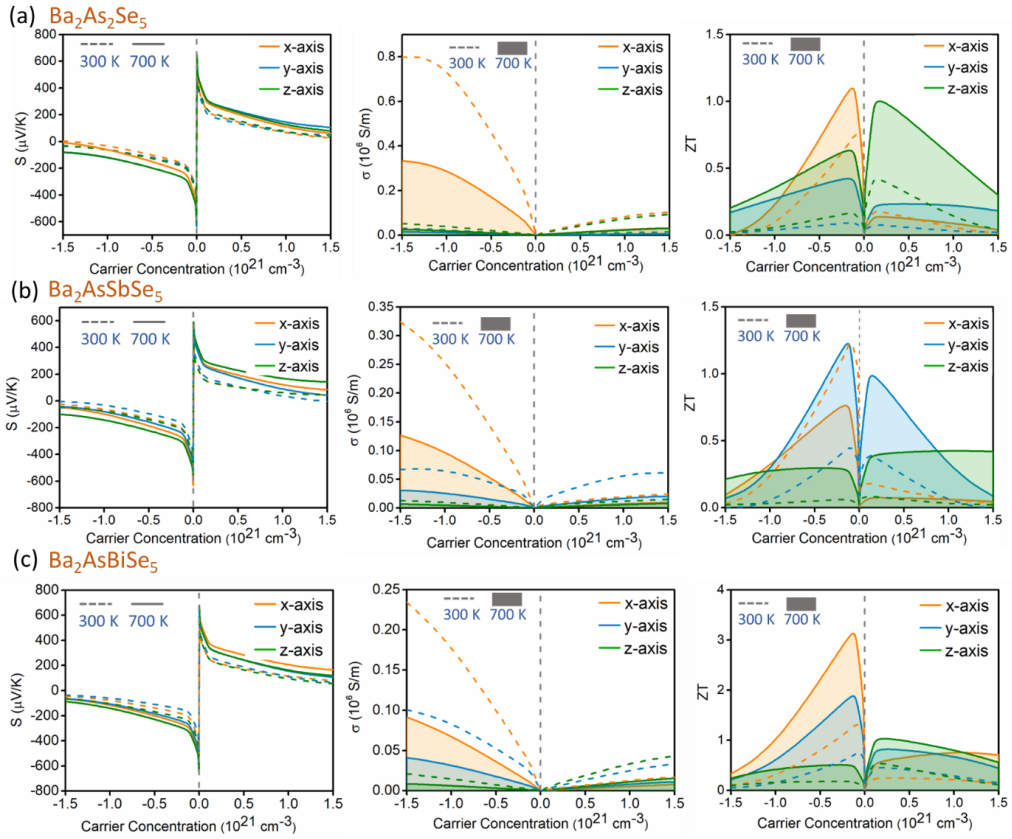


Figure 5.38: Thermoelectric properties of **(a)** $Ba_2As_2Se_5$, **(b)** $Ba_2AsSbSe_5$, and **(c)** $Ba_2AsBiSe_5$ containing Seebeck coefficient (S), electrical conductivity (σ), and thermoelectric figure of merit (ZT), computed using AMSET derived relation times. Negative and positive carrier concentrations correspond to n-type and p-type doping, respectively. Orange, blue, and olive green represent the x-axis, y-axis, and z-axis, respectively. Dotted and solid lines indicate temperatures of 300K and 700K.

These values are further enhanced in Se terminated materials (**Figure 5.38**), reaching 0.58 (1.06), 0.64 (1.15), and 1.08 (2.92) for $Ba_2As_2Se_5$, $Ba_2AsSbSe_5$, and $Ba_2AsBiSe_5$ at 300 K (700 K), respectively. The ultralow κ_L in $Ba_2AsBiSe_5$ system originates from the pronounced influence of SCALP, edge shearing polyhedra, Pn-Pn bonding, rattling atoms, and associated phonon-scattering mechanisms, collectively enabling superior thermoelectric performance. The remarkably high ZT values result from the synergistic effect of low κ_L and optimized electronic transport properties through band degeneracy, positioning these materials among the top-performing thermoelectrics, comparable to PbTe, *[100]* SnSe, *[101]* Cu_2Se, *[56]* Cu_3SbSe_3, *[57]* and KCu_5Se_3 *[58]*.

5.8. Summary

In summary, we systematically explored the intrinsic thermoelectric properties of Ba_2AsPnQ_5 (Pn = As/Sb/Bi; Q = S/Se) by combining machine learning interatomic potentials with *ab initio* calculations. Our results reveal that stereochemically active lone pairs, Pn-Pn bonding and edge-sharing polyhedra play a central role in shaping the bonding and anharmonicity of these noncentrosymmetric chalcogenides, which feature $[Pn_2Q_4]^{2-}$ and PnQ_3 units. Flattened atomic displacement parameters and long-range electronic interactions enable Ba atoms to exhibit rattling-like motion, further amplifying anharmonicity. Chemical bonding analysis through Crystal Orbital Hamilton Population shows that weak σ-interactions between Bi(6s)-Se($4p_y$) and As(4s)-Se($4p_x$) orbitals facilitate antibonding states, driving strong anharmonicity. These interactions lead to nonlinear repulsive interactions between stereochemically active lone pair electrons, Se bonds, and edge sharing polyhedra, disrupting lattice symmetry, hindering vibrational modes, and ultimately reducing κ_L. Furthermore, orbital interactions reveal that spatially extended *s*-orbitals influence the *pz–pz* bonding framework in As-Bi pairs: the highly polarizing Bi^{3+} ion distorts the $4p_z$ electron cloud of the adjacent As^{3+}, weakening As-Bi bonds and enhancing anharmonicity. We quantified these effects using a suite of

chemical bonding descriptors such as the lone pair angle (θ), lone pair pnictogen distance (d_{lp}), Debye temperature (θ_D), Grüneisen parameter (γ), ionicity (r'_σ), and hybridization (r_π^{-1}), with r_π^{-1} emerging as a key fingerprint capturing both linear and non-linear anharmonicity trends. Among the studied systems, $Ba_2AsBiSe_5$ exhibits ultralow κ_L (~ 0.14 $Wm^{-1}K^{-1}$) and the highest ZT (~2.91), outperforming all others. Overall, this study provides a bonding-centric design framework for tuning lattice dynamics through targeted manipulation of SCALPs, orbital hybridization, and polyhedral connectivity, offering a predictive pathway toward next-generation high-performance thermoelectric materials.

5.9. References

1. Walsh A., Watson G.W. (2005), The origin of the stereochemically active Pb(II) lone pair: DFT calculations on PbO and PbS, *J Solid State Chem*, 178, 1422–1428 (DOI: 10.1016/j.jssc.2005.01.030)

2. Medina-Gonzalez A.M., Yox P., Chen Y., et al. (2022), Solution-grown ternary semiconductors: Nanostructuring and stereoelectronic lone pair distortions in I–V–VI_2 materials, *Chemistry of Materials*, 34, 6847–6857 (DOI: 10.1021/acs.chemmater.2c01410)

3. Wuttig M., Yamada N. (2007), Phase-change materials for rewriteable data storage, *Nat Mater*, 6, 824–832 (DOI: 10.1038/nmat2009)

4. Azuma M., Hojo H., Oka K., Yamamoto H., Shimizu K., Shigematsu K., Sakai Y. (2021), Functional transition metal perovskite oxides with $6s^2$ lone pair activity stabilized by high-pressure synthesis, *Annu Rev Mater Res*, 51, 329–352 (DOI: 10.1146/annurev-matsci-080819-125533)

5. Skoug E.J., Morelli D.T. (2011), Role of lone-pair electrons in producing minimum thermal conductivity in nitrogen-group chalcogenide compounds, *Phys Rev Lett*, 107, 235901 (DOI: 10.1103/PhysRevLett.107.235901)

6. Yan M., Xue H.G., Guo S.P. (2021), Recent achievements in lone-pair cation-based infrared second-order nonlinear optical materials, *Cryst Growth Des*, 21, 1095–1113 (DOI: 10.1021/acs.cgd.0c01407)

7. Feng Z., Jia T., Zhang J., Wang Y., Zhang Y. (2017), Dual effects of lone-pair electrons and rattling atoms in $CuBiS_2$ on its ultralow thermal conductivity, *Phys Rev B*, 96, 235205 (DOI: 10.1103/PhysRevB.96.235205)

8. Guin S.N., Chatterjee A., Negi D.S., Datta R., Biswas K. (2013), High thermoelectric performance in tellurium-free p-type $AgSbSe_2$, *Energy Environ Sci*, 6, 2603–2612 (DOI: 10.1039/C3EE41935E)

9. Roychowdhury S., Ghosh T., Arora R., Samanta M., Xie L., Singh N.K., Soni A., He J., Waghmare U.V., Biswas K. (2021), Enhanced atomic ordering leads to high thermoelectric performance in $AgSbTe_2$, *Science*, 371, 722–727 (DOI: 10.1126/science.abb3517)

10. Xiao C., Qin X., Zhang J., An R., Xu J., Li K., Cao B., Yang J., Ye B., Xie Y. (2012), High thermoelectric and reversible p–n–p conduction type switching integrated in dimetal chalcogenide, *J Am Chem Soc*, 134, 18460–18466 (DOI: 10.1021/ja308936b)

11. Guin S.N., Biswas K. (2013), Cation disorder and bond anharmonicity optimize the thermoelectric properties in kinetically stabilized rocksalt $AgBiS_2$ nanocrystals, *Chemistry of Materials*, 25, 3225–3231 (DOI: 10.1021/cm401630d)

12. Nielsen M.D., Ozoliņš V., Heremans J.P. (2013), Lone pair electrons minimize lattice thermal conductivity, *Energy Environ Sci*, 6, 570–578 (DOI: 10.1039/C2EE23391F)

13. Walsh A., Payne D.J., Egdell R.G., Watson G.W. (2011), Stereochemistry of post-transition metal oxides: Revision of the classical lone pair model, *Chem Soc Rev*, 40, 4455–4463 (DOI: 10.1039/C1CS15098G)

14. Tan G., Hao S., Zhao J., Chi H., Zhang X., Uher C., Wolverton C., Dravid V.P., Kanatzidis M.G. (2017), High thermoelectric performance in electron-doped $AgBi_3S_5$ with ultralow thermal conductivity, *J Am Chem Soc*, 139, 6467–6473 (DOI: 10.1021/jacs.7b02399)

15. Jana M.K., Pal K., Warankar A., Biswas K. (2017), Intrinsic rattler-induced low thermal conductivity in Zintl-type $TlInTe_2$, *J Am Chem Soc*, 139, 4350–4353 (DOI: 10.1021/jacs.7b01434)

16. Minhas H., Das S., Sharma R.K., Pathak B. (2024), Rattling-induced bonding hierarchy in Li–Cu–Ti chalcotitanates for enhanced thermoelectric efficiency: A machine learning potential approach, *J Mater Chem A*, 12, 1642–1655 (DOI: 10.1039/D3TA07461G)

17. Dutta M., Pal K., Waghmare U.V., Biswas K. (2019), Bonding heterogeneity and lone pair induced anharmonicity resulting in ultralow thermal conductivity and promising thermoelectric properties in n-type $AgPbBiSe_3$, *Chem Sci*, 10, 490–501 (DOI: 10.1039/C9SC00485H)

18. Pal K., Xia Y., He J., Wolverton C. (2019), Intrinsically low lattice thermal conductivity derived from rattler cations in an $AMM'Q_3$ family of chalcogenides, *Chemistry of Materials*, 31, 1847–1858 (DOI: 10.1021/acs.chemmater.9b02484)

19. Bera T.K., Jang J.I., Song J.H., Malliakas C.D., Freeman A.J., Ketterson J.B., Kanatzidis M.G. (2010), Soluble semiconductors $AAsSe_2$ (A = Li, Na) with a direct band gap and strong second harmonic generation, *J Am Chem Soc*, 132, 3484–3495 (DOI: 10.1021/ja9094846)

20. He J., Iyer A.K., Waters M.J., Sarkar S., Zu R., Rondinelli J.M., Kanatzidis M.G., Gopalan V. (2022), Giant non-resonant infrared second-order nonlinearity in γ-$NaAsSe_2$, *Adv Opt Mater*, 10, 2101729 (DOI: 10.1002/adom.202101729)

21. Fu L., Kornbluth M., Cheng Z., Marianetti C.A. (2019), Group theoretical approach to computing phonons and their interactions, *Phys Rev B*, 100, 014303 (DOI: 10.1103/PhysRevB.100.014303)

22. Bandi S., Marianetti C.A. (2023), Precisely computing phonons via irreducible derivatives, *Phys Rev B*, 107, 174302 (DOI: 10.1103/PhysRevB.107.174302)

23. Xiao E., Marianetti C.A. (2023), Anharmonic phonon behavior via irreducible derivatives, *Phys Rev B*, 107, 094303 (DOI: 10.1103/PhysRevB.107.094303)

24. Novikov I.S., Gubaev K., Podryabinkin E.V., Shapeev A.V. (2021), The MLIP package: Moment tensor potentials with MPI and active learning, *Mach Learn Sci Technol*, 2, 025002 (DOI: 10.1088/2632-2153/abc9fe)

25. Mortazavi B., Podryabinkin E.V., Novikov I.S., Shapeev A.V., Rabczuk T. (2020), Efficient machine-learning based interatomic potentials for exploring thermal conductivity in two-dimensional materials, *JPhys Materials*, 3, 02LT02 (DOI: 10.1088/2515-7639/ab7cbb)

26. Mortazavi B., Podryabinkin E.V., Novikov I.S., Shapeev A.V., Rabczuk T. (2021), Accelerating first-principles estimation of thermal conductivity by machine-learning interatomic potentials: A MTP/ShengBTE solution, *Comput Phys Commun*, 258, 107583 (DOI: 10.1016/j.cpc.2020.107583)

27. Blöchl P.E. (1994), Projector augmented-wave method, *Phys Rev B*, 50, 17953–17979 (DOI: 10.1103/PhysRevB.50.17953)

28. Kresse G., Furthmüller J. (1996), Efficient iterative schemes for ab initio total-energy calculations using a plane-wave basis set, *Phys Rev B*, 54, 11169–11186 (DOI: 10.1103/PhysRevB.54.11169)

29. Perdew J.P., Burke K., Ernzerhof M. (1996), Generalized gradient approximation made simple, *Phys Rev Lett*, 77, 3865–3868 (DOI: 10.1103/PhysRevLett.77.3865)

30. Perdew J.P., Chevary J.A., Vosko S.H., Jackson K.A., Pederson M.R., Singh D.J., Fiolhais C. (1992), Atoms, molecules, solids, and surfaces: Applications of the generalized gradient approximation for exchange and correlation, *Phys Rev B*, 46, 6671–6687 (DOI: 10.1103/PhysRevB.46.6671)

31. Grimme S., Antony J., Ehrlich S., Krieg H. (2010), A consistent and accurate ab initio parametrization of density functional dispersion correction (DFT-D) for the 94 elements H–Pu, *J Chem Phys*, 132, 154104 (DOI: 10.1063/1.3382344)

32. Perdew J.P., Ernzerhof M., Burke K. (1996), Rationale for mixing exact exchange with density functional approximations, *J Chem Phys*, 105, 9982–9985 (DOI: 10.1063/1.472933)

33. Heyd J., Scuseria G.E., Ernzerhof M. (2003), Hybrid functionals based on a screened Coulomb potential, *J Chem Phys*, 118, 8207–8215 (DOI: 10.1063/1.1564060)

34. Wien T.U., Hauptstrasse W. (1994), Ab initio molecular-dynamics simulation of the liquid-metal–amorphous-semiconductor transition in germanium, *Phys Rev B*, 49, 14251–14269

35. Nosé S. (1984), A molecular dynamics method for simulations in the canonical ensemble, *Mol Phys*, 52, 255–268 (DOI: 10.1080/00268978400101201)

36. Mortazavi B., Podryabinkin E.V., Roche S., Novikov I.S., Shapeev A.V., Rabczuk T. (2020), Machine-learning interatomic potentials enable first-principles multiscale modeling of lattice thermal conductivity in graphene/borophene heterostructures, *Mater Horiz*, 7, 2359–2367 (DOI: 10.1039/D0MH00787K)

37. Li W., Carrete J., Katcho N.A., Mingo N. (2014), ShengBTE: A solver of the Boltzmann transport equation for phonons, *Comput Phys Commun*, 185, 1747–1758 (DOI: 10.1016/j.cpc.2014.02.015)

38. Ganose A.M., Park J., Faghaninia A., Woods-Robinson R., Persson K.A., Jain A. (2021), Efficient calculation of carrier scattering rates from first principles, *Nat Commun*, 12, 2222 (DOI: 10.1038/s41467-021-22440-5)

39. Ying P., Li X., Wang Y., Liu W., Chen L., Tang X. (2017), Hierarchical chemical bonds contributing to the intrinsically low thermal conductivity in α-MgAgSb thermoelectric materials, *Adv Funct Mater*, 27, 1604145 (DOI: 10.1002/adfm.201604145)

40. Pal K., He J., Wolverton C. (2018), Bonding hierarchy gives rise to high thermoelectric performance in layered Zintl compound $BaAu_2P_4$, *Chemistry of Materials*, 30, 7760–7768 (DOI: 10.1021/acs.chemmater.8b03130)

41. Minhas H., Das S., Sharma R.K., Pathak B. (2024), Rattling-induced bonding hierarchy in Li–Cu–Ti chalcotitanates for enhanced thermoelectric efficiency: A machine learning potential approach, *J Mater Chem A*, 12, 1642–1655 (DOI: 10.1039/D3TA07461G)

42. Silvi B., Savin A. (1994), Classification of chemical bonds based on topological analysis of electron localization functions, *Nature*, 371, 683–686 (DOI: 10.1038/371683a0)

43. Morelli D.T., Jovovic V., Heremans J.P. (2008), Intrinsically minimal thermal conductivity in cubic I–V–VI_2 semiconductors, *Phys Rev Lett*, 101, 035901 (DOI: 10.1103/PhysRevLett.101.035901)

44. Saha K., Légaré K., Garate I. (2015), Detecting band inversions by measuring the environment: Fingerprints of electronic band topology in bulk phonon linewidths, *Phys Rev Lett*, 115, 176405 (DOI: 10.1103/PhysRevLett.115.176405)

45. Tadano T., Gohda Y., Tsuneyuki S. (2015), Impact of rattlers on thermal conductivity of a thermoelectric clathrate: A first-principles study, *Phys Rev Lett*, 114, 095501 (DOI: 10.1103/PhysRevLett.114.095501)

46. Xie L., Feng J.H., Li R., He J.Q. (2020), First-principles study of anharmonic lattice dynamics in low thermal conductivity $AgCrSe_2$: Evidence for a large resonant four-phonon scattering, *Phys Rev Lett*, 125, 245901 (DOI: 10.1103/PhysRevLett.125.245901)

47. Zheng J., Shi D., Liu S., Tadano T., Tsuneyuki S. (2022), Effects of high-order anharmonicity on anomalous lattice dynamics and thermal transport in fully filled skutterudite $YbFe_4Sb_{12}$, *Phys Rev Mater*, 6, 093801 (DOI: 10.1103/PhysRevMaterials.6.093801)

48. Minhas H., Das S., Pathak B. (2022), Ultralow thermal conductivity and high thermoelectric performance of γ-GeSe: Effects of dimensionality and thickness, *ACS Appl Energy Mater*, 5, 9914–9928 (DOI: 10.1021/acsaem.2c01600)

49. Zhao L.D., He J., Berardan D., Lin Y., Li J.F., Nan C.W., Dragoe N. (2014), BiCuSeO oxyselenides: New promising thermoelectric materials, *Energy Environ Sci*, 7, 2900–2924 (DOI: 10.1039/C4EE01380H)

50. Liu Z., Zhang W., Gao W., Mori T. (2021), A material catalogue with glass-like thermal conductivity mediated by crystallographic occupancy for thermoelectric application, *Energy Environ Sci*, 14, 1146–1158 (DOI: 10.1039/D1EE00738F)

51. Zhao L.D., Chang C., Tan G., Kanatzidis M.G. (2016), SnSe: A remarkable new thermoelectric material, *Energy Environ Sci*, 9, 3044–3060 (DOI: 10.1039/C6EE01755J)

52. Nelson R., Ertural C., George J., Deringer V.L., Dronskowski R. (2020), LOBSTER: Local orbital projections, atomic charges, and chemical-bonding analysis from projector-augmented-wave-based density-functional theory, *J Comput Chem*, 41, 1931–1940 (DOI: 10.1002/jcc.26353)

53. Shen X., Pal K., Acharyya P., Xia Y., Wolverton C., Biswas K. (2024), Lone pair induced one-dimensional character and weak cation–anion interactions: Two ingredients for low thermal conductivity in mixed-anion metal chalcohalide $CuBiSCl_2$, *J Am Chem Soc*, 146, 10245–10256 (DOI: 10.1021/jacs.4c10520)

54. Tan G., Zhao L.D., Kanatzidis M.G. (2016), Rationally designing high-performance bulk thermoelectric materials, *Chem Rev*, 116, 12123–12149 (DOI: 10.1021/acs.chemrev.6b00255)

55. Lalonde A.D., Pei Y., Wang H., Snyder G.J. (2011), Lead telluride alloy thermoelectrics, *Mater Today*, 14, 526–532 (DOI: 10.1016/S1369-7021(11)70278-4)

56. Liu H., Shi X., Xu F., Zhang L., Zhang W., Chen L., Li Q., Uher C., Day T., Snyder G.J. (2012), Copper ion liquid-like thermoelectrics, *Nat Mater*, 11, 422–425 (DOI: 10.1038/nmat3273)

57. Tyagi K., Gahtori B., Bathula S., Bhattacharyya S., Singh N., Awana V.P.S. (2014), Thermoelectric properties of Cu_3SbSe_3 with intrinsically

ultralow lattice thermal conductivity, *J Mater Chem A*, 2, 15829–15835 (DOI: 10.1039/C4TA02590C)

58. Li F., Liu X., Ma N., Wang J., Shi D., Fu C., Li Y., Nan C.-W. (2023), Overdamped phonon diffusion and nontrivial electronic structure leading to a high thermoelectric figure of merit in KCu_5Se_3, *J Am Chem Soc*, 145, 11543–11553 (DOI: 10.1021/jacs.3c04871)

59. Gibson Q.D., Zhao T., Daniels L.M., Wu K.J., Ma J., Lee S., Goodenough J.B., Uher C., Kanatzidis M.G., Toberer E.S. (2021), Low thermal conductivity in a modular inorganic material with bonding anisotropy and mismatch, *Science*, 373, 1017–1022 (DOI: 10.1126/science.abh1619)

60. Bhui A., Dutta M., Mukherjee M., Dixit A., Sood A.K., Biswas K. (2021), Ultralow thermal conductivity in earth-abundant $Cu_{1.6}Bi_{4.8}S_8$: Anharmonic rattling of interstitial Cu, *Chemistry of Materials*, 33, 3965–3974 (DOI: 10.1021/acs.chemmater.1c00659)

61. Xia Y., Ozoliņš V., Wolverton C. (2020), Microscopic mechanisms of glasslike lattice thermal transport in cubic $Cu_{12}Sb_4S_{13}$ tetrahedrites, *Phys Rev Lett*, 125, 085901 (DOI: 10.1103/PhysRevLett.125.085901)

62. Fabini D.H., Laurita G., Bechtel J.S., Stoumpos C.C., Evans H.A., Kontos A.G., Raptis Y.S., Kanatzidis M.G., Seshadri R. (2016), Dynamic stereochemical activity of the Sn^{2+} lone pair in perovskite $CsSnBr_3$, *J Am Chem Soc*, 138, 11820–11832 (DOI: 10.1021/jacs.6b06287)

63. Pathak R., Paul S., Das S., Roychowdhury S., Biswas K. (2024), Deciphering Pauling's third rule: Uncovering strong anharmonicity and exceptionally low thermal conductivity in TlAgSe for thermoelectrics, *Angew Chem Int Ed*, 63, e202408908 (DOI: 10.1002/anie.202408908)

64. Burdett J.K., McLarnan T.J. (1982), An orbital explanation for Pauling's third rule, *J Am Chem Soc*, 104, 672–678 (DOI: 10.1021/ja00383a041)

65. Pathak R., Sharma M.K., Biswas K. (2025), Pauling's third rule as a guide for designing low thermal conducting chalcogenides, *Chemistry of Materials*, 37, – (DOI: 10.1021/acs.chemmater.5c01050)

66. Lencer D., Salinga M., Grabowski B., Hickel T., Neugebauer J., Wuttig M. (2008), A map for phase-change materials, *Nat Mater*, 7, 972–977 (DOI: 10.1038/nmat2330)

67. Minhas H., Jena M.K., Sharma R.K., Pathak B. (2024), Insights into thermal conductivity of pnictogen chalcogenides: Machine-learning stereochemically active lone pairs and hybridization, *Chemistry of Materials*, 36, – (DOI: 10.1021/acs.chemmater.4c02294)

68. Jena M.K., Mittal S., Pathak B. (2024), Precision basecalling of single DNA nucleotide from overlapped transmission readouts with machine-learning-aided solid-state nanogap, *ACS Appl Mater Interfaces*, 16, 29891–29901 (DOI: 10.1021/acsami.4c04858)

69. Sharma R.K., Minhas H., Pathak B. (2025), Machine learning–guided discovery of alloy nanoclusters: Steering morphology-based activity and selectivity relationships in bifunctional electrocatalysts, *ACS Appl Mater Interfaces*, 17, – (DOI: 10.1021/acsami.5c07198)

70. Sharma R.K., Jena M.K., Minhas H., Pathak B. (2024), Machine-learning-assisted screening of nanocluster electrocatalysts: Mapping and reshaping the activity volcano for the oxygen reduction reaction, *ACS Appl Mater Interfaces*, 16, 63589–63601 (DOI: 10.1021/acsami.4c14076)

71. Iyer A.K., Cho J.-B., Waters M.J., Li S., Bozin E.S., He J., Yan J., Kanatzidis M.G. (2022), Ba_2MAsQ_5 (Q = S, Se) family of polar structures with large second-harmonic generation and phase matchability, *Chemistry of Materials*, 34, 5223–5233 (DOI: 10.1021/acs.chemmater.2c00962)

72. Perdew J.P., Chevary J.A., Vosko S.H., Jackson K.A., Pederson M.R., Singh D.J., Fiolhais C. (1992), Applications of the generalized gradient approximation for exchange and correlation, *Phys Rev B*, 46, 6671–6687

73. Minhas H., Das S., Pathak B. (2023), Importance of four-phonon interactions in lattice thermal conductivity and thermoelectrics: A case

study, *ACS Appl Energy Mater*, 6, 11475–11485 (DOI: 10.1021/acsaem.3c01147)

74. Maria I., Arora R., Dutta M., Tyagi K., Biswas K. (2023), Metavalent bonding-mediated dual $6s^2$ lone-pair expression leads to intrinsic lattice shearing in n-type $TlBiSe_2$, *J Am Chem Soc*, 145, 13502–13512 (DOI: 10.1021/jacs.3c02146)

75. Minhas H., Sharma R.K., Pathak B. (2025), Exploring combined stereochemically active lone-pair and rattling effects in thermoelectrics with machine learning potentials, *J Phys Chem Lett*, 16, 5051–5061 (DOI: 10.1021/acs.jpclett.5c00952)

76. Ogawa K., Abe R., Walsh A. (2024), Band gap narrowing by suppressed lone-pair activity of Bi^{3+}, *J Am Chem Soc*, 146, 9480–9488 (DOI: 10.1021/jacs.4c00150)

77. Laurita G., Seshadri R. (2022), Chemistry, structure, and function of lone pairs in extended solids, *Acc Chem Res*, 55, 271–281 (DOI: 10.1021/acs.accounts.1c00741)

78. Dutta M., Pal K., Waghmare U.V., Biswas K. (2019), Bonding heterogeneity and lone-pair-induced anharmonicity resulting in ultralow thermal conductivity and promising thermoelectric properties in n-type $AgPbBiSe_3$, *Chem Sci*, 10, 490–501 (DOI: 10.1039/C9SC00485H)

79. Becke A.D., Edgecombe K.E. (1990), A simple measure of electron localization in atomic and molecular systems, *J Chem Phys*, 92, 5397–5403 (DOI: 10.1063/1.458517)

80. Minhas H., Majumdar A., Pathak B. (2023), Advancing thermal management with machine-learning potentials on boron nitride and other group-13 nitrides, *ACS Appl Energy Mater*, 6, 11612–11622 (DOI: 10.1021/acsaem.3c01161)

81. Zuo Y., Chen C., Li X., Ong S.P., Wood B.M., Faghaninia A., Ley C., Heinz H., Reuter K., Ceder G., Persson K.A., Jain A. (2020), Performance and cost assessment of machine learning interatomic potentials, *J Phys Chem A*, 124, 731–745 (DOI: 10.1021/acs.jpca.9b08723)

82. Zhang L., Han J., Wang H., Car R., E W. (2018), Deep potential molecular dynamics: A scalable model with the accuracy of quantum mechanics, *Phys Rev Lett*, 120, 143001 (DOI: 10.1103/PhysRevLett.120.143001)

83. Batzner S., Musaelian A., Sun L., Geiger M., Mailoa J.P., Kornbluth M., Molinari N., Smidt T.E., Kozinsky B. (2022), E(3)-equivariant graph neural networks for data-efficient and accurate interatomic potentials, *Nat Commun*, 13, 2453 (DOI: 10.1038/s41467-022-29939-5)

84. Hajibabaei A., Myung C.W., Kim K.S. (2021), Sparse Gaussian process potentials: Application to lithium diffusivity in superionic conducting solid electrolytes, *Phys Rev B*, 103, 214102 (DOI: 10.1103/PhysRevB.103.214102)

85. Willow S.Y., Hajibabaei A., Ha M., Wood B.M., Perederiy J.V., Stetina T.F., Remsing R.C., Kim S.W., Park C.W., Asahi R., Ceriotti M., Kang K., Arias T.A., Srolovitz D.J. (2024), Sparse Gaussian process–based machine-learning first-principles potentials for materials simulations, *Chem Phys Rev*, 5, 011301 (DOI: 10.1063/5.0231265)

86. Thompson A.P., Swiler L.P., Trott C.R., Foiles S.M., Tucker G.J. (2015), Spectral neighbor analysis method for automated generation of quantum-accurate interatomic potentials, *J Comput Phys*, 285, 316–330 (DOI: 10.1016/j.jcp.2014.12.018)

87. Shapeev A.V. (2016), Moment tensor potentials: A class of systematically improvable interatomic potentials, *Multiscale Model Simul*, 14, 1153–1173 (DOI: 10.1137/15M1054183)

88. Drautz R. (2019), Atomic cluster expansion for accurate and transferable interatomic potentials, *Phys Rev B*, 99, 014104 (DOI: 10.1103/PhysRevB.99.014104)

89. Hajibabaei A., Kim K.S. (2021), Universal machine learning interatomic potentials: Surveying solid electrolytes, *J Phys Chem Lett*, 12, 7415–7423 (DOI: 10.1021/acs.jpclett.1c01605)

90. Li B., Wang H., Kawakita Y., Zhang J., Shi L., Chen L., Li D., Singh D.J., Zhang X., Snyder G.J., Wolverton C., Kanatzidis M.G. (2018), Liquid-like thermal conduction in intercalated layered crystalline solids, *Nat Mater*, 17, 226–230 (DOI: 10.1038/s41563-017-0004-2)

91. Kim J.H., Chung D.Y., Bilc D.J., Mahanti S.D., Kanatzidis M.G. (2005), Crystal growth, thermoelectric properties, and electronic structure of $AgBi_3S_5$ and $AgSb_xBi_{3-x}S_5$, *Chemistry of Materials*, 17, 3606–3614 (DOI: 10.1021/cm0502931)

92. Jiang Y., Jia F., Chen L., Wu L.-M. (2019), $Cu_4Bi_4Se_9$: A thermoelectric symphony of rattling, anharmonic lone pair, and structural complexity, *ACS Appl Mater Interfaces*, 11, 35426–35434 (DOI: 10.1021/acsami.9b11115)

93. Al Rahal Al Orabi R., Mecholsky N.A., Hwang J., Stevanovic V., Toberer E.S., Stokes D.L. (2016), Band degeneracy, low thermal conductivity, and high thermoelectric figure of merit in SnTe–CaTe alloys, *Chemistry of Materials*, 28, 376–384 (DOI: 10.1021/acs.chemmater.5b04365)

94. Fajans K. (1924), Die Eigenschaften salzartiger Verbindungen und Atombau, *Z Kristallogr*, 61, 18–46 (DOI: 10.1524/zkri.1924.61.1.18)

95. Das A., Debnath K., Maria I., Bhattacharya A., Pal K., Acharyya P., Biswas K. (2024), Influence of subvalent twin-rattler for high n-type thermoelectric performance in $Bi_{13}S_{18}Br_2$ chalcohalide, *J Am Chem Soc*, 146, 30518–30528 (DOI: 10.1021/jacs.4c11738)

96. Das A., Pal K., Acharyya P., Bhui A., Summers C.J., Dutta M., Biswas K. (2023), Strong antibonding I(p)–Cu(d) states lead to intrinsically low thermal conductivity in $CuBiI_4$, *J Am Chem Soc*, 145, 1349–1358 (DOI: 10.1021/jacs.2c11908)

97. Chelikowsky J.R., Phillips J.C. (1978), Quantum-defect theory of heats of formation and structural transition energies of liquid and solid simple metal alloys and compounds, *Phys Rev B*, 17, 2453–2465 (DOI: 10.1103/PhysRevB.17.2453)

98. Zhou H., Deng Z., Xia Y., Fu M. (2016), A new sampling method in particle filter based on Pearson correlation coefficient, *Neurocomputing*, 216, 208–215 (DOI: 10.1016/j.neucom.2016.07.036)

99. Adler J., Parmryd I. (2010), Quantifying colocalization by correlation: The Pearson correlation coefficient is superior to the Mander's overlap coefficient, *Cytometry A*, 77, 733–742 (DOI: 10.1002/cyto.a.20896)

100. Heremans J.P., Jovovic V., Toberer E.S., Saramat A., Kurosaki K., Charoenphakdee A., Yamanaka S., Snyder G.J. (2008), Enhancement of thermoelectric efficiency in PbTe by distortion of the electronic density of states, *Science*, 321, 554–557 (DOI: 10.1126/science.1159725)

101. Zhao L.-D., Tan G., Hao S., He J., Pei Y., Chi H., Wang H., Gong S., Xu H., Dravid V.P., Uher C., Snyder G.J., Wolverton C., Kanatzidis M.G. (2016), Ultrahigh power factor and thermoelectric performance in hole-doped single-crystal SnSe, *Science*, 351, 141–144 (DOI: 10.1126/science.aad3749)

CHAPTER 6

Scaling and Quantifying Anharmonicity using GNN Potentials

CHAPTER 6

Chapter 6

6.1. Introduction

Chemical bonding intricacies fundamentally govern phonon behavior and thermal transport, making them critical in the rational design of materials with intrinsically low lattice thermal conductivity (κ_L), especially for thermoelectric applications *[1–3]*. In pnictogen chalcogenides (pn-chg), a unique bonding arises from the presence of stereochemically active lone pairs (SCALPs), where $AgSbTe_2$ (0.6 W/mK) with an active Sb^{3+} lone pair exhibits significantly reduced κ_L compared to $AgInTe_2$ (1.8 W/mK), which lacks lone-pair activity *[4, 5]*. Similarly, Cu_3SbSe_3, which contains Sb^{3+} with an active lone pair, exhibits an ultralow κ_L of approximately 0.49 W/mK, whereas Cu_3SbSe_4, containing Sb^{5+} without an active lone pair, shows a significantly higher κ_L of about 2.90 W/mK *[6]*. Notably, $K_2Bi_8Se_{13}$, *[6]* $LiAsSe_2$, *[7]* Bi_2Se_3, *[6]* and Sb_2Te_3, *[6]* all of which feature pnictogens in the +3-oxidation state demonstrate comparatively high lattice thermal conductivities of 3.1 W/mK, 2.06 W/mK, 2.40 W/mK, and 3.5 W/mK, respectively. This highlights that not all pn-chg compounds exhibit low κ_L, underscoring the importance of additional factors influencing bonding asymmetry and phonon transport. These insights are crucial for developing chemically intuitive strategies to design next-generation low-κ_L.

Capturing anharmonicity in non-centrosymmetric materials requires accurate vibrational Hamiltonians to describe phonon-phonon interactions, making first-principles methods computationally prohibitive, especially for complex or low-symmetry systems *[8–10]*. To address this challenge, machine learning interatomic potentials (MLIPs) have emerged as transformative tools, offering near first-principles accuracy at a fraction of the computational cost *[11]*. Among these, graph neural network (GNN)-based MLIPs have shown remarkable progress due to their ability to represent atomic structures as graphs, effectively encoding local atomic environments and complex bonding topologies. This framework provides strong chemical and structural generalizability, enabling the development

of "universal" or "foundational" MLIPs such as Materials 3-body Graph Network (M3GNet), *[12]* atomistic line graph neural network-based force field (ALIGNN-FF), *[11]* MACE, *[13]* Crystal Hamiltonian Graph Neural Network (CHGNet), *[14]* and MatterSim, *[15]* which are trained on chemically and structurally diverse datasets spanning the periodic table. While many models enable large-scale exploration of energy landscapes, thermodynamic stability, and harmonic vibrational properties, their often struggle with accuracy in certain domains and typically require fine-tuning through transfer learning *[11, 12, 16]*.

The CHGNet framework stands out for its ability to accurately capture both valence variations and long-range electrostatic interactions, making it particularly suitable for polar or non-centrosymmetric crystals *[14, 16]*. The MACE (Message Passing with Atomic Cluster Expansion) architecture further enhances representational power by incorporating higher-order many-body message passing, enabling a more complete description of local atomic environments and long-range correlations *[13]*. The recently introduced MatterSim integrates both M3GNet and Graphormer backbones to combine physically informed representations with global attention mechanisms, achieving state-of-the-art accuracy and transferability across diverse chemistries *[15]*. In this chapter, we used CHGNet, MACE, and MatterSim, which substantially enhances its capability to model phonon-phonon interactions and κ_L in complex systems, offering a scalable and efficient alternative to the conventional first-principles method.

Leveraging this, we employ a data-driven framework to screen and predict ultralow κ_L materials within the class of pnictogen chalcogenides from the Materials Project database *[17]*. The initial step of our approach involves an unsupervised machine learning analysis to explore the structural and compositional diversity within the dataset. Leveraging a fine-tuned MatterSim model, we accelerate the extraction of interatomic force constants by incorporating alchemically transferable knowledge, thereby significantly reducing data requirements while maintaining high accuracy.

Subsequently, we employed the Wigner formulation theory of heat transport to predict κ_L in solids and glasses with high accuracy, *[18–20]* as it effectively captures both anharmonic phonon interactions and disorder-induced scattering, addressing key limitations of conventional methods in thermoelectric materials design. Further, we extend our approach to demonstrate the capabilities of chemical bonding descriptors derived to capture the bonding environment of SCALP and beyond SCALPs. We demonstrate that integrating universal machine-learned interatomic potentials (MLIPs) with high-throughput screening and bonding descriptors are capable of rapid and scalable evaluation of lattice thermal conductivity across a wide range of materials with diverse crystal symmetries and chemical compositions.

6.2. Computational Details

6.2.1. Density Functional Theory (DFT) Calculations. The first-principles spin polarized calculations were performed using the projector augmented wave (PAW) pseudopotentials as implemented in the Vienna *ab initio* simulation package (VASP) *[21, 22]*. The generalized gradient approximation (GGA) within the Perdew-Burke-Ernzerhof (PBE) functional was used to describe the exchange-correlation potential, with a plane wave cutoff energy set to 520 eV *[23, 24]*. Structural relaxations were carried out considering the Hellmann-Feynman force convergence criterion of 0.01 eV/Å, and the energy convergence criterion of 10^{-6} eV. All calculations were performed using a $3 \times 3 \times 3$ k-point grid. Further, the chemical bonding characteristics were evaluated through Crystal Orbital Hamiltonian Population (COHP) and Crystal Orbital Overlap Population (COOP) analyses, as implemented in the LOBSTER package *[25]*.

6.2.2. Fine-Tuning of MatterSim. To fine-tune MatterSim, the models were trained using energy, forces, and stress as labels. We generated a $2 \times 2 \times 2$ supercell containing approximately 100-200 atoms based on relaxed structures. AIMD simulations were performed on 31 pnictogen-

chalcogenide systems with diverse bonding chemistries at three temperatures (300 K, 500 K, and 700 K) using the NPT ensemble in the VASP code. Each simulation consisted of 2,000 steps with a 1 fs timestep, yielding 6,000 configurations per material (a total of 186,000 configurations). To reduce redundancy while maintaining configurational diversity, every 20th snapshot was selected, producing a filtered dataset of 9300 unique structures. This dataset was split into training, validation, and test subsets in an 80:10:10 ratio. This strategy is a standard and widely adopted to train and fine tune the MLIP to improve sampling diversity while maintaining computational feasibility *[16, 26]*. Fine-tuning was conducted using a batch size of 32, a learning rate of 2×10^{-4}, with stepwise decay every 20 epochs, for a total of 200 epochs, and early stopping with a patience of 30 epochs. The checkpoint exhibiting the lowest validation loss was subsequently used for structural relaxations, phonon dispersion calculations, and the extraction of interatomic force constants. Instead of training separate models for each compound, we developed a single transferable MatterSim potential encompassing a wide range of pn-chg structures, ensuring robust generalization across chemically and structurally diverse systems.

6.2.3. Lattice Thermal Conductivity Calculations. For all dynamically stable structures, κ_L was computed using the Phono3py, which solves the Wigner formulation of heat transport for calculating the particle-like and wave-like lattice thermal *[20, 27, 28]*. Calculations were performed at room temperature using a uniform 10 × 10 × 10 reciprocal-space mesh to ensure convergence.

6.3. Results and Discussion

6.3.1. High throughput screening of Pnictogen-Chalcogenide

First, we performed a high-throughput screening of 154,718 inorganic materials from the Materials Project (MP) database *[17]* to identify promising thermoelectric candidates containing pnictogen (pn = As, Sb, and

Bi) and chalcogens (chg = S, Se, and Te).[26, 60, 61] From this database, a subset of 2100 materials exhibiting pnictogen-chalcogenide (pn-chg) bonding motifs was screened, and an unsupervised machine learning approach was employed to explore their structural and compositional for further screening.

Using the matminer library, we extracted 150 compositional and structural descriptors, *[32]* eliminated highly correlated features, and reduced dimensionality via principal component analysis (PCA), *[33]* retaining the top 30 components. These were further projected into a two-dimensional latent space using t-distributed stochastic neighbor embedding (t-SNE), *[34]* which preserves local chemical similarities. To elucidate latent groupings, K-means clustering was applied (**Figure 6.1(a)**), *[35]* with the optimal number of clusters (K = 8) identified through the elbow method and silhouette analysis (**Figure 6.2**). The resulting clusters, arranged in a clockwise orientation in the t-SNE embedding space, reveal chemically interpretable groupings that reflect recurring bonding motifs and elemental compositions (**Table 6.1**).

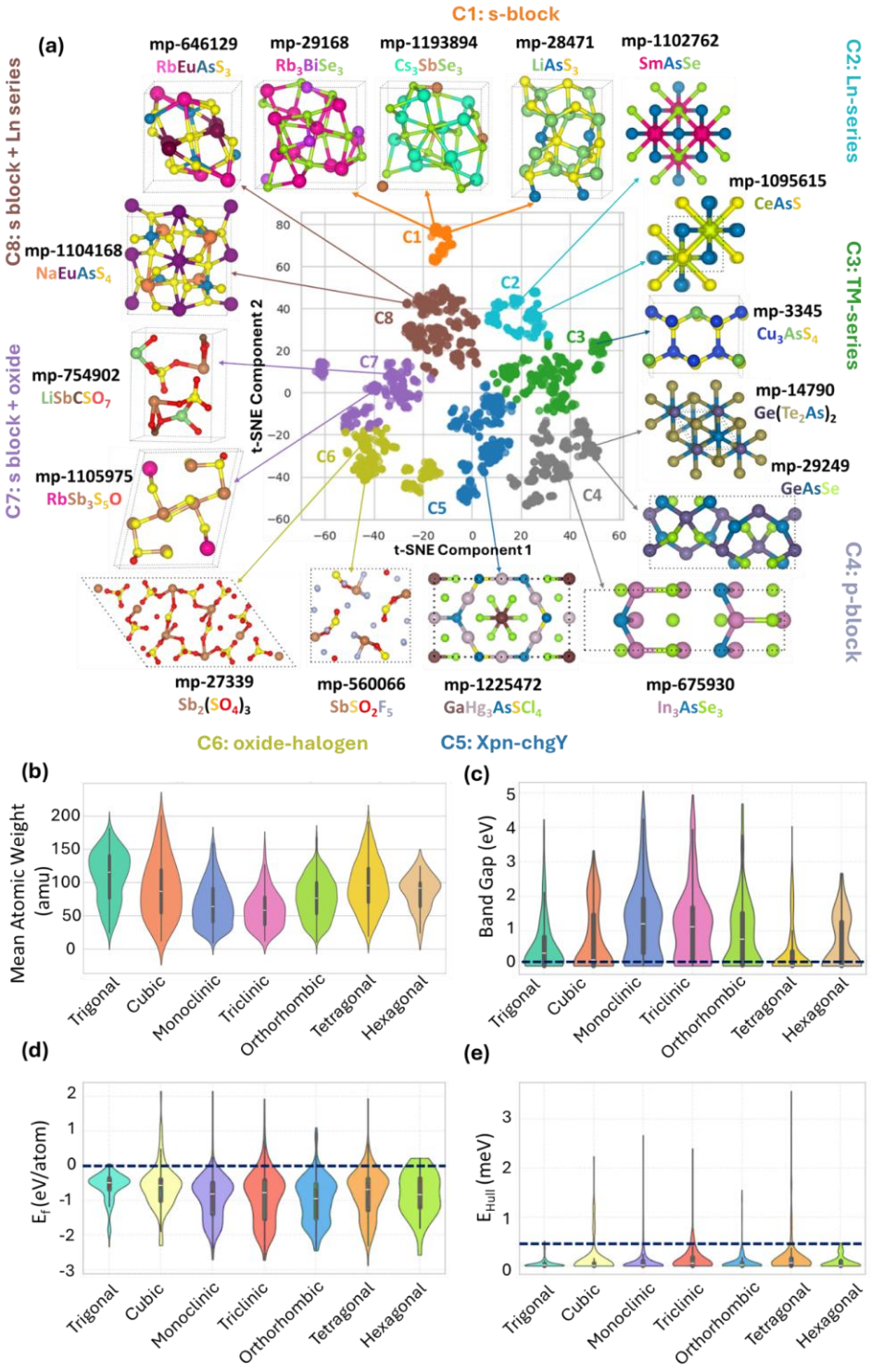


Figure 6.1: (a) Two-dimensional t-SNE projection of the pnictogen-chalcogenide (pn-chg) chemical space based on structural and compositional descriptors (perplexity = 30, learning rate = 50, iterations =

300). Each point represents a pn-chg material, color-coded according to eight distinct clusters (C1-C8) identified through K-means clustering. Representative crystal structures are illustrated for each cluster are described in **Table 6.1**. Violin maps showing the distribution of key property values for pn-chg from seven prototypes identified in Materials Project database. For each prototype showing distribution for **(b)** atomic weight, **(c)** electronic band gap, **(d)** formation energy (E_f), and **(e)** energy above convex hull (E_{Hull}), the blue-dashed line denotes the selection criterion, used in current study.

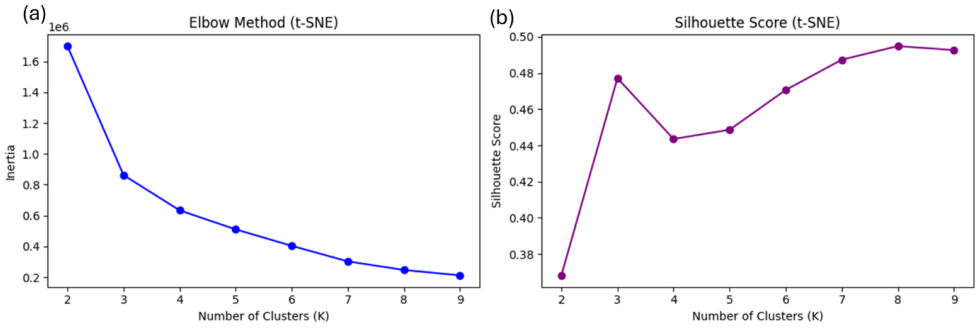


Figure 6.2: Determination of the optimal number of clusters using k-means clustering. **(a)** Elbow method plot showing the decrease in inertia (within-cluster sum of squares) as the number of clusters (K) increases, with the optimal K suggested at the point where the decrease begins to level off. **(b)** Silhouette score plot illustrating the average silhouette coefficient for each K, where higher values indicate better-defined clusters.

Table 6.1: K-means Cluster Descriptions for Pnictogen Chalcogenide (pn-chg) Systems Based on Chemical and Structural Properties

Cluster	Chemical and Structural Description
C1	Comprises alkali-metal arsenic chalcogenides enriched in s-block cations
C2	Dominated by lanthanide-centered frameworks with f-block chemistry
C3	Encompasses transition-metal-based compounds
C4	Composed of systems rich in p-block elements

C5	Features halide-chalcogenide hybrids coordinated by p-block metal centers
C6	Includes fluorinated and halogen-dense materials with anionic frameworks
C7	Contains s-block-rich compositions frequently coexisting with oxide anions
C8	Multinary systems incorporating alkali/alkaline-earth metals and lanthanides

Materials with similar chemical motifs, such as cation types (e.g., s-block, p-block, and transition metals) or anionic species (e.g., oxides and halides), tend to cluster systematically within the embedded space. For instance, clusters C1, C7, and C8 are enriched with s-block elements, while C2 and C8 demonstrate significant lanthanide elements, reflecting f-block character. Interestingly, both clusters C6 and C7 are associated with oxide-containing compositions, reflecting shared anionic frameworks. Cluster C5, comprising halide-rich pn-chg systems with p-block cations, bridging properties between C6 and C4, capturing mixed anionic and cationic characteristics, and aligns closely with C3, indicative of partial overlap with transition metal coordination environments. These chemically coherent clusters underscore the effectiveness of the unsupervised learning framework in capturing subtle chemical patterns and bonding preferences, offering a powerful strategy to navigate the vast pn-chg materials space for targeted thermoelectric discovery.

Figure 6.1(b-e) illustrates the distribution of key thermoelectric-relevant properties, including atomic weight, electronic band gap (E_g), formation energy (E_f), and energy above the convex hull (E_{Hull}) across seven structural prototypes of pn-chg materials extracted from Materials Project database. The blue dashed lines represent the selection criteria used in our high-throughput screening workflow (**Figure 6.3(a)**). In the next stage two thermodynamic stability criteria were applied, formation energy (E_f <0.00 eV/atom) and energy above the convex hull (E_{Hull} < 0.50 meV), retaining 1971 energetically favorable materials. These were further screened using

an electronic band gap filter (2.75 eV> E_g > 0.10 eV), identifying 1378 semiconductors with suitable band gaps, essential for optimizing electrical conductivity and suppressing electronic thermal conductivity. Finally, to capture chemically driven lattice anharmonicity, we applied an oxidation-state filter targeting pnictogens in the +3 state, leveraging the lone-pair effect known to reduce lattice thermal conductivity.[62] This final criterion narrowed the pool to 217 semiconducting materials that satisfy both structural and electronic prerequisites for efficient thermoelectric performance. To assess dynamical stability, we used a pre-trained universal MatterSim model to predict phonon dispersion curves. Among these, 78 pn-chg compounds from clusters C1, C2, C3, C4, C5 and C8 collectively representing motifs from s-, p-, and d-block elements were confirmed to be dynamically stable, exhibiting real phonon modes throughout the Brillouin zone (**Figure 6.3b**, **detailed in ref 18**). The distribution of E_f, E_{Hull} and E_g for this representative subset is **detailed in ref 18**. This hierarchical screening pipeline, integrating chemical, thermodynamic, electronic, and dynamical criteria, ensures retention of stable materials for further analysis.

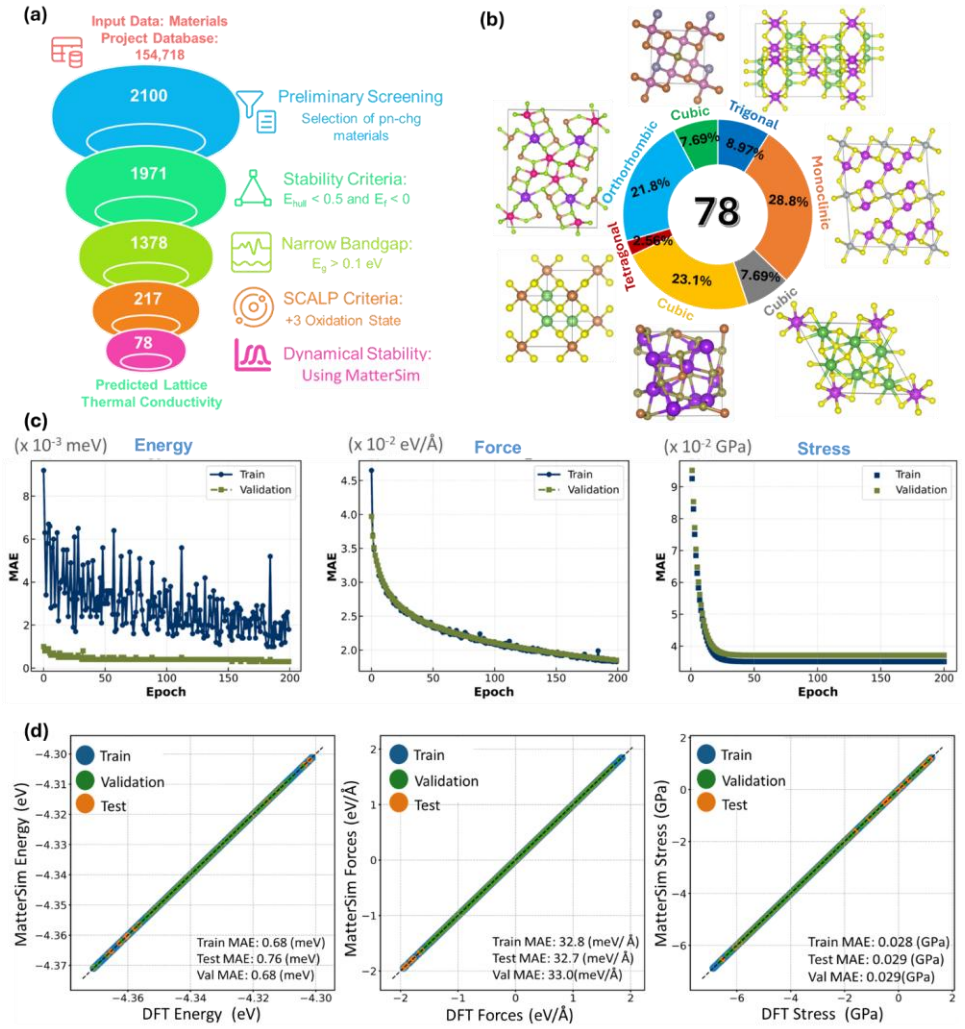


Figure 6.3: (a) Schematic workflow illustrating the high-throughput screening of the pnictogen chalcogenides dataset starting from 154,718 compounds in the Materials Project database. The candidate space is progressively narrowed using successive filters based on chemical criteria, thermodynamic stability ($E_f < 0$ eV/atom and $E_{Hull} < 0.50$ meV), electronic band gap ($E_g > 0.1$ eV), oxidation state constraints, and dynamical stability, ultimately yielding 78 promising thermoelectric candidates. **(b)** Structural classification of the final 78 screened compounds, categorized by their crystal symmetries, highlighting the diversity of crystallographic motifs, **(c)** Fine-tuning learning curves for the MatterSim model, showing the reduction in mean absolute error (MAE) for energy, forces, and stresses as

a function of training epochs, **(d)** Parity plots comparing MatterSim-predicted and DFT-calculated values for energy, forces, and stresses, confirming high fidelity of the MatterSim model in reproducing DFT-level accuracy.

6.3.2. Fine-Tuning Universal MatterSim for Accurate Interatomic Force Constants

While the pretrained MatterSim provides a strong baseline for extracting interatomic force constants (IFCs), critical for modeling phonon behavior and thermal transport, *[14, 37, 38]* universal MLIP (uMLIP) models often struggle to generalize to chemically complex or out-of-distribution systems. *[16]* To address this limitation, we performed transfer learning by fine-tuning the pretrained MatterSim model using a minimal, yet representative dataset generated from *ab initio* molecular dynamics (AIMD) simulations on selected pnictogen chalcogenide systems *[14, 37, 38]*. This targeted fine-tuning was designed to improve the potential energy surface (PES) mapping, particularly capturing subtle force perturbations relevant to lattice dynamics. Notably, we implemented a simple linear correction scheme based on the AIMD reference data to mitigate residual PES softening, a known limitation of uMLIP predictions (Detailed in Methods Section) *[14]*. This correction significantly improved both the accuracy and robustness of the MatterSim model, with convergence achieved within 200 training epochs (**Figure 6.3c**). The refined model offers enhanced sensitivity to force variations, thereby enabling more precise interatomic force constants (IFC) extraction. Parity plots in **Figure 6.3d** show strong agreement across total energies, atomic forces, and stress tensors, yielding mean absolute errors (MAEs) of 0.76 meV (energy), 32.7 meV/Å (forces), and 0.029 GPa (stresses) for test set. The low training, validation, and test performance metrics confirm the model's reliability and readiness for high-fidelity lattice dynamical modeling (**Table 6.2**). Further, the accuracy of the fine-tuned MatterSim was quantitatively validated by benchmarking its predictions against density functional theory (DFT) results **(Figure 6.4)**. The improved

agreement between the fine-tuned model and DFT results highlights the effectiveness of the fine-tuned approach in capturing the vibrational properties of these complex systems.

Table 6.2: Mean absolute errors (MAEs) for energy, forces, and stresses across screened pnictogen chalcogenide materials at final epochs. Each row corresponds to a material, and each column represents the MAE for energy, forces, and stresses on training (Train), validation (Val), and test (Test) datasets in meV, meV/Å or GPa.

mp-id_Formula	Energy			Force			Stress		
	Train	Val	Test	Train	Val	Test	Train	Val	Test
mp-1224757_In4Bi3S10	0.53	0.34	0.35	35.16	35.44	34.98	0.027	0.029	0.029
mp-1193673_Na3SbS3	0.68	0.61	0.6	23.24	23.23	23.12	0.04	0.039	0.039
mp-1192303_Pr2Mn3SbS34	1.01	1.04	1.05	36.17	36.71	36.78	0.031	0.032	0.032
mp-23474_AgBi3S5	0.72	0.63	0.65	30.92	31.02	31.22	0.032	0.033	0.033
mp-555113_Rb3Cu2BiS25	1.32	1.06	0.95	48.16	47.24	48.12	0.055	0.055	0.055
mp-1193265_Na3SbSe3	0.40	0.34	0.35	15.77	15.94	15.96	0.020	0.021	0.021
mp-2227993_Na3MgSbS4	0.36	0.27	0.32	19.89	19.79	20.18	0.014	0.015	0.014
mp-1229202_AgBi3PbS6	0.74	0.80	0.80	29.68	30.28	29.82	0.026	0.026	0.027
mp-1225886_CuBi3PbS6	0.70	0.65	0.68	36.72	37.16	37.59	0.033	0.034	0.034
mp-1194339_Li3SbS3	0.84	0.84	0.81	19.75	20.15	19.88	0.024	0.024	0.024
mp-504646_In5BiS43	0.53	0.44	0.47	31.68	32.4	31.81	0.022	0.023	0.023
mp-542302_CuBi3PbS6	0.57	0.42	0.42	40.42	40.8	41.06	0.03	0.031	0.032
mp-1229291_AgSb3PbS6	0.73	0.85	0.87	21.97	22.43	22.82	0.023	0.023	0.024
mp-1223584_KBi3S5	0.52	0.55	0.50	26.18	26.62	26.54	0.024	0.024	0.025
mp-766409_Li3BiS3	0.47	0.40	0.46	22.11	22.43	22.28	0.02	0.02	0.02
mp-9191_Na3SbTe3	0.67	0.38	0.42	22.25	21.91	22.61	0.033	0.033	0.034
mp-1227695_Bi2PbS23	0.69	0.76	0.69	32.83	32.79	33.08	0.029	0.03	0.029
mp-1194583_Ba3Sb2Se7	0.39	0.36	0.33	23.13	23.41	23.53	0.014	0.014	0.013
mp-753720_Li3BiS3	1.18	0.98	1.18	79.71	78.61	78.28	0.135	0.119	0.121
mp-17912_Rb3SbSe3	0.95	1.05	0.95	22.04	22.56	21.84	0.029	0.029	0.029
mp-1225886_CuBi3PbS6	0.70	0.64	0.68	36.72	37.15	37.58	0.032	0.034	0.034
mp-1193894_Cs3SbS3	0.15	0.14	0.14	58.53	60.73	58.92	0.052	0.062	0.090
mp-755463_Li3SbS3	1.71	1.74	1.76	20.87	20.95	21.53	0.027	0.026	0.027
mp-559356_Tl3AsS3	1.69	1.68	1.71	20.79	20.85	21.16	0.014	0.014	0.015
mp-554950_Hg3SbAsS3	1.43	1.45	1.43	20.76	20.78	0.77	0.014	0.014	0.014
mp-29295_Sr3Sb4S9	1.06	1.14	1.09	75.10	74.17	70.25	0.070	0.070	0.069
mp-2227993_Na3MgSbS4	0.35	0.27	0.31	19.78	19.78	20.18	0.014	0.014	0.014

mp-2223708_K3MgSbS4	0.28	0.28	0.25	14.05	14.21	14.30	0.013	0.013	0.013
mp-1227414_BiSbTe23	0.64	0.62	0.62	66.08	67.79	66.21	0.075	0.076	0.076

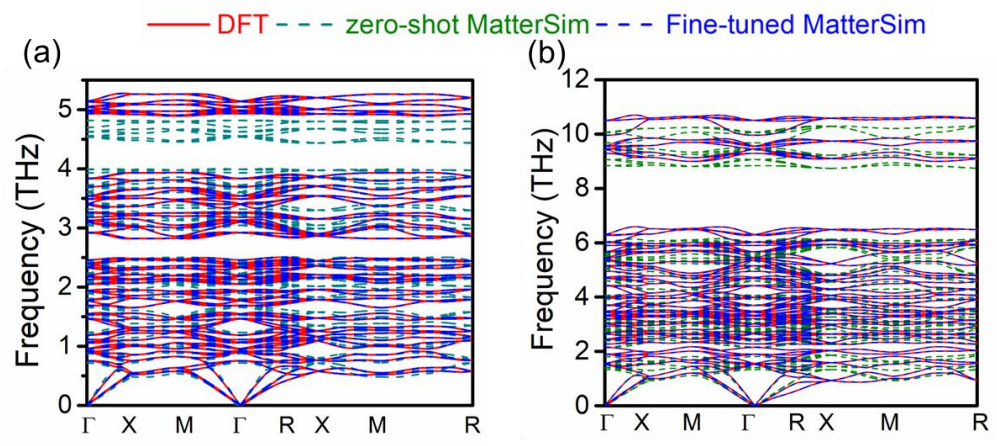


Figure 6.4: The phonon dispersion curves for (a) K_3SbTe_3 and (b) Na_3SbS_3 comparing density functional theory (DFT) results with predictions from MatterSim, both in its zero-shot and fine-tuned forms.

6.3.3. Wigner formulation of heat transport for Lattice Thermal Conductivity. To assess the thermal transport behavior of pnictogen chalcogenides and identify promising candidates for thermoelectric applications, we employed a modeling approach grounded on the unified theory of heat conduction in crystals and disordered solids, as proposed by Simoncelli, Marzari, and Mauri.[63–66] This theoretical framework is based on the Wigner heat-transport equation, named after the Wigner formulation of quantum mechanics used in its derivation, which naturally encompasses the coexistence of particle-like and wave-like conduction mechanisms, unifying and extending the Peierls and Allen-Feldman formulations *[20, 39]*. It provides comprehensive treatment of various heat carriers, including propagating phonons and localized, diffusive Wigner distribution elements, and is crucial for understanding the thermal behavior of complex, anharmonic materials. Using the unified theory approach, we computed particle-like (κ_P) and wave-like (κ_C) along the x-, y-, and z-axes, and the total κ_T values, for a dataset of 78 pnictogen chalcogenide materials,

as shown in **Figure 6.5(a)**. A pronounced anisotropy in κ_L was observed across the dataset, with the lowest value typically occurring along the x-direction. This directional dependence is likely a result of variations in chemical bonding hierarchies within the crystal structures. We have expanded our validation to multicomponent chalcogenide systems, where MatterSim predicted κ_L values reflect excellent agreement with experimentally reported or first-principles Boltzmann transport results. For example, κ_L is predicted as 0.41 W/mK for Cu_3SbS_3 and 0.24 W/mK for Cu_3SbSe_3, consistent with corresponding experimental values of 0.45 W/mK and 0.30 W/mK, respectively *[40, 41]*. For $Nb_3Sb_2Te_5$, the predicted κ_L of 1.84 W/mK closely matches the experimentally measured value of 1.90 W/mK *[42]*. Similarly, for Ag_3SbS_3, the predicted of 0.35 W/mK aligns well with the first-principles value of 0.39 W/mK *[43]*. Collectively, these results demonstrate that MatterSim provides reliable and accurate κ_L predictions not only for binary compounds but also for chemically complex multicomponent systems. This performance arises from its robust long-range interaction modeling and enhanced message-passing architecture, further strengthened through transfer learning.

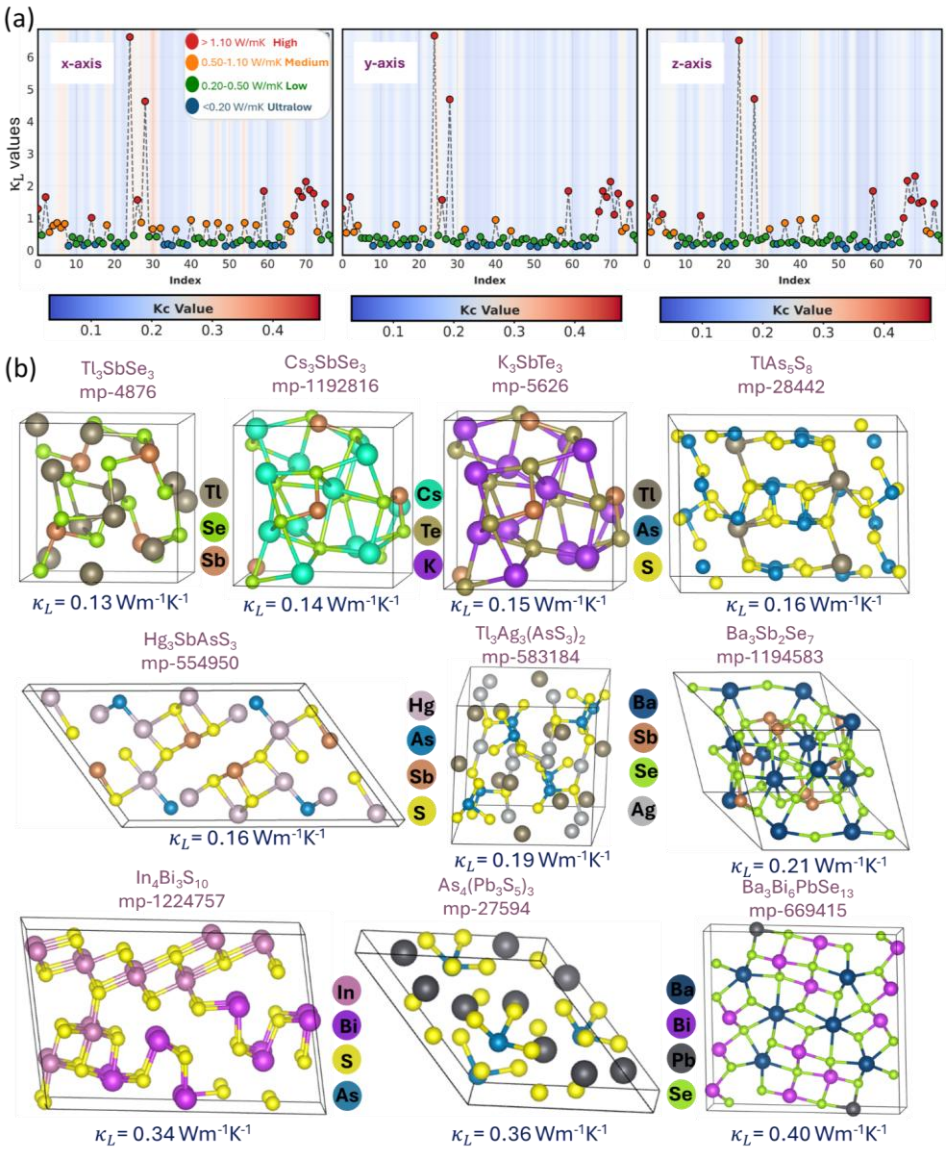


Figure 6.5: (a) Directional lattice thermal conductivity (κ_L) along the crystallographic x, y, and z-axes for 78 screened pnictogen chalcogenide systems. The materials are categorized into four regimes on their κ_L values: ultralow (<0.20 W/mK, blue), low (0.20-0.50 W/mK, green), medium (0.50-1.10 W/mK, yellow), and high (>1.10 W/mK, red). The background gradient represents the magnitude of the κ_C value defines wave-like conductivity, **(b)** representative crystal structures of ten materials with average κ_L ~0.40 W/mK at room temperature, along with their corresponding Materials Project (MP-ids).

Based on these calculated κ_L values, the materials were classified into four regimes: ultralow (<0.20 W/mK), low (0.20-0.50 W/mK), medium (0.50-1.10 W/mK), and high (>1.10 W/mK). Among these, several materials such as Tl_3SbSe_3, Cs_3SbSe_3, K_3SbTe_3, Hg_3SbAsS_3, $Ba_3Sb_2Se_7$, and $Tl_3Ag_3(AsS_3)_2$ from clusters C1, C3 and C4 exhibited ultralow κ_L along the x-axis at room temperature. The supressed κ_L in these materials can be attributed to a combination of structural and chemical features, including complex bonding hierarchies, rattling modes from loosely bound atoms, and stereochemically active lone pairs on pnictogen atoms.[27, 67–69] To provide a more comprehensive understanding, we also computed the average κ_L values across all directions. As shown in **Figure 6.5(b)**, nine materials with average κ_L values ≤ 0.40 W/mK were identified. Among these, Tl_3SbSe_3, Cs_3SbSe_3, K_3SbTe_3, $TlAs_5S_8$, Hg_3SbAsS_3, and $Tl_3Ag_3(AsS_3)_2$ emerge as promising ultralow κ_L materials, while others such as $Ba_3Sb_2Se_7$, $In_4Bi_3S_{10}$, $As_4(Pb_3S_5)_3$, and $Ba_3Bi_6PbSe_{13}$ exhibit remarkably low κ_L values ranging from 0.21 to 0.40 W/mK. To rationalize these observed trends, we emphasize the significance of chemical bonding descriptors as performance indicators. These descriptors offer microscopic insight into the structural origin of phonon scattering and anharmonicity and are essential for interpreting and predicting κ_L in chemically and structurally diverse systems.

6.3.4. Validation of uMLIP Predicted κ_L. Further to validate our uMLIP performance, we have considered 103 compounds representing rocksalt, zincblende, and wurtzite-type structures from first principles κ_L data as reference *[48, 49]*. To benchmark the predictive performance of κ_L values, we compared three state-of-the-art universal machine learning potentials (uMLIPs), including CHGNet,[36] MACE,[35] and MatterSim,[37] as shown in **Figure 6.6(a)**. To understand the origin of deviations between DFT-PBE and uMLIP-predicted κ_L, we analyzed thermal conductivities using three error metrics: the symmetric relative mean error (SRME) on

single phonon conductivity, the symmetric relative error (SRE), and the symmetric relative difference (SRD), defined as follows: *[50]*

$$\mathrm{SRME}[\{\kappa(q)_s\}] = \frac{2}{N_c \nu} \frac{\sum_{qs} |\kappa_{uMLIP}(q)_s - \kappa_{DFT}(q)_s|}{\kappa_{uMLIP} - \kappa_{DFT}}$$

$$\mathrm{SRE}[\kappa] = 2 \frac{|\kappa_{uMLIP} - \kappa_{DFT}|}{\kappa_{uMLIP} + \kappa_{DFT}}$$

$$\mathrm{SRD}[\kappa] = 2 \frac{\kappa_{uMLIP} - \kappa_{DFT}}{\kappa_{uMLIP} + \kappa_{DFT}}$$

Here $\kappa(q)_s$ represents the contribution of an individual phonon mode to κ_L, $(q)_s$ denotes the eigenstate corresponding to the same wavevector q. N_c is the number of q-points used to sample the Brillouin zone, and ν is the unit cell volume of the crystal. κ_{uMLIP} and κ_{DFT} refer to the κ_L predicted using uMLIP and DFT, respectively. SRD values range from negative to positive, indicating tendencies towards overestimation and underestimation, as they include unstable structures with negative phonon frequencies. **Figure 6.6(b)** represents the narrow and centered violin distributions, along with low mean SRE, SRME, and SRD, indicating higher predictive accuracy. Among the models, CHGNet exhibits the largest scatter (R^2 = 0.21), suggesting a weaker transferability to diverse chemistries whereas, MACE achieves a substantial improvement (R^2 = 0.90), capturing phonon transport trends more accurately. MatterSim, however, demonstrates the lowest mean errors across all metrics (SRE, SRME, SRD), reflecting its superior ability to reproduce DFT-level κ_L values consistently. The enhanced accuracy of MatterSim arises from its robust representation of long-range interactions and improved message-passing architecture, enabling better modeling of anharmonic lattice dynamics *[15]*.

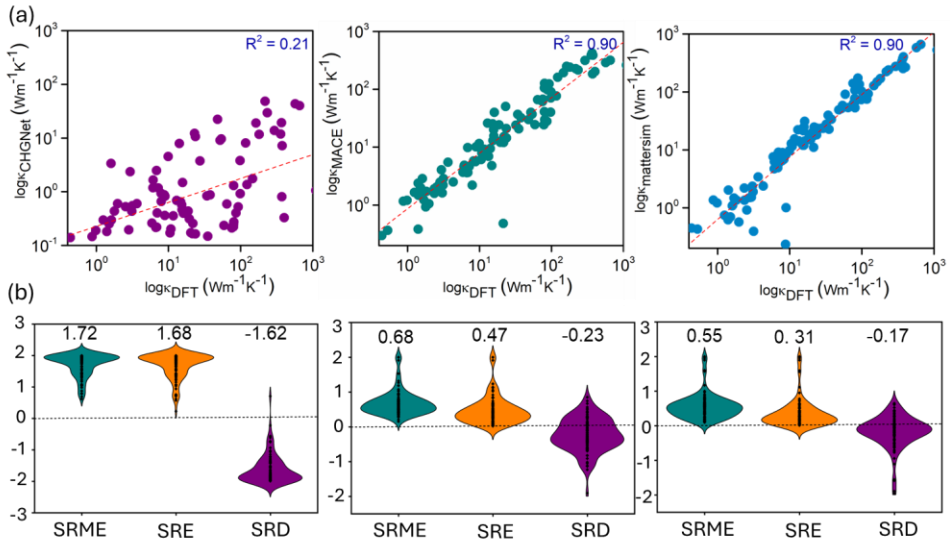


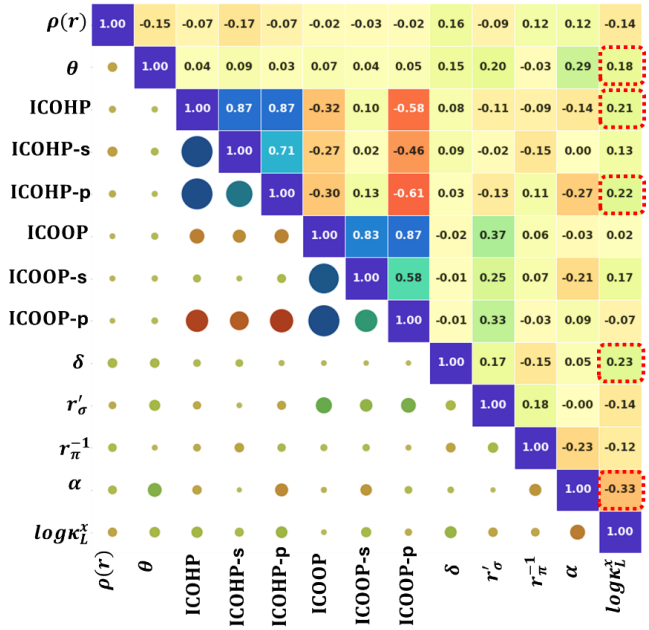
Figure 6.6: Comparative performance of CHGNet, MACE and MatterSim in predicting the lattice thermal conductivity (κ_L) **(a)** scatter plots of uMLIP-predicted versus DFT-calculated κ_L values, showing model correlation coefficient (R^2). CHGNet displays large deviations ($R^2 = 0.21$), whereas MACE and MatterSim exhibit high correlations with DFT ($R^2 \approx 0.90$), highlighting substantial accuracy gains. **(b)** Violin plots of Symmetric Relative Error (SRE), Symmetric Relative Mean Error (SRME), and Symmetric Relative Difference (SRD). The narrower, centered distributions for MatterSim confirm their minimal bias and high predictive reliability in reproducing phonon-mediated thermal transport.

6.3.5. Structural Fingerprinting of SCALPs. To uncover the underlying bonding principles governing the low average lattice thermal conductivity (κ_L^{avg}) in SCALP containing materials, we performed a correlation analysis using a set of structural and chemical bonding descriptors to understand the contributions from SCALP as well as other origins. The Pearson correlation coefficient (PCC) matrix identifies the influential descriptors dictating thermal transport behaviour, providing quantitative insights into structure-property relationships (**Table 6.3 and detailed in ref 18**) *[51, 52]*. Building upon our prior on κ_L descriptor design, we included parameters capturing

essential bonding characteristics, including ionicity (r'_σ), hybridization (r_π^{-1}), polarizability (α), and number mismatch (δ) *[44]*. To refine the representation of bonding energetics and orbital-specific interactions, we introduced the integrated crystal orbital Hamilton population (ICOHP) along with its s- and p-orbital-resolved components (ICOHP-s and ICOHP-p). These descriptors effectively quantify the bonding contributions associated with SCALP and non-SCALP interactions.

Table 6.3: Pearson correlation coefficient (PCC) matrix between structural/bonding descriptors and the κ_L^{avg} of SCALP materials. The red dotted squares highlight descriptors with the strongest negative correlations with κ_L^{avg}

Descriptor	Symbol
Bond angle	θ
Mismatch	δ
Ionicity	r'_σ
Hybridization	r_π^{-1}
Polarizability	α
ELF	$\rho(r)$
ICOHP	ICOHP
ICOHP-s	ICOHP-s
ICOHP-p	ICOHP-p
ICOOP	ICOOP
ICOOP-s	ICOOP-s
ICOOP-p	ICOOP-p
Average thermal conductivity	κ_L^{min}



SCALP Descriptors. Among these, COHP and ICOHP-p shows a significant negative correlation with κ_L^{avg} (PCC = 0.22), highlighting the importance of p-orbital-mediated bonding in phonon scattering mechanisms. More negative ICOHP-p values correspond to stronger p-type

interactions, which enhance structural rigidity and reduce phonon scattering efficiency, thereby increasing κ_L. Conversely, weaker p-orbital bonding interactions (less negative ICOHP values) facilitate enhanced phonon scattering, resulting in lower κ_L.

Non-SCALP Descriptors. To elucidate bonding asymmetry and its influence on κ_L^{avg}, we considered several electronic structure-based descriptors. The ionicity parameter (r_σ') and hybridization index (r_π^{-1}) quantify the ionicity and covalency of bonds, respectively, capturing the extent of charge separation and orbital mixing in pn-chg systems *[44, 53]*. Additionally, a larger mismatch (δ) between cation and anion orbitals leads to increased electronic imbalance, inducing local bonding distortions that enhance phonon scattering and reduce κ_L *[54]*. To further capture local geometric effects and the influence of adjacent chemical motifs, we evaluated the bond angle (θ) around the pnictogen center, which reflects geometrical distortions and exhibits a strong inverse correlation with κ_L (Pearson correlation coefficient = 0.23). Similarly, the electron localization function (ELF), ρ(r), exhibits a negative correlation with κ_L, where higher values around pnictogen atoms indicate localized lone pairs that induce asymmetric bonding and enhance phonon scattering *[55, 56]*. This framework reveals the intricate bonding hierarchies that govern κ_L in structurally complex SCALP systems and underscores the interplay between SCALP-driven and non-SCALP mechanisms.

6.3.6. Quantifying SCALP and Bonding Hierarchies To extend the insight provided by bonding descriptors and evaluate their influence on lattice dynamics, we employ the Sure Independence Screening and Sparsifying Operator (SISSO) approach to identify the most impactful descriptor governing intrinsically low κ_L values *[57]*. **Figure 6.7(a)** shows that the SISSO analysis reveals two dominant contributors to low κ_L values: electronic effects associated with SCALP activity and geometric distortions or asymmetry induced by beyond-SCALP effects. These bonding-specific

features, particularly, s- and p-orbital weighted ICOHP and ICOOP values, which capture the strength and anharmonicity of pn-chg interactions essential to SCALP behaviour account for approximately 40% influence on κ_L, with a correlation coefficient of 0.38 (**Table 6.4**). This provides a quantitative link between the SCALP mechanism, driven by s-p orbital mixing near the E_f, and its influence on thermal transport. In line with the revised lone-pair model, the presence of occupied antibonding states, (pn(ns)-chg(np)), induces local symmetry breaking through on-site sp hybridization, thereby enhancing lattice anharmonicity *[58]*. In contrast, structural distortions descriptors associated with capturing geometric asymmetries and their impact on anharmonic lattice behavior. These features reflect the intrinsic complexities of the lattice framework and its propensity for anharmonic vibrations, resulting in a stronger correlation (0.58) with κ_L, emphasizing the dominant role of geometric asymmetry in reducing thermal conductivity. Collectively, these results confirm that while SCALP-related electronic descriptors account for ~40% of the κ_L variation, the remaining ~60% arises from geometric factors that enhance phonon scattering through lattice anharmonicity *[58]*.

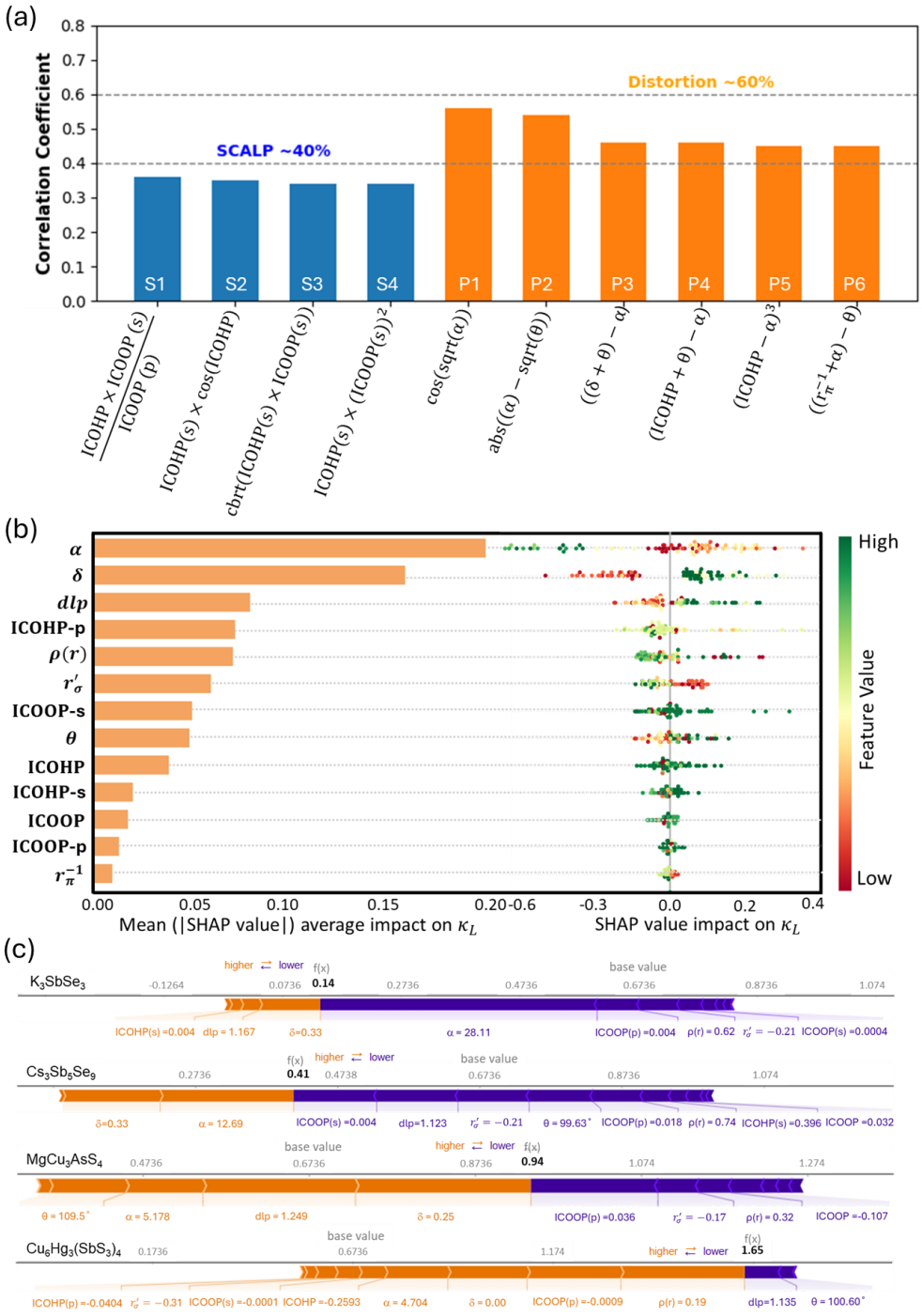


Figure 6.7. (a) Bar plot showing the correlation coefficients between κ_L and two categories of descriptors: SCALP descriptors (~40%, shown in blue) and beyond SCALP-distortion descriptors (~60%, shown in orange). Descriptor details are provided in **Table 6.3-6.4**. **(b)** Global interpretability of the GBR model obtained from SHAP feature importance and beeswarm

plots, highlighting the key chemical bonding descriptors contributing most significantly to κ_L based on mean SHAP values. **(c)** SHAP force plots illustrating the interplay between SCALP and geometric activity across representative pn-chg materials. The sequence from K_3SbSe_3 to $Cs_3Sb_5Se_9$ to $MgCu_3AsS_4$ to $Cu_6Hg_3S_{12}$ demonstrates a decrease in SCALP-activity that led to high κ_L.

Table 6.4: Chemical Bonding Descriptor Correlations highlighting the SCALP and Structural Distortion mechanisms influencing κ_L

Mechanism	Chemical Bonding Descriptor Design	Correlation Coefficient	Parameters
SCALP	$\frac{\mathrm{ICOHP} \times \mathrm{ICOHP(s)}}{\mathrm{ICOOP(p)}}$	0.38	ICOHP/ICOOP (s/p)
SCALP	$\mathrm{ICOHP(s)} \times \cos(\mathrm{ICOHP})$	0.36	ICOHP (s)
SCALP	$\mathrm{cbrt}(\mathrm{ICOHP(s)} \times \mathrm{ICOOP}(s))$	0.35	ICOHP/ICOOP (s)
SCALP	$\mathrm{ICOHP(s)} \times (\mathrm{ICOOP(s)})^2$	0.34	ICOHP/ICOOP (s)
Structural Distortion	$\cos(\mathrm{sqrt}(\alpha))$	0.58	α
Structural Distortion	$\mathrm{abs}((\alpha) - \mathrm{sqrt}(\theta))$	0.54	α, θ
Structural Distortion	$((\delta + \theta) - \alpha)$	0.46	δ, θ, α
Structural Distortion	$((\mathrm{ICOHP} + \theta) - \alpha)$	0.46	$\mathrm{ICOHP}, \theta, \alpha$
SCALP + Structural Distortion	$(\mathrm{ICOHP} - \alpha)^3$	0.45	$ICOHP, \alpha$
Structural Distortion	$((r_\pi^{-1} + \alpha) - \theta)$	0.45	$r_\pi^{-1}, \alpha, \theta$

*abs=absolute value function; cbrt=cube root function; cos/sin=trigonometric functions; exp=exponential function

To further interpret the role of individual bonding descriptors, we utilized gradient boosting regression model to perform SHapley Additive

exPlanations (SHAP) analysis, which decomposes the model prediction into additive feature contributions using principles of cooperative game theory.[45] As illustrated in **Figure 6.7(b)**, the global SHAP feature-importance plot ranks polarizability (α), mismatch (δ), lone pair distance (dlp), ICOHP-p and ELF (ρ(r)) as the five most influential factors determining κ_L. The accompanying beeswarm plot visualizes how each descriptor affects κ_L across the dataset, where green points indicate features that increase κ_L, while red points correspond to features that decrease it. High values of polarizability, ICOHP-p, and ELF, combined with low mismatch and shorter lone-pair distances, consistently lead to reduced κ_L, highlighting their cooperative role in enhancing anharmonic phonon scattering. Local SHAP force plots (**Figure 6.7(c)**) further reveal instance-specific interactions between features, where the direction and magnitude of each contribution are represented as "push" (orange) or "pull" (purple) forces relative to the model's base value. These local explanations illustrate the *tug-of-war* between opposing electronic and structural factors in determining the final κ_L value. In K_3SbSe_3, short dlp, low mismatch (δ), and high ELF promote strong sp-hybridized distortions, enhancing SCALP activity and minimizing κ_L. $Cs_3Sb_5Se_9$ represents an intermediate state where increased polarizability and moderate distortions maintain a balanced electronic-geometric competition. In $MgCu_3AsS_4$, geometric effects dominate through large bond-angle and low polarizability, sustaining high κ_L with reduced SCALP influence. In contrast, $Cu_6Hg_3S_{12}$ exhibits a rigid, symmetric lattice with large dlp, zero δ, and low polarizability, suppressing SCALP activity and yielding high κ_L (1.65 W/mK).

6.3.7. Cs_3SbS_3, $Ba_3Sb_2Se_7$, and Li_3BiS_3: a case study. To further elucidate the SCALP and non-SCALP governing factors for ultralow κ_L, we examine three representative pnictogen chalcogenides, Cs_3SbS_3 ($\kappa_L = 0.14$ W/mK), $Ba_3Sb_2Se_7$ ($\kappa_L = 0.21$ W/mK), and Li_3BiS_3 ($\kappa_L = 1.95$ W/mK) that exhibits varying κ_L (**Figure 6.8(a-c)**). We visualized the ELF to access the degree

of electron localization on pnictogen atoms which incorporates the influence of Pauli exclusion principle and provides the spatial morphology of the lone pair electron cloud *[56]*. Higher ELF values indicate more localized lone pairs, which can strongly interact with neighboring atoms, enhancing anharmonicity. Cs_3SbS_3 exhibits the highest ELF value (0.76), followed by $Ba_3Sb_2Se_7$ (0.72) and Li_3BiS_3 (0.54), which reflects a progressive decrease in SCALP activity and corresponding κ_L values. This trend is corroborated by the topology of lone pair electron densities, where Sb atoms in $Ba_3Sb_2Se_7$ and Cs_3SbS_3 show prominent asymmetric "mushroom" or "bean"-shaped electron densities (**Figure 6.8**), reflecting pronounced stereochemical expression. In contrast, Li_3BiS_3 appear as more symmetric, "flattened mushroom" projections on Bi, indicating reduced nonbonding character and weaker lattice anharmonicity. The impact of structural anharmonicity is further captured by the asymmetry parameters, such as a more negative r_σ' and moderate r_π^{-1} indicate stronger electron repulsion and distortion *[44]*. These descriptors suggest that Cs_3SbS_3 has the most distorted bonding environment, leading to stronger anharmonicity and lower κ_L. Another key indicator is the chg-pn-chg angle, which reflects strong deviations from the ideal tetrahedral geometry (109.5°) as a result of repulsion between lone pairs and bonding electrons *[6]*. For instance, in Cs_3SbS_3, angle is compressed to 102.57°, compared to 96.36° in $Ba_3Sb_2Se_7$and 98.94° in Li_3BiS_3. Such deviations induce polyhedral distortions that enhance phonon scattering and higher Grüneisen parameters, ultimately contributing to a reduction in κ_L.

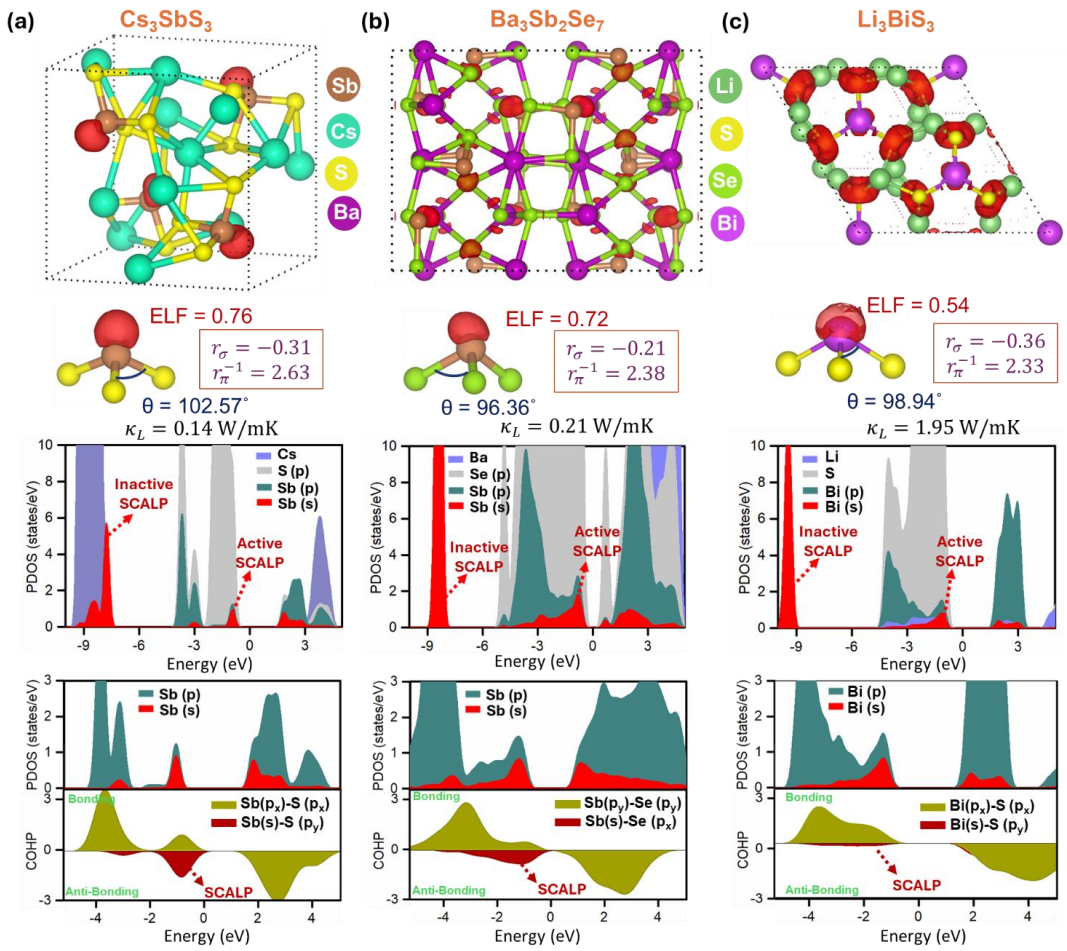


Figure 6.8: Crystal structures with SCALP projection on pnictogens using electron localization function (ELF), projected density of states (PDOS), and crystal orbital Hamilton population (COHP) analysis of **(a)** Cs_3SbS_3, **(b)** $Ba_3Sb_2Se_7$, and **(c)** Li_3BiS_3. The 3D view of the electron localization function (ELF) at isosurface values of 0.91 eV/Å^3. The comparison of ionicity (r'_σ), hybridization (r_π^{-1}), bond angle (θ), with lattice thermal conductivity (κ_L). PDOS and COHP analyses were used to visualize the bonding characteristics of the SCALP near the Fermi energy, where a positive overlap population indicates a bonding interaction, while a negative overlap population indicates an antibonding interaction.

Further, the real space visualization of SCALP activity can indeed be explained by the interaction strength and energy separation between unoccupied Sb/Bi np and occupied S/Se np and Sb/Bi ns states. To

investigate nature of bonding, we performed the partial density of states (PDOS) and COHP analysis to locate relevant *s*/*p* states relative to the Fermi level (E_f) *[25]*. The PDOS indicates that the valence bands are dominated by S/Se-3*p*/4*p* states with significant contributions from Sb 6*s* and 6*p* orbitals. All three materials exhibit electronic states labelled as "active SCALP" near the E_f, where $Ba_3Sb_2Se_7$ indicate the intense and localized Sb(s) states represent enhanced SCALP activity. Further, COHP analysis represents a distinct separation between bonding and antibonding interactions, from cation *s*- and *p*-orbitals, and anion *p*-orbitals, with antibonding states predominantly located near the E_f. In Cs_3SbS_3, strong Sb *s*- and Se *p* antibonding interactions are evident just below E_f, supporting the presence of the SCALPs *[44, 60, 61]*. These interactions exemplify stereochemical activity as described by the revised lone pair model, driven by orbital hybridization and stabilization mechanism *[7]*. Specifically, the occupied antibonding states, primarily arising from Sb (5s)-S (3p) interactions, are further stabilized through mixing with Sb (5p) orbitals, leading to local symmetry breaking and enabling on-site *sp* hybridization. Similar trends are observed in $Ba_3Sb_2Se_7$ and Li_3BiS_3, where Sb (*s*)-S (*p*) and Bi (*s*)-S (*p*) antibonding interactions, respectively, enable local distortion, enhance lattice anharmonicity, and activate lone pairs. These antibonding interactions, by inducing local symmetry breaking, play a critical role in enhancing the SCALPs, promoting strong phonon scattering and intrinsically low κ_L. The integration of chemically informed descriptors thus provides a robust and interpretable framework for capturing both SCALP-driven electronic mechanisms and beyond-SCALP lattice distortions, guiding the rational design of ultralow κ_L materials.

6.4. Summary

In summary, we have developed a unified, data-driven framework that leverages fine-tuned MatterSim-based interatomic potentials to enable accurate and efficient predictions of lattice thermal conductivity (κ_L) across

a diverse set of 78 pnictogen chalcogenides. By integrating high-throughput screening, unsupervised machine learning, and Wigner transport theory, our approach overcomes the scalability limitations of conventional DFT methods while retaining high precision. This framework successfully identifies several ultralow κ_L candidates, including Tl_3SbSe_3, Cs_3SbSe_3, K_3SbTe_3, $TlAs_5S_8$, Hg_3SbAsS_3, and $Tl_3Ag_3(AsS_3)_2$ (κ_L < 0.20 W/mK), highlighting its effectiveness for rapid materials discovery. Furthermore, we reveal that approximately 40% of the ultralow κ_L arises from SCALP-driven electronic asymmetry, with the remaining contribution linked to non-SCALP descriptors such as ionicity, atomic mismatch among others. Our results not only elucidate the fundamental origins of ultralow thermal transport but also establish a scalable and interpretable path forward for the rational design of next-generation thermoelectric materials.

6.5. References

1. Snyder G.J., Toberer E.S. (2008), Complex thermoelectric materials, Nat Mater, 7, 105–114 (DOI: 10.1038/nmat2090)

2. He J., Xia Y., Lin W., Mario B., Yang P., Kanatzidis M.G. (2022), Accelerated discovery and design of ultralow lattice thermal conductivity materials using chemical bonding principles, *Adv Funct Mater*, 32, 2108532 (DOI: 10.1002/adfm.202108532)

3. Dutta M., Pal K., Waghmare U.V., Biswas K. (2019), Bonding heterogeneity and lone pair induced anharmonicity resulted in ultralow thermal conductivity and promising thermoelectric properties in n-type $AgPbBiSe_3$, *Chem Sci*, 10, 490–501 (DOI: 10.1039/c9sc00485h)

4. Morelli D.T., Jovovic V., Heremans J.P. (2008), Intrinsically minimal thermal conductivity in cubic I–V–VI_2 semiconductors, *Phys Rev Lett*, 101, 035901 (DOI: 10.1103/PhysRevLett.101.035901)

5. Nielsen M.D., Ozoliņš V., Heremans J.P. (2013), Lone pair electrons minimize lattice thermal conductivity, *Energy Environ Sci*, 6, 570–578 (DOI: 10.1039/c2ee23391f)

6. Skoug E.J., Morelli D.T. (2011), Role of lone-pair electrons in producing minimum thermal conductivity in nitrogen-group chalcogenide compounds, *Phys Rev Lett*, 107, 235901 (DOI: 10.1103/PhysRevLett.107.235901)

7. Minhas H., Sharma R.K., Pathak B. (2025), Exploring combined stereochemically active lone-pair and rattling effects in thermoelectrics with machine learning potentials, *J Phys Chem Lett*, 16, 5051–5061 (DOI: 10.1021/acs.jpclett.5c00952)

8. Fu L., Kornbluth M., Cheng Z., Marianetti C.A. (2019), Group theoretical approach to computing phonons and their interactions, *Phys Rev B*, 100, 014303 (DOI: 10.1103/PhysRevB.100.014303)

9. Bandi S., Marianetti C.A. (2023), Precisely computing phonons via irreducible derivatives, *Phys Rev B*, 107, 174302 (DOI: 10.1103/PhysRevB.107.174302)

10. Xiao E., Marianetti C.A. (2023), Anharmonic phonon behavior via irreducible derivatives: Self-consistent perturbation theory and molecular dynamics, *Phys Rev B*, 107, 094303 (DOI: 10.1103/PhysRevB.107.094303)

11. Choudhary K., DeCost B., Major L., Butler K., Thiyagalingam J., Tavazza F. (2023), Unified graph neural network force-field for the periodic table: Solid state applications, *Digital Discovery*, 2, 346–355 (DOI: 10.1039/D2DD00096B) DOI

12. Chen C., Ong S.P. (2022), A universal graph deep learning interatomic potential for the periodic table, *Nat Comput Sci*, 2, 718–728 (DOI: 10.1038/s43588-022-00349-3) Nature

13. Batatia I., Kovács D.P., Simm G.N.C., et al. (2023), MACE: Higher order equivariant message passing neural networks for fast and accurate force fields, *Machine Learning: Science and Technology*, 4, 015028 (DOI: 10.1088/2632-2153/ace988)

14. Deng B., Zhong P., Jun K.J., Riebesell J., Han K., Bartel C.J., Ceder G. (2023), CHGNet as a pretrained universal neural network potential for charge-informed atomistic modelling, *Nat Mach Intell*, 5, 1031–1041 (DOI: 10.1038/s42256-023-00716-3)

15. Yang H., Hu C., Zhou Y., Liu X., Shi Y., Li J., Li G., Chen Z., Chen S., Zeni C., Horton M., Pinsler R., Fowler A., Zügner D., Smith J., Kong L., Hao H., Lu Z. (2024), MatterSim: A deep learning atomistic model across elements, temperatures, and pressures, *arXiv preprint*, arXiv:2405.04967

16. Deng B., Choi Y., Zhong P., Jun K.J., Han K., Bartel C.J., Ceder G. (2024), Overcoming systematic softening in universal machine learning interatomic potentials by fine-tuning, *npj Comput Mater*, 10, 150 (DOI: 10.1038/s41524-024-01500-6)

17. Jain A., Ong S.P., Hautier G., Chen W., Richards W.D., Dacek S., Cholia S., Gunter D., Skinner D., Ceder G., Persson K.A. (2013), Commentary: The Materials Project: A materials genome approach to accelerating materials innovation, *APL Mater*, 1, 011002 (DOI: 10.1063/1.4812323)

18. Minhas, H.; Sharma, R. K.; Pathak, B. (2026), Unravelling Lone Pair-Induced Bonding Effects on Thermal Conductivity in Metal Chalcogenides Using Machine Learning Potentials, J. Mater. Chem. A, 14 (DOI: 10.1039/D5TA08916F)

19. Isaeva L., Barbalinardo G., Donadio D., Baroni S. (2019), Modeling heat transport in crystals and glasses from a unified lattice-dynamical approach, *Nat Commun*, 10, 3853 (DOI: 10.1038/s41467-019-11572-4)

20. Simoncelli M., Marzari N., Mauri F. (2019), Unified theory of thermal transport in crystals and glasses, *Nat Phys*, 15, 809–813 (DOI: 10.1038/s41567-019-0520-x)

21. Blöchl P.E. (1994), Projector augmented-wave method, *Phys Rev B*, 50, 17953–17979 (DOI: 10.1103/PhysRevB.50.17953)

22. Kresse G., Furthmüller J. (1996), Efficient iterative schemes for ab initio total-energy calculations using a plane-wave basis set, *Phys Rev B*, 54, 11169–11186 (DOI: 10.1103/PhysRevB.54.11169)

23. Perdew J.P., Burke K., Ernzerhof M. (1996), Generalized gradient approximation made simple, *Phys Rev Lett*, 77, 3865–3868 (DOI: 10.1103/PhysRevLett.77.3865)

24. Perdew J.P., Chevary J.A., Vosko S.H., Jackson K.A., Pederson M.R., Singh D.J., Fiolhais C. (1992), Atoms, molecules, solids, and surfaces: Applications of the generalized gradient approximation for exchange and correlation, *Phys Rev B*, 46, 6671–6687 (DOI: 10.1103/PhysRevB.46.6671)

25. Nelson R., Ertural C., George J., Deringer V.L., Rinke P., Ceriotti M., Blum V. (2020), LOBSTER: Local orbital projections, atomic charges, and chemical-bonding analysis from projector-augmented-wave-based density-functional theory, *J Comput Chem*, 41, 1931–1940 (DOI: 10.1002/jcc.26353)

26. Qi J., Ko T.W., Wood B.C., Deringer V.L., Csányi G. (2024), Robust training of machine learning interatomic potentials with dimensionality reduction and stratified sampling, *NPJ Comput Mater*, 10, 227 (DOI: 10.1038/s41524-024-01227-4)

27. Allen P.B., Feldman J.L. (1993), Thermal conductivity of disordered harmonic solids, *Phys Rev B*, 48, 12581–12588 (DOI: 10.1103/PhysRevB.48.12581)

28. Xia Y., Gaines D., He J., Wolverton C., Ozoliņš V. (2023), A unified understanding of minimum lattice thermal conductivity, *Proc Natl Acad Sci U S A*, 120, e2302541120 (DOI: 10.1073/pnas.2302541120)

29. Guin S.N., Biswas K. (2013), Cation disorder and bond anharmonicity optimize the thermoelectric properties in kinetically stabilized rocksalt $AgBiS_2$ nanocrystals, *Chem Mater*, 25, 1482–1489 (DOI: 10.1021/cm401630d)

30. Guin S.N., Chatterjee A., Negi D.S., Roychowdhury S., Biswas K. (2013), High thermoelectric performance in tellurium-free p-type $AgSbSe_2$, *Energy Environ Sci*, 6, 2603–2612 (DOI: 10.1039/C3EE41935E)

31. Rathore E., Juneja R., Culver S.P., Biswas K., Oganov A.R. (2019), Origin of ultralow thermal conductivity in n-type cubic bulk $AgBiS_2$: Soft Ag vibrations and local structural distortion induced by the Bi $6s^2$ lone pair, *Chem Mater*, 31, 1421–1432 (DOI: 10.1021/acs.chemmater.9b00001)

32. Ward L., Dunn A., Faghaninia A., Zimmermann N.E.R., Bajaj S., Montoya J., Chen J., Bystrom K., Persson K., Jain A. (2018), Matminer: An open-source toolkit for materials data mining, *Comput Mater Sci*, 152, 60–69 (DOI: 10.1016/j.commatsci.2018.05.018)

33. Abdi H., Williams L.J. (2010), Principal component analysis, *Wiley Interdiscip Rev Comput Stat*, 2, 433–459 (DOI: 10.1002/wics.101)

34. Tang J., Liu J., Zhang M., Mei Q. (2016), Visualizing large-scale and high-dimensional data, In: *Proceedings of the 25th International World Wide Web Conference (WWW '16)*, Montreal, Canada, 287–297 (DOI: 10.1145/2872427.2883085)

35. Sinaga K.P., Yang M.S. (2020), Unsupervised K-means clustering algorithm, *IEEE Access*, 8, 80716–80727 (DOI: 10.1109/ACCESS.2020.2988796)

36. Burdett J.K., McLarnan T.J. (1982), An orbital explanation for Pauling's third rule, *J Am Chem Soc*, 104, 433–436 (DOI: 10.1021/ja00383a041)

37. Chen C., Ong S.P. (2021), AtomSets as a hierarchical transfer learning framework for small and large materials datasets, *NPJ Comput Mater*, 7, 63 (DOI: 10.1038/s41524-021-00639-w)

38. Lee J., Asahi R. (2021), Transfer learning for materials informatics using crystal graph convolutional neural network, *Comput Mater Sci*, 190, 110314 (DOI: 10.1016/j.commatsci.2021.110314)

39. Simoncelli M., Marzari N., Mauri F. (2022), Wigner formulation of thermal transport in solids, *Phys Rev X*, 12, 041011 (DOI: 10.1103/PhysRevX.12.041011)

40. Dutková E., Levinský P., Hejtmánek J., Toman P., Pathak B., Minhas H. (2025), Mechanochemically synthesized Skinnerite Cu_3SbS_3 and Wittichenite Cu_3BiS_3 nanocrystals and their promising thermoelectric properties, *Crystals (Basel)*, 15, 511 (DOI: 10.3390/cryst15060511)

41. Kirkham M., Majsztrik E.J., Skoug E.J., Morelli D.T. (2011), High-temperature order/disorder transition in the thermoelectric Cu_3SbSe_3, *J Mater Res*, 26, 1989–1996 (DOI: 10.1557/jmr.2011.43)

42. Wang S., Snyder G.J., Caillat T. (2002), Thermoelectric properties of $Nb_3SbxTe7$-x compounds, In: *Proceedings of the International Conference on Thermoelectrics (ICT 2002)*, Dresden, Germany, 107–110

43. Govindaraj P., Murugan K., Veluswamy P., Sundararajan K. (2023), Efficacy of pyrostilpnite (Ag_3SbS_3) mineral as thermoelectric material: A first-principles study, *Mater Sci Semicond Process*, 162, 107513 (DOI: 10.1016/j.mssp.2023.107513)

44. Minhas H., Jena M.K., Sharma R.K., Pathak B. (2024), Insights into thermal conductivity of pnictogen chalcogenides: Machine learning stereochemically active lone pairs and hybridization, *Chem Mater*, 36, 4562–4575 (DOI: 10.1021/acs.chemmater.4c02294)

45. Jana M.K., Pal K., Warankar A., Kumar S., Pathak B. (2017), Intrinsic rattler-induced low thermal conductivity in Zintl-type $TlInTe_2$, *J Am Chem Soc*, 139, 4350–4353 (DOI: 10.1021/jacs.7b01434)

46. Maria I., Arora R., Dutta M., Pal K., Minhas H., Pathak B. (2023), Metavalent bonding-mediated dual $6s^2$ lone pair expression leads to intrinsic lattice shearing in n-type $TlBiSe_2$, *J Am Chem Soc*, 145, 13502–13512 (DOI: 10.1021/jacs.3c02146)

47. Minhas H., Das S., Sharma R.K., Pathak B. (2024), Rattling induced bonding hierarchy in Li-Cu-Ti chalcotitanates for enhanced thermoelectric efficiency: A machine learning potential approach, *J Mater Chem A*, 12, 17450–17461 (DOI: 10.1039/d3ta07461g)

48. Togo A., Chaput L., Tanaka I. (2015), Distributions of phonon lifetimes in Brillouin zones, *Phys Rev B*, 91, 094306 (DOI: 10.1103/PhysRevB.91.094306)

49. Togo A. (2023), First-principles phonon calculations with Phonopy and Phono3py, *J Phys Soc Jpn*, 92, 012001 (DOI: 10.7566/JPSJ.92.012001)

50. Póta B., Ahlawat P., Csányi G., Simoncelli M. (2025), Thermal conductivity predictions with foundation atomistic models, *arXiv preprint*, arXiv:2501.01234

51. Zhou H., Deng Z., Xia Y., Fu M. (2016), A new sampling method in particle filter based on Pearson correlation coefficient, *Neurocomputing*, 216, 208–214 (DOI: 10.1016/j.neucom.2016.07.036)

52. Adler J., Parmryd I. (2010), Quantifying colocalization by correlation: The Pearson correlation coefficient is superior to the Mander's overlap coefficient, *Cytometry Part A*, 77, 733–742 (DOI: 10.1002/cyto.a.20896)

53. Lencer D., Salinga M., Grabowski B., Hickel T., Neugebauer J., Wuttig M. (2008), A map for phase-change materials, *Nat Mater*, 7, 972–977 (DOI: 10.1038/nmat2330)

54. Deng T., Wei T.R., Huang H., Zhang W., Chen C., Ong S.P. (2020), Number mismatch between cations and anions as an indicator for low lattice thermal conductivity in chalcogenides, *NPJ Comput Mater*, 6, 82 (DOI: 10.1038/s41524-020-00355-x)

55. Becke A.D., Edgecombe K.E. (1990), A simple measure of electron localization in atomic and molecular systems, *J Chem Phys*, 92, 5397–5403 (DOI: 10.1063/1.458517)

56. Silvi B., Savin A. (1994), Classification of chemical bonds based on topological analysis of electron localization functions, *Nature*, 371, 683–686 (DOI: 10.1038/371683a0)

57. Ouyang R., Curtarolo S., Ahmetcik E., Scheffler M., Ghiringhelli L.M. (2018), SISSO: A compressed-sensing method for identifying the best low-dimensional descriptor in an immensity of offered candidates, *Phys Rev Mater*, 2, 083802 (DOI: 10.1103/PhysRevMaterials.2.083802)

58. Walsh A., Payne D.J., Egdell R.G., Watson G.W. (2011), Stereochemistry of post-transition metal oxides: Revision of the classical lone pair model, *Chem Soc Rev*, 40, 4455–4463 (DOI: 10.1039/c1cs15098g)

59. Lundberg S.M., Erion G., Chen H., DeGrave A., Prutkin J.M., Nair B., Katz R., Himmelfarb J., Bansal N., Lee S.-I. (2020), From local explanations to global understanding with explainable AI for trees, *Nat Mach Intell*, 2, 56–67 (DOI: 10.1038/s42256-019-0138-9)

60. Walsh A., Watson G.W. (2005), The origin of the stereochemically active Pb(II) lone pair: DFT calculations on PbO and PbS, *J Solid State Chem*, 178, 1422–1428 (DOI: 10.1016/j.jssc.2005.01.030)

61. Walsh A., Watson G.W. (2005), Influence of the anion on lone pair formation in Sn(II) monochalcogenides: A DFT study, *J Phys Chem B*, 109, 18868–18875 (DOI: 10.1021/jp051822r)

Chapter 7

CHAPTER 7

Structure Generation and Deep Learning Transfer Learning strategies for Low κ_L

Chapter 7

Chapter 7

7.1. Introduction

The journey of materials design has undergone a remarkable evolution, characterized by four distinct paradigms *[1]*. The first paradigm relied on trial-and-error experiments, while the second utilized fundamental scientific theories to understand materials behavior. The third paradigm leveraged computational methods, such as density functional theory (DFT), to efficiently simulate materials at the atomic level and identify numerous functional materials *[2,3]*. The fourth paradigm represents a transformative leap by harnessing accumulated data and machine learning (ML), significantly accelerating materials discovery through rapid and accurate property predictions *[3,6]*. Notably, generative models within this paradigm enable the inverse design of novel material structures, including semiconductors, zeolites, and metal-organic frameworks, thereby overcoming the limitations of traditional ML methods that are restricted to known structures *[7,10]*.

Designing high-performance crystal structures is a central research goal in materials science. Traditional approaches, relying on DFT and high-throughput calculations, demand substantial computational resources and human expertise *[9, 11]*. Generative deep learning (DL) methods offer a promising alternative by learning atomic assembly rules from existing materials to generate chemically viable hypothetical structures. Recent advances, including large language models *[12]*, geometric graph neural networks *[13,14]*, and generative AI *[15]*, have demonstrated significant advantages in material generation and screening, enabling the discovery of unique materials in previously unexplored design spaces *[16]*. ML models can predict material properties based on either composition or structure, with performance strongly dependent on algorithm choice, feature selection, and dataset quality and size. Composition-based ML models offer fast screening of large-scale hypothetical materials *[17-20]*; however, most material properties depend on detailed atomic structure, making structure-based ML models generally more accurate *[21]*.

Graph neural networks (GNNs) are particularly effective for structure-based property prediction. They convert crystal structures from Euclidean space into graph representations, where atoms form nodes and bonds form edges, allowing graph convolutional operations to extract structural information and establish implicit structure-property relationships *[22]*. The Crystal Graph Convolutional Neural Network (CGCNN) *[23]* was one of the first GNN models for materials, although it primarily encodes distance-based interactions, neglecting many-body and directional information. Advanced models, such as Atomistic Line Graph Neural Network (ALIGNN), *[24]* explicitly incorporate geometric information like bond angles, while attention-based models, such as GATGNN and DeeperGATGNN, define chemical bonding strength and address oversmoothing issues in deeper networks *[25]*. Despite their accuracy, deep learning models require large datasets, limiting performance in smaller datasets compared to classical regression methods.

To overcome data scarcity, transfer learning (TL) has been widely employed. TL involves transferring model weights trained on large datasets to models targeting smaller datasets, either for the same property or cross-property predictions *[26-28]*. For example, models trained on formation energies from large databases such as OQMD[29] have been successfully fine-tuned to predict properties like band gaps or elastic moduli, improving accuracy in smaller datasets *[30-32]*.

In this chapter, we systematically fine-tune scratch models using CGCNN, ALIGNN, and DeeperGATGNN architectures with lattice thermal conductivity (LTC) datasets. We further explore the efficacy of same-property and cross-property transfer learning using ALIGNN as the base model. Six properties band gap, convex hull, formation energy, dielectric constant, bulk modulus, and AFLOW lattice thermal conductivity were considered for cross-property TL. Additionally, we used CrystaLLM to generate a pool of novel structures, which were screened to identify ultra-

low κ_L materials for potential thermoelectric applications. The detailed workflow has been illustrated in **Figure 7.1**.

7.2. Data Set Construction and Processing

The low thermal conductivity (κ_L) dataset has been considered from DFT based phonon transport calculations reported in the literature, with the corresponding crystal structures identified using their Open Quantum Materials Database (OQMD) structure IDs and associated metadata *[29, 33]*. The initial dataset comprised 4041 crystalline materials, including 3317 cubic and 724 non-cubic structures. For anisotropic systems, the reported directional components of thermal conductivity (κ_L^x, κ_L^y, κ_L^z) were averaged to obtain an effective scalar κ_L, enabling uniform comparison across different crystal symmetries. After, careful structure curation, 3925 materials with known κ_L were retained to train the deep neural network models, as represented in **Figure 7.1(a)**. The curated dataset spans a broad spectrum of crystallographic prototypes. Binary compounds constitute the largest subset (30.4%), encompassing ionic, covalent, and mixed-bonding frameworks. Complex systems are represented, including quaternary Heusler compounds (22.6%) and low-symmetry complex structures (17.8%) characterized by large primitive cells and multiple atomic sublattices. In addition, full-Heusler (14.7%) and half-Heusler (14.3%) phases prototypical thermoelectric material families account for a substantial fraction of the dataset. This balanced compositional and structural distribution ensures exposure to both highly ordered lattices and chemically disordered frameworks, thereby capturing diverse phonon scattering environments. Further, the κ_L values span a broad range, from 0.01 to 2960 $Wm^{-1}K^{-1}$, covering more than five orders of magnitude. This extensive dynamic range enables the model to learn phonon transport behavior across extreme regimes, from strongly anharmonic systems to highly crystalline solids with long phonon mean free paths.

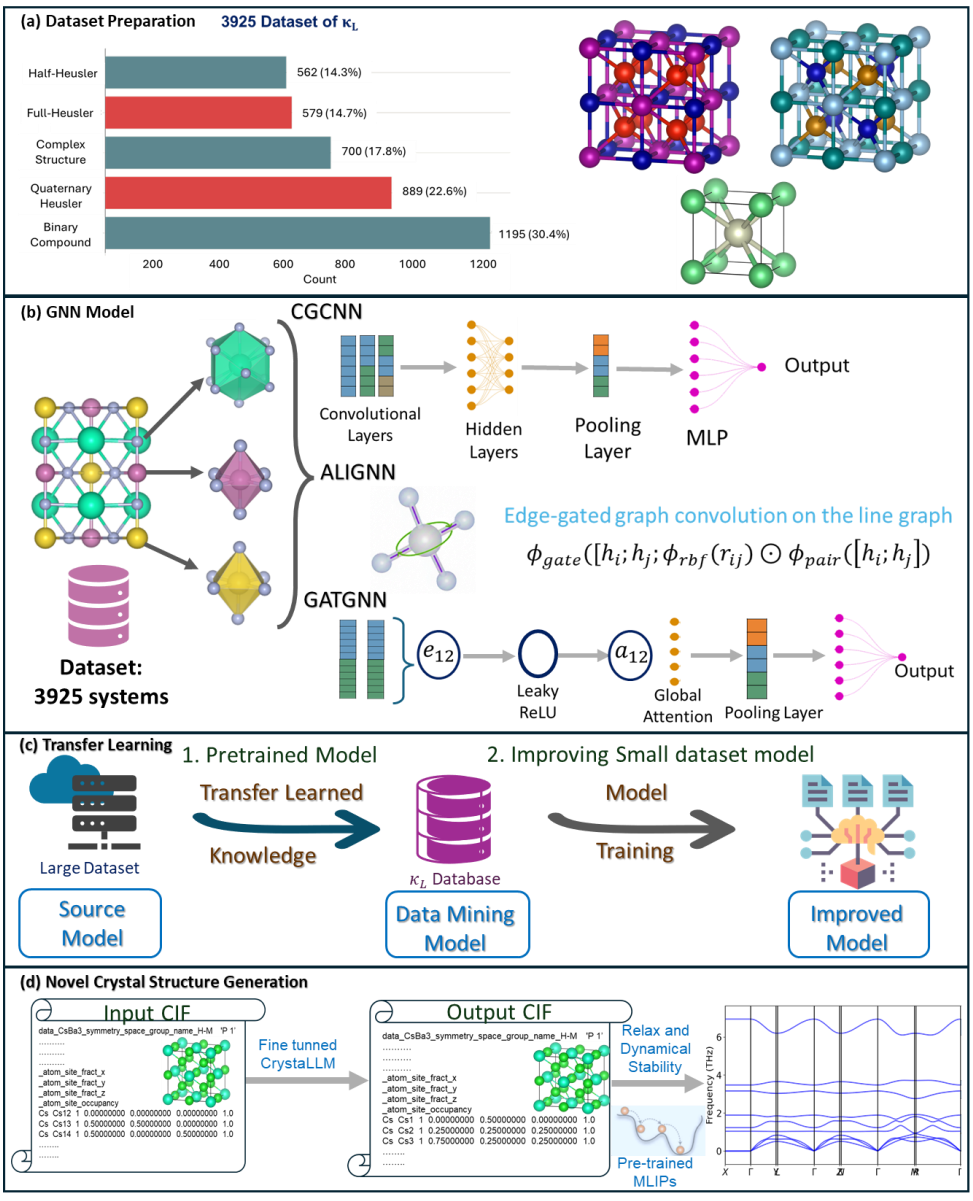


Figure 7.1: Data-driven framework for scalable prediction and optimization of κ_L. **(a)** Distribution of crystal chemistries and structural families within the 3,925-material κ_L dataset, highlighting the chemical and topological diversity used to train the model. **(b)** Edge-gated graph convolution networks operating on GNN models, enabling bond-centric message passing that captures anharmonic and local structural effects governing phonon transport. **(c)** Knowledge-transfer paradigm in which representations learned from a large materials corpus enhancing predictive accuracy and data efficiency for smaller or compositionally constrained

datasets. **(d)** Closed-loop crystal optimization workflow integrating fine-tuned CrystaLLM generation, structural relaxation, and dynamical stability screening with pre-trained machine-learning interatomic potentials.

7.3. Results and Discussion

7.3.1. Scratch Model Training

To evaluate the effectiveness of different graph neural network (GNN) architectures in predicting κ_L, we trained three representative models CGCNN, DeeperGATGNN, and ALIGNN from scratch using a dataset of 3,925 crystalline materials *[23-25]*. For scratch model training, the dataset was randomly partitioned into 80% training, 10% validation, and 10% test sets, while ensuring chemical and structural diversity across all subsets. Each crystal structure was encoded as a graph, with atoms represented as nodes and interatomic interactions as edges, enabling the models to directly learn structure–property relationships without reliance on handcrafted descriptors. All models were trained for 300 epochs, and optimal configurations were selected based on the lowest validation mean absolute error (MAE). We systematically explored the influence of key hyperparameters learning rate, batch size, and the number of graph convolution (GC) layers on predictive performance. The resulting MAE trends are summarized in **Figures 7.2(a–c)**, while parity plots comparing predicted and DFT-calculated $\log(\kappa_L)$ values for both training and test sets are shown in **Figures 7.2(d–f)**.

For CGCNN, test MAE values range from ~0.26 to 0.31 across the explored hyperparameter space. The lowest MAE (~0.26) is achieved with a learning rate of 0.001–0.003, batch size of 60, and six GC layers. Increasing the depth beyond this configuration does not yield significant improvement, suggesting limited benefit from additional layers in distance-based message-passing architectures.

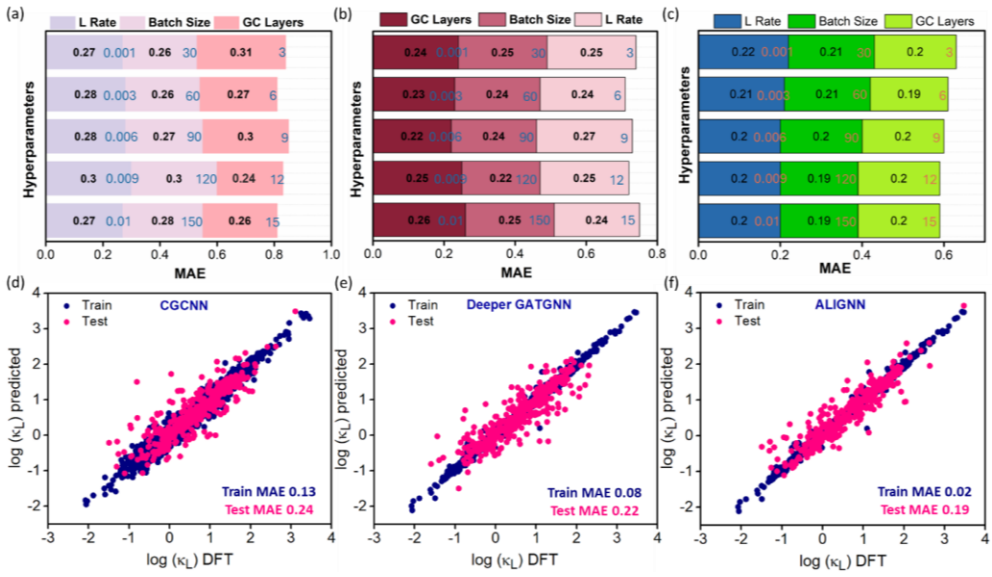


Figure 7.2: Model comparison and hyperparameter sensitivity. **(a–c)** Mean absolute error (MAE) contributions from key hyperparameters including learning rate, batch size, and number of graph convolution (GC) layers for CGCNN, deeper-CGCNN, and ALIGNN models, respectively, illustrating their relative influence on predictive performance **(d–f)** Predicted versus DFT-values for the training and test sets GNN models.

Further, DeeperGATGNN demonstrates improved performance relative to CGCNN, with test MAE spanning ~0.22–0.26. The optimal configuration corresponds to a learning rate of 0.006, batch size of 90–120, and six GC layers, resulting in a minimum MAE of ~0.22. The attention mechanism in DeeperGATGNN enhances neighbor information aggregation; however, performance saturates for deeper networks. Subsequently, ALIGNN consistently outperforms both CGCNN and DeeperGATGNN across all hyperparameter settings, with test MAE tightly clustered between ~0.19 and 0.22. The best performance (~0.19) is obtained at a learning rate of 0.003–0.009, batch size of 120–150, and 6–12 GC layers. Notably, ALIGNN exhibits reduced sensitivity to hyperparameter variations, demonstrating robust and stable convergence.

The superior performance of ALIGNN arises from its bond-centric message-passing framework, which explicitly incorporates angular

information and three-body interactions into the learned representations. By encoding bond angles and local coordination environments, ALIGNN captures subtle structural features that strongly influence phonon scattering and lattice anharmonicity. This is particularly important for materials with complex bonding topologies, where pairwise distance-based descriptors are insufficient. In contrast, CGCNN primarily relies on two-body interactions and radial descriptors, limiting its expressiveness. While DeeperGATGNN leverages attention mechanisms to improve aggregation, it still lacks explicit angular descriptors. Collectively, these results highlight ALIGNN as the most effective GNN for predicting lattice thermal conductivity in crystalline materials.

7.3.2. Fine-tuned Strategies using Transfer Learning

In data-limited regimes, training deep graph neural networks (GNNs) from scratch often leads to suboptimal generalization. To address this challenge, we develop an ALIGNN-based transfer learning (TL) framework that leverages pretrained atomistic representations learned from large materials datasets to enhance predictive accuracy for κ_L. Within this framework, κ_L is considered both as source task and target task, while additional thermodynamic, mechanical, and electronic properties are employed to systematically evaluate cross-property transferability[26,34]. This design enables a rigorous assessment of how pretrained atomistic representations generalize across disparate materials properties. To this end, we consider six materials properties with varying datasets sizes spanning a broad range of dataset sizes, from 1,056 to 132,752 data points (**Table 7.1**) including κ_L (AFLOW), formation energy, energy above hull, bulk modulus, band gap, and dielectric constant. Together, these datasets encompass bonding, thermodynamic stability, mechanical stiffness, and electronic response, thereby providing a comprehensive testbed for transfer learning in crystalline materials.

ALIGNN Architecture: The Atomistic Line Graph Neural Network (ALIGNN) consists of seven layers in total, as illustrated in **Figure 7.3**. The

architecture explicitly encodes both two-body and three-body interactions, which is critical for accurately learning κ_L.

Embedding layers (Layers 1–3) The first three layers transform raw crystallographic information into continuous, learnable embeddings at the atom, bond, and bond-angle levels. For a crystal structure represented as a graph $\mathcal{G} = (\mathcal{V}, \mathcal{E})$, the initial embeddings are defined as:

$$\mathbf{h}_i^{(0)} = \phi_{\text{atom}}(Z_i),\ \mathbf{e}_{ij}^{(0)} = \phi_{\text{bond}}(r_{ij}),\ \mathbf{a}_{ijk}^{(0)} = \phi_{\text{angle}}(\theta_{ijk}),$$

where Z_i denotes the atomic number of atoms i, r_{ij} is the interatomic distance between atoms i and j, and θ_{ijk} represents the bond angle formed by atoms i, j, and k. The functions ϕ_{atom}, ϕ_{bond}, and ϕ_{angle} are learnable embedding functions.

ALIGNN Convolution Layers (Layers 4–5) The embedded features are propagated through two edge-gated graph convolution layers, referred to as ALIGNN layers. These layers jointly update atomic representations by incorporating bond- and angle-dependent message passing:

$$\mathbf{h}_i^{(l+1)} = \sum_{j \in \mathcal{N}(i)} \mathbf{g}_{ij}^{(l)} \odot \psi\left(\mathbf{h}_i^{(l)}, \mathbf{h}_j^{(l)}, \mathbf{e}_{ij}^{(l)}, \mathbf{a}_{ijk}^{(l)}\right),$$

where $\mathcal{N}(i)$ denotes the neighborhood of atom i, $\mathbf{g}_{ij}^{(l)}$ is an edge-gating function that modulates message importance, $\psi(\cdot)$ is a learnable nonlinear transformation, and $\odot$ denotes element-wise multiplication. This formulation enables the model to encode higher-order local structural correlations that are absent in conventional atom-bond GNNs.

Pooling and Prediction Layers (Layers 6–7) Following message passing, node-level representations are aggregated via global average pooling to obtain a fixed-length crystal-level descriptor:

$$\mathbf{h}_{\text{global}} = \frac{1}{|\mathcal{V}|} \sum_{i \in \mathcal{V}} \mathbf{h}_i^{(L)},$$

where Ldenotes the final ALIGNN convolution layer. The pooled representation is subsequently mapped to the target property through a fully connected prediction layer:

$$\hat{y} = f_{\text{out}}(\mathbf{h}_{\text{global}}),$$

where $\hat{y}$ corresponds to the predicted material property, such as lattice thermal conductivity κ_L.

7.3.3. Transfer Learning Formulation

Let a pretrained ALIGNN model be optimized on a source dataset $\mathcal{D}_s = \{(\mathcal{G}_n, y_n^{(s)})\}_{n=1}^{N_s}$, yielding pretrained parameters:

$$\Theta^{(s)} = \arg\min_{\Theta} \frac{1}{N_s} \sum_{n=1}^{N_s} | f_\Theta(\mathcal{G}_n) - y_n^{(s)} |$$

Transfer learning is then performed on the target lattice thermal conductivity dataset $\mathcal{D}_t = \{(\mathcal{G}_m, \kappa_{l,m})\}_{m=1}^{N_t}, N_t = 3925,$ by selectively optimizing a subset of parameters $\Theta \subseteq \Theta^{(s)}$:

$$\Theta^{(t)} = \arg\min_{\Theta} \frac{1}{N_t} \sum_{m=1}^{N_t} | f_\Theta(\mathcal{G}_m) - \kappa_{l,m} |$$

7.3.3.1. Fine Tuning Strategies

To systematically evaluate the role of transfer learning in the GNN-based ALIGNN framework, we employ four complementary fine-tuning strategies, as illustrated in **Figure 7.3**. These strategies differ in the extent to which pretrained parameters are updated during training, thereby enabling a controlled evaluation of model flexibility and representation transferability for learning κ_L.

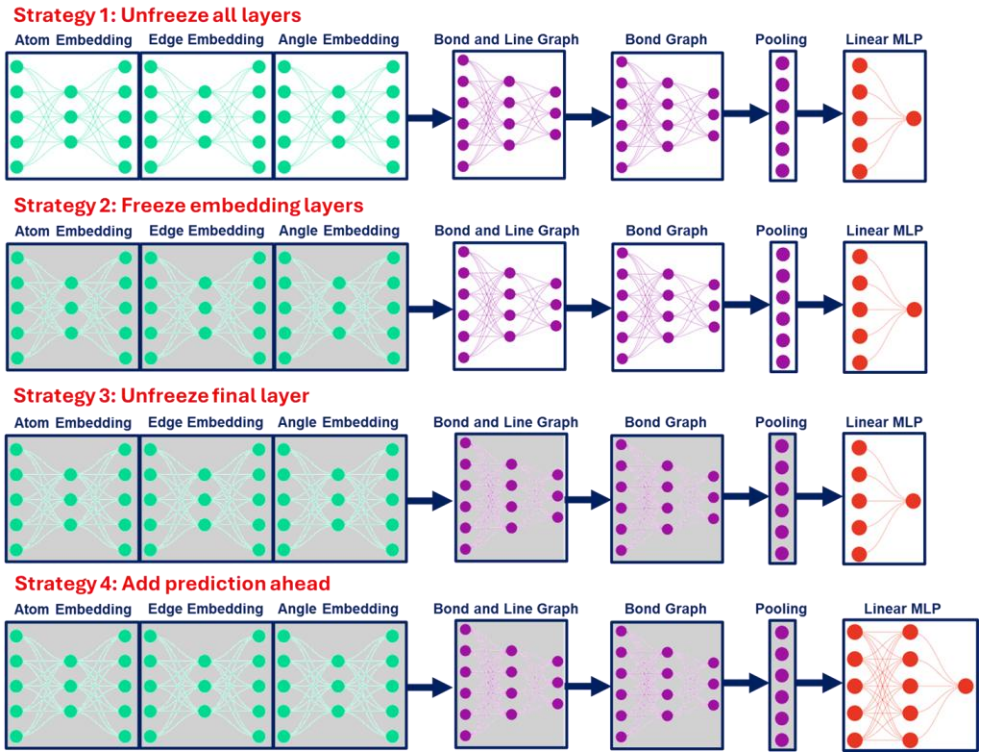


Figure 7.3: Fine-tuning strategies for a pretrained graph neural network model. Schematic illustration of four transfer-learning strategies applied to a graph-based architecture comprising atom, edge, and angle embedding layers, followed by bond and line graph message passing, pooling, and linear MLP head. **Strategy 1** unfreezes all layers for full fine-tuning. **Strategy 2** freezes the embedding layers while fine-tuning the downstream graph and MLP layers. **Strategy 3** freezes all pretrained layers except the final prediction layer. **Strategy 4** retains all pretrained layers and adds an additional prediction head for task-specific learning.

Fine Tune Strategy 1: Unfreeze all layers. In this strategy, all parameters of the pretrained ALIGNN model are loaded and fully unfrozen during fine-tuning. The model, consisting of atom, edge, and angle embedding layers followed by graph convolution, pooling, and prediction layers, is therefore allowed to update its representations at every level. This approach provides the highest degree of freedom for adapting representations at all hierarchical levels.

Fine Tune Strategy 2: Freeze Embedding Layers. Here, the atom, edge, and angle embedding layers are kept fixed, while the subsequent graph convolution and prediction layers are fine-tuned. Since these embedding layers capture general chemical and structural descriptors learned during large-scale pretraining, freezing them helps retain physically meaningful representations, while allowing higher-level features to adjust to κ_l-specific trends.

Fine Tune Strategy 3. Unfreeze last layer. This strategy permits retraining of only the final prediction layer, with all preceding layers remaining frozen. As a result, the model learns a new mapping from the pretrained latent representation to κ_L without modifying the underlying feature extraction process. This represents the most constrained fine-tuning scheme and serves as a useful reference for assessing the intrinsic transferability of the pretrained ALIGNN features.

Fine Tune Strategy 4. Add Prediction Ahead. In the final approach, an additional multilayer perceptron (MLP) is introduced immediately before the prediction head. All parameters of the original pretrained ALIGNN model are frozen, and only the newly added MLP is optimized using the κ_l dataset. This design enables task-specific nonlinear refinement of the pretrained representations while preserving the original learned chemical and structural information, thereby reducing the risk of catastrophic forgetting.

7.3.4. Dataset Description and Pretrained Models. The distribution of data across the six materials property datasets is summarized in **Table 7.1**, together with the mean absolute error (MAE) achieved by the corresponding pretrained ALIGNN models prior to fine-tuning. These pretrained models act as source tasks for both same-property and cross-property transfer learning. The source datasets span κ_L from the AFLOW database, thermodynamic properties (formation energy and energy above the convex hull), mechanical properties (bulk modulus), and electronic properties (band gap and dielectric constant). Within this framework, deep transfer learning

enables the transfer of feature representations learned from large source datasets to smaller target datasets. In addition, we used pretrained scratch models across multiple property ranges to provide a baseline comparison, allowing us to assess how transfer learning exploits underlying physical and chemical interactions and elemental similarities to improve predictive performance.

Table 7.1: The lists the target material property, dataset size, and the mean absolute error (MAE) achieved by the corresponding pretrained ALIGNN model prior to fine-tuning. These pretrained models serve as source tasks for both same-property and cross-property transfer learning analyses.

Property	Data Size	MAE of Pretrained Model
Lattice thermal conductivity (AFLOW)	5658	0.18
Band Gap (eV)	106,113	0.134
Ehull (eV/atom)	55,323	0.080
Bulk Modulus (GPa)	19,542	11.50
Formation Energy (eV)	132,752	0.127
Dielectric Constant	1056	0.158

Together, above four strategies consider a broad spectrum of fine-tuning flexibility, from full retraining to minimal adaptation, and provide clear insights into how pretrained graph representations can be most effectively leveraged for predicting κ_L. The transfer learning performance shown in **Figure 7.3** is governed by three strongly coupled factors: (i) the size of the source dataset, (ii) the physical nature of the source and target properties, and (iii) the extent of fine-tuning applied to the pretrained model. These

dependencies are directly reflected in the relative MAE values across the four strategies and six target properties.

7.3.4.1. Effect of Dataset Size. The correlation between source dataset size and achievable MAE is evident in **Figure 7.4**. Pretrained models based on large datasets such as formation energy (132,752 entries), band gap (106,113 entries), and convex hull energy (55,323 entries) consistently yield lower validation and test MAEs, typically remaining close to or below 0.20, the dashed reference line in each panel. In contrast, properties trained on comparatively smaller datasets, such as dielectric constant (1,056 entries) and bulk modulus (19,542 entries), exhibit noticeably higher MAEs and larger train–test gaps, particularly under constrained fine-tuning strategies (S3 and S4). This trend indicates that large-scale pretraining enables ALIGNN to learn more transferable chemical and structural representations, which remain effective across different target properties.

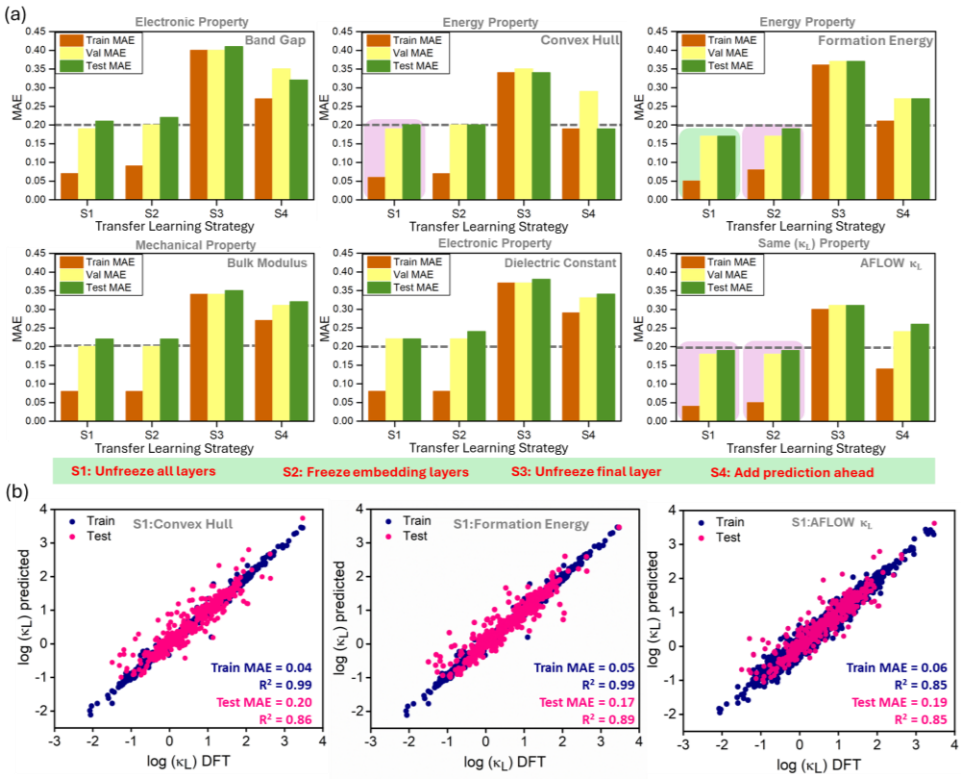


Figure 7.4: Performance of same-property and cross-property transfer learning using different fine-tuning strategies. (a) Bar plots show the train,

validation, and test MAE obtained for six target properties, band gap, convex hull energy (E_{hull}), formation energy, bulk modulus, dielectric constant, and lattice thermal conductivity (κ_L) using four fine-tuning strategies: S1 (unfreeze all layers), S2 (freeze embedding layers), S3 (unfreeze final layer only), and S4 (add prediction head). Results include both same-property transfer and cross-property transfer, yielding a total of 24 trained models. (b) Parity plots for the best-performing transfer learning models under the S1 strategy.

7.3.4.2. Energy vs Electronic vs Mechanical Properties. **Figure 4** reveals a clear hierarchy in cross-property transfer effectiveness across different classes of source properties. Energy-related properties formation energy and energy above the convex hull (E_{hull}) consistently emerge as the most effective source tasks for transfer learning. When transferred to electronic (band gap, dielectric constant), mechanical (bulk modulus), or lattice thermal conductivity (κ_L) prediction, energy-pretrained models achieve systematically lower validation and test MAEs than models pretrained on electronic or mechanical properties, particularly under the more flexible fine-tuning strategies S1 (unfreeze all layers) and S2 (freeze embedding layers). This superior transferability can be attributed to the fact that energy-based quantities encode fundamental information about bonding strength, coordination environments, and local structural stability, which underpins a wide range of materials properties. **Figure 7.4b** further corroborates this trend through parity plots of the best-performing S1 transfer models. Predictions derived from energy-pretrained representations exhibit a tight clustering around the parity line for convex hull energy, formation energy, and κ_L, with high coefficients of determination ($R^2 \approx 0.85$–0.99) and low test MAEs. In contrast, larger errors observed for models transferred from non-energy source tasks, particularly at the extremes of the property distributions. These results indicate that energy-informed representations not only reduce average prediction error but also improve robustness across chemically and structurally diverse regimes, including low-κ_L materials

governed by complex phonon and anharmonic effects. Electronic properties, such as band gap and dielectric constants, display moderate cross-property transfer performance. Although band-gap-pretrained models benefit from their large dataset size, their MAEs increase more sharply when transferred to κ_L or bulk modulus, indicating limited overlap between purely electronic descriptors and lattice- or phonon-dominated properties. Mechanical properties, represented here by bulk modulus, show the weakest cross-property transfer, with relatively high MAEs across most strategies, likely due to their dependence on long-range elastic response that is not fully captured by pretrained local graph embeddings.

7.3.4.3. Same-Property vs Cross-Property Transfer. As expected, same-property transfer consistently produces the lowest MAEs, with minimal differences between training, validation, and test errors across all properties. This indicates strong alignment between the pretrained and target feature distributions and confirms that ALIGNN effectively reuses representations when the physical nature of the source and target tasks is identical. In contrast, cross-property transfer introduces a systematic increase in MAE, the magnitude of which depends strongly on the physical similarity between the source and target properties. Importantly, cross-property transfer from formation energy and E_{hull} often yields MAEs that approach those of same-property transfer, particularly under S1 and S2. This observation highlights the robustness and generality of ALIGNN-learned energy representations, even when applied to physically distinct target properties such as κ_L.

7.3.4.4. Role of Fine-Tuning Strategy. The influence of fine-tuning strategy is pronounced across all properties and source–target combinations. Strategy S1 (unfreeze all layers) almost universally achieves the lowest test MAEs, particularly for κ_L and other structurally sensitive properties. This behavior confirms that full adaptation of atomistic representations is essential when the target property depends on subtle bonding distortions, angular correlations, and anharmonic effects. Strategy

S2 (freeze embedding layers) delivers performance comparable to S1 in many cases, especially for large target datasets. This indicates that the pretrained atom, bond, and angle embeddings already capture chemically meaningful low-level features, while allowing higher-level message-passing layers to adapt to task-specific trends. In contrast, Strategy S3 (unfreeze final layer only) consistently results in the highest MAEs across properties, demonstrating that linear remapping of pretrained latent representations is insufficient for effective cross-property learning. Strategy S4 (add prediction head) improves upon S3, particularly for small target datasets, as the added nonlinearity enables limited task-specific refinement while mitigating overfitting and catastrophic forgetting.

7.3.5. Crystal Structure Generation Using CrystaLLM

We introduce a generative framework for crystalline materials based on CrystaLLM, a transformer-based, decoder-only language model trained autoregressively on the Crystallographic Information File (CIF) format. Unlike conventional generative approaches that rely on hand-designed structural features, our method directly models standardized and tokenized CIF text, enabling the generation of complete crystalline structures through sequential sampling. This treatment harnesses the capacity of large language models to learn complex joint distributions over space group, lattice parameters, fractional coordinates, and atomic species simultaneously [12]. The training dataset consists of inorganic crystal structures filtered to emphasize low-κ_L materials ($\kappa_L < 5$ $Wm^{-1}K^{-1}$), biasing the learned distribution toward structurally complex and phonon-soft compounds. Raw CIF files are first standardized and serialized into token sequences encoding lattice parameters, space-group symmetry, atomic species, and fractional atomic coordinates. We perform unconditional sampling of 10,000 CIF structures from the trained large-scale model. Out of the 10,000 CIF files generated, 8800 were valid, and 5300 represented structurally distinct (i.e., unique) materials. We performed relaxation and

dynamical stability of the 4479 novel structures, and 758/567 stable structures within threshold of -0.10/-0.05 THz.

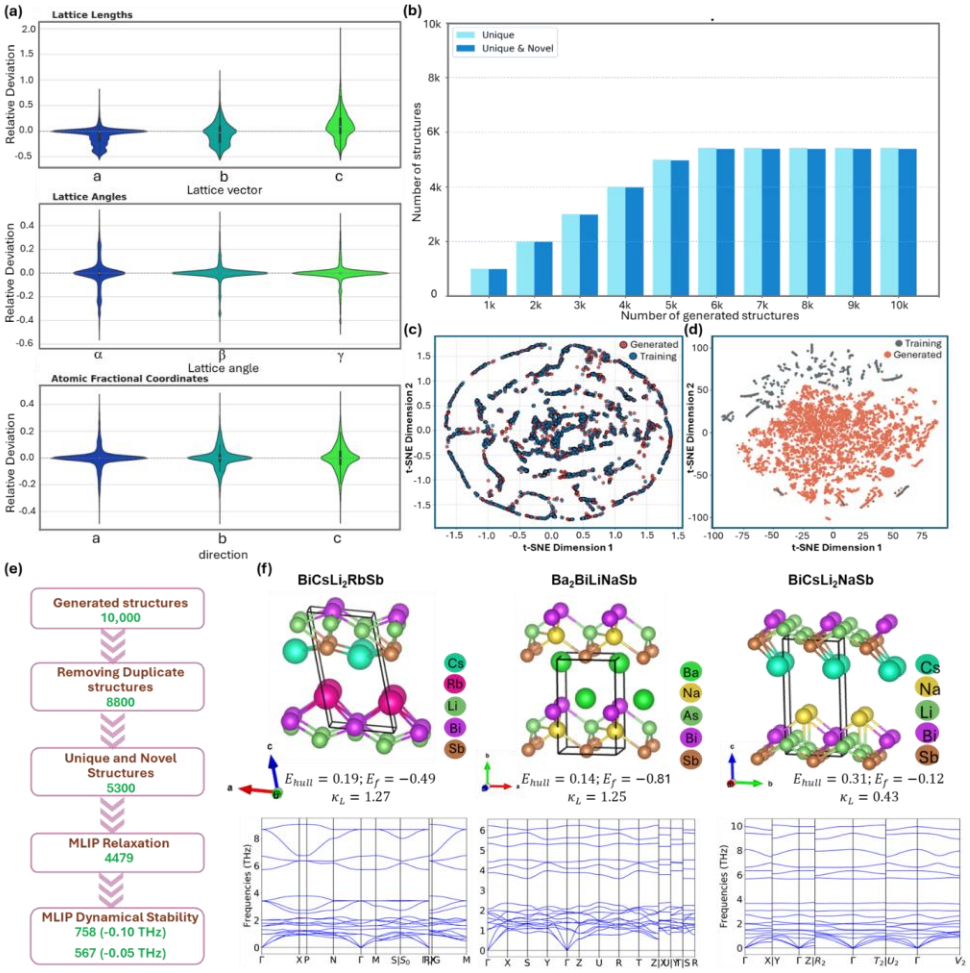


Figure 7.5. Evaluation of generative crystal structures and discovery of low lattice thermal conductivity candidates. (a) Violin plots comparing the distributions of lattice lengths, lattice angles, and atomic fractional coordinates for generated structures against the training dataset, demonstrating close agreement in crystallographic statistics. (b) Cumulative counts of generated, unique, and unique-novel structures, highlighting efficient novelty generation after duplicate removal. (c,d) Low-dimensional embeddings comparing generated and training structures, indicating strong coverage of the learned structural manifold while extending into previously unexplored regions. (e) Workflow summarizing structure filtering from

10,000 generated candidates to dynamically stable materials. (f) Representative unique and novel crystal structures identified by the model along with the phonon dispersion relations confirming the dynamical stability of selected candidates, with no imaginary frequencies observed. Here, E_{hull}, E_f and κ_L represents convex hull (meV/atom), formation energy (eV/atom) and lattice thermal conductivity (W/mK).

7.3.5.1. Validity of Generated Structures. The crystallographic validity of the generated structures is assessed by comparing key geometric descriptors against the training dataset. As shown in **Figure 7.5(a)**, the distributions of lattice lengths (a, b, c), lattice angles (α, β, γ), and atomic fractional coordinates for generated structures closely overlap with those of the training data. This strong agreement indicates that CrystaLLM successfully internalizes fundamental crystallographic constraints, producing geometrically consistent and physically meaningful crystal structures rather than arbitrary atomic arrangements. Therefore, the validity analysis reflects structural realism, while energetic and dynamical stability are evaluated separately.

7.3.5.2. Uniqueness and Novelty of Generated Structures. The structural similarity is evaluated using the StructureMatcher class in pymatgen [35], with tolerances set to fractional length tolerance (ltol) = 0.2, site tolerance (stol) = 0.3, and angle tolerance (angle_tol) = 5°. CrystaLLM exhibits strong generative diversity. After duplicate removal, 8,800 unique structures remain, of which 5,860 are both unique and novel relative to the training dataset (**Figure 7.5(b)**). The high fraction of unique-novel samples confirms that the model does not merely reproduce training examples but instead generates genuinely new crystalline configurations. To further quantify novelty, we visualize the generated and training datasets using t-SNE embeddings of compositional and structural descriptors (**Figure 5(c,d)**). Compositional diversity is quantified using the ElementProperty featurizer from Matminer [36], based on Magpie elemental descriptors [36].

Structural features are extracted using the CrystalNNFingerprint featurizer [37], producing site-level fingerprints that are averaged to yield structure-level representations. All features are standardized using training-set statistics to ensure consistent scaling across datasets. The generated structures are broadly distributed across the training manifold, with no artificial clustering or mode collapse. This indicates that CrystaLLM samples the learned chemical space smoothly while maintaining diversity and structural coherence.

To examine how well CrystaLLM captures the underlying structural manifold of known materials, we compare generated and training structures using low-dimensional embeddings of structural descriptors (**Figure 7.5(e)**). The generated samples show substantial overlap with the training distribution, confirming that the model learns realistic crystal chemistry. Further, a subset of generated structures extends beyond the dense regions of the training space, indicating controlled extrapolation into previously unexplored structural regimes. This balance between distributional fidelity and exploratory generalization is essential for effective materials discovery.

Table 7.2: List of predicted low lattice thermal conductivity (κ_L), formation energy (E_f), convex hull (E_{hull}) for generated novel and unique structures.

Formula	$\boldsymbol{\kappa_L}$	$\boldsymbol{E_f}$	$\boldsymbol{E_{hull}}$
Cs_2Na_3Sb	0.21	-0.32	-0.04
$CsNa_3Sb$	0.37	-0.36	-0.04
CsRbSb	0.42	-0.12	0.17
Ba_2CdP	0.67	-0.70	0.11
BaCdS	0.72	-1.36	0.05
CsNaSb	0.73	-0.42	0.09
BaCdSn	0.79	-0.56	-0.02
KNa2P	0.80	-0.35	0.10
KNaO	0.87	-1.12	0.19

The physical realizability of the generated structures is assessed through a multi-stage stability screening workflow (**Figure 7.5f**). From the pool of unique and novel candidates, 4,879 structures were retained after eliminating entries with incomplete energetic predictions. Based on predicted formation energies (E_f) and energies above the convex hull (E_{hull}), a substantial fraction of candidates satisfies commonly accepted stability criteria. Specifically, 817 structures lie within 0.10 meV atom^{-1} of the convex hull, 575 structures fall within 0.05 meV atom^{-1}, and 246 compounds are predicted to be thermodynamically stable with $E_{hull} \leq 0.00$ meV atom^{-1}. The overall distribution of E_{hull} values exhibit a mean of 0.61 meV atom^{-1}, with more than 60% of candidates (2,760 structures) residing below 0.50 eV atom^{-1}, indicating a large reservoir of potentially stable phases, detailed in ref 38. These results demonstrate that the generative–screening pipeline effectively biases the search toward low-energy regions of the compositional and structural space. To further assess dynamical stability, phonon dispersion calculations were performed on a down-selected subset of energetically favorable candidates. Based on the minimum phonon frequencies, 758 structures are dynamically stable within a tolerance of −0.10 THz, while 567 systems remain stable under a stricter criterion of −0.05 THz, as evidenced by the absence of significant imaginary phonon modes across the Brillouin zone.

Among the dynamically and thermodynamically viable candidates, several compounds exhibit exceptionally low predicted lattice thermal conductivity. In particular, alkali- and alkaline-earth–based pnictides and chalcogenides such as Cs_2Na_3Sb, $CsNa_3Sb$, and CsRbTe display κ_L values below 0.5 W/mK (**Table 7.2**), while remaining close to or on the convex hull. Many of these systems also exhibit soft phonon modes, with minimum frequencies approaching zero or slightly negative values, indicative of incipient lattice instabilities and strong anharmonicity. Notably, compounds such as Ba–Cd–X (X = S, Sn, O) and Ba–Te–based phases combine low κ_L with favorable formation energies, highlighting them as promising

candidates for ultralow thermal conductivity materials. Collectively, these results underscore the ability of the generative–screening workflow to identify chemically diverse, low-energy structures with intrinsically suppressed lattice thermal transport.

7.4. Summary

In summary, this chapter presents a comprehensive machine-learning framework that integrates scratch-trained graph neural networks, systematic transfer learning, and generative crystal design to accelerate the discovery of ultralow κ_L materials. Comparative training of CGCNN, DeeperGATGNN, and ALIGNN from scratch reveals that models explicitly encoding angular and higher-order interactions, particularly ALIGNN, deliver superior predictive accuracy. This highlights the decisive role of local bonding geometry and many-body effects in governing phonon transport, which cannot be captured adequately by purely distance- or attention-based architectures. The core contribution of this work lies in the rigorous dissection of transfer learning strategies. Same-property transfer consistently achieves the lowest MAEs due to optimal alignment between source and target feature distributions. In cross-property scenarios, pretraining on energetically grounded tasks especially formation energy and convex hull yields markedly improved performance compared to electronic or mechanical source properties. We further demonstrate a strong dataset-size dependence: large-scale pretraining ($>10^5$ samples) significantly enhances representation transferability and reduces MAE, whereas smaller datasets limit generalization. Full-network fine-tuning emerges as the most effective strategy, enabling task-specific adaptation of atomistic representations. Finally, CrystaLLM enables inverse crystal design, generating diverse, structurally valid, and genuinely novel compounds, from which dynamically stable ultralow-κ_L candidates are identified.

7.5. References

1. Agrawal, A., Choudhary, A. (2016) Perspective: Materials informatics and big data: Realization of the “fourth paradigm” of science in materials science, *APL Mater.*, 4(5), 053208 (DOI: 10.1063/1.4946894)

2. Gómez-Bombarelli, R., Aguilera-Iparraguirre, J., Hirzel, T.D., Duvenaud, D., Maclaurin, D., Blood-Forsythe, M.A., Chae, H.S., Einzinger, M., Ha, D.G., Wu, T., Markopoulos, G., Jeon, S., Kang, H., Miyazaki, H., Numata, M., Kim, S., Huang, W., Hong, S.I., Baldo, M., Adams, R.P., Aspuru-Guzik, A. (2016) Design of efficient molecular organic light-emitting diodes by a high-throughput virtual screening and experimental approach, *Nat. Mater.*, 15(10), 1120–1127 (DOI: 10.1038/nmat4717)

3. Xu, Y., Elcoro, L., Song, Z.D., Wieder, B.J., Vergniory, M.G., Regnault, N., Bernevig, B.A., Felser, C. (2020) High-throughput calculations of magnetic topological materials, *Nature*, 586(7829), 702–707 (DOI: 10.1038/s41586-020-2837-0)

4. Butler, K.T., Davies, D.W., Cartwright, H., Isayev, O., Walsh, A. (2018) Machine learning for molecular and materials science, *Nature*, 559(7715), 547–555 (DOI: 10.1038/s41586-018-0337-2)

5. Weng, B., Song, Z., Zhu, R., Yan, Q., Sun, Q., Grimaud, A., Ceder, G. (2020) Simple descriptor derived from symbolic regression accelerating the discovery of new perovskite catalysts, *Nat. Commun.*, 11, 3513 (DOI: 10.1038/s41467-020-17263-9)

6. Chen, X., Lu, S., Chen, Q., Jiang, P., Xu, L., Wang, T., Ren, W., He, Y., Zhang, X., Zhang, J. (2024) From bulk effective mass to 2D carrier mobility accurate prediction via adversarial transfer learning, *Nat. Commun.*, 15, 49686 (DOI: 10.1038/s41467-024-49686-z)

7. Kim, B., Lee, S., Kim, J. (2020) Inverse design of porous materials using artificial neural networks, *Sci. Adv.*, 6(38), eaax9324 (DOI: 10.1126/sciadv.aax9324)

8. Noh, J., Kim, J., Stein, H.S., Sanchez-Lengeling, B., Gregoire, J.M., Aspuru-Guzik, A., Jung, Y. (2019) Inverse design of solid-state materials

via a continuous representation, *Matter*, 1(5), 1370–1384 (DOI: 10.1016/j.matt.2019.08.017)

9. Zeni, C., Pinsler, R., Zügner, D., Fowler, A., Koumoutsakos, P., Csányi, G., Battaglia, P., De Fabritiis, G. (2025) A generative model for inorganic materials design, *Nature*, 639, 128–134 (DOI: 10.1038/s41586-025-08628-5)

10. Lu, S., Zhou, Q., Chen, X., Zhang, Y., Wang, J., He, Y. (2022) Inverse design with deep generative models: Next step in materials discovery, *Natl. Sci. Rev.*, 9, nwac111 (DOI: 10.1093/nsr/nwac111)

11. Merchant, A., Batzner, S., Schoenholz, S.S., Aykol, M., Cheon, G., Cubuk, E.D. (2023) Scaling deep learning for materials discovery, *Nature*, 624, 80–85 (DOI: 10.1038/s41586-023-06735-9)

12. Antunes, L.M., Butler, K.T., Grau-Crespo, R. (2024) Crystal structure generation with autoregressive large language modeling, *Nat. Commun.*, 15, 54639 (DOI: 10.1038/s41467-024-54639-7)

13. Han, X.Q., Wang, X.D., Xu, M.Y., Zhang, Z., Wang, L. (2025) AI-driven inverse design of materials: Past, present, and future, *Chin. Phys. Lett.*, 42(1), 011201 (DOI: 10.1088/0256-307X/42/1/011201)

14. Han, J., Cen, J., Wu, L., Zhang, Y., Li, H. (2025) A survey of geometric graph neural networks: Data structures, models and applications, *Front. Comput. Sci.*, 19, 191301 (DOI: 10.1007/s11704-024-3123-1)

15. Song, Y., Sohl-Dickstein, J., Kingma, D.P., Kumar, A., Ermon, S., Poole, B. (2021) Score-based generative modeling through stochastic differential equations, *ICLR 2021 Proc.* (DOI: 10.48550/arXiv.2011.13456)

16. Jiao, R., Huang, W., Lin, P., Han, X., Zhang, Y., Liu, Y. (2023) Crystal structure prediction by joint equivariant diffusion, *Adv. Neural Inf. Process. Syst.*, 36 (DOI: 10.48550/arXiv.2303.06513)

17. Goodall, R.E.A., Lee, A.A. (2020) Predicting materials properties without crystal structure, *Nat. Commun.*, 11, 6285 (DOI: 10.1038/s41467-020-19964-7)

18. Wang, A.Y.T., Kauwe, S.K., Murdock, R.J., Sparks, T.D. (2021) Compositionally restricted attention-based network, *npj Comput. Mater.*, 7, 77 (DOI: 10.1038/s41524-021-00545-1)

19. Ihalage, A., Hao, Y. (2022) Formula graph self-attention network, *Adv. Sci.*, 9, 2200164 (DOI: 10.1002/advs.202200164)

20. Dan, Y., Zhao, Y., Li, X., Li, J., Hu, W., Peng, J. (2020) GAN based efficient sampling of composition space, *npj Comput. Mater.*, 6, 84 (DOI: 10.1038/s41524-020-00352-0)

21. Bergerhoff, G., Hundt, R., Sievers, R., Brown, I.D. (1983) The inorganic crystal structure database, *J. Chem. Inf. Comput. Sci.*, 23(2), 66–69 (DOI: 10.1021/ci00038a003)

22. Scarselli, F., Gori, M., Tsoi, A.C., Hagenbuchner, M., Monfardini, G. (2009) The graph neural network model, *IEEE Trans. Neural Netw.*, 20(1), 61–80 (DOI: 10.1109/TNN.2008.2005605)

23. Xie, T., Grossman, J.C. (2018) Crystal graph convolutional neural networks, *Phys. Rev. Lett.*, 120(14), 145301 (DOI: 10.1103/PhysRevLett.120.145301)

24. Choudhary, K., DeCost, B. (2021) Atomistic line graph neural network, *npj Comput. Mater.*, 7, 65 (DOI: 10.1038/s41524-021-00650-1)

25. Omee, S.S., Louis, S.Y., Fu, N., Tian, Y., Koyuturk, M., Zhang, Y. (2022) Scalable deeper graph neural networks, *Patterns*, 3, 100491 (DOI: 10.1016/j.patter.2022.100491)

26. Chen, C., Ong, S.P. (2021) AtomSets framework, *npj Comput. Mater.*, 7, 39 (DOI: 10.1038/s41524-021-00639-w)

27. Chen, C., Zuo, Y., Ye, W., Li, X., Ong, S.P. (2021) Learning properties from multi-fidelity data, *Nat. Comput. Sci.*, 1, 46–53 (DOI: 10.1038/s43588-020-00002-x)

28. Lee, J., Asahi, R. (2021) Transfer learning using CGCNN, *Comput. Mater. Sci.*, 190, 110314 (DOI: 10.1016/j.commatsci.2021.110314)

29. Saal, J.E., Kirklin, S., Aykol, M., Meredig, B., Wolverton, C. (2013) OQMD database, *JOM*, 65(11), 1501–1509 (DOI: 10.1007/s11837-013-0755-4)

30. Wang, A., Kingsbury, R., McDermott, M., Horton, M., Aykol, M. (2021) DFT uncertainty framework, *Sci. Rep.*, 11, 94550 (DOI: 10.1038/s41598-021-94550-5)

31. Kim, G., Meschel, S.V., Nash, P., Chen, W. (2017) Experimental formation enthalpies, *Sci. Data*, 4, 170162 (DOI: 10.1038/sdata.2017.162)

32. Devi, R., Butler, K.T., Sai Gautam, G. (2024) Pre-train/fine-tune strategies, *npj Comput. Mater.*, 10, 1486 (DOI: 10.1038/s41524-024-01486-1)

33. Ojih, J., Shen, C., Rodriguez, A., Tran, F., Ceder, G. (2023) Ultralow κ discovery, *J. Mater. Chem. A*, 11, 16524–16540 (DOI: 10.1039/D3TA04874H)

34. Gupta, V., Choudhary, K., Tavazza, F., Cohn, R., Sankaranarayanan, S. (2021) Cross-property transfer learning, *Nat. Commun.*, 12, 26921 (DOI: 10.1038/s41467-021-26921-5)

35. Ong, S.P., Richards, W.D., Jain, A., Hautier, G., Kocher, M., Cholia, S. (2013) Pymatgen library, *Comput. Mater. Sci.*, 68, 314–319 (DOI: 10.1016/j.commatsci.2012.10.028)

36. Ward, L., Dunn, A., Faghaninia, A., Zimmermann, N.E.R., Bajaj, S., Wang, Q., Montoya, J., Chen, J., Bystrom, K., Dylla, M., Chard, K., Aykol, M., Steeves, E., Antono, E., Tran, H., Wu, Z., Zhou, H., Ong, S.P., Persson, K., Snyder, G.J., Foster, I. (2018) Matminer toolkit, *Comput. Mater. Sci.*, 152, 60–69 (DOI: 10.1016/j.commatsci.2018.05.018)

37. Zimmermann, N.E.R., Jain, A. (2020) Local structure order parameters, *RSC Adv.*, 10(10), 6067–6081 (DOI: 10.1039/C9RA07755C)

38. https://github.com/Harpriyaminhas/Thesis_chapter7.git

Chapter 7

CHAPTER 8

Future Perspectives

Chapter 8

8.1. Scope for Future Work

The traditional paradigm of materials discovery has largely relied on forward screening, where properties are predicted for known or enumerated crystal structures. While effective within limited design spaces, this approach becomes inefficient when targeting extreme or rare functionalities such as ultralow κ_L, where multiple structural, chemical, and bonding motifs can lead to similar macroscopic behavior. Moreover, the mapping from structure space to property space is highly non-unique, rendering the inverse problem fundamentally ill-posed. As illustrated in **Figure 8.1**, inverse design offers a more direct route by seeking material structures conditioned on targeted properties. This shift is particularly important for thermal transport engineering, where suppressing κ_L can arise from diverse mechanisms including mass disorder, bonding heterogeneity, anharmonic lattice dynamics, and complex crystal structure. Consequently, inverse design frameworks are increasingly necessary to efficiently navigate the vast and complex materials design space beyond what is accessible through conventional forward screening.

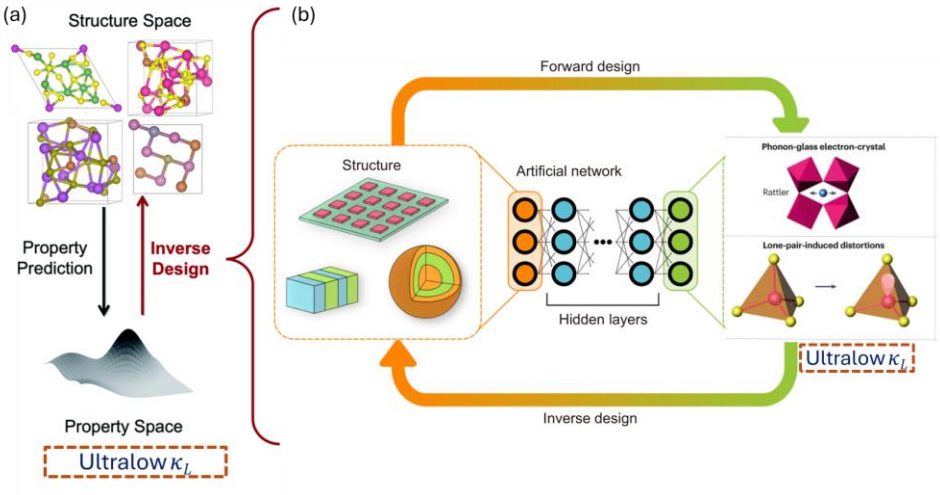


Figure 8.1: Schematic illustration of forward and inverse materials design paradigms enabled by machine learning. **(a)** Traditional forward design maps material structures to properties, while inverse design seeks to generate candidate structures conditioned on targeted properties within a highly ill-posed and non-unique design space. **(b)** A generative inverse-

design framework, where conditional deep neural networks learn probabilistic mappings between structure representations and physical responses, enabling efficient exploration of complex materials spaces and the discovery of novel, out-of-distribution materials with targeted functionalities, such as ultralow lattice thermal conductivity.

Future inverse-design methodologies for thermal conductivity optimization should therefore integrate physically informed generative or conditional learning frameworks that explicitly account for stability and phonon transport constraints. In practice, this requires coupling structure generation with key energetic and vibrational descriptors, including formation energy, energy above the convex hull (E_{hull}), and dynamical stability from phonon spectra, to ensure thermodynamic and experimental viability. Simultaneously, property conditioning should extend beyond κ_L alone to include phonon-related quantities such as group velocities, anharmonicity indicators, and mode-resolved scattering tendencies, enabling more controlled manipulation of thermal transport mechanisms. Embedding these constraints directly into the inverse-design workflow rather than applying them as post hoc filters can significantly improve the reliability of generated candidates. Such physics-aware inverse design strategies provide a promising pathway toward the rational discovery of stable, low-κ_L materials and represent a critical step toward closing the gap between computational prediction and experimental realization.